COMMUNAUTÉ EUROPÉENNE DE L'ÉNERGIE ATOMIQUE
EUROPEAN ATOMIC ENERGY COMMUNITY
EURATOM

SHOCK STRUCTURE INTERACTIONS IN REACTOR VESSELS

Symposium

Bruxelles, octobre
Brussels, October 1968

COMMUNAUTÉ EUROPÉENNE DE L'ÉNERGIE ATOMIQUE
EUROPEAN ATOMIC ENERGY COMMUNITY
EURATOM

SHOCK STRUCTURE INTERACTIONS IN REACTOR VESSELS

Symposium
Bruxelles, octobre 1968
Brussels, October

COMMUNAUTÉ EUROPÉENNE DE L'ÉNERGIE ATOMIQUE
EUROPEAN ATOMIC ENERGY COMMUNITY
EURATOM

RÉUNION DE SPÉCIALISTES SUR LES INTERACTIONS ENTRE LES PHÉNOMÈNES DE CHOC ET DES STRUCTURES DE RÉACTEURS

MEETING OF EXPERTS ON SHOCK STRUCTURE INTERACTIONS IN REACTOR VESSELS

organisée par
l'Agence Européenne pour l'Energie Nucléaire (Paris, France)
et
le Centre Commun de Recherche de l'Euratom (Ispra, Italie)

organised by
the European Nuclear Energy Agency (Paris, France)
and
the Euratom Joint Research Centre (Ispra, Italy)

Ispra, Italie — 27-30 juin 1966
Ispra, Italy — June 27-30, 1966

Publié par
le Centre d'Information et de Documentation — C.I.D.

Published by
the Centre for Information and Documentation — CID

Bruxelles, Octobre
Brussels, October 1968

EUR 4101 f, e

EUR 4101 f, e

Price : FB 500,— DM 40,— FF 50,— Lit. 6.240 Fl. 36,— $ 10,—

The Meeting of Specialists on "Shock Structure Interaction in a Reactor" was organized under the auspices of ENEA , following an initiative of the CREST (Committee on Reactor Safety Technology) . This Meeting took place at the Joint Research Establishment of Ispra and his Organization was done jointly by ENEA and the EURATOM Ispra Centre.

The contribution of Specialists of various countries, although the number of participants was restricted , as usual in this kind of Meeting , was very valuable and enthousiastic.

EURATOM thanks ENEA and all the autors of the papers for the authorization of publishing the proceedings of the Meeting. The discussions on the papers are not included in the proceedings and they can be demanded at ENEA.

Contents

SESSION III

SHOCK EFFECTS ON STRUCTURES (contd.)

a) Material Strength (contd.)

SESSION IV

SHOCK EFFECTS ON STRUCTURES (contd.)

a) Material Strength (contd.)

b) Results of Mock-up Experiments

SESSION V

SHOCK EFFECTS ON STRUCTURES (contd.)

b) Results of Mock-up Experiments (contd.)

DEPRESSURISATION AND WAVE PROPAGATION IN WATER COOLED REACTORS

by

A. R. Edwards

U. K. A. E. A., Risley

United Kingdom

1. INTRODUCTION

In the field of reactor safety investigations, disruptive pressure forces generally originate from one of two principal mechanisms. There is the class of accident which starts from a change in reactivity, leading to fuel overheating and melting. Dispersion of this hot material may then give rise to rapid vapour production with the consequent rise in local pressure which will propagate through the system. The initiating mechanism might be control rod or fuel movement or a change in flow condition aggravated by positive temperature or void coefficients. The other principal mechanism occurs in water cooled reactors when the normal fluid temperature is above atmospheric boiling conditions. Normally using a high system pressure, failure of the pressure boundary will allow loss of the coolant. If the failure occurs suddenly pressure waves will propagate through the reactor system subjecting internal components to large forces, the duration of these forces will be dependent on the length of the path available for wave propagation. Of principle concern is the fact that the core and its surrounding structure may be distorted causing reactivity changes and preventing the insertion of control rods, thus aggravating the course of the accident.

In addition to the pressure loading on the internal components of a reactor system, it is also necessary to consider the effects of an accident on the external components. This would include consideration of the containment structure or other building over the reactor and also equipment installed inside. Two main mechanisms exist for producing these pressure forces, firstly with a high temperature water reactor, release of the coolant will allow some of it to flash into steam and the resultant volume changes will give rise to pressure waves. The second mechanism is basically a chemical reaction which liberates energy, giving again a volume change and a pressure

rise. The chemical reaction might be that of hydrogen-oxygen, the hydrogen having been generated by a metal-steam reaction inside the reactor core. Alternatively it could be a direct reaction of the coolant with oxygen, such as might happen on a sodium cooled fast reactor system. This mechanism is considered in a separate paper at this conference, other papers consider the reaction of structures to the pressure forces we are discussing. In this paper we are concerned with the possible means of generating the forces inside the reactor primary circuit.

2. PROPAGATION OF PRESSURE WAVES IN TWO-PHASE MIXTURES

A number of theoretical and experimental studies [1, 2, 3] have been made into the speed of propagation of small amplitude waves in two-phase media. However much of the work has been carried out on two-component systems, that is using a liquid with a non-condensible gas. In such mixtures heat transfer between the phases is of minor importance and reasonable correlation between theoretical predictions and experimental measurements has been obtained. However, when a single-component system is considered, the problem becomes more complex. Heat transfer between phases now plays an important role in determining whether the appropriate amount of condensation or evaporation can take place, this is dependent on the frequency of the disturbance and the size of the bubbles present. The calculations of Walle [3] indicate that for a water-steam mixture, at a voidage between 40-60%, the sonic speed is about 10% of the liquid sonic speed for frequencies above 10^5 c.p.s. and is independent of bubble size in the range 10^{-2} to 10^{-4} m. radius. As the frequency is reduced, the effect on the smallest bubble size soon becomes marked, and the sonic speed ratio falls to 1 1/2% at 1 c.p.s. This is because heat transfer between the phases is now effective. Slightly larger bubbles, 10^{-3} m. rad., do not vary so much, effects are small down to 10^2 c.p.s., with the sonic velocity ratio falling to 4% at 1 c.p.s. The large bubbles, 10^{-2} m. rad., are virtually unaffected by frequencies down to 1 c.p.s., indicating that heat transfer is completely ineffectual as an energy transfer mechanism in this situation.

The fact that propagation velocity is so dependent on the heat transfer capabilities of the two-phase mixture raises a query regarding the relevance of wave propagation limits on the discharge flow rate of two-phase mixtures,

for example, does critical flow have a characteristic frequency controlling propagation velocity? This will be referred to again later in the section dealing with theoretical studies.

Of great importance in reactor safety studies is the propagation of the large disturbance, rather than the small amplitude sonic wave. It is well known that the propagation of large amplitude waves can be significantly different from small waves, here again, heat transfer between the phases can be expected to play a controlling part. In the case of the large compression wave, travelling through an initially two-phase mixture, heat transfer prevents instantaneous collapse of vapour bubbles; hence it affects the depth of the wave front and any subsequent pressure amplification effects, which may occur when the last of the bubbles are collapsed.

The case of the large expansion, or decompression, wave propagating into an initially sub-cooled liquid is even more complex, as bubble nucleation mechanisms will control the time and rate at which bubbles are formed, with heat transfer controlling their subsequent growth. At the moment there is some evidence from the pressure measurements taken from shock tubes [4], which indicates that vapour bubbles are not formed immediately, but only after a delay of a millisecond or so. This allows the pressure behind the wave front to fall to nearly atmospheric conditions, as the expansion of water, as a liquid, will not create a significant pressure wave in the air into which it is expanding. As has been mentioned earlier this effect would allow the core of a reactor to be subjected to a very large pressure difference for the extent of this delay period. It is expected that a number of factors will have an influence on the initial delay and growth period; amongst these are the water temperature, controlling surface tension, the presence of dissolved gases or other particles and ionizing radiation, controlling the number of nucleation sites available. Some of these aspects are already receiving detailed investigation [6, 7], but at this stage it is impossible to say whether any one effect will predominate.

It is important that a better understanding of wave propagation is obtained, as it is impossible to calculate transient flow phenomena without introducing wave effects.

3. THE DEPRESSURISATION ACCIDENT

Insufficient knowledge exists to allow accurate calculations to be carried out on the sequence of events after a high temperature water reactor suffers a pressure circuit failure. But it is possible to carry out simplified calculations [5], which indicate the main areas of uncertainty and the problems to be answered if the safety of a reactor system and the effectiveness of emergency cooling arrangements are to be properly assessed.

Briefly, the core will be subjected to an initial transient, caused by the sudden rupturing of the system boundary. It must be demonstrated that the core has not been so distorted that heat transfer conditions are unpredictable in the later stages of the accident study. Subsequent stages of the blowdown may subject the structure to long duration loads significantly greater than normal design values, depending on the size and location of the break. Unacceptable distortion must again be avoided.

At the other extreme, adequate strength must also be demonstrated to exist for smaller breaks, when, although the loads are low, over heating may take place leading to loss of strength.

In all but the minor break case, the reactor system will lose most of its original coolant, allowing the fuel to heat up before emergency coolant can be supplied. Most proposals to date, involve either an overhead spray or a vessel flooding system, which does not operate until the circuit pressure has fallen to a few atmospheres, so that heating up can take place over a period of several minutes.

The various limitations will not all occur in the course of any one accident, so a range of break sizes and positions must be investigated to ensure adequate coverage has been obtained. At one extreme, with a break near the outlet of the core, rapid loss of pressure on this side will allow the core structure to feel the full circuit pressure as a pressure differential across it. The duration will depend on bubble nucleation, which will tend to restore the pressure near the break to the saturation condition, and wave propagation velocity, which will eventually reduce the pressure acting on the bottom of the core. Subsequently the pressure difference across the core falls to a value dependent on the break size and discharge rate, but this may still

be several times that normally applied to the structure so there is great interest in knowing discharge rates as accurately as possible.

The other extreme condition arises from a break positioned between the entry to the core and the circulating pumps. Such a break may divert the pump flow causing rapid stagnation of the core flow; the time scale involved in stopping the core flow will again be dependent on wave propagation effects as liquid inertia and compressibility will be important factors. Here again, the designer is interested in knowing as accurately as possible the discharge rate, particularly how it may vary as the circuit pressure falls and more and more vapour is produced, as this will influence the time that the core flow remains stagnant.

Stagnant core flow conditions, particularly if it occurs before the reactor has been shut-down and temperature equalisation taken place in the fuel, leads to rapid clad failure and potential problems of explosive vapour generation when some coolant eventually returns. In this context, for a typical cylindrical oxide-fuel pin, temperature equalisation will take 10-20 secs to occur. Without cooling for this period, the equalisation temperature would be around 900-1000^{o}C, clad failure would occur within a few seconds of the circuit pressure falling below the fission product gas pressure inside the pin. These conditions can be avoided if cooling persists for the 10-20 secs., the clad temperature will be held around 300^{o}C and subsequently rising at 10-20^{o}C/sec., if cooling is then lost, hence a period of a few minutes is available before failure temperatures are reached.

To obtain a better understanding of the depressurisation accident the Americans are building the LOFT facility. This consists of a 50 Mw P. W. R. installed in a large containment building. Studies of the forces acting and the response of the reactor system to depressurisation will be made by opening a large vent in the primary circuit. To obtain the maximum possible information from these tests preliminary model tests are being carried out by both the British and Americans.

4. MODEL SCALING CONSIDERATIONS

Many discussions have taken place between the British and Americans regarding the appropriate method of scaling to be adopted. As is usual, it is

impossible to satisfy all the criteria governing the flow distribution and losses once a departure from a full size copy of the system under consideration is made.

The scaling laws for single phase fluids are fairly well understood and if a geometric model of a reactor system is built, and the pressure against time curve obtained for a specified break using compressed gas as the test medium, then fairly reliable estimates can be made of the appropriate curve for the full scale reactor with the same filling gas. This would involve making some correction for the initial starting transient, where wave propagation effects play a part, the correcting the quasi-steady-state blowdown for the effect of Reynold's number on the friction factor in the piping.

When we look at the problem for two-phase flow conditions, however, large uncertainties exist. Not enough is known about wave propagation and the part played by bubble nucleation on wave speeds to correct the initial starting transient. Then at later times, the same correction factors will not apply to the different parts of the system (e.g., bends, sudden enlargements or contractions, pipes etc.) as the proportions of the two phases vary during the course of the depressurisation. It is, therefore, necessary to decide what information one hopes to extract from any particular series of model tests and then chose the scaling method.

The Americans have decided to use strict geometric scaling and are to investigate the performance of a 1/4 scale model of their reactor system. On such a system the time scale of events would, therefore, be shortened by a factor 4 if no distortion is introduced in the smaller system. It is argued that, if wave propagation does affect the initial part of the transient, then the scaled answers will be suitably pessimistic for the estimation of the duration of high pressure differences across the core structure. Also, in the context of their programme, the later stages of depressurisation are considered to be more important, and it is thought that geometric scaling is the most suitable.

For the British programme it was decided that the initial starting transient was the important effect and we are using transverse scaling only. This leaves the flow path lengths unaltered hence the time scale of events should

be the same as for a full sized system, allowing for easier study of wave propagation and initial bubble nucleation. It was also decided that, whilst we would not attempt to model the American LOFT reactor system exactly, we would at least simulate the core accurately. This means using a group of full size fuel rods, spaced at the appropriate centre distances. The external circuit is to be as simple as possible, using constant diameter piping, consistent with giving the right order of overall blowdown time, in order to facilitate comparison with analytical methods. As the LOFT reactor only uses one external circulation loop, it has been decided to carry out two series of tests to simulate one and four external loops to see if significant differences arise in the flow patterns.

5. EXPERIMENTAL PROGRAMME

The experimental programme is being carried out at the AWRE test establishment at Foulness, and is divided into three phases.

Phase I consists of a series of tests, utilising lengths of straight piping, to investigate on the simplest possible geometry, nucleation delays and wave propagation. Two pipe sizes will be used (1" and 3" i.d.) and the length will be 12 ft. Each pipe will have an instrumentation section every 3 ft. along the length (fig. 1). Measurements of pressure, temperature and voidage will be taken as the system depressurises. The starting pressure will be 500-2500 psi (33-160 atm) with the water temperature from 50°C subcooled up to the saturation value.

Heating elements are clamped around the outside of the pipe, with thermal insulation fitted over everything. The heater ratings are sufficient to raise the water temperature in less than one hour and a period of a few minutes is allowed for temperature equalisation to take place before depressurisation. The system pressure is controlled by a gas pressuriser, partially water filled, which is isolated just before blowdown.

Preliminary proving tests have indicated that a double diaphragm bursting disc assembly is not an entirely satisfactory method of initiating the blowdown, as the volume change caused by the stretching of the diaphragm prior to bursting affects the system pressure. It is now intended to use a glass disc, fracture being initiated by the firing of a steel pellet, or alternatively

a single strong closure disc, sheared by a pressure operated ring.

Phase II consists of a similar series of tests, but with a reservoir connected to one end of the pipe. This means that the initial wave reflection is now a compression wave, instead of a further expansion wave. The differences in wave propagation and nucleation will be studied. The reservoir will be 5 1/4 ins. i.d., and 8 ft. high, the piping will be 1 in. and 2 in. i.d., 12 ft. long. The same range of initial pressures and temperatures will be covered as that used for Phase I tests.

Some additional tests will also be carried out using a simple bend and a pipe loop with a tee piece for the discharge. These pieces will be later used in the Phase III tests. Typical configurations are illustrated in fig. 2. Phase III consists of a reactor vessel simulation with a section of a core represented full size. The general proportions are based on the American LOFT reactor proposals, which uses a core length of 3 ft. and cylindrical fuel rods 0.39 in. dia. at 0.58 in. centres. A group of 25 rods will be used with internal heaters designed to raise the temperature of the rods to the normal operating condition. It is hoped that the rod-heater unit can be designed to have the correct heat storage capacity, so that as the blowdown proceeds the appropriate heat transfer conditions will be reproduced. The external circuit of the actual reactor will not be reproduced, but a simple pipe loop of the right order of internal volume and path length will be used to simulate the effects (fig. 3). It has been estimated that a pipe loop 180 ft. long and between 1 1/2 - 2 in. i.d., will have a flow resistance of the same order as that encountered in the reactor, when computed for single phase conditions. To simulate the effect of different break positions provision will be made to install the blowdown tee piece at alternative locations round the pipe loop.

The heating on the reactor vessel and pipework will be so controlled that the top half of the system can be raised to a higher temperature, so simulating the differential temperature across the core which exists in a working reactor. It is considered important to include this effect in the tests as it will control the region first producing steam. Similarly it is also considered important to include core heating as the hot core may produce sufficient vapour to disrupt the normal heat transfer mechanism. As flow conditions change to restore liquid flow through the core effective cooling may not be regained if

the rod surface temperatures have risen too fast.

6. THEORETICAL WORK

Studies on the experimental data published by many workers in the field of two-phase critical flow discharges have been in progress for some time. Most of this is concerned with steady-state discharges from pipes and it has become evident that the common assumption of thermal equilibrium between phases is erroneous, see for example work by Fauske [8]. This lack of thermal equilibrium is probably the reason for the discrepancy between theoretical predictions and experimental results, particularly in the case of short pipes.

A theoretical model has been built up, based on the concept of a cloud of small vapour bubbles, which are carried along in the flow. The growth of the bubbles is controlled by the heat conduction lags between the bulk of the liquid and the liquid-vapour interfaces. The set of equations has now been programmed for a restricted range of cases. At the moment entry conditions are limited to sub-cooled or just saturated approach flow, with the acceleration pressure drop into the pipe entry sufficient to cause nucleation in the bulk of the fluid. It is assumed that no slip exists between a bubble and its surrounding fluid.

A number of approximations have to be made to enable the computations to proceed. These are:

a) a short initial growth period in a constant pressure field with no interference between bubbles. The results of Plesset and Zwick [9] are used to give the bubble growth in this region.
b) a period where the pressure is falling along the axis of the pipe, but the temperature fields around the bubbles are too limited to interfere with one another. Heat conduction is based on a finite difference system for an infinite slab, with a correction factor applied to the temperature gradient to allow for the spherical geometry and moving interface.
c) a final period where interaction effects are present. In this region a function is introduced to compensate for the coalescing of bubbles, which causes a loss of heat transfer area. Also the temperature field is distorted by the rapidly changing distance between the bubbles, and a moving

co-ordinate system has to be applied to the heat conduction calculation.

At the moment the programme is limited to relatively low voidage conditions, say up to 60%, at the outlet plane, because of the bubble assumption. It is, however, ideally suited to examine the flow in short pipes and it is hoped that it will successfully cover the region of zero length up to, may be, L/D = 50.

The method of calculation is to assume an entry flow rate and then follow the growth of the bubbles, calculating the rate of change of pressure with length at successive points along the pipe. The end of the calculation is reached when the pressure gradient runs off to minus infinity. The form of the choking criterion is fairly complex as it contains terms which originate from the rate of change of quality as well as the usual pressure terms. The full implications of this limit have not yet been assessed.

Preliminary results indicate that the model predicts the right trend of critical flow variation with changing pipe length, and that the results are not too sensitive to the initial number of bubbles assumed in the calculation. It is obvious, however, that more information is needed on the factors affecting the initial number of nuclei available. It is hoped to be able to extend the method to handle two phase approach flow conditions and alternative assumptions will be tried for the third stage of the calculation which may be more appropriate at high voidage conditions.

The main implication of this particular theoretical model is to indicate that the flow system cannot be scaled in a geometric manner, but has a strong dependent on the time of transit along the pipe. It is hoped that some curves showing the effect of number of bubbles etc., will be available for the conference.

When the steady-state flow studies are further advanced, and assuming that the postulated heat transfer model is still thought to be a reasonable one, it is intended to start writing a similar programme for transient flow conditions. This will involve the introduction of wave transit times and will depend to a great extent on the experimental information obtained from Phase I of the test programme described earlier.

7. CONCLUDING REMARKS

The paper attempts to outline, very briefly, the areas where pressure wave effects could be important to reactor safety. The uncertainties that exist on wave propagation velocities have been mentioned and some tests to be carried out in the U.K. to improve our understanding of these phenomena are outlined.

The uncertainties which arise in interpreting model results and the effects of scale are also mentioned. The tests to be carried out by ourselves when correlated with the American work on the LOFT project should help to clarify many of our present doubts.

On the analytical side it would appear that the relatively straight forward concepts of phase slip are not sufficient to explain critical flow phenomena in all cases, and the thermal conduction lags must be introduced. In this context it is necessary to obtain a better understanding of the factors affecting nucleation. The work in Sweden on the effects of irradiation on nucleation and that at Ispra on depressurisation is particularly interesting.

REFERENCES

(1) KARPLUS, H.B., Propagation of Pressure Waves in a Mixture of Water and Steam, ARF. 4132-12 (Jan. 1961)

(2) GOUSE, S.W. Jr., and BROWN, G.A., A Survey of the Velocity of Sound in Two-Phase Mixtures, A.S.M.E. Paper 64-WA/FE-35

(3) WALLE, F.V.D. et al., A Study of the Application of Acoustical Methods for Determining Void Fractions in Boiling Water Systems, EUR 2336.e. (1966)

(4) BROWN, E.A., Experiments on the Explosive Decompression of Water, ARF 4132-9.

(5) EDWARDS, A.R. and HUNT, D.L.M., Post Incident Cooling of a P.W.R. Core, AHSB(S)R.86 (1965)

(6) FRIZ, G., Coolant Ejection Studies with Analogy Experiments. Paper presented at Fast Reactor Conference A.N.L. Oct. 1965.

(7) BLOMBERG, P.E., Measurement of Pressure and Void as a Function of Time and Ionisation Radiation Intensity at Rapid Decrease of Pressure in Saturated Water, E.N.E.A. Meeting of Specialists at Cadarache, April, 1966.

(8) FAUSKE, H.K., Two Phase Two- and One-Component Critical Flow, Two-Phase Flow Symposium, Exeter, June, 1965

(9) PLESSET, M.S. and ZWICK, S.A., The Growth of Vapour Bubbles in Superheated Liquids, J. Applied Physics, Vol. 25, No. 4, April, 1954

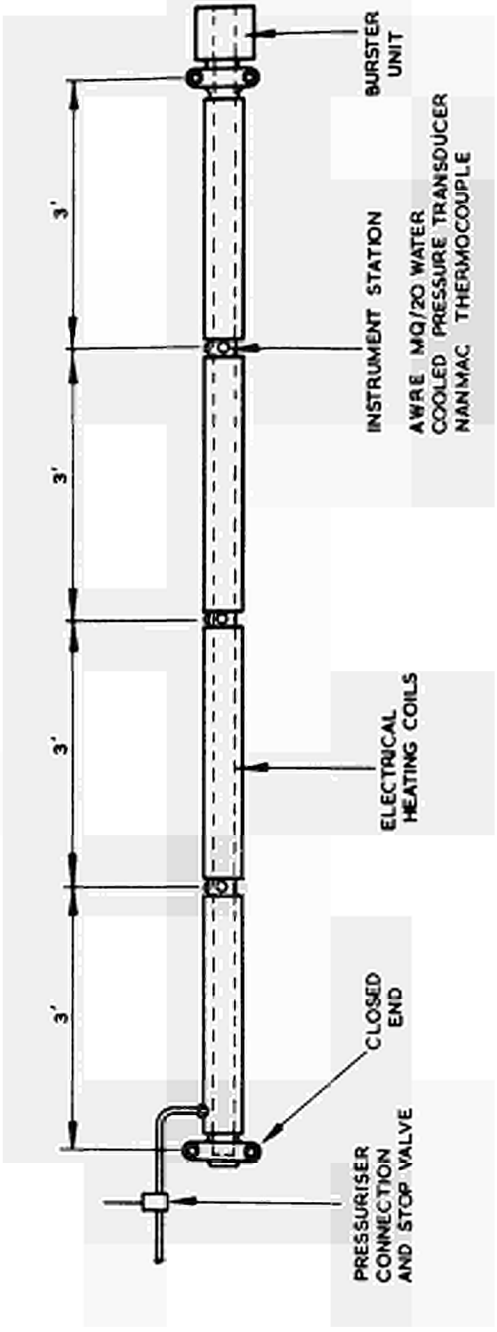

FIG.1 PHASE I - BLOWDOWN OF 3 INCH DIAMETER PIPE

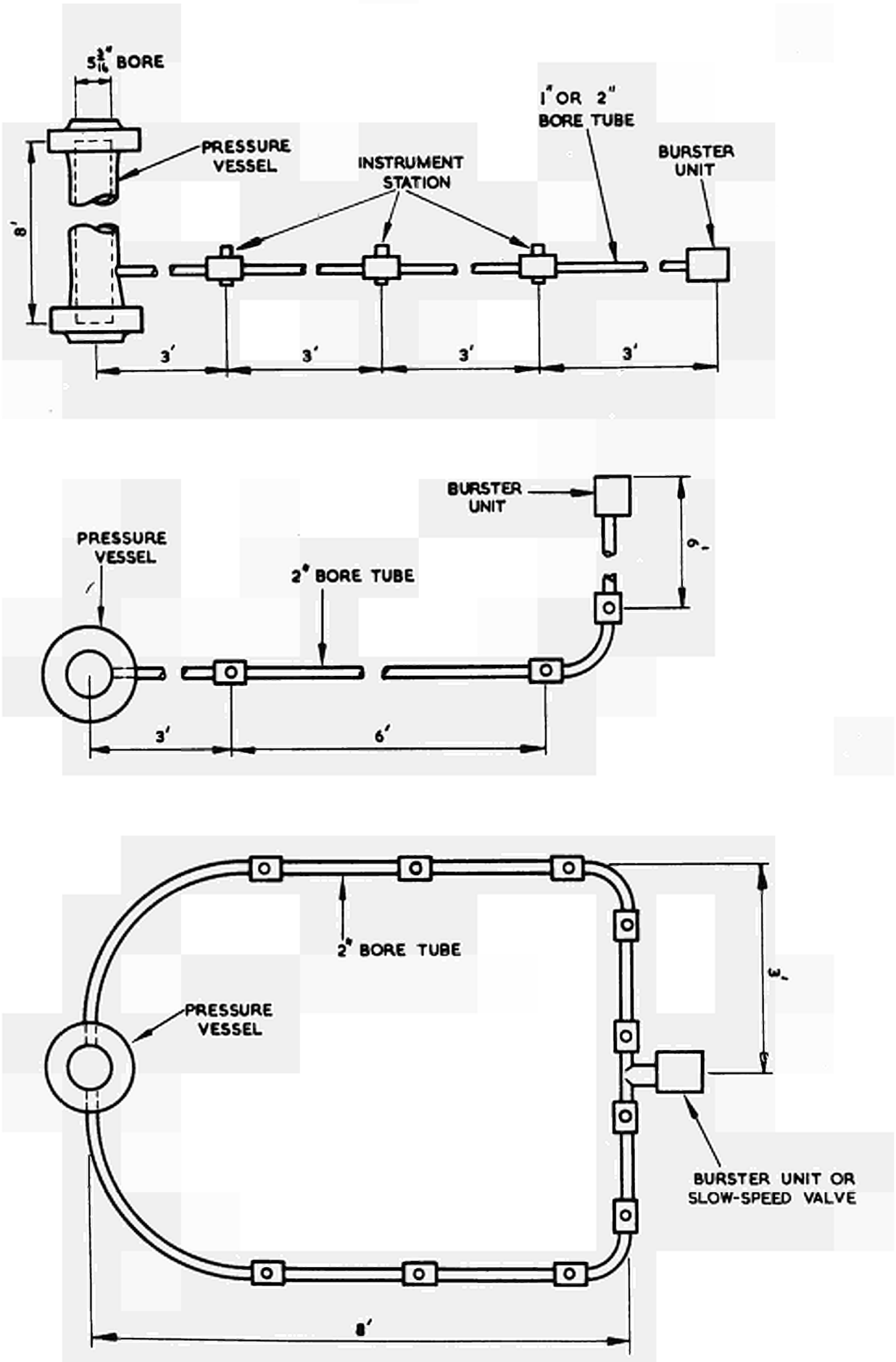

FIG. 2 PHASE II - BLOWDOWN OF RESERVOIR THROUGH VARIOUS PIPE GEOMETRIES

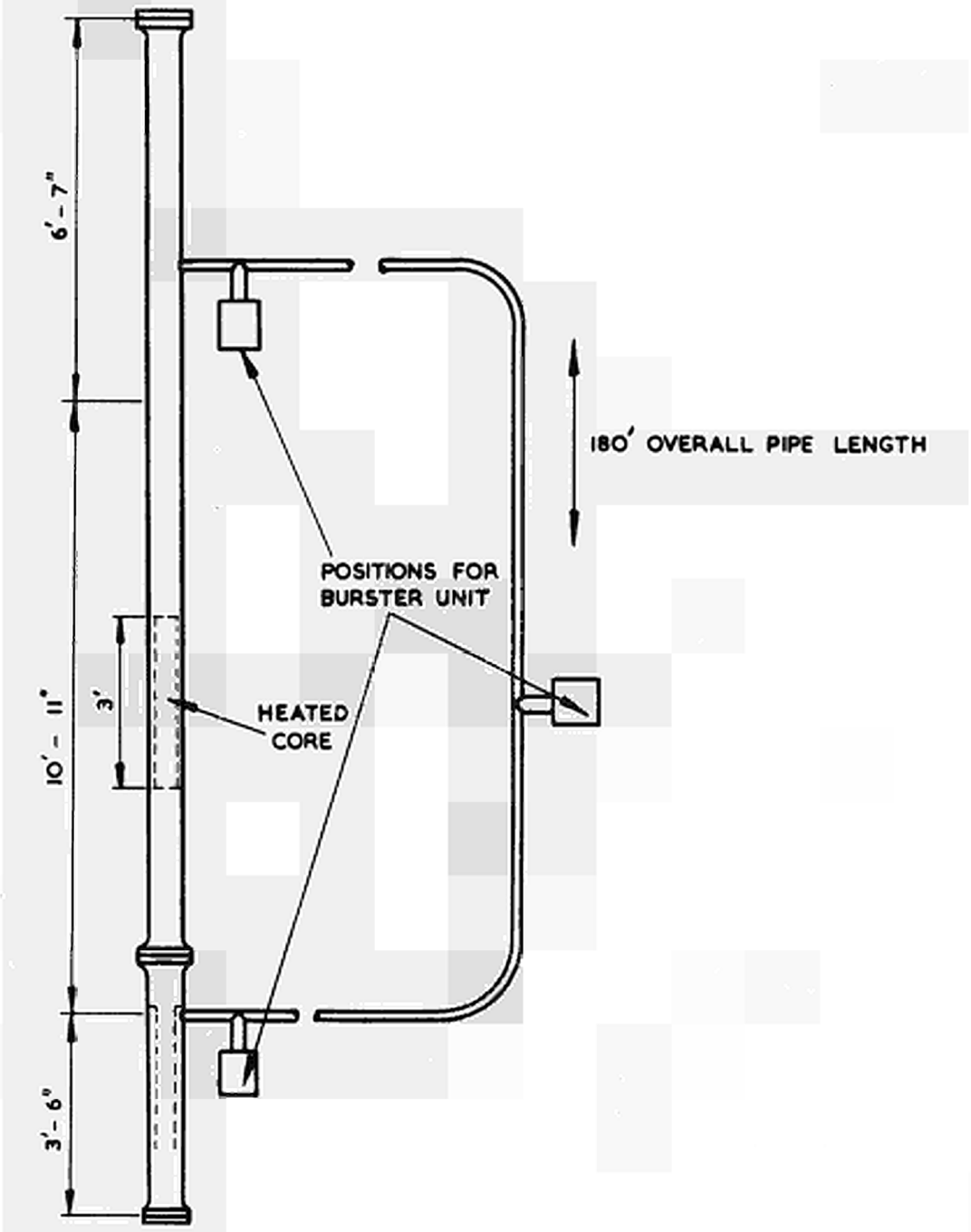

FIG.3 PHASE III-TESTS ON SIMULATED SINGLE LOOP REACTOR CIRCUIT (LOFT)

SOME THEORETICAL CONSIDERATIONS AND EXPERIMENTAL DATA ON PROPAGATION AND REFLECTION OF UNDERWATER PRESSURE AND SHOCK WAVES

by

H. Holtbecker and A. Maserati

Euratom, CCR Ispra
Italy

INTRODUCTION

The study of the containment of accidental overpressures that may be created inside a reactor vessel by the actual vessel structures calls for a knowledge of their magnitude, the point at which the overpressure originates, the mode of wave propagation, i.e. whether they decay or grow stronger during propagation, and the response of the structure and materials to such stresses. This report deals with the modes of propagation of waves due to rapid pressure rises caused, for example, by an uncontrolled reactor power excursion or, in the case of pressure-tube reactors, by the failure of one of these tubes, or else to reactions between a metal such as Al or UC with the water used as moderator or coolant, where the waves are propagated in water.

The main interest was to see how a pressure wave generated by any cause decays during propagation, and what values the pressure reaches if the wave is reflected from a structure.

A cylindrical propagation geometry was chosen because, first, the failure of a reactor pressure-tube leads to that geometry, secondly, it is easy to generate waves of approximately that form by means of line-charge detonating explosives, and thirdly, for model experiments the idealized structure sometimes chosen is a cylindrical shell, struck by a wave of cylindrical form, as described in the report No. EUR/C-IS/673/66 e "The Response of a Vessel to an Internal Blast Loading - Limits of Model Tests - Influence of Strain-Rate"[1].

The present report contains three sections ; the first concerns the propagation of a wave from source to structure, the second studies the behaviour of the wave from the moment of impact on the structure, and the third, dealing with the events that occur when a pressure wave impinges on a reactor channel, considers

the shadow phenomena due to the tube, the diffraction of the wave, its possible enhancement as a result of its travel through pressure tube reactor lattice and, lastly, the reflection from a pressure tube.

1. PROPAGATION OF A PRESSURE WAVE

1.1. Statement of the problem

The problem can be expressed in the following terms : inside the reactor pressure vessel, which contains light or heavy water, an accidental cause sets up overpressure in a certain zone, with a peak value that may range from tens to hundreds of atmospheres[2].

It is desired to know how the wave is propagated, whether the propagation geometry and dissipating factors will cause it to decay, and how these events can be predicted in theory.

1.2. Hydrodynamic considerations

A violent power excursion, failure e a pressure-tube, a metal-water reaction, any of these will provoke a rapid pressure transient in a certain zone in the water. There will be liquid or vapour pressures applied to water across a certain surface of separation. The boundary surface will move, generating disturbances which will be propagated in the form of waves. The first thing to establish is whether these are to be treated as shock or acoustic waves. This will depend on the magnitude of the pressure exerted on the water by the liquids or vapours, which may be considered as "pistons".

As a guide parameter for the wave propagation phenomena, we may take the variations of density ρ due to a certain variation of pressure p[3].

The fluids considered are water and heavy water ; the latter will be approximated to ordinary water in respect of all the characteristics involved here[4].

Since the equation of state of the water is [5] [6]

$$p = A \left(\frac{\rho}{\rho_o}\right)^7 - B$$

where p = pressure

ρ = density of water at pressure p

ρ_o = density of water at 1 atm, and

with the coefficients A and B practically independent of temperature for variations of the order of 80°C, it is obvious that very great variations of pressure are necessary to produce the significant density variations required to form shock waves[3].

With pressure variations of the order of 500 kg/cm^2, the water density varies to the extent of about 2 %, which can be regarded as a negligible value. In these conditions the wave propagated may be approximated to an acoustic wave, and its motion can be described by the wave equation[3] :

$$\nabla^2 V = \frac{1}{pc^2} \cdot \frac{dp}{dt} \qquad (2)$$

where

V = velocity potential

p = pressure

t = time

c = velocity of sound in the medium under consideration.

As stated in the introduction, a cylindrical propagation geometry was chosen.

With this geometry and with waves that fulfil the above description, the pressure decay is in inverse proportion to the square root of the radius, when the radius of the wave surface has become much larger than the water-"piston" boundary surface, as may be verified by integrating equation (1).[7]

For higher pressures the mathematical description of the events must take into account the fluid density variations and the equations concerned are changed.

In general, with what are defined as strong shocks, in which the pressure behind the front is far higher than that of the fluid not yet affected by the shock (the

expression "far higher" must be understood in relation to the equation of state of the fluid ; for a gas it may be greater by a factor of some tens or hundreds only, but for a liquid, by a factor of tens or hundreds of thousands), account must also be taken of the dissipation phenomena that affect the front and are characterized by an increase of entropy.

Numerous authors agree, however, that as regards water, even with extremely high pressures, such entropy variations can be neglected. In reference[6] it is stated that for water, pressure is a function of the density only and not of the internal energy, i.e. the coefficients A and B of equation (1) are independent of the entropy, whose variations can thus be neglected. Stanyucovitch[7] states that for pressures up to 10^5 kg/cm^2 the density variations are such that the entropy can be shown to be virtually constant.

The field of pressure we are concerned with ranges from a few tens of atmospheres up to the pressures, estimated at 0.5×10^5 to 10^5 kg/cm^2, due to a line charge of high explosives encased in a sheath ; the reason is that both in the experiments reported here and in the model experiments on cylindrical shells [1], the pressure wave to be expected from a reactor accident was generated by high explosives of that type.

Under these conditions the equations describing the wave can be reduced to the two fluid dynamics equations for conservation of mass and conservation of momentum, which may be expressed as [5]

$$\frac{d\rho}{dt} + \text{div } \bar{v} = 0 \qquad (3)$$

where $\bar{v}$ is the vector of velocity of a fluid element and conservation of momentum :

$$\rho \frac{\partial v}{\partial t} + (\bar{v} \times \text{grad}) \bar{v} = - \text{grad } p \qquad (4)$$

1.3. Calculation methods

A calculating system was required that would describe the propagation of a wave in cases where the density variations were no longer negligible.

The problem was submitted to a group of mathematicians at the Ispra computer centre and a report entitled "Computation of shock waves in water" is being prepared by L. Guerri and P. Stella.

Various calculating methods were tested and will be described in the above-named report.

The calculation is at present being effected only in one spatial coordinate.

One system, evolved by R.D. Richtmyer and Von Neuman[8], is a finite difference calculating method, in which the equations are the fundamental equations of fluid dynamics. Its main characteristic is that it describes a shock front without having recourse to mathematical discontinuities, but introducing a parameter - pseudoviscosity - which automatically creates steep pressure and density gradients where a shock is located.

It is based on certain physical phenomena to which real fluids are subject, namely viscosity and heat conduction. These are the factors which make discontinuity of density and pressure physically impossible on the shock front. The discontinuity surface, as considered by Rankine and Hugoniot, is indeed a thin transition layer in which the parameters vary rapidly but continuously.

The method in question introduces into the general equations a term which accounts for the dissipation phenomena, and the equations thus written are valid everywhere, so that there is no need for boundary conditions corresponding to shock. This is the term which the authors have called pseudoviscosity.

Another method tested is a finite difference method of implicit type in Lagrange coordinates, in which the Rankine-Hugoniot conditions are introduced directly

into the calculation (shock fitting method). Yet another line of study was the feasibility of directly solving the partial-derivative fluid dynamics equations with a simplifying hypothesis, as K.P. Stanyucovitch did [7].

The second method seems to give the best results at present. Richtmyer's method for boundary conditions of very high pressures (i.e. over 10,000 kg/cm^2) gives strong oscillations in the wave pressure profile near the front.

Certain considerations are called for in this connection. The calculating methods mentioned describe the motion and the characteristic parameters of the wave being propagated, as a function of the action of the explosive. It is thus necessary to determine what pressure the explosive exerts on the water through the interface, which is assumed to transmit pressure only.

The pressures on the explosive detonation front are known and in the case of TNT are evaluated at about 189,000 kg/cm^2 [9]. In our case the charge is initiated at one end and the detonation front proceeds at a speed of about 7,000 m/sec. As a consequence the pressure is not uniform, at a given instant, throughout the line charge.

In the calculations, a simplifying hypothesis is assumed, namely that the detonating velocity is infinite and that the space initially occupied by the explosive is filled at the zero instant with a gas already at the same pressure as that at the detonation front. Since a rarefaction wave is propagated from the interface towards the axis of the explosive, so that the pressure at the interface varies with time, changing the boundary conditions for the equations relating to the wave in the time following the initial instant, this phenomenon needs to be described, and the hydrodynamic equations are written likewise for the gases produced by the detonation.

The equation of state for these is [21]

$$p = A\ \rho^{\gamma}$$

where $\gamma = \frac{c_p}{c_v} = 3$; A is a function of the explosive.

But another factor must be considered. In the case of the line charge used, not the explosive but a casing of hemp and plastic was in contact with the water.

The wave generated by the explosive has to pass through this before reaching the water, and undergoes pronounced decay, greater than the decay that would ensue in water (which is already very considerable, considering that for a spherical charge experimental data show that at a distance of 3 diameters the pressure with TNT fell from 189,000 kg/cm^2 to about 3,700 kg/cm^2) [10].

It was assumed, then, that the pressure in the detonation products was lower than the real pressure, and that they were in direct contact with water.

Various boundary conditions were then tested ; the envelope of the pressure wave peak versus the distance from the charge axis is shown in Fig. 1, for boundary conditions of 30,000 kg/cm^2 and 50,000 kg/cm^2. The graph also shows the experimental profile of the decay of the peak (determined as will be explained in paragraph 4), and if we compare it with the profile calculated for these boundary conditions, the calculated curves are quite satisfactory.

In the same graph, for comparison purposes, is shown the pressure peak envelope given by the second method and the one given by the Richtmyer method, for boundary conditions of 10,000 kg/cm^2.

We intend to determine the boundary conditions (water explosive interface) better by means of pressure measurements or, for the line charge with lead casing, by calculating the wave travel through the casing. It will then be possible to provide a definite check for the calculating methods.

1.4. Experimental results

In the experiments carried out on full scale model for the ESSOR test reactor [11] on the failure of a reactor channel containing organic liquid at 30 atm, it was found

that the wave, registered by a pressure transducer positioned about 20 cm away from the point of generation of the disturbance, had a rise time of approximately 500 μ sec with a peak of 15 kg/cm^2.

A problem for consideration was whether waves of this type could be regarded as acoustic from their start in the generating zone. That is to say, we wanted to see experimentally whether a shock wave can be propagated in water (the term "shock wave" is used here, for convenience, to signify a wave with a very steep front and a rise time of less than 1 μsec), if the "piston" behind it applied a pressure not exceeding about 500 atm, even assuming that the "piston" exerts the pressure in step form with a rise time of less than 1 μsec. We likewise wished to verify the law of propagation, as regarding peak decay, of a wave of the type generated by a high explosive in cylindrical geometry.

The method adopted for the first question was as follows. In order to obtain a pressure step of known value, the lower end of a vertical gas shock-tube was filled with water to various know levels, as shown in Fig. 2. When the diaphragm fails a shock is, of course, propagated (12) through the low-pressure chamber until it encounters the free surface of the water. The shock wave is reflected at this free surface and passes through the water at the reflected pressure value down to the end of the tube, where it is again reflected. At the tube end is positioned a pressure transducer of the steel bar and strain-gauge types, as described in the above-cited report, which registers the evolution $p = p(t)$ of the wave pressure.

Experiments effected with various water-levels and various pressures for the wave impinging on the water, apparently showed how with pressure values ranging up to about 500 kg/cm^2 the pressure-wave rise time increases with the travel. This tends to show that with these pressure levels, even if the initial wave is a shock wave, it must shortly lose this character. The oscillographs illustrating this event are given in Figs. 4-13.

Fig. 3 shows the signal given by the transducer used for these experiments, in a calibrating test on the gas shock-tube. The pressure is about 120 kg/cm^2. The time bases are 2 μsec per square for the upper trace and 10 μsec per square for the lower. This shows that the transducer rise time is approximately 2 μsec.

Figs. 4-6 give the oscillographs for a wave propagated in water over the distances indicated, at a pressure of 20 kg/cm^2. The rise times increase gradually up to 30 μsec.

Figs. 7-10 show the oscillographs for the same distances of travel in water, but at a pressure of 120 kg/cm^2. The rise time is unchanged over 3 cm travel in water, then increases to about 15μ sec. In Figs. 11-13, with the same travels in water but with a pressure of 476 kg/cm^2, the rise time increases to about 7μ sec. These findings are in contrast with what was found by several authors, i.e. a steepening up of a wave front even at low pressure levels, and therefore, doubting that the effect found was due to a secondary effect of the gas shock tube, we have interposed rubber between the air and the water section, and substituted the steel low pressure section with one of aluminium. Nevertheless, no change in transducer signals were found. Furthermore, on reference (5) increase in rise time of a shock wave propagating in water is reported.

It must be observed, however, that in the measurements effected on shock waves generated in water by an explosive - dealt with more fully in the next paragraph - even with the transducer positioned at such distances that the peak pressure has fallen to levels of about 100 kg/cm^2, the wave front is still very steep, with rise times of the order of 1 μsec. This would indicate that if a wave has initially the character of a violent shock wave it will continue to be propagated with a steep front even at pressures for which the density variations are very small. Nevertheless, the wave front is no longer as steep as it was when nearer to the explosive, where the pressure

values are higher (some thousands of atm.). In the zone where the wave is still very violent, many authors [5] consider that its rise time is of the nanosecond order.

Using a beryllium transducer [12] with a rise time of the order of 0.3 μsec (Fig. 14) we measured a wave generated by line-charge, at a distance at which the peak pressure of the incident wave was 350 kg/cm^2 and, as Fig. 15 shows, the pressure rise time was about 2 μsec.

It was decided to use a detonating explosive to propagate a wave simulating the wave caused by a reactor accident. The limitations of this method have been discussed at length by various authors[13][14][15][16][17] ; nevertheless the almost perfect reproducibility afforded by these explosives, the ease with which the wave intensity can be varied with their quantity, the simple scale laws governing them, all recommended their use.

The aim was to secure information on the pressure values obtaining when the disturbance reaches a structure at a given distance. The experimental and theoretical data on the argument in cylindrical symmetry, as known to us[18], were insufficient and new measurements were needed to provide information for use in further research.

In particular, information was required on the type of wave and its decay, in relation to the explosives we intended to use both for the experiments reported here and for the model and materials experiments on cylindrical shells[1] ; these are the explosives mentioned in the introduction and under head 1.2.

The choice of explosive was based on the following criteria :

a) Generation of a cylindrical wave.

A line charge completely submerged in water and detonated at one end generates a wave which has approximately the form [5][9] shown in Fig. 16.

If the ignition end is positioned out of the water, this will cut out the detonator effect which can be fairly

considerable[18], and the wave generated will be approximately conical, the angle of aperture of the cone depending of course on the relation of the explosive detonation velocity to the velocity of propagation of the wave.

Since the explosive used has a detonation velocity of 7 mm/μ sec and the velocity of propagation of the shock wave in water - if we except a zone of about 20 diameters in the immediate neighbourhood of the explosive, where the pressures are extremely high - is approximately 1.5 mm/μsec, the angle of aperture will be about 12°.

It was therefore concluded that the wave could be considered as approximately cylindrical.

b) Use of limited quantity of explosive.

The line charge had to be of very small diameter (a few mm), so that, in order to ensure satisfactory detonation, the explosive had to be contained in a casing. The explosive used here is a PETN primacord made by the firm of Montecatini.

The arrangement for the experiments described in this report were as follows :

the water in which the wave was to be propagated was contained in a parallelepiped tank, internal dimensions 1.70 x 1 m, height 0.60 m.

The water level in the tank was 0.40 m. The primacord was positioned vertically and detonated at its top end, outside the water so as to cut out the detonator effect.

The pressure transducer was positioned 0.20 m from the tank bottom (Fig. 17). The measured pressure varies, of course, according to the transducer's position in depth, as there is an effect due to the rarefaction to which the wave is subjected towards the free surface of the water.

The line charge is detonated with a Montecatini I.E.P.S. detonator, which in turn is detonated by the discharge

from a condenser forming part of a circuit illustrated in the Appendix.

The pressure peak envelope as a function of distance from the charge axis is described in Fig. 18. For the pressure measurements the transducer, a steel bar type with strain-gauge sensitive element[12] was mounted on a heavy-gauge steel plate as in Fig. 19.

The reason underlying this assembly is that in order to obtain a correct pressure measurement, the impact of the wave front must be perpendicular to the axis of the bar. As will be seen from the drawing of the transducer[12] the bar, of 6 mm diameter, is surrounded by a support clamp which has a diameter of 12 mm at the bar head. Under these conditions the incident wave, which starts reflecting at the head of the transducer, almost doubling its pressure in that region, is subjected to a rarefaction wave coming from the zone surrounding the head where the incident wave is not reflected, and reaches the edge of the bar in about 2μ sec.

As the pressure duration for the incident waves is about 40 μsec, it was necessary to prevent the rarefaction wave from reaching the bar in this time. Assuming that the rarefaction wave is propagated at the velocity of sound, a plate of at least 60 mm radius had to be fitted around the transducer head, so this was done.

Figs. 20 and 21 give two oscillographs of the pressure versus time, the first without the plate and the second with the plate in position, and both obtained under exactly the same conditions of charge and distance from charge. The influence of the plate is manifest.

The pressures measured are therefore the pressures transmitted from the water into the bar, and the ratio between incident and reflected pressure is 0.52, as will be shown in Chapter 2. In Fig. 18 different zones can be distinguished, in which the peak decay versus distance follows different laws, according to the distance from the axis of the explosive charge.

From the first measuring point, 5 cm away from the charge axis, to the measuring point 30 cm away, the decay curve is intermediate between type $\frac{1}{\sqrt{r}}$ and type $\frac{1}{r}$.

From a zone of about 40 cm distance out to about 80 cm the decay is of the $\frac{1}{r}$ type.

Beyond that point it is reasonably close to the $\frac{1}{\sqrt{r}}$ type.

All this is in partial agreement with the theory predictions described in paragraph 2.

A typical graph of the pressure generated by the line charge used, as a function of time, is shown in Fig. 21. Here, the pressure attained is 900 kg/cm^2, the time base is 10 μsec/square.

The pressures, as stated in the report No. EUR/C-IS/698/66e[12], can be calculated on the base of the signal given by the strain-gauge, the strain-gauge factor and the constants for the circuit used, and the results are in close agreement with the calibration readings. The error assumed to occur in the peak value is due chiefly to the transducer and amounts to $\pm$ 10 %.

Good reproducibility was found with respect to the pressure peaks in the various explosions, as shown by the experimental points on the graph at Fig. 18, and to the evolution of the pressure with time. The pressure curve after the peak is nearly exponential, as was to be expected.

2. REFLECTION

2.1. Statement of the problem

We wished to find out to what extent a pressure wave, having once struck a structure could, as well as damaging it, be reflected so as to reach and damage other structures. Wave reflection from a rigid wall is a familiar topic which has been dealt with theoretically by a number of authors[5]. We wished, however, to obtain experimental evidence on the

subject. We also wanted to know how the bulk movement of a structure that is shifted considerably by an incident wave influences the reflected wave. There could be cavitation phenomena[19][20] which could have a great influence on reflection at the wall, but here we are only interested with the wave as it is travelling away from the wall.

The problem falls into two parts :

a) reflection from a rigid wall

b) reflection from a wall which is shifted significantly by the incident wave.

This chapter deals with the acoustic type of wave, bearing in mind that the pressure peaks of disturbances resulting from a reactor accident would most probably be in that range by the time they reach the vessel wall. It is intended, however, to extend the research to cover shock waves with higher pressure peaks.

2.2. Case a) General considerations and experimental data

The rigid wall concept is, of course, ideal. But since the parameters involved in the transmission and reflection of a wave from one medium to another are the density and elastic modulus of the media, or their acoustic impedances ρc, and since the media we are considering are water and steel, then from the formulae that express the ratio between transmitted pressure p_t (which coincides with the pressure of the reflected wave when the latter is still in contact with the wall and is therefore in a zone of fluid at the incident wave pressure) and incident pressure p_i, we find[5]

$$\frac{P_t}{P_i} = \frac{2\ \rho_2 c_2}{\rho_2 c_2 + \rho_1 c_1} \qquad (6)$$

where the indices 2 refer to the steel and the indices 1 to the water. This is valid where the wave is of the acoustic type and its impact is normal to the wall ;

substituting the relevant values for ρ and c, we obtain a ratio

$$\frac{p_t}{p_i} \approx 1.92 ,$$

which is very close to the value 2 which would be obtained in the case of a rigid wall under the conditions stated.

A steel wall of such thickness that it will not undergo bulk movement during the brief time when it reflects a wave of the explosive-generated type may therefore be considered as practically rigid.

For the purpose of determining a wave reflected from such a wall, pressure measurements were effected for waves reflected from a steel plate of 30 mm thickness, a gauge adopted as permitting the incident wave to be reflected long enough to involve the front and part of the wave without the plate undergoing bulk displacement. With this thickness the wave takes about 10 µsec to travel back and forth through the plate.

The waves were, as usual, generated by a pentrite line charge ; Fig. 22 shows the layout as seen from above.

The measurements were of necessity effected on the oblique reflection, because a true measurement of the pressure of a perpendicularly-reflected wave cannot be obtained, since the transducer must be positioned between the explosive and the wall. If, alternatively, the explosive is placed between transducer and wall a similar difficulty arises, as the gas bubble generated by the explosive obstructs the path of the reflected wave ; so that some arrangement on the lines of Fig. 22 had to be adopted.

So that the shock wave generated by the explosive should not disturb measurement by reaching the transducer ahead of the reflected wave, a shock damper, consisting of a steel plate with rubber cemented to both sides, was placed between the explosive and the transducer. Tests effected to see what signal the transducer would give in spite of the damper showed that it was wholly negligible.

It is possible to work out what the peak pressure of the reflected wave should be, from the formulae which express it in the acoustic theory.

These formulae derive[5] from the relation

$$p = \rho . c . u \qquad (7)$$

where

p = pressure

ρ = density of medium in which wave is propagated

u = particle velocity

and from the condition that the tangential velocities of the incident and transmitted waves (see Fig. 23), in relation to the boundary surface of the two media, are equal :

$$c_1 \cdot \sin\alpha_i = c_2 \cdot \sin\alpha_t \qquad (8)$$

where

c_1= velocity of wave in medium 1

c_2= velocity of wave in medium 2

α_i= angle formed by front of incident wave with the boundary plane between the two media, A-A

α_t= angle formed with plane A-A by wave transmitted in medium 2.

(7) of course is only valid where the motion can be described by an equation of type (1).

Moreover, there must be continuity of velocity of the particles on the boundary surface :

$$u_1 \cos\alpha_i - u'_1 \cos\alpha_r = u_2 \cos\alpha_t \qquad (9)$$

where

α_r= angle formed with plane A-A by reflected wave

u_1= velocity of particles in the incident wave in medium 1,

u_2= velocity of particles in the transmitted wave in medium 2,

u'_1= velocity of particles in the reflected wave in medium 1.

From (7), (8), (9) we can derive the desired equations[5] :

$$\frac{p_r}{p_i} = \frac{\rho_2 c_2 \cos\alpha_i - \rho_1 c_1 \cos\alpha_t}{\rho_2 c_2 \cos\alpha_i + \rho_1 c_1 \cos\alpha_t} \qquad (10)$$

$$\frac{p_t}{p_i} = \frac{2\rho_2 c_2 \cos\alpha_i}{\rho_2 c_2 \cos\alpha_i + \rho_1 c_1 \cos\alpha_t} \qquad (11)$$

(10) is relevant here.

If medium 1 consists of water and medium 2 of steel, in the case of waves of small amplitude such as we are considering, the wave velocity is equal to the velocity of sound in the medium, so that

$$\sin\alpha_t = \frac{c_1}{c_2} \sin\alpha_i = \frac{1.5}{6.1} \sin\alpha_i = 0.246 \sin\alpha_i \qquad (12)$$

where the velocities are expressed in mm/μsec.

In (10) the numerator differs from the denominator in that whereas in the numerator the second term is subtracted, in the denominator it is added.

But it is clear from (12) that the angle α_t will be small even where α_i assumes very high values, hence the variation of the cosines of α_t will be very small and the two terms of the ratio cannot differ greatly from one another.

e.g. for $\alpha_i = 15°$ we find $\alpha_t = 3°39'$

and the ratio $\frac{p_r}{p_i}$ is therefore :

$$\frac{p_r}{p_i} = 0.934$$

Similarly for $\alpha_i = 60°$, we obtain $\alpha_t = 12°18'$,

and the ratio $\frac{p_r}{p_i}$ becomes :

$$\frac{p_r}{p_i} = 0.884 \ .$$

Hence even with wide angles of incidence the value of the reflected pressure is not much lower than that of the

incident pressure, where the media are water and steel.

We wished to verify these laws experimentally. The arrangement used is shown in Fig. 22. The type, quantity and positioning of the explosive and the position of the transducer are as described in Chapter 1, in order to ensure the same experimental conditions.

The angle α_i selected is 28°. The distance of the explosive from the steel plate and of the plate from the transducer is 29.3 cm. The measured pressure of the wave reflected from the steel plate was found in two tests to be 150 kg/cm^2 and 130 kg/cm^2 respectively. The first test signal is shown in Fig. 24(*).

To calculate the pressures by expression (10) we used the graph shown in Fig. 18 to evaluate the pressure incident on the plate. At the distance adopted this is 262 kg/cm^2. From (10) with an angle of 28° we obtain

$$p_r = 0.932\ p_i = 245 \text{ kg/cm}^2$$

The wave thus reflected now travels another 29.3 cm, and from the above-mentioned graph we obtain an indicated pressure of 133 kg/cm^2, which tallies well with the measurements quoted above.

Fig. 25 shows the signal given by the pressure wave propagated for 60 cm on an unobstructed path.

It will be noted that the two signals have peaks of about the same value, whilst the pulse diminishes in the case of the reflected wave. This is thought to be due to the the fact that after 10 µsec the steel plate begins to undergo a bulk shift which subtracts impulse from the reflected wave.

(*) The pressure in the graphs are relative to the wave transmitted in the transducer steel bar, whereas we refer here to the pressure of the incident wave.

2.3. Case b) General considerations. Experimental results. Comparison with previous case

In order to have a wall that would undergo a bulk shift after a time of insufficient length to allow the entire front of the wave to be reflected, a sheet of 0.5 mm thickness was selected, through which the impinging wave travels in less than 0.1 μ sec.

The same distance between charge and sheet was adopted as in the case a) experiments, i.e. giving a peak value of about 250 kg/cm^2 for the incident wave pressure. As stated in Chapter 1.4., the rise time for the type of wave in question was found to be of the order of 2 μ sec. The sheet is therefore sufficiently thin to start its bulk movement before the entire front has been reflected.

It was also imperative that there should be no water behind the sheet, as this would oppose rapid movement of the sheet. We therefore devised an assembly (see Fig. 26) in which the sheet is bolted all along its edge on to the open side of a water-tight metal box, the whole being mounted so that there is air in the box behind the sheet.

We then set this up in the geometry (see Fig. 22) used for reflection from a thick plate, so as to compare the reflected wave intensities.

The transducer signal for the wave reflected from the thin sheet is shown in Fig. 27, the peak value being 54 kg/cm^2. A comparison of Fig. 27 with Fig. 24 shows that the wave reflected from the thin sheet is considerably weaker.

2.4. Numerical wave-reflection calculations.

While endeavouring to find a calculation method to describe the propagation of a wave, attempts were also made to describe its reflection both from a "rigid" wall and from a wall that is displaced by the wave. On the subject of the numerical processing of this problem, a report by L. Guerri and P. Stella is in course of publication.

We wished to investigate by calculation the evolution of the pressure values in the reflected wave, in cases where the wave pressure rise-time is 100 ÷ 500 μ sec., and the wave is reflected from a structure which undergoes a considerable bulk displacement.

The calculation method employed is Richtmyer's, which is applicable here as the pressure peaks involved are not very high.

It was also desired, in connection with the cylindrical shell model experiments[1] to describe the reflection of a cylindrical wave generated by explosives impinging on a cylindrical wall coaxial with the wave.

As stated in the above report, the equation for the motion of the wall of the cylindrical shell was written, and it was found experimentally that the calculated wall motion approximates satisfactorily to the measured value.

Also for the wave with large rise-time a cylindrical geometry was chosen. The result in this case shows that the peak pressure of the reflected wave is not doubled at the structure wall but is becoming lower with increasing bulk movement of the wall (Fig. 28 A).

The result for the wave generated by explosives is given in detail in the next paragraph.

The calculation was effected for an incident wave generated by a pentrite line charge with step pressure peak of 355 kg/cm^2 and nearly exponential decay, for which the pressure curve $p = p(t)$ had been obtained by means of the bar and strain-gauge pressure transducer already cited. This $p(t)$ was converted to a graph $p(x)$ (Fig. 28), where x is the spatial co-ordinate, supposing that every part of the wave travels at the velocity of sound in water, i.e. 1500 m/sec, and assuming the decay of each of its pressure levels to be that shown in the graph at Fig. 18.

At the moment of impact on the wall the wave front is reflected with a pressure of the order of 700 kg/cm^2(*). This means that the movement of the wall is in this case negligible in the first instants when the front is reflected (the calculation takes the wall thickness into account for wall-mass purposes, but the traversing time of the wave is not taken into consideration). The front now starts its return travel in a pressurized region since the fluid is affected by the wave tail which is duly approaching the wall. As the pressure levels of the incident wave fall off towards the tail, the reflected wave peak will also fall until on reaching the undisturbed zone the wave assumes its normal pressure value.

The wave peak pressure envelope versus distance travelled is illustrated in Fig. 28.

An interesting feature is that, as the graph shows, after entering the zone where the water is no longer affected by the incident wave tail, the reflected wave, which is propagated towards the cylinder axis, heightens its peak pressure. This is explained by the fact that it is an imploding cylindrical wave, and a geometric factor of pressure-level enhancement is therefore present.

3. EFFECT OF THE PRESENCE OF REACTOR CHANNELS ON THE PROPAGATION OF PRESSURE WAVES

3.1. Statement of problem

We wished to throw light on the complex events that occur

(*) The peak value achieved cannot be precisely stated because, as this is a finite difference calculation, that value will not usually coincide with one of the instants in which the calculation is written, but will generally fall into one of the time intervals between those instants.

where pressure waves are generated inside a vessel containing reactor channels of various types (see report No. EUR/C-IS/683/66 e - "Full scale experiment on the consequence of the rupture of a pressure tube in Essor reactor vessel"[11]).

Our particular concern was with the ESSOR test reactor and the problems encountered in experiments carried out on full scale.

We attempted to reduce the general question to separate more easily formulated problems, with the dual aim of achieving the more general experimental conditions with fewer full-scale tests and of obtaining a clearer interpretation of the events encountered.

The following points have been dealt with so far :

1. Shadow and diffraction effects due to a channel located in the path of a wave.
2. Influence of a tube lattice on the propagation of a wave.
3. Wave reflection from a channel.

Up to now the problems have been tackled from the experimental angle, because no calculating processes have yet been devised to describe these complex phenomena.

To effect measurements we employed the tank described in Chapter 1.4., using the same type and arrangement of explosive.

The reactor calandria-tube diameters were adopted for the tubes simulating the reactor channels, i.e. 108 mm external, 104 mm internal. The material chosen was aluminium ; for the type of measurements effected the choice of material is considered to be of no importance. The tubes were always positioned at a distance where they would not be exposed to incident wave peak pressures of more than 200 kg/cm^2. The wave is characterized by a steep front, with a rise time of about one microsecond, whereas in reality the waves propagated in reactor may have much longer rise times as stated in Chapter 1.4.

We intend to extend our research to that type of wave as well, to ascertain its behaviour.

3.1.1. Shadow and diffraction effects

The tube axis is positioned parallel to the axis of the line charge, i.e. vertically.

The tube is fixed rigidly at both ends. Tests were effected with a water-filled tube and with a tube containing air.

The experimental arrangement is shown in Fig. 29 (seen from above). The distance selected between the explosive and tube axes is 100 cm. The transducer was positioned behind the tube as shown in Fig. 29, at various distances from it.

The results were as follows :

Case a - tube containing water

Figs. 31, 32, 33 show the oscillographs given by the transducer at distances of $\frac{1}{10}$, $\frac{1}{2}$, and 1 tube-diameter from the tube wall. These oscillographs, compared with the one in Fig. 30 for the pressure under the same conditions but without tube (peak pressure value 42 kg/cm^2), show that the tube shadow effect is not very significant. The pressure reaches an initial peak of about 11 kg/cm^2, remains nearly steady for about 40 μ sec, then reaches a second peak, again of fairly low magnitude, and thereafter a peak of considerable magnitude (31 kg/cm^2 with transducer at 1 diameter from tube)(*).

It is thought that the phenomena can be explained as follows. The pressure wave colliding with the tube generates a wave in the tube wall which is propagated as a transversal wave ; this, on reaching the area diametrically opposite the impact area, transmits into the water a disturbance which is the

(*) The pressure in the graphs are relative to the wave transmitted in the transducer steel bar, whereas we refer here to the pressure of the incident wave.

first to reach the transducer, since the velocity of the transversal wave in the wall is greater than that of a wave in water.

The wave which collided with the tube also travels as a longitudinal wave through the tube wall, through the water contained in the tube, through the wall in the area diametrically opposite the impact area, and finally into the water surrounding the tube. This wave appears to be represented on the oscillograph by the highest peak, which occurs about 50μ sec after the first.

The time difference between these two peaks corresponds to a transversal wave velocity of about 2,500 m/sec in the tube. Before the principal peak there appears a peak of far lower intensity for which it is difficult to find an explanation. One characteristic shown by the oscillographs is that the intensity of the principal peak increases with the distance of the transducer from the tube wall.

Since some diffraction of the incident wave is to be expected after it has passed round the outside of the tube, and since that wave must be travelling only slightly behind the wave which passed through the tube (the delay being caused by the fact that the latter wave travels through 6 mm of aluminium in which the speed of sound is approximately 6,500 m/sec) it was thought that the peak enhancement can be explained by the diffracted wave.

At a greater distance from the tube the transducer still registers a pressure with the same shape but, naturally, with lower levels.

Case b - tube containing a gaseous medium (air)

The chief effect of the absence of water in the tube is, predictably, the elimination of the wave transmitted across the tube ; this is demonstrated in Figs. 34 and 35, where the higher peak, present in the previous

oscillographs, is absent, thus confirming the prediction.

Another feature is that the wave caused by the transmission of the disturbance by the tube wall is of greater duration when the transducer is positioned at a distance of one diameter away from the wall, a fact which seems to indicate that this greater duration is due to the superimposing of the diffracted wave. If this assumption is true, then the intensity of the diffracted wave would be of the order of 10 ÷ 12 kg/cm^2.

In conclusion it may be said that with an incident wave of the type described, the shadow effect of a reactor channel is only significant if the channel is filled with a gaseous fluid in which the wave transmitted thereto by the tube wall is negligible - i.e. the incident wave cannot travel through the tube.

Where the channel is filled with a liquid, the wave transmitted to the liquid from the wall is considerable and the incident wave travels through the tube.

The diffracted wave, at distances of up to two or three diameters from the tube, is of no great significance. A disturbance is furthermore transmitted by the transversal waves travelling in the tube wall.

3.1.2. Influence of a tube lattice on the propagation of a wave

We were interested in discovering how the wave would be affected by travel through a lattice of the type of tubes used in the ESSOR reactor.

As before, we used the wave generated by a line charge. The initial arrangement chosen was that shown in Fig. 36 ; the distance x between the tubes was varied, while the distances of the line charge and the transducer from the tubes remained constant.

In this experiment we found ourselves faced with an interesting phenomenon. With x = 10 cm the pressure wave,

after travelling through the space between the two tubes, has a peak enhanced from 139 kg/cm^2 without tubes present (Fig. 37) to 201 kg/cm^2 with the tubes present (Fig. 38). Thus the pressure is some 1.45 times greater in the second case.

It will be seen from the oscillographs that the pressure decay behind the front is more rapid in the second case. Although an exact calculation was not effected, it appears that the ratio between the impulses does not correspond to the peak ratio. The event still occurs even at greater distances from the tubes, but weakens. The transducer, positioned 60 cm from the tube axes, registered an incident wave pressure of 62 kg/cm^2, as against the 57 kg/cm^2 recorded with the tubes absent.

With shorter distances between the tube the phenomenon is attenuated, but with distance x = 6 cm the enhancement ratio is still 1.15.

A qualitative explanation of the phenomenon may be as follows : The wave colliding with the tubes is affected in the same way as a wave propagated in a cone, i.e. guided laterally by the walls of the two tubes, the particles are driven towards the centre and the wave emerges enhanced. After having travelled between the tubes the wave undergoes a lateral dilation which weakens it.

We then tried passing the wave through a lattice of 4 tubes of the ESSOR reactor type (see Fig. 39). The figure also shows the relative positions of the line charge and transducer. Fig. 40 gives the oscillograph for a pressure measurement and Fig. 41 the oscillograph signalled by the transducer with lattice absent but at the same distance from the charge. It will be seen that the pressure peak enhancement observed when only two tubes were present is far less conspicuous.

A transducer so positioned as to be "covered" by two tubes (Fig. 42) gave a signal (Fig. 43) wholly similar in

form to those described under head 3.1.1.

It was also desired to ascertain whether the enhancement phenomenon was evident with the arrangement as in Fig. 36 and x = 10 cm, but with the tubes filled with a gaseous medium (air, in our case).

The transducer signal is as shown in Fig. 44, and the pressure peak in this measurement is 149 kg/cm^2 (it should be observed here that all measurements quoted in this report were found reproducible within $\pm$ 5 %).

In this case, too, the enhancement effect is considerably lower.

3.1.3. Reflection of a wave from a pressure-tube

Various experiments in reflection from a tube simulating a channel were carried out.

The most pessimistic conditions were adopted as regards the intensity achieved by the reflected wave. The test channel is filled with water, is fixed at its two ends and is much shorter than a real channel, so that it is far more rigid than the real one ; its bulk movement will therefore be less, so that the reflected wave will be of maximum pressure. It was found that, predictably, the peak pressure of the reflected wave is a great deal lower, not only than that reflected from a heavy-gauge plate, but also than the pressure reflected from the thin sheet which had considerable bulk movement.

The arrangement is as in Fig. 45. The angle formed by the incident wave with the bisector of the angle of reflection was the same as in the previous tests, but the distances from linė charge to tube and from tube to transducer were shorter. In spite of this the pressure attained is 49 kg/cm^2 (Fig. 46).

This is easily explained by the fact that the angle of incidence varies rapidly along the periphery of the tube, and a minimal part of the wave is reflected in a direction

forming a reflection angle equal to the angle of incidence.

R E F E R E N C E S

(1) A. MASERATI, M. MONTAGNANI, G. VERZELETTI
"The Response of a Vessel to an Internal Blast Loading. - Limits of Model Tests - Influence of Strain-Rate."
Report EUR/C-IS/673/66 e

(2) J.H. BOWEN and E.V. GILBY - U.K.A.E.A.
"Review of Reactor Safety Problems due to Transient Pressure Generation - Appendix 2."

(3) R. SHARMAN
"Vibrations and Waves"
Butterworths

(4) P.W. BRIDGMAN
"The Pressure-Volume-Temperature Relations of the Liquid and the Phase Diagram of Heavy Water."
The Journal of Chemical Physics, Oct. 1935

(5) R. COLE
"Underwater Explosion."
Priceton, 1948.

(6) COURANT and FRIEDERICH
"Supersonic Flow and Shock Waves."

(7) K.P.S. STANYUCOVITCH
"Unsteady Motion of Continous Media"
Pergamon Press, 1960

(8) R.D. RICHTMYER
"Difference Methods for Initial Value Problems"
Interscience, N.Y.

(9) RINEHART, PEARSON
"Explosive Working of Metal"
Pergamon Press

(10) MELVIN A. COOK
"The Science of High Explosives"
Reinholds Publ. Co.

(11) H. HOLTBECKER, M. MONTAGNANI, G. VERZELETTI
"Full Scale Experiment on the Consequence of the Rupture of a Pressure Tube in Essor Reactor Vessel"
Report EUR/C-IS/683/66 e

(12) P. ACTIS DATO, H. HOLTBECKER, E. JORZIK, Y. LACHAPELLE, A. MASERATI, G. VERZELETTI
"Instrumentation for Rapid Mechanical Transients in Model Scale Experiments"
Report EUR/C-IS/698/66 e

(13) W.E. BAKER
"Scale Model Tests for Evaluating Outer Containment Structures for Nuclear Reactor"
Paper P/1028 Proc. Intern. Conf. Peaceful Uses of Atomic Energy - Geneva 1958

(14) J.W. HANNA, W.O. EWING JR., W.E. BAKER
"The Elastic Response of Models of Outer Containment Structures for Nuclear Reactors"
Nuclear Science and Engineering 6, 1959, pp. 214-221

(15) J.R. BOHANNON JR., W.E. BAKER
"Simulating Nuclear Blast Effect"
Nucleonics, March 1958

(16) F.B. PORZEL
"Some Hydrodynamic Problems in Reactor Containment"
Paper No. P/434 Proc. Intern. Conf. Peaceful Uses of Atomic Energy - Geneva 1958

(17) R.J. LARSON and W.C. OLSON
"Measurement of Air Blast Effects from Simulated Nuclear Reactor Core Excursion"
BRL Rep. No. 1102

(18) J.S. COLE, R.H. COLE, P.C. CROSS, J.P. SLIFKO, C.R. NIFFENEGGER, A.E. CHRISTIAN, and M.A. ROGERS
"Shock-Wave Parameters Measured Off the Ends and Perpendicular Bisector of Line Charges 25 ft. Long Containing 50 lb. of Flexed TNT."
Underwater Explosives Research Laboratory, Woods Hole Oceanographic Inst.

(19) E.N. FOX
"A Review of Underwater Explosion Phenomena"
Office of Naval Research - Department of the Navy

(20) E.H. KENNART
"Explosive Load on Underwater Structures as Modified by Bulk Cavitation"
Office of Naval Research - Department of the Navy

(21) Ya.B. ZELDOVICH and A.S. KOMPANEETS
"Theory of Detonation"
New York Academic Press, 1960

ACKNOWLEDGEMENTS

The authors would like to thank Mr. L. Guerri and Miss P. Stella for developing the calculating methods, the results of which are reported.

The discussions and suggestions of Messrs. M. Montagnani and G. Verzeletti were of great help.

Mr. Y. Lachapelle was in charge of all electronic apparatuses, Mr. P. Actis-Dato designed the experimental set-ups and assisted during the tests, and Mr. P. Brunella carried out the construction and assembly of the mechanical set-ups and assisted also during the tests.

Special thanks are due to Mrs. Doyen and Miss Zenner for the translation and preparation of the report.

APPENDIX

ELECTRONIC DETONATOR-FIRING DEVICE

(Y. Lachapelle)

It was necessary to have a noise-free firing device capable of initiating the detonator which in turn fires the line charge. Furthermore, a signal was needed that, at the instant of ignition of the charge, starts the oscilloscope traces through a delay-line.

The detonators used, of commercial type, are characterized by a response time, from the instant when the wire that fires the primary charge burns to the moment when the terminal section detonates, of about 57 μ sec, reproducible within a range of $\pm$ 4 μ sec.

It was then possible to devise an electronic circuit in which a condenser feeds current to the detonator, and from the instant its wire burns, the current decreases to zero in about 4 μ sec. This transient is used to trigger the delay-line.

The control circuit (Fig. 47) comprises a 2 N 1671 A unijunction transistor. The power circuit consists of the condenser C5 and the controlled silicon rectifier. The resistor R 13 picks up the triggering signal.

If I1 is closed, a single pulse switches the controlled silicon rectifier and a current passes abruptly into the detonator wire and R 13.

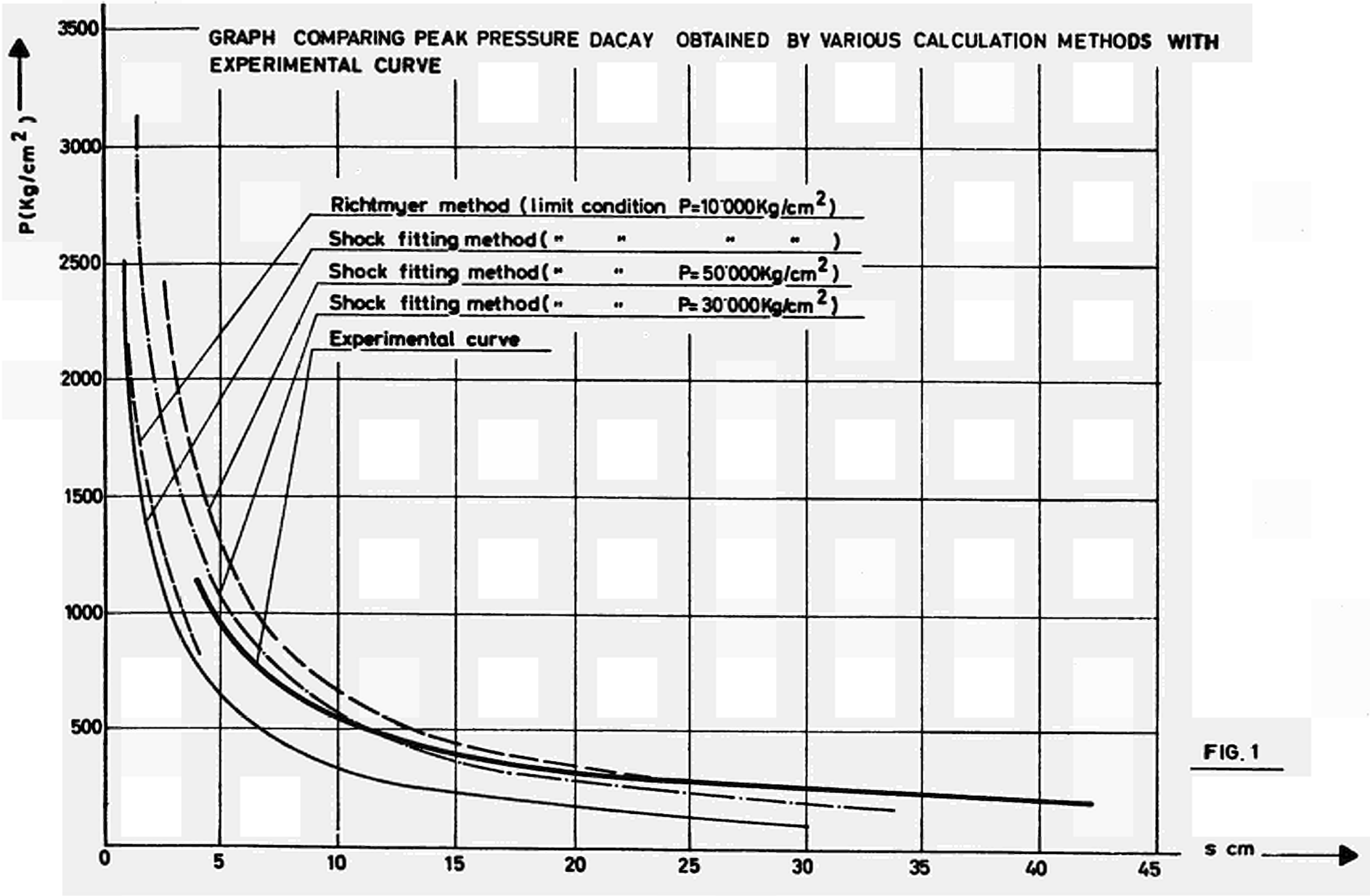
GRAPH COMPARING PEAK PRESSURE DACAY OBTAINED BY VARIOUS CALCULATION METHODS WITH EXPERIMENTAL CURVE
P(Kg/cm²)
3500
3000
2500
2000
1500
1000
500
0
5
10
15
20
25
30
35
40
45
s cm
Richtmyer method (limit condition P=10'000Kg/cm²)
Shock fitting method(" " " ")
Shock fitting method(" " P=50'000Kg/cm²)
Shock fitting method(" " P=30'000Kg/cm²)
Experimental curve

FIG. 1

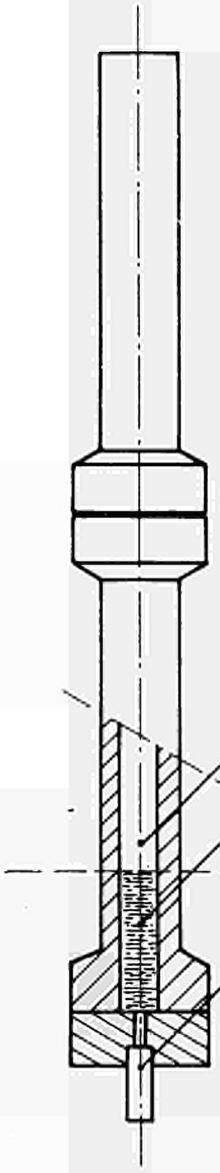

FIG. 2 GAS-WATER SHOCK TUBE IN VERTICAL POSITION

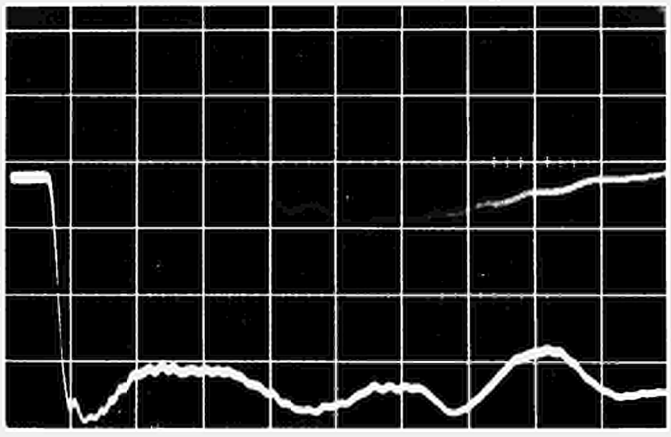

FIG. 3 CALIBRATING TEST ON GAS SHOCK TUBE FOR TRANSDUCER USED IN THE EXPERIMENTS ILLUSTRATED IN FIGS. 4 ÷ 13

→ 2 μsec/square

→ 10 μsec/square

PRESSURE 120 kg/cm²

FIG. 4

10 μ sec/square

TRAVEL IN WATER 55cm

FIG. 5

10 μ sec/square

TRAVEL IN WATER 90 cm

WAVE FRONT RISE TIME INCREASING WITH DISTANCE OF TRAVEL IN WATER (PRESSURE 20 kg/cm²)

FIG. 6

20 μ sec/square

TRAVEL IN WATER 125 cm

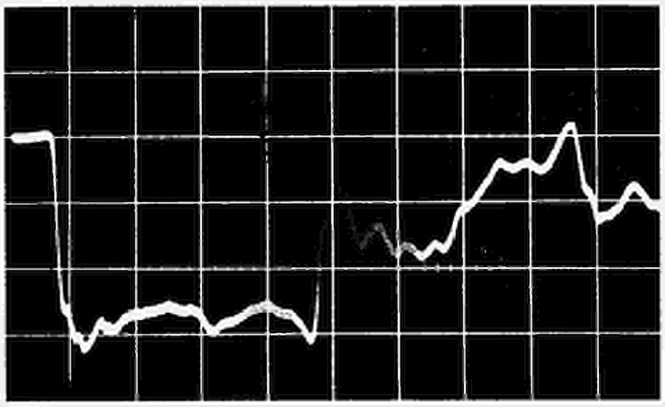

Fig. 7
travel in water 3 cm
pressure 120 kg/cm^2

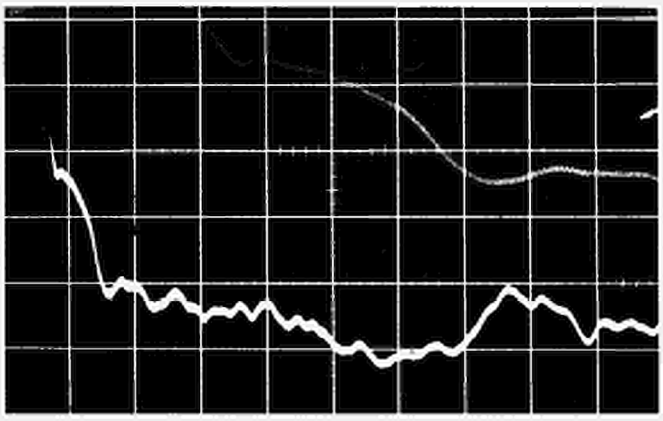

Fig. 8
travel in water 55 cm
pressure 120 kg/cm^2

WAVE FRONT RISE TIME INCREASING WITH DISTANCE OF TRAVEL IN WATER

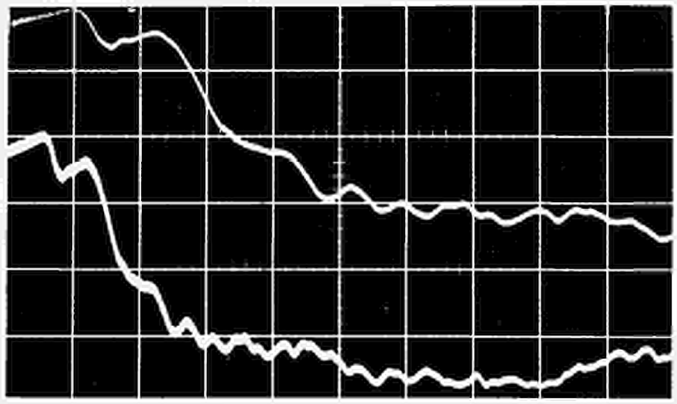

Fig. 9
travel in water 90 cm
pressure 120 kg/cm^2

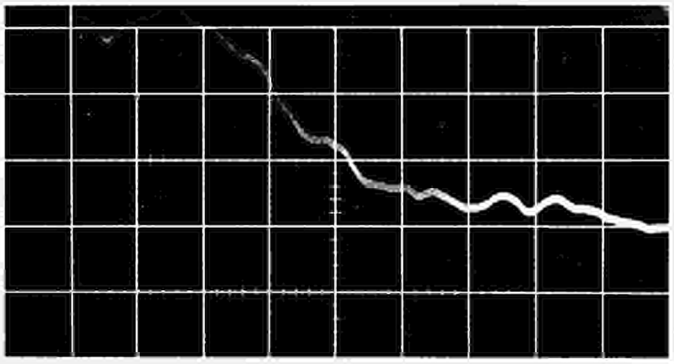

Fig. 10
travel in water 125 cm
pressure 120 kg/cm^2

WAVE FRONT RISE TIME INCREASING WITH
DISTANCE OF TRAVEL IN WATER

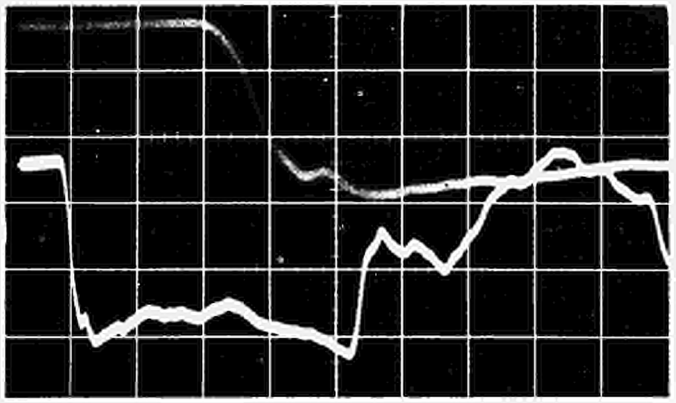

Fig. 11
travel in water 3 cm

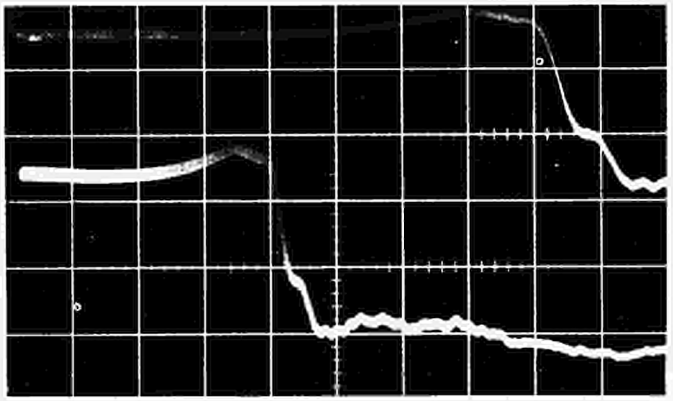

Fig. 12
travel in water 55 cm

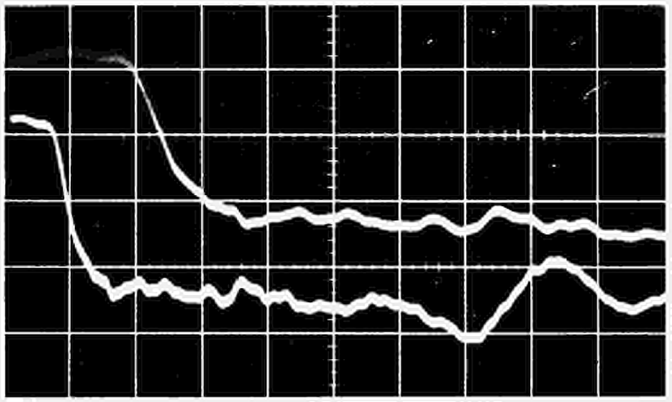

Fig. 13
travel in water 125 cm

WAVE FRONT RISE TIME INCREASING WITH
DISTANCE OF TRAVEL IN WATER
pressure 475 kg/cm^2

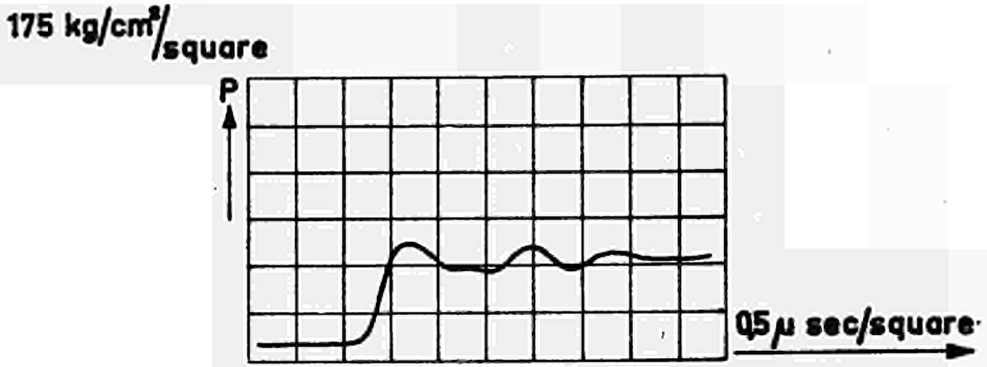

FIG. 14

CALIBRATING TEST IN GAS SHOCK TUBE FOR TRANSDUCER USED TO RECORD THE PROFILE SHOWN IN FIG. 15

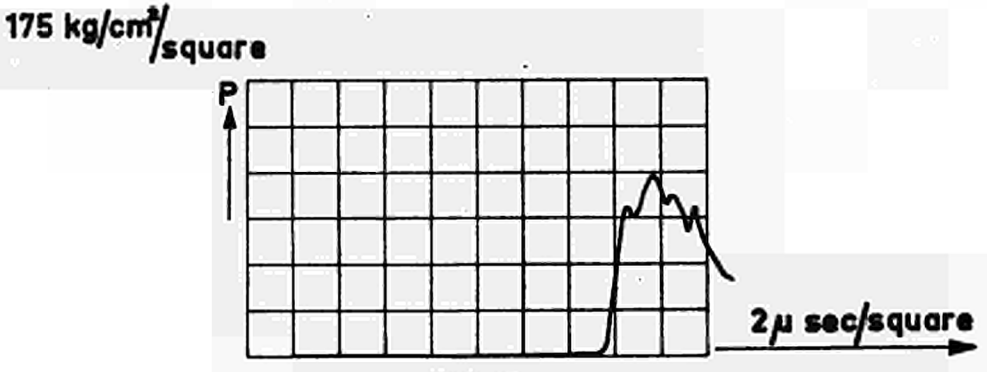

FIG. 15

PRESSURE RECORD SHOWING RISE TIME OF PRESSURE WAVE IN WATER

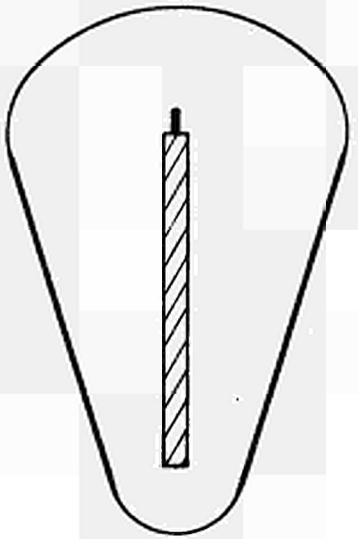

FIG. 16

SHAPE OF THE SHOCK WAVE THROWN OUT BY A LINE CHARGE IN WATER.
(FROM R.H. COLE–UNDERWATER EXPLOSIONS)

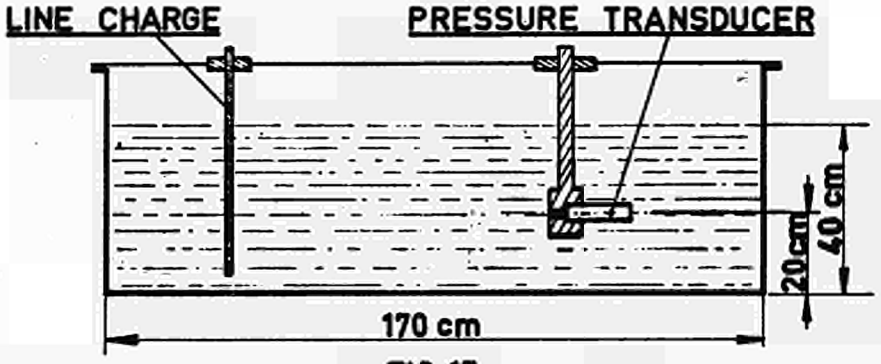

FIG. 17

RECORDING THE PRESSURE WAVE EMITTED BY LINE-CHARGE. DIAGRAM OF EXPERIMENTAL SET–UP

——— Peak pressure decay vs. distance of the shock wave thrown out by a PETN line charge of 10g/m measured along the perpendicular bisector. Length of the charge: 40 cm, vertically positioned
The pressure points refer to the wave at moment of reflection on steel plate
– – – – Peak pressure presumed values, in the same conditions, for the incident wave.

FIG. 18

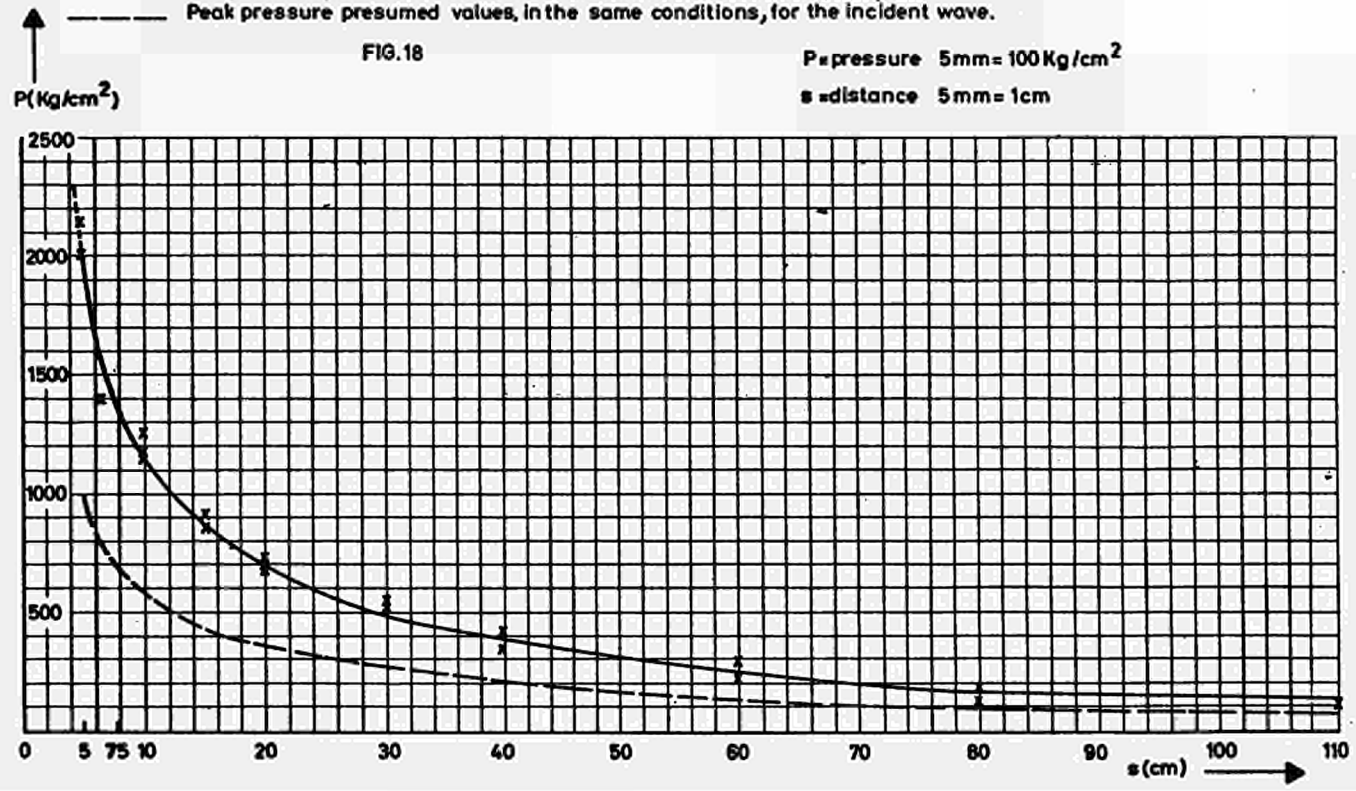

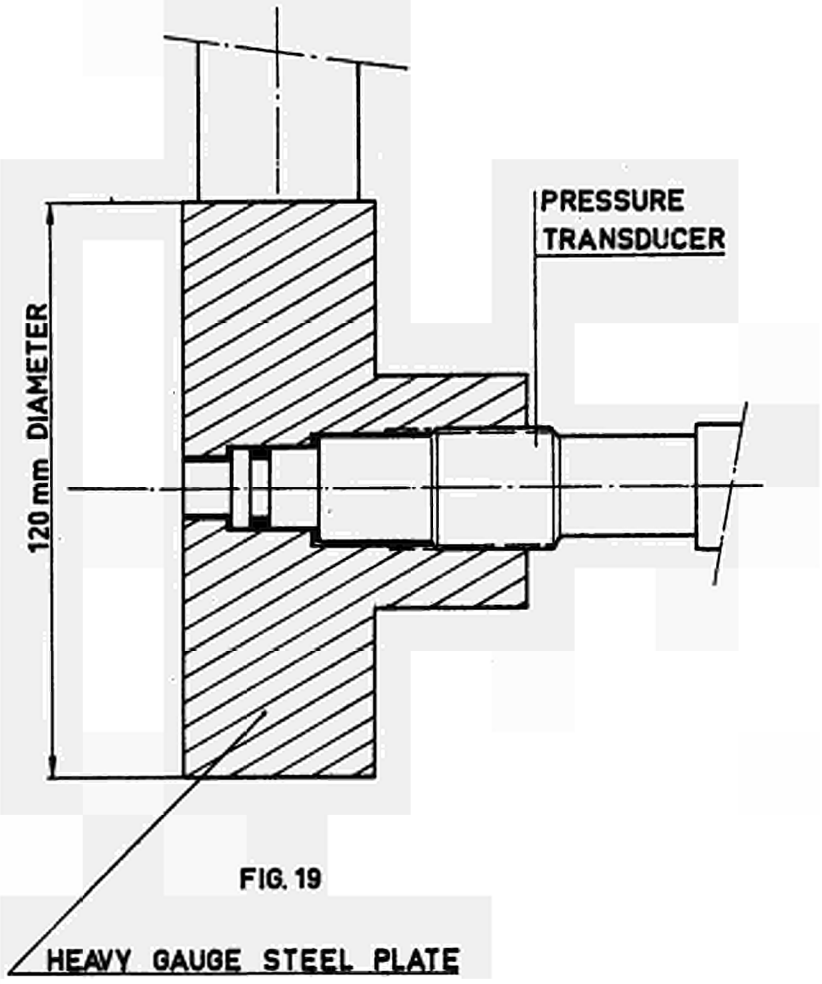

FIG. 19

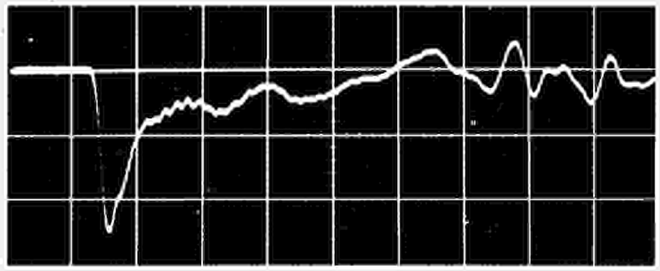

Fig. 20
transducer without plate

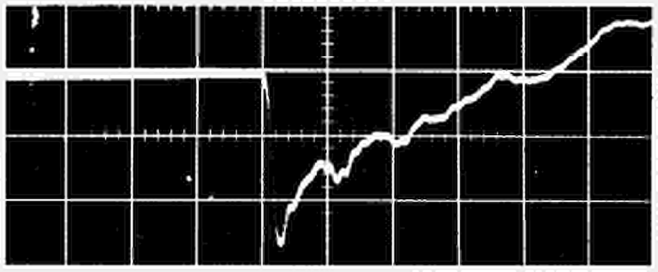

Fig. 21
transducer with plate

COMPARISON OF TWO PRESSURE RECORDS:

- Transducer without plate
- Transducer mounted on plate as in Fig. 19

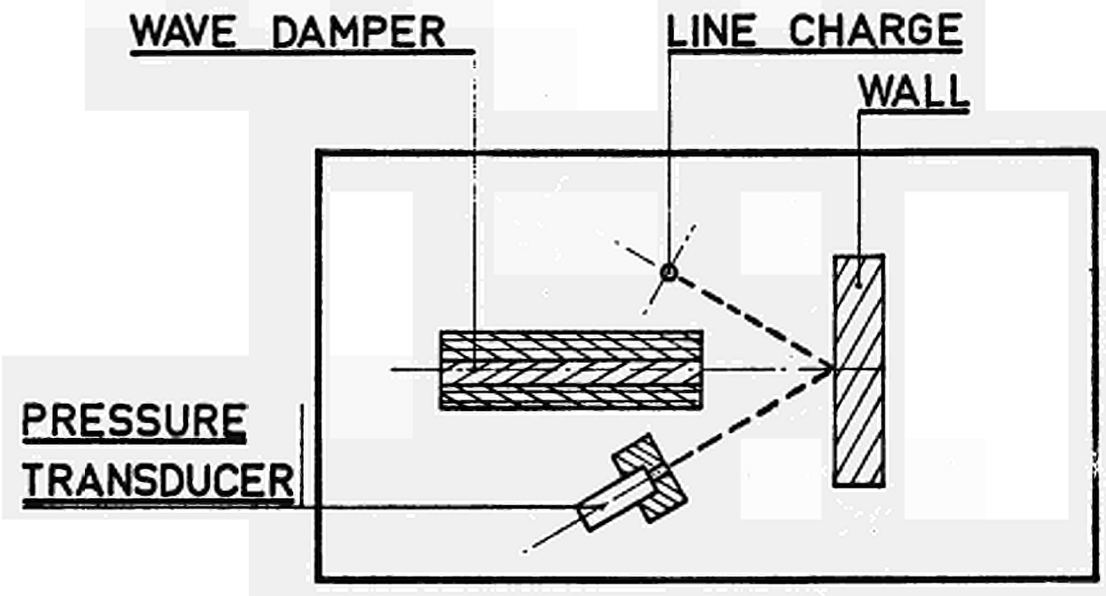

FIG. 22

RECORDING THE PRESSURE-WAVE REFLECTED BY A THICK PLATE: DIAGRAM OF EXPERIMENTAL SET-UP

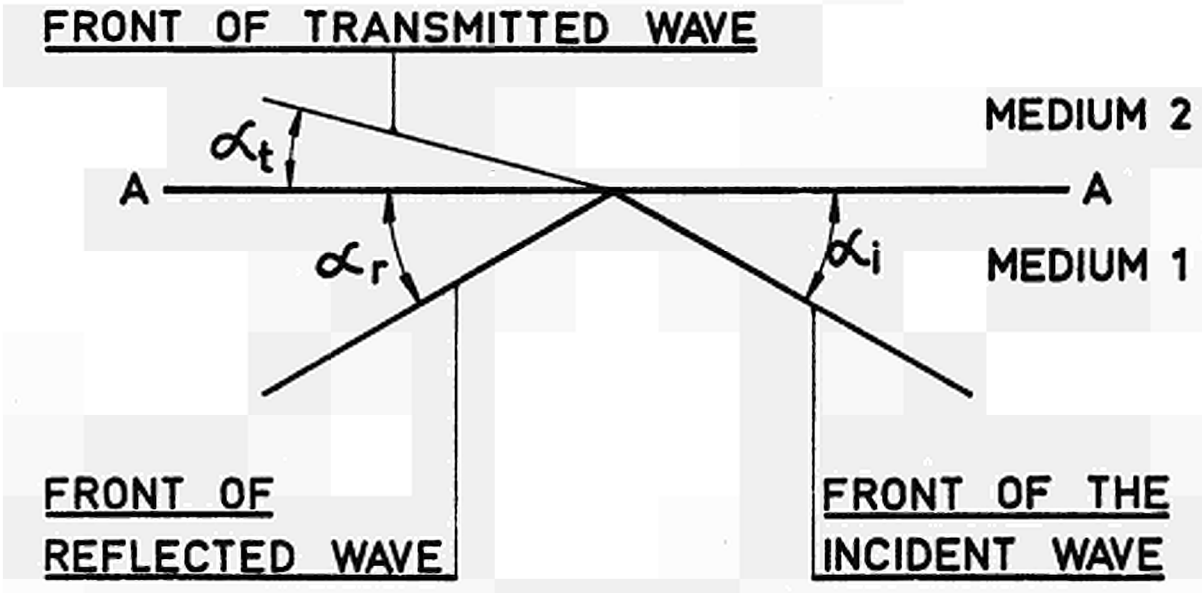

FIG. 23

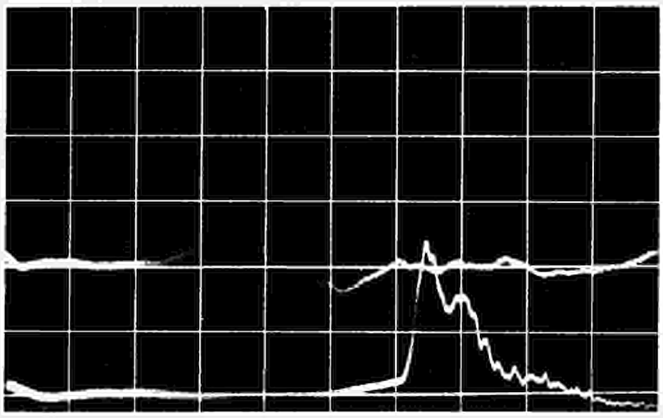

Fig. 24
reflected wave

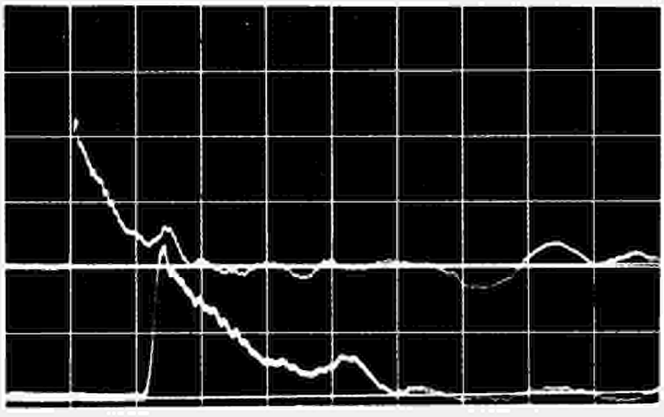

Fig. 25
non-reflected wave

COMPARISON OF CURVES FOR:

- pressure of a wave reflected from a thick steel plate
- pressure of a non-reflected wave measured over same distance

FIG. 26

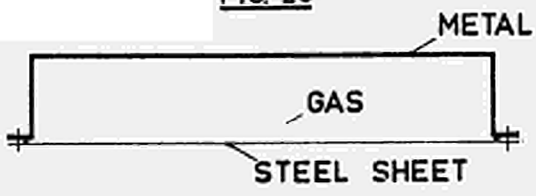

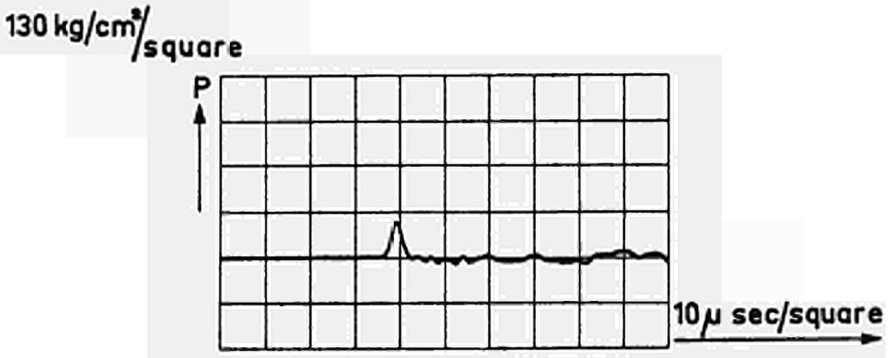

FIG. 27

RECORD OF PRESSURE WAVE REFLECTED FROM STEEL SHEET (SEE FIG. 26)

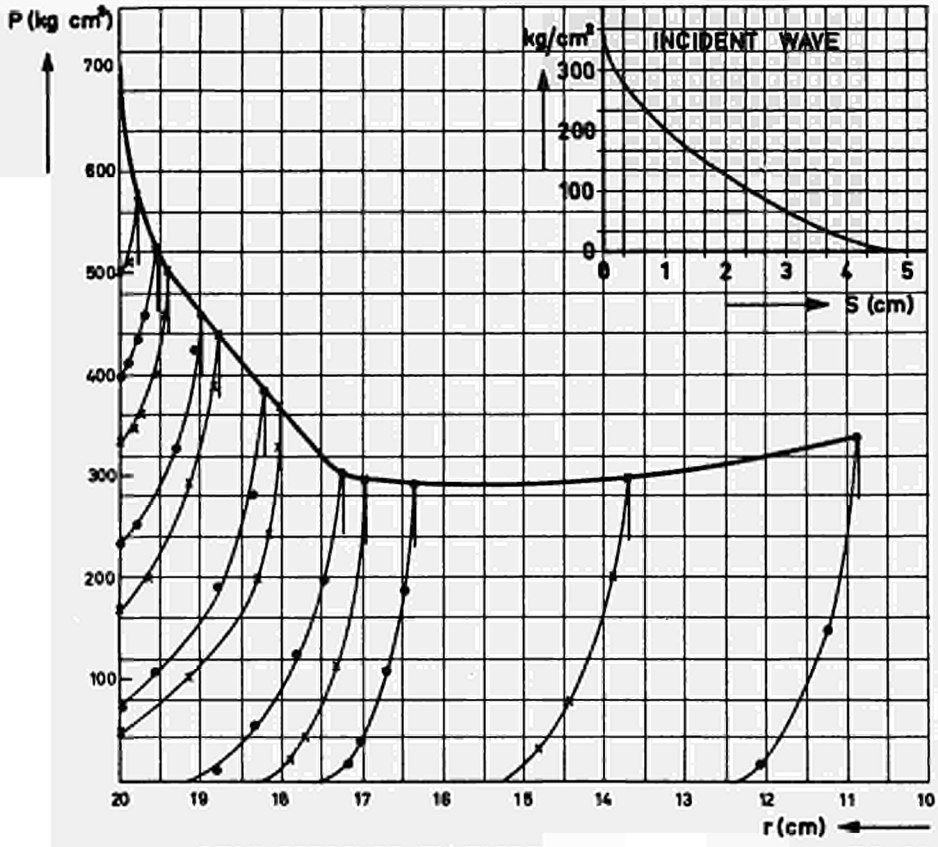

FIG. 28

EVOLUTION OF A CYLINDRICAL PRESSURE WAVE REFLECTED FROM A CYLINDRICAL WALL, AS A FUNCTION OF DISTANCE

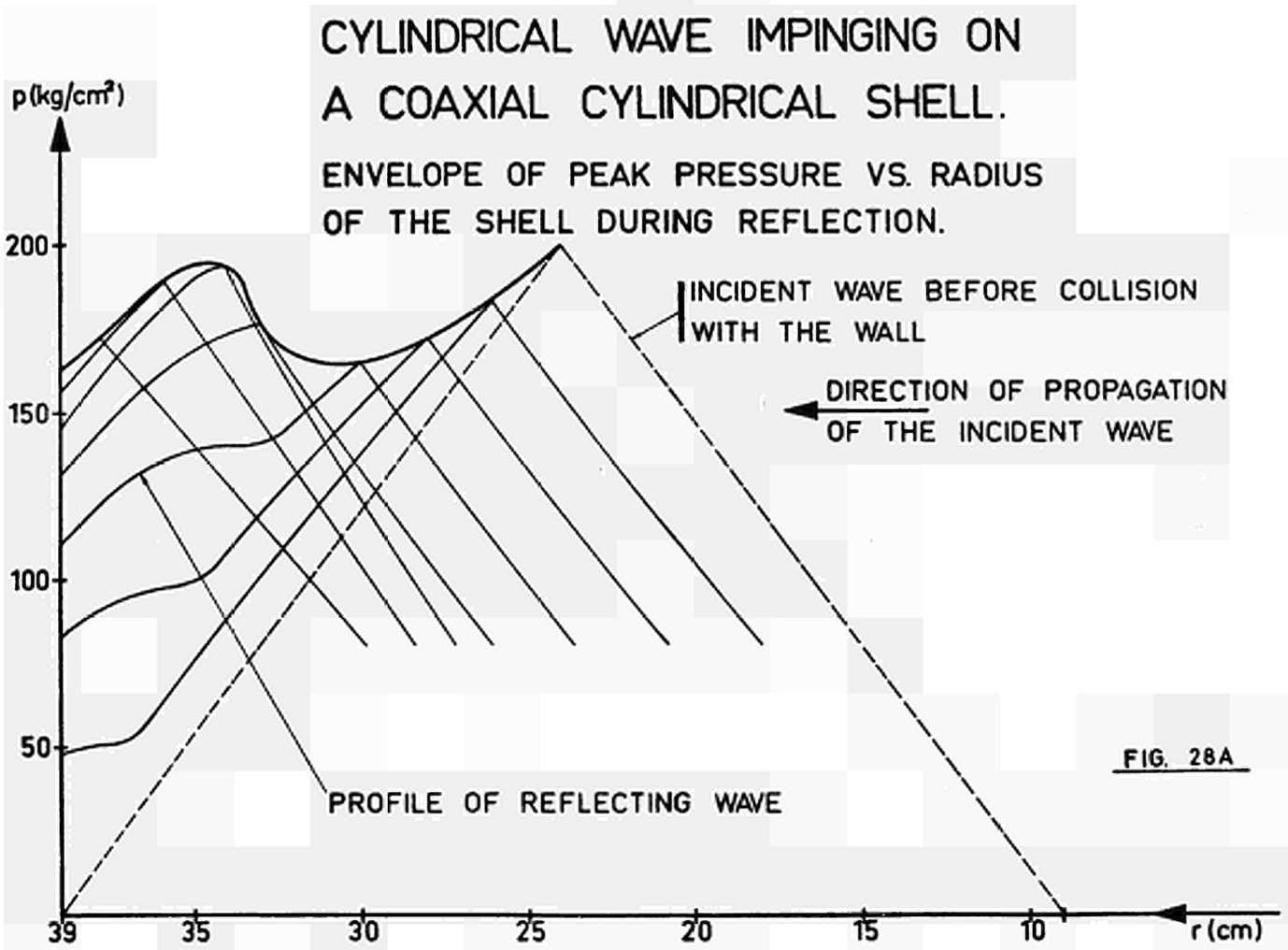

FIG. 28A

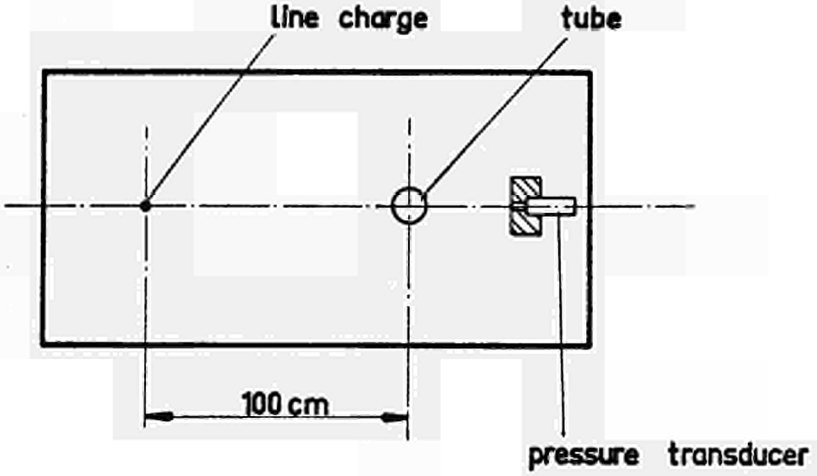

FIG. 29

SHOWING SHADOW AREA AND WAVE DIFFRACTION

EXPERIMENTAL SET – UP

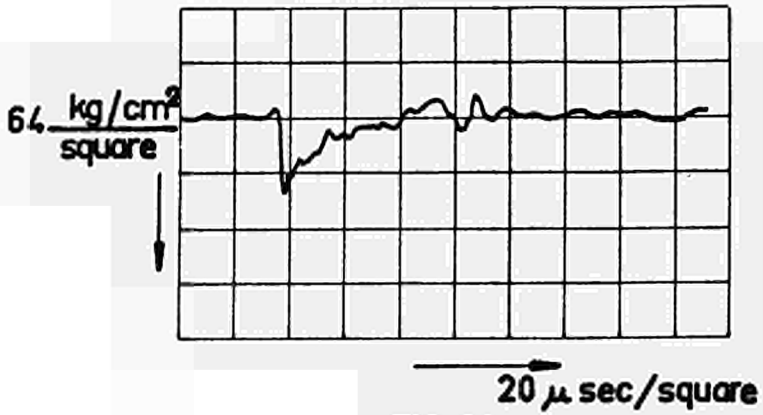

FIG. 30

PRESSURE RECORD OF WAVE AFTER TRAVELLING UNDISTURBED

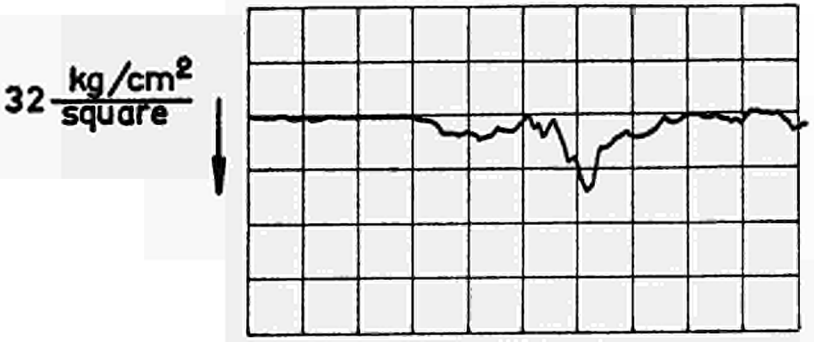

FIG.32

PRESSURE VERSUS TIME OF WAVE RECORDED AT 1/2 DIAMETER BEHIND WATER-FILLED TUBE

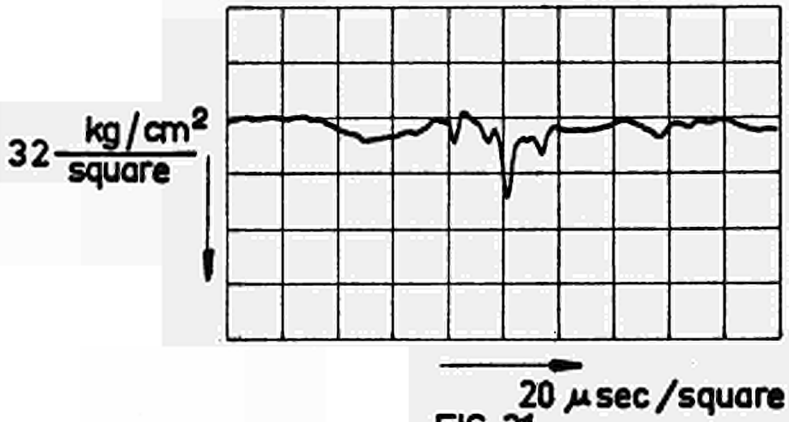

FIG. 31

PRESSURE VERSUS TIME OF WAVE RECORDED AT 1/10 DIAMETER BEHIND WATER-FILLED TUBE

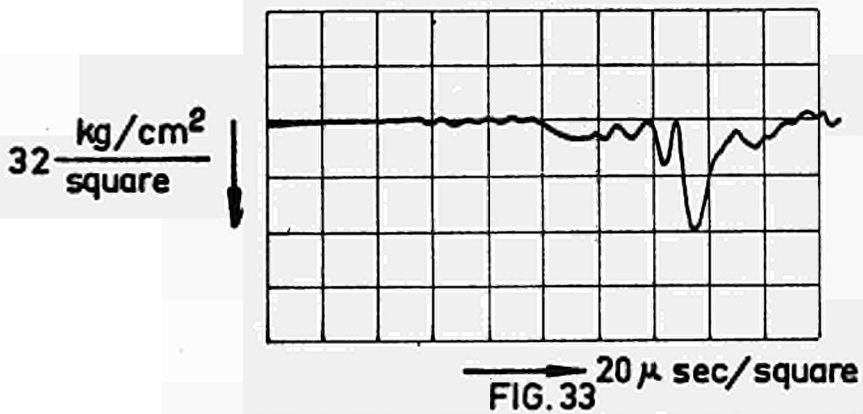

FIG. 33

PRESSURE VERSUS TIME OF WAVE RECORDED AT 1 DIAMETER BEHIND WATER-FILLED TUBE

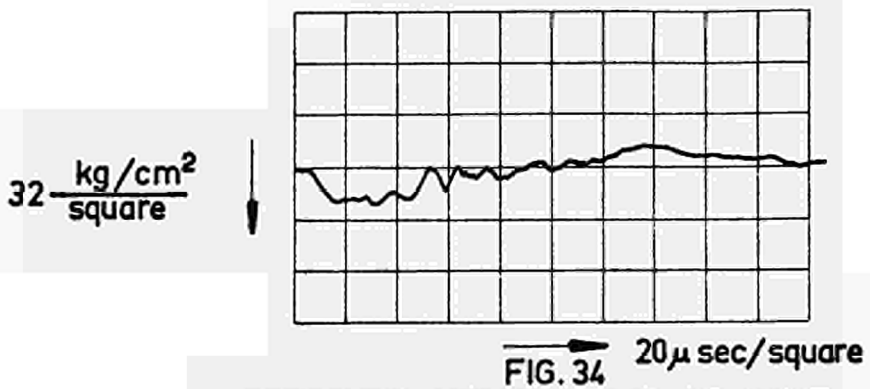

FIG. 34
PRESSURE VERSUS TIME OF WAVE RECORDED AT 1/10 DIAMETER BEHIND GAS-FILLED TUBE

FIG. 35
PRESSURE VERSUS TIME OF WAVE RECORDED AT 1 DIAMETER BEHIND GAS-FILLED TUBE

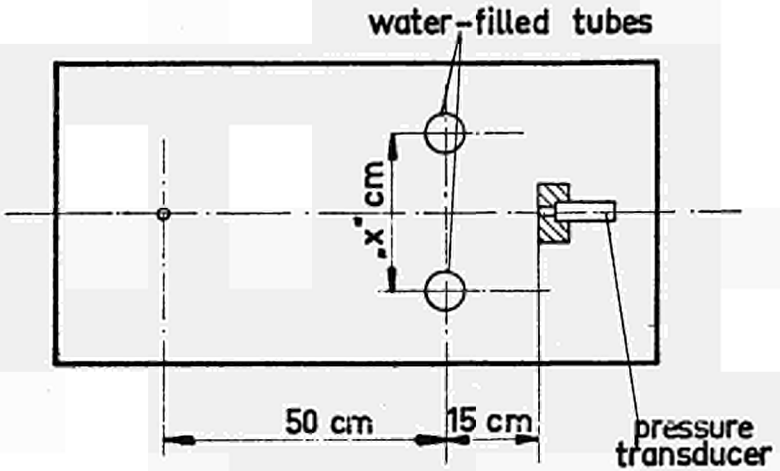

FIG. 36
RECORDING THE PRESSURE WAVE AFTER TRAVELLING BETWEEN TWO TUBES

EXPERIMENTAL SET-UP

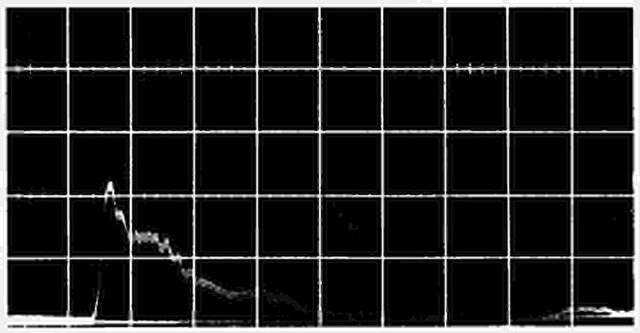

Fig. 37

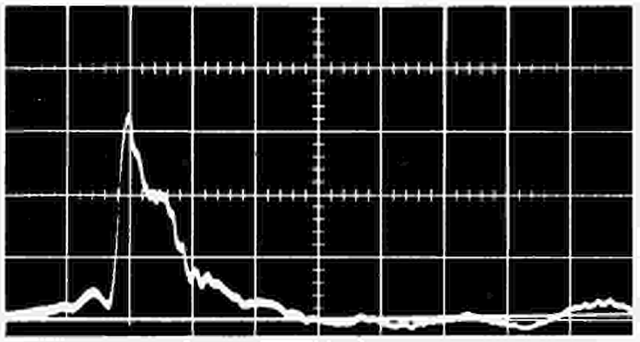

Fig. 38

PEAK-PRESSURE COMPARISON:

Fig. 38 - wave after travelling in the space between two water-filled tubes

Fig. 37 - wave after travelling undisturbed for the same distance

FIG. 39

EXPERIMENTAL SET-UP FOR STUDY OF INFLUENCE OF NETWORK ON PRESSURE WAVE

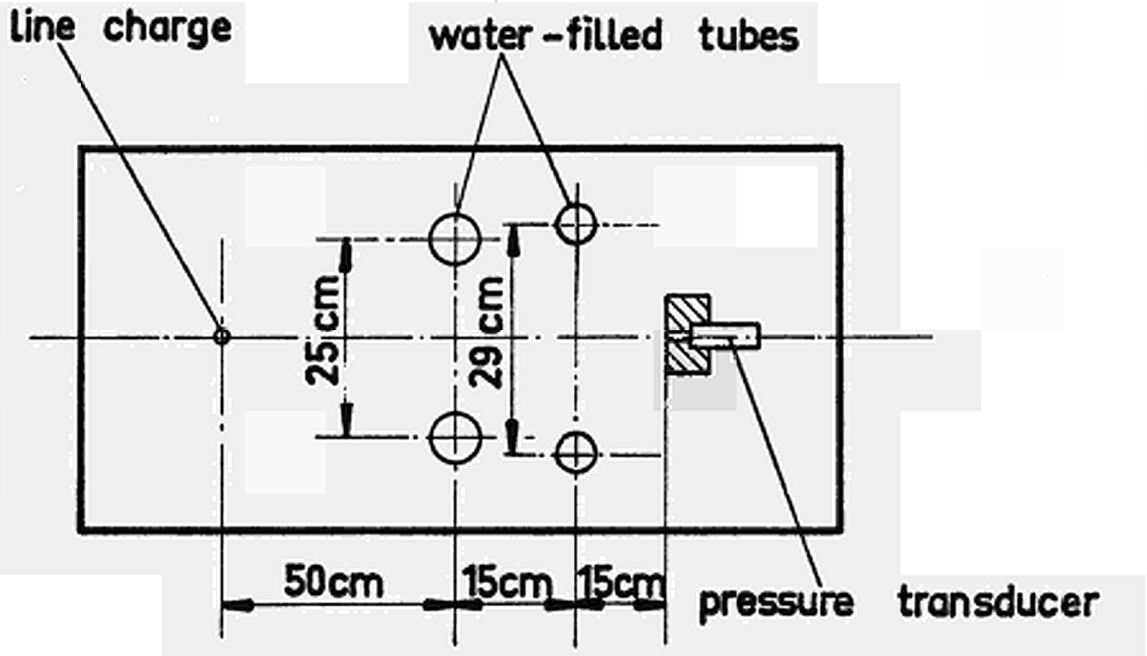

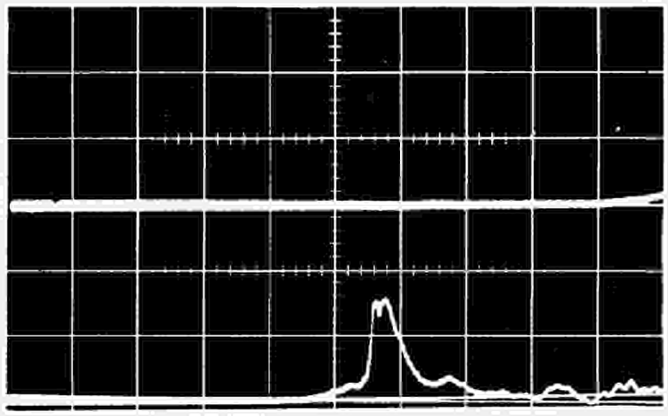

Fig. 40
wave after travelling through network

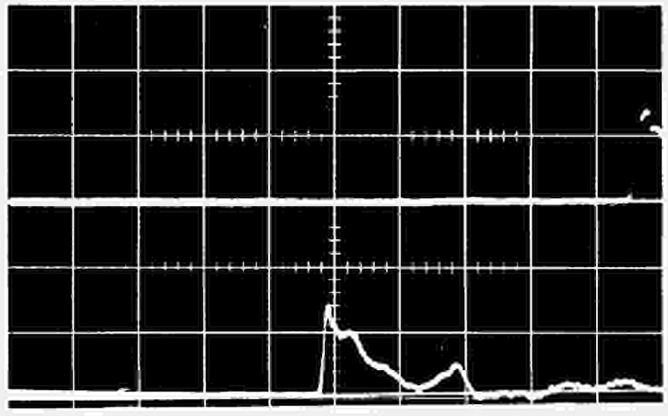

Fig. 41
wave after travelling undisturbed

PEAK-PRESSURE COMPARISON:

- wave after travelling through network of tubes as in Fig.39
- wave after travelling undisturbed for the same distance

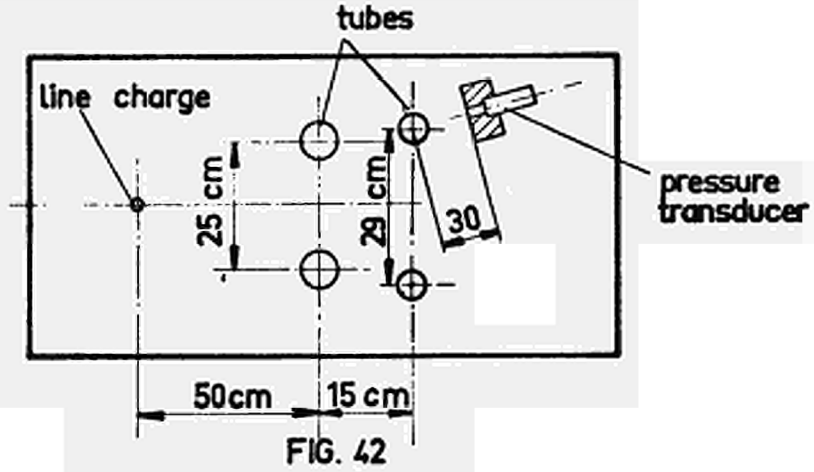

FIG. 42

EXPERIMENTAL SET-UP

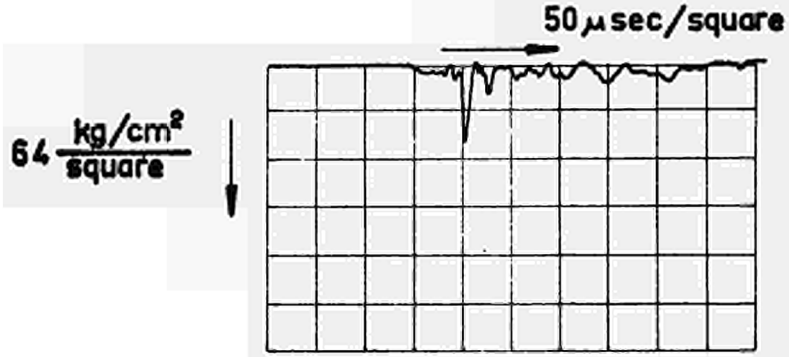

FIG. 43

PRESSURE RECORD OF WAVE AFTER TRAVELLING THROUGH NETWORK AS IN FIG. 42

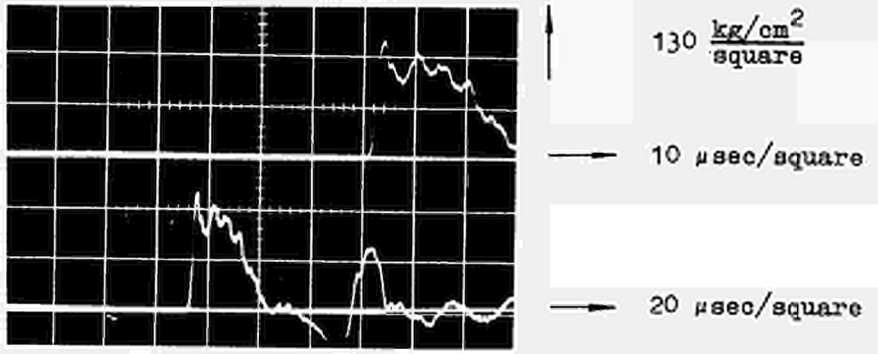

Fig. 44

PRESSURE RECORD OF WAVE AFTER TRAVELLING BETWEEN TWO GAS-FILLED TUBES

FIG. 45

EXPERIMENTAL SET-UP

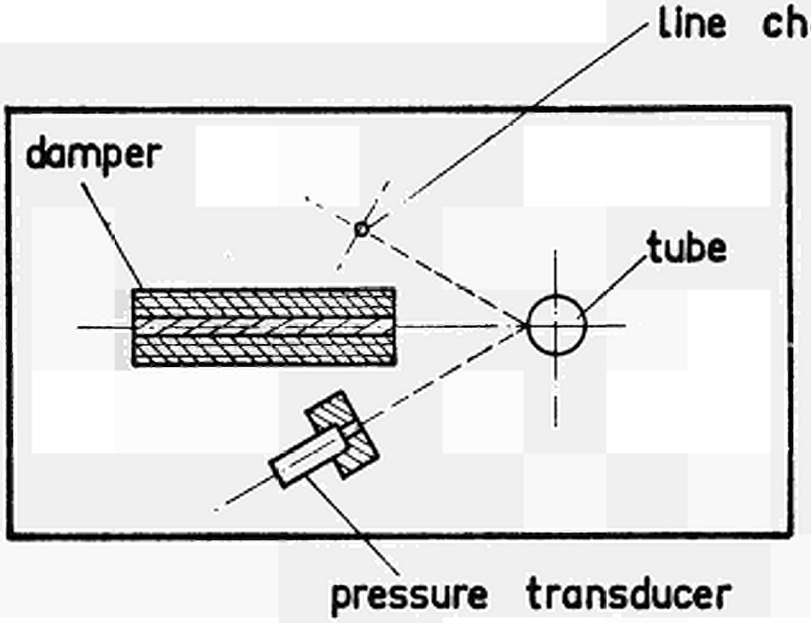

FIG. 46

RECORD OF WAVE REFLECTED FROM WATER-FILLED TUBE AS SHOWN IN FIG. 45

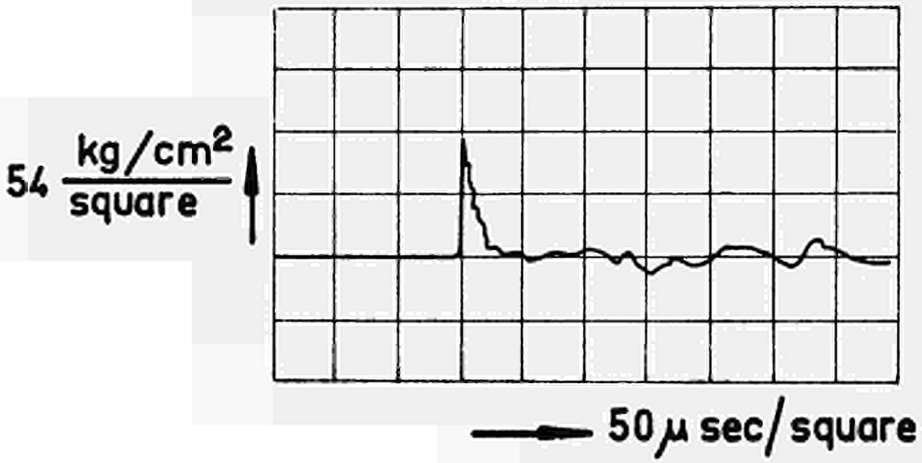

ELECTRONIC DETONATOR FIRING DEVICE
CIRCUIT LAYOUT

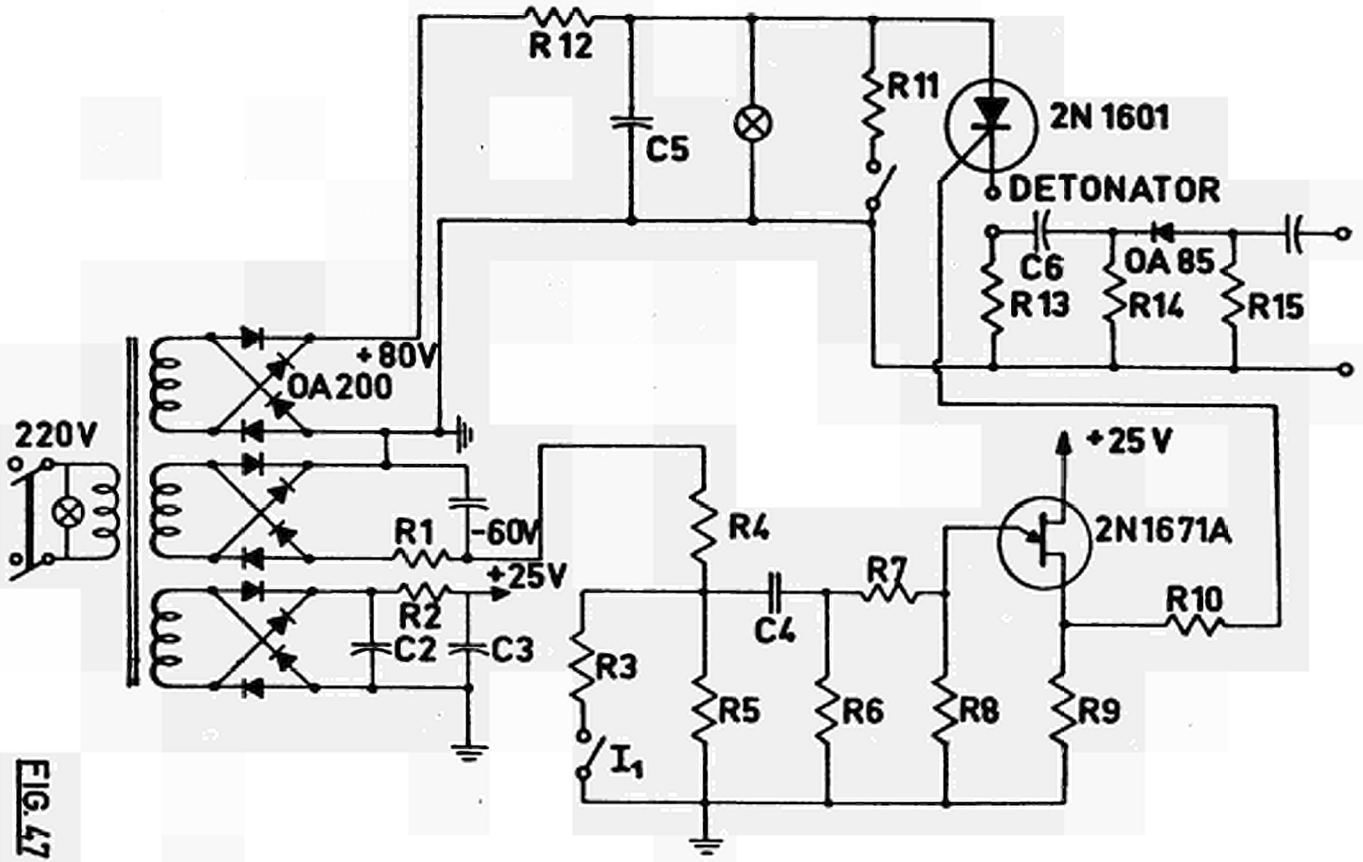

FIG.47

SHOCK WAVES AND TRANSIENT LOADING FROM CHEMICAL REACTIONS

by

J.G. Moore
U.K.A.E.A., Risley
United Kingdom

Design problems can arise in any system in which shock waves can be produced and transient loading occur as a result. There are a number of possible causes of such shock waves including chemical reactions, the sudden release of a pressurized medium and the rapid conversion of thermal energy into mechanical energy. This paper is chiefly concerned with the problems arising from chemical reactions.

The Sodium-Air Reaction

One hazard which has been envisaged in sodium cooled reactors in the release of a fine spray of sodium which partly fills an air filled enclosure. The problem is to estimate the transient loading on the enclosure during combustion of the sodium; this has been reported in ref. (1). The pressures produced when sodium is uniformly dispersed throughout the enclosure may be obtained from experimental work done in the U.S. ref. (2).

Form of Combustion

The basic mechanism for shock wave formation during combustion is the expansion of combustion products producing compression of the surrounding gas in the form of pressure waves. The pressure waves may be formed immediately as shock waves or may subsequently coalesce to form shock waves as they travel out from the combustion region, depending on the rate of reaction considered.

The problem of calculating the formation of shock waves from the combustion of a fuel air mixture can be described by a set of partial differential equations which cannot be solved analytically. The usual method of solution, known as the method of characteristics, consists of constructing a wave diagram which shows the propagation of the pressure waves. The method can become tedious, especially when the entropy of the system is varying but in some cases certain simplifying assumptions can be made which enable wave diagram construction to be limited to certain regions or eliminated entirely. These assumptions form the basis of the three methods of calculations.

The simplest and most pessimistic assumption is that the combustion takes place instantaneously throughout the whole mixture. This is the basis of the "instantaneous combustion model".

The second model assumes that chemical reaction takes place instantaneously as the unburned gas passes through an advancing flame front. This is referred to as the "flame front model".

The third model assumes that combustion is taking place uniformly throughout the volume involved but at a finite rate. This is the "uniform combustion model".

Since the kinetics of the sodium-air system are not known the results from all three theoretical models were compared and their relevance assessed. In order to simplify the calculations spherical symmetry was assumed for the combustion zone and enclosure; this enabled the attenuation due to three-dimensional spreading of the shock system to be calculated fairly easily. The pressure on the enclosure was calculated by adding the momentum of the gas behind the wave to its static pressure profile.

The shock pressures were calculated as a function of mass of sodium released and size of enclosure which was characterised by a linear dimension. The flame front model gave very low pressures as was expected. The uniform combustion model gave pressures which varied up to a maximum of about 2 atmospheres assuming a total combustion time of 30 msec. This was the shortest experimentally measured time of reaction. The instantaneous combustion model produced pressures up to a maximum of about 14 atmospheres. The results are shown in fig. (1) for stoichiometric mixtures of sodium and oxygen. Calculations were also done for different molar ratios of sodium to oxygen. The shock pressure was found to be relatively insensitive for ratios greater than unity, as shown in fig. (2). This is because dilute mixtures correspond to large initial volumes which therefore means less attenuation of the shock wave due to three-dimensional spreading.

The rate of reaction between sodium and air is a function of the temperature and the rate of exposure of the sodium surface which in turn depends upon the mass of sodium involved and the degree of dispersion. In the experiments described in ref. (2) liquid sodium was explosively injected into a vessel. It might be expected that the injection energy would increase the surface to volume ratio of the sodium and hence reaction rate. It was

found however that provided the injection energy was greater than about 5 cal/gm of sodium, the peak pressure produced were relatively insensitive to variations in injection energy. The highest peak pressures occured however when the injection energy per unit weight of sodium was greatest.

Humphreys has suggested that the insensitivity of peak pressure to ejection energy is due to a secondary dispersion mechanism. The explosive ejection of finely divided sodium into a large atmospheric volume leads to an intense local heating about the point of injection. This results in a violently expanding turbulent gas zone within which a large portion of the ejected sodium is trapped. This secondary dispersion phenomenon has the characteristic of a mild explosion ignited by the initial sodium reaction. Once initiated, the thermal expansion dispersion mechanism is progressive. As the larger sodium particles are broken apart, the resulting increase in reaction rate supplies additional energy to the expanding gas zone, thus promoting further breakdown and dispersion of the entrapped sodium particles.

It will therefore be seen that none of the theoretical models explains this phenomenon in detail but is partly described by the uniform combustion model and partly by the instantaneous combustion model.

In the design of the containment vessel for a nuclear reactor the instantaneous combustion model would certainly provide the most pessimistic values of pressure. The restriction on design may not be too severe for the case of small amounts of sodium producing a relatively small combustion region though undoubtedly this approach is over-pessimistic when the theoretical combustion region almost fills the containment vessel. In this latter case it is suggested that the uniform combustion model be used; the calculation being done at least to the point where the shock front first reaches the wall.

The existing measurements by Humphreys apply only to the case where the sodium is mixed, relatively uniformly throughout the whole test volume. A more realistic test as regards reactor containment design, and which would also confirm the appropriateness of the various models, could be performed in which sodium was dispersed locally in a much larger volume of confined air.

Explosion Hazard Following a Release of Hydrogen into a Reactor Containment (Ref. 3)

In a water cooled reactor a loss of coolant due say to a fracture in the primary circuit can cause fuel overheating which can in turn lead to a metal-

water reaction which will liberate hydrogen. The hydrogen produced may react with the air in the containment system and it is the purpose of this section to consider the possible hazards from this reaction.

When hydrogen is released into a vessel containing steam and air the possibility exists of spontaneous ignition. If the hydrogen burns as it enters the containment volume additional energy will be released. In any calculations of pressure therefore this additional energy will have to be included in the heat balance for the containment. The rate of burning in this instance will be determined by the rate of metal water reaction. Provided the rate of heat release from hydrogen burning is not too large compared with the rate of loss of heat from the system the pressure rise should be much less than the explosion pressure rise.

If however hydrogen collects in the containment instead, then an explosion could occur which may destroy the building. The spontaneous ignition of the hydrogen-steam mixture as it escapes into the containment will depend on the temperature of the escaping mixture and the proportion of hydrogen in the mixture. Since these quantities are likely to be different for every accident, in any safety assessment it would seem necessary to assume that the hydrogen did not react with the air as it escaped.

The results of the theory of spontaneous ignition and the limited available data indicated that spontaneous ignition was unlikely to occur when the hydrogen collected in the containment. It is necessary therefore to consider initiation of an explosion by external means. However since the spark ignition energy requirements are so small it must be considered in any safety analysis that a large enough spark would be available to cause an explosion if the other conditions are favourable. The flammability limits of the hydrogen-air-steam mixture were also estimated from the limited data available.

The explosion pressure was calculated for mixtures lying within the flammable limit by assuming adiabatic conditions. The heat generated by combustion was equated with the heat of dissociation of combustion products and the heat required to raise the temperature of the final mixture to the final temperature. The final pressure was then the sum of the partial pressures of the constituents at this temperature.

Calculations of this type were carried out for a typical PWR with a high pressure, low leakage containment design, typical parameters are given in

Table I. It was not possible to do a typical case for a BWR or SGHWR since the distribution of air is not fixed as with a PWR due to the use of pressure suppression containment.

TABLE I

TYPICAL PWR PARAMETERS

Thermal power	=	1500 MW
Mass of primary water	=	450,500 lb.
Mass of UO_2 fuel	=	168,000 lb.
Mass of zirconium clad	=	25,000 lb.
Can surface area	=	34,000 $ft.^2$
Net containment volume	=	1.5×10^6 $ft.^3$
Cooler area	=	19,000 $ft.^2$
Cooler inlet temperature	=	18^oC
Cooler heat removal capacity/unit	=	1 MW at 90^oF containment temp.
	=	18.8 MW at 250^oF containment temp.

Calculations were performed of the containment pressure during depressurisation as a function of time following a fracture of the primary circuit. The results are shown in fig. (3) with various assumptions about the emergency heat removal capacity. It should be noted that a high concentration of steam and hence a high containment pressure is effective in preventing an explosion.

The mass of hydrogen liberated as a function of time was specified in fig. (4). Curve B, represents hydrogen generation with no cooling to the cladding during blowdown and unlimited steam for the reaction whereas A2 represents cooling during blowdown with a limited supply of steam. The intersection of the curve of required hydrogen and hydrogen produced from the metal-water reaction gives a time at which a hydrogen explosion is first possible. The final explosion pressures calculated were about 60 to 80 psia.

These calculations however assume a uniform distribution of hydrogen; if non-uniform concentrations are assumed to occur then a calculation similar to the one for the sodium air case can be carried out. This mode of explosion in which a local concentration burned very quickly and in expanding produced

a shock wave was found to give pressures about 200 psia using the instantaneaous combustion model. These shook pressures are shown in fig. (5).

In addition to explosion there is the possibility of detonation in which the chemical reaction takes place in a shock wave travelling through the gas. Available theories on detonationhave been extended to the hydrogen-air-steam mixtures without any experimental confirmation. In particular the detonation limits for various mixtures were computed and also the detonation pressures if these mixtures were ignited. The detonation pressures were found to be several hundred psia. However, because detonation in free space requires at least an initiation energy of several joules as compared with millijoules for an explosion and the fact that steam is a very efficient diluent, detonation is less likely to occur.

When explosion occurs due to a combustion wave travelling through the mixture, the pressure is more or less uniform throughout the volume though increasing with time until the whole mixture is burnt. The rate of rise of pressure on the vessel wall will determine whether the loading is effectively applied statically or under transient conditions. The rise time of an explosion in a typical PWR vessel will always be greater than about a second for all conceivable hydrogen-air mixtures. Since the natural period of vibration of the vessel will be very much less than this the loading can obviously be treated as if applied statically.

Shock waves generated from local pockets will have a duration depending on the original size of the pocket so that each case would have to be considered separately. Very approximately the duration of the pulse will be the time taken for a rarefaction wave to travel the diameter of the local pocket before explosion, assuming the theoretical model of instantaneous combustion.

In the case of a detonation wave as with most shock waves the leading edge is a pressure discontinuity and therefore loads the structure dynamically. However, the actual duration of the pulse will probably depend on the configuration, mixture composition and shock strength. Experimental measurements made of stoichiometric hydrogen-oxygen mixtures showed that the pressure fell exponentially after the initial peak. If the presssure at any point is written therefore as $P = P_o e^{-t/T}$, where t represents time and T the time taken for the pressure to fall by a factor e, then ref. (4) showed for stoichiometric mixtures that T was about 220 microseconds. This type of pressure time profile is identical to that of shock waves generated from conventional high explosives.

The Hazard Associated with a Sodium-Water Reaction in a Sodium Heated Steam Generator

Most present day designs of heat exchangers for sodium cooled reactions have a single tube arrangement rather than a double walled construction separating the sodium and water. This produces a saving of capital costs but also leads to an increased possibility of a tube leak leading to a sodium-water reaction.

If a leak occurred then shock pressures can arise from the expanding hydrogen bubble formed from the chemical reaction. It can be shown ref. (5) using a simplified mathematical model that the maximum pressure in the sodium surrounding the hydrogen bubble is given by $p_{max} = 500\ W^{1/2}/r$ psi, where W is the leak flow rate in lb/sec. from the pressurized water tube and r the distance in in. from the fracture. Thus if the flow rate is 20 lb/sec. the pressure will be 500 psi at a distance of 4.5 in., which on reflection will produce a pressure of 1000 psi. Dynamic analysis of the hydrogen gas bubble formed shows that these pressures last for a fraction of a millisecond and therefore are unlikely to produce damage.

After several pressure reflections the bubble will fill the whole diameter of the vessel and the pressure will remain more or less constant until the first rarefraction wave returns from the liquid surface. The pressure during this time may be several hundred psi depending on flow rate and geometry of the system. The duration of the loading will be at least the time taken for a pressure wave to travel to the nearest free surface and back. It is during this period of time that the most severe loading will occur on the vessel. It is significant that bursting discs in the gas space above the liquid do not relieve the pressures during this phase of the loading.

The UKAEA has undertaken experimental work with a view to ultimately producing a safe design and refining methods of analysis, and therefore have constructed a sodium water rig which is a scaled version of a typical heat exchanger, fig. (6, 7 and 8). Experiments are being done with the rig in which a tube failure is simulated by fracturing a bursting disc on a tube containing pressurized water which is surrounded by a ring of pressurized tubes as shown in fig. (9). The parameters under investigation are pressures and temperatures as a function of initial temperature, leak rate etc. In tests carried out so far the maximum pressures measured have been about 300 psi. These pressures occured at about one second after the tube failure.

Figure (9) shows bowing of the tubes around the reaction point and fig. (10) a localised view of one of the damaged tubes showing that failure propagation had taken place.

No shock wave effects have been observed so far although this is probably due to inadequate instrumentation. The test vessel which has been designed to 300 psi has withstood all the tests without any visible signs of damage.

The results of the tests so far have shown that the propagation of tube failure cannot be ruled out as tubes adjacent to the fracture have sometimes failed, fig. (10). The mechanisms for failure propagation are also being investigated. It has been suggested that there are two main mechanisms for failure propagation namely, corrosion/erosion processes and the loss of tube strength due to the high temperatures of the exothermic reaction. Temperatures as high as 1300°C have been measured. A larger rig is at present being built with a view to increasing the head of sodium in the vessel since this will increase the duration of the pressure loading and corrosion processes. In addition the new rig is to have larger pressurized water supplies so that more realistic discharges can be achieved. Tests on the new rig are expected to begin in early 1967.

REFERENCES

(1) J.G. MOORE : "The formation of shock waves from the combustion of gaseous mixtures with special consideration of the sodium-air reaction". Nuclear Engineering and Design, Vol. 3 (1966) No.2 pp. 320-337.

(2) J.R. HUMPHREY : "Sodium-air reactions as they pertain to reactor safety and countainment". A/CONF 15/P/1893 June 1958.

(3) J.G. MOORE and E.V. GILBY to be published.

(4) S.P. HARRIS and C.F. BUMPUS : "Pressure and temperature instrumentation for dynamic measurements in the KEWB program". NAA-SR-4709, 1960.

(5) M.A. SALMON : "Effects of tube leaks in sodium heated steam generators". NAA-SR-8140, 1963.

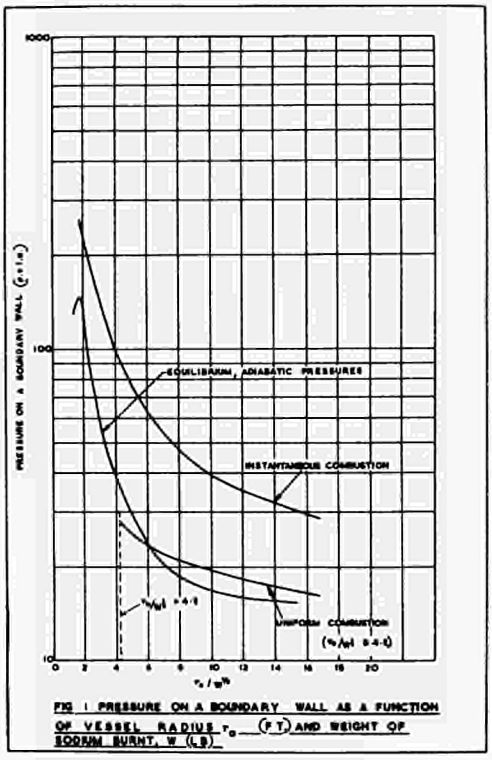

FIG 1 PRESSURE ON A BOUNDARY WALL AS A FUNCTION OF VESSEL RADIUS r_o (FT) AND WEIGHT OF SODIUM BURNT, W (LB)

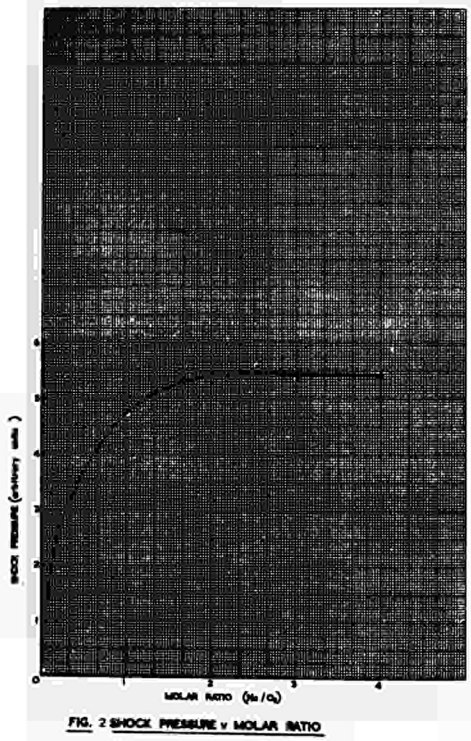

FIG. 2 SHOCK PRESSURE v MOLAR RATIO

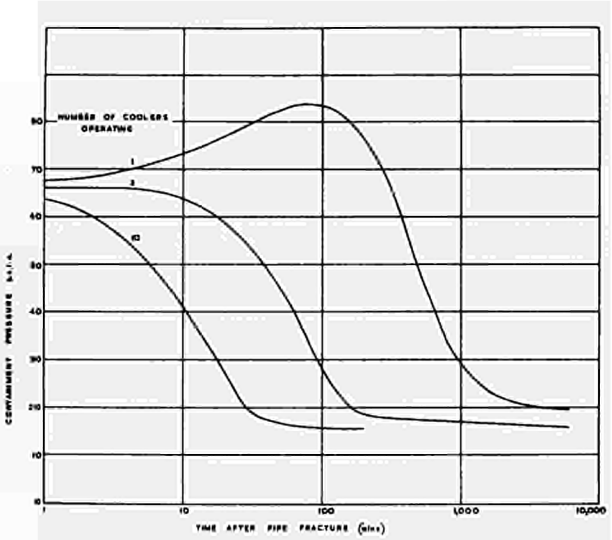

FIG 3 REACTOR CONTAINMENT PRESSURE DURING DEPRESSURISATION WITH DIFFERENT DEGREES OF HEAT EXTRACTION

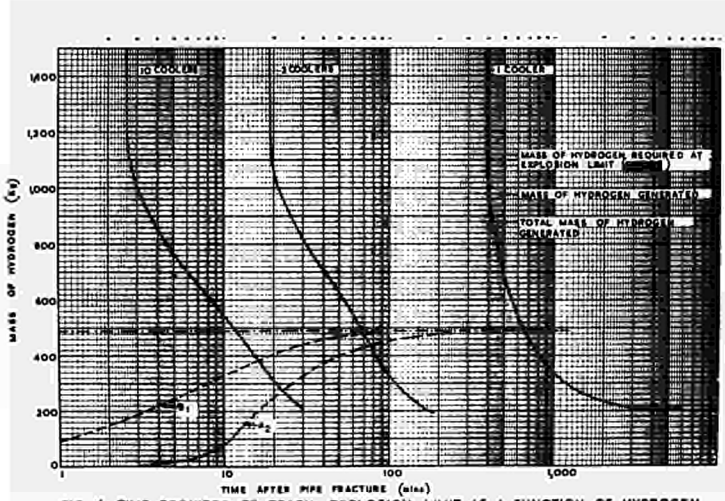

FIG. 4 -TIME REQUIRED TO REACH EXPLOSION LIMIT AS A FUNCTION OF HYDROGEN GENERATION AND CONTAINMENT CONDITIONS

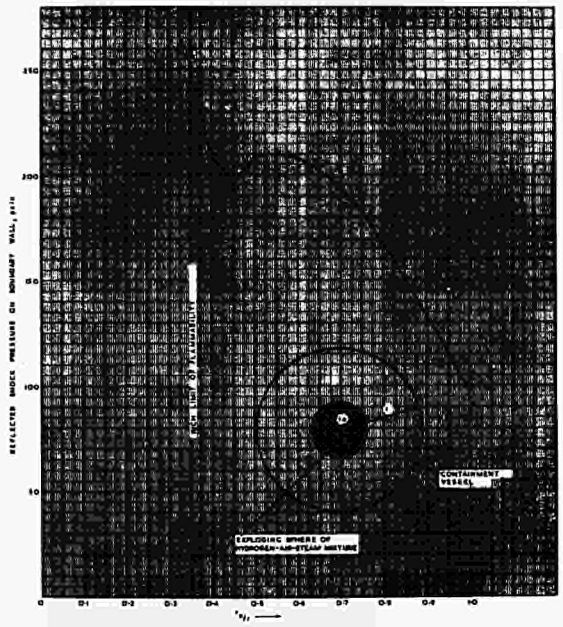

FIG. 5 SHOCK PRESSURES ON BOUNDARY WALL FOR VARIOUS DISTRIBUTIONS OF 500KG OF HYDROGEN IN A CONTAINMENT VOLUME OF 1·5 X 10^5 FT^3

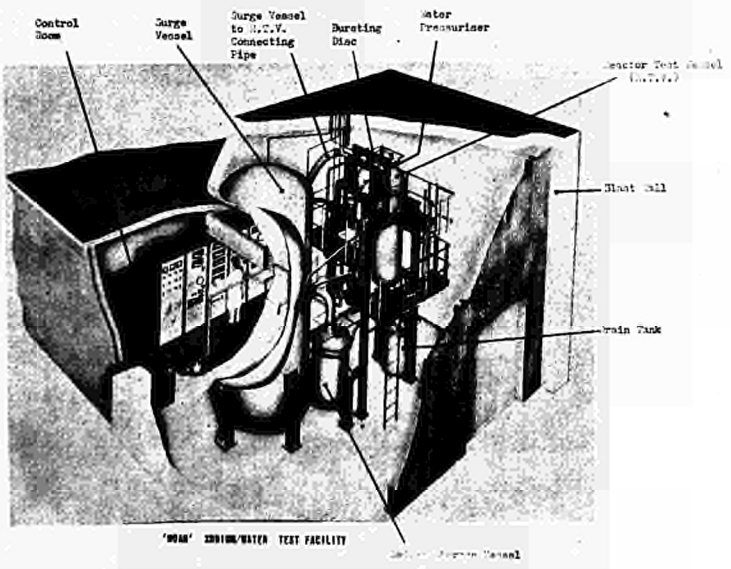

'HDAR' STEAM/WATER TEST FACILITY

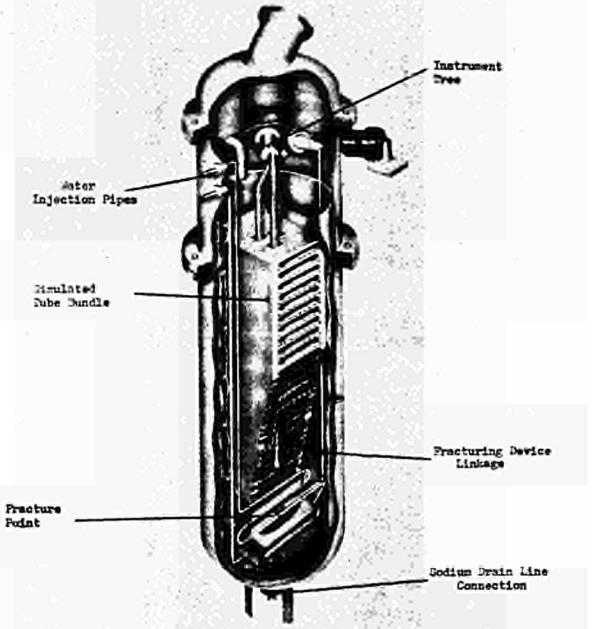

Fig. 7 'HDR' REACTION VESSEL

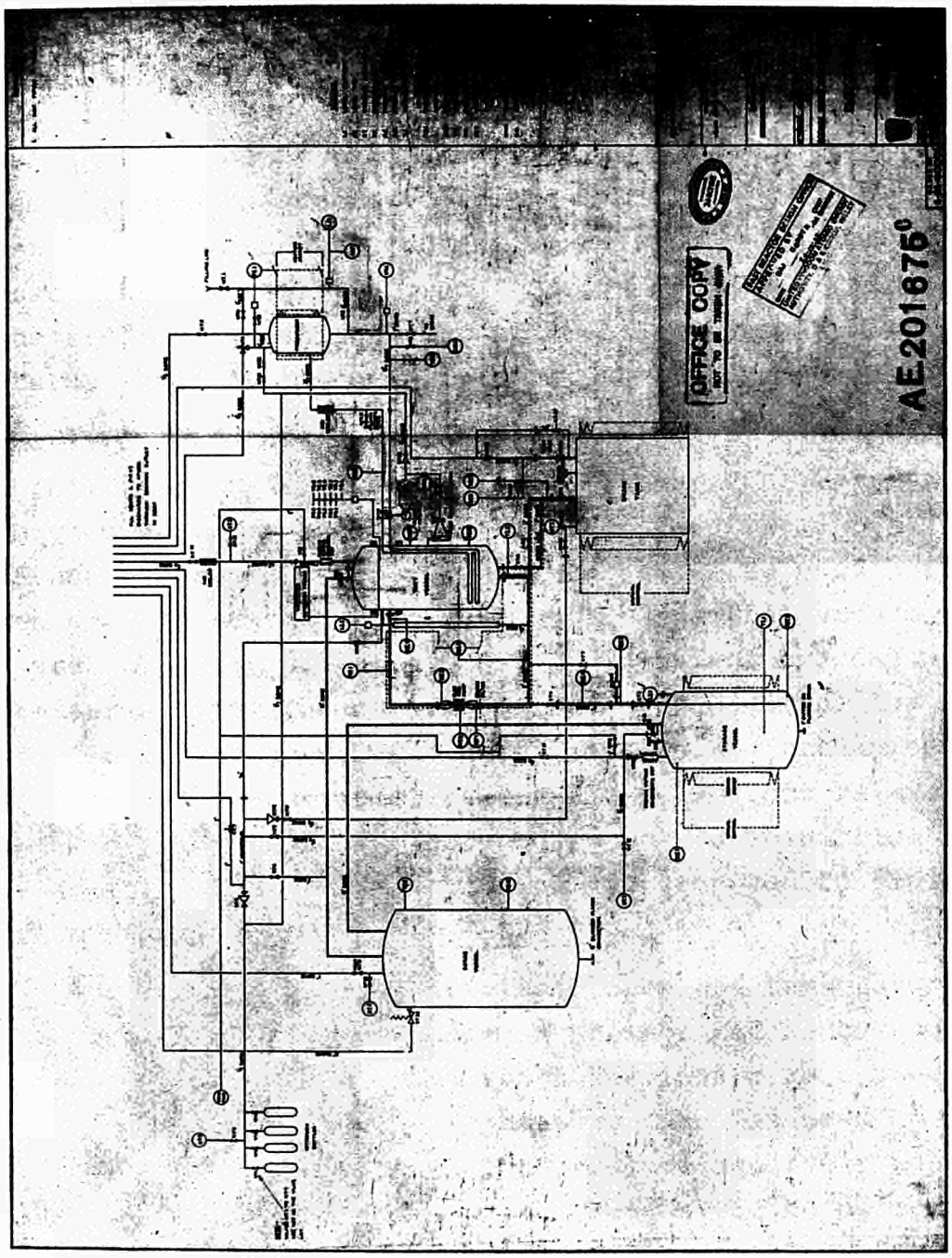
OFFICE COPY
AE201876

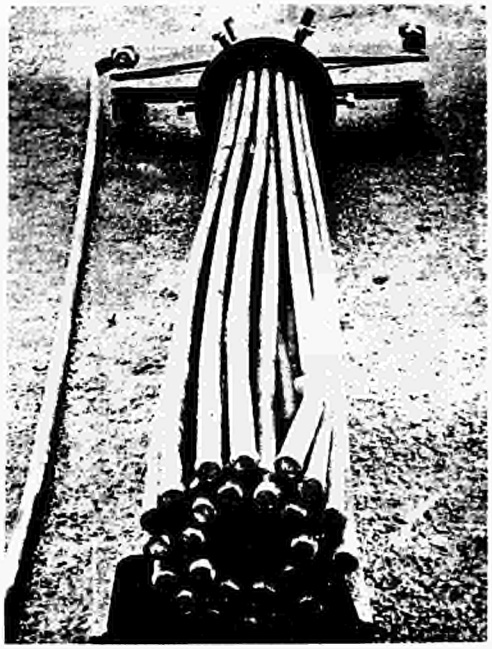

Fig. 9

Fig. 10

WATER DEPRESSURISATION STUDIES*

by

T.A. Zaker and A.H. Wiedermann
IIT Research Institute
Chicago, United States

I. INTRODUCTION

Sudden rupture of a pressure tube in a pressurized-water reactor leads to a decompression or blowdown process accompanied at early times by transient wave propagation through the system. Pressures generated in the containment volume, and thrust forces induced on coolant circuits, are of importance in assessing the safety of such reactor systems. These effects can be studied conveniently in a laboratory depressurization apparatus which is essentially a water-driven shock tube.

Early experimental studies with a water-driven shock tube were performed at IIT Research Institute by E. A. Brown.[1*] Brown used water as the driver fluid at temperatures up to about 212°F and at pressures up to about 25 psia. He used air in the driven section of the shock tube under a partial vacuum at pressures of about 0.5 to 6.0 psia. Transient overexpansions to pressures below the saturation pressure, lasting for the order of a millisecond, were attributed to the attainment of nonequilibrium (metastable) states and subsequent relaxation effects in the fluid. A theory based on the assumption of a two-stage, nonequilibrium expansion was proposed to explain the phenomenon.

In more recent work, initial pressure and temperature conditions representative of those in pressurized-water coolant loops have been examined. In some experiments an expansion tube equal in diameter to the pressure tube has been used, while in others a much larger low-pressure reservoir has been coupled to the pressure tube, the volume ratio being roughly representative of coolant loading and containment volumes in power reactor facilities.

II. EXPERIMENTAL STUDIES

This section presents a brief description of equipment used in depressurization experiments and some observations on blowdown phenomena.

---

* Superscript numerals designate appended references.

A. Equipment and Instrumentation

The pressure tube used in current studies is of stainless steel 6 feet in length, 2 inches in inside diameter, and has a 1/2-inch wall thickness. Ports are provided at several positions to accommodate transient pressure and temperature gages. An expansion tube of the same dimensions as the driver has been used in some experiments (Fig. 1). In others, the expansion chamber is a vessel 3-1/2 feet in diameter with a 1/4-inch wall thickness (Figs. 2 and 3). Initial pressures and temperatures up to the critical state (3200 psia, 705°F) can be contained in the driver. The driver water is heated by electric coils in insulation blocks external to the tube. About two hours is generally required for heating.

The pressure tube has two 1-1/4-inch diameter ports located about an inch upstream of the diaphragm. These permit visual observation of the flow field using high-speed photography to observe bubble formation. The diaphragm is of tempered glass, ranging in thickness from 1/4 inch to 3/8 inch, clamped between the driven and driver sections. Rupture of the glass is initiated by impact of a small lead pellet fired from a gas gun mounted at the closed end of the expansion chamber.

A longitudinal section at the junction between the pressure tube and expansion chamber is shown in Fig. 4. The method of mounting the glass diaphragms and the glass porthole windows to prevent leakage, and breakage from clamping pressures, is depicted in this figure.

Instrument stations are located at five positions in the pressure tube. These accommodate either transient pressure sensors or fast-response thermocouples in appropriate adapter units.

The pressure transducers used are Kistler Model 601 piezoelectric quartz-crystal gages. Since the output of these gages is affected by temperature above 300°F, each transducer is mounted in a water cooling jacket.

Two types of thermocouples are used. One type has the junction of dissimilar metals encased in a stainless-steel sheath, and is used for control of temperature during heating. The second type has the junction of dissimilar metals exposed to the flow, and has a very short response time.

B. Pressure Records

Typical pressure-time records obtained at the closed end of the pressure tube are shown in Fig. 5. These represent data from different shots at the same gage location, where different temperatures (as noted) were used on each shot. In each case the plateau on the left represents the pressure level in the water prior to arrival of the decompression wave at the gage location. At the extreme right in each record is another pressure plateau which represents the magnitude of the saturation pressure. Between the two pressure plateaus there is a sudden drop in pressure from the initial value to nearly zero for a very short period of time.

The records from pressure gage locations in the expansion tube were quite similar to each other and showed no qualitative difference with variations in the temperature and pressure of the driver fluid. The arrival time of the wavefront at any given gage location depends on the distance of the gage from the diaphragm, and yielded wave velocities consistent with the magnitudes of the overpressures observed. Some representative pressure and temperature records taken simultaneously are shown in Fig. 6.

The overexpansions visible on the records taken in the pressure tube have been considered tentatively as evidence of the momentary attainment of nonequilibrium states in the expanding fluid. These have been observed consistently. The time duration has been observed to be as high as 1 msec for an initial driver temperature of 400°F, and generally less than 0.5 msec for temperatures of 500°F and higher.

It is possible, however, that these overexpansions can be explained on the basis of initially nonuniform temperature or fluid quality (see Section III). The effect of a vapor blanket adjacent to the diaphragm is to induce supersonic flow at the exit after the vapor is blown out of the pressure tube (Fig. 19). On the other hand, a blanket of liquid at lower temperature than the bulk of the fluid in the pressure tube leads to a water-hammer type pressure-time history immediately inside the exit (Fig. 22).

C. Photographic Observations

A Fastax high-speed moving-film camera with a rotating-prism shutter has been used for visual observations of flow at the test section in the driver near the diaphragm station.

The layout of the camera and light source, relative to the test section porthole windows, is shown in Fig. 7. Fig. 8 shows three individual frames of film obtained at a framing rate of 3000/sec in this case. In the first of the three frames no vapor can be seen in the flow field. The camera views the face of a flush-mounted thermocouple at the opposite port.

In the second frame of Fig. 8, the first frame differing in appearance from those preceding, a region of vapor appears in the center of the frame and three or four much smaller regions appear on the face of the thermocouple. In the third frame of Fig. 8, the vapor region is seen to be larger than the previous frame, and a cloud of vapor appears to be moving very slowly to the right toward the freshly broken diaphragm. On subsequent frames of this film, motion to the right continued as more vapor was formed in the field of view, and finally a frothy mixture of liquid and vapor filled the entire field of view.

III. DEPRESSURIZATION ANALYSIS

Some theoretical studies of one-dimensional depressurizing systems have been performed. The objective of these studies is to predict the transient phenomena observed in specific experiments, and thus to assist in interpreting the observed results. This type of analysis can also be used to design experiments and establish response criteria for the instrumentation systems which are needed to define better the decompression process. Finally, some insight into the scaling laws of the phenomena can be established.

A significant characteristic of the decompression process is its transient nature. That is, significant changes in pressures, reactions, and internal loads occur in relatively short periods of time. Pressure waves are generated, and thus the effects of inertia of the fluid medium are significant. If a small break occurs in the system, a quasisteady flow process develops after the initial flow transients. In this type of sit-

uation the usual steady flow process predominates, and transient inertia effects are unimportant. The geometries of pressurized water systems can be roughly categorized as combinations of long narrow ducts, tubes, and reservoirs. Pressure-wave propagation within the ducts and possibly within the reservoirs can be treated by a one-dimensional nonsteady flow analysis. Water is known to exhibit some metastable effects near saturation states; however, it appears that these states exist for times of the order of a millisecond, and hence they will not significantly influence phenomena which occur over many tens of milliseconds or longer. These metastable effects will be even less important in the prototype situations which are dimensionally much larger than typical laboratory apparatus.

A. Fundamental Considerations

For the problem of one-dimensional nonsteady flow both mass and momentum are conserved. One form of these basic equations is:

$$\frac{\partial u}{\partial t} + u \frac{\partial u}{\partial x} + \frac{1}{\rho} \frac{\partial p}{\partial x} = 0 \qquad \text{(momentum)} \qquad (1)$$

$$\frac{\partial \rho}{\partial t} + u \frac{\rho}{\partial x} + \rho \frac{\partial u}{\partial x} = 0 \qquad \text{(mass)} \qquad (2)$$

where: u = particle velocity
p = pressure
ρ = density
x = distance
t = time

An energy equation could also be formulated. However, we will defer writing this equation and assume that the flow process is adiabatic; that is, no heat transfer occurs between adjacent particles of the fluid, or between the fluid and the walls of the pressure vessel.

A third equation describes the behavior of the fluid medium in the environment of interest. This equation is called the equation of state. It relates one thermodynamic variable to the others, e.g.

$$p = p\ (\rho, s) \qquad (3)$$

where s = entropy. If this equation can be simplified to the form

$$p = p\ (\rho) \qquad (4)$$

in any solution zone (region of x,t), then we can eliminate either p or ρ and reduce the system of equations to two equations.

These two equations form a system of quasilinear partial differential equations of the first order for functions of two independent variables. A fairly complete and elegant mathematical theory[2]—the method of characteristics— has been formulated for the case where the system of equations is of the hyperbolic type. The notion of characteristics plays a dominant role in this type of mathematical problem.

Characteristic lines, along which certain flow parameters are constant, exist in the planes of both the independent and dependent variables. The solution of a problem is obtained by calculating corresponding changes along and across characteristics in each of the two domains.

A weak disturbance of intensity Δp propagates through a medium at the sound velocity c, and changes the particle velocity u by an amount $\pm \Delta u$. Conservation of momentum across such a wavelet can be written as:

$$\Delta p = \pm (\rho c)\ \Delta u \tag{5}$$

The characteristics in the hodograph or state plane (p,u) (i.e. the plane of the dependent variables) are the loci of these infitesimal changes of state. The characteristics, which we can designate as C^+ and C^-, are given by

$$u = \pm \int \frac{dp}{(\rho c)} + \text{constant} \tag{6}$$

where the quantity (ρc) is a function of p alone. Such a weak disturbance propagates in both directions in a medium at the velocity c relative to the medium; hence in any fixed coordinate system, a weak disturbance propagates at an absolute velocity

$$u \pm c \tag{7}$$

where u is the local particle velocity. These disturbance paths are the characteristic lines in the wave diagram (x,t), the plane of independent variables. There are two sets associated with the double sign. We designate these sets of characteristics D^+ and D^-.

Changes of state which occur along the characteristic C^-

in the hodograph plane occur across the characteristic D^+ or along the characteristic D^- in the wave diagram. Similarly, changes in state which occur along the characteristic C^+ correspond to changes along D^+. Boundary conditions are specified in both the hodograph plane and in the wave diagram and will generally be given on some noncharacteristic curve.

B. Equation of State of Water

We assume that the water is always in thermodynamic equilibrium and that the process is locally isentropic. If this is the case then sufficient data[3] exist and an analysis can be initiated. Metastable states are ignored and complete equilibrium between the vapor and liquid phases is assumed when two-phase flow occurs.

1. Compressed Liquid

In the compressed liquid state an isentropic change in state is also approximately an isothermal change in state, provided that the temperature is not greater than approximately 600°F. Figure 9 presents the sound velocity[4] over a wide range of pressures and temperatures. The acoustic impedance (ρc) varies over the range from approximately 60 psi/fps at 32°F to approximately 20 psi/fps at 600°F. These large values indicate that for significant pressure changes relatively little motion is induced in the medium. The resulting state is one of low subsonic ($u \ll c$) flow. Relatively little energy is released during a decompression to the saturation pressure, and the wave propagation closely resembles a classical "water-hammer" phenomenon provided the pressure does not drop below the saturation pressure.

2. Mixture Region

Steam-table data were used to construct the density variation with pressure for a number of specific entropy values. The tabular data were then numerically differentiated to obtain the corresponding sound velocity. The sound velocity in saturated liquid states is of the order of hundreds of feet per second.* The characteristic curves of the hodograph plane were plotted from these data with initial states on the saturation line, and

*The sound velocity changes in a discontinuous manner across the saturation line (see Ref. 4).

it was discovered that the characteristics were straight lines in a ln p versus u representation (see Fig. 10). Subsequent investigation indicated that this behavior still exists at higher values of entropy corresponding to the saturated vapor phase.

Thus it is possible to write a simple equation for the characteristics in the mixture phase:

$$\ln \frac{p}{P_o} = \pm \frac{u}{u_o} + \text{constant} \tag{8}$$

where P_o = saturation pressure

u_o = inverse slope of the characteristic.

This equation is valid for any initial state in the mixture region, a fact which permits us to develop the equation for all isentropes in the mixture region.

We can rewrite Equation (8) for the case of a saturated initial state as:

$$p = P_o \exp(-u/u_o) \tag{8a}$$

noting that $p = P_o$ when $u = 0$.

Differentiating Equation (8) or (8a) yields:

$$\frac{dp}{du} = -\frac{P_o}{u_o} \exp(-u/u_o) = -\frac{p}{u_o} \tag{9}$$

for the C^+ characteristic.

Recall that the momentum equation corresponding to this characteristic is

$$\frac{dp}{du} = \rho c$$

Hence

$$\rho c = \frac{p}{u_o}$$

$$c^2 = \frac{dp}{d\rho} \tag{10}$$

Therefore

$$\frac{dp}{d\rho} = \left[\frac{p}{\rho u_o}\right]^2 \tag{11}$$

Separating and integrating yields the isentrope

$$\frac{\rho_o}{\rho} = \frac{v}{v_o} = \frac{u_o}{c_o}\left[\frac{P_o}{p} - 1\right] + 1 \qquad (12)$$

where v is the specific volume $\left(= \frac{1}{\rho}\right)$, and the subscript zero refers to the saturation state. Use was made of Equation (10), in that

$$u_o = \frac{P_o}{c_o \rho_o} \qquad (13)$$

We can now derive an expression for the sound velocity. From Equation (10) we obtain

$$\frac{c}{c_o} = \frac{P}{P_o} \times \frac{\rho_o}{\rho} = \frac{u_o}{c_o} - \frac{p}{P_o}\left(\frac{u_o}{c_o} - 1\right) \qquad (14)$$

Thus the sound velocity varies linearly with pressure from the value c_o along the saturation curve to the value u_o at zero pressure. The constant u_o is a function of entropy only.

In some problems it will be necessary to consider constant-energy processes, that is, changes of state in which

$$h + \frac{1}{2} u^2 = \text{constant} \qquad (15)$$

where h is the enthalpy per unit mass. For an isentropic process

$$dh - \frac{1}{\rho} dp = 0 \qquad (16)$$

Using Equation (12), one can integrate Equation (16) from an arbitrary initial state (subscript 1) in the mixture region to an expanded state (unsubscripted), with the result

$$\frac{h_1 - h}{u_o^2} = \frac{1}{P_o}\left(1 - \frac{c_o}{u_o}\right)(p - p_1) - \ln \frac{p}{p_1} \qquad (17)$$

For initial states on the saturation curve, $p_1 = P_o$ and $h_1 = h_o$. On the vapor branch of the saturation curve the logarithmic term on the right in Equation (17) dominates, and the relation is well approximated by a family of straight lines in a ln p versus Δh_o representation, where $\Delta h_o = h_o - h$ (Fig. 11).

Substituting Equation (17) into Equation (15), one obtains the relation between pressure and velocity in constant-energy processes:

$$\frac{u^2 - u_1^2}{2u_o^2} = \frac{1}{P_o}\left(1 - \frac{c_o}{u_o}\right)(p - p_1) - \ln\frac{p}{p_1} \qquad (18)$$

C. Decompression Solutions

We present a series of specific decompression solutions in this section. These solutions generally deal with the decompression process from a constant-area tube of finite length and with initial states on the saturation line.

The results have been obtained by using a conventional graphical technique,[5] modified for the peculiarities of the pressurized-water equation of state. The results are generally presented in a series of three figures: (1) the hodograph plane, (2) the wave diagram, and (3) a series of pressure histories. The pressure-time curves will generally correspond to: (A) the closed end of the pressure tube, (B) the midpoint of the pressure tube, and (C) the diaphragm station.

1. Homogeneous Region at Saturation

Consider a constant-area pressure tube closed at both ends and filled with water at rest at some saturation condition (liquid or vapor). At time t = 0, one end (the diaphragm) of the pressure tube is ruptured such that no flow restriction occurs. The region outside of the pressure tube is very large and maintained at an ambient pressure P_∞ (= 14.7 psia) which is much lower than the saturation pressure P_o. The pressurized water starts to flow from the tube and a centered rarefaction wave system propagates upstream into the water. The flow is choked (i.e., sonic flow) at the diaphragm station. The centered rarefaction wave reaches the closed end of the pressure tube, reflects, and propagates back toward the diaphragm station. The boundary condition for the closed end of the pressure tube is that of no motion (u = 0). The reflected disturbance reverberates between the two ends of the pressure tube. The pressure continues to drop as the water continues to leave the tube. As long as the

pressure at the open end or diaphragm station is greater than the ambient pressure P_∞, the fluid is further accelerated by this pressure gradient. However, the limit of this local velocity increase is given by the sonic condition, since any disturbances which could further accelerate the fluid locally would be swept out of the region. Thus the boundary condition at the diaphragm station for outflow is either sonic flow or equality of pressure to the outside ambient pressure. We have treated only the sonic boundary condition, since the most significant decompression effects are completed prior to full decompression. This is due to the fact that $P_o \gg P_\infty$. Actually at very late times the pressure within the tube will drop below P_∞ and reverse flow (inflow) will subsequently occur.

The first problem which we have solved in some detail is the case of a saturated liquid at 550°F (P_o = 1045 psia). The results are given in Figures 12 thru 14. The initial expansion through the centered rarefaction wave corresponds to the change in state from the initial state, S_o, to the sonic state S_1. The reflection of this wave system at the closed end of the pressure tube corresponds to the change of state from S_1 to S_2. Thus a series of states S_1, S_2, S_3, ... will exist which will correspond to the various reflection cycles occurring in the wave diagram. The point b in the wave diagram corresponds to state S_o and the line a-c corresponds to the initial choked state, S_1. The other states are identified by their corresponding number. For this particular case approximately five and one-half reflections are needed before the pressure drops to the ambient pressure, P_∞. It should also be noted that the characteristics ($u \pm c$) in the wave diagram become flatter at late times (i.e. speeds greater in absolute magnitude) since the sound velocity increases substantially with decreasing pressure. The pressure histories presented in Fig. 16 are characterized by a number of specific cusps due to the reflected wave systems. Furthermore, much of the axial pressure variation in the tube exists near the diaphragm station.

The solution for a saturated vapor at 500°F (P_o = 681 psia) was also obtained. We find significant differences between this case and the previous solution, although qualitatively the decompression process is the same. Characteristic of the saturated vapor states, the sound velocity is much larger than those

of the saturated liquid states, and the sound velocity does not vary as much with the pressure. For this particular case the sound velocity decreases from 1600 fps at the saturated state to approximately 1350 fps at very low pressure. The solution for this case is presented in Figures 15 through 17. The number of reflections needed to drop the pressure to the ambient level is just over three. This solution is similar to that which one would obtain for the decompression of a pressurized gas system. Perhaps the most significant feature of this decompression solution is the very short time (approximately 15 millisec) needed to reduce substantially the pressure and the decompression loads on the pressure tube.

2. Mixed Regions

We now treat cases in which two homogeneous regions of fluid of different entropies exist adjacent to each other. The fluids are initially at rest and at the same pressure. We simultaneously solve two problems, one for each entropy value, and match the solutions at the interface separating the fluids, recalling that the boundary conditions at the interface are those of equal pressure and particle velocity.

Consider a vapor blanket of length L adjacent to the diaphragm station and backed by an infinite length of saturated liquid. The only disturbance that can propagate into the saturated liquid is a simple wave system corresponding to states which exist on its initial expansion characteristic. That is, there exists only one set of characteristics, the D^- characteristic set. The left-hand boundary condition for the vapor is this liquid expansion characteristic. The right-hand boundary condition for the vapor is the choked outflow condition at the diaphragm station. The left boundary of the vapor (the liquid-vapor interface) is a moving boundary whose path is determined as the solution is advanced in time. The wave diagram of Fig. 18 indicates the interface as the path b-c. The vapor behaves much as it does in the simple decompression process in that a centered rarefaction wave originates at the diaphragm station and propagates into the saturated vapor. The interaction of this wave system with the interface results in the transmission of disturbances into the saturated liquid and the reflections of signals back into the vapor, now actually a mixture.

The initial outflow of the liquid is supersonic. The interaction of these characteristics with the diaphragm station will not result in a reflected wave due to the supersonic nature of the flow. At late times the outflow of the liquid will approach the sonic condition which would exist in the absence of a vapor blanket. Fig. 19 presents the pressure histories at three positions: (A) at the original interface position x=-L, (B) at x=-L/2, and (C) at the diaphragm station. The pressure at the diaphragm position drops down to 300 psia corresponding to the sonic state, and then continues to drop as the interface reflected signals interact with this boundary. After the vapor is blown out of the pressure tube $\left(\frac{tc_o}{L} = 3.46\right)$ the pressure rises to the liquid sonic expansion pressure (525 psia for c_o = 1600 fps).

Consider the case where a short section adjacent to the diaphragm station is filled with a liquid whose temperature is slightly below that of the remainder of the liquid. The bulk of the liquid is at a saturation state (T_o = 550°F, P_o = 1045 psia) and the short section of liquid is at a temperature of 500°F. Both regions of liquid are initially in pressure equilibrium at 1045 psia. The saturation constants for the compressed liquid are T_o = 500°F, P_o = 681 psia.

When the diaphragm is removed an initial disturbance propagates rapidly through the compressed liquid region, dropping the pressure to the saturation pressure (681 psia) corresponding to its temperature. This wave propagates at approximately 2800 fps. The hodograph plane is presented in Fig. 20 and shows this initial change in state (from S_o to S_1). A centered rarefaction wave system is also generated at the diaphragm station, and propagates into the liquid region behind the initial disturbance as shown in Fig. 21. The head characteristic will propagate at a much slower velocity. This centered rarefaction wave system will expand the fluid from state S_1 to its sonic outflow state, S_5.

The only possible states for the saturated liquid (T_o = 550°F) are those associated with its initial expansion characteristic passing through state S_o; hence we have a simple wave system in this region. A small change in pressure in the saturated liquid results in an appreciable particle velocity increment, whereas a large change in pressure of the compressed liquid pro-

duces only a small increment of particle velocity. Thus the initial interaction at the interface results in the reflection of a rather strong compression wave and only a small drop in pressure in the saturated liquid. The state S_2 exists as a result of this interaction.

The reflected wave interacts with the centered rarefaction wave system and further accelerates the fluid. This wave is reflected and reverberates between the interface and the rarefaction wave system, alternately expanding and compressing the liquid. The disturbance which penetrates the rarefaction wave system accelerates the fluid to a supersonic state, and as a result this signal is not reflected from the diaphragm station. In fact, the rarefaction wave system is completely blown out of the pressure tube at the point a in the wave diagram. Thereafter the disturbances in the compressed liquid reverberate between the interface and the diaphragm station. The interface is further accelerated and reaches the diaphragm station at the point b in the wave diagram. Both the compressed liquid and the saturated liquid (now a mixture) reach state S_3 at this time. Since state S_3 is a subsonic state for the saturated liquid, the fluid expands through a centered rarefaction wave system to the sonic outflow state, S_4.

The pressure histories at three stations are presented in Fig. 22. Station A is at x = -5 inches (the original interface position), station B is at x = -2 inches, and station C is at the diaphragm station.

3. Area Change Solution

This section treats a problem in which a change in flow cross-sectional area is present. In one-dimensional nonsteady flow problems it is assumed that the values of the flow variables which are used are average values for the cross section of interest. Area changes in such systems can be treated locally as discontinuities across which steady-state flow equations are valid. This implies that the local two-dimensional transient effects associated with diffraction phenomena from incident disturbances are short-lived compared to the time scale of interest.

The steady-state equations which must be satisfied at the area change are continuity of mass,

$$\rho u A = \text{constant} \tag{19}$$

and possibly the energy equation, (15). One can also use some type of modified momentum equation to account for pressure losses which might occur in some special cases.

Consider an area enlargement (area ratio = 1.5) in a pressure tube containing saturated vapor at 500°F. The area change is located a distance L from the diaphragm station.

When the diaphragm is removed the vapor expands from the initial state S_o to the sonic state S_1. The centered rarefaction wave system propagates towards the area change. The only permissible state which can exist upstream of the area change for this pressure tube are those associated with the initial expansion characteristic of the vapor. These states will be located between state S_o and the sonic state S_1. Thus we can expect to observe a simple wave upstream of point B.

We must now establish the upstream boundary condition for the larger area pressure tube, that is at point B. Since the permissible states at B_+ are those given by the initial expansion characteristic, we can map these states into a single compatibility characteristic with the aid of the energy and mass conservation equations. State S_1' at B_- corresponds to state S_1 at B_+. If the pressure at B_- drops below the pressure associated with state S_1' it becomes impossible to satisfy both the energy and mass conservation equations simultaneously. It is quite clear that mass must be conserved; hence we can expect that some non-isoenergetic process will exist at the area change. The smaller-area pressure tube will become choked at B and a standing shock forms. The upstream boundary at B_- can now be extended from state S_1' to the sonic state S_2 by requiring mass conservation. The non-isoenergetic process at B results in entropy production. We have assumed that the entropy change is sufficiently small so that it can be neglected.

The boundary conditions in the hodograph plane are illustrated in Fig. 23. The corresponding wave diagram is presented in Fig. 24. The centered rarefaction wave reflects from the area change and the states at B_- follow the compatibility characteristic until state S_1' is reached. This state occurs along the C^- characteristic from state S_3 within the centered rarefaction system. As the remainder of the centered rarefaction wave reflects, the pressure at B continues to fall. A shock forms

at the area change. At late times the flow in the larger area tube also becomes sonic. The associated pressure histories are presented in Fig. 25. The pressure at B_+ drops more rapidly than that at B_- since the particle velocity is greater. This is particularly true as the particle velocity at B_- increases. Finally the pressure at B_+ drops suddenly and the flow becomes choked. The pressure at B_- and at C (the diaphragm station) both approach the choked flow conditions associated with state S_2 (p = 160 psia).

4. Comparison with Experiment

An experiment was conducted which consisted of a liquid column whose initial average temperature was approximately 545°F and whose initial pressure was approximately 1280 psia. The equilibrium saturation pressure corresponding to 545°F is 1003 psi; therefore there existed an overpressurization of nearly 300 psi. The experimental results will be compared to the theoretical predictions for a saturated liquid column at 550°F and 1045 psia. The theoretical pressure histories for this case are presented in Fig. 14. The overpressurization results in an initial decompression wave which drops the pressure from its initial value to the corresponding saturation pressure assumed in the theoretical model. The propagation velocity of this disturbance is approximately 2300 fps, and the wave traverses the 6-foot long water column in approximately 2.6 milliseconds. The velocity change imparted to the water due to this initial decompression wave is approximately 12 fps. This value is small compared to the value of the sound velocity (130 fps) associated with the saturation state. Thus we assume that the overpressurization will not influence the decompression process significantly, and that we can compare the experimental results directly to the theoretical prediction for the case whose initial conditions correspond to a saturation state. The primary difference is the initial rapid pressure drop which occurs during the first few milliseconds.

The experimental pressure-time curves are presented in Fig. 26 for this problem. The curves are labeled with the appropriate gage position (GP). This figure also presents the corresponding predicted pressure histories, shown by the dashed curves. The pressure plateau which is predicted at A and B is observed on GP6 and GP8, except that the mean value of the plateau observed in the experiment is approximately 970 psia rather than 1003 psi

(1045 psia for T = 550°F). This difference can be accounted for by an initial temperature of 441°F, representing a measurement error of only 4°F. The pressure plateau which is predicted at C is observed approximately on GP4. The pressure level of this plateau, corresponding to a saturation pressure of 970 psia, is 580 psia. The three pressure plateaus are not perfectly flat on the experimental records; however, initial axial temperature gradients in the water column could produce this effect. Furthermore, the axial pressure gradients near the diaphragm station (GP4 and C) are quite large; hence small differences in position, initial temperature conditions, or overpressurization are reflected as large differences in pressures.

The arrival of the centered rarefaction wave (pressure drop) at GP6 does not occur at $t \cong 20$ ms as predicted (B) but does occur at a somewhat later time ($t \cong 35$ ms). On the other hand, the pressure drop predicted to occur at A at $t \cong 40$ ms does occur at GP8; however, the rate of pressure decay is smaller than predicted. At later times ($t > 60$ ms) all three experimental observations are in reasonable agreement with the theoretical predictions. During the intermediate range of time ($35 < t < 60$ ms) the experimental observations do not show a consistent major wave pattern such as is predicted theoretically. One would expect that the propagation velocities of disturbances would be consistent with the state or changes of state of the media; the experimental data do not indicate this. It may be that random or local effects may be causing some perturbation on the pressure observations such that the fine details predicted by the theoretical model cannot be observed.

In addition to comparing specific pressure time histories, we have computed and compared the reaction impulse, I, acting on the pressure tube. For the simple straight pressure tube this impulse is given as

$$I = \int_0^\infty \left[p(t) - P_\infty \right] dt \qquad (20)$$

where p(t) is the predicted or experimentally observed pressure-time curve at the closed end of the tube (GP8 or A).

Before we compare the reaction impulse observed for the experiment with the predicted value, we present a correlation of

the theoretically predicted reaction impulses for a number of cases with the total stored enthalpy in the pressure tube. Figure 27 presents the variation of enthalpy per unit volume as a function of stagnation temperature for both branches of the saturation line. It should be noted that the enthalpy per unit volume for the liquid phase is much greater than that for the vapor phase at the same temperature, except near the critical state. Furthermore, the enthalpy is not too sensitive to the saturation temperature except near the critical state.

The correlation between the reaction impulse and the total enthalpy is presented in Fig. 28. The impulse is given in units of psi-sec as measured for the 6-foot long pressure tube. A linear relationship exists between the reaction impulse and the total enthalpy and is presented in this lnI versus H representation. The constant of proportionality is 0.00269 psi-sec/Btu/ft^3. The two solid circles represent the calculated impulses for a saturated liquid at 550°F and at 600°F. The open circle represents the calculated impulse for a saturated vapor at 500°F. The half solid circles represent the calculated impulses for the two mixed (saturated liquid/saturated vapor) problems treated. Finally, the open triangle represents the calculated impulse for the pressure tube containing saturated vapor at 500°F with an area reduction (area ratio = 0.5) at the diaphragm station. All of these calculated impulses are within 10 percent of the average I/H ratio.

The value of the reaction impulse computed from the pressure-time data of the experiment considered above was 68.1 psi-sec, and is to be compared with a predicted value of 67.5 psi-sec corresponding to a total enthalpy of 25,100 Btu/ft^3. This experimental data point is shown in Fig. 28 as a small open box representing an estimate of the uncertainties in the observations. Two other experimental results for widely different initial states are also shown.

IV. CONCLUSION

Depressurization of heated pressurized water and water-steam mixtures leads to blowdown phenomena qualitatively different in some respects than those in rupture of a gas pressure tube. This is due to the variation of sound speed

with mixture quality in two-phase flow of water and steam. Blowdown of a tube 6 ft in length from an initial liquid state is essentially complete in times of the order of 100 msec. Blowdown from a vapor state at the same initial pressure occurs about an order of magnitude more rapidly, resembling more closely the behavior of a perfect gas in decompression. These blowdown times must, within broad limits, scale directly with tube length. Choked flow at the tube exit controls the decompression time, being slower in liquid depressurization owing to the low sound speeds attained in expanded states in that case.

Momentary overexpansions to very low pressures have been observed for durations of the order of a millisecond in the pressure records. If they are due to relaxation phenomena intrinsic to the fluid, these overexpansions, being of short duration, would not affect significantly the over-all response of systems of practical dimensions. In fact, the depressurization analyses presented in Section III suggest that these phenomena are possibly attributable to nonuniformities of initial fluid conditions, such as the presence of a vapor blanket or a subcooled liquid blanket at the diaphragm station. A vapor blanket can induce supersonic flow momentarily at the exit, while a subcooled liquid blanket induces local water-hammer phenomena.

The analysis of one-dimensional unsteady flow in the pressure tube during decompression assumes a homogeneous mixture of phases in thermodynamic equilibrium during the process. Slip between the phases is assumed to be zero. The analysis confirms the over-all blowdown time found experimentally for a liquid decompression, and predicts pressure-time variations having roughly the same major features as those observed experimentally.

High-speed motion picture film strips show evidence of individual bubble formation within a small fraction of a millisecond. A uniform dense population of small vapor bubbles develops throughout the field of view within a few milliseconds, indicating a finely divided two-phase mixture which persists thereafter. This tends to support the assumption of thermal equilibrium between phases which is made in the analysis.

A correlation has been found between the reaction impulse exerted axially on the pressure tube and the total enthalpy initially stored in the fluid. This thrust force is significant in determining damage to coolant-line networks in the event of gross line rupture.

REFERENCES

1. Brown, E. A., "Experiments on the Explosive Decompression of Water", Report No. ARF 4132-9, Contract No. AT(11-1)-528 (November 1959)

2. Courant, R., and K. O. Friedrichs, Supersonic Flow and Shock Waves, Interscience Publishers, Inc., New York (1948)

3. Keenan, J. H., and F. G. Keyes, Thermodynamic Properties of Steam, John Wiley and Sons, Inc., New York (1936)

4. Karplus, H. B., "Propagation of Pressure Waves in a Mixture of Water and Steam", Report No. ARF 4132-12, Contract No. AT(11-1)-528, (January 1961)

5. Korst, H. H., "Analysis of Some Thermodynamic Processes by the Method of Characteristics for Nonsteady One-Dimensional Flow", Proceedings, Midwestern Conference on Fluid Dynamics (1950)

*This work was supported by the U.S. Atomic Energy Commission under Contract No. AT(11-1)-578 with IIT Research Institute, Chicago, Illinois, USA.

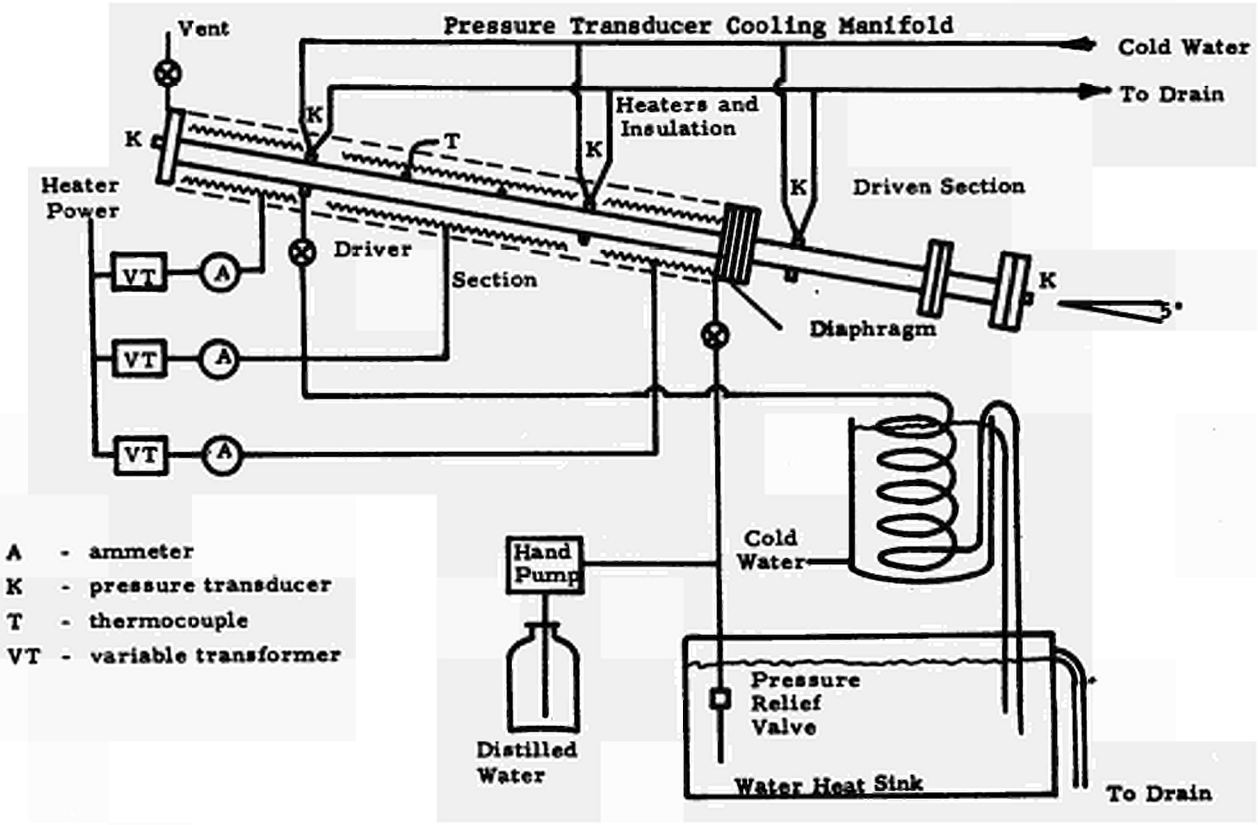

Figure 1 Constant-Area Water Shock Tube

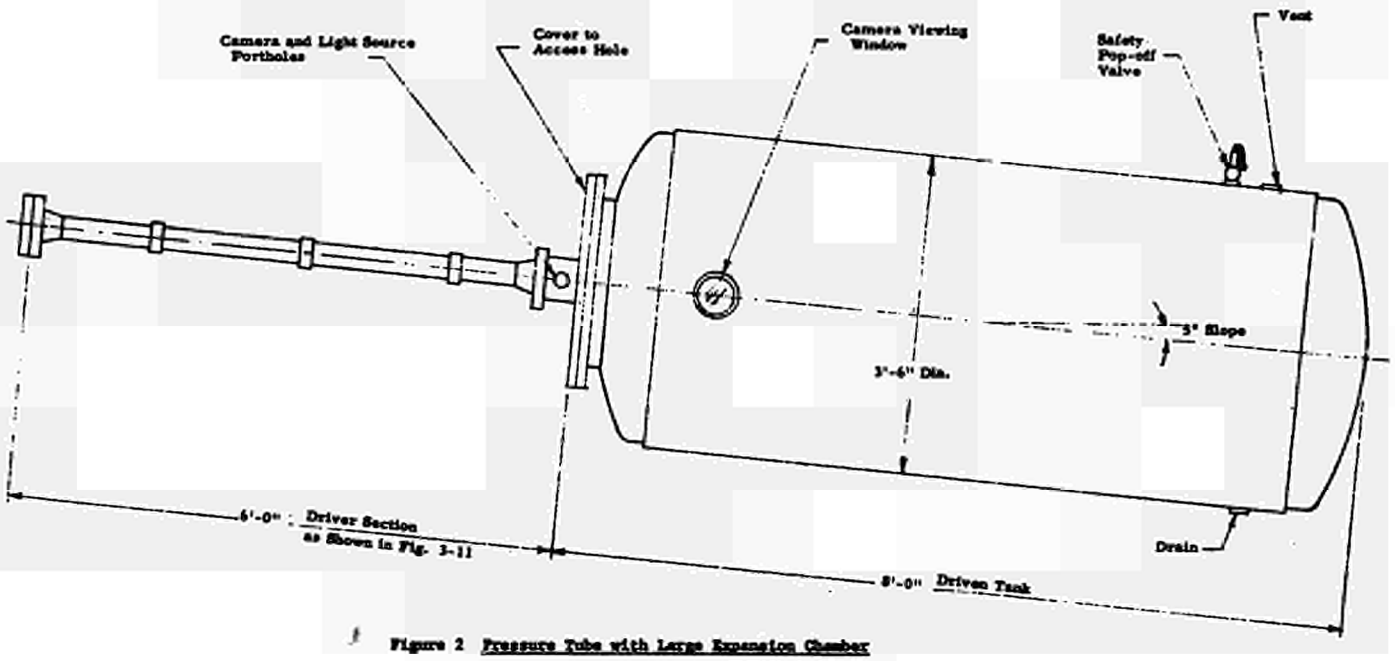

Figure 2 Pressure Tube with Large Expansion Chamber

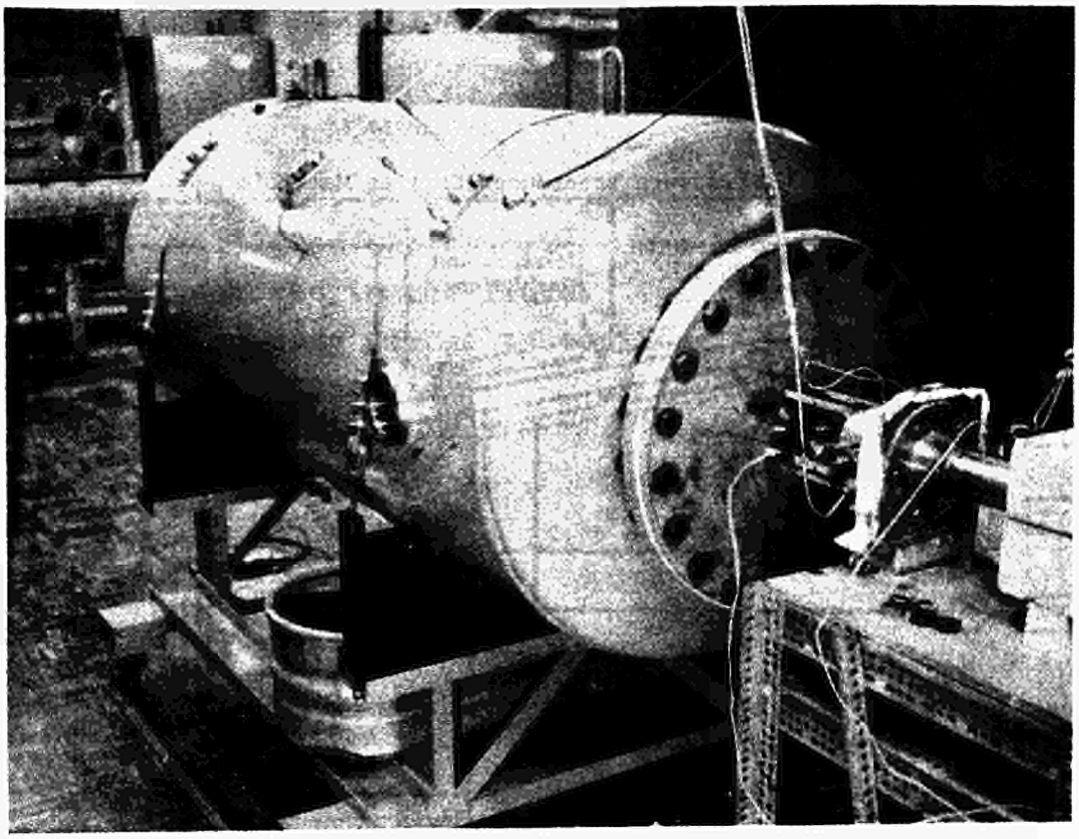

Figure 3 Photograph of Receiver Vessel

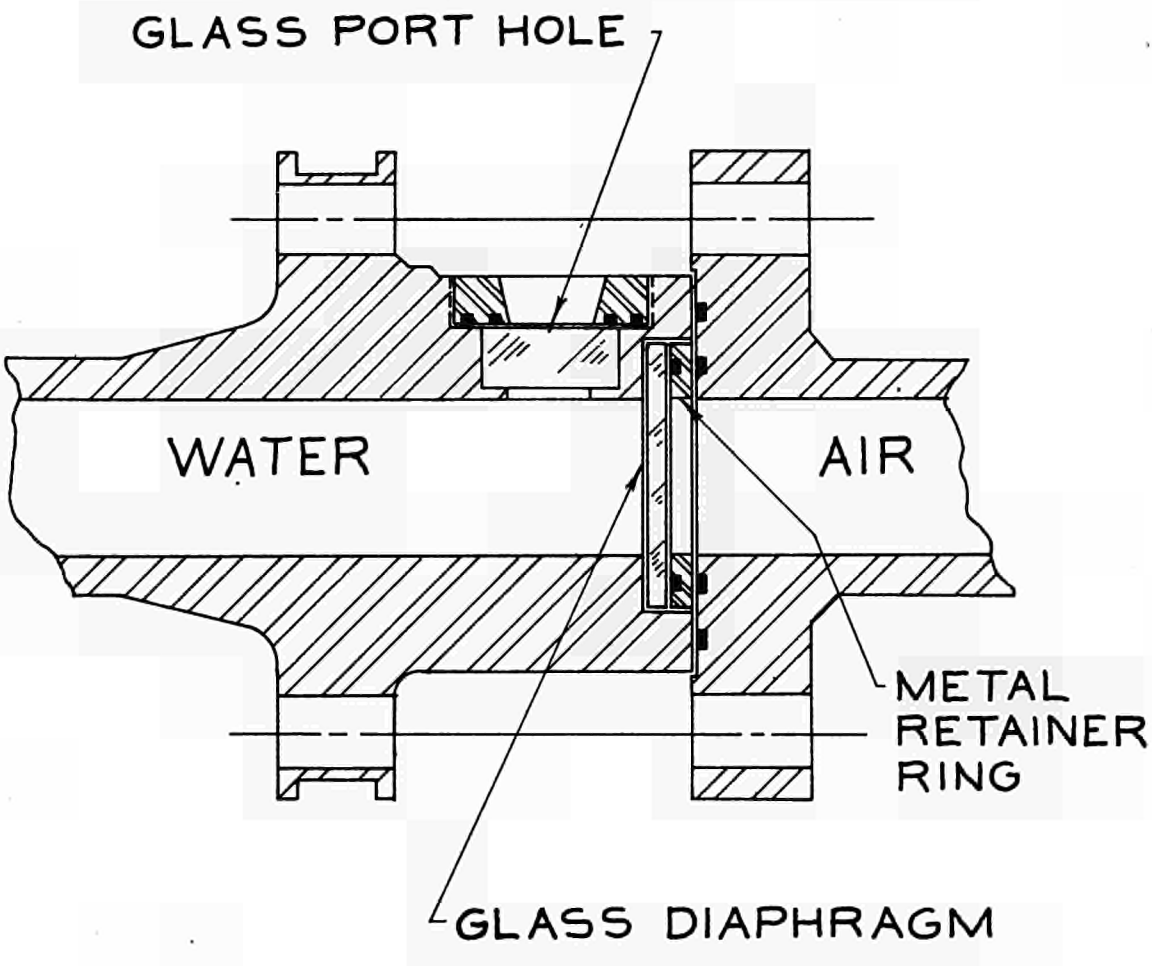

Figure 4 Section at Diaphragm Station

Pressure = psi/cm

Temperature = ms/cm

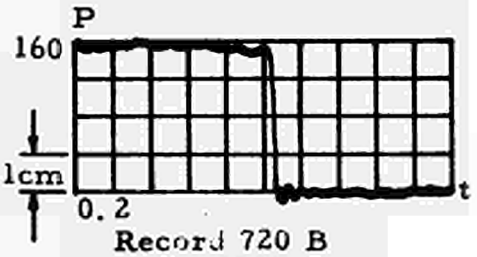

Record 720 B
IDT = 90°F
IDP = 600 psi

(a)

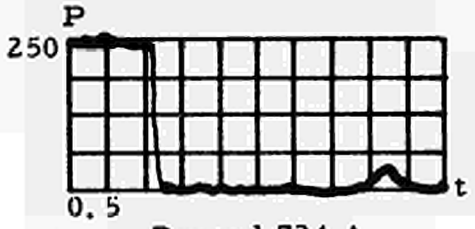

Record 724 A
IDT = 302°F
IDP = 982 psi

(b)

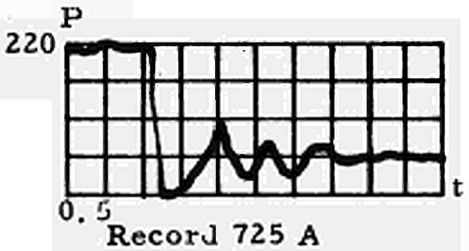

Record 725 A
IDT = 420°F
IDP = 800 psi

(c)

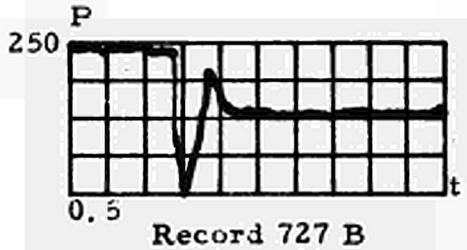

Record 727 B
IDT = 490°F
IDP = 980 psi

(d)

Note:

All Records are from Test Series A
IDT is the initial drive temperature
IDP is the initial drive pressure

Figure 5 Pressure Records at Closed End of Pressure Tube

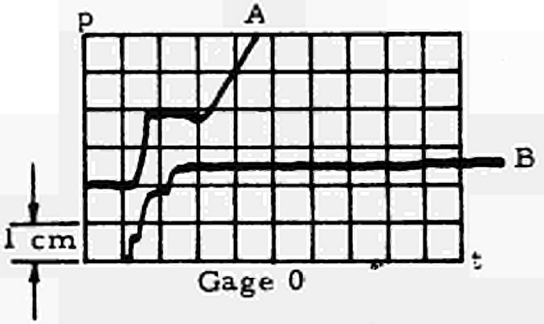

Trace A - 12.5 psi/cm, 2 msec
Trace B - 50 psi/cm, 20 msec

(a)

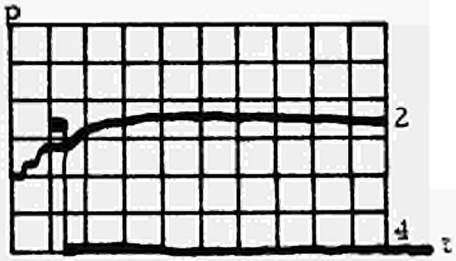

Gage 4 - 125 psi/cm, 1 msec
Gage 2 - 50 psi/cm, 20 msec

(b)

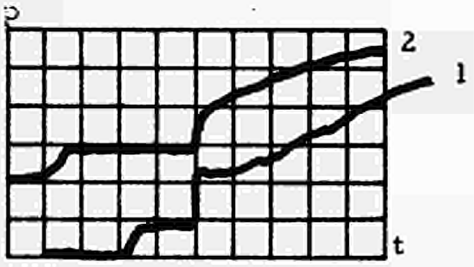

Gage 2 - 10 psi/cm, 1 msec
Gage 1 - 10 psi/cm, 1 msec

(c)

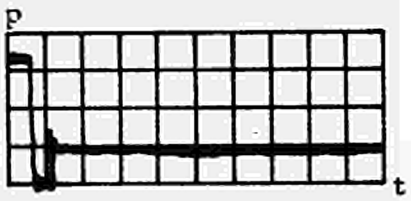

Gage 7 - 125 psi/cm, 2 msec

Note: All records are from 0707A and test series A

(d)

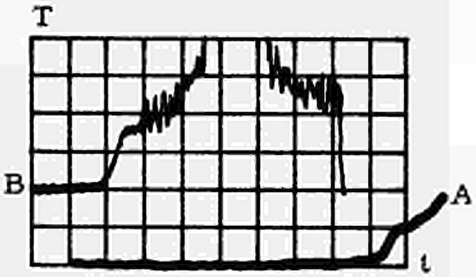

Driven Section Temperature
Trace B - 1 mv/cm, 2 msec
Trace A - 1 mv/cm, 0.5 msec
(Note: 1 mv ≃ 45 °F)

(e)

Driver Section
Temperature 0.250 mv/cm, 10 msec
Steady Calibration at 1.18 mv
(Note: 1 mv ≃ 45 °F)

(f)

Figure 6 **Representative Pressure and Temperature Records in Constant-Area Tube**

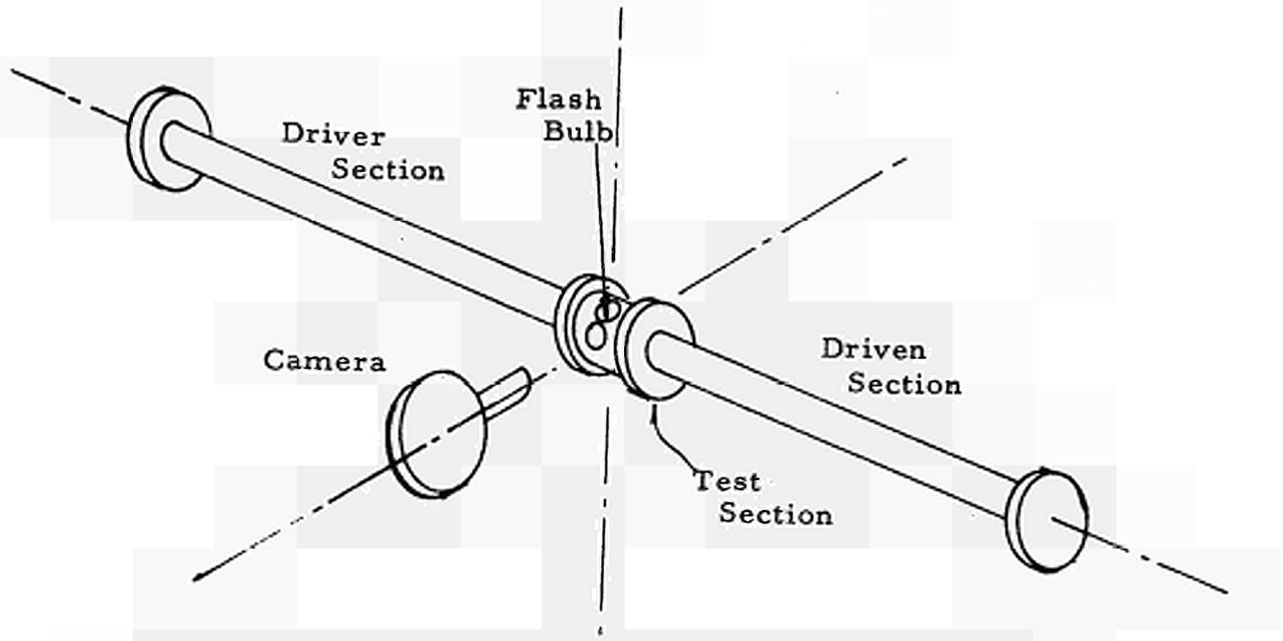

Figure 7 Arrangement of Light Source and Camera at Test Section

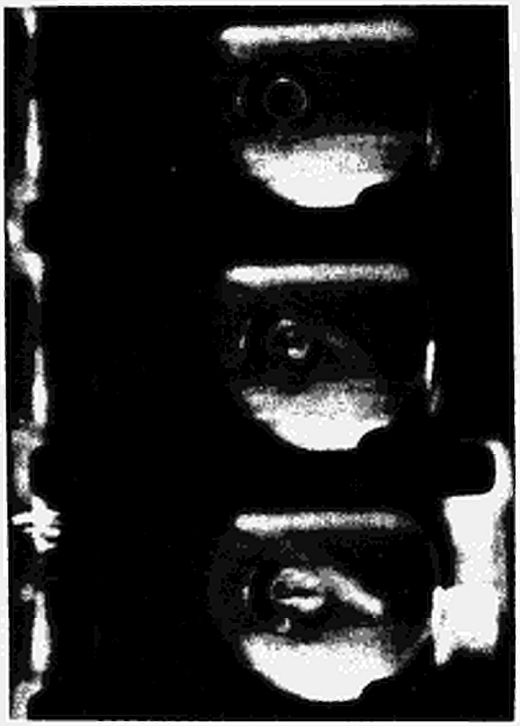

Figure 8 Frames of High-Speed Film Showing Bubble Nucleation

Framing rate: 3000/sec

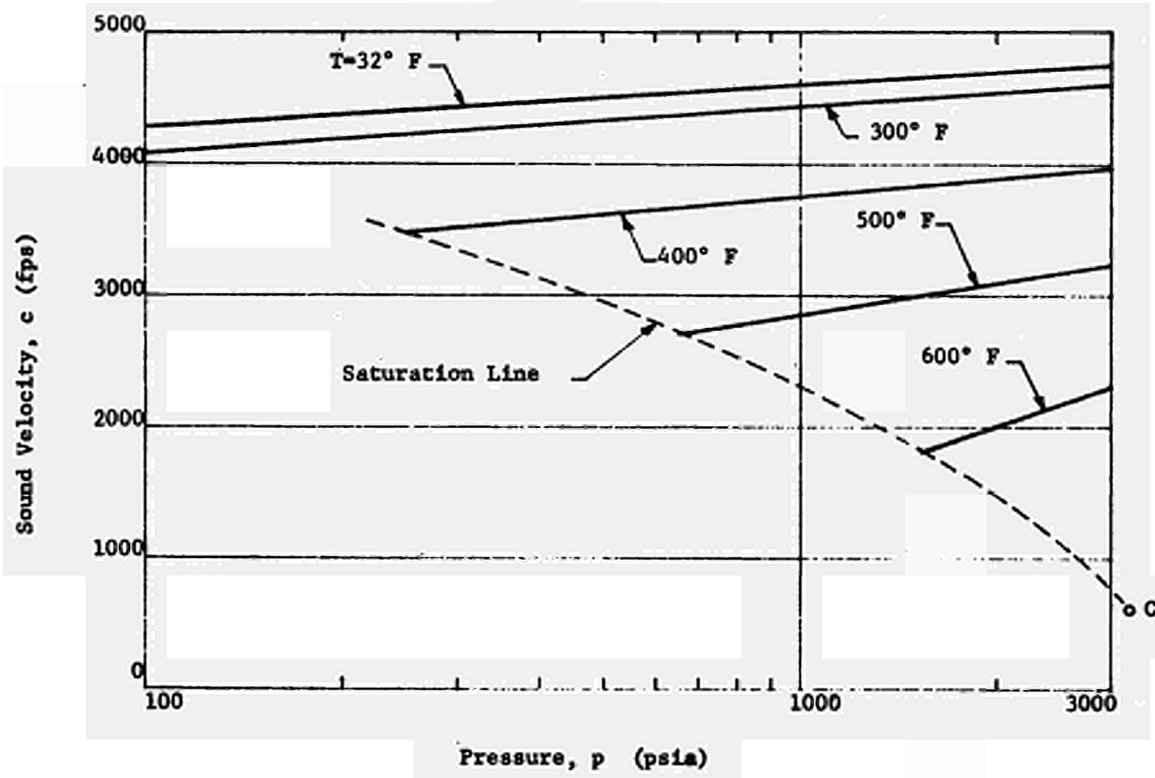

Figure 9 Sound Velocity - Compressed Liquid

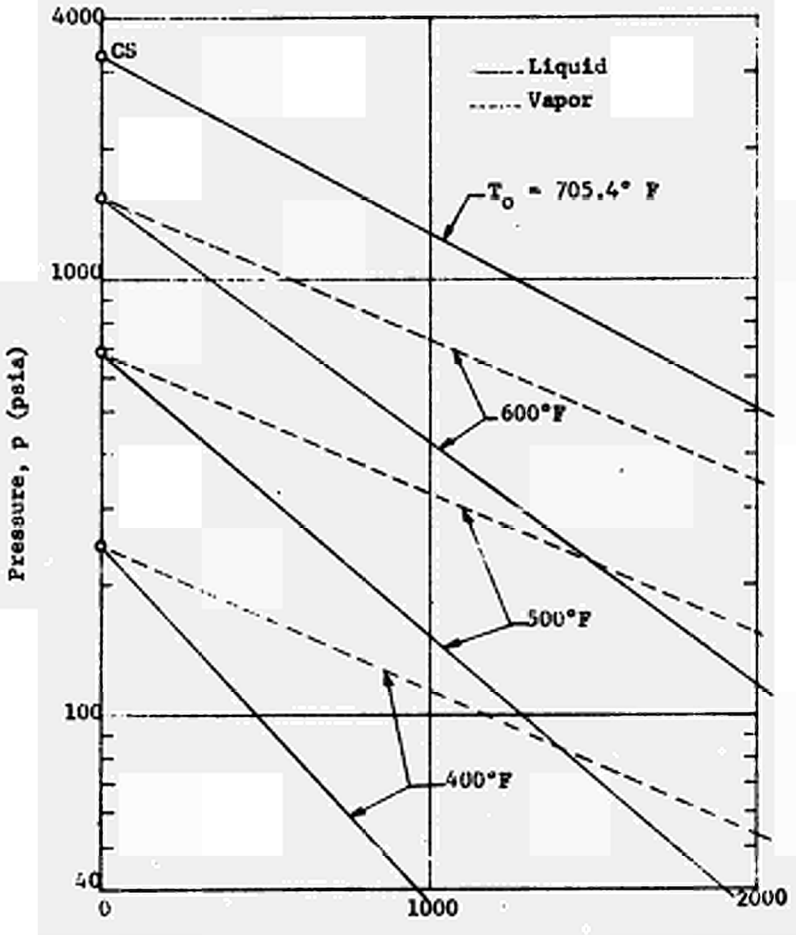

Figure 10 Hodograph Plane - Mixture Region

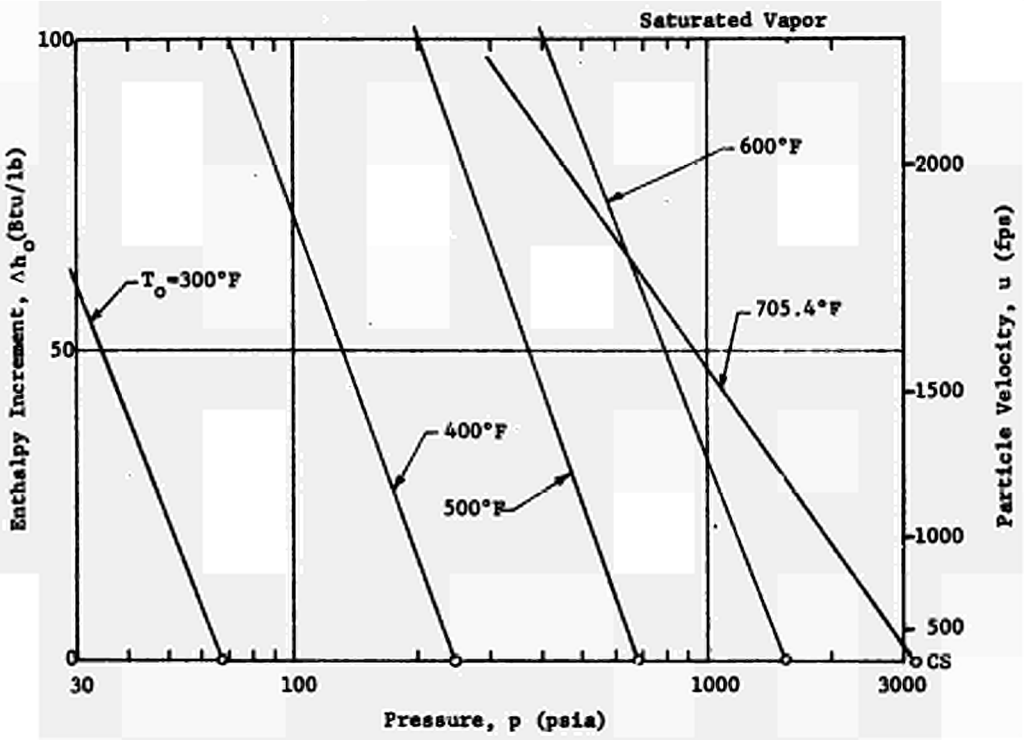

Figure 11 Enthalpy Increment in Mixture Region - Saturated Vapor

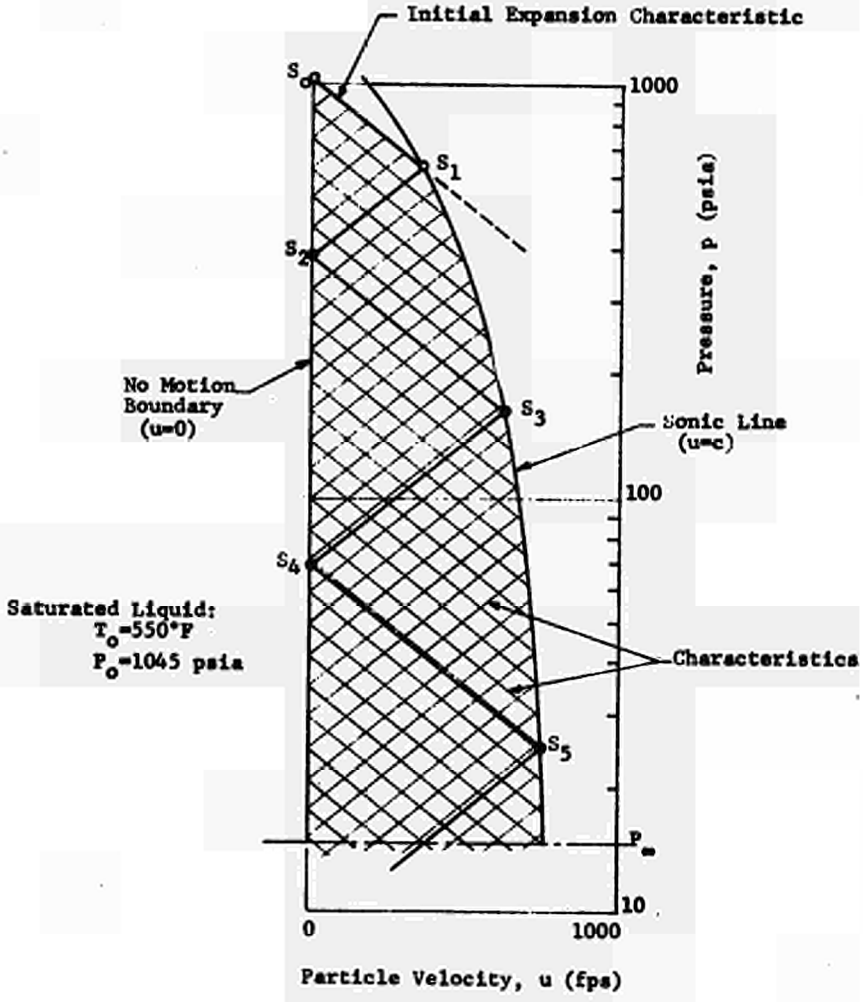

Figure 12 Hodograph Plane - Decompression Process - T_o=550°F

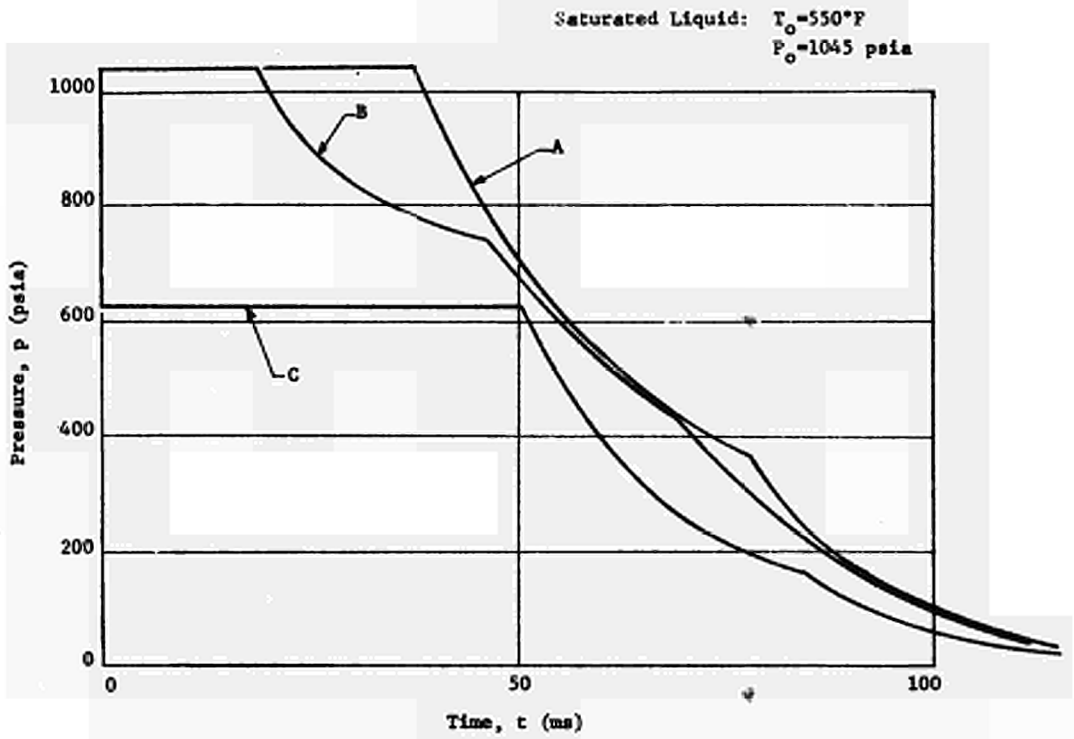

Figure 14 Pressure Histories - Decompression Solution - T_o=550°F (Liquid)

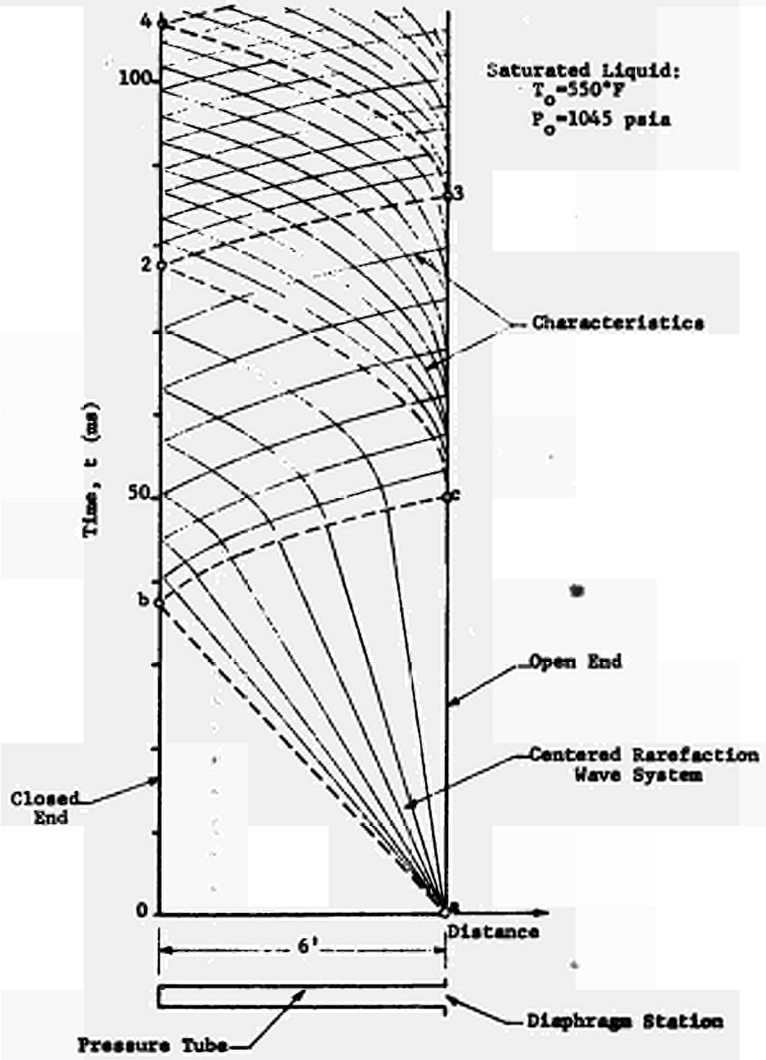

Figure 13 Wave Diagram - Decompression Process - T_o=550°F (Liquid)

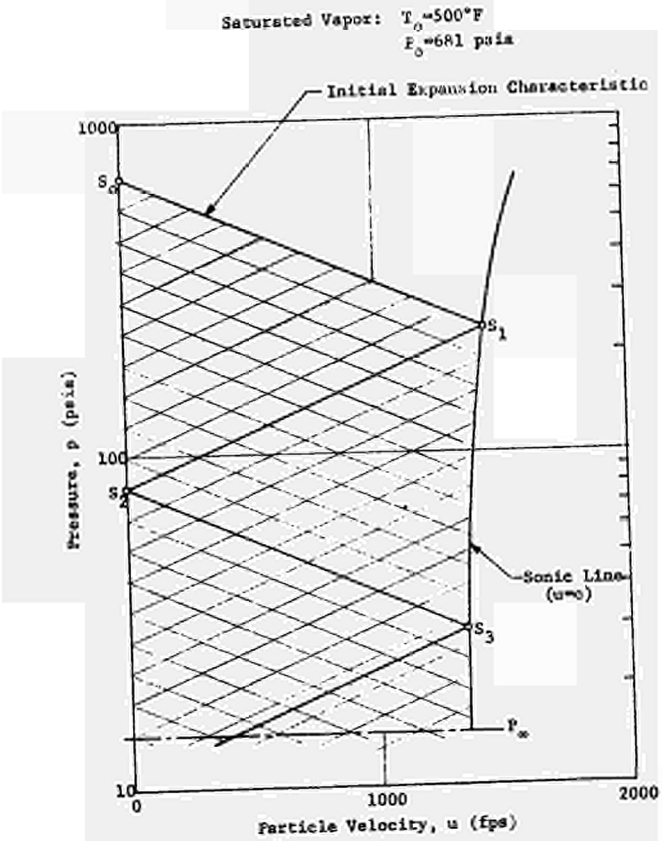

Figure 15 Hodograph Plane - Decompression Process - T_o=500°F (Vapor)

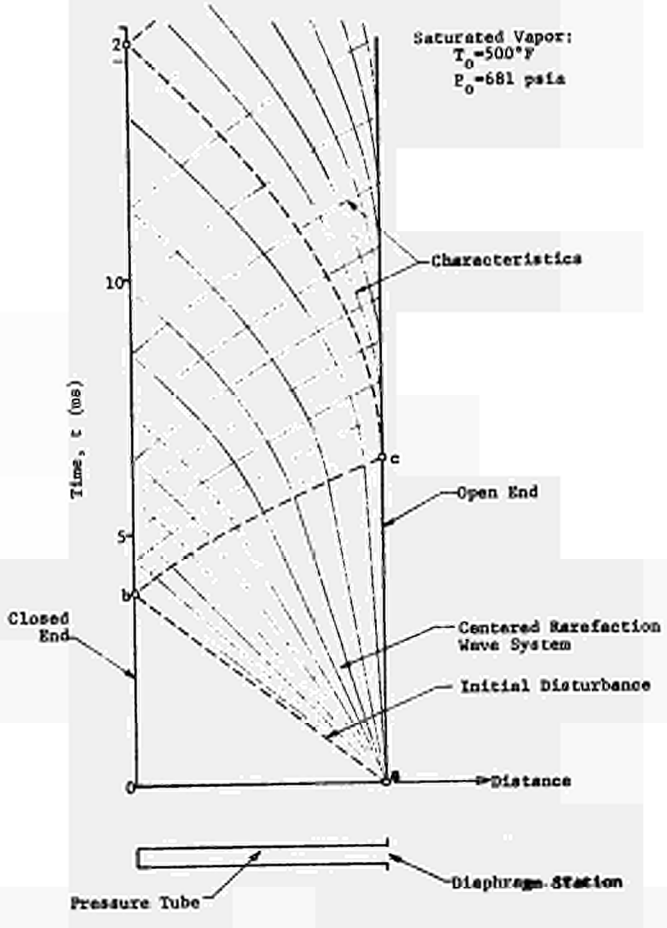

Figure 16 Wave Diagram - Decompression Process - T_o=500°F (Vapor)

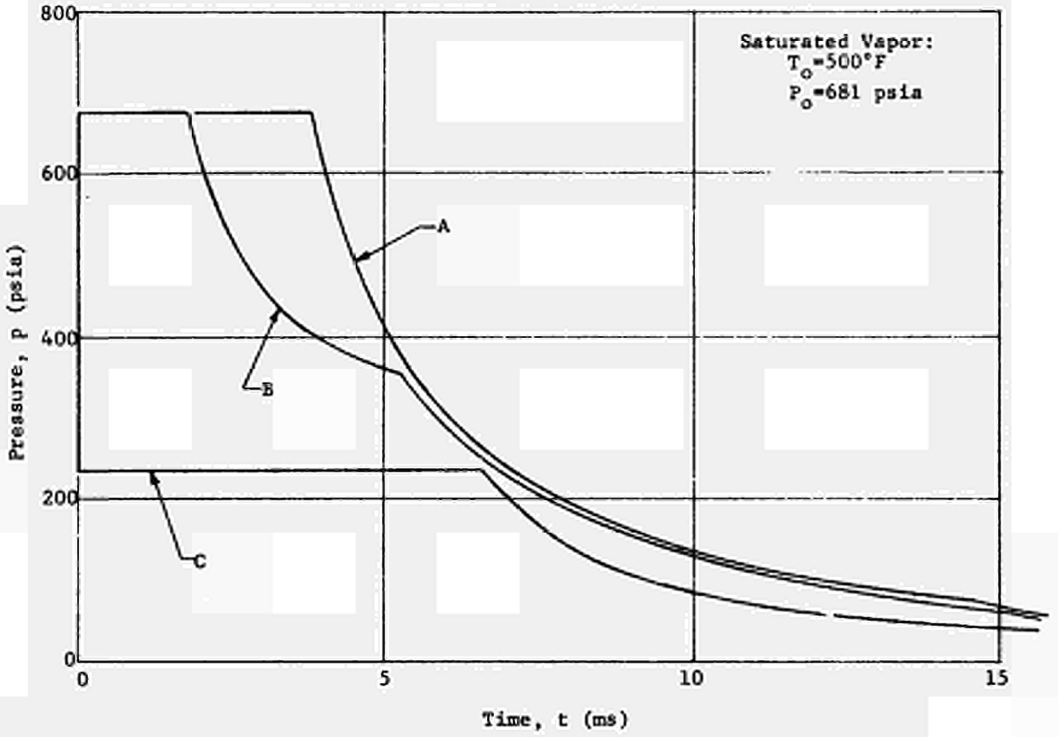

Figure 17 Pressure Histories - Decompression Solution - T_o=500°F (Vapor)

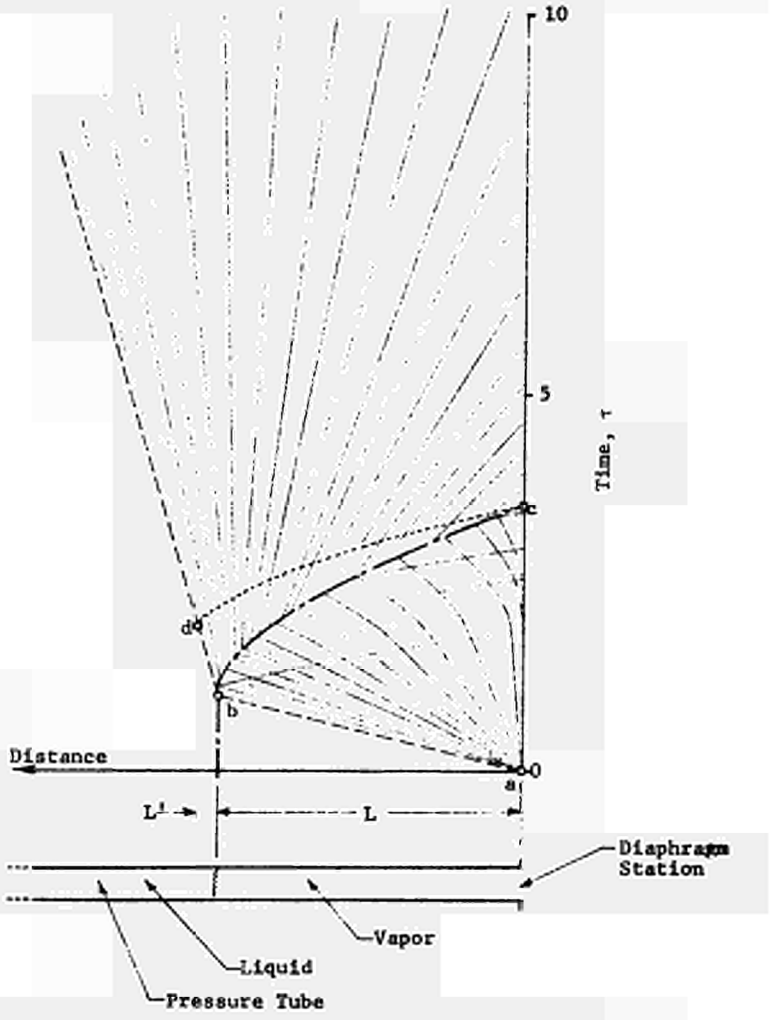

Figure 18 Wave Diagram - Uncoupled Solution for Vapor at Diaphragm- T_o=530°F

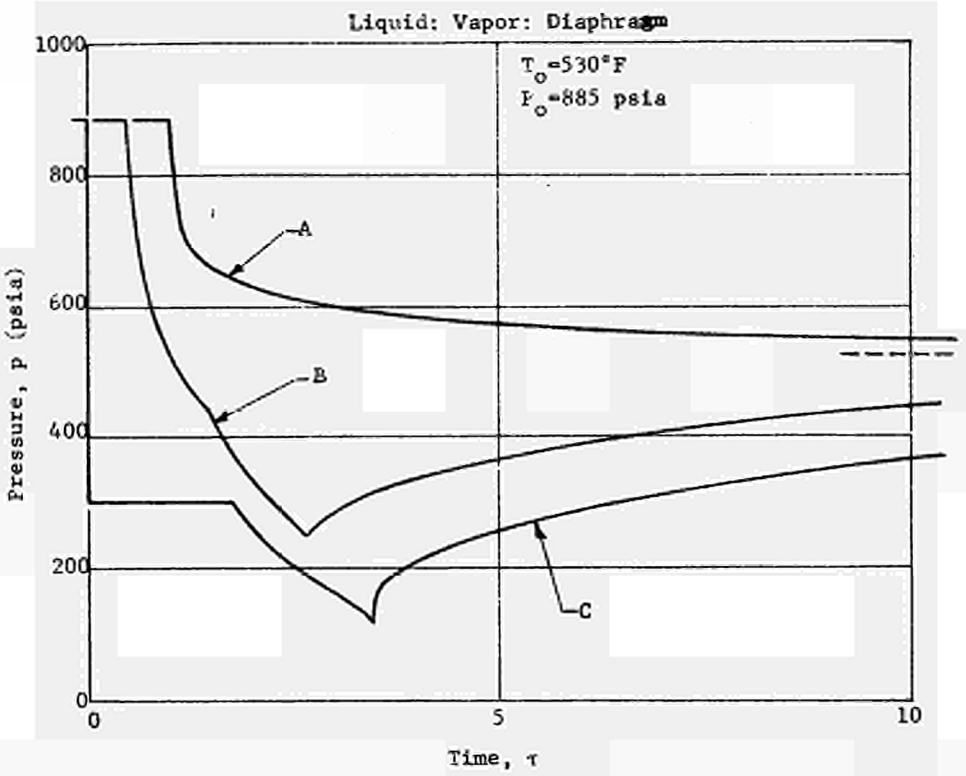

Figure 19 Pressure Histories - Uncoupled Solution for Vapor at Diaphragm- T_o=530°F

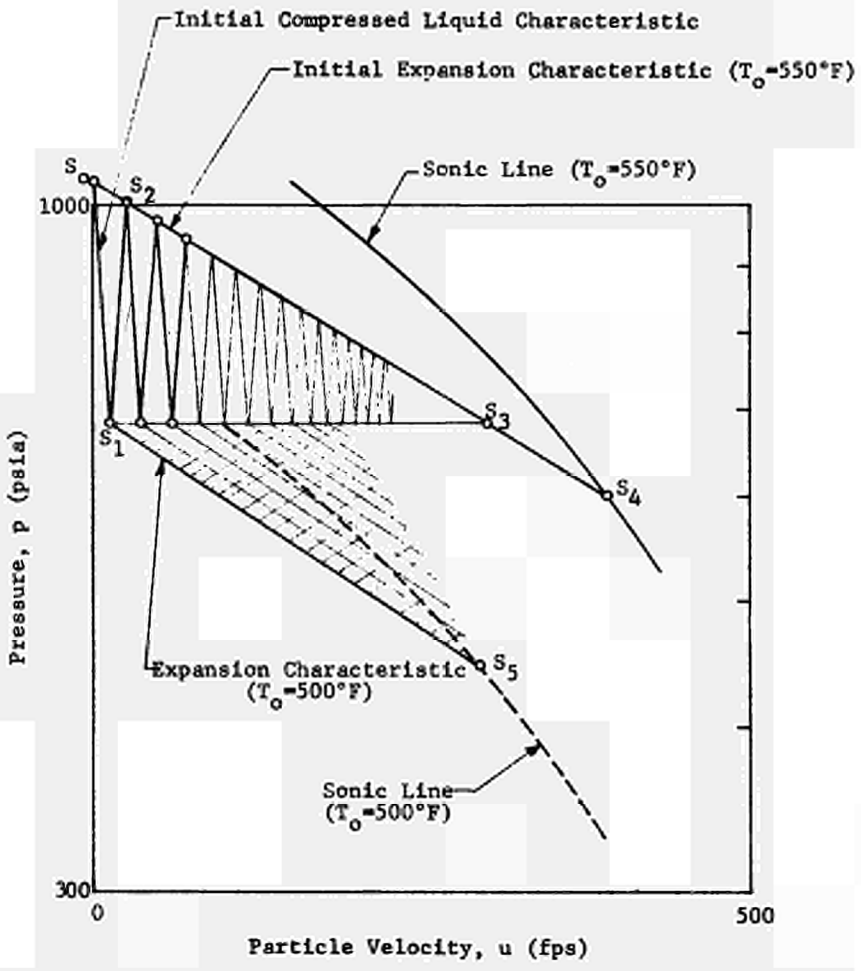

Figure 20 Hodograph Plane - Liquid/Compressed Liquid/Diaphragm

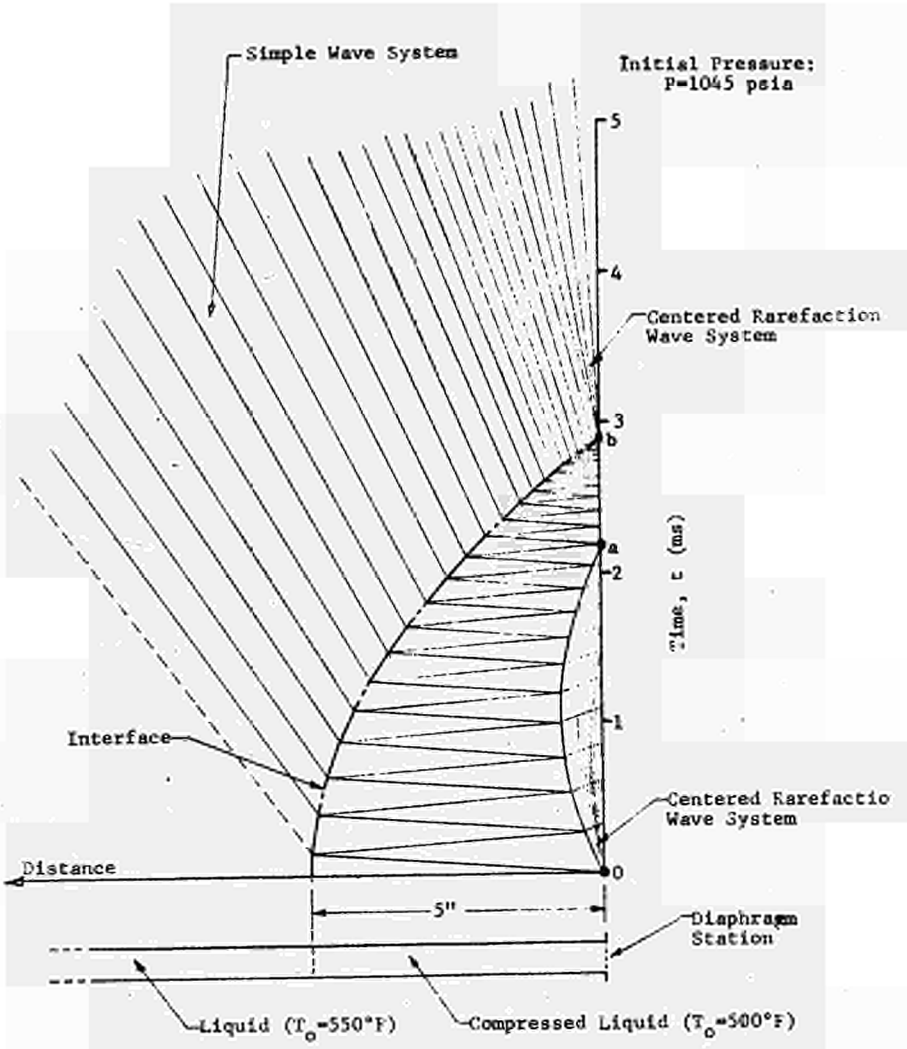

Figure 21 Wave Diagram - Liquid/Compressed Liquid/Diaphragm

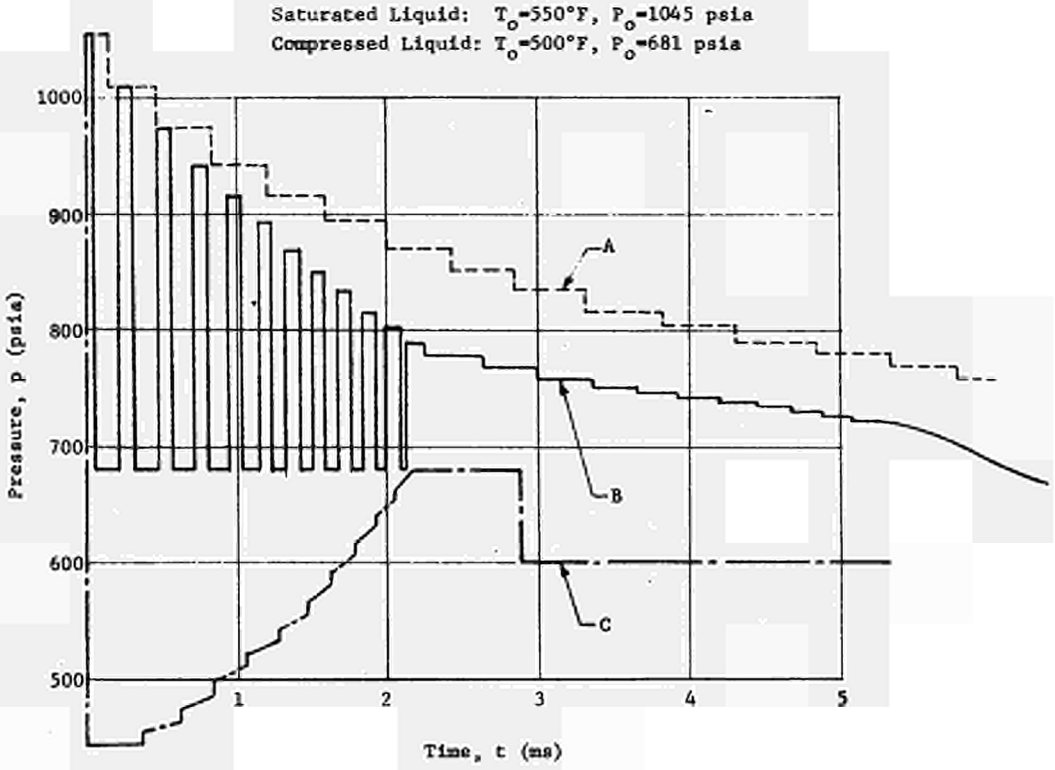

Figure 22 Pressure Histories - Liquid/Compressed Liquid/Diaphragm

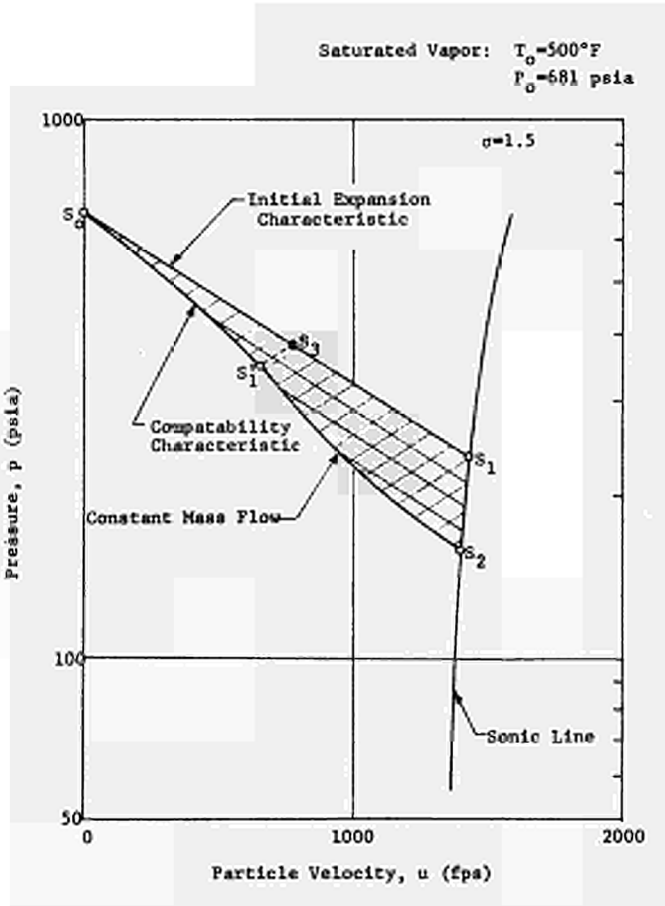

Figure 23 Hodograph Plane - Area Change Solution - σ=1.5

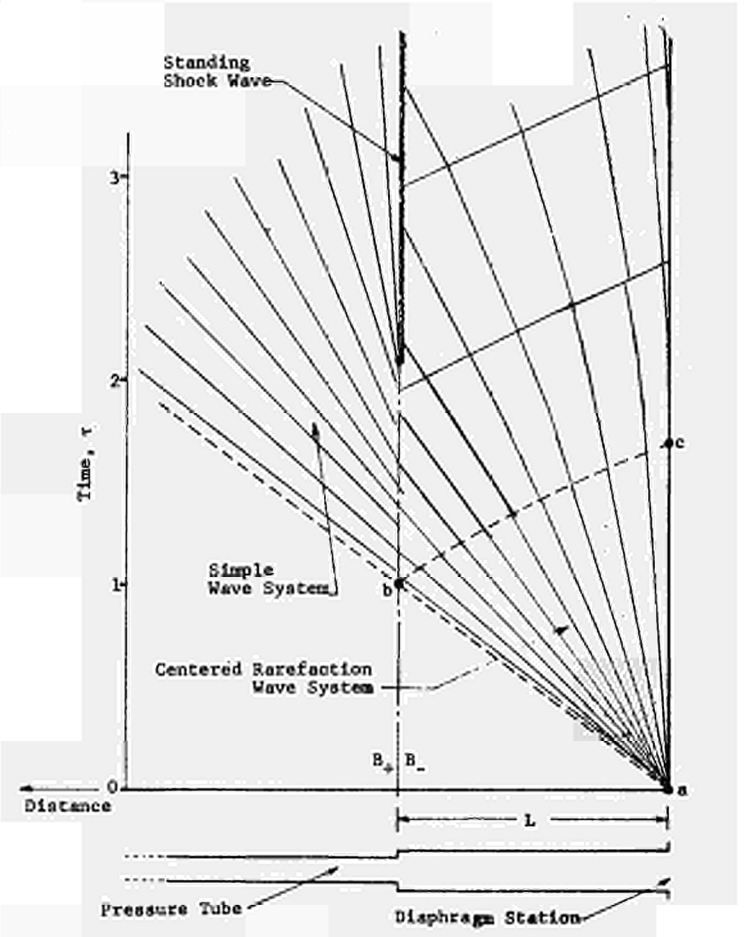

Figure 24 Wave Diagram - Area Change Solution - σ=1.5

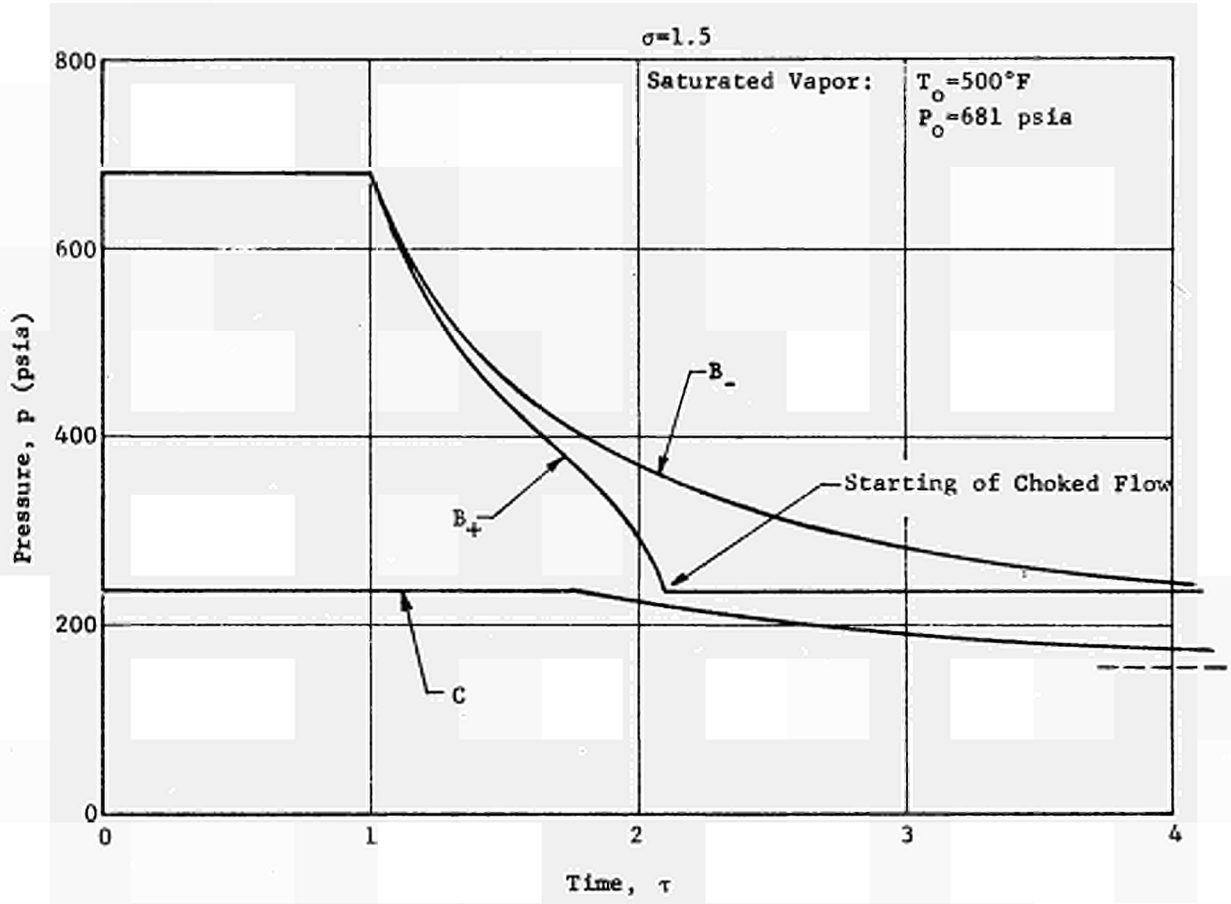

Figure 25 Pressure Histories - Area Change Solution - σ=1.5

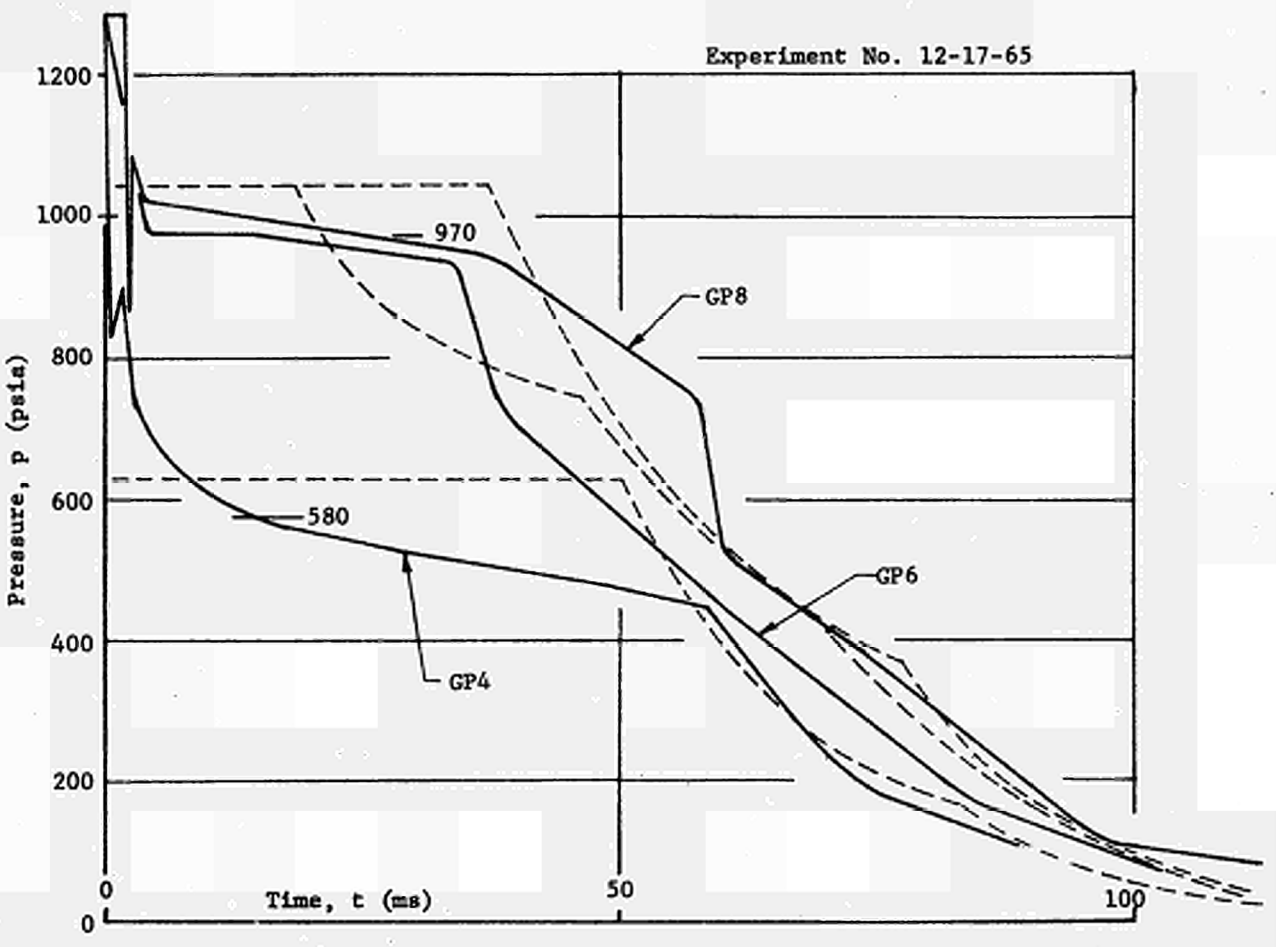

Figure 26 Comparison of Experimental Results and Theoretical Predictions (Liquid)

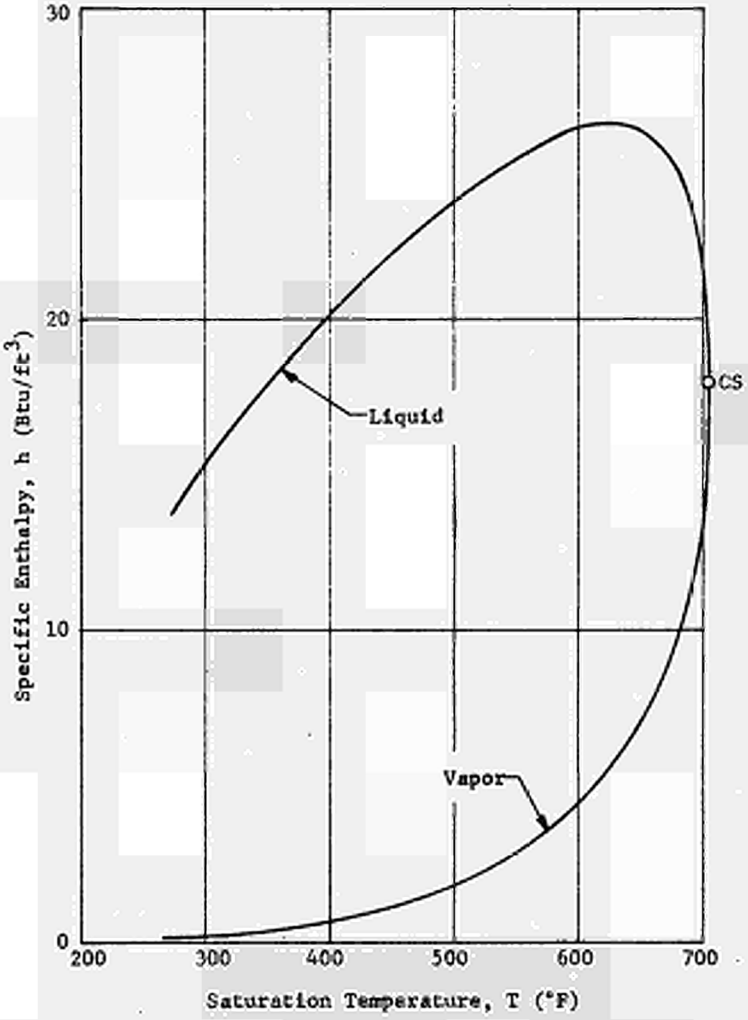

Figure 27 Specific Enthalpy along the Saturation Line

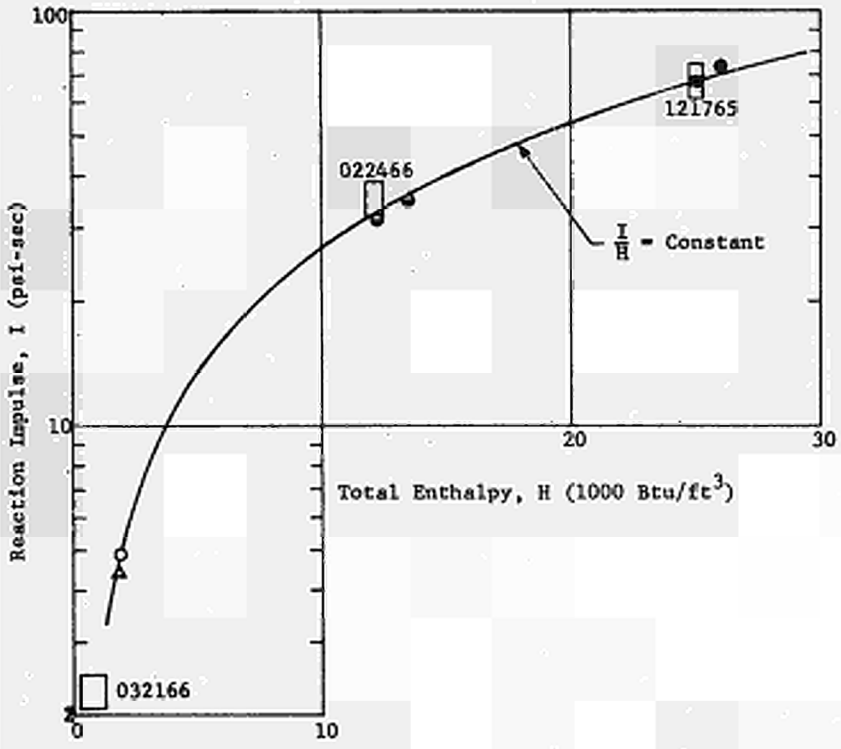

Figure 28 Reaction Impulse Correlation with Total Enthalpy

EXPERIMENTAL AND THEORETICAL INVESTIGATIONS OF SODIUM-WATER REACTIONS IN TUBES

by

K. Dumm, H. Mausbeck and W. Schnitker

Internationale Atomreaktorbau, Bensberg, Germany

1. INTRODUCTION

INTERATOM recently started the construction of the compact sodium reactor experiment (KNK). This plant, which includes a sodium-cooled zirconium hydride-moderated reactor of 20 megawatt electric output, will be equipped with two steam generators of the concentric tube-in-tube design as shown in fig. 1. The inner tube contains the upstreaming water and steam. Sodium flows downward in the surrounding annular tube. In this design, sodium and water are isolated only by a single tube wall. Because of uncertainties with regard to long-term corrosion and durability of protective magnetite-layers on the water-steam side, the possibility of tube failures cannot be excluded altogether inspite of close quality control of tubes and welds during manufacture.

The size of leaks to be considered varies from pin-holes to total rupture of the inner tube. Also a subsequent rupture of the outer tube cannot be entirely excluded. From the view point of safety we have to solve the problem to prevent the adjoining sodium-loop and intermediate heat exchanger from becoming pressurized above design pressure. In this manner it has to be ensured that the reactor system is not affected by such a conventional failure. In case of a rupture of both tubes, the system will be depressurized immediately. For a rupture of the inner tube alone, we had to develop a pressure-relief system as shown in principle in fig. 2. At the sodium outlet we install a depressurizer with an orifice at its outlet and a rupture disc at the top which, by means of a blow-out line, leads into a reaction products separation tank. At the sodium inlet the system is secured by non-reversible shut-off devices as shown in fig. 3. Additional hydrogen bubble indicators at the outlet of each sodium line serve as an early indication of small steam generator leaks. As a second remedy, remote-controlled valves which are automatically actuated by high pressure signals and independent electrical contacts behind the rupture disc, separate the leaking steam generator.

From the safety point of view the layout incident of the steam generator is the full rupture of the inner tube. Breaks of more than one tube need not be considered because of the independence of the tubes in this concentric tube design.

Basing on the aforementioned facts and in the light of the lack of representative operating experience on single-wall sodium-heated steam generators, we started an experimental and theoretical program on sodium-water reactions in tubes, in order to support the safety-layout of our steam generator by more experience. We performed a series of basic experiments with the aim of obtaining a better understanding of the reaction behaviour of sodium-water reactions in tubes and of developing an adequate mathematical program for their description. The results gained have to be verified by further experiments with a concentric tube steam generator model and its safety devices.

2. DESCRIPTION OF THE TEST FACILITY (see fig. 4)

The test facility consists of the following main components:

- high-pressure water container
- quick-action valve
- tube test section
- pressure-relief system
- reaction products tank.

The following auxiliary systems are installed:

- pressure gas system
- cover gas system
- vacuum system
- sodium filling system.

The design of the high-pressure water container permits all water conditions which may arise in a steam generator to be simulated. The usable pressure range extends from 50 to 160 kp/cm^2, the temperature range from 120 to 350°C. The container has a total volume of about 75 dm^3. Water conditions corresponding to the preheating zone of the steam generator are simulated by a nitrogen over-pressure supplied to the container via the

valves EV2 and V3. Water conditions according to the beginning of the boiling zone are reached without an additional gas cover. In addition to the safety valves, a remote-controlled relief valve EV1 allows depressurization in case of system failures. During the heat-up period the container is closed by a quick-action valve VS1. The valve has been designed by INTERATOM for this special purpose. It is kept in closed position by pressurized gas in a pneumatic cylinder. For starting the test, the gas pressure is relieved and the water pressure itself opens the valve. After a time of about 20 to 30 milliseconds the nominal valve area will be open. The closing times vary from 10 to 20 milliseconds. The nominal diameter of the valve is 25 mm.

Between the quick-action valve and the beginning of the test section, a pressure-relief section is installed. More details of this section are given following the description of the test section. A tube of 2 m length, with an inner diameter of 60 mm and a wall thickness of 8 mm, serves as test section. Ferritic steel 13 CrMo 44 (C: 0.1-0.18%, Cr: 0.7 - 1.0%, Mo: 0.4 - 0.5%) is used. At both ends the test section is closed by rupture discs B1 and B2. The rupture discs we use are nickel sheets with thicknesses from 0.07 to 0.2 mm. Burst pressures at a diameter of 50 mm up to 350°C are for instance: 0.07 mm $\hat{=}$ 8 - 9 kp/cm^2, 0.1 mm $\hat{=}$ 18 - 19 kp/cm^2, 0.2 mm $\hat{=}$ 60 - 64 kp/cm^2.

The evacuated test section is filled from a sodium container, connected to the test section by valves EV3 and V4. An expansion line between the test section and the sodium container is opened during the heat-up period. The gas dome shown in fig. 4 is closed by a steel plug. (It was used only during the initial tests).

The pressure-relief section consists of the said quick-action valve, inlet rupture disc B1 and the vacuum system. The rupture disc is necessary because it has not been possible to find a high-temperature valve with an absolutely sealed seat. On the other hand, the burst pressure of the disc must be lower than the water pressure. For this reason a leakage at the valve seat would destroy the disc at an unknown time when all the other test preparations are not yet ready. Therefore, valve EV5 is open and the section is connected to the vacuum system by valve V27 during the heat-up period. Immediately before starting the test, valve EV5 is closed electrically. For safety reasons, valve EV5 is electrically interlocked with the quick-action valve in a manner

ensuring that the quick-action valve can be opened only with valve EV5 closed.

A blow-out tube is connected to the outlet flanges of the test section. This tube has a diameter of 25 mm and a length of 1600 mm. It feeds into the pressure relief system. Sodium, reaction products, and water flow through a 250 mm diameter tube to the reaction products tank. The reaction products tank itself has a total volume of about 13 m^3. It is closed at the outlet by a rupture disc of 400 mm diameter which opens at an overpressure of about 300 mm Hg. The tank is filled with nitrogen in order to avoid hydrogen-oxygen reactions. The oxygen content is reduced to less than 4%.

The two other tanks seen in fig. 4 are already installed for the tests with the steam generator model. The whole test set-up without the reaction products tank is located in a steel tank (2 x 8 x 3 m). Between the test set-up and the control room a distance of about 25 m is provided. In case of damage in the set-up, the operators are protected by an earth wall. The test set-up is completely remote-controlled.

3. REACTION MEASURING EQUIPMENT (see fig. 5)

During the reaction, the following measurements are performed:

- Pressure characteristics at certain points of the test unit:
  - P1) Pressure in the gas area of the high-pressure water container
  - P2) Outlet line of the water container (25 Ø)
  - P3) Starting end of the test section (60 Ø)
  - P4) Centre of test section (60 Ø)
  - P5) Closing end of test section (60 Ø)
  - P6) Beginning of blow-out tube (25 Ø, behind rupture disc B2).
- Velocity of the sodium face after breakdown of B2.
  These measurements are taken at certain distances in the blow-out tube (shown in fig. 4 as Z1 to Z5).

Moreover, some tests were made to measure reaction temperature and wall stresses in the test section.

Because of the quick movement of the reaction face it has been impossible to achieve reproducible temperature characteristics. The measurement of mate-

rial stresses was also not satisfactory, as the temperature compensation during the test was not fast enough.

With respect to pressure measurements, theoretical predictions indicated that in the instant of the reaction a very rapid pressure increase will occur. Therefore it was necessary to use pressure pickups with a very high natural frequency. Only quartz pickups were taken into consideration. Based on such calculations the following equipment was chosen:

a) Pressure pickup

Supplier:	AVL Graz, Laboratory for internal combustion engines.
Range:	0 to 10,000 kp/cm^2
Pressure sensitivity:	2.2 $pC/kp/cm^2$
Natural frequency:	180 kcps
Insulation resistance:	10^{14} Ohms
Acceleration sensitivity:	0.001 $kp/cm^2/g$
Maximum temperature:	240°C

From these data it can be seen that the critical limitation for the pickups is the temperature of 240 °C max. To avoid damage and to reach sodium temperatures higher than 240°C, we use small cooling tubes with a length of about 120 mm between the pickup and the tube walls. To avoid gas bubbles inside, these tubes are filled with an organic grease. Data of interest on the grease are:

Velocity of sound:	1,500 m/s
Specific weight:	0.86 - 0.9 kg/dm^3

This shows that the compressibility of the grease is nearly equal to that of sodium.

b) Piezo-Amplifier

By means of a 35 m coaxial cable, the pickup is connected to a Piezo-amplifier.

Technical data:

Supplier:	Vibrometer AG, Fribourg/Switzerland
Input impedance:	about 10^{14} Ohms

Output:	± 5 Volts maximum
Output impedance:	about 100 Ohms
Linearity:	± 0.25% with respect to full output
Rise time:	about 5/us for 10-90%
Frequency range:	0-100 kcps (-3 d B)

c) Driver Amplifier

To drive the galvanometers of the oscillograph, an additional amplifier has been found necessary.

Technical data:

Input impedance:	100 kilo ohms nominal
Source impedance:	1 kilo ohms

Values up to 10 kilo ohms are possible, but will decrease the stability.

Input voltage:	± 0.5 - ± 1.6 Volts for full output, depending on gain adjustment.
Output voltage:	± 10 Volt, limited at 13 Volts
Output current:	± 150 mA
Output impedance:	1 ohm nominal
Noise:	less than 1/u Volt effective
Linearity:	from 0 - ± 10 Volts better than ± 0.5%
Rise time:	10-90% less than 25/us

d) Velocity of the Sodium Face

For measuring the velocity of the sodium face, we use spark plugs which are mounted into the blow-out tube. Every spark plug is connected to its own electric circuit. By the movement of the sodium face, the electric circuits are shortened. As the distances between the spark plugs are known, the velocity of the sodium face can be calculated. Moreover, as the diameters of test section and blow-out tube are known, it is possible to calculate the velocity of the reaction zone by means of this simple measuring equipment.

e) Recording Systems

Pressure characteristics and speed of the sodium face are recorded at a 25-channel galvanometer oscillograph:

Supplier:	Hartmann and Braun AG (Lumiscript 25/300)
max. speed of the registrating paper:	3 m/s

As galvanometers for the pressure measurements we use the Hartmann and Braun type HMK 4000 H:

natural frequency:	4000 cps
useful frequency range:	about 0-2500 cps
delay time:	0.055 milliseconds
time constant:	0.07 milliseconds

In the spark plug circuits we use the type HMK 100 I, with a

natural frequency:	100 cps
useful frequency range:	0-70 cps
delay time:	2.2 milliseconds
time constant:	2.8 milliseconds

The above mentioned data show, that the maximum frequency of the pressure recording system is limited by the frequency of the HMK 4000 H galvanometers. In order to improve the resolution time considerably, we use in parallel a Tectronix cathode ray oscilloscope Type 502 A, with a maximum frequency of 2 Mcps. The cathode-ray oscilloscope is connected to the output of the piezo-amplifier (max. frequency 100 kcps). The cathode-ray is triggered by the pressure signal itself. For recording purposes, we use a Polaroid-Land camera.

4. TEST PROGRAM

With the above described test set-up we have performed about 30 basic experiments during the past 1 1/2 years. In addition, we conducted a number of special tests to check the proper functioning of the shut-off devices installed at the steam generator.

The large number of basic experiments was necessary to vary the parameters which may have an influence on the reaction behaviour, namely, on the water side, temperature and pressure, for subcooled and saturated water as well; and, on the sodium side, the temperature and, to some extent, geometry of the test section.

The water temperature was varied from 120°C to 323°C. The waterside pressure was varied from 80 to 140 kp/cm^2. On the sodium side, temperatures from 150°C to 390°C were applied. For the major portion of tests, the outlet rupture disc B2 was installed in the blow-out tube behind pressure pickup P6.

5. TEST RESULTS

Fig. 6 shows a typical result recorded by the Galvanometer-oscillograph. The test parameters chosen were:

$$t_{Na} = 300°C,\ t_{H_2O} = 250°C,\ P_{H_2O} = 80\ kp/cm^2 \text{ (subcooled water)}$$

The reaction starts immediately after disc B1 is ruptured. The first pressure peak is reached after some 10^{-5} s.

This fast rise-time was measured by an additional cathode ray-oscilloscope. While only the first peak can be attributed to the reaction itself, the following peaks are due to reflection effects at the sodium surfaces. The travelling time of the first shock wave can be seen from the different pressure readings (P3, P4, P5). A second group of pressure peaks will be induced at the moment when the sodium face enters the cone between test section and blow-out tube.

These pressure peaks are observed first at P5 and travel back to the test section. The reflected high pressure waves exist in the liquid zone only. That means for the pickup, they are existent only for the time during which the pickup is in contact with sodium. They are highly damped in the compressible reaction product zone which consists mainly of hydrogen, mixed with some oxydes and water vapour. The spark plugs Z1 to Z5 indicate the velocity of the sodium face. In this case the velocity of 175 m/s in the blow-out tube corresponds to 30 m/s in the test section. After 10 to 20 ms following the start of the reaction, the test section pressure remains for some time at a point around the initial water pressure, if the leakage was sufficiently large (e.g. complete tube rupture). If, in the case of saturated water, the initial sodium temperature is much higher than the water temperature, a delayed secondary pressure surge superimposed on the primary reaction pressure can be observed (see fig. 7). The data for this special test were: t_{Na} = 370°C,

t_{H_2O} = 323°C, p_{H_2O} = 120 kp/cm^2 (saturated water). The effect can be interpreted as steam flashing due to a sudden release of heat, stored in the hot test section, to the introduced saturated water. The high temperature difference between the test section and the water causes initially steam blanketing of the wall (film boiling); the steam layer collapses some time later usually after a random pressure disturbance started at the outlet of the blow-out tube, about 40 ms after the beginning of the reaction. Before and after the second pressure oscillation, the quasi-stationary pressure equals also the initial water pressure.

Fig. 8 shows a typical test result, where the location of the rupture disc has been changed. Now the sodium filling extends to the pressure pickup P6.

The test data were: t_{Na} = 370°C, t_{H_2O} = 290°C, p_{H_2O} = 90 kp/cm^2 (slightly subcooled water). The travelling velocity of the first shock wave is seen much more clearly than in fig. 6 and 7. Included into the figure is a reproduction of the recorded cathode-ray reading. It shows clearly that due to the limited frequency resolution, the pressure peaks measured by the galvanometers are pressure-time integrals of the real pressure structure. At the cathode-ray oscillogram we found a rise time, up to the first peak, of about 2.10^{-5} s.

6. MATHEMATICAL MODEL

Existing mathematical models of the sodium-water reaction normally presume that the amount of water entering the sodium volume reacts immediately and completely with the sodium. This means no time is needed for the reaction itself. The amount of reaction materials is only given by transport phenomena. This leads to an infinite pressure at time zero, which decreases very quickly. We have developed a refined model which gives us a chance to predict more realistically the first pressure peak and the time of pressure development.

The reaction between sodium and water takes place in two steps:

$$Na + H_2O \longrightarrow NaOH + \frac{1}{2} H_2 \quad - \quad 33.7 \text{ kcal/mol}$$

$$Na + NaOH \longrightarrow Na_2O + \frac{1}{2} H_2 \quad + \quad 2.7 \text{ kcal/mol}$$

The second reaction follows the first one only if sodium is available excessively. The heat quantity of the first reaction is as large as to heat up the developed hydrogen to the boiling temperature of the sodium hydroxide or, in case of both reactions, to the sublimation temperature of the sodium oxide. Because of the vaporisation heat of NaOH or the sublimation heat of Na_2O, these temperatures will probably not be exceeded during the reaction; they are 1390°C and 1260°C respectively, at normal pressure.

The model is restricted to one-dimensional behaviour, which means for reactions in tubes only. As seen in fig. 9, we assume that immediately after the reaction has started a hydrogen bubble will disconnect the water and sodium boundaries. To maintain the reaction the water vapour has to diffuse through the hydrogen. The hydrogen bubble will be mixed with some sodium hydroxide (and no sodium oxide, as an excess of water in the diffusion zone must be assumed).

From the theory of diffusion in gases by Hirschfelder, Curtis, and Bird one can derive an approximate diffusion coefficient for hydrogen and water vapour in the interesting temperature range as under:

$$D = C' \cdot \frac{T^{(1+\alpha)}}{P} \tag{1}$$

Fick's law

$$\frac{dM}{dt} = D \cdot q \cdot \frac{dc}{dx} \tag{2}$$

can be written for our case to read

$$\frac{dM}{dt} = \frac{D \cdot C_{crit}}{S}; \; (q = 1) \tag{3}$$

Equations (3) and (1) confined to the ideal gas equation

$$P \cdot v = M \cdot R \cdot T \tag{4}$$

lead to the expression

$$\frac{dM}{dt} = C' \cdot \frac{T^{\alpha} \cdot C_{crit}}{R \cdot M} \tag{5}$$

Under the assumption of an adiabatic compressible gas bubble, finally the equation

$$\frac{dM}{dt} = C_o \cdot \frac{T^{*\alpha} \cdot S^{*\alpha \cdot (K-1)}}{M^{1-\alpha \cdot (K-1)} \cdot S^{\alpha \cdot (K-1)}} = C_o \cdot f(M,S) \qquad (6)$$

will be obtained.

The rate of hydrogen formation is influenced also by the sodium layer at the tube wall which reacts with the following water after passage of the gas bubble. This can be expressed by a second term in equation (6)

$$\frac{dM}{dt} = C_o \cdot f(M,S) + C_1 \cdot \frac{dx}{dt} \qquad (7)$$

After the sodium leaves the blow-out tube a third term in the fundamental equation is necessary to describe the influence of gas venting with critical velocity:

$$\frac{dM}{dt} = C_o \cdot f(M,S) + C_1 \cdot \frac{dx}{dt} - C_3 \cdot P_{gas} \qquad (8)$$

The pressure in the gaseous phase can be described by

$$P = \frac{R \cdot T^* \cdot S^{*K-1} \cdot M^K}{S^K} \qquad (9)$$

again under the assumption of an ideal gas and an adiabatic compression.

Equations (7), (8), and (9) are the main equations to describe the reaction. In addition we used equations to describe the movement of sodium and water and the initial conditions. Sodium was assumed to be compressible during the first few milliseconds. The program does not allow to start with M and S equal to zero. Therefore, the initial value of S was taken to be the mean free path according to the kinetic theory of gases, and the initial value of M was chosen to give a starting pressure in the hydrogen bubble of 1 kp/cm^2.

In fig. 9 the theory is compared with the experiments. They can be matched fairly by proper adjustment of the constants in equation (8). The constants can be fixed separately, because of the fact that the diffusion term is impor-

tant for times less than 2 milliseconds; the surface layer term is of main importance for times longer than 2 ms; and the vent term has to be introduced after about 150 ms, where the exact value depends on the water pressure. According to turbulence effects, the constant C_o has to be 1 to 3 times larger than given by diffusion theory, if the difference in density between water vapour and an ideal gas is taken into consideration. Adjustment of C_1 shows that the sodium layer itself has a thickness of 0.1 to 0.2 mm. C_3 finally is in accordance with an effective atomic weight of 40 for the mixture of reaction products and vapour.

Theory and experiment show that the maximum pressure peak is approximately equal to $\sqrt{C_o}$

to $\sqrt{\text{leak area}}$ (only, if leakage area < 40 to 50% of reaction tube cross-section)

to $f(C_o) + f(V_{water})$

Moreover, the measured pressures are nearly equal to the theoretical peaks. At times of more than 50 ms, experimental and theoretical pressures show approximately the same level as the water pressure.

7. CONCLUSIONS

There is good agreement between our basic experiments and the theoretical model as far as the reaction pressure is concerned. The reflected pressure pulses are not included in the theory. Further experiments will be performed to check these results with tube-in-tube steam generator models. Experiments are planned also for pool-type steam generators.

SYMBOLS USED IN THE EQUATIONS

C = concentration of one component

C' = factor of the constant values in the equation of Hirschfelder, Curtis and Bird

C_o = constant to describe vapour diffusion through hydrogen

C_{Crit} = vapour concentration at the critical point

C_1 = constant to describe the influence of sodium film reaction at the wall

C_3 = constant to describe the blow-out of reaction products at critical velocity

D = constant of diffusion

K = exponent of adiabatic expansion or pressure

M = mass of gas (Kilomol)

p = gaspressure in the reaction zone

q = cross-section of reaction zone

R = gasconstant in general

s = length of the gaseous zone

s^* = molvolume of hydrogen at 1 atmosphere and reaction temperature

x = distance between the water-hydrogen boundary and rupture disc B1

t = time

T = temperature of hydrogen

T^* = temperature of hydrogen at 1 atmosphere

V = gasvolume

α = exponent to figure the variable term of the theory by Hirschfelder, Curtis and Bird; approximately 0.65

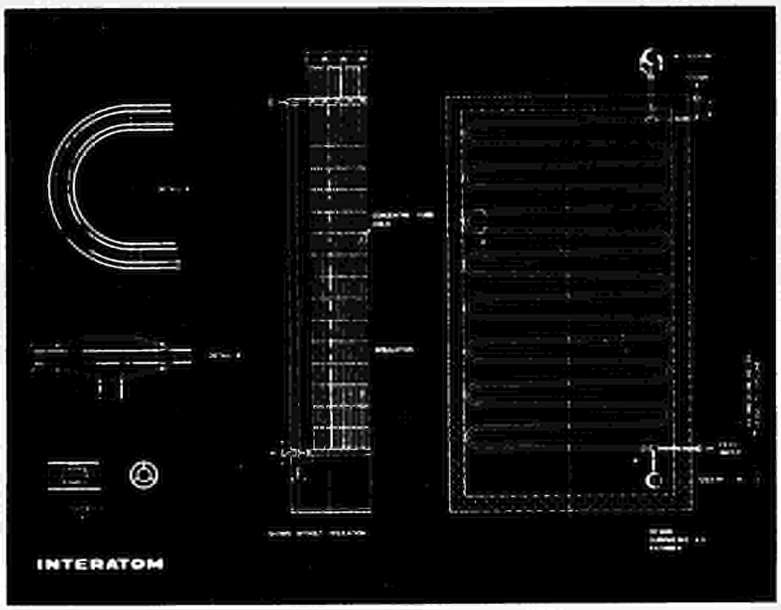
INTERATOM

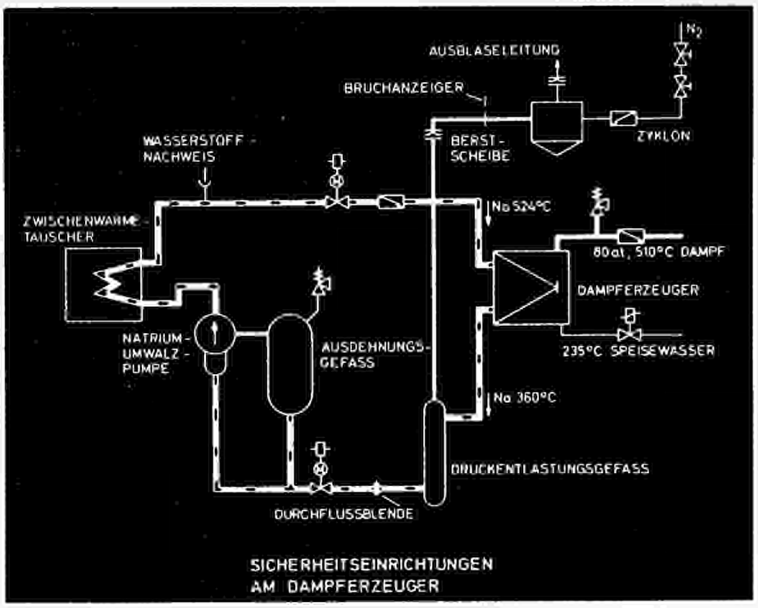
AUSBLASELEITUNG
N_2
BRUCHANZEIGER
ZYKLON
BERST-SCHEIBE
WASSERSTOFF-NACHWEIS
ZWISCHENWÄRME-TAUSCHER
Na 524°C
80 at, 510°C DAMPF
DAMPFERZEUGER
NATRIUM-UMWALZ-PUMPE
AUSDEHNUNGS-GEFÄSS
235°C SPEISEWASSER
Na 360°C
DRUCKENTLASTUNGSGEFÄSS
DURCHFLUSSBLENDE
SICHERHEITSEINRICHTUNGEN
AM DAMPFERZEUGER

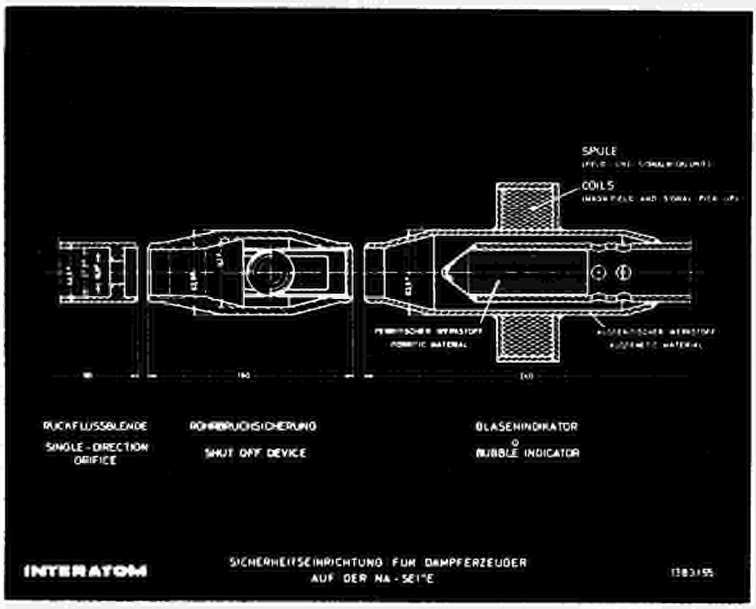
SPULE
COILS
RÜCKFLUSSBLENDE
SINGLE-DIRECTION ORIFICE
ROHRBRUCHSICHERUNG
SHUT OFF DEVICE
BLASENINDIKATOR
BUBBLE INDICATOR
INTERATOM
SICHERHEITSEINRICHTUNG FÜR DAMPFERZEUGER AUF DER NA-SEITE

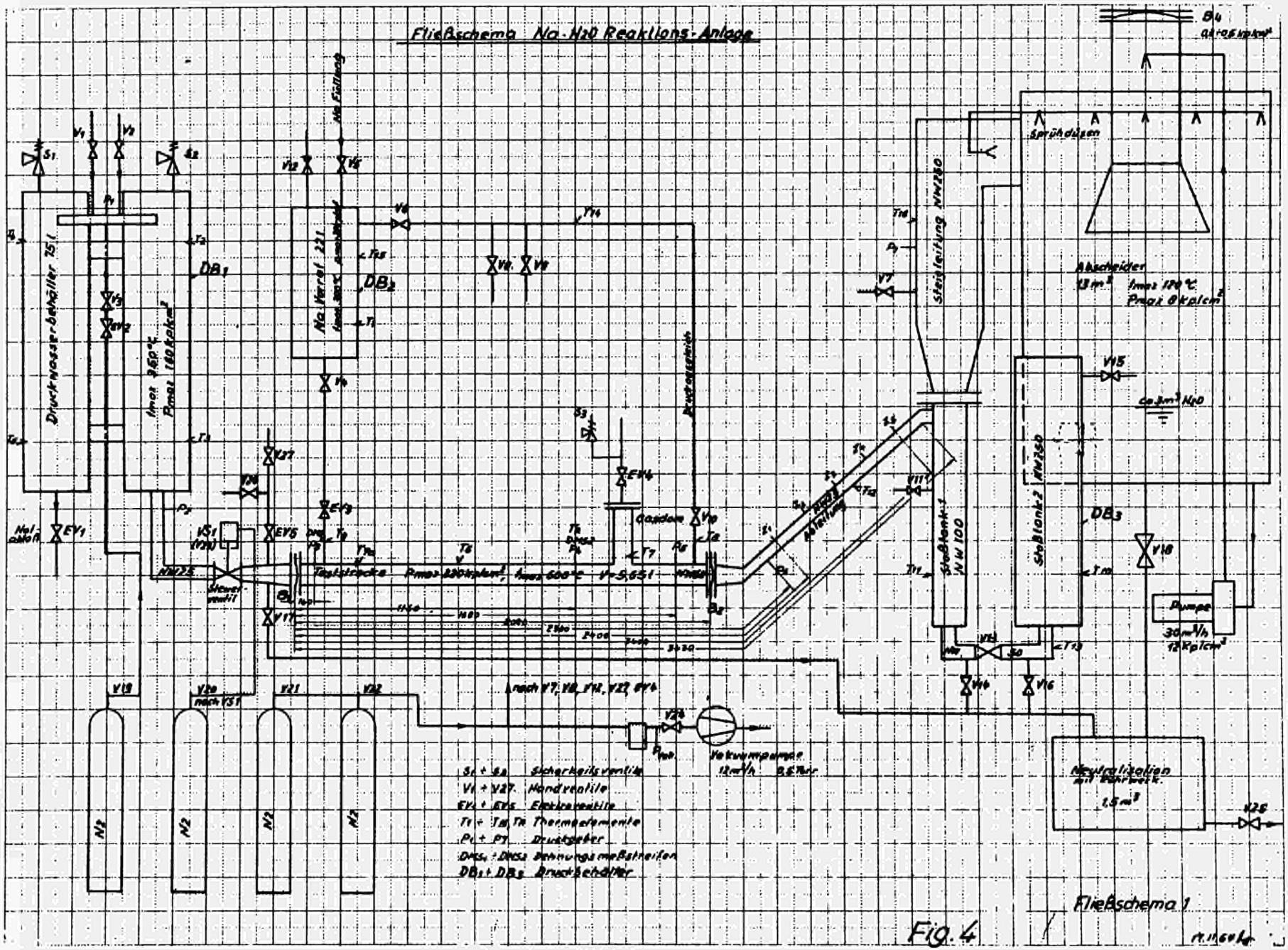
Fließschema Na-H20 Reaktions-Anlage
Druckwasser-behälter 25 l
Na Vorrat 22 l
Na Füllung
Steigleitung NW 250
Sprühdüsen
Abscheider
Stoßbank 1 NW 100
Stoßbank 2 NW 250
Pumpe
Teststrecke
Gasdom
Steuerventil
Vakuumpumpe
Neutralisation
Fließschema 1
Fig. 4

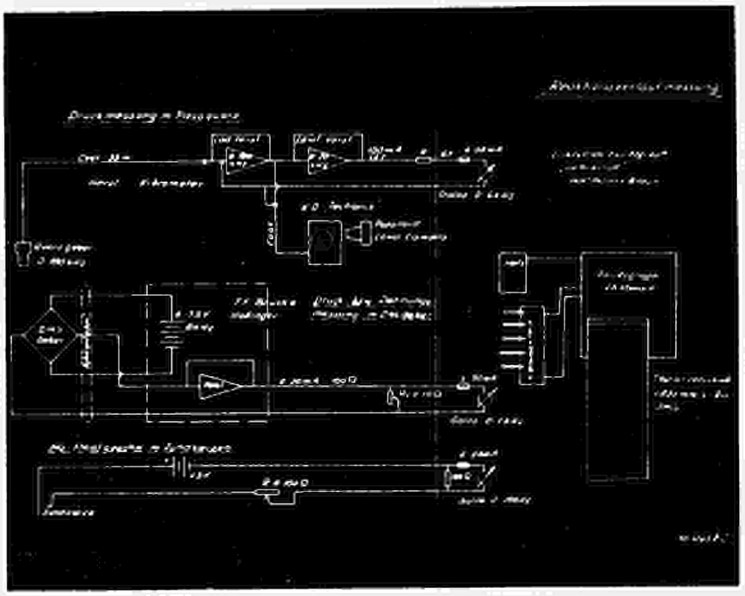

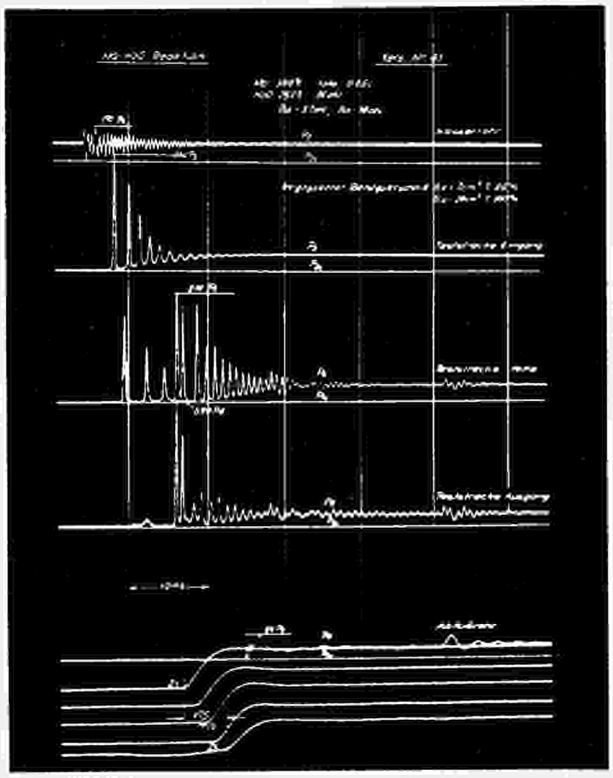

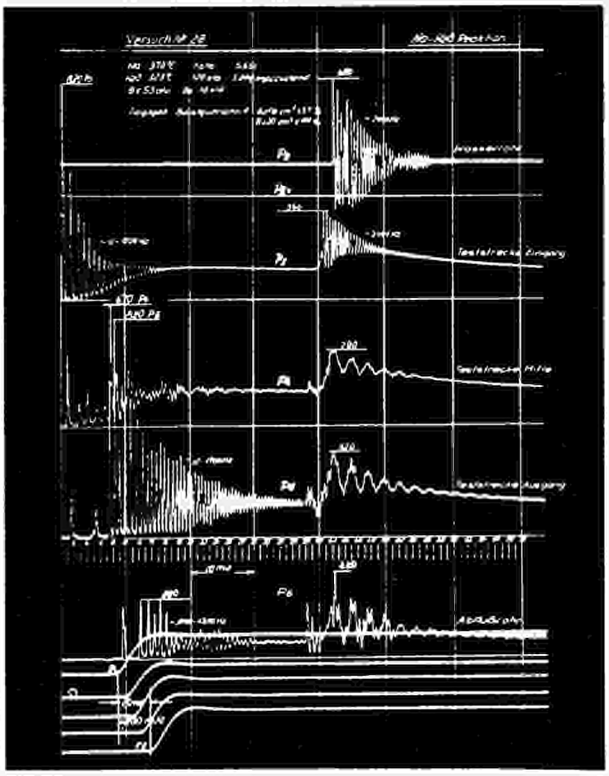

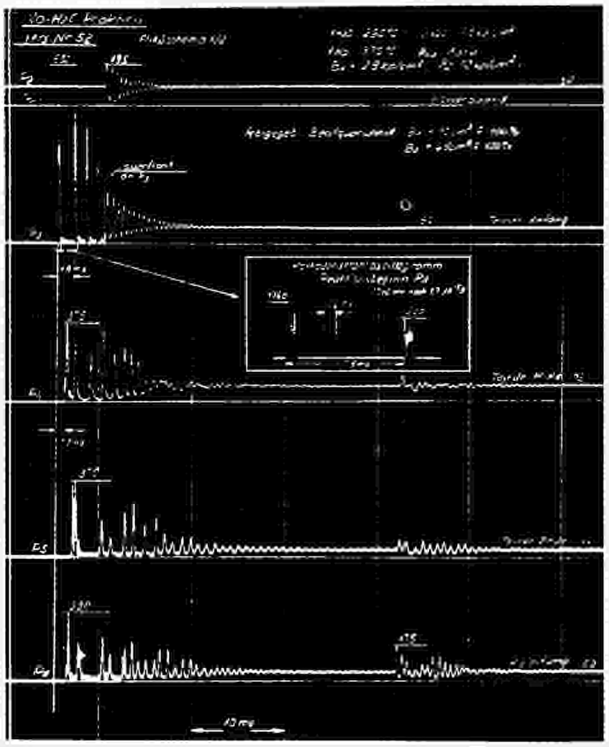

Sodium-Water-Reactions in tubes

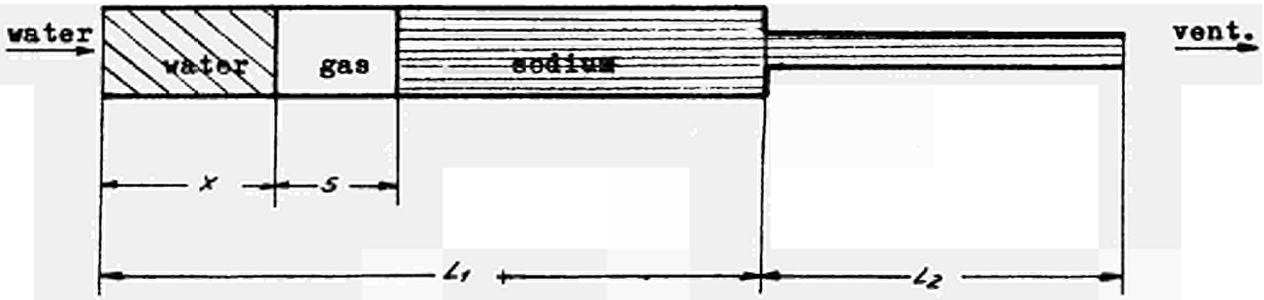

$$\frac{dM}{dt} = Co \cdot f(M,s) + C_1 \frac{dx}{dt} - C_3 \cdot P_{gas}$$

diffusion Na surface layer gas vent.

Diffusion: $Co_{exp.} = 1 - \cdot 3\ Co_{theor.}$ by turbulences; important for t< 2 ms

Na surface layer: C_1 = const. sodium layer 0,1 ... 0,2 mm;
important for t > 2 ms

Gas vent: laval-expansion C_3 ← atomic weight of gas: 40.

Equations of movement for water and sodium incl. initial conditions

Compressibility of sodium is taken into account for the first few ms.

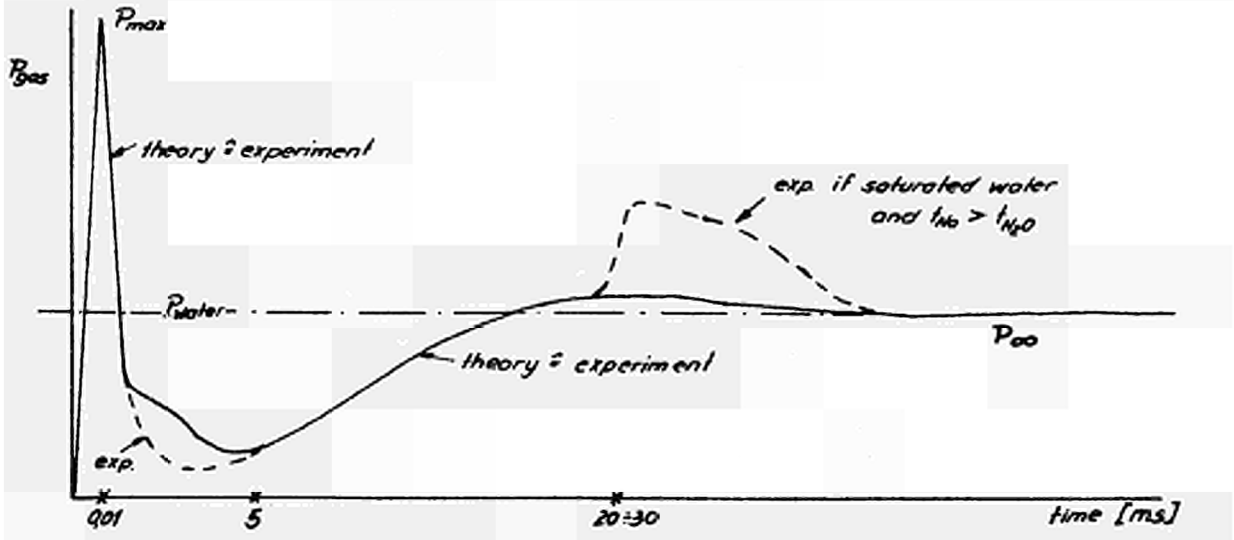

$$P_{max} \approx \sqrt{C_o} \approx \sqrt{\text{leak area}} \approx f(C_o) + f_{(V_{water})}$$

duration of $P_{max} \approx 10^{-5}$ s

Fig. 9

MODEL TECHNIQUES IN REACTOR ACCIDENT SIMULATION

by

N.S. Thumpston

AWRE, Foulness
United Kingdom

In assessing the mechanical damage to reactor components and structures under accident conditions one is concerned with problems of structural failure under the action of dynamic loads. This is outside the normal experience and practice of design engineers as their object is to design structures which do not fail.

One approach to obtaining experimental data is the destructive testing of specially built reactors. However, such tests are limited in number and scope and it is not always possible to study the effects of varying the design and the operating parameters.

A second approach, one to which we were led from our experience of work on the effect of air blast from weapons, has been to carry out studies by means of model scale experiments; the essential feature of a model study being that it is either smaller than the prototype structure or that it should be a small section only of the full scale structure. It is these model experiments which I want to discuss.

Simulation of Energy Release

The first step to be taken in an accident assessment is to define the energy release, both in magnitude and time. In general, in reactors mechanical damage occurs when energy is released more rapidly than the heat removal and containment systems can cope with it. In some cases knowledge of the power transient is available to us from full scale experiments, as in the Borax and Spert experiments, or accidents such as the SL.1 incident. For other types of reactors, for example fast reactors, we have to rely on calculation.

The second step is how to simulate this energy release in the model because how we do this determines the scale of the model approach. The problem of such energy simulation was discussed by my colleague, Mr. Samuels, at the previous Meeting of Specialists on Heat Transfer in Rapid Transients. The choice of a suitable simulation depends in part on an assessment of the way in which the damaging forces are produced by

several different mechanisms (depressurisation, flow or drag forces, liquid or solid impact, shock waves); these mechanisms must be identified and their relative importance assessed.

Thus, classifying model studies in terms of the energy source we have:

a) Those in which the forcing pressure is generated by sudden release of pressurised gas - flow studies.

b) Those in which the energy arises from changes of reactivity or chemical process in which:

(i) We obtain simulation of the incident by electrical pulse heating methods.

(ii) We obtain simulation of the incident by the detonation of an explosive charge.

Of the two simulations, (i) is more restricted in the scale size we can use. It is limited by the capacitance of our condenser banks and the care needed to avoid damage to them. We prefer to do this type of experiment in one of our indoor ranges so there may be building restrictions on firing.

The restriction on the second type of simulation arises not from charge size but from considerations of energy density and rate of energy release. For fast reactors the energy density is right, at least for the initial phases of the incident, and we have used high explosive as a simulation. For lower densities or slower energy releases we have been limited because we have not had available suitable gasless explosives or pyrotechnic mixes. We are working on producing these.

The Structural Model

Coming to the actual model which we make, two types are used for work in the U.K.

Strength scaled models in which the geometry of failure of the prototype is reproduced.

Geometrically scale overstrong models in which transient forces are reproduced and are measured by means of instruments mounted in the model, the response of the instruments not being affected by the deformation of the model.

For some investigations, the two types of models may be combined and structurally scaled components, which are critical to the construction, incorporated in a geometrical overstrong model.

Scaling

Before discussing examples of the model work that we have done at Foulness I would like to briefly describe the scaling laws and instrumentation.

The behaviour of the model is related to that of the prototype through the principle of dynamic similarity. Two independent relationships between the physical variables define the correspondence between the model and prototype systems, as the scaling law for any other physical parameter may be deduced from these relationships by dimensional considerations. The scale relationships usually chosen are $T \propto L$, $M \propto L^3$, where M, L, T represent mass, length and time respectively. In this system most of the relevant material properties (density, specific heat, stress) are invariant, so the prototype materials may be used for constructing the model. In particular, for energy, dimensions $ML^2 T^{-2}$, we have the so-called cube root law for energy comparison, model to prototype. Other invariant quantities are velocity, pressure, energy density, energy flux and temperature.

Limitations sometimes arise in the application of the scaling laws to models, for example, not all material properties are independent of the scale factor. Examples are thermal conductivity, viscosity and surface tension. Again, the gravitational field cannot be altered, so that the self-weight of a model and the flight of missiles do not scale correctly. These limitations should be recognised when planning an investigation as their effects can often be minimised or allowed for in the interpretation of the results.

Instrumentation

The reduced time scale of events in a model experiment makes it essential to use instruments having a rapid response. However, many of the quantities to be measured (pressure, strain, velocity, density, temperature) are of the same magnitude as in the prototype, so there are no stringent sensitivity requirements. Transducers must have low thermal or mechanical inertia and yet be sufficiently rugged to withstand the large forces involved in destructive experiments.

In the work at Foulness pressures are usually measured by quartz piezo-electric transducers. These were originally developed for air blast measurement but have been modified and improved for reactor safety applications. They have a response time of a few microseconds and sensitivities ranging from 0.1 p.s.i. to 40,000 p.s.i. In a cooled mount they have been used to record the impact pressures of liquid metals at temperatures up to 500°C. Both foil and wire resistance strain gauges are used. Both types are light and are capable of following the movement of any structural component to which they may be attached. They are also used on load cells for force measurement. The measurement of rapid temperature changes presents a problem. Wire resistance thermometers and thermocouples have good stability but it is difficult to make them with a time constant less than about one milli-second. Thin metal films can be deposited on an insulating surface and have a time constant better than 1 microsecond, but after the first few microseconds they measure the temperature of the backing rather than that of the fluid in which they are immersed. However, this gap in response time has recently been filled by a thermocouple comprising a large number of micro-junctions formed across the edge of a mica insulator by friction welding. The device has a response time of about 10 μS. The recording system used must have a frequency response matching that of the transducers and must also be capable of recording for a considerable length of time.

Examples of Model Work

(a) Model in which Energy Source is Pressurised Gas

I would like first of all to deal with a model study in which the energy source was depressurised gas, an investigation on a scale structure based on the Calder Hall geometry, a geometrically scale overstrong model instrumented with PE gauges for pressure measurements. What we were considering was what would happen in a gas cooled reactor if there was a sudden loss of coolant due to a complete duct failure. The problem was to assess the pressure difference across the core and also the flow of gas through the core. A pressure difference across the core could give rise to core movement, a cold duct failure could give the possibility of stagnation and unsatisfactory cooling of the fuel elements. The model which was about one twentieth the size of a reactor circuit consisted of a pressure vessel connected to four circuits, each of which contained a chamber to represent a heat exchanger unit. A flow of air was used to calibrate the equipment and to adjust the flow resistance of the core and heat exchangers to the required values. Although this particular model

study started by being related to an existing reactor system, it ultimately became a parametric study in which the relative importance of assumptions made in a theoretical analysis of the transient were subjected to experimental checking.

The study was not a model study as commonly accepted; we were not, for example, attempting to scale the results to full scale conditions. The basic assumption that had to be made was that the theory as applied to this particular "model experiment" was the same theory that could be applied when considering flow in a larger reactor. The validity of this assertion could, of course, be checked by repeating experiments on a number of scales, but by starting with a model that was big enough we did not anticipate any major scale effects to appear. Some simplifications that were made in the model study were incorporated to make the theoretical analysis easier, for example rotors were not used in the impellers; orifice plates were placed in the discs on the outside of the impeller cases.

Top and bottom duct bursts were investigated, both air and CO_2 being used in the system for pressures of 60, 100 and 150 p.s.i. The pressure gauges had to withstand a high steady pressure and record the subsequent fall to atmospheric pressure with a high degree of accuracy. This was achieved by performing replicate experiments.

A second investigation on depressurisation of gas cooled systems used a smaller model, about one fiftieth full size. Here we were interested in measuring the internal loading on a bioshield following catastrophic failure of the reactor vessel. The model pressure vessel was made in two halves which could be bolted together with any desired circumferential gap. The gap was sealed from inside by a piston which could be moved rapidly to uncover the gap. Pressure measurements taken with PE gauges showed both the uniform pressure rise on the shield and the local high pressures caused by the jetting of the emergent gas can be observed.* Different vessel venting areas and shield leak rates were investigated.

(b) Models with Energy Insertion by Electrical Pulse Heating Methods

The best example of work that we have done in this field has been

*Reference: Symposium on Studies to Determine the Safety Margins Available on Magnox Type Gas Cooled Reactors. British Nuclear Energy Society, July, 1964.

the model investigation of the SL.1 reactor incident. This accident, which is well documented from U.S. sources, is believed to have given an energy release of 130 MWS in an excursion of 4 ms. The approach at Foulness was to model this at 1/30th scale, a structurally scaled model incorporating pressure gauges. On the final model the structural damage and mechanical effects produced by the accidental excursion were very closely reproduced in the models. During the course of this work it became apparent that to produce the correct mechanical effects the most important factor was to get the right energy density in that part of the core which melted during the excursion. In the full scale structure it was seen that some 20 per cent of the fuel elements, those on the centre of the core, were melted in the excursion. To reproduce the correct energy density in the centre of the model core the core was made up in two zones, which were heated from two independent condenser banks. Earlier firings in this model study where we put the energy homogeneously into a single zoned core did not give a distortion pattern of the correct type, although we did achieve a very close simulation of the power time relationship. With a properly made core in two zones we got a correct dispersion of the molten metal and rapid steam production. The energy deposited in the rest of the core did not affect the damage.

The SL.1 study has enabled us to simplify our approach to excursion simulation. The essential thing to determine from a study of the energy distribution in the core is when part of the fuel will melt and to model this region by correctly scaling the mass and the surface area. The metal used for the model must have similar thermal properties to the fuel plates, and the model should be constructed so that the coolant water is in contact with the metal surface. The time scale of the pulse is not critical but it should not be longer than the scale duration of the excursion.

Before going on to describe typical experiments that we have done using explosives for energy simulation, it is worth mentioning that as part of the SL.1 study we investigated the effect of releasing 30 per cent of the energy by the explosion of a detonator in our structural scaled model. The distortion near the head of the vessel is comparable with what one obtains from the electrical transient but that extensive damage to the bottom of the vessel has been caused by reflection of the shock wave from the detonator. This underlies the desirability of identifying the damaging mechanism, which in the case of the SL.1 reactor was the impact of the water on the lower surface of the vessel, the water being

driven upwards by the expansion of steam. The peak pressure measured at the time of impact was about 10,000 p.s.i. and it was this that distorted the vessel flange and the wall immediately below, and the control rod guide tubes.

(c) Models with Energy Insertion by Explosive Charge

The best examples of our work in this field is the programme of work carried out on fast reactor systems. There are two basic types of fast reactors.

(i) Reactor vessel and heat exchangers contained in a concrete vault as with Dounreay and Fermi reactors.

(ii) Single tank integral designs like EBR II and the current U.K. design where reactor vessel and heat exchangers are contained in the large tank of sodium.

We have carried out model experiments on both types.

For the Dounreay reactor we decided a major hazard following an explosive transient was the ejection of the loading plugs which, if they rise 30 ft. would hit the overhead gantry and breach containment. Initial experiments to study plug ejection was made at 1/65 scale using ¼ grm charges of PETN to simulate energy release using two types of models - a steel model with overstrong walls and a weak graphite model, with a lead sleeve to simulate the breeder. From such greatly simplified structures we were able to assess the proportion of available energy imparted to the plugs was low falling between the limits of 0.4 and 3%, the variation being produced by the degree of venting due to the changing strength of the model.

For a more detailed investigation 1/10th scale models were used enabling us to incorporate the main structural details of the pressure vessel, support stands and plugs scaled to the correct static strength. In these tests water was used to simulate the sodium coolant. These larger scale models confirmed the results at smaller scale.

In experiments on single tank designs we were initially attracted to the idea of providing containment design data by determining the sequence of physical events resulting from an explosion in a nearly filled coolant tank. In one series of model firings we measured the pressure loading on the roof and walls of an overstrong two foot diameter by two

foot high steel tank, partially filled with water when a 2 oz. charge was detonated inside. A loosely fitted plug was fitted and its ejection photographed. The air gap above the coolant was varied in depth. From the records the initial and reflected shocks and the rarefaction from the surface are all clearly distinguishable. The shock reflection at the water surface causes cavitation with layers of water breaking away and impacting on the roof. We were able to determine the spray velocity and by further experiments in a perspex tank watch the process.

The present U.K. fast reactor reference design has been under continuous development for some years and during this period significant changes in the design have been examined by model studies. The objectives of this work have been to determine the time sequence of the major physical events following an energy transient to measure the pressure loadings, strains and deflections on the important reactor components and to demonstrate the structural integrity.

The work on PFR has been done at 1/32, 1/25 and 1/16 scale and has included both work on overstrong models and structurally scaled ones. The latter are interesting because they have included examples of our work on composite reinforced concrete structures where we have used mortar to model concrete. Where one goes, as in this case, to a slightly different material in the model the relationship between stress and strain for both the model material and the prototype must be the same. The sand we use on the cement mortars is graded in the same way as the aggregate in normal concrete and since what evidence we have suggests a similar failure mechanism, mortar to concrete, we can think of these mortars as micro-concretes. One point to watch carefully in modelling reinforced concrete is that the model scale reinforcing is similar in its physical properties to the full scale, by the use of suitably annealed drawn wires. As part of our protective structures programme we have made and tested models over a variation of scale sizes and are confident that we can accurately simulate both reinforced and prestressed concretes throughout their entire stress change right up to the point at which they fail.

We have evolved a number of useful techniques in weaving and casting models, including a technique of using collapsible expanded polystrene mould cores to model awkward re-entrant surfaces.

One point in the structural modelling of PFR which we have not solved has been the sealing around the core plugs because this has

required a detail unattainable at 1/16 scale. Our current work is on ¼ scale model of the roof structure to cover this point, but it will give interesting scale comparisons with the 1/16 scale work as an incidental.

It has been usual in our fast reactor studies to use cold water to simulate sodium. A direct comparison of the explosive effects in the two liquids has been conducted in a series of collaborative firings between the CEA Euratom and UKAEA at Cadaracne.

Conclusion

What I have given is a survey of the range of model work which we have done or are doing, illustrating a whole armoury of model approaches and techniques.

With this experience you might ask, how do we set about tackling new jobs, or what advice can be given to someone embarking on model studies? This can be summed up as follows:-

(1) Your basic problem is energy simulation - much of our background work in reactor safety is aimed at a better understanding of this. It is as well to remember right from the outset that any non-nuclear method of simulating a reactor transient is approximation.

(2) Decide what you want out of your model which can be either a vehicle for measurements or a direct indicator of structural response. One can carry out measurements on the whole system or an essential part of it; on the whole structure or on selected components. But remember any degree of simplification introduced must be based on a thorough engineering appraisal and that in model studies the quality of fabrication and the properties of material used must be examined with especial care.

(3) Check that your instrumentation is adequate to cope with the shorter response times.

INSTRUMENTATION FOR RAPID MECHANICAL TRANSIENTS IN MODEL SCALE EXPERIMENTS

by

P. Actis Dato, H. Holtbecker,
E. Jorzik, Y. Lachapelle, A. Maserati and G. Verzeletti

Euratom, CCR Ispra, Italy

INTRODUCTION

For a study on models of the response of a structure to dynamic loading by means of explosives, it is necessary to know certain characteristic dynamic parameters, namely the law for the variation with time of the load acting on the structure, and the law for strain versus the time.

This means that two gauges are needed, one for the pressures, the other for the strains.

P A R T I

PRESSURE TRANSDUCER

The transducer characteristics required for this study are:

1) small bulk and least possible interference with the event;
2) good time resolution (< 1 μ sec) and sufficiently constant signal (200 μ sec);
3) linearity of signal;
4) high signal/noise ratio;
5) strong, simple construction able to withstand high pressures.

The wide range of standard pressure transducers are not as a rule calibrated dynamically and the values indicated for precision and frequency response are usually calculated values.

From analysis of the catalogue information and from experience of the calibration of such transducers, it was concluded that they do not possess the characteristics we required and the decision was adopted to design and construct a measuring instrument to meet our requirements.

There are various methods of measuring dynamic pressure; after a study of the literature (1)(2)(3)(4)(5), the following types were short-listed:

capacitative

Baganoff has described a transducer fabricated wholly of plastic material. The condenser consists of two conductorized high-polymer plates, the dielectric material is an insulating high-polymer.
With a voltage of 4 KV applied to the two poles, a pressure of 1 atm gives a signal of ~10 mV. The transducer is limited to pressures ranging no higher than the elastic limit of the material.

inductive

The mechanical and electrical assembly is not suitable for obtaining a high time resolution. High sensitivity can be achieved only by long travels which cannot be effected in the required time.

magnetostrictive

The magnetic behaviour of certain materials is influenced by anisotropies in the crystal structure which undergo changes when a force is applied.
This effect is particularly noticeable in Ni or Ni-Fe alloys. Permeability variations of 17% have been recorded for a pressure of 1000 atm (8). Recent advances in the field of ferrites for high-frequency purposes have brought even higher sensitivity within reach.

In a number of experiments, performed by us, pressure waves were applied to Ni wires. The system allows of determining the amplitude of the impulse and is particularly suitable when a transducer of small diameter (wire) is required.

piezoelectric)
(These systems will be discussed
strain-gauge) in detail further on.

A review of the characteristics of the types listed above and of others whose description we omit for the sake of brevity, led to the choice, for highly dynamic high-precision tests, of the two last-named types, i.e. bar transducers with piezoelectric or strain-gauge sensitive element.

These transducers are of fairly similar geometry. In both there is a wave-guide consisting of a bar, the material of which is selected by acoustic criteria, which is mounted in such away as to cut out vibrations due to the actual wave-impact or to oscillations of the structure.

The dynamic calibration of the transducers is effected on a shock tube, the characteristics of which are given in the Appendix.

1. THE PIEZOELECTRIC TRANSDUCER

1.1. Theoretical considerations

The choice of a ceramic material for the piezoelectric apparatus was governed by the determination of the following conditions:

maximum operational temperature
sensitivity
maximum operational pressure

Quartz was selected in our case, on account of its very high Curie point (550°C) and the minor effect of temperature on the output signal.

On the other hand, quartz is not very highly sensitive and where pressures of less than one atmosphere are to be measured it is necessary, to avoid amplifying the signal, to connect the cathode follower directly to the transducer.

In view of the very short rise time required ($< 1\ \mu$sec) the geometrical dimensions of the quartz must be small.

The resonance frequency is calculated, in a first approximation, from the relation

$$f = \frac{1}{2l}\sqrt{\frac{E}{\rho}}$$

where $\sqrt{\frac{E}{\rho}}$ represents the velocity of sound which, for quartz, is 5,500 m/sec.

The theoretical rise time for a shock wave striking a quartz

of length l = 1.5 mm is 0,3 μsec.

The mechanical assembly follows the principle of the Hopkinson pressure bar. The quartz forms an integral part of a bar in which the wave is guided without reflections (ρ. c = const.). The position of the quartz on this bar is conditioned

- by the rise time required
- by the mechanical problems involved in mounting the quartz.

The dispersion of the wave along the bar (described in detail for the bar transducer) increases the rise time. This effect is reduced as far as possible by cementing the quartz on the head of the bar. This type of mounting is preferable as it also allows of reducing the injurious bending effects that might occur if the quartz were mounted between two bars. Such bending could damage the cement attaching the quartz to the bar. As the quartz forms a single unit with the bar, to which it is cemented by a thin layer of high-strength adhesive, the resonance frequency of the quartz-bar system is very low and cannot disturb the measuring.

Owing to the dispersion phenomena, the wave reflected at the bottom end of the bar has a very long rise time and a greatly diminished amplitude. Because the sensitive component is small, the wave on reaching it causes negligible disturbances in the signal registered, as the sensitive component receives the sum of two signals of opposite sign (dilatation and compression waves).

The amplitude of the disturbance signal decreases directly with the thickness of the quartz and inversely with the length of travel of the wave in the bar and the consequent lengthening of the front rise time.

In order to eliminate the influence of the reflected wave, it is necessary to lengthen the bar so that the measurement is completed by the time the reflected wave reaches the sensitive component, or to damp the reflected wave with special devices (see bar transducer).

At the same time as a wave is propagated longitudinally, transversal vibrations are generated through contraction of

the bar. If the longitudinal wave length is comparable to the diameter of the bar there is serious transversal resonance.

In calculating the resonance frequency, the dispersion of the longitudinal wave and the influence of the Poisson ratio for the material must be taken into account.

The radial oscillations, which are very ample at the resonance frequency, affect the longitudinal deformations; producing an apparent variation of the E modulus. In consequence the phase velocity and the amplitude of the longitudinal oscillations are affected. These events can be simulated (6) with a damped oscillating electric circuit with resonance frequency

$$f_o = \frac{1}{2\pi\sqrt{L \cdot C}}$$

This equation is compared with the equation for the vibration of the bar, and the parameters are determined by analogy, giving

$$f_o = 0.448 \frac{c_o}{D} ,$$

in which the constant takes into account the damping effects and the influence of Poisson's modulus.

For the geometry used here (diameter D = 4 mm, velocity of sound c_o = 5,500 m/sec) the calculated frequency is 620 kc/sec.

As will be described further on, the reducing of the radial oscillation effects was a very laborious task based on a series of experiments.

1.2. Mechanical construction

The problem of the mechanical construction of the transducer can be summarized under two heads:

- to effect a perfect connection between the sensitive component and the Al-Mg alloy bar so as to ensure perfect passage of the wave from one material to the other without any reflection;

- to construct a mechanical assembly capable of withstanding pressures up to 1,000 atm and temperatures up to 100°C and ensuring a rise time of < 1 μsec, perfect leaktightness to water and a measuring time of ~ 200 μsec.

To cement the quartz (thickness 1.5 mm, diameter 4 mm) to the Al-Mg bar various organic adhesives were utilized, the aim being to achieve as thin a layer as possible. The ratio between the reflected wave and the wave impinging on a thin layer is calculated (10) from the expression

$$R = \frac{m^2 - 1}{m} \quad \frac{\pi d}{\lambda} \quad ,$$

where m is the ratio of the acoustic impedance of the two materials

$$m = \frac{\rho_o \cdot c_o}{\rho_s \cdot c_s}$$

s = layer
d = thickness of the layer
λ = length of the wave in the layer

To obtain minimum reflection the impedance of the two materials must be chosen as equal as possible and the adhesive thickness cut down.

The bar thus prepared is mounted inside the transducer shell; care must be taken to achieve perfect electrical insulation between the two (> 1000 MΩ). A coating of conductor paint connects the transducer shell to the free face of the quartz. The other pole is formed by the bar.

At first we followed the suggestion of various authors and filled the annular gap between the transducer shell and the bar with a high polymer (Fig. 1).

The calibration readings obtained in this way on the shock tube were not reproducible and it was impossible to make any modifications in case of faulty working because the transducer could not be disassembled.

We then tried to devise an assembly that would allow of varying the type of clamp holding the bar (see Fig. 2).

It will be seen from the results obtained that the grip of the clamp which holds the quartz laterally must be extremely light, in order to reduce the signal oscillations (see photographs 1 and 2).

Obviously this requirement adds to the insulation difficulties and renders the use of the transducer in conductor liquids problematic.

The adjustable clamp is visible in the drawing of the transducer at Fig. 2. The performances achieved with good reproducibility are shown in photographs 3 and 4.

When the transducer is to be used in water the quartz head is protected with a light layer of PVC, which has proved satisfactorily leaktight in water at 100°C for over 24 hours.

1.3. The electrical circuit

Fig. 3 gives the block diagram of the electronic equipment.

The recording system has an R-C time constant of a few milliseconds. The cathode follower input impedance is 40 MΩ and the amplification factor approximately 0.8.

1.4. Discussion of the transducer characteristics

1.4.1. Sensitivity

The transducer is particularly suitable for low and intermediate pressures of 1 - 400 atm; above this range the quartz often comes unstuck after a few experiments.

1.4.2. Temperature limits

In theory the limit is set by the Curie point of the sensitive component. In view of the differential thermal expansion of the various materials involved, and the chemical stability of the organic component actually used, it is considered unadvisable for the present to use the transducer at temperatures of over 100°C. The calibrations

effected in water at 100°C and 20°C showed no appreciable difference in the signal.

1.4.3. Linearity error

The component is linear, with an error lower than the level of the oscillations.

1.4.4. Accuracy

On the various records effected for calibration, an oscillation frequency of about 600 Kc/sec is found. This corresponds approximately to the resonance frequency of the lateral vibrations calculated above.
The amplitude of these signals is such as to hold the error on the absolute pressure measurement down to ± 10%.

1.4.5. Response time

The measured response time of the transducer varies within a range of 0.6 ÷ 1 μ sec (photographs 5, 6 and 7).
For frequencies higher than 500 Kc/sec, which occur with explosives in water, the signal decays to below the zero line during the pressure decrease. Experiments are in progress to discover the cause of this phenomenon, which did not occur, however, when a bar-quartz-bar assembly was used.

The response time of the piezoelectric transducer can be improved by reducing the thickness of the sensitive component; this may be done by vapour-depositing layers of barium titanate directly on the bar head.

2. STRAIN-GAUGE BAR TRANSDUCER

With the object of obtaining a transducer capable of measuring higher pressures, also more robust and less tricky as regards insulation, a bar type was designed and made. The sensitive component consists of a strain-gauge cemented to the side of the bar.

2.1. Theoretical details

There is a good deal of literature available on the subject of strain in bars. In the first approach an elementary theory may be used (11) which does not take the bar transversal strains into account; this treatment of the problem takes as its only spatial variable the coordinate z measured along the axis of the bar. The bar component, of radius a and length dz, may be written as:

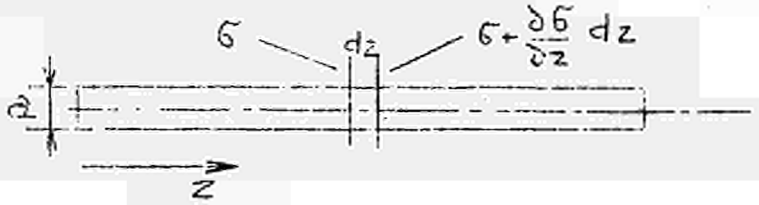

$$\rho \pi a^2 dz \frac{\partial^2 u}{\partial t^2} = \pi a^2 \left(\sigma + \frac{\partial \sigma}{\partial z} dz - \sigma \right) \qquad (1)$$

where

ρ = density of material forming the bar,

$u = u(z,t)$ is the displacement of the z coordinate cross-section.

Since

$$\sigma = E.\epsilon \ , \quad \epsilon = \frac{\partial u}{\partial z} \ , \quad \frac{\partial \sigma}{\partial z} = E \frac{\partial^2 u}{\partial z^2} \ .$$

Substituting in (1) and cancelling where appropriate, we obtain

$$\rho . \frac{\partial^2 u}{\partial t^2} = E \frac{\partial^2 u}{\partial z^2} \ . \qquad (2)$$

This is the equation for the propagation of the plane waves, with velocity

$$c_o = \sqrt{\frac{E}{\rho}}$$

If this theory were valid an elastic strain propagated in the bar would not be deformed.

This condition is approached in reality when the wave lengths of the sinusoidal components into which the stress may break up are long by comparison with the bar radius.

Where this condition is not satisfied, the phase velocity of the plane sinusoidal waves varies as a function of the wave length and of the Poisson ratio.

Thus the strain is distorted and the waves of highest frequency precede the others. Poisson's ratio intervenes as Miklowitz has demonstrated (12).

Fox, Curtis and Skalak (13)(14)(15) applied the almost-exact theory in stating the equation for wave propagation in a bar; almost exact, because in establishing the boundary conditions for the problem, they assumed that the end of the bar at which the step-function pressure load is applied undergoes no radial strain, and furthermore that the bar is subjected to no lateral constraint. Using this theory the results obtained agree satisfactorily, for distance of several diameters from the end of the bar, with the same authors' experimental findings.

Where a pressure step is applied to the bar, their theory leads to the expression

$$\frac{\epsilon}{\epsilon_o} = \frac{1}{3} + \int_o^B A_i\,(-B)\,dB \qquad (3)$$

$$B = (t - \frac{z_o}{c_o})\,(4c_o^3 / 3\,\nu^2 a^2 z)^{\frac{1}{3}}$$

where

ϵ_o is the strain corresponding to the static pressure,
z_o is the coordinate of the point where the measuring element is positioned,
c_o is the velocity of sound in the bar
$A_i(x)$ is the Airy function
t is the time measured from the moment the wave enters the bar.

Formula (3) yields the strain curve shown in Fig. 4. From this figure it will at once be seen that if the wave has to approximate the original step of the pressure wave, i.e. to have a short rise time, the factor $(4\,c_o^3 / 3\,\nu^2 a^2 z)^{1/3}$ appearing on the abscissae must be large.

For this reason the material selected must have a low Poisson's ratio and a very high sound velocity. It is also advisable to have a bar of small diameter and to position the sensitive component close to the end of the bar.

2.2. Experimental procedure

We started with steel bars of radius a = 3 mm, with a strain-gauge cemented on at a distance of 50 mm from the end.

The measuring circuit is shown in Fig. 5.

The voltage V corresponding to a strain ϵ is given by the formula

$$V = I_o K \epsilon \frac{R_s \cdot R_c}{R_s + R_c}$$

$I_o = 25 \cdot 10^{-3}$ A = current in circuit
K = gauge factor, i.e.,
2 for the wire strain-gauges and
120 for the semi-conductor gauges.
ϵ = strain
R_s = strain-gauge resistances = 120 + 120 Ω
R_c = damping resistance = 1600 Ω.

To have some idea of the output voltages obtainable with the various types of strain-gauge, a calculation was effected with an assumed pressure of 100 kg/cm^2.

V_{100} = 0.52 mV with metal foil strain-gauges

V_{100} = 31.3 mV with semi-conductor gauges.

As the background noise amounts to ~ 0.5 millivolts, the semi-conductor strain-gauges have to be used for pressures of less than 500 kg/cm^2.

The calibrating tests were effected on the shock tube described in the appendix.

2.3. Problems encountered

2.3.1. Bending of bar

In the first experiments with the shock tube a very serious phenomenon was observed straight away; this was an oscillation of great amplitude and fairly low frequency. It was thought that this was due to bending of the bar.

Two strain-gauges were then placed diametrically opposite one another, i.e. with their two generatrices at an angle of 180°, and the two oscillations were found to be in phase opposition (see photograph 8).

By connecting the strain-gauges in series so as to obtain the sum of the two signals, the effect of this oscillation was completely cut out, as may be seen from photograph 9 which was taken with the same transducer after the strain-gauges had been connected in series.

2.3.2. Sealing problems

In order to ensure insulation of the sensitive component and to prevent the wires from being swept away by the flow of gas or liquid in which the transducer has to operate, it is necessary to enclose the latter in a special leak-tight clamp on the region where the pressure is applied.

The head clamp was observed to have an extraordinary effect; in fact, unless it was practically disengaged it produced compressive stresses on the lateral wall of the bar, with resultant longitudinal waves. Photographs 10 and 11 show an example of this effect.

Actually in the two tests only one alteration was made, in that the compression of the rubber ring was varied experimentally.

The need to keep the bar free is, of course, in direct opposition to the need to ensure the sealing especially at high pressures.

In the end a satisfactory compromise was adopted, which led to the results that will be given further on (photographs 12 to 17).

2.3.3. Absorbing the return wave

When the pressure wave propagated through the bar reaches the end, it is reflected as a dilatation wave, which arrives at the strain-gauge and is recorded (see photograph 9). It is therefore impossible to effect pressure measurements for a time greater than the travel time of the wave through the bar and back.

With a view to removing this disadvantage without making the bars too long, the expedient was adopted of placing an acoustically adapted dispersing section at the far end of the bar (16). The adaptation was achieved by terminating the bar in a cone and cementing an Araldite semiellipsoid directly on to the cone, with its centre coinciding with the cone apex. This form satisfies the condition

$$\rho_s c_s S_{zs} + \rho_e c_e S_{za} = \text{constant}$$

ρ = density
c = velocity of sound
S_z = cross section area
s and a are the indices for the steel and the Araldite.

With this arrangement, the wave travelled on into the Araldite, which has only about half the sound velocity of steel and a very high damping factor; so that the return wave was almost totally destroyed.

Photograph 18 and Fig.6 show a transducer constructed on the above principle and a section drawing of the unit.

For certain experiments we needed a transducer capable of measuring two short pulses widely separated in time. To cut out even the weak residual return wave, a transducer was built consisting of two bars laid end to end in contact but not joined (Fig. 7). The first pulse passes through the first bar, is registered, passes through the second bar, is reflected at the end as a tensile wave and, on reaching the point where the bars meet, does not pass into the first one; the latter is therefore free to receive a second pulse which can arrive a considerable time later

without any risk of being confused with a return wave in the transducer.

2.4. Comparison between the theoretical predictions and the experimental results

For a given bar of a given material, with the sensitive component located in a given position, the adimensional magnitude

$$B = (t - \frac{z_o}{c_o}) \left(\frac{4\, c_o^3}{3\, \nu^2 a^2 z_o}\right)^{\frac{1}{3}}$$

assumes the significance of a measured time from the moment when the disturbance propagated with velocity c_o reaches the abscissa point z_o where the gauge is positioned.

Then by converting the scale for a bar in which:

$a = 3$ mm
$c_o = 5{,}300$ m/sec
$\nu = 0.3$
$z = 30$ mm

$$B = (t - \frac{30 \cdot 10^{-3}}{5.3 \cdot 10^3})\, 5.3 \cdot 10^3 \left(\frac{4}{3.9 \cdot 10^{-2}\, 9 \cdot 10^{-6} 30 \cdot 10^{-3}}\right)^{\frac{1}{3}} =$$

$$= (t - \frac{3 \cdot 10^{-5}}{5.3})\, \frac{5.3 \cdot 10^6}{9}\, \sqrt[3]{40} =$$

$$= (t - 5.66 \cdot 10^{-6})\, 2.04 \cdot 10^6$$

whence

$$t = \left(\frac{B}{2.04} + 5.66\right) 10^{-6} \text{ seconds.}$$

Hence in Fig. 4 each interval corresponding to increments of $B = 3.5$ corresponds to time increments of

$$t = \frac{3.5}{2.04} = 1.72 \quad \mu \text{ seconds.}$$

A similar conversion was made in the case of a steel bar in which

$a = 2$ mm
$c_o = 5300$ m/sec

ν = 0.3
z = 30 mm

It was found that

$$t = \left(\frac{B}{2.68} + 5.66\right)10^{-6} \text{ seconds.}$$

In the case of a beryllium bar with

a = 3 mm
c_o = 12,800 m/sec
ν = 0.035
z = 30 mm

we find

$$t = \left(\frac{B}{8.6} + 2.34\right)10^{-6} \text{ seconds.}$$

In Figs 8, 9 and 10 the diagram at Fig. 4 is retraced with the time shown on the ordinate. The same figures also show a registration record.

All three cases agree very closely as to the rise time; as regards the oscillation frequency, however, the beryllium record is not in agreement; nevertheless, taken as a whole, it may be said that the theory agrees satisfactorily with the experimental findings even with regard to the amplitude of the oscillations.

Photographs 12, 13, 14, 15, 16 and 17 give some examples of registrations effected during the calibration process.

3. CONCLUSIONS

The transducer studied has the following characteristics:

3.1. Sensitivity

Pressures as low as 10 kg/cm^2 can be measured with a satisfactory signal/noise ratio and without recourse to amplifying systems.

By cutting out the highest noise frequencies the figure can be brought down to 4-5 kg/cm^2.

Maximum pressures, using standard strain-gauges, can range

from 10,000 to 15,000 kg/cm^2.
Experiments were carried out up to 2,500 kg/cm^2.

Higher sensitivities can be achieved by using a material of lower elastic modulus for the bar.

3.2. Temperature and irradiation limits

The temperature limits are imposed by the strain-gauge; standard models are obtainable for high-temperature work (400 - 800°C). In such work a bar is used, without rubber rings. The semiconductor strain-gauges can operate up to 200°C, being compensated up to 100°C by the gauge-factor shift.

Irradiation tests are in progress on strain-gauges with ceramic insulation (EUR 2649 e - "In-Pile Application of Strain-Gauges" by P.S. Weltevreden). So far results have been obtained up to a flux of almost 10^{18} n.v.t. (fast neutrons). In addition it is possible to reduce the neutron flux by shielding the sensitive component.

3.3. Linearity error

The element is linear with an error lower than the level of the internal oscillations. No difference was found between the calculated value of the signal and the value recorded during calibration.

3.4. Accuracy

Exact evaluation of the pressure is impeded by the presence of oscillations connected with the mechanism of wave transmission on the real bar, as all the appended photographs show. The error can be estimated at $\pm$ 10%. This value can be lowered to $\pm$ 5% for pressures <400 atm.

Another source of error is the length of the strain-gauge which lengthens the pulse by a time

$$t = \frac{l}{c_o}$$

l = 2 mm length of strain-gauge
c_o = velocity of sound in the bar.

For a steel bar $t = 0.32\ \mu$sec,
for a beryllium bar $t = 0.15\ \mu$sec.

3.5. Rise time

In order to reduce the rise time, the 6 mm diameter steel bar, which gave a rise time of 1.8 μsec (photographs 14 and 15), was abandoned for a bar of the same material but with a diameter of 4 mm, which gives a rise time of 1.2 μsec (photographs 12 and 13). To bring the figure still lower we used beryllium, which has a very high sound velocity (12,800 m/sec as against 5,300 m/sec in steel) and an extremely low Poisson's modulus (0.035 as against 0.29 in steel).

In this way we obtained a transducer with a rise time of 0.3 μsec (photographs 16 and 17), which is comparable with the time of travel of the wave through the strain-gauge. It must be borne in mind, however, that beryllium is a toxic substance and special precautions are necessary.

The transducer that we constructed is extremely easy to use in that it gives highly reproducible readings (as demonstrated in the underwater measurements), is strong, needs no special calibrations, can be taken apart and reassembled with the utmost ease, and is not subject to moisture on account of its low resistance (240 Ω).

P A R T II

DYNAMIC STRAIN MEASUREMENTS

In order to effect dynamic strain measurements of structures the behaviour of strain-gauges has been studied.

For small elongations as occur in the elastic field (up to 3,000 μstrain, corresponding for steel to a stress of about 60 kg/mm^2) semi-conductor strain-gauges were utilized, per-

mitting (especially for very small elongation) a very high signal/noise ratio. It has been seen that there are virtually no problems:
The strain-gauges follow a strain-rate of 500 μstrain/μ sec, without showing phenomena of hysteresis, which, as was thought initially, could be developed in the thin cement coat.

The strain-gauges used are of the type PO1-16-120 and PO1-05-120 of MICRO SISTEM and KGN 3,5 E1 and KGN 3,5 E2 of KYOWA with Eastman 910 cement, which has given satisfactory results.

Up to strains of 3% normal strain-gauges of type BUDD, Fine Line Gauges C.9-F1x4-M 25, and FRISCHEN, MFS-F6 120-19/0.9.1 Ib, have been used. No particular difficulties have been encountered. Accurate controls have been effected comparing the residual strain measured by the strain-gauges with the permanent strain measured with a micrometer and with optical methods. The differences found fell within the measurement errors.

On the contrary, at higher strains, in the order of magnitude of 5-10%, difficulties occurred. In the cases where strain-gauges of BUDD, type HE 121 with GA-5 cement, and BALDWIN-LIMA-HAMILTON, type PA-3, were used, which in statics are capable of measuring an elongation up to 15%, it was found that in dynamics, when the strain-rate went up to some hundreds of μstrain/μsec, the strain-gauges broke away from the structure before reaching 4% elongation. However, due to a special thermal treatment of the cement, elongation values of 7% were obtained.

If the strain of a structure is associated - as in the case of a sphere or a cylinder referred to in the report No. EUR/C-IS/673/66 e - "The response of a vessel to an internal blast loading - Limits of model tests - Influence of strain-rate" - with the displacement, in a perpendicular direction, of the wall on which the strain-gauge is cemented, and if this displacement has a velocity of 100 ÷ 200 m/sec, accelerated by 1 ÷ 2.10^6 m/sec^2, the strain-gauge will break due to the great forces of inertia which act on the welded ends. In such cases it is advisable to utilize very fine

connection-wires welded only in one point, so as to reduce to a minimum the masses involved.

REFERENCES

(1) E. BAILITIS
"Der Schallimpuls eines Flüssigkeitsfunkens"
Zeitschrift für angewandte Physik einschließlich Nukleonik
9. Band, Heft 9, Sept. 1957

(2) D.H. EDWARDS
"A Piezo-Electric Pressure Bar Gauge"
Journal of Scientific Instruments, Vol. 35, 1958

(3) M.O. STERN and E. N. DACUS
"Piezoelectric Probe for Plasma Research"
The Review of Scientific Instruments, Vol. 32, No. 2,
Feb. 1961

(4) A.W. BLACKSTOCK, H.R. KRATZ, M.B. FENNEY
"Piezoelectric Gauges for Measuring Rapidly Varying
Pressures up to Seven Kilobars"
The Review of Scientific Instruments, Vol. 35, No. 1,
Jan 1964

(5) J.H. GERRARD
"Piezoelectric Pressure Gauges for Use in a Shock Tube"
Acustica, Vol. 9, 1959

(6) H. WUTZ
"Die Entwicklung und Erprobung einer piezoelektrischen
Drucksonde für die Messung hoher Druckstöße kürzester
Dauer"
Dissertation TH Hannover, 1961

(7) D. BAGANOFF
"Pressure Gauge with One-Tenth Microsecond Risetime for
Shock Reflection Studies"
The Review of Scientific Instruments, Vol. 35, No. 3,
March 1964

(8) W. HOLZMÜLLER
"Technische Physik - Band I"
VEB Verlag Technik Berlin, 1959

(9) H. KUTTRUFF and J. WOLFRUM
"Akustischer Nachweis von elektromagnetisch erzeugten
Stoßwellen"
Acustica, Vol. 15, No. 6, 1965

(10) P. WOLF
"Ultraschallreflexion an dünnen Koppelschichten zwischen Verzögerungsleitungen aus Quarzglas im Frequenzbereich von 5 MHz bis 45 MHz"
Acustica, Vol. 15, 1965, pp. 39 - 44.

(11) H. KOLSKY
"Stress Waves in Solids"
Oxford University Press, Fairlawn, N.J., 1953

(12) J. MIKLOWITZ
"The Propagation of Compressional Waves in a Dispersive Elastic Rod"

(13) R. FOLK, G. FOX, C.A. SHOOK and C.W. CURTIS
"Elastic Strain Produced by Sudden Application of Pressure to One End of a Cylindrical Bar. - I. Theory"
The Journal of the Acoustical Society of America, Vol. 30, No. 6, June 1958

(14) G. FOX and C.W. CURTIS
"Elastic Strain Produced by Sudden Application of Pressure to One End of a Cylindrical Bar. II. Experimental Observations"
The Journal of the Acoustical Society of America, Vol. 30, No. 6, June 1958

(15) R. SKALAK
"Longitudinal Impact of a Semi-Infinite Circular Elastic Bar"
Journal of Applied Mechanics, 1957

(16) J.K. WRIGHT
"Shock Tubes"
Methuen & Co. Ltd., London, 1961

ACKNOWLEDGEMENTS

The authors wish to thank Messrs. G. Giudici and U. Guerrini, who assembled the mechanical set-ups and assisted during the experiments.

They are also grateful to Mr. P.S. Weltevreden, who advised on choice and application of strain-gauges, and to Messrs. C. Haider and W. Schnabel for the strain-gauge instrumentation.

Special thanks are due to Mrs. D. Doyen and Miss E. Zenner for the translation and preparation of the report.

APPENDIX

S H O C K T U B E

In order to calibrate the transducers it was necessary to construct a shock tube, which we used to generate pressure steps of exactly known height. To obtain the high pressures needed, we used helium for the high and argon for the low pressure.

These two gases were chosen because they are almost perfect and have widely different sound velocities (1020 m/sec and 321 m/sec at 20°C), so that a ratio can be established between the reflected pressure value and the very high driver pressure value.

Figure No. 11 shows the general design of our tube. Photograph 20 shows the rig mounted on tracks. Photograph 21 shows the coupling system on the driver-driven sections.

There are three lateral measuring windows into which probes are inserted, to determine the travel time of the wave from point to point and thus measure its velocity, from which the incident and reflected shock pressures can be calculated via the Rankine-Hugoniot equations.

The velocity is measured by two methods:

first, by a probe with a light-ray which is interrupted by the shock wave passing along the tube; the photomultiplier gives a 2-volt signal with a rise time of 0.5 μsec. As the measuring base is traversed in about 500 μsec, the relative error is 1 °/oo, which is well below the limit for practical requirements. With this system the wave speed was most carefully checked on two adjacent bases, and the differences observed were easily comprised within the measuring errors ($< 0.5\ \mu$ sec).

The second method consists in the use of piezoceramic transducers (Fig. 12). No particular gear was used to break the

diaphragm, which fails automatically when the helium pressure is raised.

A special study was carried out on the diaphragm. To prevent fragments from breaking away and damaging the transducers at the end of the tube, failure must be primed by cutting grooves in the diaphragm. If they are cut too deep, however, the diaphragm does not open completely, thus setting up distrubances which delay the formation of the shock wave and reduce its amplitude.

Measurements of the time of opening of the diaphragm yielded values varying from 30 to 70 μsec with grooves of the right dimensions.

As a result of the prestraining of the diaphragm, the opening is perfect (see photograph 22).

Our tube was designed for a pressure of 3,000 kg/cm^2 and is at present operational up to 2,000 kg/cm^2. Up to now, however, there has never been more than 1000 kg/cm^2 in the high-pressure chamber, giving reflected shock pressures of about 1500 kg/cm^2.

In our experiments the transducer was mounted on the end, its axis parallel with the tube axis. In this way the whole pressure-sensitive surface of the transducer receives the impact of a wave whose rise time is of the order of one nanosecond.

Wishing to obtain pressure waves of variable rise time, in order to study the behaviour of the transducer in such conditions, we mounted a vertical shock tube (see photograph 19) and filled it with water to various levels. With this arrangement the wave, which is propagated in the argon, has to travel a certain distance in water before reaching the transducer.

With pressures of up to 500 kg/cm^2, the wave front is blunted and rise times of up to 10 μsec can be obtained.

These phenomena are studied in report No. EUR/C-IS/705/66 e - "Some theoretical considerations and experimental data on propagation and reflection of underwater pressure and shock waves" by H. Holtbecker and A. Maserati.

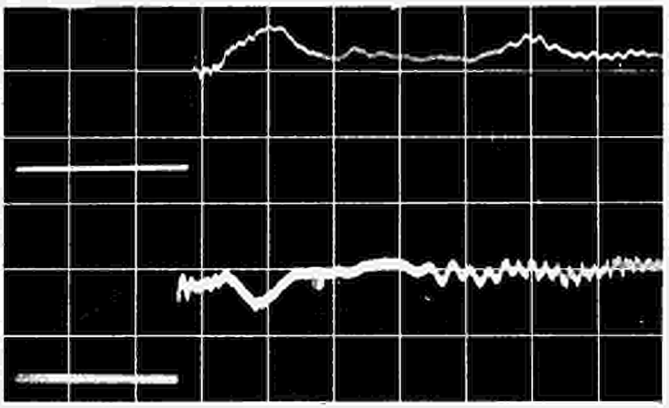

PHOTOGRAPH 1

pressure 125 atm.
upper beam - clamp too loose
lower beam - clamp too tight

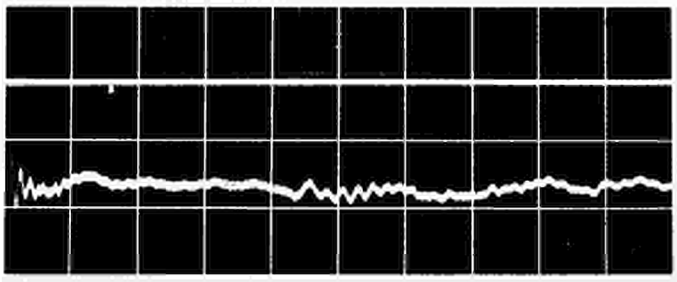

PHOTOGRAPH 2

pressure 125 atm.
correct clamp tightness

QUARTZ PRESSURE TRANSDUCER
INFLUENCE OF HEAD CLAMP ON SIGNAL OSCILLATIONS

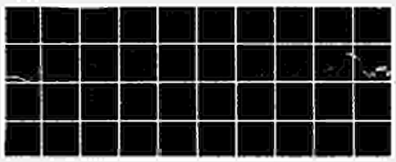

1 V/square

10 μsec/square

PHOTOGRAPH 3
pressure 122 atm.

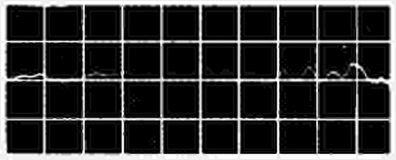

2 V/square

10 μsec/square

PHOTOGRAPH 3a
pressure 242 atm.

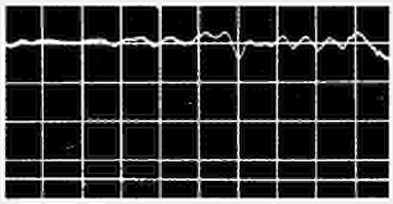

2 V/square

10 μsec/square

PHOTOGRAPH 4
pressure 462 atm.

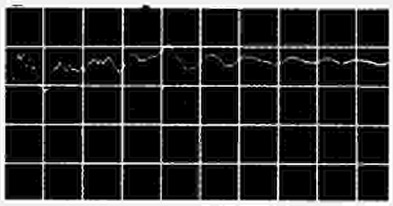

5 V/square

10 μsec/square

PHOTOGRAPH 4a
pressure 860 atm.

QUARTZ TRANSDUCER
RECORDS AT VARIOUS PRESSURES

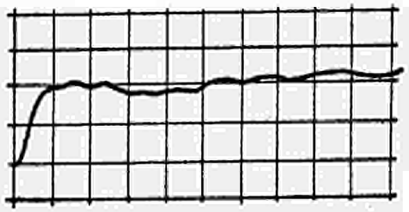

Photograph 5
pressure 250 atm.

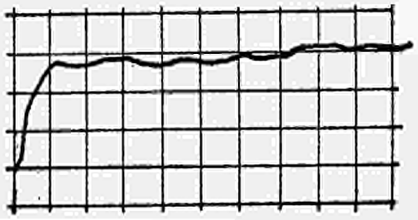

Photograph 6
pressure 125 atm.

QUARTZ TRANSDUCER
RECORD SHOWING TRANSDUCER RISE TIME

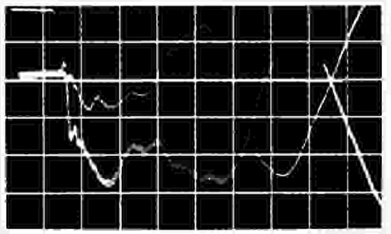

PHOTOGRAPH 8
signals from two strain-gauges mounted diametrically opposite each other on steel bar of 4 mm diameter

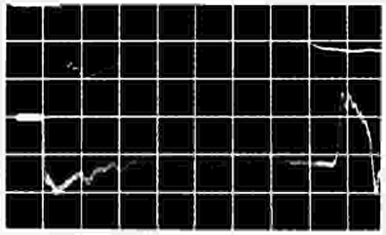

PHOTOGRAPH 9
signal from the same two strain-gauges when connected in series

BAR TRANSDUCER
BAR BENDING COMPENSATION

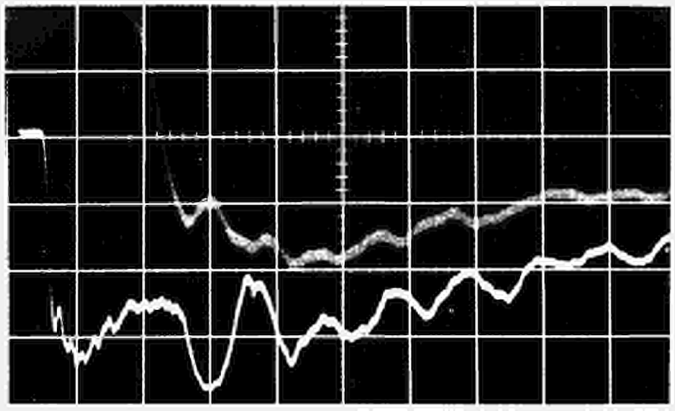

→ 2 μsec/square

→ 10 μsec/square

PHOTOGRAPH 10
Clamp too tight

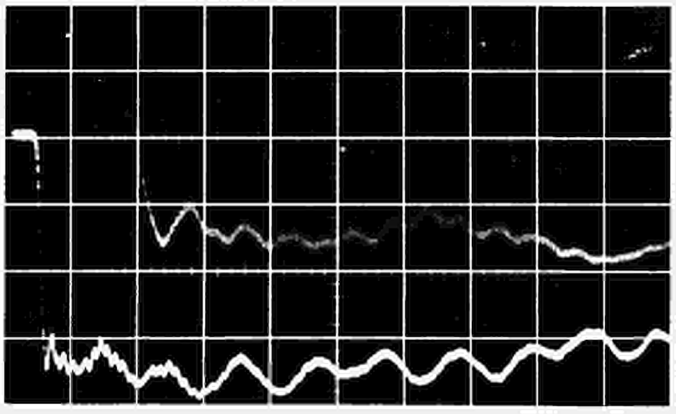

→ 2 μsec/square

→ 10 μsec/square

PHOTOGRAPH 11
Clamp loose

BAR TRANSDUCER
INFLUENCE OF HEAD CLAMP ON SIGNAL OSCILLATIONS

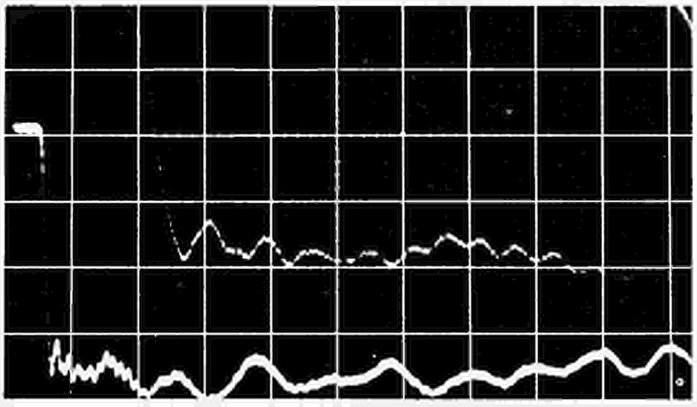

10 mV/square

2 μ sec/square

10 μsec/square

PHOTOGRAPH 12
pressure 125 atm.

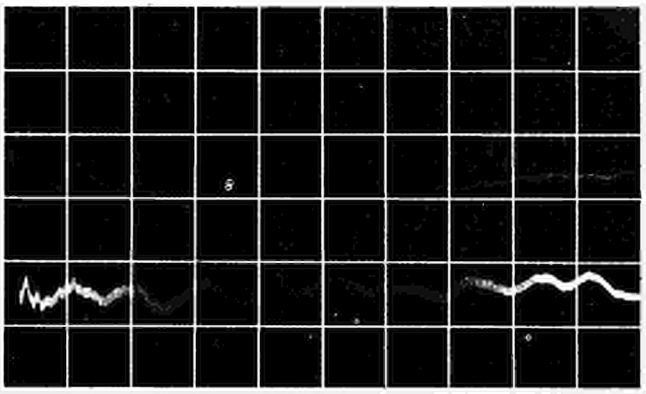

50 mV/square

2 μsec/square

10 μ sec/square

PHOTOGRAPH 13
pressure 440 atm.

4 mm diameter steel bar transducer
Records showing the transducer rise time

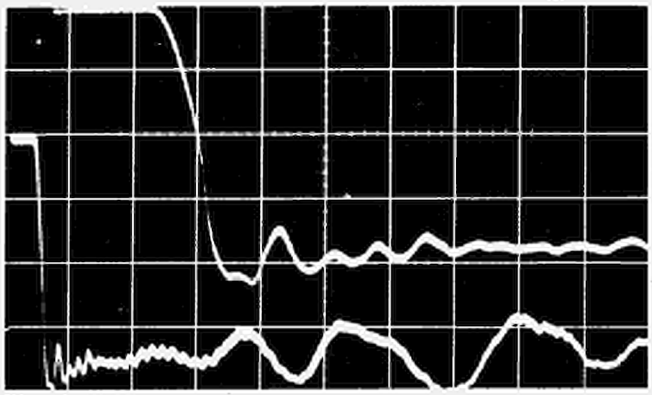

125 atm

→ 2 μsec/square

→ 10 μsec/square

Photograph 14

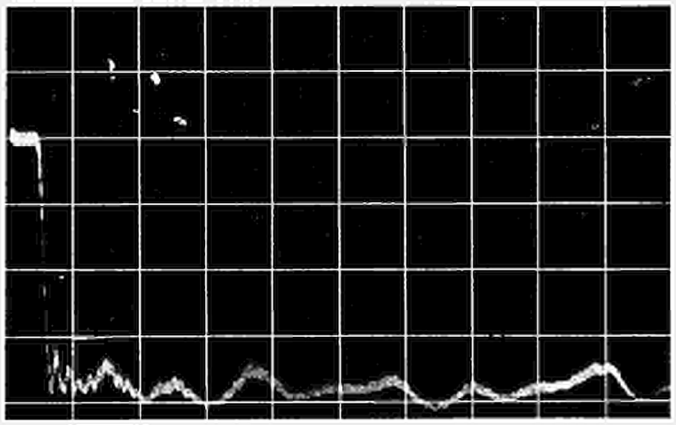

225 atm

→ 2 μsec/square

→ 10 μsec/square

Photograph 15

6 mm diameter steel bar transducer
records showing - transducer rise time
- damping of the return wave

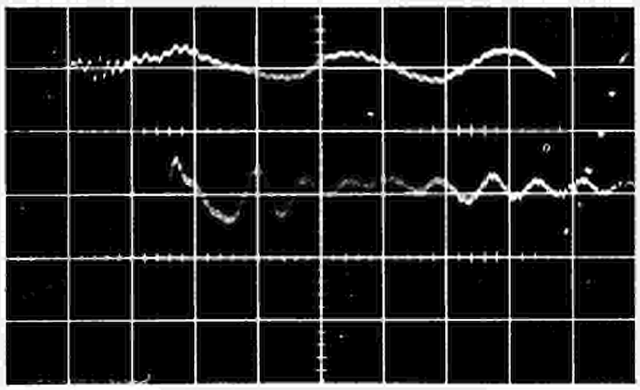

5 μsec/square

1 μsec/square

PHOTOGRAPH 16
pressure 125 atm.

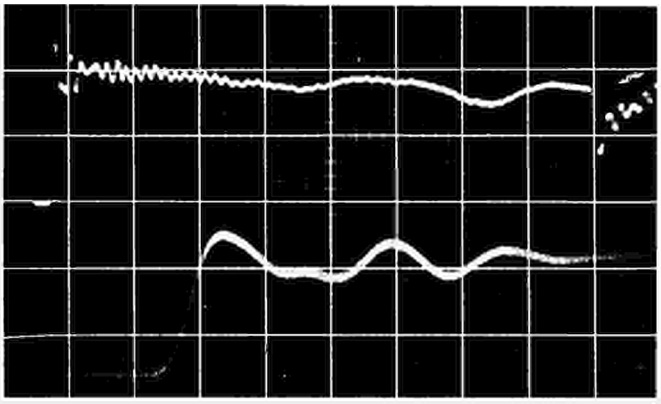

5 μsec/square

0,5 μsec/square

PHOTOGRAPH 17
pressure 375 atm.

6 MM DIAMETER BERYLLIUM BAR TRANSDUCER
RECORDS SHOWING RISE TIMES

A

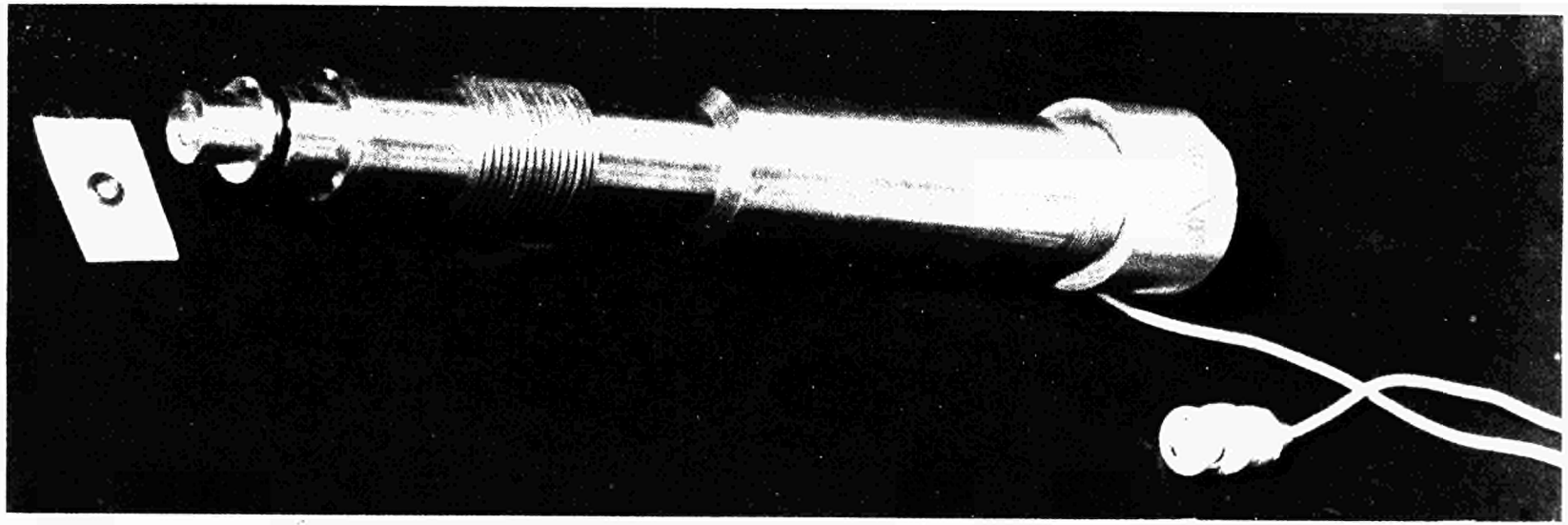

B

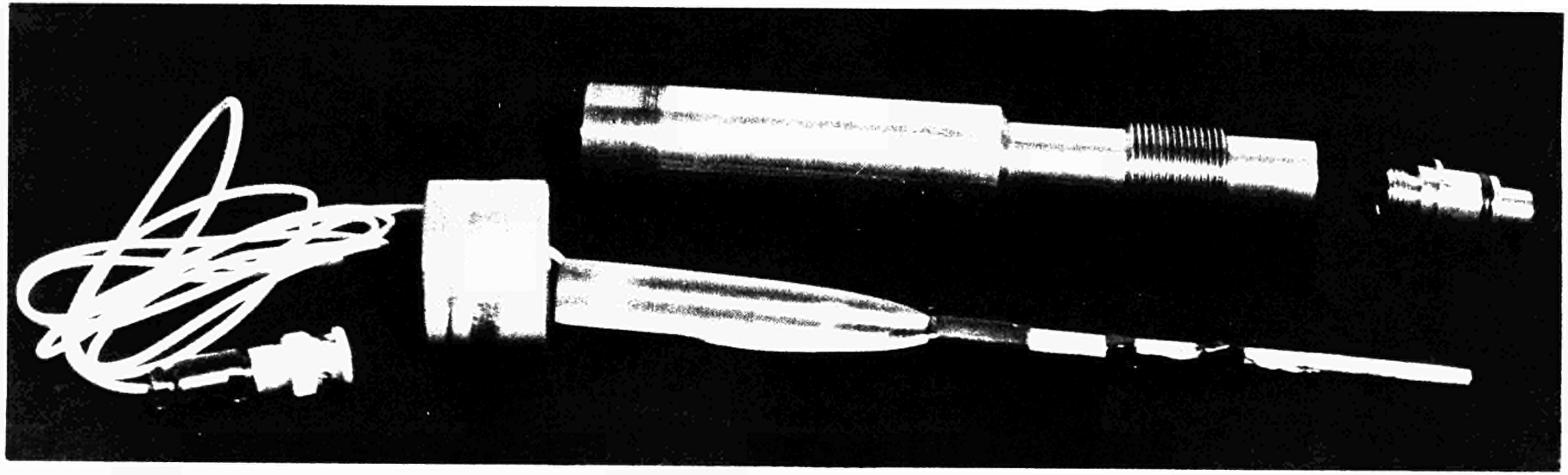

PHOTOGRAPH 18 BAR-TRANSDUCER

A Assembly
B - Components

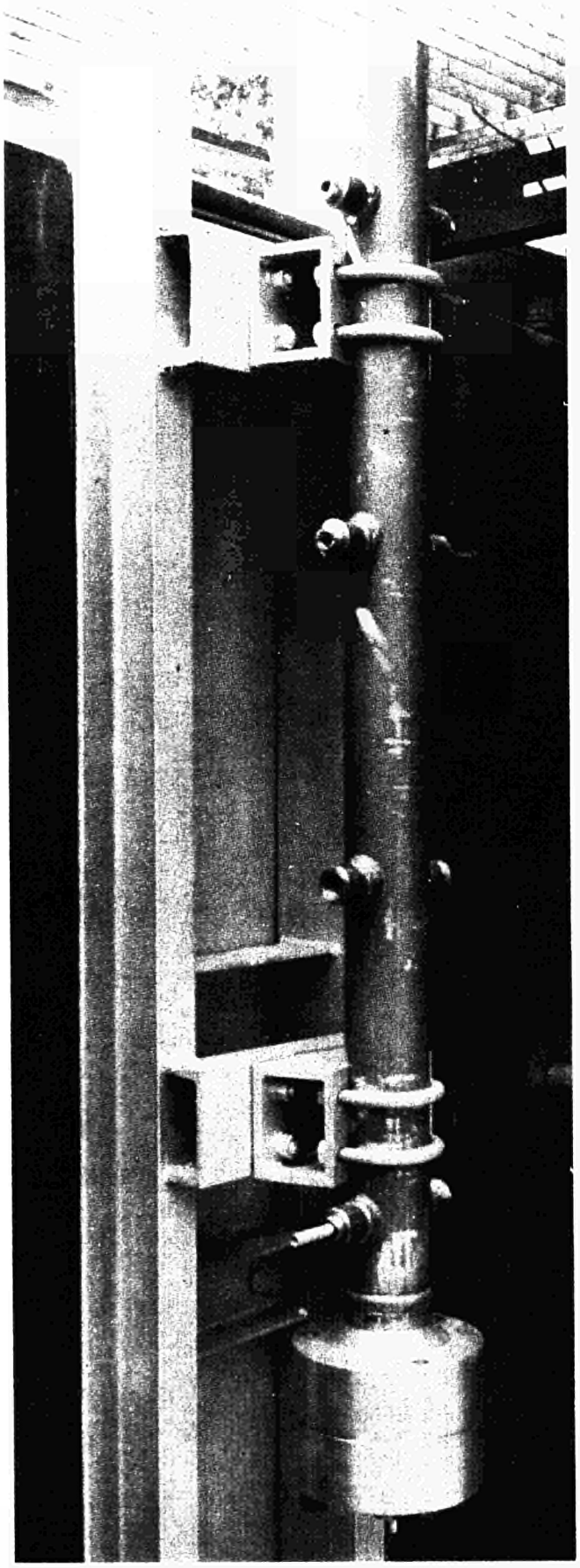

PHOTOGRAPH 19

DRIVEN SECTION OF VERTICAL SHOCK TUBE

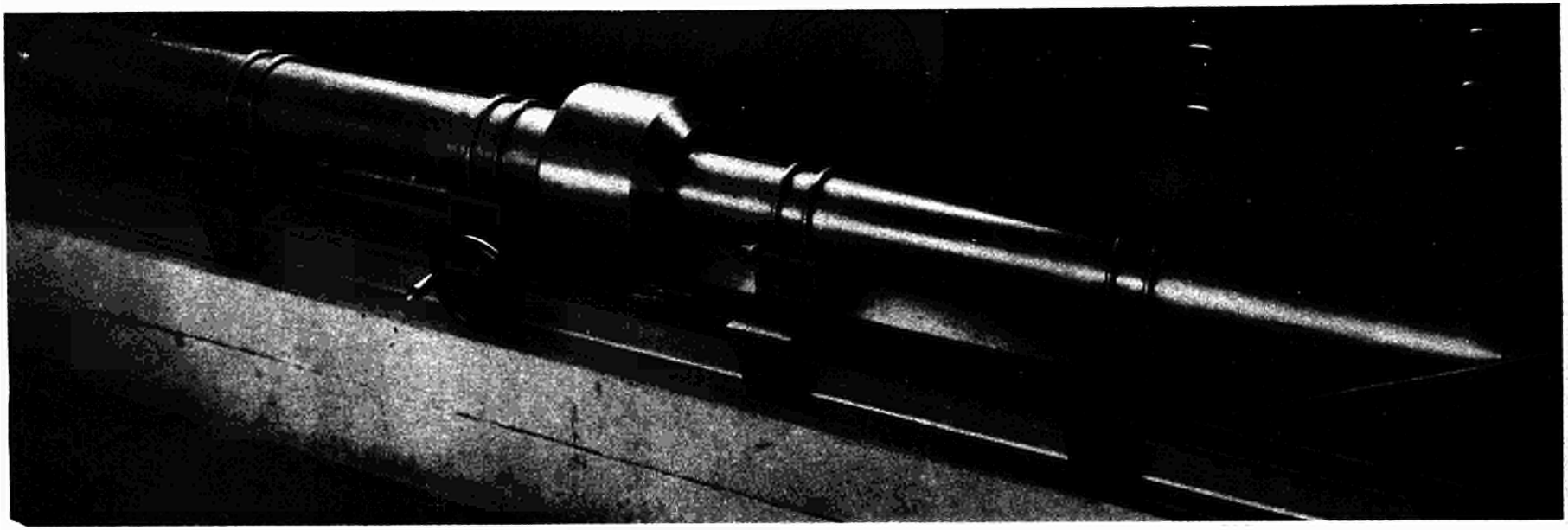

PHOTOGRAPH 20

HIGH-PRESSURE SHOCK TUBE

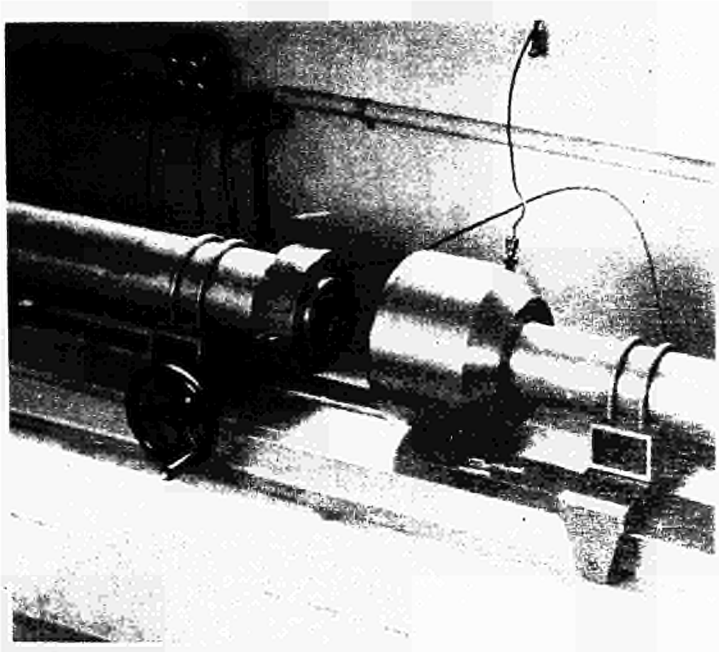

PHOTOGRAPH 21

COMPRESSED AIR CONNECTION
BETWEEN DRIVER AND DRIVEN SECTIONS

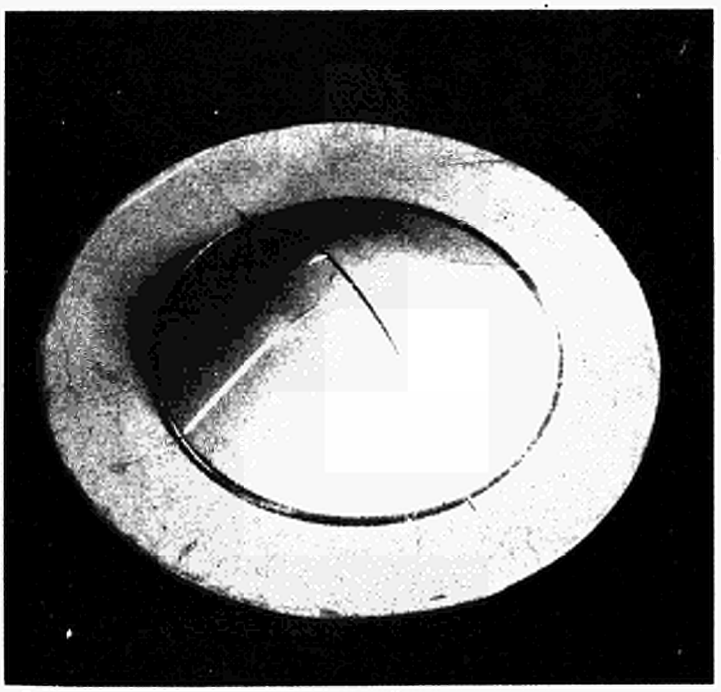

prestrained diaphragm

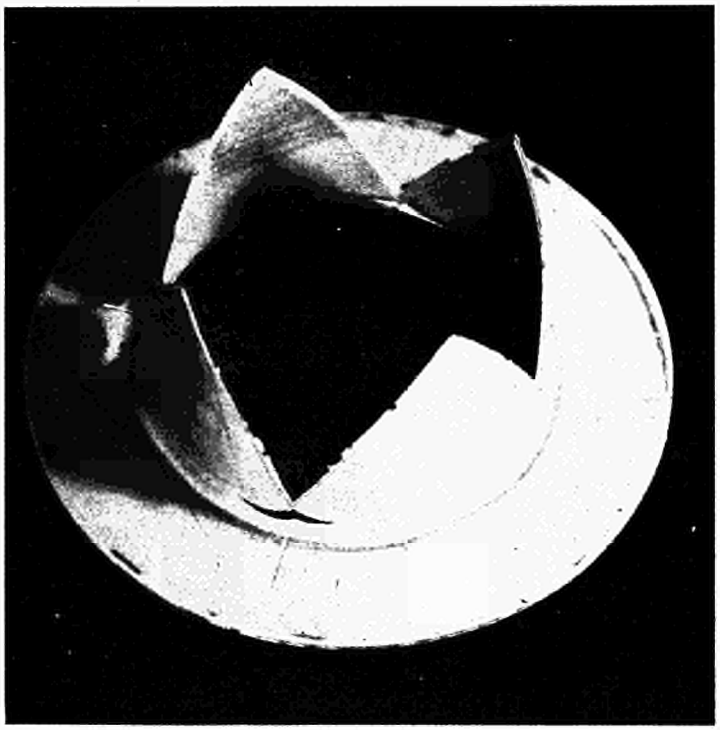

diaphragm after test effected
with open driven section

PHOTOGRAPH 22

SHOCK TUBE DIAPHRAGM

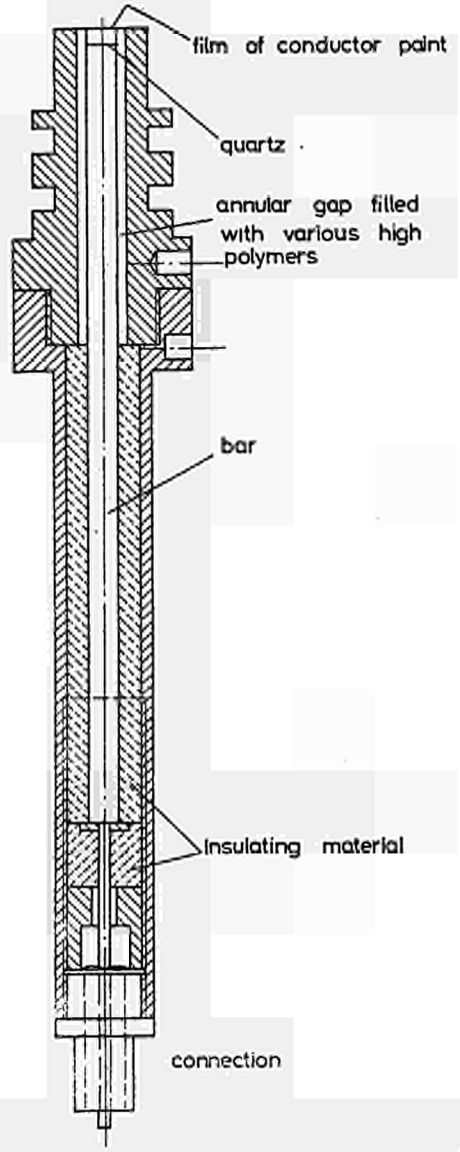

FIG. 1 QUARTZ TRANSDUCER (first solution)

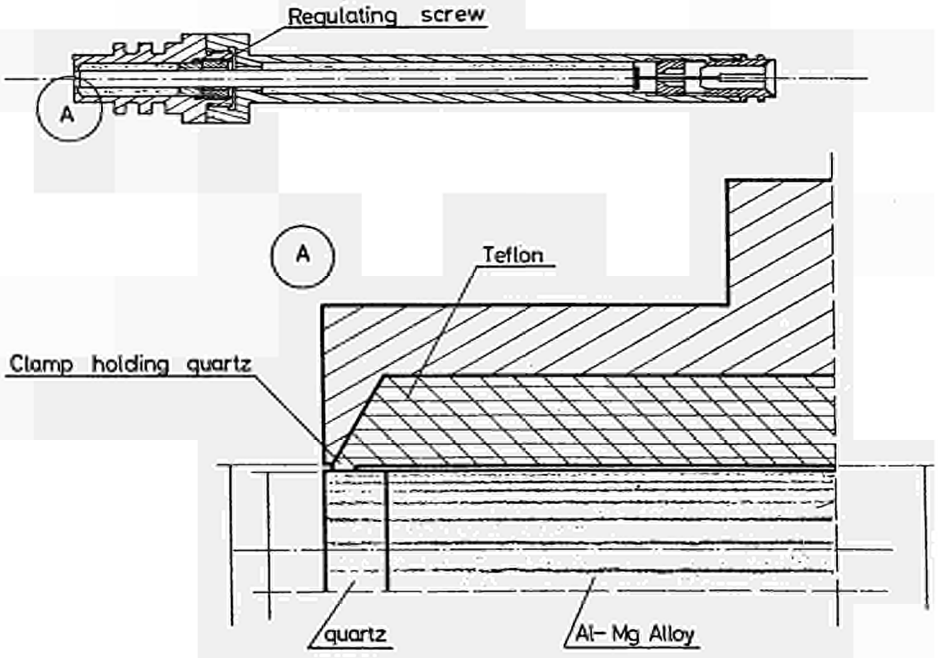

QUARTZ TRANSDUCER FINALIZED SOLUTION | FIG. 2

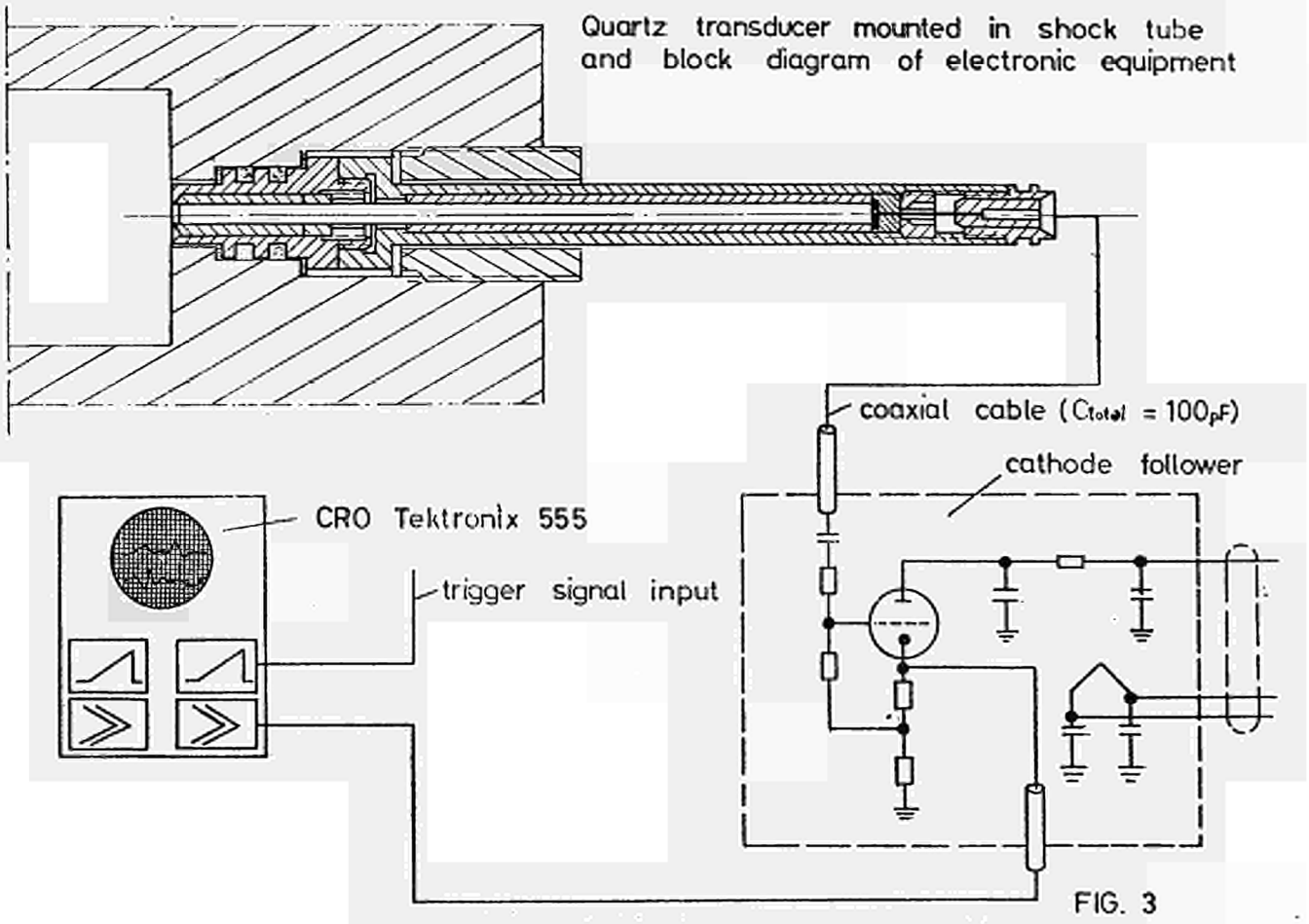

FIG. 3

Curve for strain ratio $\varepsilon/\varepsilon_o$ as a function of the adimensional parameter $B = \left(t - \frac{z_o}{c_o}\right)\sqrt[3]{\frac{4\,c_o^3}{3a^2.\gamma^2.z_o}}$

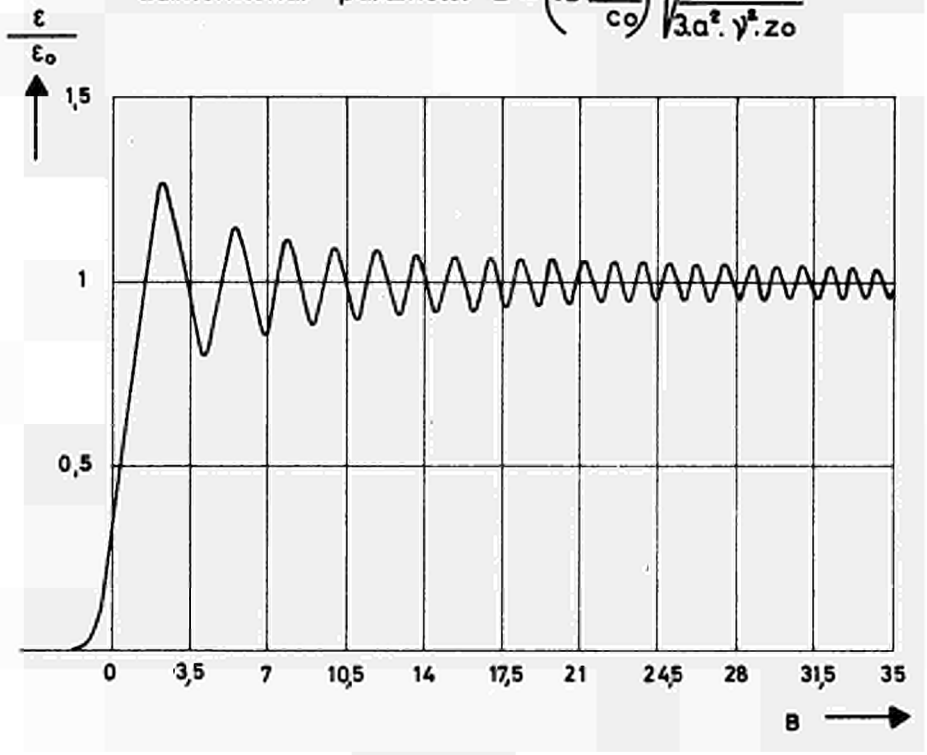

Fig. 4

BAR TRANSDUCER
DIAGRAM OF ELECTRONIC EQUIPMENT

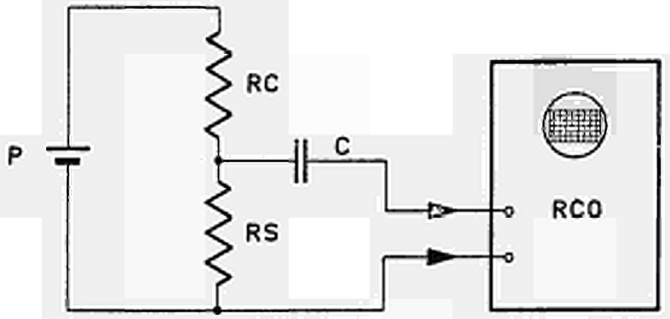

RC: DAMPING RESISTANCE
RS: STRAIN-GAUGE RESISTANCE
P : PILE
C : BLOCKING-CAPACITOR

FIG.5

BAR TRANSDUCER FIG. 6

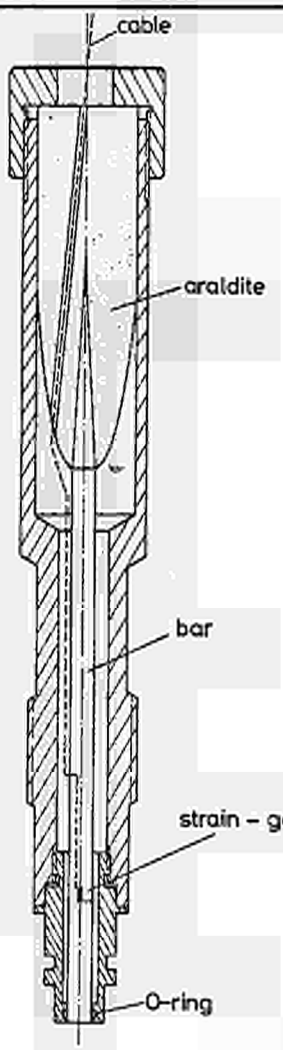

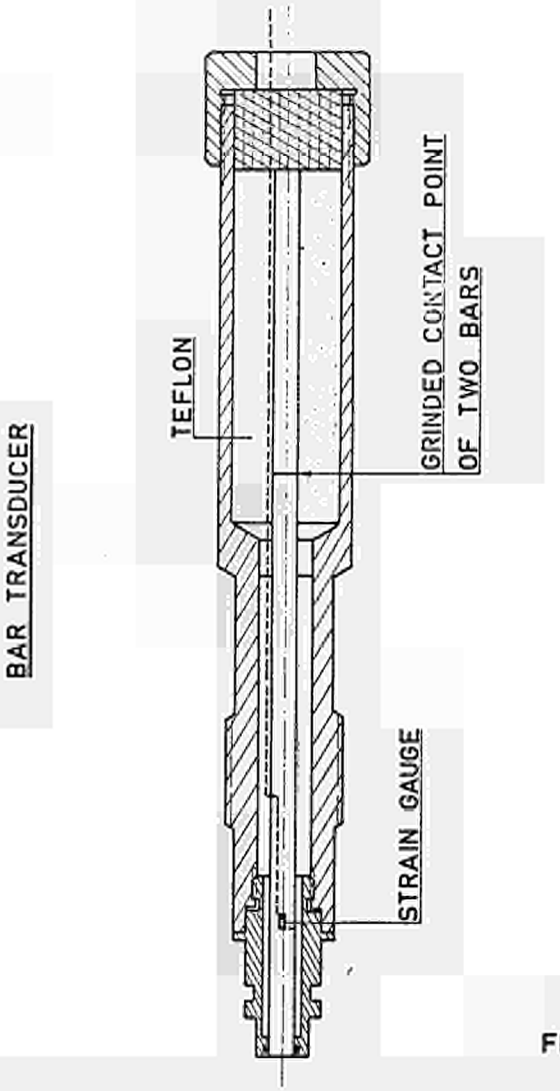
BAR TRANSDUCER
TEFLON
GRINDED CONTACT POINT
OF TWO BARS
STRAIN GAUGE

FIG. 7

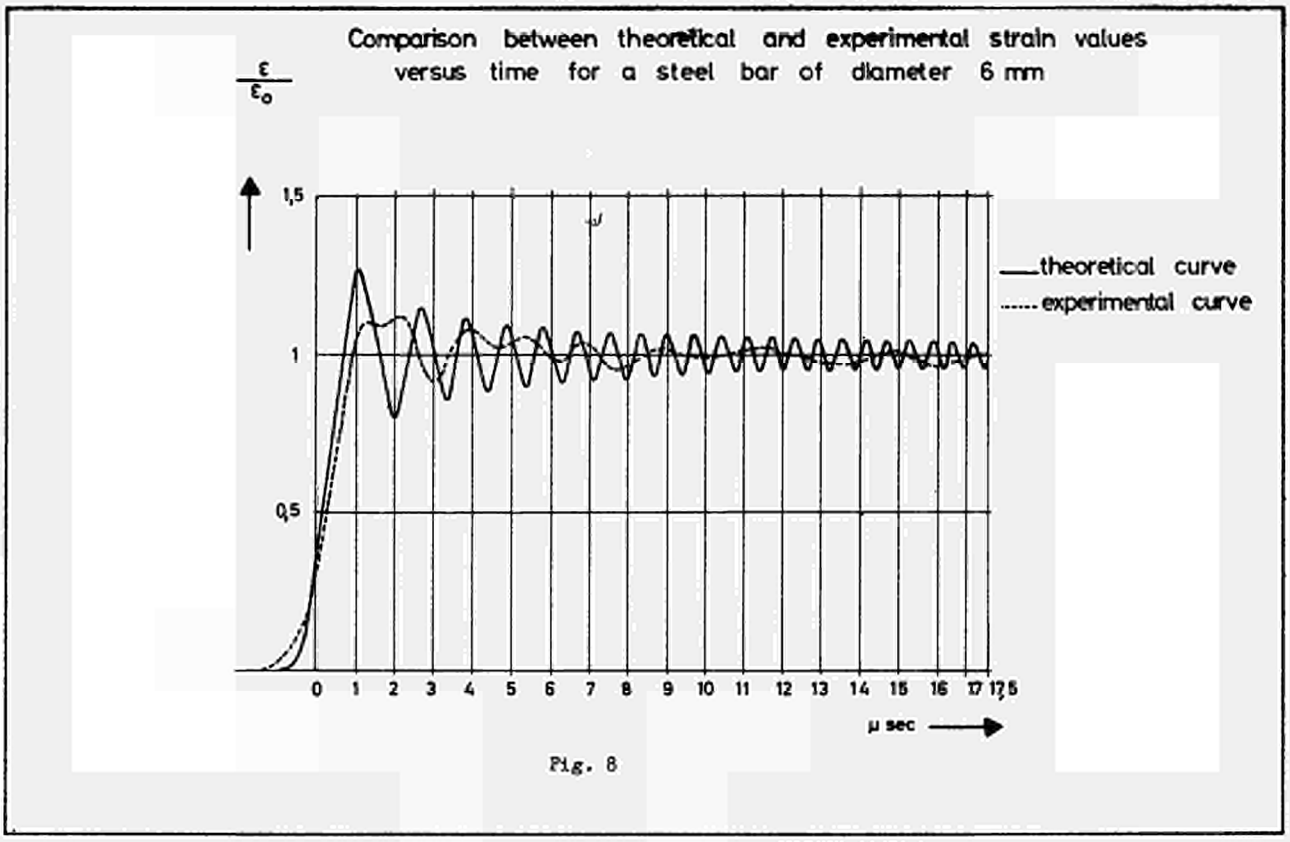
Comparison between theoretical and experimental strain values
versus time for a steel bar of diameter 6 mm
ε/ε₀
1,5
1
0,5
0 1 2 3 4 5 6 7 8 9 10 11 12 13 14 15 16 17 17,5
μ sec
theoretical curve
experimental curve

Fig. 8

Comparison between theoretical and experimental strain values versus time for a steel bar of diameter 4mm

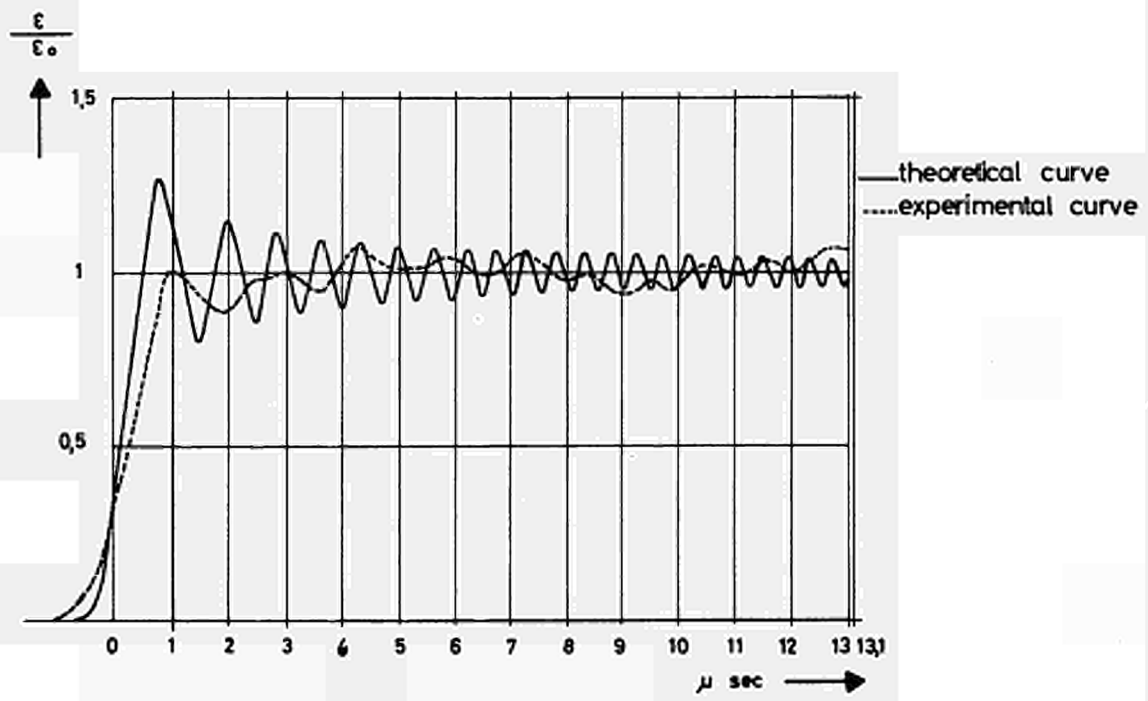

Fig. 9

Comparison between theoretical and experimental strain values versus time for a beryllium bar of diameter 6 mm

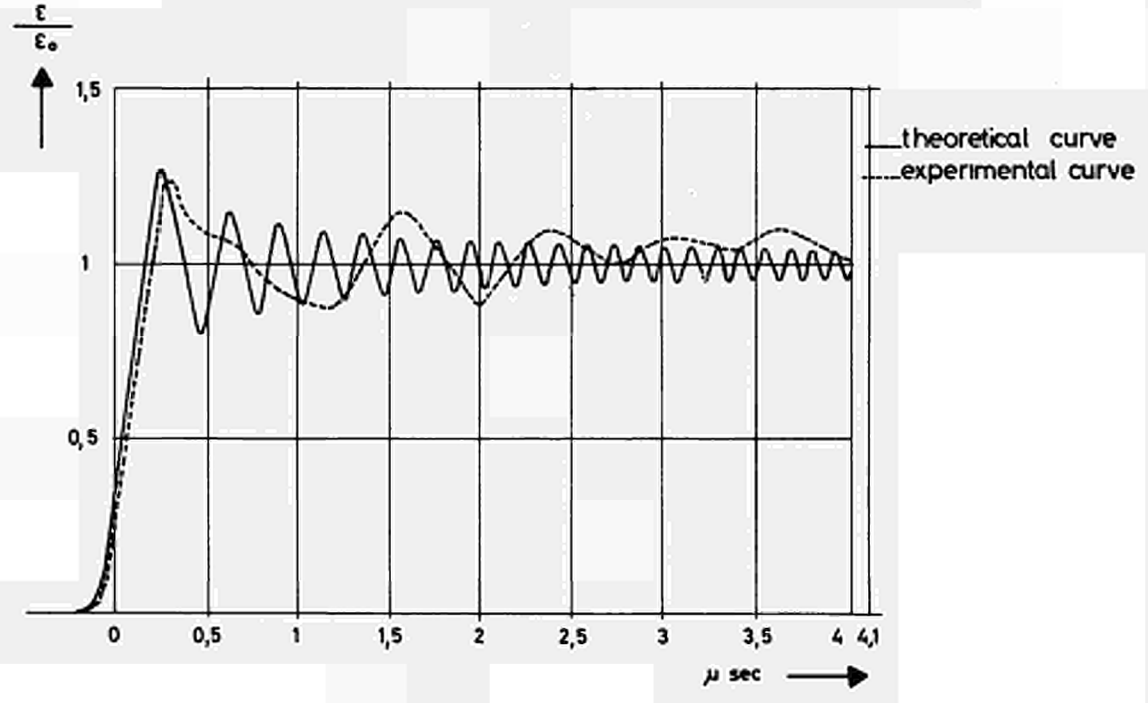

Fig. 10

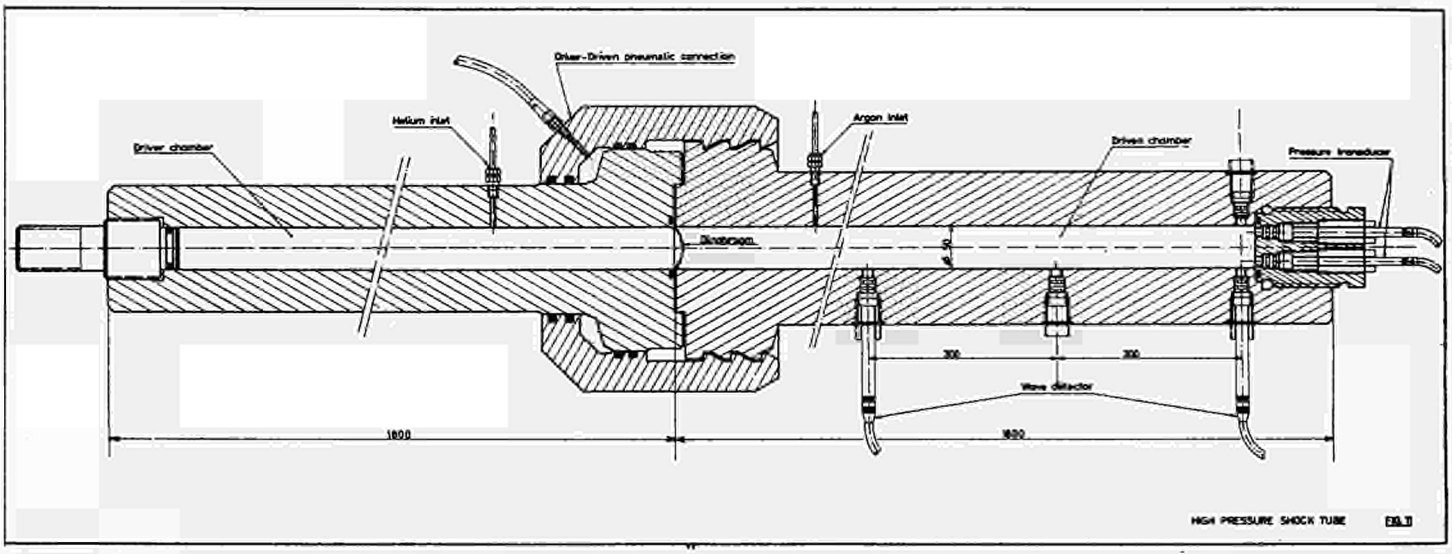

Piozoeletric (quartz) transducer for measuring velocity of wave in shock tube.

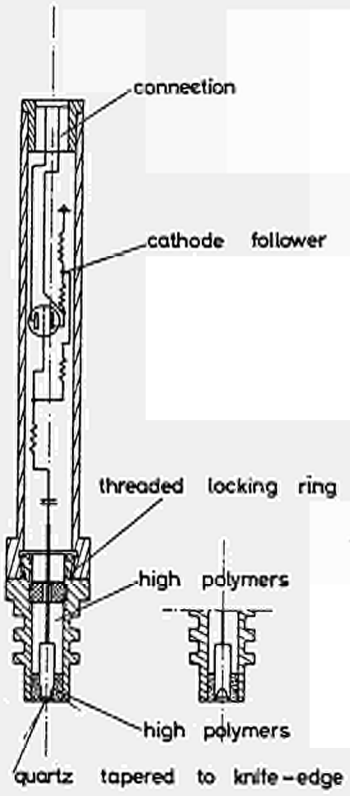

FIG 12

EVALUATION OF THE TENDENCY TO FRACTURE IN MATERIAL UNDERGOING IMPULSIVE LOADING USING SMALL SPECIMENS

by

H.C. Van Elst
TNO, Delft
The Netherlands

1. Introduction

If the time of load application to a body until its maximum value becomes of the order of the time for propagation of mechanical disturbances in this body, one has to do with transient impulsive loading.For a small body, even at high stress rates, multiple reflextions cause a smearing out of the stress configuration, which then more resembles the situation at static or quasi-static loading; however the mechanical properties, as elastic constants and (yield) strength values, can be quite different.
Material in contact with detonating explosives or exploding gas- or liquid mixtures or impacted at failure of pressurized construction parts, usually will be submitted to impulsive loading.
The generated pulse at this impulsive loading is qua amplitude proportional to the acquired velocity of the struck free bounding surface.
When the striking occurs by fast impact of a projectile the length of this impacting projectile will determine the time width of the generated pulse. Striking the free end of a pressure bar centrically with a projectile bar of the same material and diameter as the pressure bar and with length 1, which can e.g. be fired from a gas gun, one obtains a time width of the generated block-pulse of $2\frac{1}{c}$ (c = sound velocity in bar material).
Detonating a small explosive mounted on an anvil of the same diameter and material as the pressure bar and contacting this pressure bar, stress pulses of ca 5 /usec half value time and peak values over 100 kgf/mm^2 can be generated, when for the material of the pressure bar a (hard) material is chosen, with

yield strength well above 100 kgf/mm^2. General aspects of impulsive loading of metals are reviewed in [1], [2], [3].

Stress changes in time similar to these latter pulses have been found to occur at the tip of a running brittle fracture in steel plate. This was observed by application of ultra high speed photographic and electronic equipment with which the detailed propagation of the brittle fracture and its connected dynamic strain configuration at the apex was recorded in the Robertson test (cf. [4], [5]). It might be memorized that these recordings revealed an intermittent propagation of the brittle fracture in discrete steps, with length d, which need a certain time τ for realization. Both d and τ decrease with decreasing temperature; their ratio $\frac{d}{\tau}$ representative for the average fracture velocity only slightly increases with decreasing temperature. In a particular case for a low carbon steel, near its arrest temperature of ca 20 degrees centigrade, these step lengths d and their step times τ amounted to 25 mm and 20 μsec resp.; some 50 degrees centigrade lower d and τ were diminished to less than 2 mm and 2 μsec resp. The realization of the fracture propagation steps is connected with the depicted fast stress time changes (cf. [4], [5]).

It might be stressed that in our opinion the Robertson test can be considered to be fairly well representative for brittle fracture as occurring in practice, for the length and width of the specimen are large as in a real construction; the thickness of the plate, which has a pronounced influence on brittleness is retained and the specimen is under a static load (of e.g. 60% of the yield strength) like in a real construction.

The arrest temperature as determined in the Robertson test, being the temperature at and above which an initiated fracture will be arrested and below which it will be propagated, can consequently be regarded as a relevant indication for the danger of brittle fracture with respect to the working

conditions of stress and temperature. The large size of the specimens in the Robertson test makes it however desirable to look for a representative test on small specimens, indicating brittleness in a reliable way. In particular when one wishes to study the influence of neutron radiation damage on brittleness of steel this becomes of obvious importance. It was anticipated that the communication to small specimens of stress changes in time, as occurring at the tip of a running brittle fracture in the Robertson test, will allow to deduce from their effect on these specimens an indication of brittleness.
In the following is described how small specimens can be submitted to such stress time pulses, artificially generated in a pressure bar as mentioned, and how an estimate of brittleness (or embrittlenement) of the specimen material thus can be found.

2. Experimental

A cylindrical specimen with length and diameter of 6 mm, is mounted between two similar pressure bars of 6 mm diameter and length 250 mm. Cf. fig. 1. The specimen is submitted to a certain stress time performance when the free end of a pressure bar is impacted.
Striking this pressure bar via an anvil of the same material and diameter as the pressure bar by detonation of a fast explosive one generates an elastic pulse of ca 130 kgf/mm^2 and 5 μsec half value time, incident to the specimen. This pulse will be partially reflected and partially transmitted into the second bar.
All endfaces are polished and perpendicular to the axis to avoid stray reflections.
The recording of the pulses in the pressure bars proceeds with the aid of strain gauges or cylinder condensers to these bars on a C.R.O., triggered to a suitable single sweep by the detonation of the explosive. Examples are given in fig. 2.

The bars are made from a hardened steel (PCN4-Demka-Holland) with hardness Rc = 55 and yield strength $\approx$ 150 kgf/mm^2, causing the stress waves to remain elastic and allowing to ignore their attenuation in the bars, compared to that by the specimen (cf. fig. 3). The temperature of the specimen can be adjusted with a surrounding brass container in which a liquid is circulated from a thermostat. When the performance of the elastic stress σ in the pressure bar is:

$$\sigma = 0 \text{ for } t > \frac{x}{c} + \frac{1}{2}\tau \text{ and } t < \frac{x}{c} - \frac{1}{2}\tau \text{ and } \sigma = \sigma(x,t) \text{ for } \frac{x}{c} - \frac{1}{2}\tau \leqslant t \leqslant \frac{x}{c} + \frac{1}{2}\tau,$$

one can assume for the energy contents H of this pulse:

$$H = \frac{cA}{E} \int_{t = \frac{x}{c} - \frac{1}{2}\tau}^{t+\tau} \sigma^2 dt$$

with A = cross section of the pressure bar; E = Young's modulus;

$c = \sqrt{\frac{E}{\rho}}$ = sound velocity in the pressure bar material with density ρ;

τ = time width of the pulse.

The energy absorption by the specimen can now be approximated as $H_I - H_R - H_T$, with H_I, H_R and H_T the energy contents of the incident, reflected and transmitted pulse.

This can be plotted in a relative way as $\eta = (H_I - H_R - H_T)/(H_I - H_R)$ versus temperature.

For steel, generally b.c.c. metals, a transition phenomenon can be observed, i.e. a fast increase of the energy absorption with temperature in a rather small temperature interval ($\approx$ 50 degrees centigrade), preceded and followed by a small increase of energy absorption with increasing temperature. This can be connected with the brittleness of the material, as to the arrest temperature of a steel plate with a certain thickness will correspond a certain (relative) energy absorption level in the above described stress wave attenuation test.

This will roughly indicate the restriction of tolerable (elastic) energy changes in ca 5 μsec just avoiding fracture.

The embrittlement by deterioration as e.g. aging or irradiation can be followed from the shift in temperature of the relative energy absorption levels, in particular that belonging to the arrest temperature, which will rather equal the shift in arrest temperature, as could be verified (cf. fig. 4).

It might be remarked that these brittleness interpretations can be similarly

given for notch impact results.

Besides the energy absorption, also the dynamic stress train diagram of the time-endurance to which the specimen is submitted at transmittance of the stress pulse, can be deduced from the recordings.
Denoting the displacement of the first face of the specimen by $\xi_1(t)$ and of the second face by $\xi_2(t)$ one has:

$$\sigma_I(t) + \sigma_R(t) = \rho c \dot{\xi}_1(t) \text{ and } \sigma_T(t) = \rho c \dot{\xi}_2(t)$$

(I, R and T refer to incident, reflected and transmitted pulse resp.)
Consequently the length decrease $\xi(t)$ of the specimen is:

$$\xi(t) = \xi_1(t) - \xi_2(t) = \frac{1}{\rho c} \int_o^t \left\{ \sigma_I(t') + \sigma_R(t') - \sigma_T(t') \right\} dt'$$

The stress $\sigma(t)$ in the specimen, correpsonding to $\xi(t)$ will be on average:
$\sigma(t) = \left\{ \sigma_I(t) - \sigma_R(t) + \sigma_T(t) \right\} /2.$
The dynamic stress strain diagram i.e.: $\sigma(t)$ versus $\varepsilon(t)$, can thus be determined. Pending a direct electronic recording this proceeded manually with a mechanical integrator from the optically magnified oscillograms of the incident, reflected and transmitted waves.

A more detailed description of the applied experimental technique and the evaluation methods is given in [6], where also is referred to other literature dealing with versions and aspects of this "split Hopkinson bar experiment".

3. Results

"Energy absorption versus temperature" curves for some steels in delivery condition and after increasing neutron radiation fluence values, as deduced from recordings in the stress wave attenuation tests are given in fig.5,6,7 and 8. In the figures 5a, 6a, 7a and 8a the temperature shift ΔT_{c_1} in the temperature $T = T_{c_1}$, bounding equal areas between the relative energy absorption curve and the lower and upper level of the relative energy absorption resp., is indicated. In the figures 5b, 6b, 7b and 8b the temperature shift ΔT_{c_2} in the temperature $T = T_{c_2}$, referring to the 50% relative change in the relative energy absorption level and the temperature shift ΔT_{c_3} according to the persistent relative energy absorption at the isothermal Robertson test crack arrest temperature (C.A.T. = T_{c_3}) is indicated.

Dynamic stress-strain diagrams deduced from such recordings at -50 and +150 degrees centigrade are given in fig. 9, 10 and 11.

4. Discussion

The influence of neutron fluences on the "energy absorption versus temperature" curves, determined in the stress wave attenuation test and the evaluation of embrittlement from these are discussed in [7] and [8].
The dynamic stress-strain diagrams apparently show sometimes a considerable increase in Young's modulus (unfortunately however the data of the stress-strain diagrams at (quasi) static loading are not yet available). Moreover, an increase of plastic deformation at decrease of the stress occurs, ie. a delayed yield is suggested. This effect is stronger with aluminium than with steel and becomes more pronounced at higher temperature.
The jump in the "energy absorption versus temperature" curve at transition in the stress wave attenuation test is much smaller than is notch impact tests. This is connected in our opinion to the fact that the deformation is not proceeded to fracture as in usual technological destructive tests. At destructive tests the increase in temperature also implies an increase in test time, as the deformation can proceed longer at higher temperatures before it is terminated by fracture.
With b.c.c. metals the additional effect of the brittle-ductile transition enhances this increase with temperature. Below the transition temperature b.c.c. metals choose a deformation mechanism (cleavage and (or) twinning), which restricts the allowable deformation to a rather small value; fracture thus terminates the deformation process rather soon and therewith the test time. Above transition the b.c.c. metals choose a deformation mechanism (glide) that allow deformation to extend to a much larger value. When fracture finally terminates this deformation process the test time might have reached duration values ten times as large as below transition. Consequently , the energy absorption above transition also becomesconsiderably larger than below transition. From a physical point of view the change of the time parameter when changing the temperature implies a complication at interpretation.
The advantage is of course the larger dispersion in results below and above transition. The fact that in technological destructive tests the result is obtained after an integration in time, instead of being based on a state of equilibrium or a moment photo as in physical experiments, implies a dependence on the followed path during this time integration. The sometimes

pronounced scale influence and occurring contradiction in results of different tests, which can lead to inversions in the order of merit are well known consequences connected with this.

In the stress wave attenuation test the deformation is not proceeded to fracture and the test time is mainly determined by the incident stress wave. Yet a temperature effect remains, due to the increased dispersion effect and decreased propagation velocity of the plastic stress wave in the specimen at increase of temperature, in particularly when passing transition.

At deterioration of the material a shift in the transition region of the "energy absorption versus temperature" curves at stress wave attenuation or notch impact tests can usually be observed, allowing to estimate the increase in transition (arrest) temperature.

Also a decrease of the energy absorption in the ductile region indicates embrittlement. As after aging usually the strength values increase and the deformation rate $\dot{\varepsilon}$ decreases (at least does not increase) one can expect an increase of the energy absorption rate per volume unit $\sigma\bar{\dot{\varepsilon}}$, if the increase of the strength figures predominates the decrease of the deformation rate values. A decrease of the test duration time τ can account for the decrease in energy absorption. This decrease will occur, if deformation is determined earlier by fracture, i.e. when embrittlement takes place.

References

1. "Behaviour of metals under impulsive loads" - Rinehart J.S. and Pearson J. (Americam Society for Metals, Cleveland, Ohio, 1954; Dover ed. 1965).
2. "Stress waves in solids" - Kolsky H. (Oxford 1953, Clarendon Press; Dover ed. 1963).
3. "Response of metals to high velocity deformation" - Hauser F.E., Simons H.A. and Dorn J.E. (Interscience, New York 1961).
4. Elst H.C. van - Trans. of the Met. Soc. of AIME, 230, no. 3, pp. 460-469 (1964).
5. Elst H.C. van - Bulletin de la Soc. Belge de Physique, Série IV no. 3-4, pp. 238-268 (1964).
6. Elst H.C. van - Proc. of the 2nd Conf. on Dimensioning and Strength Calculations, pp. 483-507. Budapest (1965).
7. Elst H.C. van - Proc. of the Euratom-colloquium on "Brittle fracture in steel". Brussels 1966 (to be published).
8. Elst H.C. van - Communication au 10ème colloque de métallurgie: Fragilité et effets de l'irradiation - C.E.N. Saclay 1966.

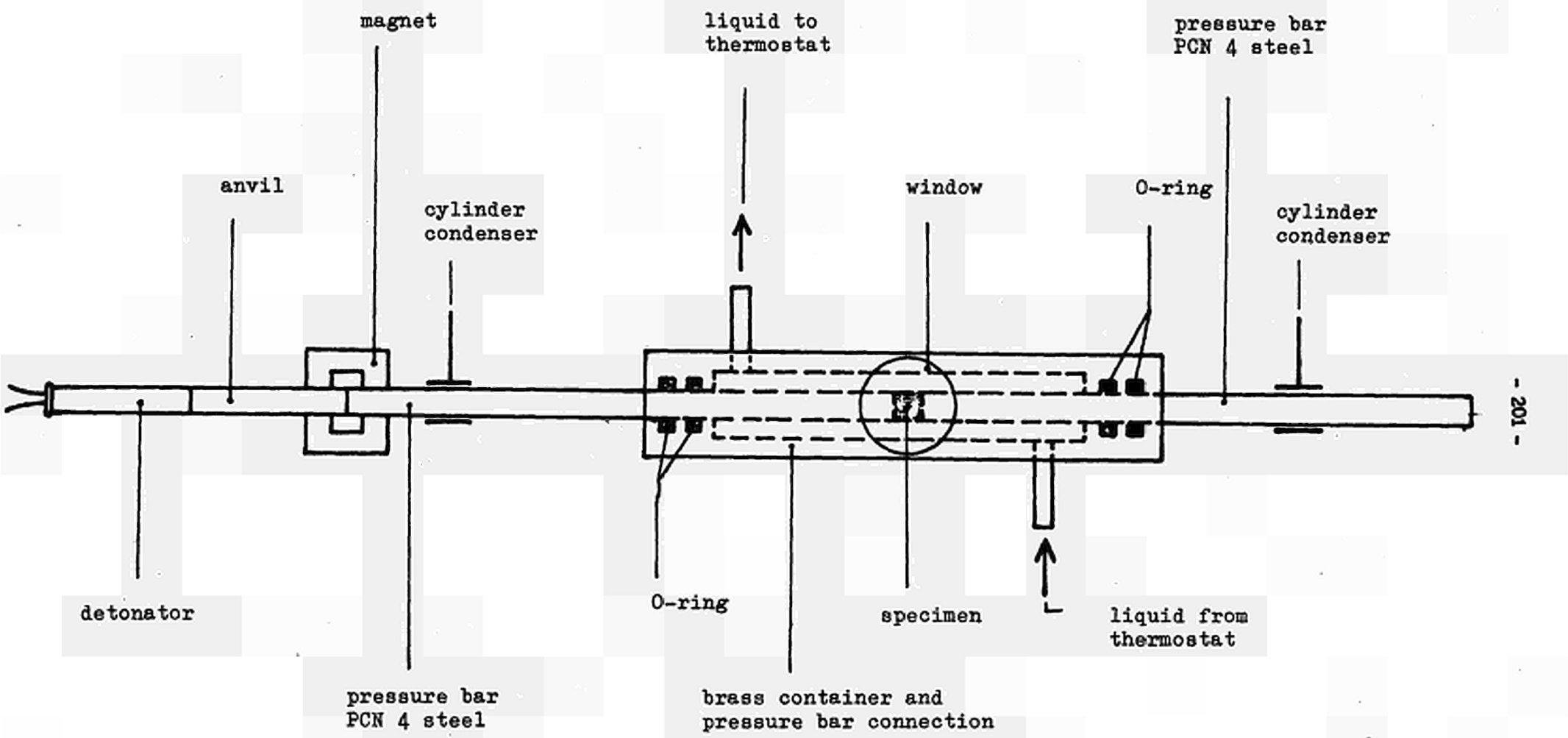

Fig. 1

Experimental set-up for the measurement of the attenuation of stress waves by a small cylindrical specimen at several temperatures.

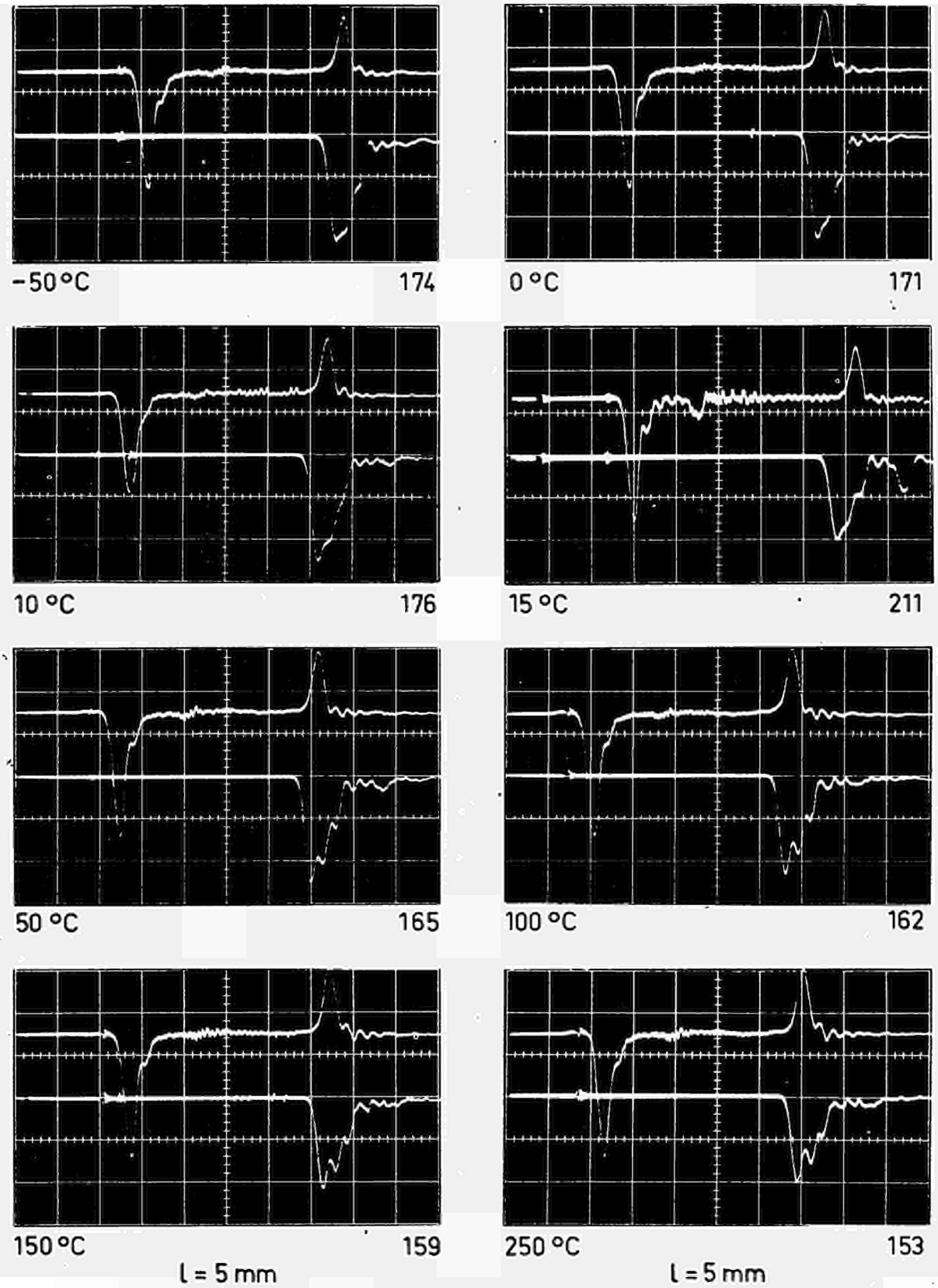

upper beam: 1 s.d. ↑ = 64.6 kgf/mm^2; 1 s.d. → = 10 /usec
lower beam: 1 s.d. ↑ = 26.2 kgf/mm^2; 1 s.d. → = 10 /usec

Fig. 2

Recordings of the incident, reflected and transmitted pulse at performance of the stress wave attenuation test on a low carbon construction steel at several temperatures.

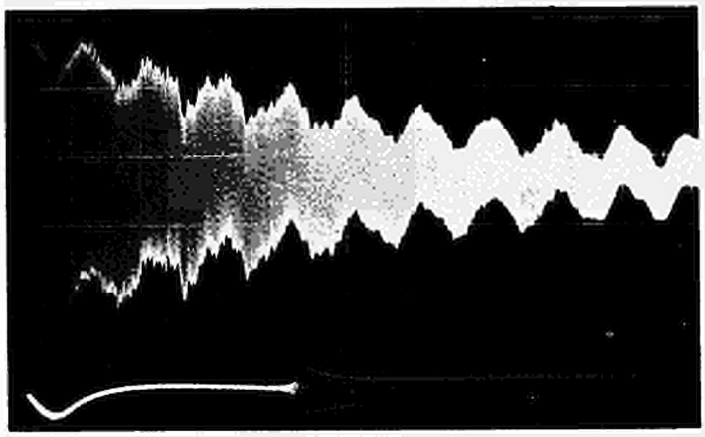

→ 20 msec/cm

$E = 19.7 \times 10^3$ kgf/mm^2

$\nu = 25.237$ kHz

$\frac{\Delta W}{W} = 6.68 \times 10^{-4}$

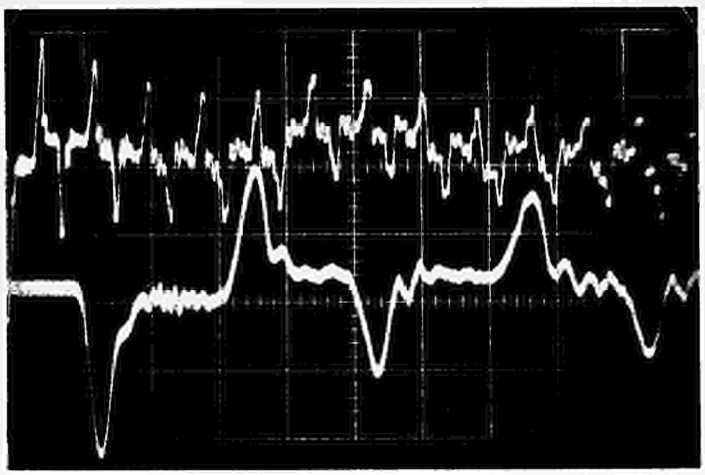

→ 50 μsec/cm

↑ 64 kgf.mm^2/cm

→ 10 μsec/cm

$\frac{\Delta W}{W} = 0.17$

Fig. 3

Attenuation of stress wave in pressure bar.

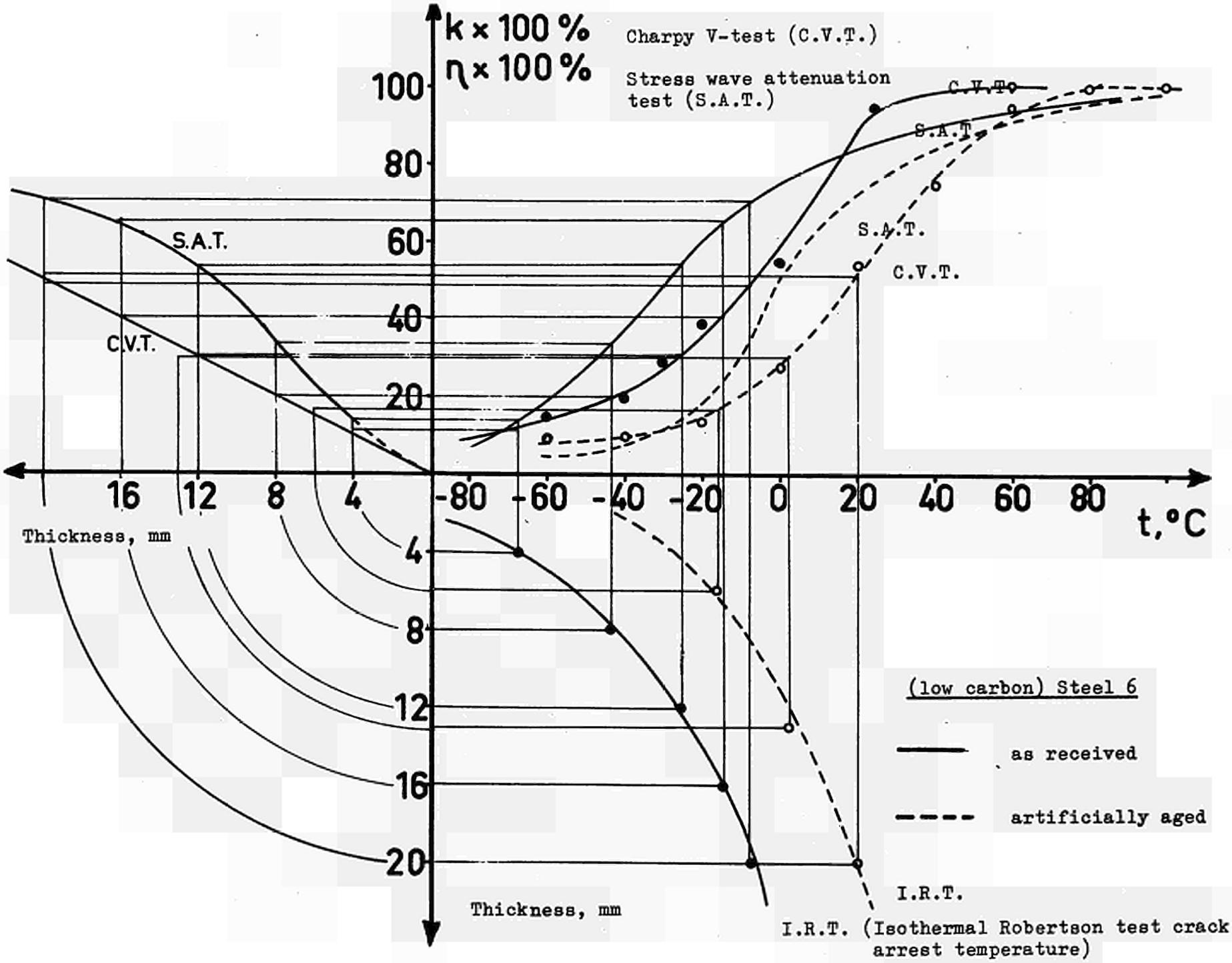

Fig. 4

Relation between energy absorption in notch impact or stress wave attenuation test for steel and arrest temperature in the isothermal Robertson test for a certain thickness of this steel, before and after aging.

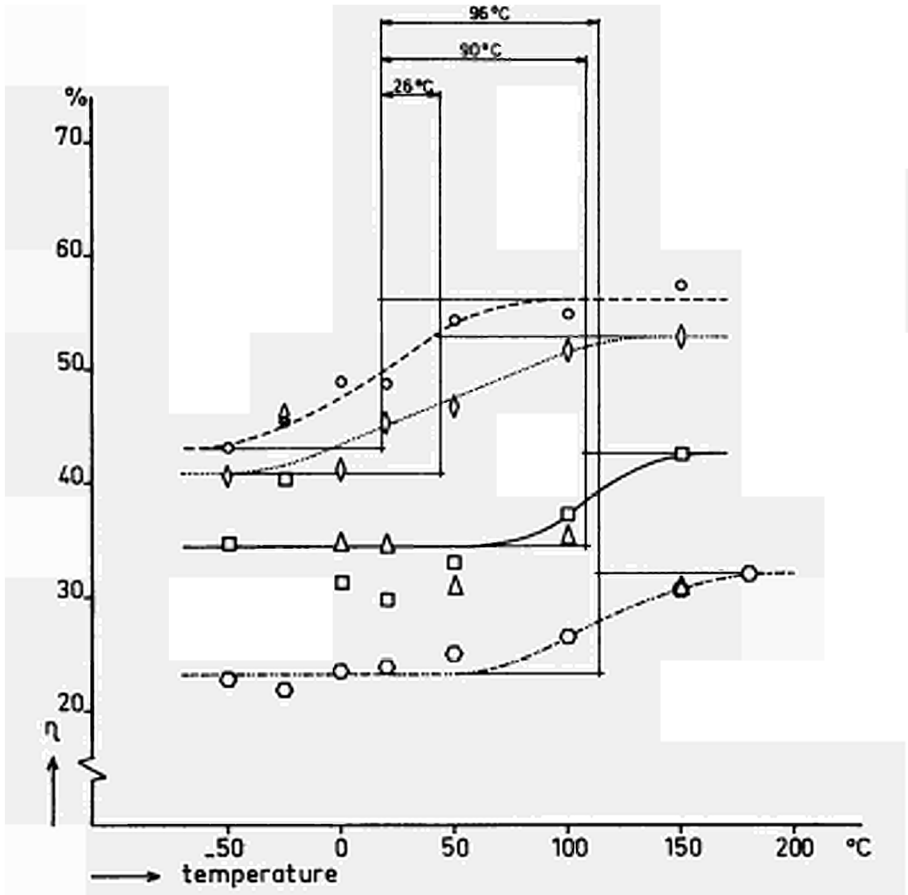

Fig. 5a

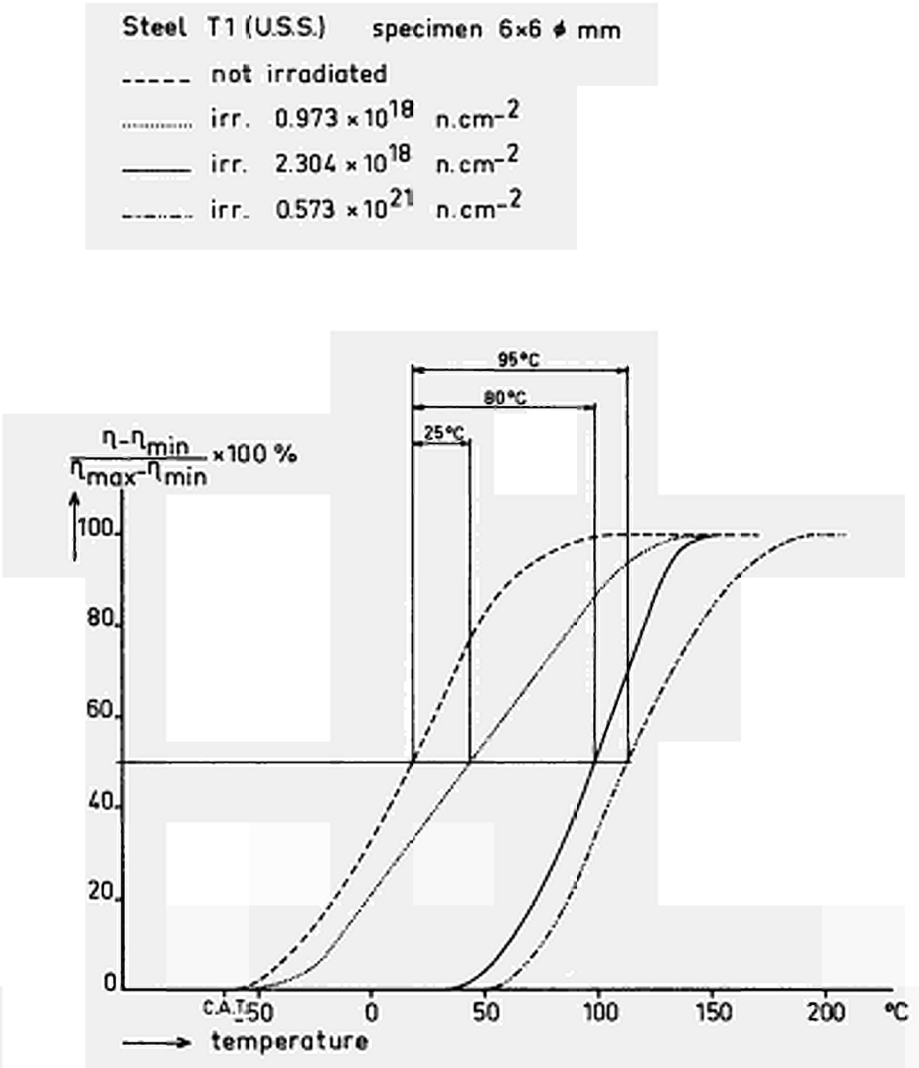

Fig. 5b

5. The influence of neutron radiation damage on the energy absorption versus temperature curves of the stress wave attenuation test for T_1-steel of U.S.S.

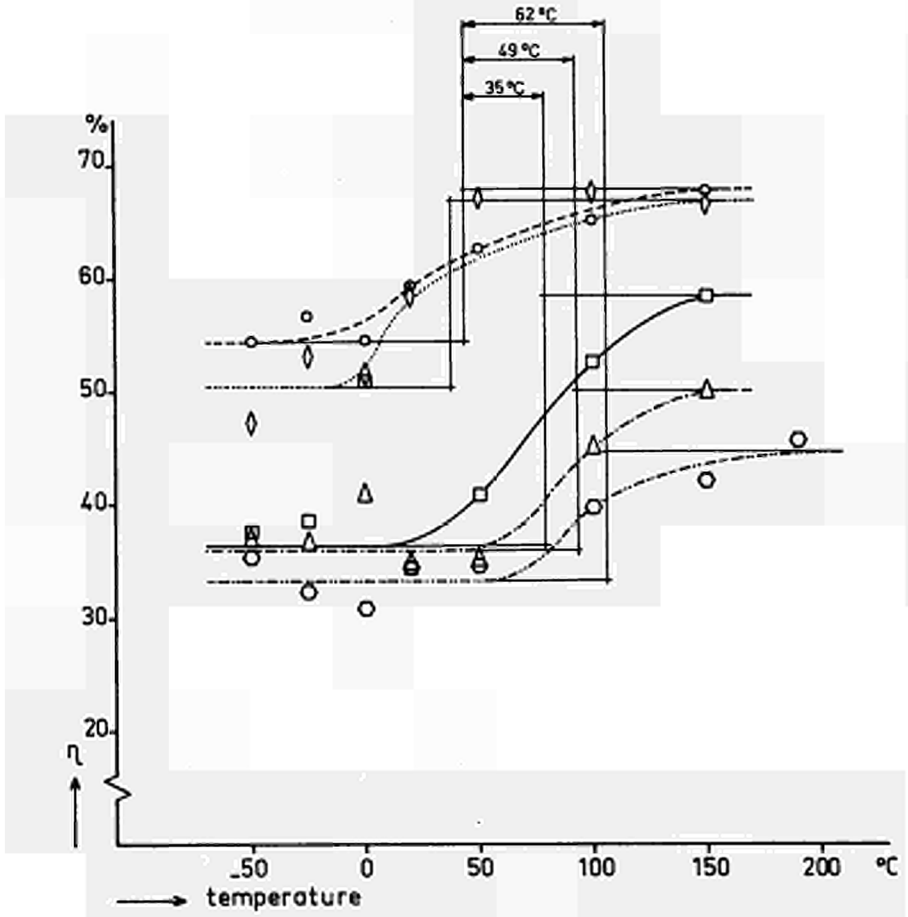

Fig. 6a

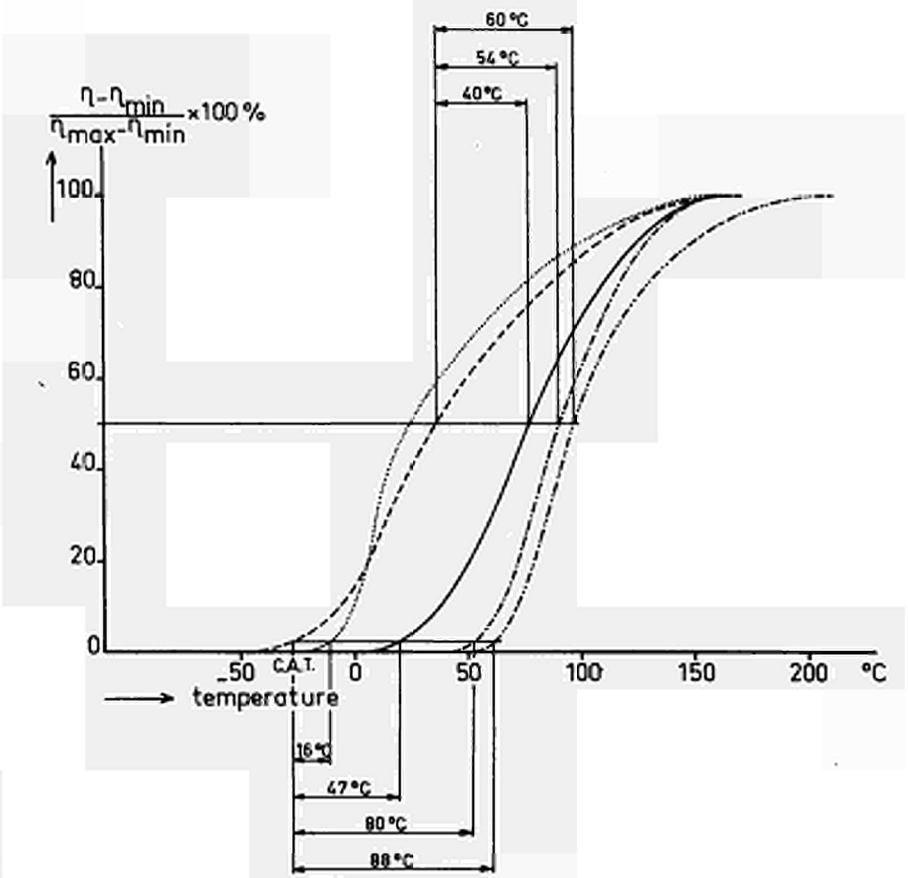

Fig. 6b

6. Ditto for Soudotenax - 56 steel of Cockerill-Ougrée.

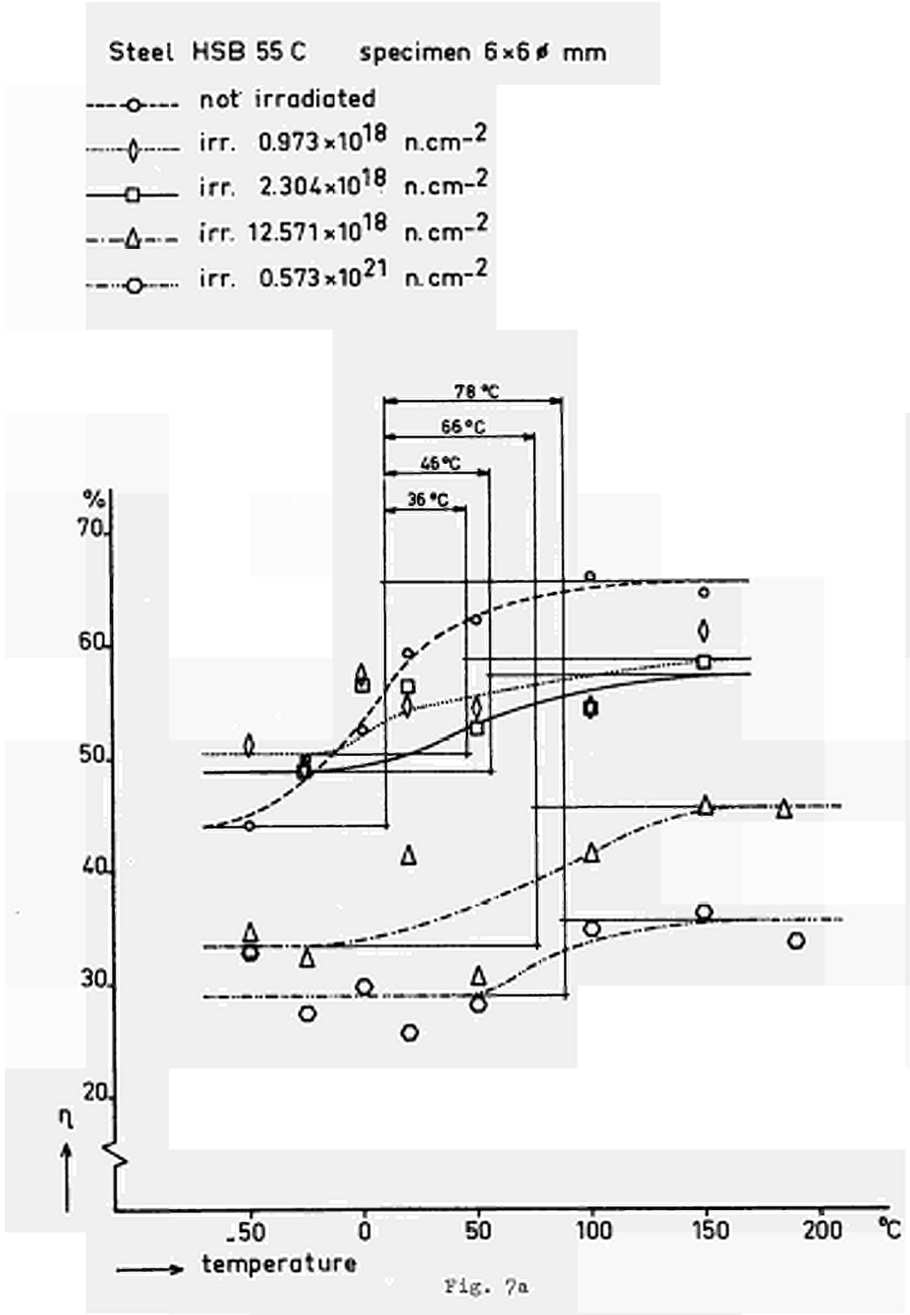

Fig. 7a

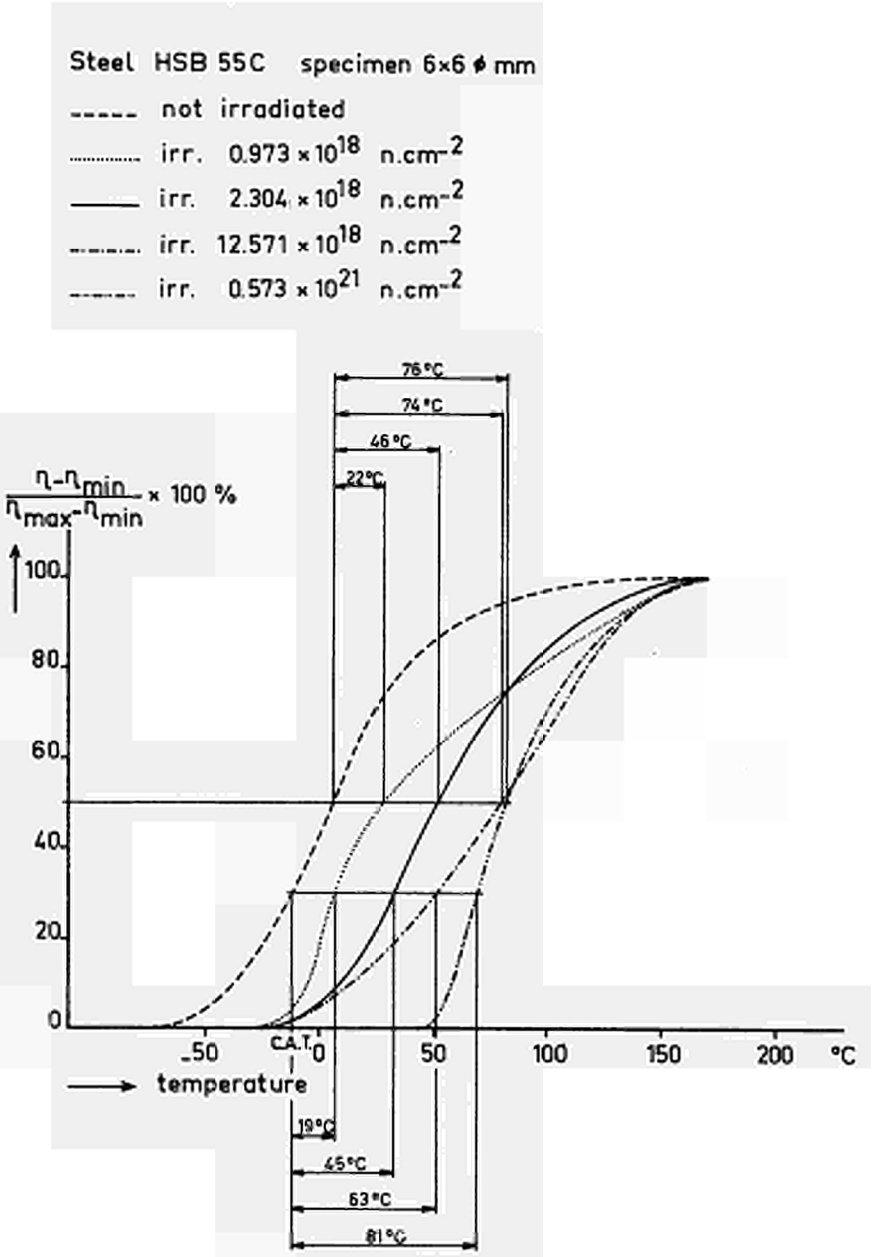

Fig. 7b

7. Ditto for HSB 55 C - steel of Phoenix Rheinrohr.

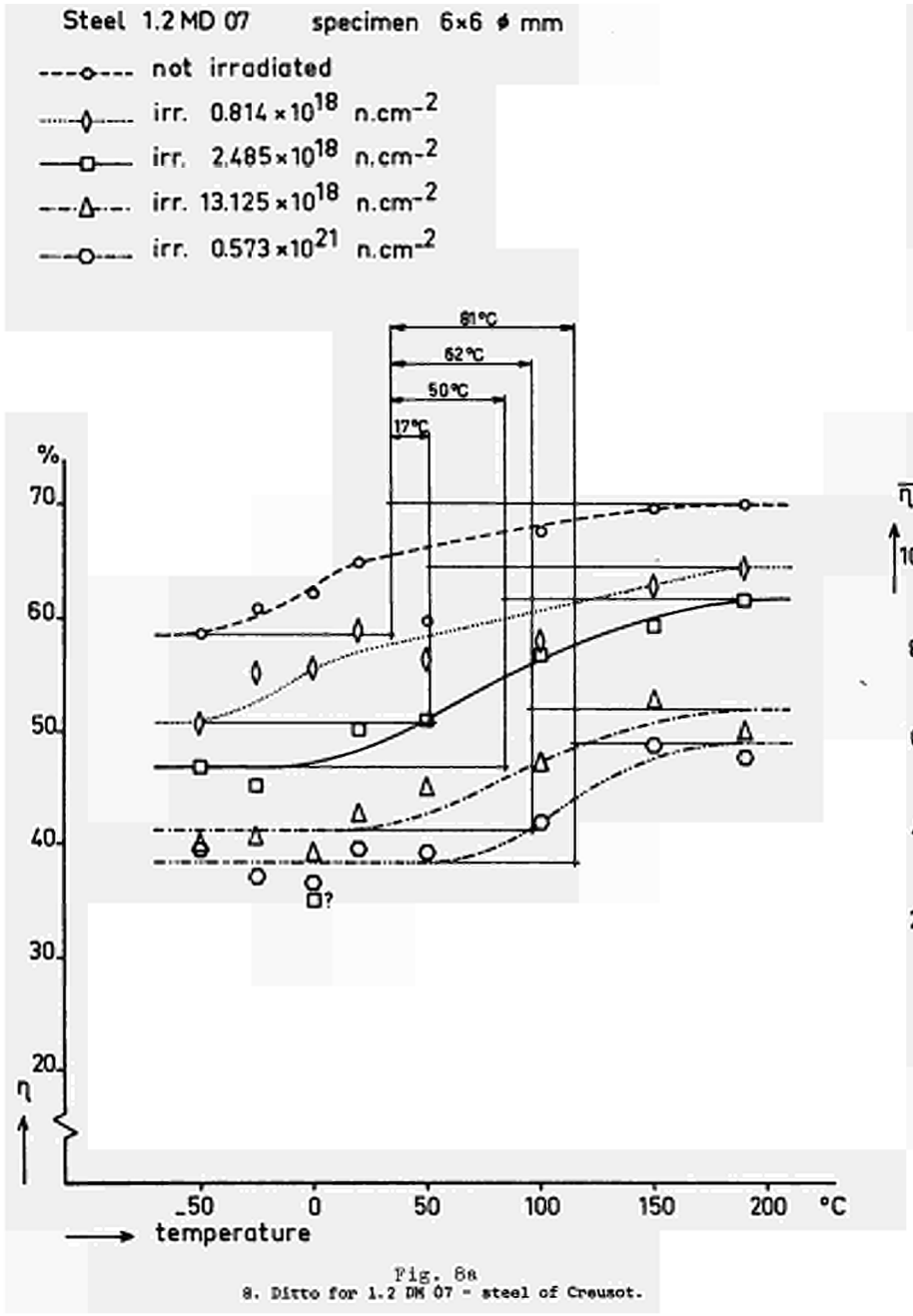

Fig. 8a
8. Ditto for 1.2 DM 07 - steel of Creusot.

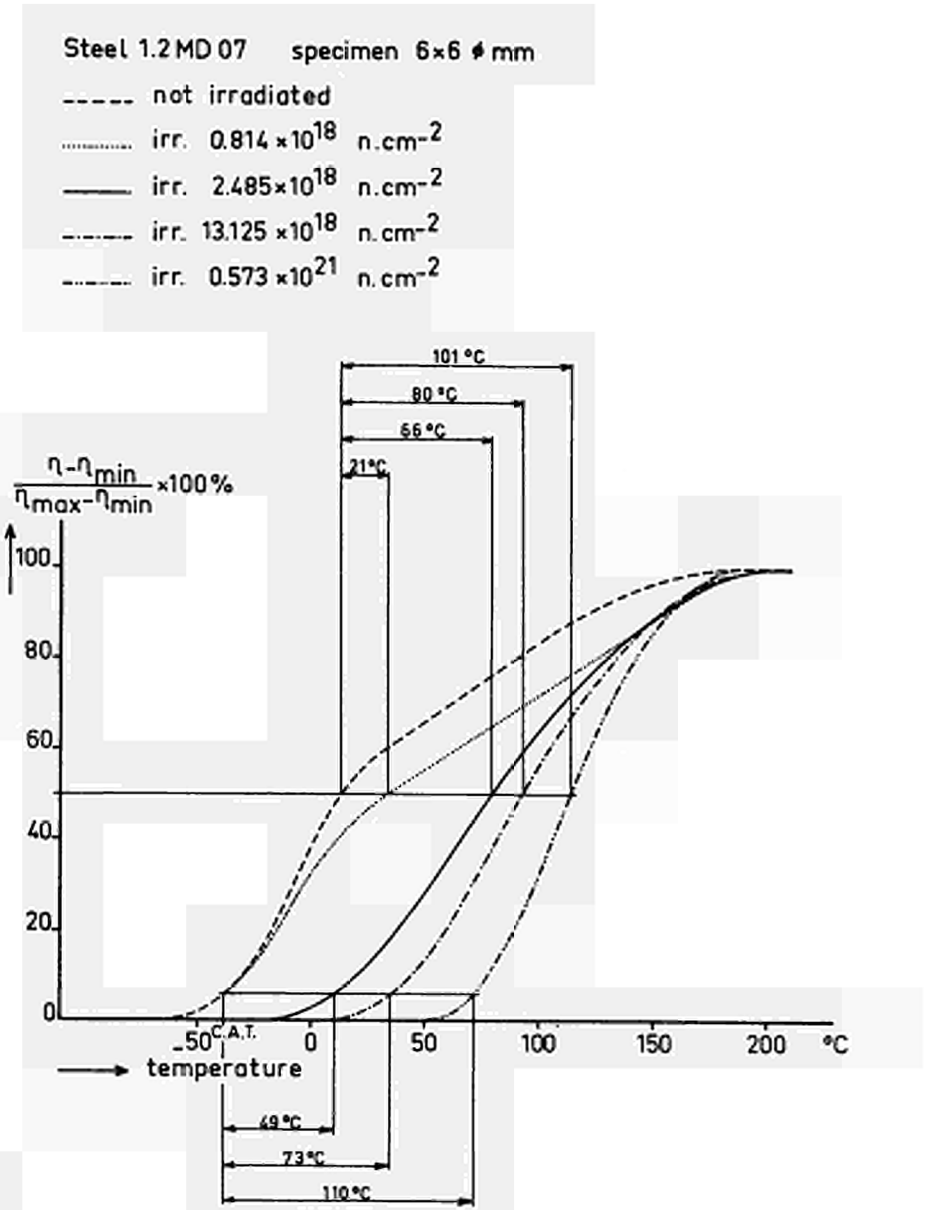

Fig. 8b

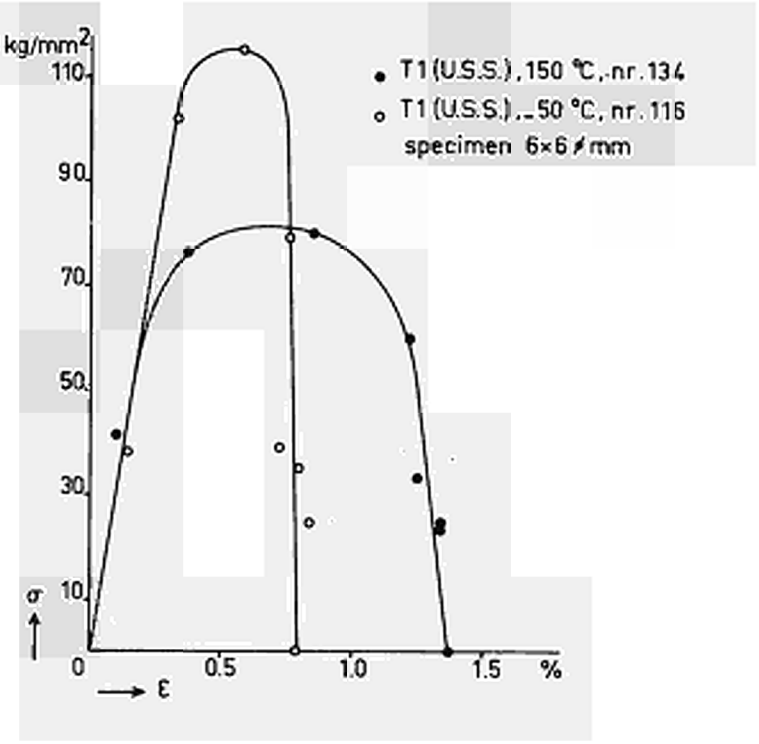

Fig. 9. Dynamic stress strain diagram at 150 and +150 degrees centigrade of T1-steel specimen in the stress wave attenuation test, deduced from recordings of the incident, reflected and transmitted pulse.

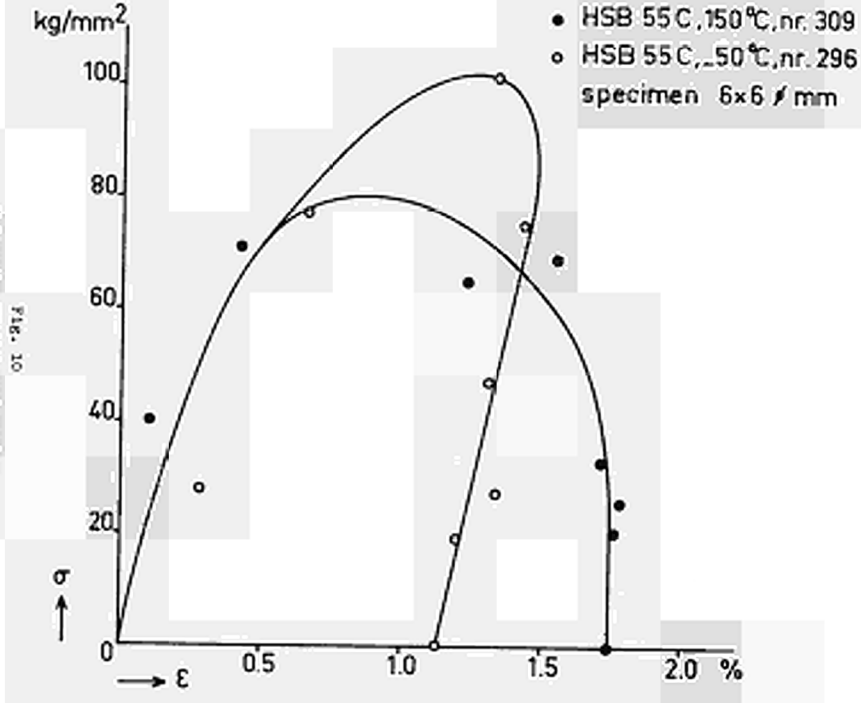

Fig. 10. Stress-strain curves for HSB 55 C steel specimen.

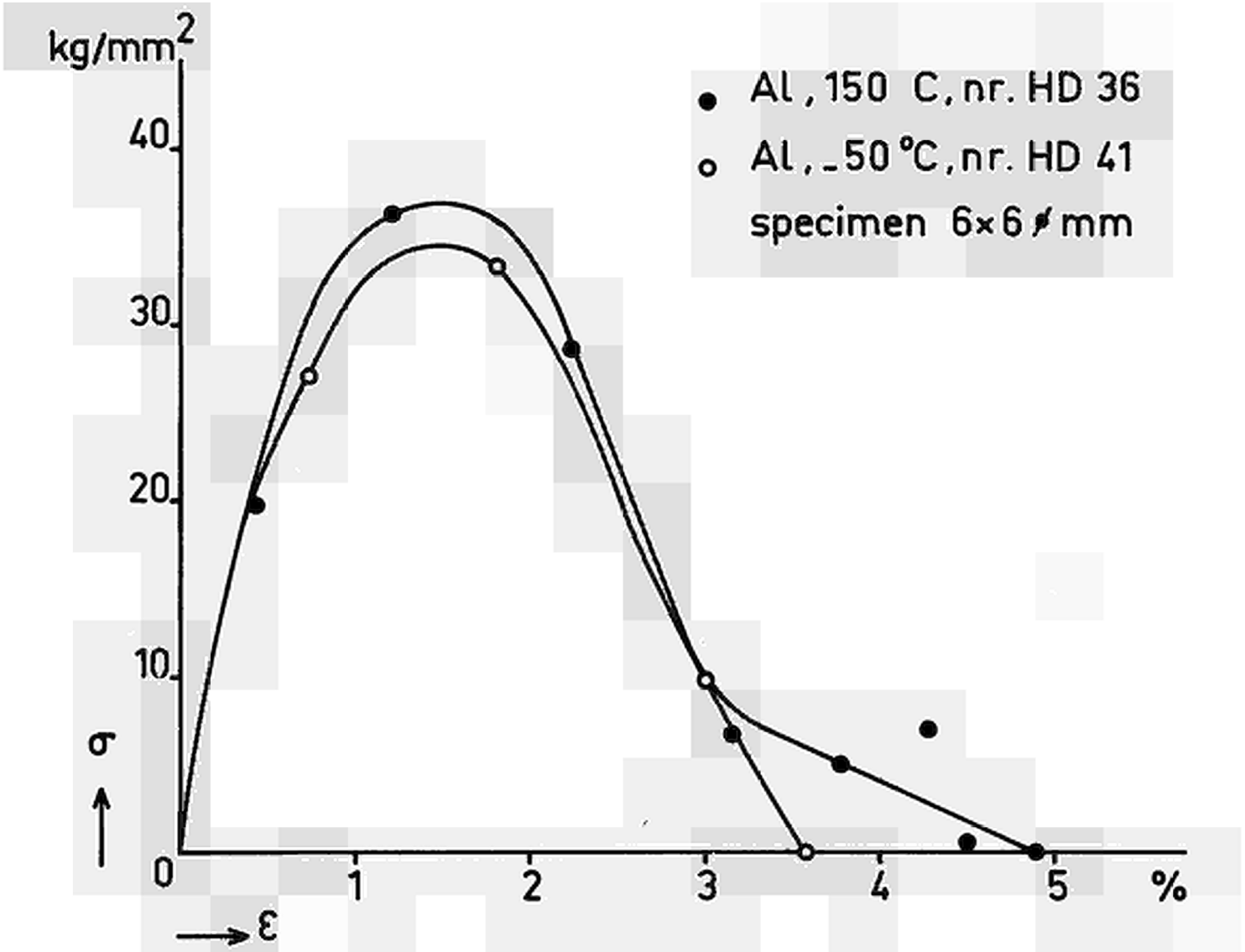

Fig. 11
11. Ditto for aluminium specimen.

EXPERIMENTS TO EXAMINE THE EFFECT OF RAPID STRAIN RATES ON FULL SCALE AND MODEL SCALE REACTOR MATERIALS

by

N.J.M. Rees

AWRE, Foulness
United Kingdom

1. Introduction

A mechanical system and a scale model of it are said to be dynamically similar when scaled forces are exerted at scaled times on similar portions of the system and the model. Dynamic similarity will be maintained between the model and a full scale explosion if the linear dimensions of the explosive charge and the mechanical system are divided by a factor S and the model constructed of similar materials. Thus if M is the mass of the full scale charge, R is a full scale length and t a full scale time, then the corresponding model scale values are M/S^3, R/S and t/S. Shock wave pressures on the full and model scales will be the same (1,2). The scaling factors for some physical parameters that are often measured in full and model scale experiments are listed in Table 1.

Certain parameters cannot be correctly scaled in a model which has been derived from a mechanical system by simple linear scaling. The acceleration due to gravity does not change between the model and full scales. It is also necessary to use substitutes for some of the full scale materials or components. For example the usual coolant used in fast reactors is liquid sodium. However in model experiments to investigate the mechanical safety of fast reactors to internal explosion using chemical explosive charges water is often used to represent the sodium, as safety problems are difficult to solve if hot liquid sodium is used as coolant in the model. The safe introduction of a temperature sensitive explosive charge into hot sodium in the model reactor would require a major modification of the structure round the charge, thus impairing the dynamic similarity between the model and the full scale system.

Experiments on single tank reactor systems (3,4) have shown that only a few percent of the energy released in an explosion in the core

is available to damage the major containment structures such as the main sodium tank and the vault roof. The energy absorbed from the shock wave by the breeder, the core support structure and the reflector has an important effect on the strength of the shock reaching the outer containment structures. Thus to preserve similarity between the model and the full scale structure the parts of the model that will be deformed by the explosion should be made of a steel having a (stress, strain) curve similar to that of the full scale structure at its operating temperature. Suitable dynamic (stress, strain) curves for stainless steels at elevated temperatures are not currently available and the best match that can be obtained at present is to equate the statically measured yield stress, ultimate tensile stress and the permanent elongation after failure. Due to the substitution of cold water for the hot sodium coolant, the model will now be at about 20°C instead of 400°C. If the model reactor were made of stainless steel, then it would be much stronger at room temperature and have a greater elongation at the maximum stress; this is shown in Table 2. The properties, in the temperature range 300 to 500°C, of a commonly used stainless steel, EN58B, are similar to those of the mild steel EN2 at 20°C, and this mild steel was used to make the model of PFR design shown in my other paper (5).

Thus the problem is to compare the dynamic properties of the stainless steel at elevated temperatures, say 250°C and 450°C, at the full scale rate of straining with the properties of the mild steel being used to make the models when it is strained at the model rate of strain. The ratio of the model rate of strain to the full scale rate is equal to the scale factor. (Table 1).

2. Experiments with Small Specimens

A high rate of strain specimen testing device similar to the type described by Austin & Steidel (6), based on an original design by Shepler (7), was available (Figure 1). This was considered suitable to compare empirically the tensile properties of the two steels at the appropriate rates of strain. In our models most of the main tank, diagrid support structure and the breeder are made of sheet steel 1/16th in thick. This sheet material was used to make the specimens, based on British Standard specification 3A, 4, having a gauge length of one inch. Both EN2 and EN58B certified material was made up; it was found necessary to reinforce the ends of the specimens to prevent slipping and deformation at the clamping bolt hole. Four square metal

plates, the same size as the square ends of the specimens, were spot welded, one on each side of the gripping ends of the specimen. The spot welds were arranged so that the test section was not reached by the heated zones near the welds.

The straining system was originally activated by exploding a charge of black powder in the explosion chamber. However black powder is dangerous to handle and the pressure developed in the chamber depends on the confinement i.e., the properties of the specimen being tested, and was considered an unsatisfactory explosive material for these tests. This was replaced by an electric detonator equivalent to 1.1g of PETN. To attenuate the direct shock from the explosion the chamber was lined with a thin layer of polythene and the remaining free space packed with expanded mica granules. The velocity of the piston was reduced when testing the stainless steel specimens by using a smaller detonator and increasing its mass.

In our 1/16th scale model PFR experiments (5) the time required to rupture the breeder and reflector structure was in the range 0.5 to 1 ms. In the tensile test apparatus the time required to break the specimen was measured and adjusted to give times of just under 1 ms. Under these conditions most specimens break near the middle of the gauge length.

A small furnace was designed to fit round the stainless steel specimens and heat them uniformly. The temperature was maintained with a thermocouple throughout the experiment.

A number of parameters were measured in each experiment: two recessed pressure gauges (type MQ20) measured the loading pressure in the explosion chamber; accelerometers measured the acceleration of both the piston and the base; a capacitance displacement transducer measured piston movement and strain gauge load cells measured the forces acting on each end of the specimen. The device was supported on a massive steel and concrete base so that the piston moved vertically upwards. The transducer signals were recorded on a DC to 250 kc/s response tape recording system for analysis on playback into an analogue computer.

If M_P is the mass of the piston, M_F the mass of the frame, x_1 the vertical displacement of the piston end of the specimen and x_2 the displacement of the frame end of the specimen, both measured from an arbitrary fixed zero, then $M_P \ddot{x}_1 + F_1(t) + M_P g = A_P P(t)$ .....(2,1)

and $M_F \ddot{x}_2 - F_2(t) + M_F g = -A_B \bar{P}(t)$ .....(2,2)

where P(t) is the mean measured pressure in the explosion chamber, A_P is the piston area and A_B is the base area on which this pressure acts; $F_1(t)$ and $F_2(t)$ are the forces measured at top and bottom ends of the specimen. In our experiments since the specimen is short and the piston velocity low, the number of reflexions of stress pulses in the piston will be large and the mean force $\bar{F}(t)$ can be used in equations (2,1) and (2,2). Since $(x_1 - x_2)$ is also measured directly it should be possible to derive two versions of the specimen (load, deflexion) curve from the measured data, one from the direct measurements and the other by solution of the above equations (2,1) and (2,2) using an analogue computer.

The experiments with this equipment have just begun; satisfactory measurements are being obtained, though no analysis of the data has yet been carried out.

A series of static tests on EN2 and EN58B in this specimen size are also being carried out for comparison with the dynamic results.

References

1. N.S. Thumpston, "Model Techniques in Reactor Safety Studies" OECD Committee on Reactor Safety Technology. Meeting of Specialists on Shock-Structure Interactions in a Reactor. Ispra, June 27th - 29th 1966.

2. R.H. Cole, "Underwater Explosives" Princeton University Press.

3. N.J.M. Rees, "A Model Investigation of Explosion Containment in Single Tank Fast Reactors". Conference on Safety, Fuels and Core Design in Large Fast Reactors. Argonne National Laboratory, October 1965.

4. D.E.J. Samuels, "Design Factors Influencing the Containment of Internal Explosions in Fast Reactors". Conference on Safety, Fuels and Core Design in Large Fast Reactors. Argonne National Laboratory, October 1965.

5. N.J.M. Rees, "The Calculation of the Response of Model and Full Scale Reactor Structures to Dynamic Loading". OECD Committee on Reactor Safety Technology. Meeting of Specialists on Shock-Structure Interactions in a Reactor. Ispra, June 27th - 29th 1966.

6. A.L. Austin and R.F. Steidel, "The Tensile Properties of some Engineering materials at High Rates of Strain". American Society Testing Materials Vol. 59 pp 1292-1308.

7. P.R. Shepler, "Explosive Impact Tests". Journal of Experimental Stress Analysis.

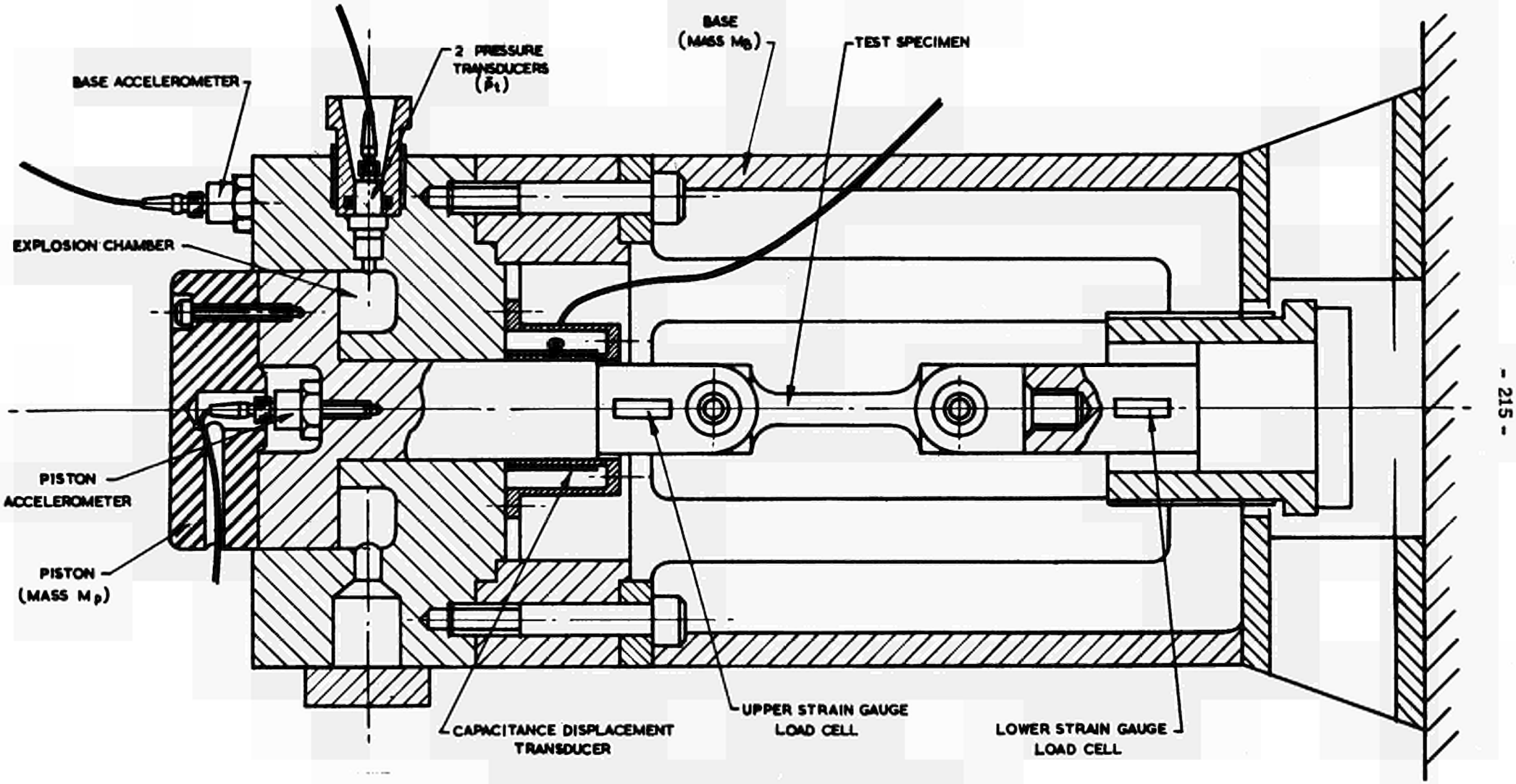

FIGURE 1. CROSS-SECTION OF RAPID STRAINING DEVICE

TABLE 1

PARAMETERS ON FULL SCALE AND ON A MODEL SCALE OF $\frac{1}{S}$

Physical Quantity	Dimensions	Full Scale Value	Model Scale Value
Charge Mass and other Masses	M	Z	Z/S^2
Shock Wave Pressures	$ML^{-1}T^{-2}$	P	P
Length, e.g., Distance from Charge	L	R	R/S
Time, e.g., Duration of Shock Pressure	T	t	t/S
Area	L^2	A	A/S^2
Impulse Per Unit Area	$ML^{-1}T^{-1}$	I	I/S
Force	MLT^{-2}	F	F/S^2
Velocity	LT^{-1}	V	V
Acceleration (Except Gravity)	LT^{-2}	a	aS
Stress	$ML^{-1}T^{-2}$	σ	σ
Strain		ξ	ξ
Rate of Strain	T^{-1}	$\dot{\xi}$	$\dot{\xi}S$
Energy	ML^2T^{-2}	E	E/S^2

TABLE 2

PUBLISHED PROPERTIES OF STAINLESS STEEL TYPE EN58B AND MILD STEEL EN2

Steel	Temperature ^oC	0.5% Proof Stress, tsi	Maximum Stress, tsi	Elongation, %
Stainless Steel EN58B	20	16.7	42.6	53.4
	100	13.7	34.0	48.8
	200	13.0	30.7	40.7
	300	12.2	30.0	38.4
	400	12.4	30.2	40.7
	500	11.2	27.9	38.3
Mild Steel EN2	20	13.2	20.1	36

EFFECT OF STRAIN RATE ON FRACTURE STRENGTH OF CONVENTIONAL STRUCTURAL STEELS

by

W.S. Pellini
Office of Naval Research
US Naval Research Laboratory
Washington, D.C., United States

The most desirable attribute for a structure that is expected to withstand fast loading (in the sense of the application of forces exceeding usual design limits) is the ability to withstand plastic deformation coupled with an inherent resistance to the initiation and propagation of fracture. In broad terms, the specific level of elastic or plastic strain that may result in the development of fracture is a crucial factor in determining the response of the structure to fast loading. This factor must be analyzed in terms of the inherent response of structural material to conditions that induce the initiation of fracture. Accordingly, the starting point for any analysis of structural response to a spectrum of loading conditions is the fracture toughness of the metal.

As a first approximation in analyses of structural strength, one of two assumptions must be made: (1) that the material is free of crack-like defects or that (2) it contains such defects. It is well known that steels which can propagate brittle fractures will deform extensively in the absence of crack defects, at either low or high rates of loading. Explosion bulge tests have provided extensive proof of this fact. Realistic analyses of the effects of dynamic loading must include the assumption that defects may be present, if limiting conditions are to be considered. Otherwise, the analyses will be optimistic to a degree that may be seriously misleading.

Extensive studies of the ductility of conventional mild steels in the presence of notches or cracks have demonstrated that dynamic loading may decrease resistance to fracture initiation to low levels, under certain conditions. In fact, these studies have concentrated on the question of the specific conditions that either provide or preclude marked decreases in notch ductility due to dynamic loading. For steels having transition temperature features the most important factor is the temperature of loading relative to

the transition temperature range.

As a starting point of such analyses it is most instructive to consider the effect of temperature on the fracture propagation of the steel. This provides an assessment of the size of the plastic zones at crack tips (fracture toughness) under the most rapid (limiting) conditions of loading rate. The plastic zone size is the factor which determines the energy absorbed in the fracture process for initiation or for propagation. Rapid loading cannot reduce the size of the plastic zone in initiation for the base material to below that which is developed under conditions of dynamic propagation of the fracture. Dynamic fracture propagation studies have shown that a critical temperature exists above which a rapid increase in plastic zone size (fracture toughness) is developed.

Above this critical temperature, plane strain stress conditions at crack tips are relaxed through the thickness and plane stress fracture (shear lips) become manifest at the fracture surfaces. With increasing temperature the nature of the fracture reverts entirely to plane stress (45° shear) and the effects of dynamic loading on fracture initiation are eliminated. Below the critical temperature, fractures are of plane strain type (90° flat fractures) and the plastic zone size is relatively small. In the temperature region of plane strain fracture, rate of loading has a major influence in reducing the size of the plastic zone at the point of instability (fracture initiation). This has the effect of reducing the level of applied nominal stress required to initiate fracture for a specific size of flaw.

The described critical temperature may be deduced as the NDT (Nil Ductility Temperature); the temperature of first development of surface shear lips; or the temperature of first rise of the Robertson Crack Arrest Temperature curve (CAT). All of these definitions are exactly equivalent and relate to a narrow range of temperatures, which from an engineering point of view may be considered a specific temperature. The concept of NDT + 60°F may thus be reconciled with the fracture mechanics definition of a temperature corresponding to the development of large plastic zones at crack tips and therefore high fracture toughness. The effects of dynamic loading are minimized in the presence of large size plastic zones at crack borders.

Conversely, temperatures below the NDT temperature relate to small plastic zones and to high sensitivity to dynamic loading. Dramatic illustrations of this effect have been made in studies conducted in USA and in various European laboratories. Typical examples are represented by bend tests of fatigue-cracked bars at temperatures slightly below the NDT temperature. By slow loading, the bars show relatively large crack opening displacements and plastic loading is required for fracture initiation. By impact loading the crack opening displacements are reduced to very small values and the general level of fracture load may decrease to below the yield point. The level of dynamic deformation load required to initiate fracture increases rapidly with increase in temperature above the NDT.

The NDT temperature represents a critical point above which the effects of dynamic loading are rapidly suppressed due to a change in the basic mode of microfracture of the steel. This represents a change of the fracture from pure cleavage to mixed fracture, partly cleavage and partly ductile ruptures of the individual grains.

Formal methods of fracture mechanics based on determining fracture strength of flawed structures on a basis of laboratory tests conducted at slow rates are not directly applicable to the case of dynamic loading of structures. It is essential that such tests include rapidly applied loading, and specific conditions of metallurgical damage at the crack tips which are pertinent to the condition in the structure. The virtue of ensuring the use of metal of fracture toughness level that prevents the use of fracture mechanics is that variables of "low stress fracture" are eliminated in large degree.

It is not recognized generally that dynamic loading effects in fracture initiation (for tangible steels) may result from three separate sources which are equivalent insofar as the fracture process is concerned:

(1) Dynamic application of the full load.

(2) Super-imposition of small transient dynamic loads which are added to the static loads.

(3) Local cracking of small embrittled regions which result in dynamic propagation of the fracture to the base material which is loaded statically.

All three conditions effectively subject the plastic zone at crack tips to dynamic conditions and fracture toughness then is controlled by the "dynamic case." For example, it becomes possible to initiate fractures at levels of nominal stress considerably below those which would not cause fracture in a slowly loaded proof test. The virtue of ensuring that transition temperature steels are used at temperatures above the NDT derives from the elimination of "low stress fracture" induced by any of the three processes described above.

Obviously, there is a relationship of flaw-size and stress to be considered in addition to purely dynamic effects. The larger the flaw and the higher the stress, the higher the requirement for fracture toughness, i.e., the higher the temperature above the NDT point that is required. The NDT + 60°F criterion for pressure vessels normally provides protection against fracture initiation for loading conditions that do not result in gross plastic overload of regions containing flaws of less than 2 to 3 times the wall thickness. If gross (high level) plastic loading is considered as a design requirement covering cases of extreme overload, it is necessary to ensure that the material is utilized in its fully ductile state. Such a requirement forces consideration of metal of properties such that fractures are restricted to ductile 45° shear tearing of high energy absorption characteristics.

These factors emphasize that structural safety must be analysed in terms of both the level of assumed loading and of the characteristic fracture toughness of the steel.

EXPERIMENTS AND ANALYSIS ON THE PERFORMANCE OF CRUSHABLE BLAST SHIELDS

by

T.A. Zaker and P. Lieberman
IIT Research Institute,
Chicago, United States

This work was supported by the U.S. Atomic Energy Commission under Contract No. AT(11-1)-578 with IIT Research Institute, Chicago, Illinois, USA.

I. INTRODUCTION

The construction of nuclear power plants presents a number of problems to the design engineer. Among these is the need for adequate safeguards against a violent malfunction of the reactor system. It is necessary to provide for the absolute containment of gaseous products and radioactive debris which may result from such an incident, in order to prevent any hazard to nearby populated areas. For this reason, the reactor system and primary heat-exchange equipment of a megawatt-range nuclear power plant are commonly enclosed in a leak-tight containment shell, the integrity of which must be maintained under the effects of the maximum credible explosive-like energy release which can be associated with the given system. Theoretical and experimental studies have been conducted to determine the effectiveness of crushable materials as shields or attenuators in the event of a violent release of energy at the reactor core. The specific objective of this work was to develop systematic techniques for observation and analysis of the transmission of disturbances in one-dimensional layered systems of generalized mechanical properties. Analytical techniques are based on the use of quite general piecewise linear stress-volume relations for the uniaxial strain condition, and on stepwise approximations to arbitrary time-varying surface loadings.

Graphical methods for the solution of problems of one-dimensional impact in rate-independent elastic-plastic materials have been advanced by DeJuhasz [1*], by von Karman, Bohnenblust and Hyers [2], and by White and Griffis [3]. In the present work, these methods have been extended to the case of elastic-crushable-compactible material behavior, and the procedures have been adapted for machine calculation. With very general material behavior exhibiting strong property changes and the phenomenon of irreversible straining, quite complicated stress and velocity fields develop in the position-time space of independent variables, thus necessitating the use of high-speed computing equipment for the numerical solution of these pro-

* Superscript numerals designate references listed at end of paper.

blems. In this paper we present the methods by which various wave interactions are analyzed. The computational scheme developed for this work is described.

A considerable experimental effort paralleled the analytical work reported here. A conventional strong shock tube was modified for the performance of gas shock impingement experiments on crushable solid specimens. The purpose of the experiments was to obtain the relevant dynamic stress-volume relations of the materials, and to provide over-all verification of the analysis of wave transmission and attenuation in such materials.

II. EXPERIMENTS TO DETERMINE EQUATIONS OF STATE

An experiment was devised for determining the equation of state of a porous solid under shock loading. A shock-tube facility was designed and constructed to induce and measure stresses and displacements in a porous solid during shock impingement. One porous solid, balsa wood, was extensively tested; redwood, sugar pine, styrofoam, foamglass, and Celotex were studied to a limited extent.

The equation of state of a porous solid is usually represented in the stress-volume plane. Direct measurement of stress and volume during blast loading is not usually attempted; rather, measurement of the wavefront velocity and particle velocity is sought. Direct measurement would require the development of new instrumentation and instrumentation techniques, and the accuracy of resultant data would be influenced only by the measurement error. The indirect approach permits the use of standard instrumentation and controlled accuracy, and the accuracy of the resulting data is influenced by the measurement error amplified by the data reduction process. Both approaches were evaluated considering the available blast load amplitudes and the complications introduced by the multiple reflections of the plastic wave and dispersive wave train behind the elastic precursor.

The determination of the shock compression (Hugoniot) equation of state required more than twelve channels of oscilloscope data display and approximately nine piezoelec-

tric pressure sensors. Determination of the isentropic unloading paths of media in the stress-volume plane, from several Hugoniot states, required different arrangements of the test specimen in the holder. The shock compression and isentropic unloading data can be used to predict the attenuation of a blast wave propagating through a crushable material. The test arrangement can be used for the determination of the equation of state of various porous solids and the calculation of stress wave motion in a layered material composed of porous solids.

A. Apparatus

The shock tube was selected as a blast generator device because it can impart impact loads of controlled amplitude and duration, and utilizes instrumentation which can record data in both the impinging gases and in the impacted solid. A shock tube of circular cross section, having a 2-in. inside diameter and a 1-in. wall thickness, was used in this work. This tube was constructed with lengths of cold-rolled steel, cold-pierced, with a corrosion-resistant interior finish of hard chrome plating 0.002 in. thick (Figs. 1 and 2).

To establish large and easily observed constant-state regions in the test specimen, the applied load should be an impulse of long time duration and constant pressure amplitude. The lengths of the shock tube driver section, driven section, and test specimen, and the magnitudes of the initial pressures, were selected in such a manner as to establish a range of desired wave motion patterns in the test specimen. The lengths of the shock tube driver and driven sections were each selected to be 12 ft to produce at least 4 msec of constant-pressure duration. Various helium driver pressures were used in combination with normal atmospheric driven chamber pressure in air. Helium driver gas and air driven gas in the shock tube permitted the use of reasonable driver pressures to attain up to 2400 psi blast impingement pressures.

Accurate control of the applied load is readily achieved. Elementary shock tube theory shows that large variations in the driven gas pressure result in rather small variations in incident shock wave strength.

B. Instrumentation

A specimen holder was designed to accommodate up to 42 in. of test specimen. Access ports were incorporated in the holder walls for side-mounted piezoelectric crystals, end-mounted crystals, and internally-mounted wave arrival sensors. Crystal sensor stations at 6-in. intervals permitted various combinations of specimen lengths and sensor locations to best distribute the data points for determining a wavefront network (Fig. 3).

To determine strain-rate and friction effects, an additional array of seven crystal sensors was placed at 1-in. intervals from the upstream end of the holder. To determine unloading wave data, the axis of the holder was turned 180 degrees so that the additional array of seven sensors then occupied the position nearest the end plate.

Although typical loadings were between 20 and 2000 psi for 5 msec, compaction of the specimen against the rigid downstream end surface produced loadings as high as 150,000 psi for a few microseconds.

Wave motion in the impingement gas adjacent to the upstream end surface of the test specimen, in the test specimen, and at the downstream end surface of the test specimen was measured to obtain the complete equation of state of the material in shock compression.

The measurements in the gas were obtained by the use of quartz crystal sensors at two stations upstream of, and close to, the test specimen. The first sensor measured the flat-topped waveform of the reflected wave. The primary result of these data was the amplitude of the applied pressure. Additional quantitative results were obtained from these data concerning subsequent waves which were sufficiently strong to be transmitted from the solid back into the gas.

Measurements in the solid were obtained using nine quartz crystal sensors at axial positions on the lateral surface of the test specimen. The sensor mounted in the stationary test specimen holder and the moving lateral surface of the crushing test specimen were coupled with vacuum grease. This mechanical arrangement resulted in a pressure-time history near the loaded end which first showed the radial component of the elastic stress precursor, then the radial component of stress in the shock state, and finally the still higher amplitude gas pressure when the test specimen end surface moved beyond the gage station.

A typical data record for a sensor close to the downstream end surface shows the arrival time of the elastic precursor, the plastic wave, and the subsequent plastic wave reverberations between the upstream and downstream end surfaces. The elastic and plastic wavefronts are readily detected as before, but the free surface never arrives at the downstream stations. Rather, the passage of the plastic wavefront is followed by reverberations of the plastic wavefront between the constant applied-pressure upstream surface and the zero-particle-velocity downstream surface.

C. Results

The primary result of this study is the development of a blast wave generating facility, instrumentation, and experimental technique to determine the dynamic equation of state of porous solids under shock compression and unloading. A second important result is the development of an analytical procedure for using data obtained from the shock-tube blast facility to construct the equation of state of any porous solid.

1. Shock Compression

The slope of the Hugoniot in the elastic range was obtainable from the experimentally determined velocities of the elastic wave. These elastic wave speeds were derived from time-of-arrival measurements of the elastic precursor. However, the elastic limit was not known. It was assumed that

this point was equal to the static crushing pressure, and this assumed value was used to calculate the plastic wave velocities associated with the higher pressures. The calculated plastic wave velocities were in agreement with the experimentally determined plastic wave speeds obtained from time-of-arrival measurements. This verified that the assumed values were correct.

The upper portion of the strain-hardening regime and the compaction regime were obtained in the dynamic tests. The static and dynamic stress-volume relations were found to be nearly coincident within the limits of reproducibility of the material behavior.

2. Unloading from Shock Compressed States

In the strain-hardening region, static tests showed hysteresis loops for the unloading and reloading paths in the stress-volume plane. These loops became narrower with increased pressure of the shock-compressed state. At each Hugoniot state in the strain-hardening region close to the elastic region, the dynamic tests showed that the dynamic unloading path was tangent to the static unloading path. At each Hugoniot state in the strain-hardening region close to the compaction region, the dynamic unloading path was less steep than the tangent to the static unloading path. The dynamic unloading path was tangent to the Hugoniot curve in the compaction region. For impact loads at extremely high pressures, the slope of the unloading isentrope is less than the slope of the Hugoniot in the upper portion of the compaction region.

3. Typical Results for Celotex

A typical pressure-time record obtained from a piezoelectric transducer mounted in the tube wall in contact with the lateral surface of a Celotex specimen is shown in Fig. 4. The record is displayed at different sensitivities and sweep speeds on the two channels of a dual-beam oscilloscope. Arrival times of waves and of the gas-solid interface are identifiable on the record, and are used together with data

from other stations to construct a wavefront network in position-time space (Fig. 5). Correspondingly lettered points identify the events observed on the pressure record.

Repeated shock impingement of the same test specimen in succeeding dynamic experiments similarly yielded wavefront networks for compressed initial states (Figs. 6 and 7). In each case, the direct observations of impinging gas pressure and axial stress at the fixed end of the specimen provided additional data for consistency checks on the stresses deduced from the observed wave and interface velocities.

Typical dynamic results are shown in stress-velocity coordinates in Fig. 8. The data points lie somewhat above the curve computed from the results of a static compression test, which is shown as the solid line.

Hugoniot and unloading curves in stress-specific volume coordinates are calculated from the wave and particle velocity data by application of jump conditions for mass and momentum conservation across the observed waves. The data for Celotex resulting from experiments on two specimens at different pressure levels, together with repeated dynamic recompressions of the same specimens, are shown in Fig. 9. For comparison, a portion of a static compression curve for the same material is shown as the dashed line.

III. ANALYSIS OF WAVE PROPAGATION IN CRUSHABLE SOLIDS

The solution of a one-dimensional impact problem can be accomplished by a single method regardless of whether the material behaves as an elastic, plastic, or compactible substance. By assuming that all types of impacts generate constant-state regions within the impacted material, we are able to connect the properties in each region by a set of algebraic equations. The extent of each region can be represented in the wave diagram or physical plane, while the properties of each region can be presented in the stress-volume and stress-particle velocity diagrams of the dependent-variable (state) planes.

A. Equations

When a force is suddenly applied to a deformable body, it does not immediately assume the state of stress and motion predicted by elementary rigid-body mechanics. Actually, when the force is applied, discontinuities of stress and strain propagate through the body from the point of impact. When these disturbances reach the boundaries of the body, they are partially transmitted to the surroundings and partially reflected back into the body. This process of multiple reverberation and interaction continues until the mechanical state predicted by elementary mechanics is approached in a gradual and, in general, discontinuous fashion. In small bodies subjected to long-duration loads, the process is completed so rapidly that analysis of the transient phase of the motion is usually of little interest. In bodies with dimensions such that the time of traverse of a wave across a typical dimension of the body is of the order of the characteristic time of loading or larger, however, the transient nature of the process cannot be ignored.

The assumption of stress or strain wavefronts propagating through a body and interacting with boundaries and with other waves requires the use of suitable jump conditions in the calculations which connect properties on either side of each discontinuity through the requirements of mass and momentum conservation:

$$\rho_0(W_{10}-U_0) = \rho_1(W_{10}-U_1) \qquad \text{continuity}$$

$$\sigma_0 + \rho_0(W_{10}-U_0)^2 = \sigma_1 + \rho_1(W_{10}-U_1)^2 \qquad \text{momentum} \qquad (1)$$

where

W_{10} = wavefront velocity in laboratory-fixed (Eulerian) coordinates

U = particle velocity

σ = longitudinal normal stress component

These equations can be rearranged in a form such that the stress-volume relation in uniaxial strain obtained from dynamic tests can be used to calculate the particle veloci-

ties and shock velocities induced by impact:

$$U_1 - U_0 = \pm \sqrt{(\sigma_1 - \sigma_0)\left(\frac{1}{\rho_0} - \frac{1}{\rho_1}\right)}$$

$$W_{10} - U_0 = \pm \frac{1}{\rho_0} \sqrt{\frac{\sigma_1 - \sigma_0}{\frac{1}{\rho_0} - \frac{1}{\rho_1}}} \qquad (2)$$

The positive sign applies to waves which propagate in the positive direction relative to the material particles; the negative sign applies for the negative direction relative to material particles.

B. Representation of Solutions to Impact Problems

The physical plane shows the time and spatial distribution of the constant-state regions within an impacted solid. The state planes show the value of each mechanical property associated with each constant state region. The stress particle-velocity state plane specifies the value of two dynamical properties of each state. In some cases constant-state regions may have the same dynamic properties but different specific volume values so that it is also necessary to include the stress/specific-volume state plane to specify the specific volume value or values associated with each dynamical state.

1. Wave Diagram

One-dimensional unsteady motion of a continuous medium is conveniently represented in the position-time space as independent variables, referred to as a wave diagram. Either the current position x, relative to laboratory-fixed coordinates, or the initial particle position ξ may be regarded as the independent position coordinate. (The former is the Eulerian representation and the latter the Lagrangian representation of the motion.) Regions of constant stress and particle velocity, which develop after impact in a column of material at various times t and positions x or ξ, may be depicted in such wave diagrams. Discontinuity lines which separate these constant-state regions have inverse slopes given by the appropriate wave speeds in the frame of reference used.

2. State Planes

It is evident that the wave propagation characteristics of any particular material depend directly on the form of the stress-density relations in loading and unloading. Materials impacted at stresses below their dynamic yield point, in their crushing or strain-hardening region, or in their compacting region, will develop acoustic waves, dispersive compression waves, and plastic or shock waves, respectively. After a material has been compressed to a particular state, unloading can take place either through a single discontinuity or through a series of unloading wavelets, depending upon the equation of state of the material in unloading. Finally, different equations of state govern unloadings, depending upon the maximum stress experienced by a particle in its past history.

The stress-velocity plane is a convenient state plane, because boundary conditions are usually specified in terms of these parameters. Changes in the state properties in the interior of an impacted material as a result of the interaction of wavefronts can be obtained from constructions in the σ-U plane with reference to the σ-v plane, by use of the finite-difference relations

$$\Delta\sigma \pm m \Delta u = 0 \qquad (3)$$

which hold respectively on the characteristic lines

$$\Delta\xi = \pm m v_o \Delta t \qquad (4)$$

where $m = (-\Delta\sigma/\Delta v)^{1/2}$ and $v = 1/\rho$ = specific volume. In the calculation method, the stress/specific-volume relations are approximated by straight-line segments.

C. Illustrative Wave Interaction

The calculation procedure for determining the stress in the constant-state region formed by the interaction of two waves is as follows:

estimate the stress level of the newly formed constant state region,

refer to the stress-strain relation to obtain the number of wavelets transmitted to the left and to the right, relative to particles,

calculate the particle velocity associated with each state

check the original estimate of the stress level of the newly formed region by comparing the extent of matching between the sum of particle velocity jumps in the clockwise direction and those in the counter-clockwise direction.

If there is a mismatch of the particle velocity when summing in the two different directions, starting from the initial state and ending in the newly formed state, the assumed stress level must be revised, the number of wavelets considered in the interaction revised, and again the particle velocity match must be checked for the newly formed region.

Figure 10 can be used as an illustration. Assume that the properties in states 5, 6 and 7 are already known, and it is required to determine the result of interaction of the two right-running waves 7-6 and 6-5. As an initial trial, say that there is only one right-running and one left-running wave generated, i.e. 8-5 and 8-7.

Jump Conditions

$$W_{8',5} = + v_o \sqrt{\frac{\sigma_{8'} - \sigma_5}{v_7 - v_{8'}}} \qquad U_{8'} = + \sqrt{(\sigma_{8'} - \sigma_5)(v_5 - v_{8'})}$$

$$W_{87} = - v_o \sqrt{\frac{\sigma_8 - \sigma_7}{v_7 - v_8}} \qquad U_8 = - \sqrt{(\sigma_8 - \sigma_7)(v_7 - v_8)} \tag{5}$$

Contact Surface Assumptions

$$\sigma_{8'} = \sigma_8 \quad \text{and} \quad U_{8'} = U_8 \tag{6}$$

Equations of State

$$\sigma_8 = \sigma_8 \ (\sigma^*, v_8) \qquad \sigma_{8'} = \sigma_{8'} \ (\sigma^*, v_{8'}) \tag{7}$$

where σ^* is the peak compressive stress to which the material has previously been subjected. The positive sign is used with each radical associated with the right-running wave.

The solution is accomplished by making an initial estimate of σ_8 on the basis of an acoustic approximation. The resulting values of U_8 and $U_{8'}$ are then compared. A new estimate of σ_8 is made which is higher or lower than the initial estimate according to whether the stress-strain diagram is concave upward or downward in the range of stress under consideration. Thereafter, improved values of σ_8 are determined so as to bring the values of particle velocity in states 8 and 8' into coincidence in a converging iterative fashion.

To test the physical admissibility of the solution, it is first necessary to check if the chord connecting the states (σ_5, v_5) and (σ_8, $v_{8'}$) (indicated by dotted line) lies on or above the σ-v relation in that interval, so that the assumption of a single right-running wave is not contradicted. A similar condition must hold for the left-running wave.

In loading up from region 0 to 6 a fan exists from 0 to 5 but the next vertex (not labeled) above 5 is omitted from the fan, so that only a single wave exists from 5 to 6. The fan exists from 0 to 5 because each increase in stress level is associated with a decreased slope on the σ-v curve and therefore has a decreased wave speed. However, above region 5 the fan ceases in favor of a single jump to point 6, i.e., the unlabeled vertex produces no wave. The need for this becomes evident if one attempts to impose a fan from 5 to 6. The intermediate wave between 5 and 6 has no effect since it has both lower stress and slower velocity than the single wave from 5 to 6. This is a result of the σ-v curve being concave-up between 5 and 6. A single wave rather than a fan will occur for any rise in stress above region 5 which has the chord above the curve. For points in Figure 10 which are located to the right of the point where W_{76} reaches W_{65}, the rise of stress above that of region 5 will be to a level of region 8'. The single wave causing a jump from 5 to 8' occurs instead of a two-wave fan involving the intermediate vertex. Again this is clear by first supposing that the fan occurs and then showing that this supposition leads to a contradiction. Since the higher-stress-level wave moves faster than

the lower-stress-level wave, the fan collapses into a single wave.

The stress-volume relations for any given material in uniaxial strain may be quite complicated. In a crushable-compactible solid, for example, the current mechanical state of the material is in general a function of its prior deformation history. If temperature changes induced in compressions from the initial state are negligible, it is reasonable to assume that a unique stress-volume relation governs compressions from the initial state. However, when a portion of the material is subjected to a given peak compressive stress σ^* in the crushing range and is subsequently unloaded, the stress-volume relations governing the unloading and possible later recompressions will depend on the value σ^*, the peak compressive stress to which the material has been subjected. This hysteresis phenomenon has a pronounced effect on the results when unloading waves overtake crushing waves or shocks.

In the present illustration, unloading takes place from state 6 to state 7 at zero stress as the unloading wave progresses into the material. When the unloading wave overtakes the shock, the latter is weakened (state 8'), but the adjacent material formerly compressed to state 6 and unloaded, is recompressed to state 8. Dynamical equilibrium considerations require that there be simultaneous equality of stress and particle velocity across the interface between 8 and 8', but a possible discontinuity of strain. Such a discontinuity, once formed, travels with the local particle velocity, and is referred to as a residual strain or density discontinuity. These discontinuities are exactly analogous to entropy discontinuities which develop in one-dimensional, particle-isentropic unsteady flow of gases when strong shocks are present. Such entropy discontinuities are referred to as contact surfaces in unsteady gas dynamics.

On the Lagrangian wave diagram, the wave velocities determine the slopes of the wave lines. However, residual strain discontinuities, which travel at the local particle velocity, appear as vertical lines on such a diagram. The Lagrangian wave diagram is a convenient plot because it represents the motion of waves relative to material particles. The calculation of wave speed in Lagrangian coordinates is somewhat simpler than in laboratory-fixed coordinates since they do not involve the local particle velocities. Further simplification occurs in the representation of residual strain discontinuities, which appear as vertical lines. Each region between two such discontinuities is associated with a particular peak stress σ^* experienced in prior motion. Each such value σ^*, in turn, defines the unloading curve in the σ-v plane which is associated with a particular zone between strain discontinuities.

In a more general case, it would be possible to generate multiple right-running and left-running wavelets after the interaction of two single waves. The only variation introduced into the solution technique is the determination of intermediate values of σ for each wavelet until the interior points of chords connecting the individual states on the σ-v plane lie on or above the σ-v relations.

D. Programmed Solutions of the Impact Problem [4]

Impingement of a blast wave on a layered specimen, in which each layer is composed of a material with a complicated equation of state, can induce a multiple wave system which is further complicated in internal reflections and external boundary reflections. For certain combinations of stress levels and waveforms, the stress wavefronts can become still more numerous, because residual strain discontinuities generated by stress wave interactions provide additional interfaces for subsequent interaction and perform the same type of calculation.

The solution of each wave interaction problem appears complex in its final form; however, the construction of the network is readily obtained by considering the individual in-

teractions. A general procedure can be followed which takes into account all possible complexities of any type of interaction, and it is this general procedure which is programmed for machine computation.

1. Boundary Conditions

In impact problems, boundary conditions are usually specified at the impingement surface and at the opposite end surface. The usual specifications are stress or particle velocity as functions of time at the impingement surface, and stress or displacement as functions of time at the opposite end surface.

The boundary conditions at the end surface opposite to the loaded end may be specified by either a stress-time or displacement-time relation. For instance, an unsupported surface would be considered as a free surface with a stress-free condition at all times. A partially constrained end surface may be described by the resistance which it offers to displacement or to changes in particle velocity. A fixed boundary which can support compressive but not tensile stresses may be described by the condition of zero displacement and positive stress, or possible negative displacement and zero stress.

In general, compressive waves are reflected from a fixed boundary as compressive waves, and tensile waves are reflected as tensile waves. Consider an unloading wave moving into an initially compressed region and striking a fixed boundary. If the unloading wave is sufficiently strong, tensile stresses may tend to develop in the material adjacent to the boundary. If the tension can be supported by the bond between the material and the backup surface, the particle velocity at the boundary remains zero, and the negative stress state is propagated into the material as a reflected tension wave. On the other hand, if tensile stress cannot be supported by the material, separation of the material takes place forming a free surface, and the material moves away from the rigid backup surface. This process is known as spallation.

2. Description of Flow Diagram

The flow diagram of the computer program of an impact problem is primarily composed of two types of procedures: (1) decision-making procedures which resolve the number of waves of each characteristic family generated after each interaction, and (2) iterative procedures which are used to match stress and particle velocity after summing property jumps, from clockwise and counter-clockwise directions, around each interaction point in the physical (t-ξ) plane. The flow diagram for the computations is shown in Fig. 11.

As input, one must describe the physical problem by specifying the material equation of state, the length of material, and the boundary conditions at the left-hand and right-hand surfaces. At the left boundary only right-running waves are generated; at the right boundary only left-running waves develop. In the interior, after an interaction, one wave of each family is introduced as an initial estimate.

To determine if more than one wave of each family is generated, it is necessary to assume first that only one wave of each family exists. This permits an estimate of stress, specific volume and particle velocity in the newly formed states between the resultant opposite-facing waves. To check the assumption of single waves, it is then necessary to test whether the chord connecting the σ-v state point of each newly formed region and the initial state point always lies on or above the σ-v curves. When the chord intersects a segment of the σ-v relations, it is hypothesized that an additional intermediate wavelet is generated, of amplitude such that the chords representing property jumps should lie on or above the σ-v curves. After tentative values for properties in states between the waves have been established, the resultant wave system is again tested for physical admissibility. This process is continued until all the wavelets are drawn in for both left- and right-running characteristic families. With the correct number of waves, it is then possible to calculate final values of the properties in the newly formed states between the right- and left-running wavelets. After the appro-

priate degree of accuracy is attained in establishing the properties of the newly formed region and any other intermediate states, the data are read out of the computer.

The output consists of the normal stress, specific volume, particle velocity, wave speeds, and the maximum stress experienced by the material at any time in its past history. This data output refers to a particular zone of the material at time t.

The computer is advanced to the next interaction point in time, and the wave lines and strain discontinuities are extended to their new positions. The occurrence of any interactions or change of conditions at either boundary is determined by the appearance or disappearance of any of the constant-state regions. The cycle then begins again; the number of wavelets of each family is determined and the state properties are calculated. The process continues until the zone between the resulting waves is completely solved for its properties and extent. To carry the solution to long times, weak stress or weak density discontinuities are dropped by means of systematic test routines. If this were not done, calculations would be made for an ever-increasing number of interactions while advancing the solution in time very slowly.

3. Summary of Code Characteristics

The IITRI code is best characterized as an application of the field method of characteristics (in contrast to lattice-point calculations) for one-dimensional compressible flow problems. The numerical analysis is such that small regions of uniform state separated by discontinuity lines make up the variable fields in distance-time space. Thus shock conditions can be applied where appropriate as readily as can isentropic (nondissipative) relations, without the introduction of an artificial viscosity to suppress shocks where they naturally occur.

The program has been prepared in FORTRAN language for use on IBM 7094 equipment. This computer code permits calculation of the pressure, velocity, and position profile in each of the layers of a composite shield for a given loading

at one surface. Machine capacity has been divided in such a fashion that 40 layers of material can be handled, in which each layer is characterized by a set of stress-volume relations involving as many as 27 straight-line segments for unloading from different ranges of peak stress. The pressure-time pulse applied at one surface can be approximated by as many as 75 constant-pressure intervals. The solution can be advanced in time until as many as 1022 constant-state regions have developed.

This machine code is unusual in that it is a purely algebraic code based on piecewise linearization of pressure pulses and equations of state, rather than on numerical integration of the field differential equations. As a consequence, running time is much shorter than that of analogous finite-difference codes. Finally, provisions have been made for inserting criteria for internal spallation by specifying limiting tensile stresses, and continuing the calculations of wave motion in the separated material after spallation occurs.

4. Computational Results for Layered Shields

The stress-time history at a rigid backup surface represents the load transmitted by a crushable protective shield to a relatively stiff structure assumed to be in contact with it. Computations have been carried out to obtain these transmitted loads for a series of layered shields subjected to a constant pressure pulse of 10,000 psi amplitude and 0.1 msec duration.

The results are shown in Figs. 12 and 13 for combinations of redwood and Celotex of the same total thickness (8-in.). The result for a somewhat thicker (10-in.) solid redwood shield is also shown. It is seen that the load amplitude is reduced by as much as a factor of 10. In fact, if the shield loading of 10,000 psi were produced by gas shock impingement, the same shock would produce a still higher reflected pressure at the rigid wall in the absence of the shield.

It may be noted that the transmitted impulse is virtually the same as that applied to the left-hand surface of the shield (1 psi-sec). This is because the shield material is brought nearly to rest at the time the transmitted load terminates. Actually, a small net leftward velocity on the average is calculated for the shield material at this time, representing a weak spallation condition. Therefore the transmitted impulse exceeds slightly that applied to the left-hand surface of the shield. These considerations of momentum conservation serve as an over-all check on the results of the computations.

IV. CONCLUSION

Systematic experimental and analytical methods have been developed for evaluation of the performance of blast attenuators or layered crushable material. The data are useful in optimizing the design of shields to contain the effects of the maximum credible explosive-like energy release which can be associated with a reactor system.

REFERENCES

1. DeJuhasz, K. J., "Graphical Analysis of Impact of Bars Stressed Above the Elastic Range", J. Franklin Inst. 248, 15-48, 113-142 (1949)

2. von Karman, T., H. F. Bohnenblust, and H. D. Hyers, "The Propagation of Plastic Waves in Tension Specimens of Finite Length: Theory and Methods of Integration", NDRC Report No. A-103 (October 1942)

3. White, M. P., and L. Griffis, "The Permanent Strain in a Uniform Bar Due to Longitudinal Impact", NDRC Report No. A-71, OSRD 742 (1942)

4. Lieberman, P., and T. A. Zaker, "Numerical Solution of Wave Propagation Problems in Layered Inelastic Materials", Proceedings, Symposium on the Use of Computers in Civil Engineering, Paper No. 47, Lisbon, Portugal (October 1962)

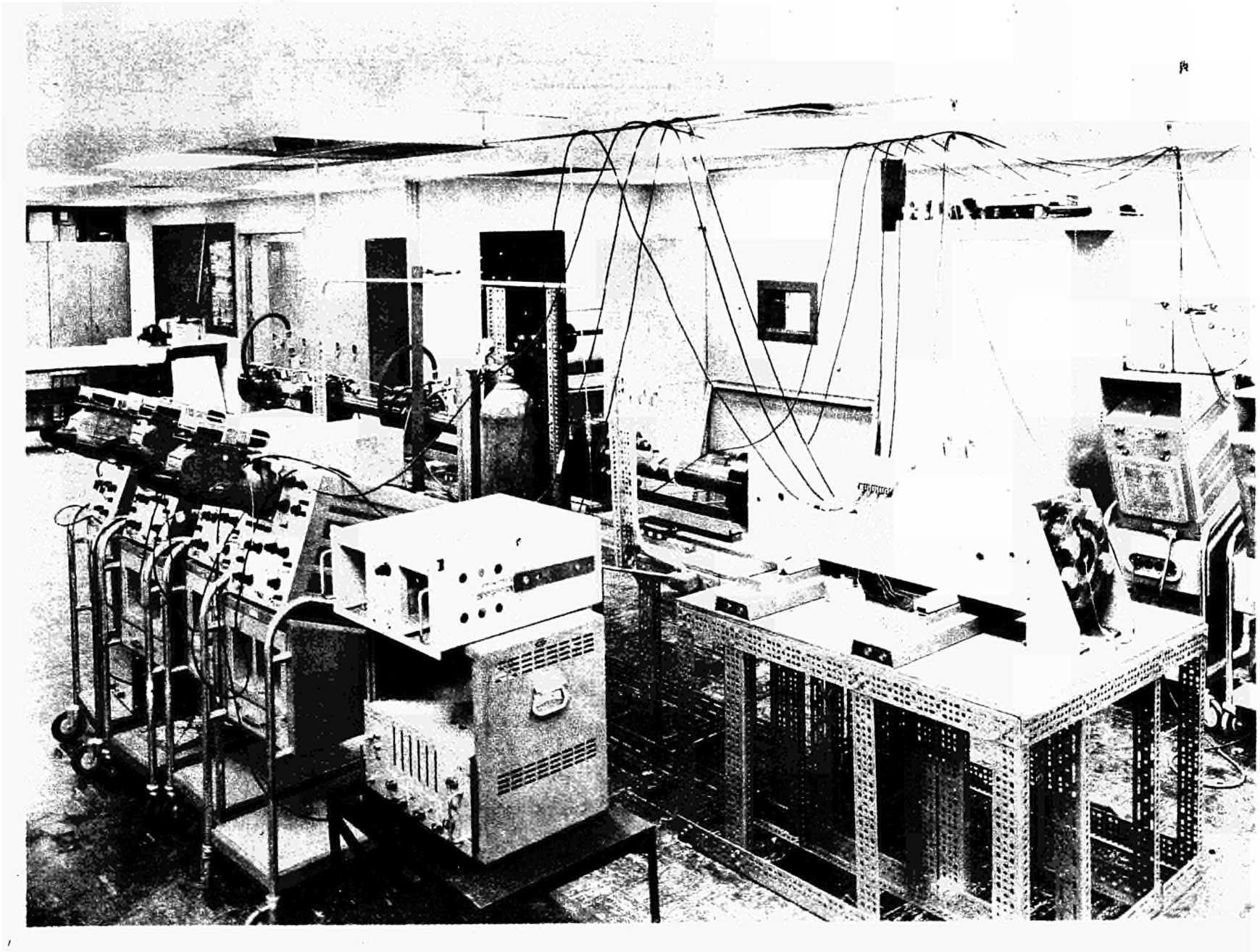

Figure 1 Photograph of Shock Tube Facility

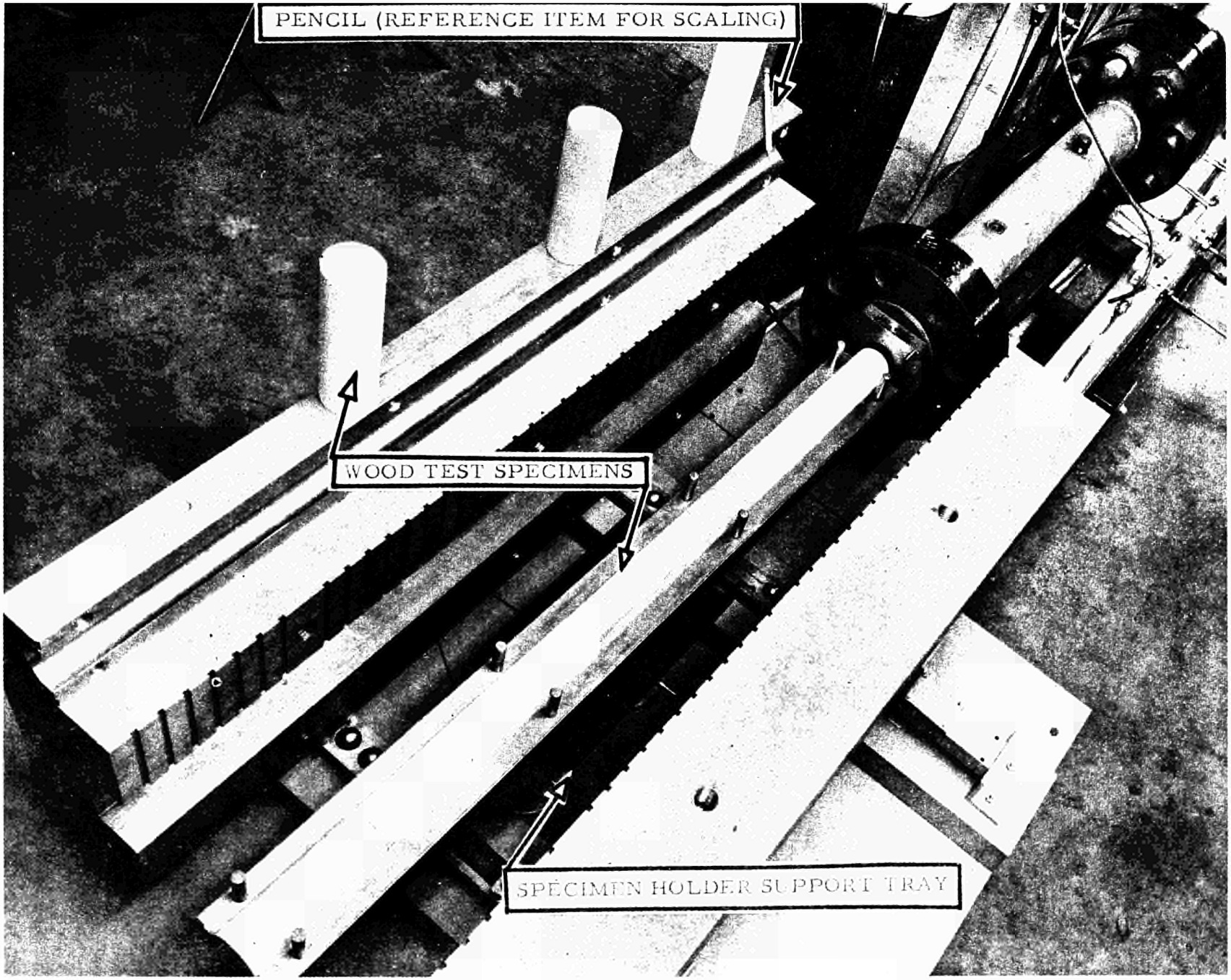

Figure 2 Shock Tube Test Section

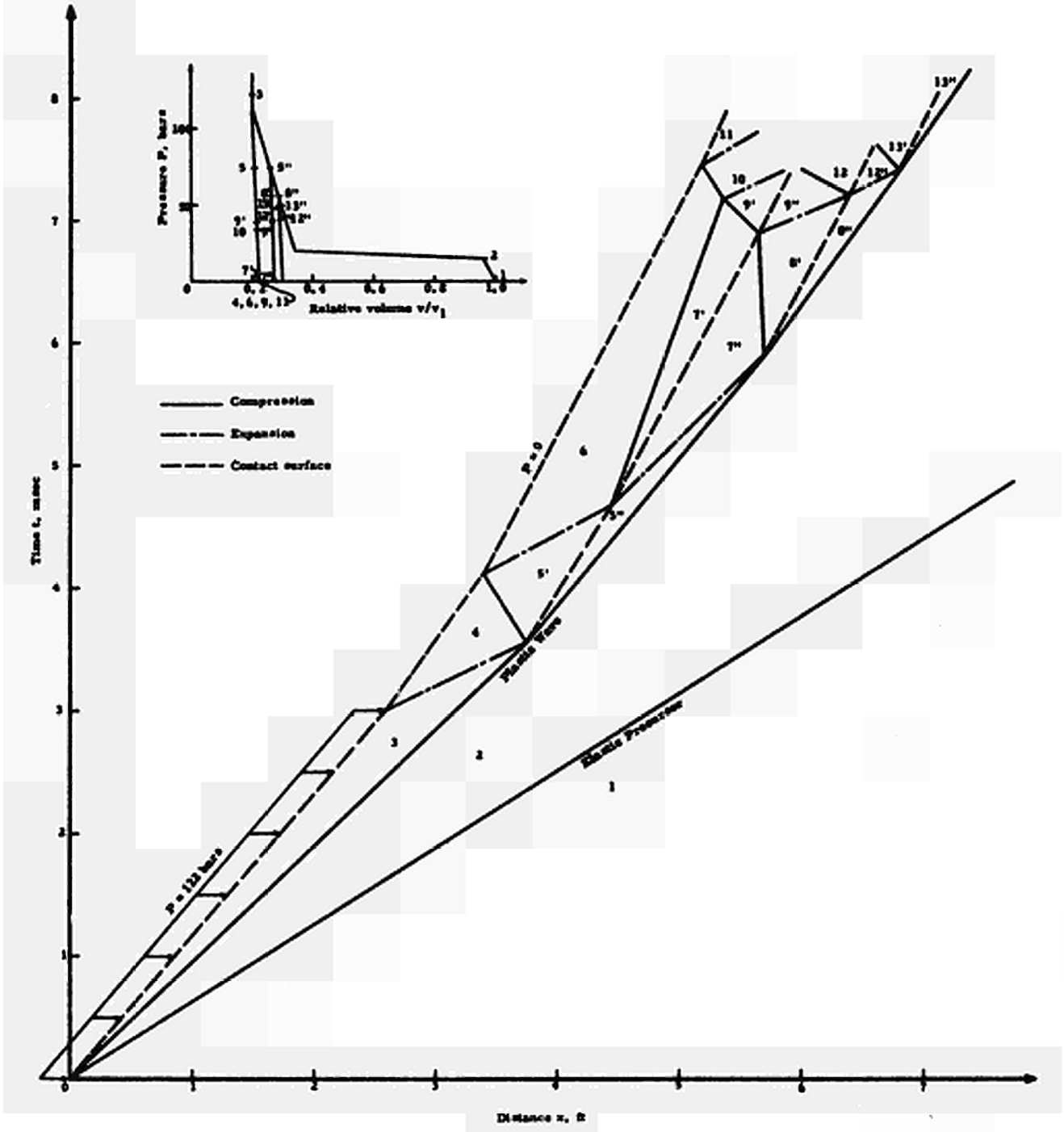

Figure 3 Response of Crushable Material to Pressure Pulse Loading

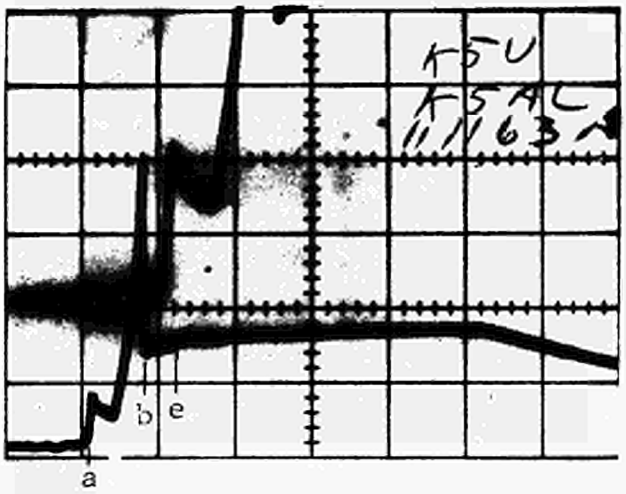

Gage 5 250 psi/cm, 500 μsec/cm
Gage 5 750 psi/cm, 1 msec/cm

Figure 4 Pressure-time Record for Initial Loading of Celotex

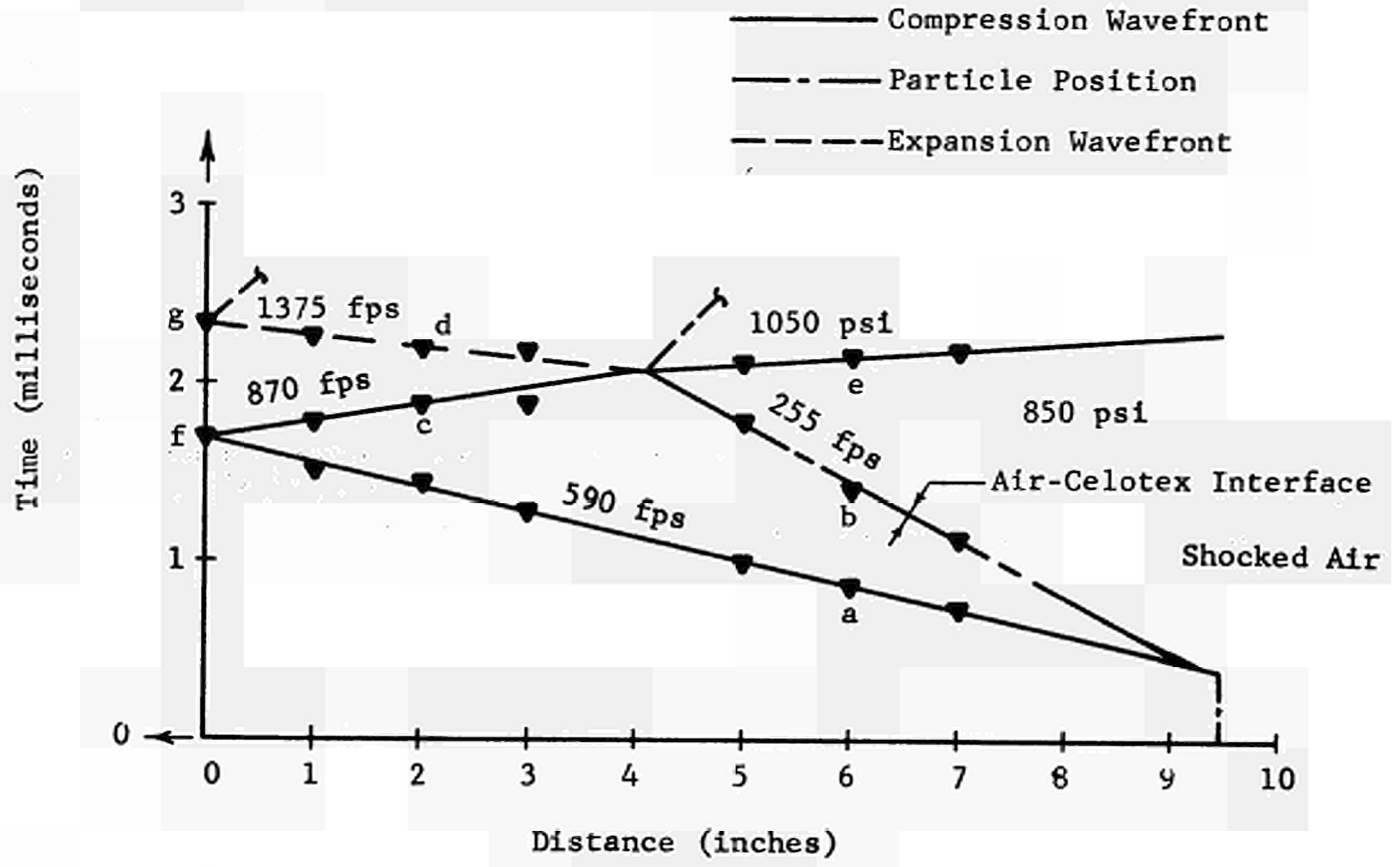

Figure 5 Wave Diagram for Initial Loading of Celotex

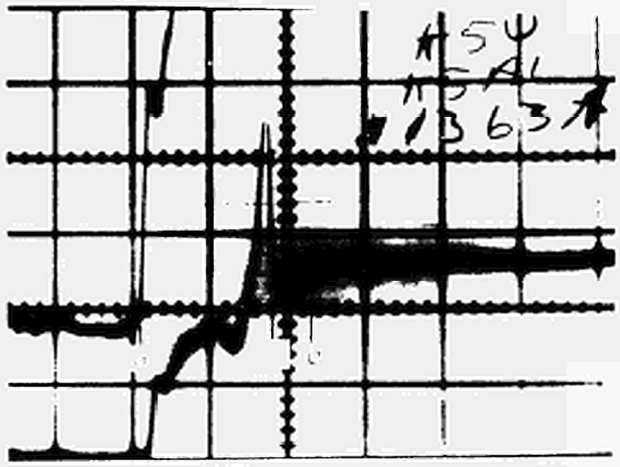

Gage 5 250 psi/cm, 500 μsec/cm
Gage 5 750 psi/cm, 1 msec/cm

Figure 6 Pressure-time Record for Reloaded Celotex

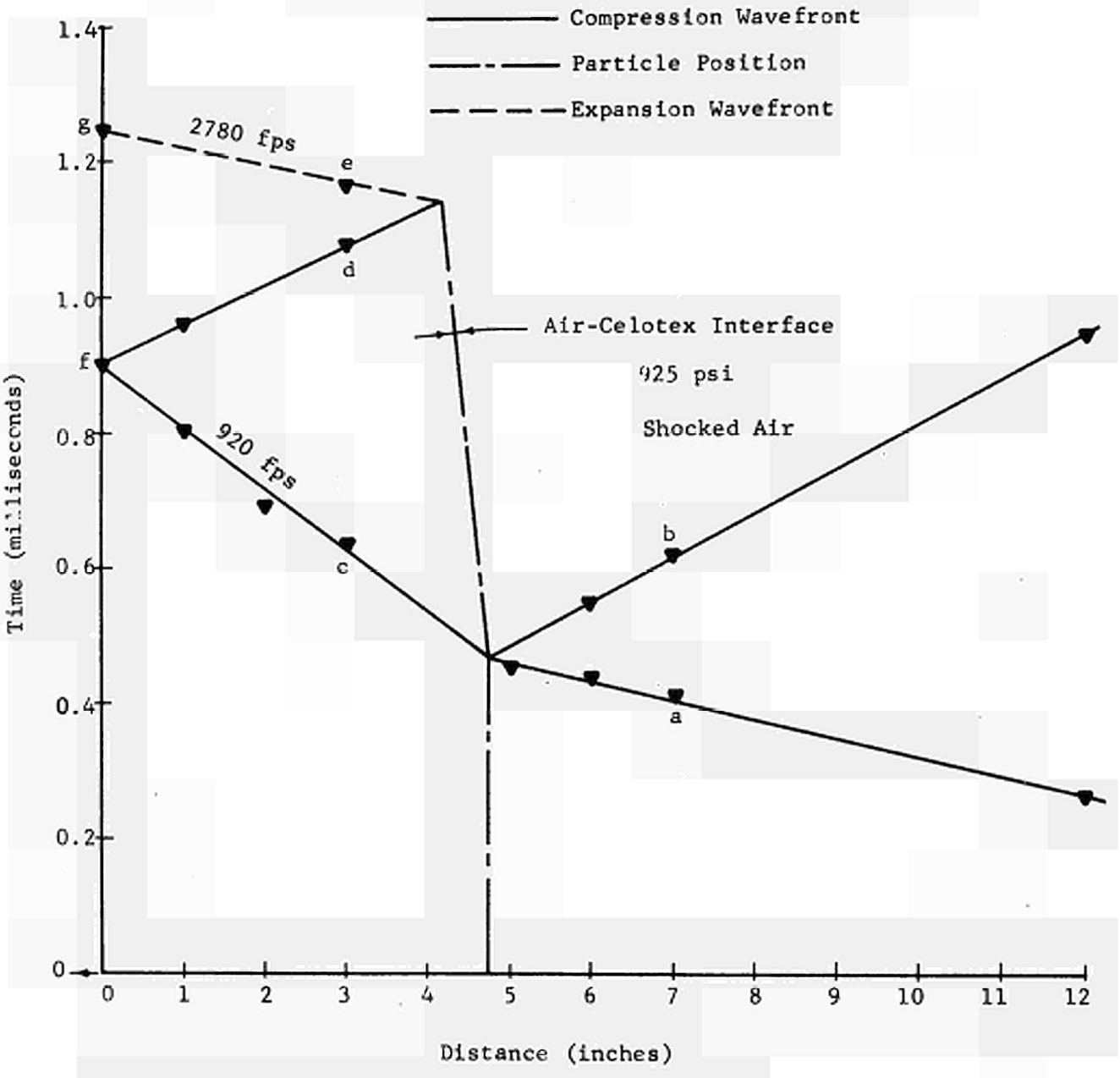

Figure 7 Wave Diagram for Reloaded Celotex

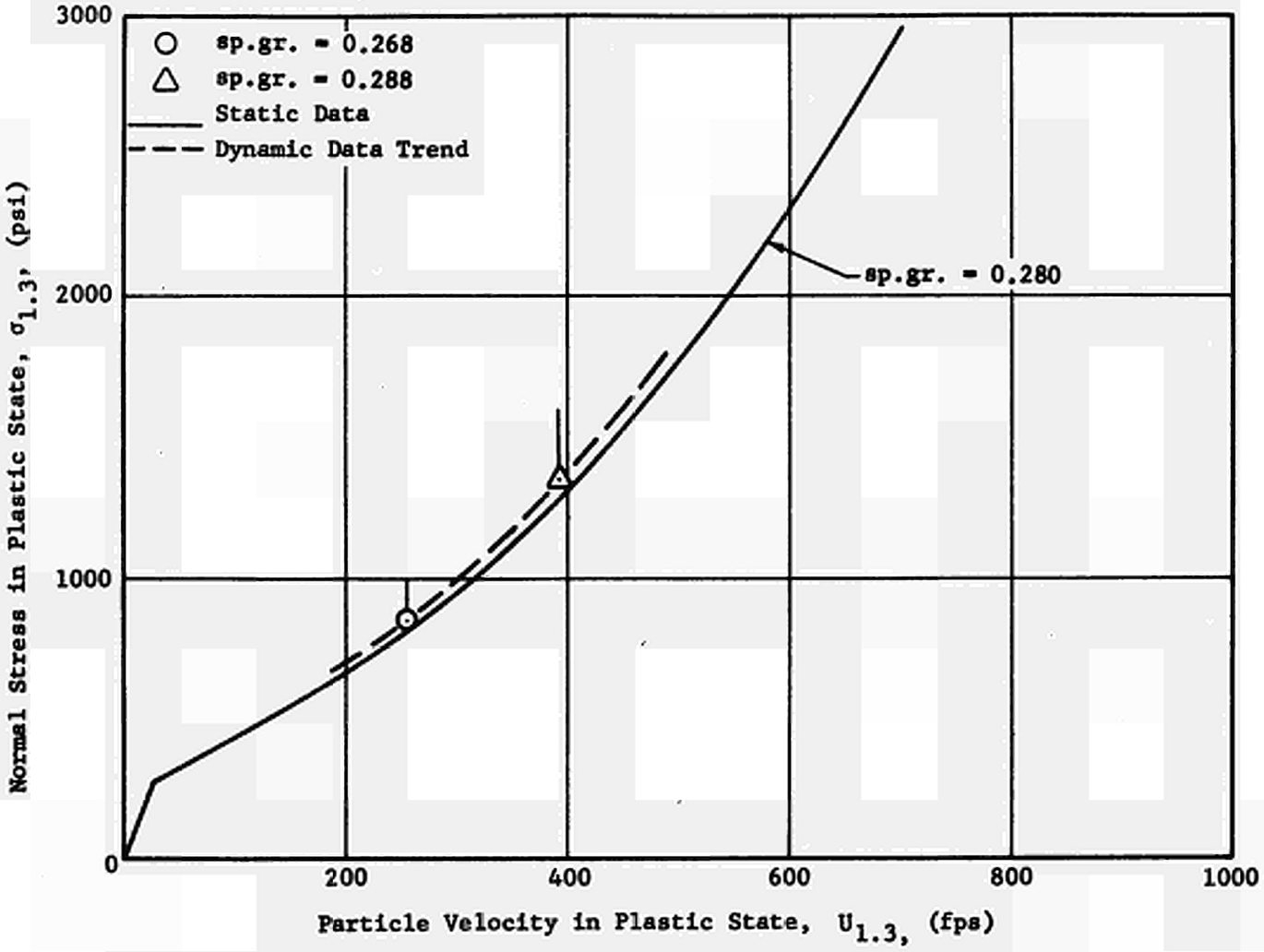

Figure 8 State Plane for Celotex Showing Static and Dynamic Data

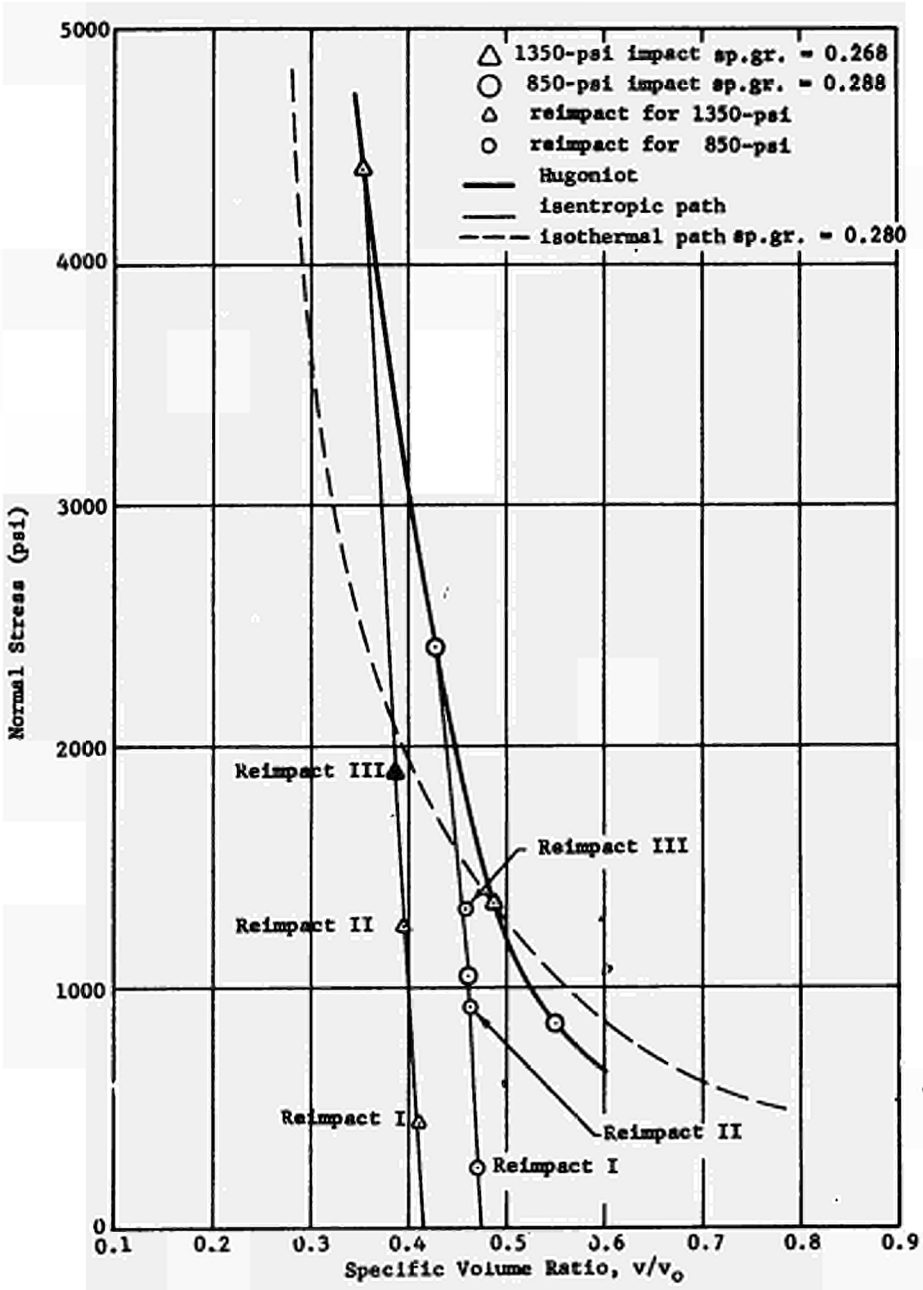

Figure 9 Stress-Volume Relations for Celotex

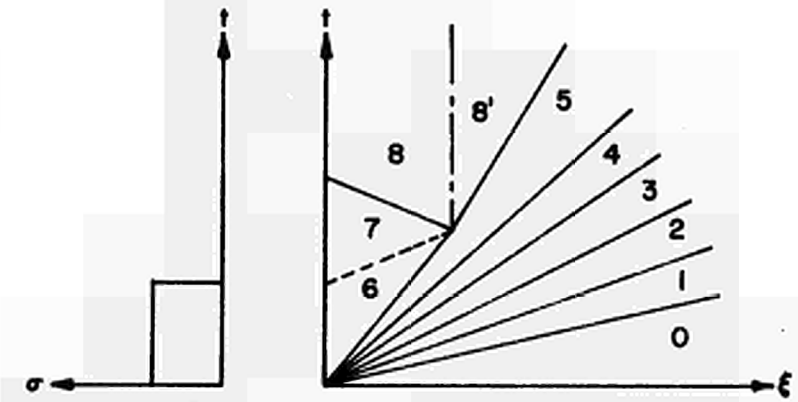

(a) LAGRANGIAN WAVE DIAGRAM

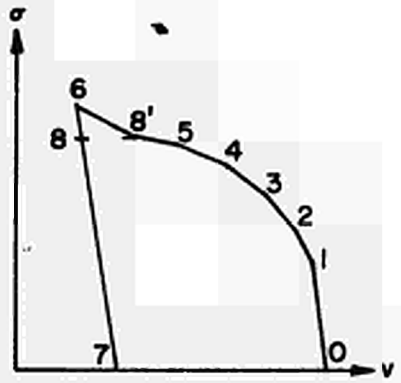

(b) DYNAMIC σ vs v STATE PLANE

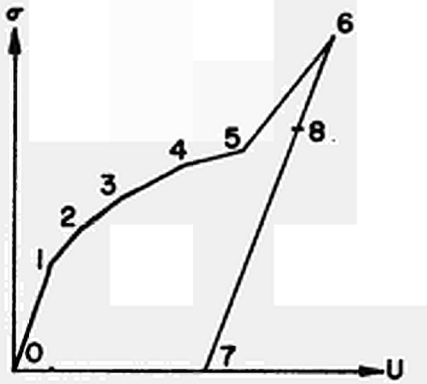

(c) STRESS vs PARTICLE VELOCITY STATE PLANE

Figure 10 Typical Wave Interaction Problem

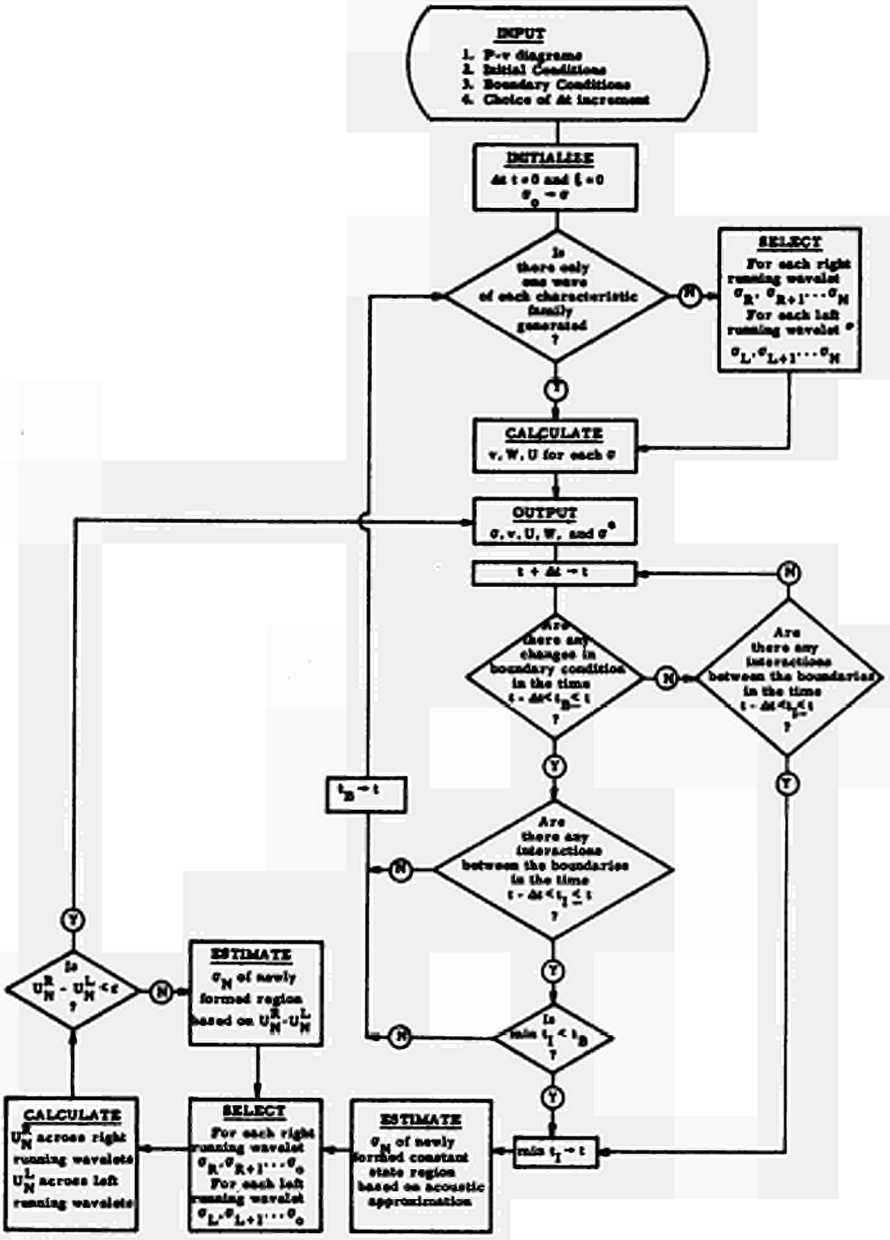

Figure 11 Flow Diagram of Computations

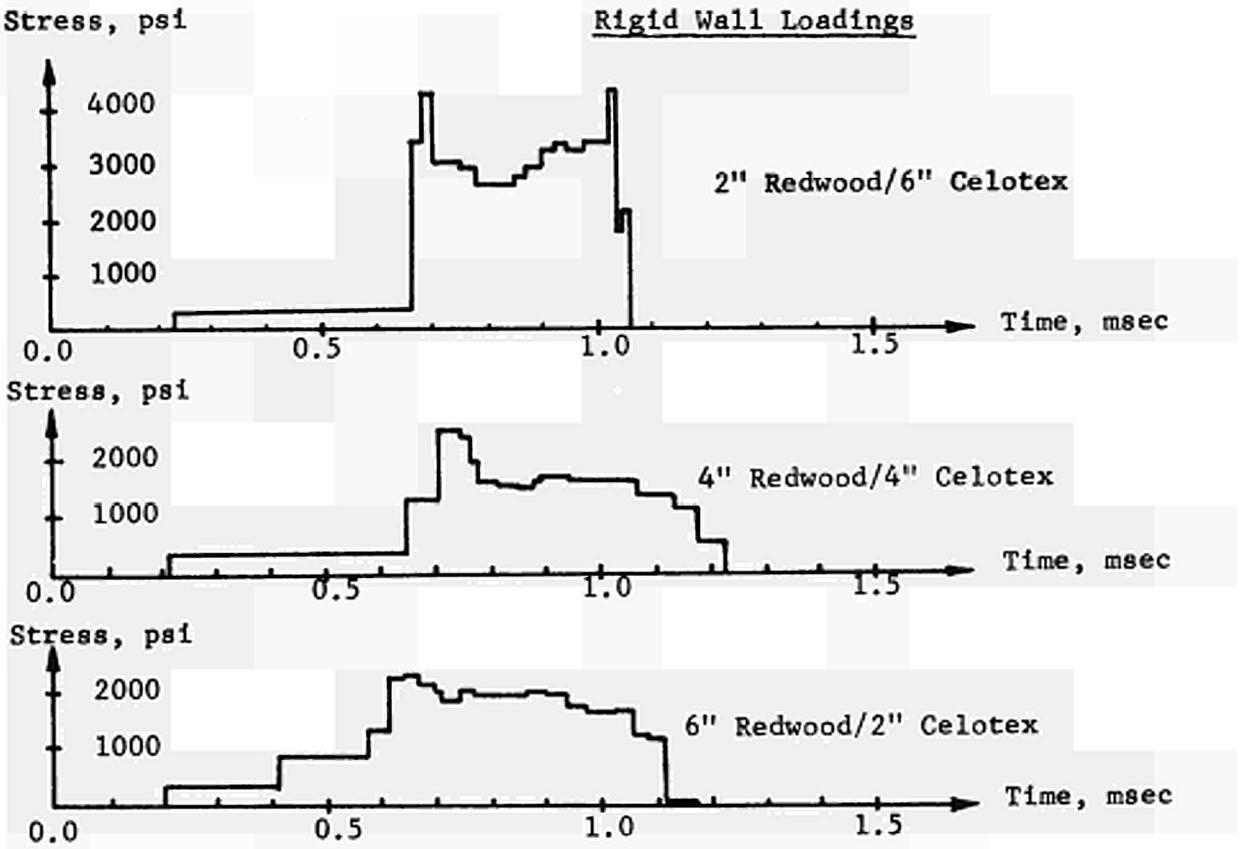

Figure 12 Load Attenuation by Crushable Shields, I
Incident Load: 10,000 psi, 0.1 msec

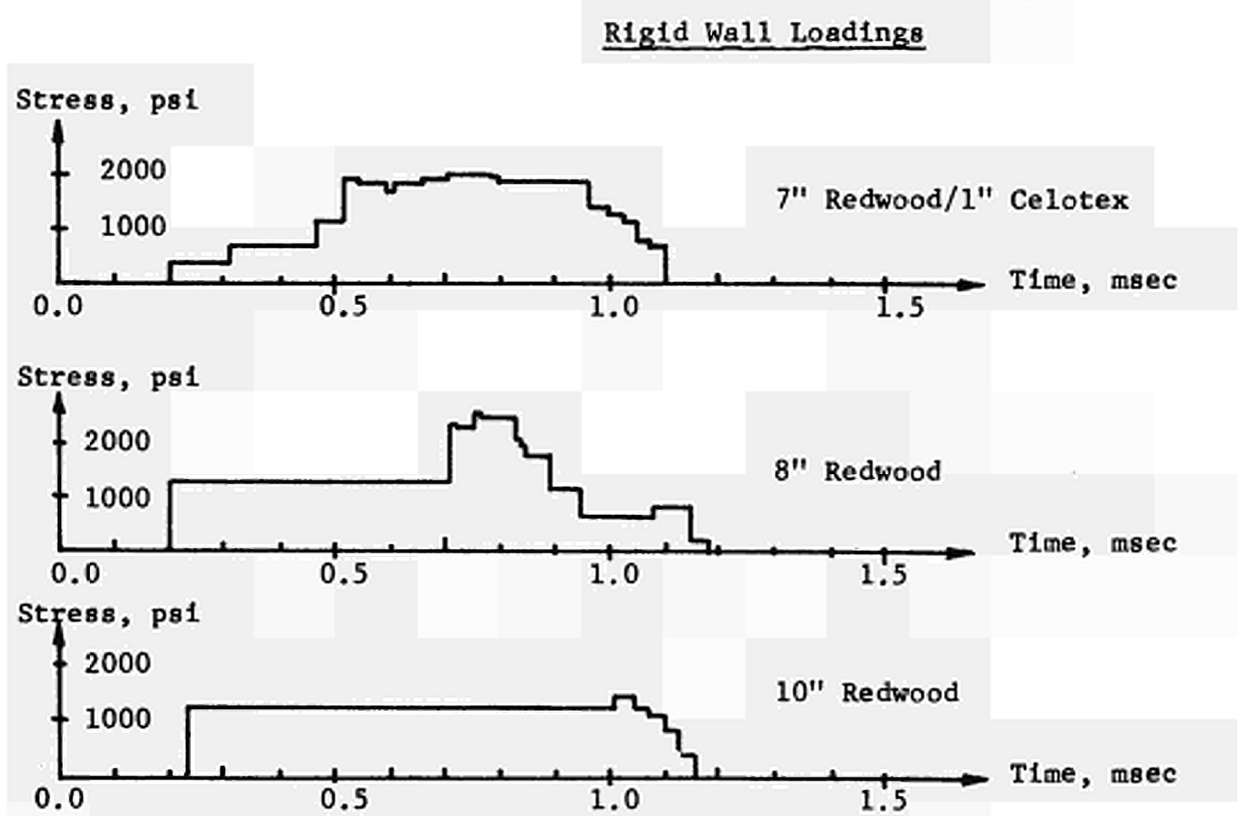

Figure 13 Load Attenuation by Crushable Shields, II
Incident Load: 10,000 psi, 0.1 msec

THE RESPONSE OF A VESSEL TO AN INTERNAL BLAST LOADING

Limits of Model Tests

Influence of Strain - Rate

by

H. Holtbecker, A. Maserati, M. Montagnani, G. Verzeletti

Euratom CCR, Ispra, Italy

1. LIMITS OF MODEL TESTS USING EXPLOSIVES

The problem of the deformation and rupture strength of a vessel as a result of internal blast has already been studied very thoroughly [1, 2], and the feasibility has been examined of carrying out tests on a reduced-scale model, using detonating or deflagrating explosives.

Apart from the influence of gravity forces (which are slight with slightly-reduced scale models) and the strain-rate effect, the validity of the following relation (W.E. Baker) was confirmed:

If a spherical charge of diameter D produces at a distance R from its centre a blast wave of intensity P and duration T, a similar charge of diameter KD will produce, at distance KR, a similar blast wave of intensity P and duration KT. It should be noted, however, that this criterion is valid only in the ideal case, where the source of energy-release is concentrated virtually in a point source. In reality, however, as Spert's destructive experiment appears to demonstrate clearly, the release source is diffused through all the melted aluminium particles, which are scattered in the core in an unknown pattern. Furthermore, the actual explosive employed to simulate the accident has its own characteristic pressure-damping curve varying with the radius. For example, a detonating explosive gives a decay curve characterized, where the wave is spherical, by 4 distinct zones (fig. 1), in which the pressure drop follows quite different exponential curves according to its distance from the centre.

With a detonating explosive a specific impulse can therefore be produced at

a specific distance from the centre. Hence the detonating explosive can be used with satisfactory approximation to ascertain the response of a vessel to an impulse originating in the centre. However, it can hardly be used to simulate eccentric blast or study its simultaneous effect on different structures located at various distances from the centre (e.g. the wall and all the internal components of the vessel simultaneously).

With deflagrating explosives, a decay curve closer to that generated by an excursion can be obtained in principle [3], but this still does not solve the problem because, to simulate the power excursion effects completely, not only must the same amount of heat be generated in the same time, but this heat must also be converted, at equal distances from the centre, into the same quantity of mechanical energy with the same pressure level. (Hence the mechanical impulse generation and heat exchange parameters of the simulating source must be in instant-for-instant scale with those of the source it simulates). Thus we still have the obstacle referred to earlier, that the most destructive effects are caused by scattered particles whose mechanism of energy conversion versus time and space is unknown.

Although these restrictions place difficulties in the way of complete simulation of blast loading in a vessel, with either detonating explosives or propellants, nevertheless, when the law for the motion of a structure acted upon by a given impulse P(t) has been found by calculation, explosives can be used, e.g. to simulate such blast-loading for the purpose of studying the strain-rate effects, or carrying out tests on real geometries with equal strain-rates.

This is the particular subject of the work reported here.

2. INFLUENCE OF STRAIN-RATE

In a tensile test with low strain-rate, elastic behaviour of the material is observable over a certain part of the diagram. After this zone the plastic deformation zone is reached and continues until rupture. Predominant in the first part is the elastic deformation of the crystal lattice, which returns to almost exactly its original position if the load is removed. Beyond the elastic limit slip is observed, in which the crystal planes slide over one an-

other. Displacement of this type is irreversible.

Certain authors [4, 5, 6] have carried out experiments on longitudinal test-pieces, investigating how the elastic limit, determined at low strain-rate, rises sharply with higher strain-rates (figs. 2 and 3). Microscopic examination effected by J. D. Campbell and J. Duby in the region of the dynamic proportional limit showed the absence of any significant slip bands and only some microscopic slip was observable.

D. S. Clark and D. S. Wood noticed that on carbon steel test-pieces a certain time is needed for slip to initiate. Within this period slip cannot initiate and the test-piece behaves elastically.

It has been attempted in various fundamental studies [7 to 15] on high velocity damping, relativistic motion of dislocations, and dislocation locking, to give a theoretical explanation of the events which occur during rapid deformation of a metal. J. D. Eshelby calculates, in the case of a screw dislocation, that the following law of relativity applied to a dislocation is valid when the speed of dislocation approaches the velocity of sound:

$$E = \frac{E_o}{\left(1 - \frac{v^2}{c^2}\right)^{1/2}}$$

where E = energy absorbed by the dynamic dislocation

v = velocity of dislocation

c = velocity of sound

E_o = rest energy of a dislocation

As well as this relativistic effect, there are considerable resistances opposing the slip induced by a shearing stress, which G. Z. Leibfried, J. D. Eshelby, J. Lothe and P. Mason identify in the mechanisms of phonon scattering, thermo-elastic damping, harmonic radiation and phonon viscosity. When the strain-rate rises, the deformation and rupture mechanism tends, owing to all the resistances against dislocation, to shift from slip to elastic strain and rupture by cleavage, in which only the surface energy is involved (fig. 4). A similar effect is produced by a temperature drop.

As the strain-rate is increased, there is a gradual change from slip strain to simple elastic deformation of the atom planes and rupture by cleavage, with consequent reduction in the ultimate elongation with the increased strain-rate.

This behaviour always occurs beyond a critical velocity, known as the transition velocity, in which the velocity of deformation at the free end of the test-piece is equal to the velocity of transmission of the plastic wave.

Below this critical velocity certain authors [13, 14] have also observed an increase in the ultimate elongation of certain materials (fig. 5). The apparent contradiction is caused by the fact that during dynamic loading the effect of restriction of area does not always allow - as in static tests - the reduction of the stress acting on the non-restricted part of the test-piece. Therefore, uniform elongation may increase during dynamic tests. Furthermore, we note that, because in dynamic tests the ultimate tensile strength increases, it is possible that the total number of dislocations involved in the strain mechanism may also increase masking, in certain conditions, the effect of locking of a single dislocation.

Although definite quantitative data on the dynamic behaviour of metals are very often lacking and sometimes are also contradictory, on the basis of all the foregoing factors two characteristic critical zones were distinguished (fig. 4) for the dynamic tests on model:

Zone a:

The increase in the strain-rate extends the field of the material's elastic behaviour versus the strain-rate. If the strain keeps within the dynamic elastic field and the deformation is therefore not sufficient to rupture or to deform the material plastically, raising the strain-rate will increase the strength of the structure.

Zone b:

If, on the other hand, the dynamic strain is generated by a sufficiently great impulse, the material may also attain the plastic deformation zone and come to fracture. The energy absorbed till fracture may decrease or increase depending on the material characteristics for a given temperature and strain-rate. It is difficult, therefore, to establish an a priori criterion.

In order to evaluate the energy absorbed till fracture it is necessary to know the true stress - true strain diagram and both the volumes of the material involved by fracture and by uniform strain.

Some of these concepts were verified experimentally by the authors with tests on simple, cylindrical and spherical geometries, which represent, on a reduced scale, idealized vessel geometries.

It must be observed that in reduced-scale models there is another factor which may affect the fracture behaviour of the material, and that is the reduction in scale of the thickness.

In fact [16], the reduction of the "plastic-zone", which governs the ductile-brittle rupture mechanism, varies in the function of the thickness of the material. This is because the lateral contractions are easier in thin plates than in thick ones.

In a reduced scale model, therefore, the behaviour of the material due to reduced thickness is more ductile than in the case of the original thickness, and this can sometimes disguise the effect of the strain-rate, which is in the opposite direction.

3. BEHAVIOUR OF A CYLINDRICAL SHELL SUBJECTED TO AN INTERNAL BLAST

3.1 Description of the set-up

The structure chosen had to be an idealized one, which could easily be constructed in different sizes and materials, and whose deformation could easily be calculated. Furthermore we needed a structure which would simulate part of a reactor vessel.

A cylindrical shell was decided upon, with wall thickness and internal diameter chosen to cover a rather wide range of thickness/diameter ratios.

The shell can be loaded by means of a detonating line charge which can throw out a wave of an approximately cylindrical shape [17, 18].
Since the chosen shell diameter is of the order of 200 mm, a very small

amount of explosive is required for the shell to reach the elastic limit. In order to obtain the complete detonation of an explosive of very small diameter it is necessary to confine it, and line charge of the primacord type was therefore used, with frequent use of a special line charge with a lead sheath (made by Montecatini).

Because several types of reactor vessels are filled with water and in addition water is capable of transmitting a pressure pulse of much greater intensity than gas, it was decided that water would be a convenient medium to transmit the pressure wave from the charge to the shell.

The containment of the water in the shell presented a problem, but a very simple system was devised to seal the water in, and yet leave the cylindrical shell completely free to deform. The set-up is illustrated in fig. 6.

The shell is simply supported on a horizontal plate of thick steel, and grease is smeared all around the shell to seal it.

A line charge is placed in position on the axis of the shell, and, when detonated at the upper end, which is outside the plate, an almost cylindrical wave starts to propagate radially.

To prevent rarefaction of the wave towards the free water surface in the upper section of the shell, another thick steel plate encloses the water contained in the shell. To avoid friction between the shell and the plate, a 1/10 mm clearance is left between the upper section of the shell and the plate by means of spacers.

This set-up is suitable for shells of not too large a diameter (not exceeding 400 mm) and for explosive charges not heavier than 30-40 gr. With diameters or charges larger than these it is no longer possible to confine the water by use of the upper plate, but it is possible to prevent the rarefaction wave by raising the water level above the test-piece.

In the set-up described the line charge is centred by means of a rubber tube, whose internal diameter matches the external diameter of the charge, and whose external diameter matches the central hole in the steel plate.

This rubber is used in order to avoid extensive damage to the plates, which would result from contact with the explosive.

This type of test on a cylindrical shell creates a loading condition noticeably different from that found in a longitudinal test-piece. In the longitudinal test-piece loaded by a longitudinal impulse a strain is created which is conditioned by the transmission of a longitudinal wave. This last is a plastic wave, if the impulse has been strong enough. If the displacement velocity of the extremity subjected to the impact is greater than the velocity of the plastic wave, there can be a considerable effect on the necking.

However, in the cylindrical shell test-pieces there is no wave propagation along the ring periphery. The wave, which is transmitted radially is reflected several times on the free surfaces of the shell. This induces a negligeable stress value compared with the tangential stress, which strains the shell.

In this type of test-piece it is therefore possible to study the strain phenomena without being affected by the propagation of strain waves. Moreover, the ring test-piece comes close to the original loading conditions of a vessel, in which, due to a centred and symmetrical wave, there is in fact no propagation of a strain wave along the periphery of the vessel.

Three main problems will be discussed here:

- Calculation of the structure deformation as a function of time.
- Increase of the yield stress of a material with the strain-rate.
- Behaviour of the material at fracture at high strain-rate.

3.2 Calculation of the structure deformation as a function of time

The main interest has been in thin cylindrical shells, and it was therefore easy to write the equation of motion of the shell wall.

If we take

$2\,d\,\alpha$ = angle at the centre of the shell made by an element on the wall of height equal to unity (see fig. 7),

σ_t = tangential stress,

$p\,(t)$ = applied pressure, function of time t

r_o = medium radius of the undeformed shell,

u = displacement of each element of the shell from the rest position at r_o,

s = thickness of the wall,

E = modulus of elasticity of the material,

ρ = density,

the equation of the motion of the element is, after suitable arrangement:

$$\rho s \frac{d^2u}{dt^2} = p - Es \frac{u}{r_o^2} \tag{1}$$

in the case where the material follows the Hook law

$$\sigma_t = E \frac{u}{r_o}$$

It follows immediately that the period T for the free oscillations is:

$$T = \frac{2\pi}{\omega} = \frac{2\pi r_o}{\sqrt{\frac{E}{\rho}}} \tag{2}$$

In tests in which the dynamic elastic limit of the material is not exceeded, it is possible to check formula (2) within the experimental error.

The strain of the shell may be recorded by means of a normal strain gauge cemented on the outer part of the shell. A record of deformation within the elastic limit is shown in fig. 8. The duration of the pressure is of the order of 15 to 25 μ sec and a typical profile of the pressure as a function of time is shown in fig. 9. This record was obtained by means of a steel bar pressure transducer [19] the head of which fits into a hole in the shell as shown in fig. 10.

It is evident from this that the pressure applied to the shell ceases before the maximum elongation of the wall is reached, and from this instant the shell undergoes free oscillation.

The oscillograph of fig. 8 relates to a shell of C 60 steel with r_o = 192 mm, and, in consequence, to a calculated period of 118 μ sec.
The period of 122 μ sec given by the oscillograph agrees very well, within experimental errors, with that calculated.

Equation (1) was given to a group of mathematicians of the Ispra Computing Centre for numerical integration, and in fig. 11 and 12 respectively are shown the deformations as a function of time calculated on the basis of (1) and recorded during a shot that produced a shock wave on the wall as shown in fig. 13. This pressure wave was used in equation (1) and the resulting wall motion is the one shown. The agreement between the calculated and experimentally recorded deformation is satisfactory.

In the calculation the material was supposed to follow the Hook law, and the calculation was a check on the accuracy of the method.

The next problem was to extend the calculation to the plastic field, and the yield stress of the material at such a strain-rate had to be known. This was easily achieved (as is described in more detail in the following paragraphs) by gradually increasing the explosive charge to discover at which point the shell becomes permanently deformed. Once this point is known the calculation method may give indication of the form of the curve $\sigma = \sigma(\varepsilon)$ in the plastic field. In fact it is possible to induce increasing peak deformations with known increased impulses. The peak deformations will be the sum of a plastic deformation, that will remain residual, and the elastic deformation.

A typical record is shown in fig. 14. With a series of tests it is possible to collect sufficient information to calculate approximately the unknown function $\sigma = \sigma(\varepsilon)$ in equation (1) in the plastic field.

If, on the other hand, the $\sigma = \sigma(\varepsilon)$ is known for a given material and a given strain-rate, it is possible to predict the deformation which the structure will undergo.

3.3 Increase of proportional limit with strain-rate

We have tried to determine the increase of the proportional limit at high strain-rate in several materials, in particular in an austenitic stainless steel, a low carbon steel (St. 37 DIN), and a C 60 UNI steel (see Appendix I). The test-pieces used are cylindrical shells mounted in the set-up described in the preceding paragraph.

The method of determining the proportional limit is, as mentioned before, to subject the shell, by gradually increased charges, to increasing impulses and therefore increasing strains, up to the point at which permanent deformation is observed. The deformation measurements are made by strain-gauges, which give excellent results even at a very high strain-rate (of the order of 100 μ strain/μ sec), for deformations of value somewhat above the proportional limit of a steel [19]. The limit is then calculated on the basis of the measured strain, supposing the modulus of elasticity of the material to be constant and equal to the static one, also at the strain-rate concerned.

The oscillographs of an experimental sequence, which was made to determine the elastic limit of St. 37, are illustrated in figs. 15 to 18.
The result was that the material did not show a residual plastic strain up to a strain of the order of 2, 300 μ strain, whereas at 2, 500 μ strain a permanent deformation was apparent.

The cylindrical shell used in this experiment was made by cutting strips from a metal sheet of St. 37, with a thickness of 5 mm, and curving them into a cylindrical shape. After the extremities had been welded together the strips were machined on a lathe to form a cylindrical shell of the outer diameter of 250 mm, the thickness of 2 mm and the height of 30 mm.

Test-pieces were made of the same sheet of steel and subjected to a uniaxial tensile test which showed the mechanical properties given in Appendix I and the stress-strain curve shown in fig. 19.

From the deformations obtained in the shell subjected to an internal blast, and on the basis of the "static" modulus of elasticity, the proportional limit (at 0. 02% residual strain) of this steel is found to be 48. 5 kg/mm^2 for a maximum strain-rate of the order of 100 μ strain/ μ sec. The strain measurements are considered to be affected by an error such as to induce an error of $\pm$ 10% in the value of proportional limit.

Next some tests were carried out on a shell of austenitic stainless steel obtained from a tube. The shell had an outer diameter of 158 mm, a thickness of 3 mm and a height of 30 mm.

In addition some tests were carried out on a shell of the carbon steel C 60 UNI obtained from a rod. The shell had an outer diameter of 194 mm, a thickness of 3 mm and a height of 30 mm. After machining the material of the shell was annealed (750°C for 15 minutes, followed by cooling in air at room temperature).

In both of these cases test-pieces of the same radius and thickness as the shell were also made. The results of the static and dynamic tests are summarized in the following table 1.

TABLE 1

MATERIAL	$E \frac{kg}{mm^2}$ static	$\sigma_{0.01} \frac{kg}{mm^2}$ static	$\sigma_{0.1} \frac{kg}{mm^2}$ static	$\sigma_{0.02} \frac{kg}{mm^2}$ at 100 $\frac{\mu strain}{\mu sec}$ dynamic
St. 37	20,900	21.6	21.9	48.5
austenitic 18/8 stainless steel	19,600	15.5	24.5	30.4
C 60 UNI	21,000	34.5	34.8	61.4

3.4 Behaviour at fracture at a high strain-rate

The study of the behaviour of the materials at fracture at high strain-rate was also carried out, for the cylindrical shell, with the set-up described in paragraph 3.1.

The charges used, which in this case had to be of considerable weight, were either cylinders of TNT with a 15 mm diameter, or cylinders of plastic explosive ("plastit" made by Dynamit Nobel, which has a density of 1.65 gr/cm^3 and a detonation velocity of about 7,000 m/sec) with diameters from 19 to 24 mm. The height of the cylinders of explosive is naturally equal to that of the shell.

Since the strain gauges are not capable of following the strain as far as rupture at the strain-rates in question [19], the elongations were measured by pin-contactors (see Appendix III). The cylindrical shell fractures at many

points as it is shown in fig. 21a. After the test we reassembled the pieces, and measured the residual deformation, determining the following parameters:

a) Uniform strain far from the fracture area which was calculated from deformation at measurement bases situated on the external periphery of the shell. These bases are delimited by marks drawn following a generatrix line at a distance of 20-30 mm from one another.

b) Reduction in the thickness, measured with a precision of $\pm$ 0.01 mm.

c) True-strain calculated from the measurements of the reduction in height and thickness of the shell at the fracture, and on the basis of the formula

$$(1 + \varepsilon_t)(1 + \varepsilon_h)(1 + \varepsilon_r) = 1 \qquad (3)$$

where:

ε_t = the tangential strain which coincides with the true-strain at the fracture

ε_h = reduction in height in percent

ε_r = reduction in thickness in percent

Formula (3) which expresses the volume constancy of the material and is valid at all points of the shell, is used also to check the measurements set out in paragraph a).

The strain-rates in question vary between 1,300 and 1,500 μ strain/μ sec. Figs. 20 and 21 give examples of strain measurements given respectively by a strain-gauge (which in this test gave the exceptional measurement of a strain of up to 14.2%) and pin-contactors.

The shells used were similar to those described in paragraph 3.3, with the sole difference that the stainless steel shell was also manufactured from metal sheet, and had an outer diameter of 202 mm and a thickness of 1 mm. The comparison between the results obtained in dynamics and those obtained on test-pieces of the same material in static is given in table 2.

The temperature of the experiments varied between 20°C and 25°C.

On one shell of C 60 UNI steel an experiment was made by putting hot water into the shell. The temperature of the shell in that experiment was 42°C.

TABLE 2

MATERIAL	strain-rate $\frac{\mu \text{ strain}}{\mu \text{ sec}}$	uniform strain %	reduction of thickness %	true strain %	temperature during experiment °C
St. 37	static	25	58.5	163	24
	1,500	42.7	32.5	103	
stainless steel 18/8	static	49.5	43.5	233	24
	1,400	43.3	31	81	
C 60	static	17.5	68	91	24
	1,400	22	13	30	
C 60	static 1,400	32	17.9	42	42

4. BEHAVIOUR OF A SPHERICAL SHELL SUBJECTED TO AN INTERNAL BLAST

4.1 Calculation of the structure deformation as a function of time

The behaviour of a spherical shell subjected to an internal pressure rapidly variable in time but constant from one place to another in the sphere can be described by the equation:

$$(\lambda + 2\mu)\ \frac{\partial}{\partial r}\ \left(\frac{\partial u}{\partial r} + 2\frac{u}{r}\right) = \rho\ \frac{\partial^2 u}{\partial t^2} \qquad (4)$$

where

t = time

λ and μ = constants of Lamé

ρ = density of the material of which the wall is built

r = initial spatial coordinate of a layer

u = $u(r, t)$ = displacement from the rest position of the layer of coordinate r.

The radial stress σ_r and tangential stress σ_t are defined in function of the

u and of the $\frac{\partial u}{\partial r}$ of the following expressions:

$$\sigma_r = (\lambda + 2\mu)\frac{\partial u}{\partial r} + 2\lambda\frac{u}{r} \tag{5}$$

$$\sigma_t = \lambda\frac{\partial u}{\partial r} + 2(\lambda + \mu)\frac{u}{r} \tag{6}$$

Given r_i the internal radius and r_e the external radius of the sphere, the boundary conditions are:

1) u, $\frac{\partial u}{\partial r}$, $\frac{\partial u}{\partial t}$, σ_r and σ_t are = 0 for $t < 0$

2) $\sigma_r = 0$ for $r = r_e$ for every t

3) $\sigma_r = -p(t)$ for $t \geq 0$ for $r = r_i$

The solution of equation (4) with the boundary conditions was done by a group of mathematicians of the Ispra computing centre and programmed on the IBM 7090 computer.

We have thus obtained, for a given $p = p(t)$, the magnitudes

$$\sigma_r = \sigma_r(r, t), \quad \sigma_t = \sigma_t(r, t) \quad u = u(r, t),$$

and $\varepsilon_t = \frac{u(r, t)}{r}$, which is also directly measurable through the strain-gauges.

Equation (4) is only valid where σ_r and σ_t are related to the u and $\frac{\partial u}{\partial r}$ of relations (5) and (6); that is, as long as the material remains in the elastic field.

When the material enters the plastic field the link between the σ and the u and $\frac{\partial u}{\partial r}$ is no longer linear, the constants λ and μ of the material vary, and the values to be introduced into the equation are no longer known.

After each experiment one can compare the measured tangential strain values ε_t with the values calculated from measurement of the pressure which has acted upon the internal surfaces of the sphere.

4.2 Experimental set-up

Two materials, of standardization DIN, have been taken into consideration: St. 37 and stainless steel 4300 (see Appendix I).

The spheres are obtained by arc-welding forged hemispheres. After the welding an annealing treatment is carried out as described in 3.3.

The external diameters of the sphere were 400 and 250 mm for each of the materials. The thicknesses were of a nominal 3 mm and 2 mm respectively for the spheres of 400 mm and 250 mm diameter.

In effect, since the manufacturing process starts from a plate of constant thickness, variations of $\pm$ 10% of the nominal value have been measured, with thicknesses decreasing from the equator to the pole of the hemisphere.

Four meridian lines and five parallels are traced on each hemisphere. At the intersection of each meridian with the various parallels the thickness may be measured with an accuracy of $\pm$ 0.01 mm.

After welding the diameters of the sphere were measured at the various traced points and values have been found ranging within $\pm$ 1% of the nominal value. On the external surface of the area near the pole, where the thickness remains constant over a large zone, strain-gauges have been cemented. The internal blast-loading is generated by a charge of "plastit". This is detonated by means of an exploding wire, on to which a condensor of 1 μF, charged to 14 KV, is discharged. We prepared the explosive charge ourselves by pressing the explosive into a spherical die divided into two halves equipped with the exploding wire. It has been pressed in order to obtain a sufficiently homogeneous density. By this procedure it is possible to obtain a spherical detonation, and consequently, the production of a spherical wave. Bar strain-gauge pressure transducers [19] carried out simultaneous measurements in different directions, and recorded differences included in the accuracy of the transducers. In each experiment two pressure measurements and two strain measurements were made. The charge was gradually increased in order to ascertain the point at which the material showed signs of plastic deformation.

The sphere was supported by the pressure transducers, as is shown in fig. 22. The explosive was introduced through a hole made on the sphere, and this hole has been reinforced as is also shown in fig. 22. By pulling a wire through the polar axis of the sphere, it was possible to centre the charge with an error of $\pm$ 1 mm.

4.3 Comparison between the experimental results and the theoretical calculations

In each experiment two pressure signals and two strain signals were recorded on two double beam oscilloscopes. Figs. 23, 24, 25 and 26 give two examples of the recordings. By taking the pressure values recorded by the two transducers we find the average $p = p(t)$ which, when introduced into the boundary conditions of equation (4), gives the profile of the ε_t, which is also obtained by strain-gauge recordings.

The comparison between the ε_t given by the two methods permits an evaluation of the validity of the mathematical method, and a check on the values of σ_t and σ_r, which the calculation methods give, not only for the points on the external surfaces but also for all the points of the sphere.

This is particularly important when the sphere is no longer thin as it is in our case. Examination of the data obtained from the calculation shows that the tangential stress σ_t increases by approximately 3% going from the external surface to the internal surface of the sphere of 400 mm diameter and thickness of 3 mm.

In fig. 24a the diagrams of the theoretical and experimental strain time curves (reproduced from fig. 26) are compared. The agreement between the experimental and theoretical results is good (within a range of $\pm$ 10%) as far as concerns the values obtained for peak strains and the time in which this peak is attained. In some cases, however, there is disagreement between the theoretical and experimental profiles of the strain curve. This disagreement, however, can be attributed to variation in the thickness from point to point.

4.4 Increase of the proportional limit with the strain-rate

The elastic limit of the material is measured in static on test-pieces, as re-

ported in Appendix I. For a closer comparison of the values of the elastic limit of the material in the true state of stress which exists in the sphere, we have carried out static tests on both the materials of the spheres.

The results are reported in fig. I-1 which shows an elastic limit of 23 ± 1 kg/mm^2 for the St. 37, although it was not possible to find the exact point at which the plastic phenomenon began in the austenitic DIN 4300 stainless steel. The limit of proportionality can be placed at about 7 ± 2 kg/mm^2; the proportional limit at 0.05% is 15 kg/mm^2 ± 10%.

In dynamics, by the same method as already described for the cylinders, we measured an elastic limit of 57 ± 10% kg/mm^2 for the St. 37 steel, and of about 45 kg/mm^2 for the austenitic steel, with a mean strain-rate of 40 μ strain/μ sec. The maximum strain was attained in 50 ± 5 μ sec. This shows for St. 37 steel an increase in the elastic limit of 140% compared to the static case. The value found for the DIN 4300 stainless steel being based on only one experiment demands further check.

4.5 Study of the rupture

Charges as described in the paragraphs concerning the elastic field were used with water as the transmission medium in order to obtain a high strain-rate with a small charge.

Since the strain-gauges are unable to follow strains above ~7% in dynamics, these higher strains were measured during the deformation by:

- the pin contactors, and
- the capacity method

which are described in Appendix III.
In this way we measured the values of the strain-rate, which was one of the parameters which were varied during our tests. After the experiment we re-assembled the pieces and measured the residual deformation by checking the following parameters:

1) The uniform tangential strain ε_u far from fracture. ε_u was determined by the formula:

$$(1 + \varepsilon_{t1})(1 + \varepsilon_{t2})(1 + \varepsilon_r) = 1$$

supposing constance of volume.

ε_{t1} and ε_{t2} are the tangential strains in two orthogonal directions and are equal to ε_u because of the symmetry of the stresses.

ε_r being the reduction of thickness, is known by thickness measurements performed at individual points before welding of the sphere and after the test.

2) The reduction of thickness measured to an accuracy of $\pm$ 0.01 mm.

3) The true strain calculated from the reduction of the area in the fracture zone, supposing that the strain along the fracture is equal to the uniform strain.

4) The aspect of the fracture, which is normally of shear type with a fracture angle varying in both materials from 47° to 54°. The fracture angle has shown a certain tendency to increase with increasing strain rate.

Experiments have been carried out which increased the strain-rates by detonating 60, 80, 100, 320 and 500 gr of explosive in water. The strain-rates thus obtained varied from 200 to 2,600 μ strain/μ sec. Figs. 28 and 29 give examples of the recording of the strain as a function of time.

From an examination of the fractured pieces of the sphere it can be seen that with low strain-rates there are only a few broken pieces, whereas we noticed that the number of pieces increased as the tests became more rapid. This increase leads us to presume that the fracture must have occured in several places independently and simultaneously. In some of these later tests on the St. 37 steel we noticed that about 5% of the total length of the fracture was of a zig-zag type characterized by the passage from shear to cleavage with a direction change of 90° and a fracture angle of 90°. Details of a fracture of this type are given in fig. 32. It has been observed that austenitic steel shows this tendency to a much less degree.

Even where the appearance of the fracture is shear, we have reason to think that at a high strain-rate it will propagate at a very high velocity of the order of 1.5 kg/sec. This figure was recorded accidentally during an experiment.

The following table 3 gives the mean values of parameters measured in various experiments.

TABLE 3

MATERIAL	diameter mm	Explosive charge medium gr	average strain-rate $\frac{\mu \text{ strain}}{\mu \text{ sec}}$	ε_u %	ε_r %	ε_t %
St. 37	400	static		14	40	46
St. 37	250	static		16	49	69
St. 37	400	80 water	300	12	44	60
St. 37	250	60 water	800	17	40	42
St. 37	400	500 water	900	24	41	37
St. 37	250	500 air	2500	30	42	33
DIN 4300	400	static		22	40	37
DIN 4300	250	static		20.5	43	45.5
DIN 4300	400	320 water	750	19	37	34
DIN 4300	250	80 water	1250	22	33	23

Test temperature about 18°C

ε_u = tangential uniform strain far from the fracture

$\varepsilon_r = \frac{s - s_o}{s_o}$ (s is the thickness at the fracture; s_o is the average initial thickness at the same point)

ε_t = true strain at the fracture

5. DISCUSSION AND CONCLUSION

On the basis of the preliminary results set out in the present report it is possible to make the following remarks:

- Experimental and calculating methods devised for the study of the response of a vessel to an impulsive loading, allow a sufficiently precise study of such phenomena, and, particularly, have made possible the study of the effects of strain-rate in vessels with thin walls in the elastic field and at rupture.

- We have been able to verify the considerable increase in dynamics of the elastic limit of two types of carbon steel and two types of austenitic steel in state of mono- and biaxial stress. The dynamic elastic limit of biaxial stress for St. 37 exceeds by about 19% that of monoaxial stress.

- We have noticed rupture phenomena which were not entirely foreseeable on the basis of existing literature, and which prove that modification of the strain-rate can bring about considerable changes in the deformation and rupture mechanism. This can distort the results of an experiment on a reduced-scale model. The zig-zag shear cleavage fracture as shown in fig. 32 presents a peculiar characteristic. This can perhaps be accounted for by the strain wave which precedes the shear fracture and profoundly alters the state of stress at the point where the cleavage fracture starts.

- The increase of the strain rate has brought about an equally considerable increase of the uniform strain and the decrease of the true strain, both in the tests on cylindrical and spherical shells. In the experiments on cylindrical shells uniform strain decrease was proved in the case of stainless steel. This finding requires further tests for better checking.

  Tests were carried out for the UNI C 60 steel also at higher temperature, which caused a sharp strain increase, both uniform and true.

- The behaviour of the material at rupture in the various experiments can be explained by the strain-hardening effect. This, in the biaxial experiments, is sufficient to create a decrease in plasticity of the material in the restricted area, whereas in the monoaxial experiments, where the material is freer to flow, this effect takes place to a smaller extent. The increase of both uniform and true strain with increase of temperature shown by UNI C 60 steel leads us to presume that the material is in the neighbourhood of the transition temperature for the deformation velocity employed.

- It has not yet been possible to determine the influence of all parameters observed upon the energy necessary for rupture. It follows that, whereas zone a) in fig. 4 has been fully verified, we have only a few elements for defining zone b). Therefore, it is necessary to be very careful in evaluating rupture tests on the reduced-scale model.

- It must be noted in addition that the manner in which the structure is deformed can be of great importance to the rupture mechanism, since this is related to the exact state of stress of the structure at the fracture point. The condition of loading for the symmetrical internal dynamic pressure of a structure is really a very special condition which it is difficult to simulate completely in a test-piece of a different shape and state of stress.

The methods employed in the present study are suitable for a test on a prototype, in which the test-piece is built of the same material, with the same thickness, and the same weldings, but using (see fig. 33) a ring of reduced height compared to the original. In such a test, however, the same strain-rates as in the original structure should be reproduced.

The test can be carried out in an open experimental area with the use of simple equipment. Such a test will obviously not be a substitute for experiments on the test-piece (20, 21, 22, 23), whose importance is due to their extreme simplicity, but it will provide complementary information, which comes close to that provided by a full-sized experiment at very much reduced cost.

Naturally, for such a test to be valid, the impulse of the structure which is to be simulated should be known. This calls for a deeper knowledge than that at present available on the effects of a release of energy on the value of the mechanical impulse.

The research work begun shows that further investigation of the following points would be of considerable interest:

- Tests on a prototype (see preceding comment) with special regard to the influence of strain-rate on transition temperature.
- Investigation into the shear-cleavage type of fracture which propagates itself at great speed, and on the state of stress at the running fracture tip.
- The influence of defects or stress concentration caused e.g. by nozzles upon the origin and propagation of a fracture induced and pushed dynamically.

ACKNOWLEDGEMENTS

We wish to thank Messrs. A. Benuzzi and L. Guerri and Miss P. Stella for the integration of motion equations and computation work.

We are much indebted to Mr. P.S. Weltevreden who made helpful criticisms on the evaluation of the results.

We thank Messrs. Berthmann, Schenk and Röh of Dynamit Nobel as well as Messrs. Formento, Morganti and Tessaro of Montecatini, who all gave advice on the utilization of the explosives and prepared special explosive charges for us.

Messrs. P. Actis Dato, E. Jorzik and Y. Lachapelle were responsible for the instrumentation and the measurements.

Messrs. P. Brunella, G. Giudici, U. Guerrini and G. Bevilacqua assembled the test set-ups.

Messrs. P. Golinelli and E. Soma carried out measurements on test-pieces after rupture. Mr. Jung performed tests in order to define material characteristics in static conditions.

Special thanks are due to Mrs. P. Doyen, Mrs. J. Varekamp and Miss E. Zenner for the translation and preparation of the report.

REFERENCES

(1) F. B. PORZEL, "Some Hydrodynamic Problems in Reactor Containment", P/434 USA, Geneva Conf. 1958

(2) W. E. BAKER, "Scale Model Tests for Evaluating Outer Containment Structures for Nuclear Reactors", P/1028 USA, Geneva Conf. 1958

(3) A. PASCOUET, "Nuclear Power Excursion - Simulation in France", Nuclear Safety, Fall 1965

(4) A. H. COTTRELL, "Dislocations and Plastic Flow in Crystals", Oxford at the Clarendon Press, 1961

(5) D. S. CLARK and D. S. WOOD, "The Time Delay for the Initiation of Plastic Deformation at Rapidly Applied Constant Stress", Proceedings of Am. Soc. for Testing Materials, Vol. 49, 717-737 (1949)

(6) J. D. CAMPBELL and J. DUBY, "The Yield Behaviour of Mild Steel in Dynamic Compression", Proceedings of Royal Society, Vol. A 236, 1956

(7) J. WEERTMAN, "High Velocity Dislocations", Proceedings of a Technical Conference, Estes Park, Colorado, July 11-12, 1960

(8) G. T. HAHN, "A Model for Yielding with Special Reference to the Yield-Point Phenomena of Iron and Related BCC Metals", Acta Met. 10, 1962, p. 727

(9) J. D. ESHELBY, Proc. Phys. Soc. (London), A 62, 307 (1949)

(10) G. Z. LEIBFRIED, Z. Physik, 127, 344 (1950)

(11) W. P. MASON, "Phonon Viscosity and its Effect on Acoustic Wave Attenuation and Dislocation Motion", J. Acoust. Soc. Am. 32 (4), 1960, p. 458

(12) E. R. PARKER, "Brittle Behavior of Engineering Structures", John Wiley and Sons, Inc., New York, 1957

(13) K. G. HOGE, "The Effect of Strain Rate on Mechanical Properties of Some Widely Used Engineering Metals", UCRL-14599, Dec. 1965

(14) D. S. CLARK, "The Behavior of Metals under Dynamic Loading", 1953 Edward de Mille Campbell Memorial Lecture

(15) C. ZENER and J. H. HOLLOMAN, "Effect of Strain-Rate Upon Plastic Flow of Steel", J. Appl. Phys. 15, 1944, p. 22-32

(16) W. H. IRVINE, A. QUIRK, E. BEVITT, "Fast Fracture of Pressure Vessels: an Appraisal of Theoretical and Experimental Aspects and Application to Operational Safety", J. Brit. Nucl. Energy Soc., Jan. 1964

(17) R. H. COLE, "Underwater Explosions", Princeton University Press, 1948

(18) H. HOLTBECKER, A. MASERATI, "Some Theoretical Considerations and Experimental Data on Propagation and Reflection of Underwater Pressure and Shock Waves", Report EUR/C-IS/705/66 e

(19) P. ACTIS DATO, H. HOLTBECKER, E. JORZIK, Y. LACHAPELLE, A. MASERATI, G. VERZELETTI, "Instrumentation for Rapid Mechanical Transients in Model Scale Experiments", Report EUR/C-IS/698/66 e

(20) W. S. PELLINI, P. P. PUZAK, "Fracture Analysis Diagram Procedures for the Fracture-Safe Engineering Design of Steel Structures", NRL Report 5920, March 1963

(21) H. M. SCHNADT, "A New Approach to the Solution of Brittle Fracture Problems in Modern Steel Construction", Document N 33 (1962) - Private Communication

(22) C. A. VERBRAAK, "Determination of Brittle-Ductile Transition in Steel With Small Specimens, in Particular with Respect to Irradiation", Colloquium on Brittle Fracture, Brussels, Jan. 1966

(23) H. C. VAN ELST, "Relation Between Brittle Fracture Tests, in Particular With Small and Large Specimens", Colloquium on Brittle Fracture, Brussels, Jan. 1966

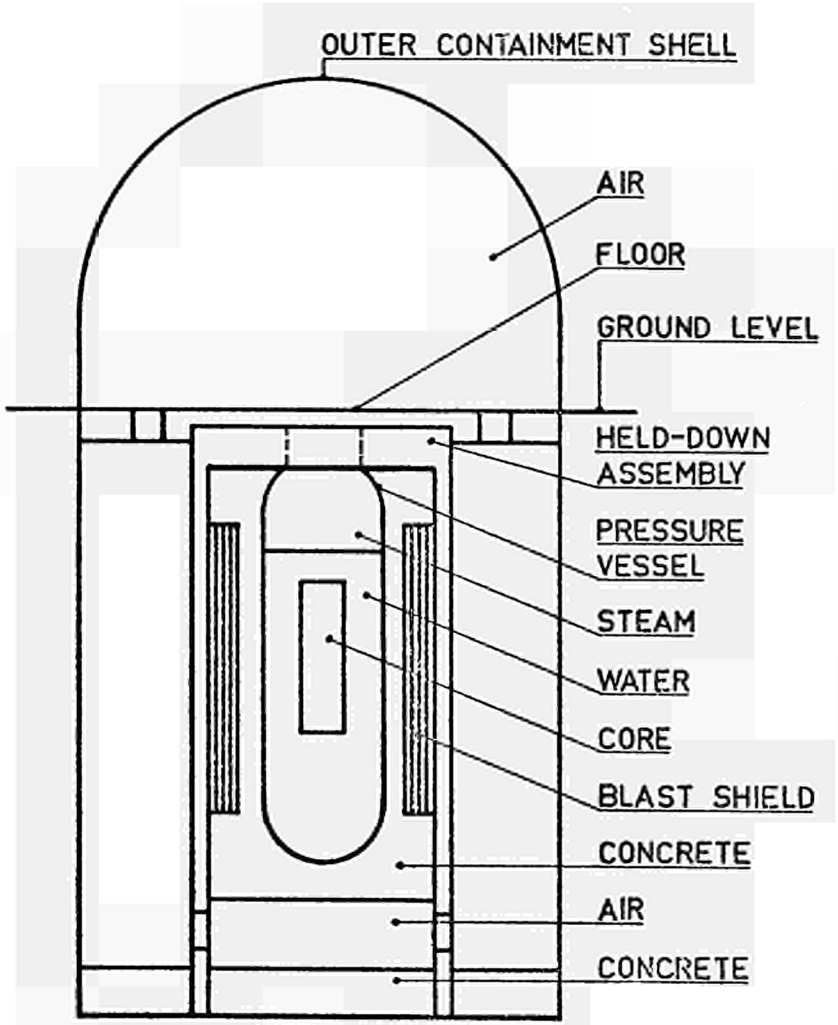

IDEALIZED COMPONENTS OF A POWER REACTOR

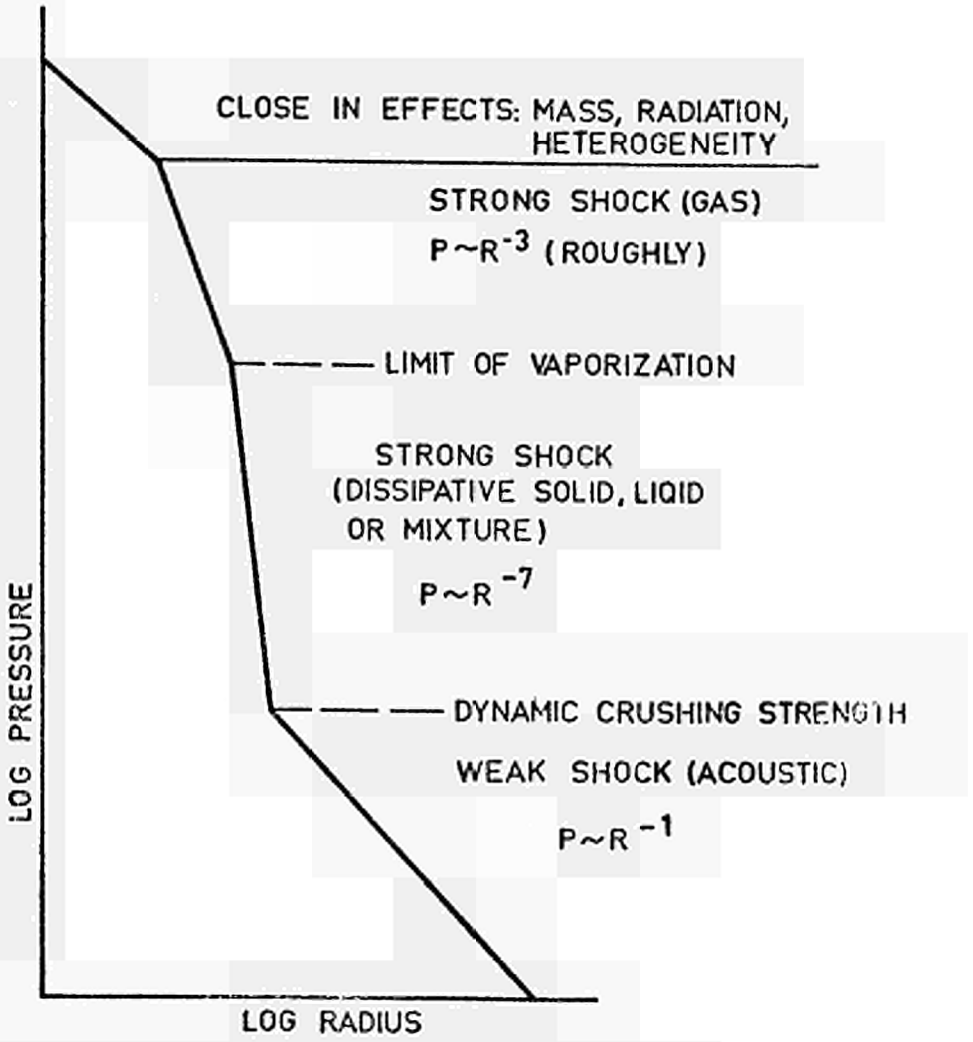

CURVE OF PRESSURE DISTANCE FROM A DETONATING CHARGE

(FROM F. B. PORZEL)

FIG. 1

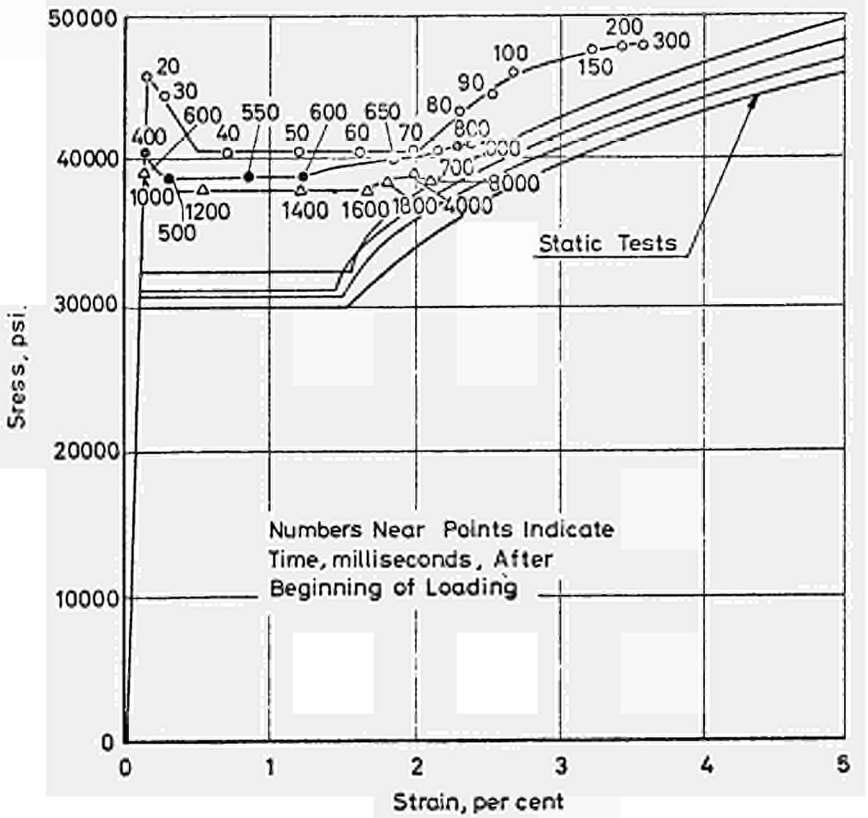

Stress versus Strain for Three Rapid Load Tests on 0,19 per cent Carbon Annealed Steel

(from D.S. Clark & D.S. Wood)

FIG. 2

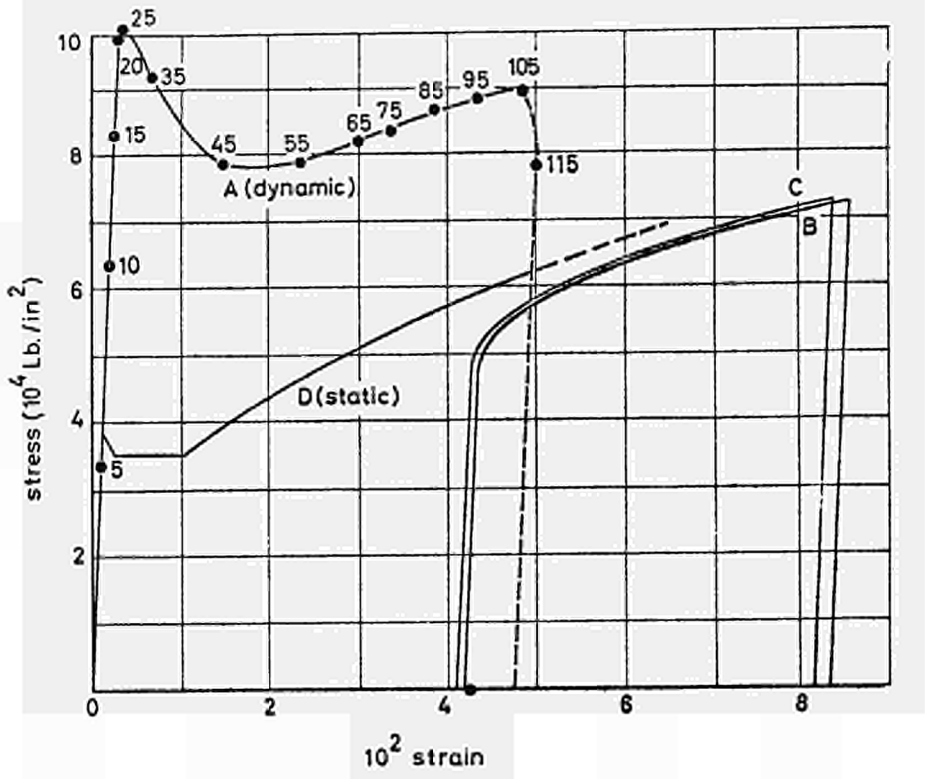

Static and dynamic stress-strain curves for 0·5 in. mild steel specimens. Curve A, dynamic loading of annealed specimens (numbers denote time in microseconds); B and C, static reloading of dynamically strained specimens; D, static loading of annealed specimen.

(from J.D. Campbell & J. Duby)

FIG. 3

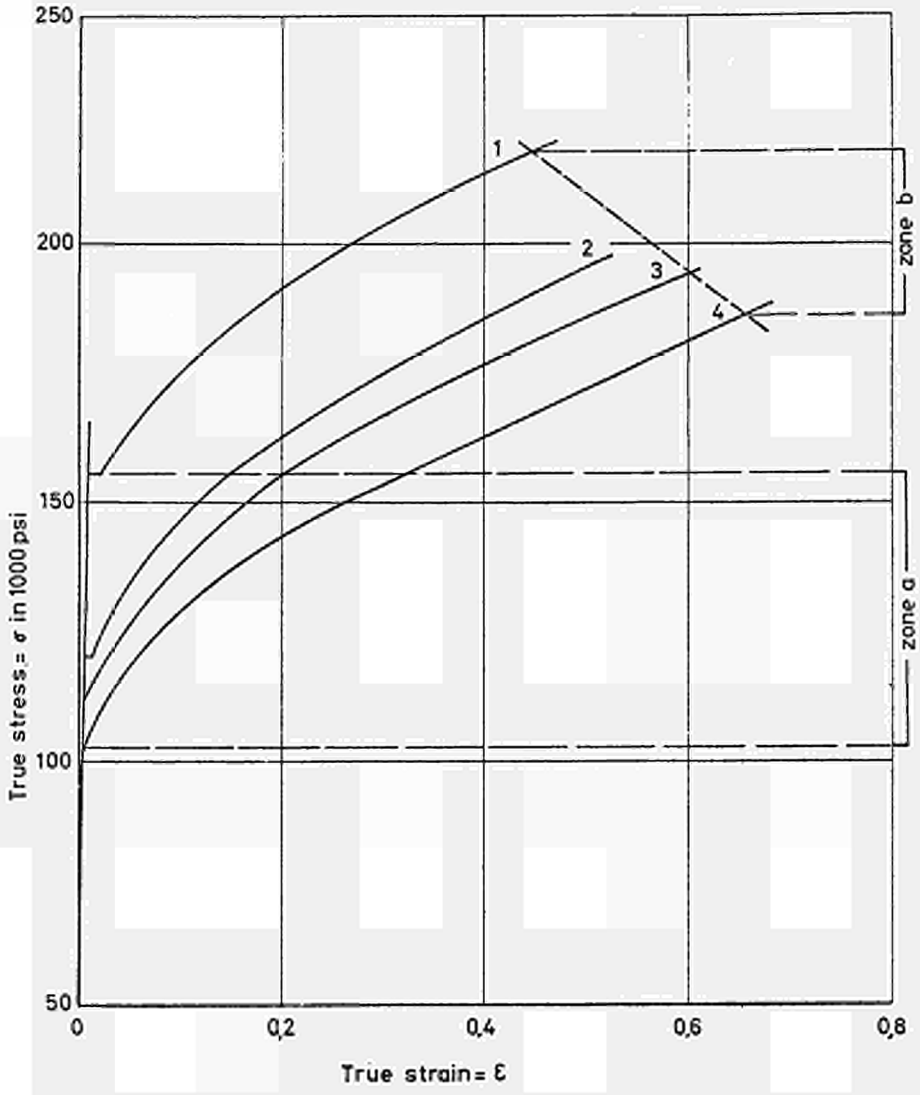

Effect of strain rate or temperature on stress-strain diagram (from curve 1 to 4 temperature is increasing and strain rate decreasing) (from C. Zener and J.H. Hollomon)

FIG. 4

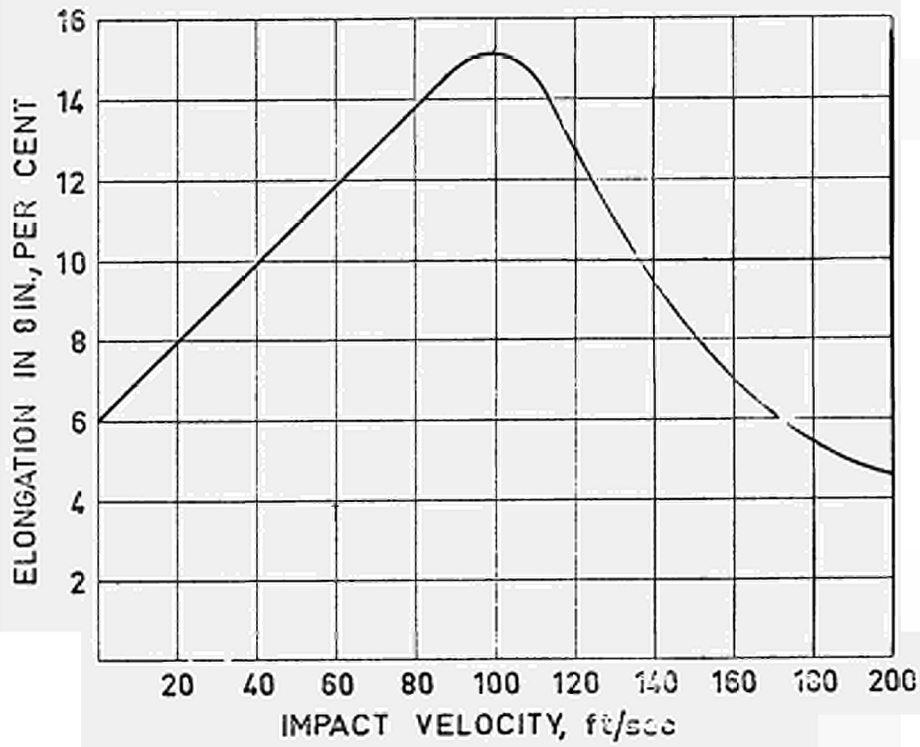

EFFECT OF IMPACT VELOCITY ON PERCENTAGE ELONGATION OF SAE 1020 STEEL, COLD-ROLLED

(FROM D.S. CLARK)

FIG. 5

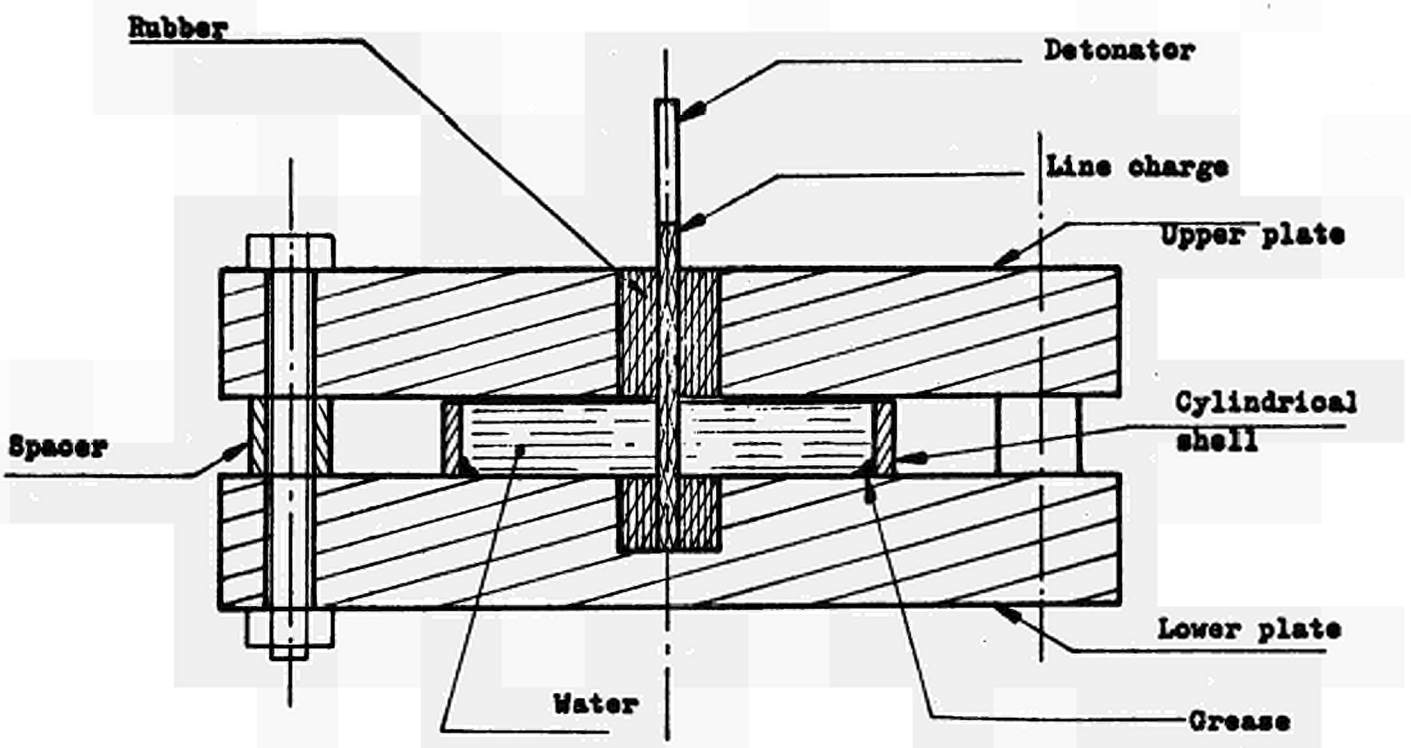

Fig.6
Cross-section showing the set-up for tests on cylindrical shell

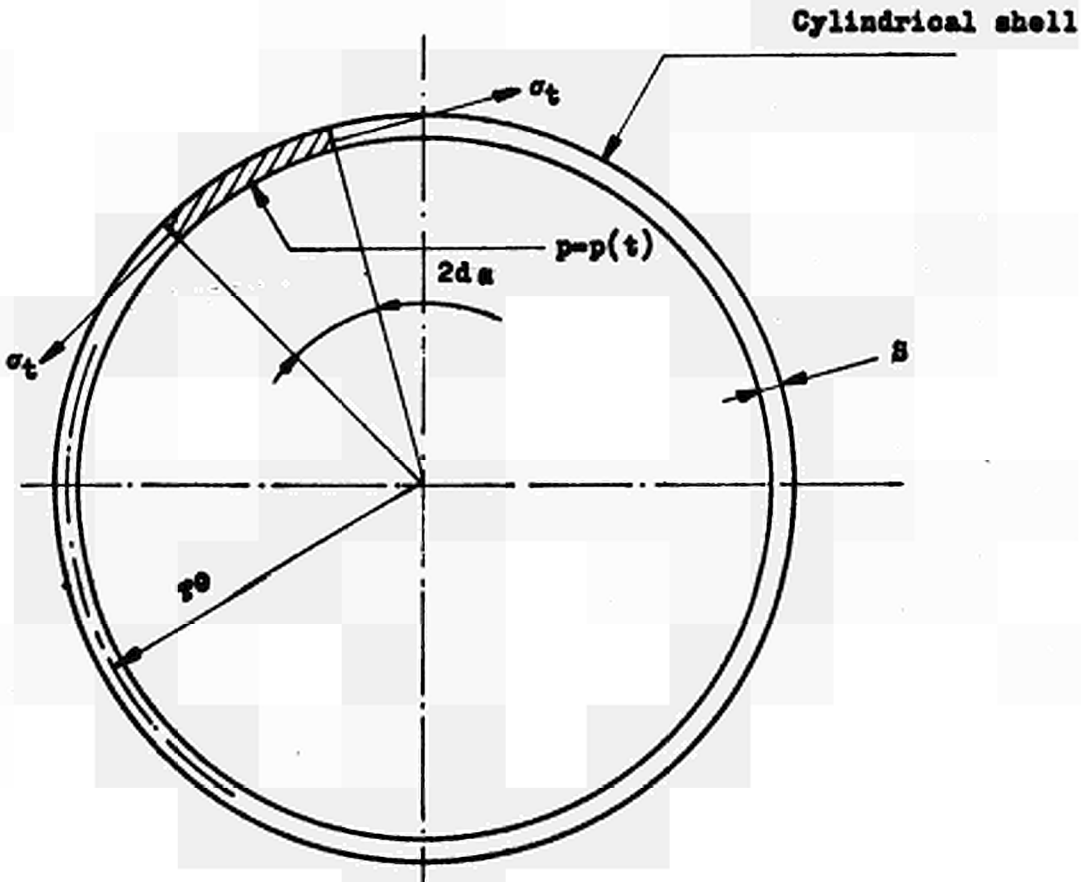

Fig.7

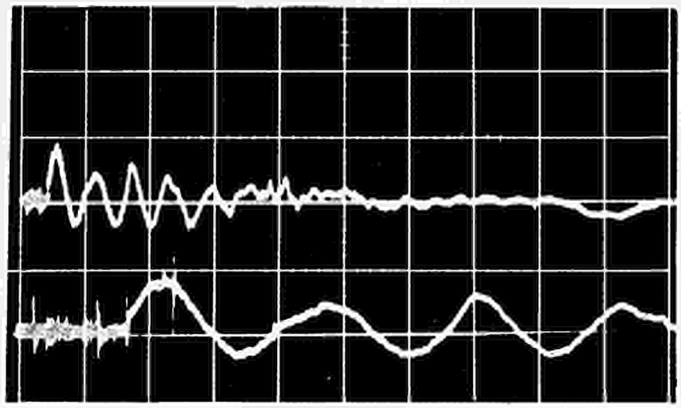

Fig. 8

Typical record of a strain induced in a cylindrical shell by an internal blast loading

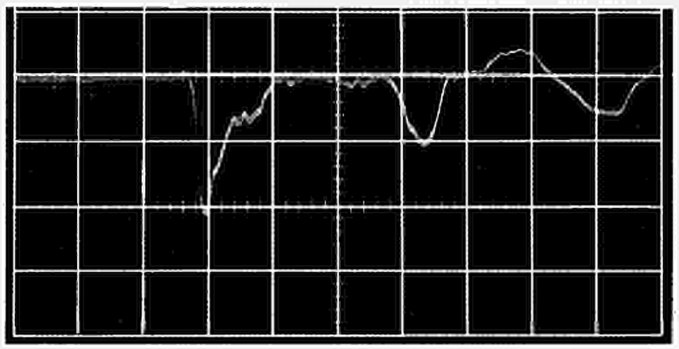

Fig. 9

Typical record of the shock wave impinging on the cylindrical shell

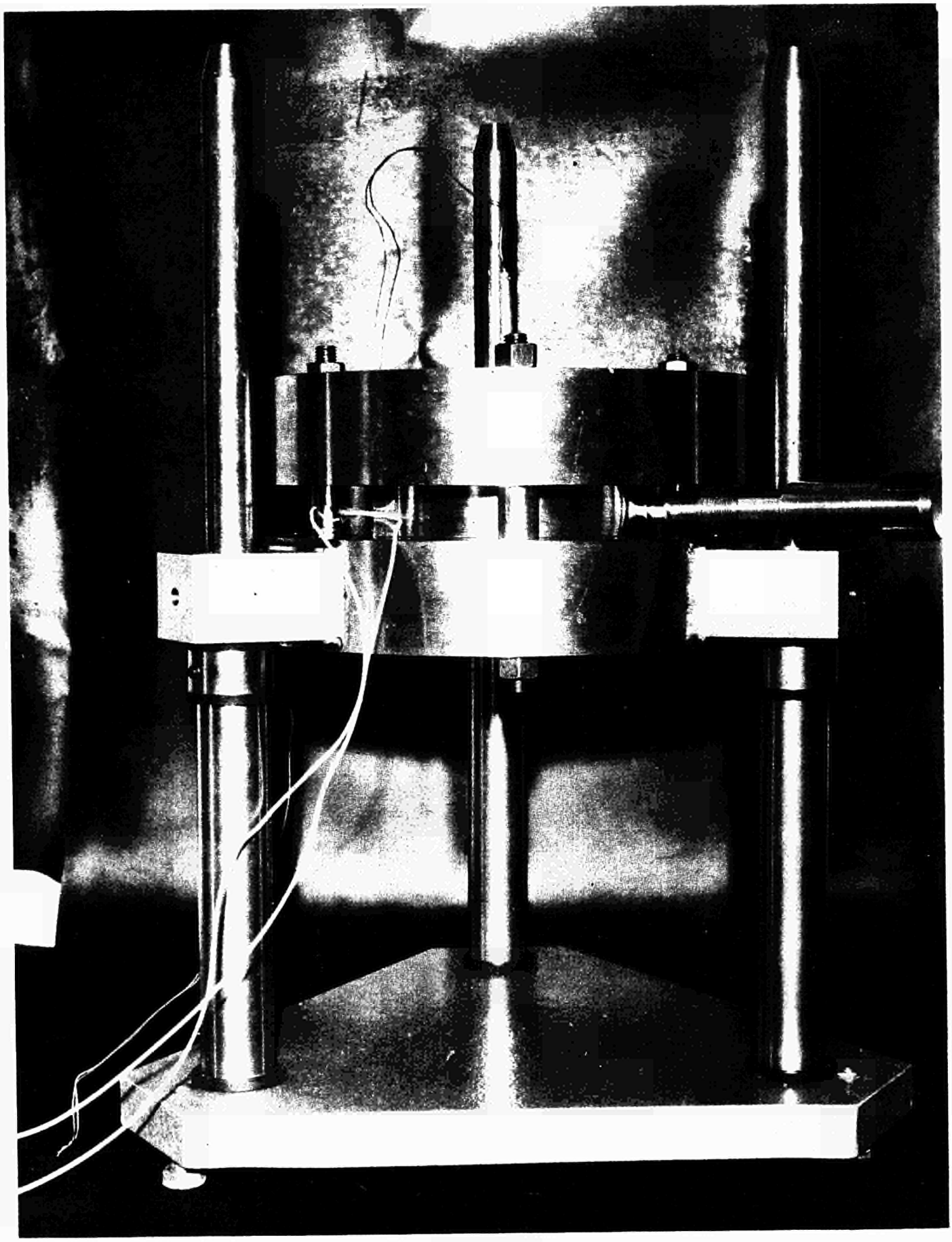

Fig. 10

SET-UP FOR TESTING CYLINDRICAL SHELLS

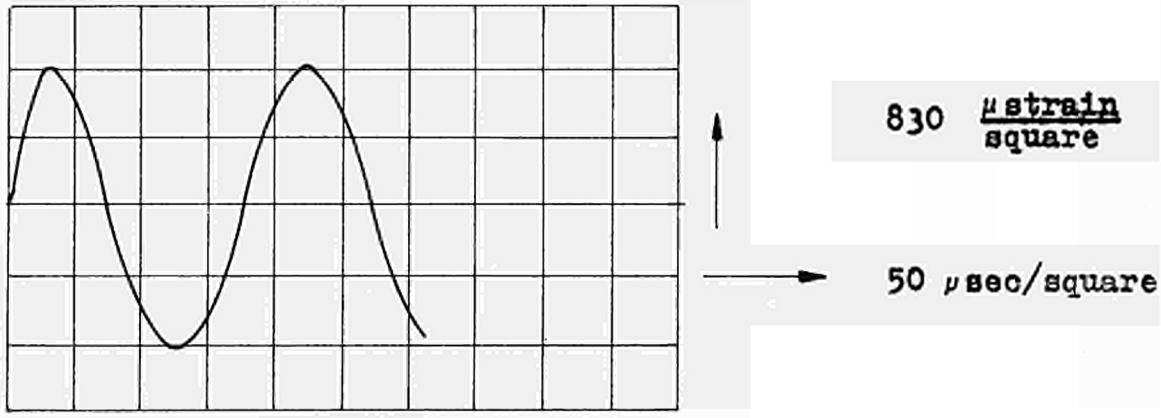

Fig. 11

Strain versus time calculated from numerical integration of equation (1) on the basis of the incident pressure wave obtained in the experiment of Figs. 12 and 13.

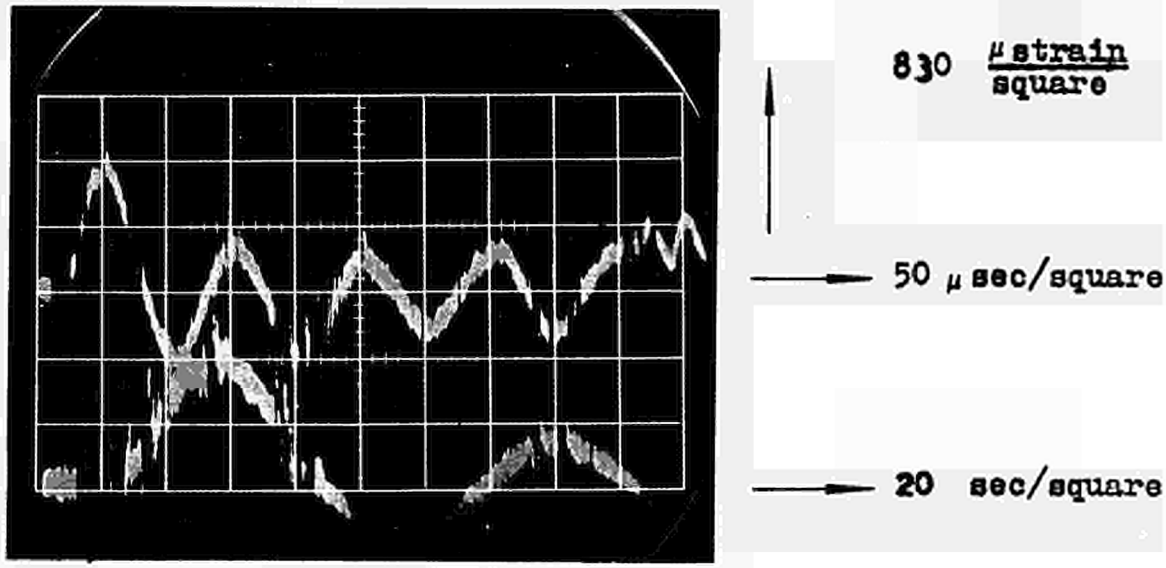

Fig. 12

Record of strain versus time. The drop of the amplitude after the first half cycle is due to water mass displacement during elastic spring-back.

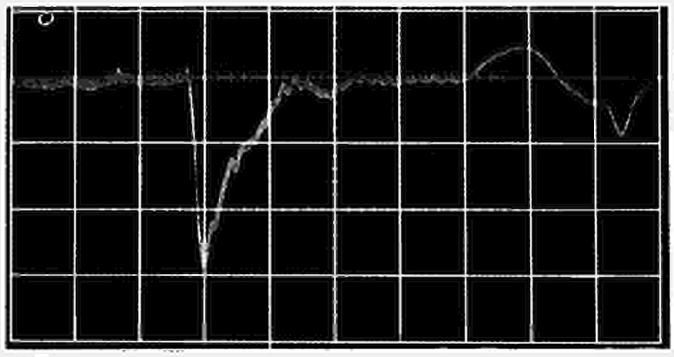

Fig. 13

Pressure record of shock wave reflected from the cylindrical shell in the same experiment as in Fig. 12.

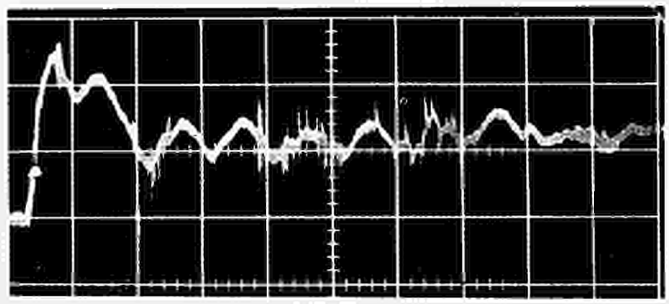

Fig. 14

Strain record of an experiment in the plastic field

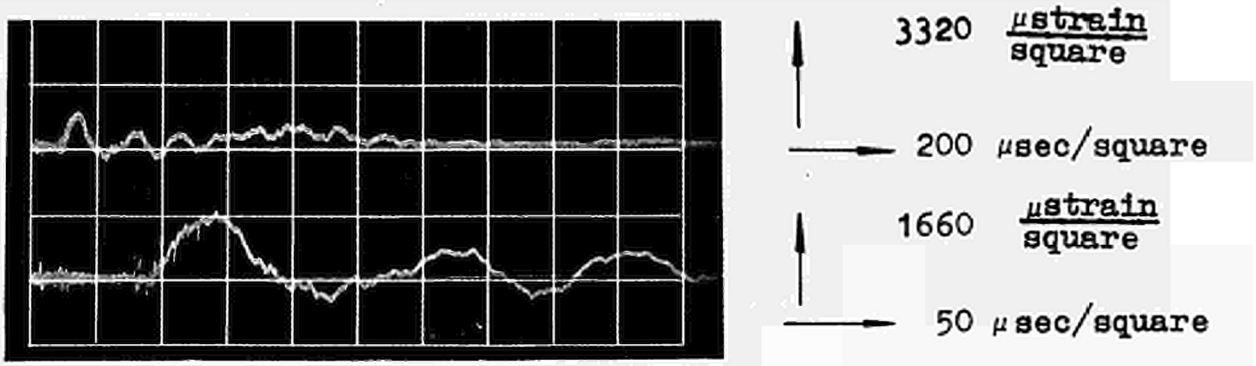

Fig. 15

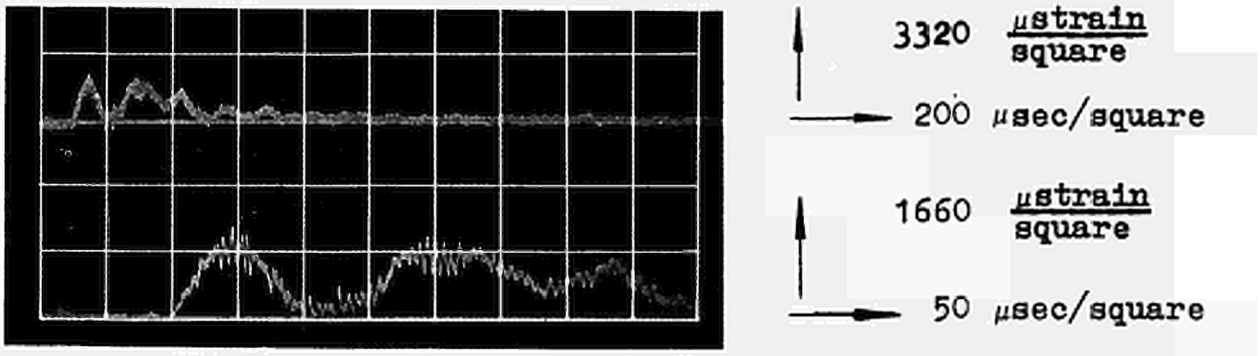

Fig. 16

Explosive charge: a twist of three lead sheathed line charges, each containing 1 gr/m of PETN.

SERIES OF TESTS FOR DETERMINING THE ELASTIC LIMIT OF DIN St. 37 STEEL

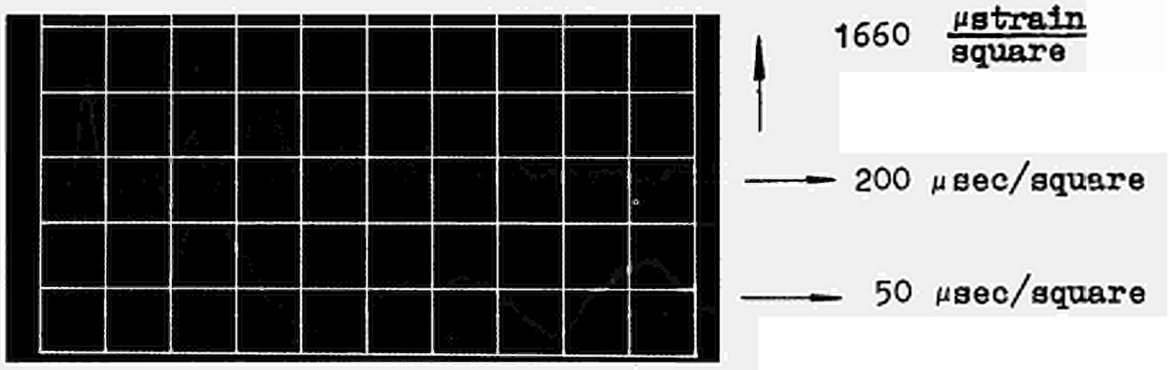

Fig. 17

Explosive charge: a twist of four lead sheathed line charges, each containing 1 gr/m of PETN.

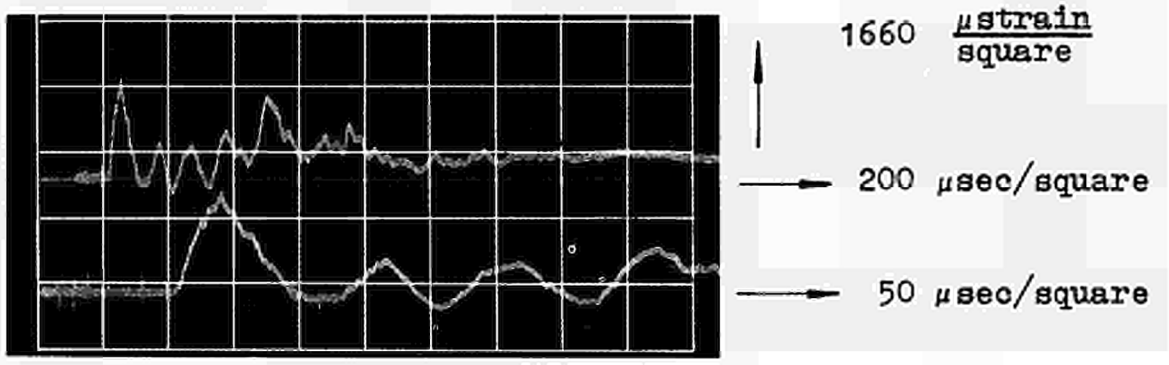

Fig. 18

Explosive charge: one lead-sheathed line charge containing 5 gr/m of PETN

SERIES OF TESTS FOR DETERMINING THE ELASTIC LIMIT OF DIN St. 37 STEEL (continued)

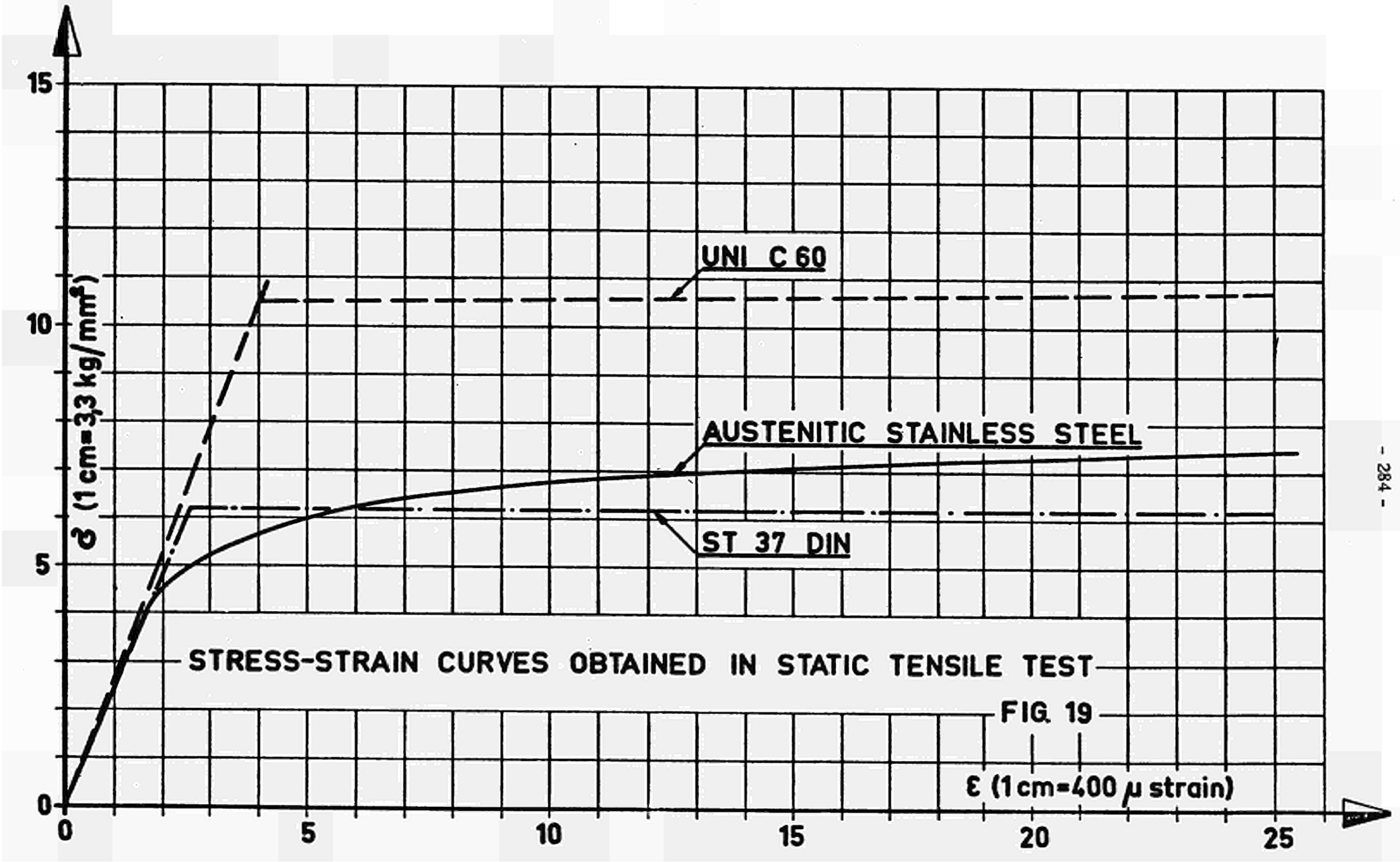

STRESS-STRAIN CURVES OBTAINED IN STATIC TENSILE TEST

FIG. 19

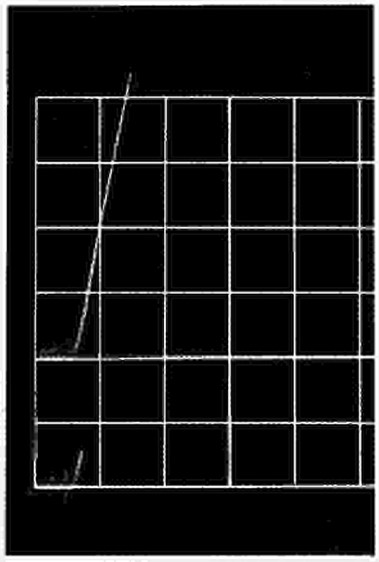

ϵ = 3.22% per square

100 μsec/square

100 μsec/square

Fig. 20

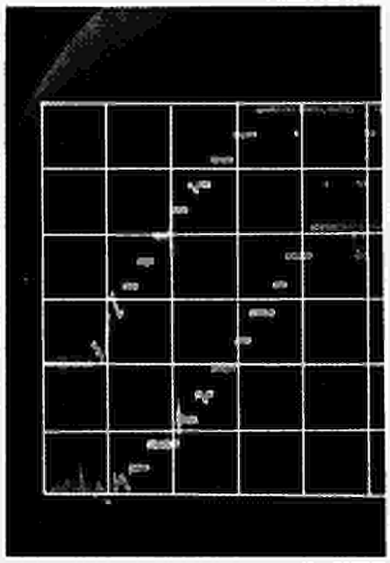

s = 3.5 mm/step

100 μsec/square

100 μsec/square

Fig. 21

Strain records obtained simultaneously by strain-gauges and pin contactors during explosion test which resulted in the rupture of the cylindrical shell.

Fig. 21a

CYLINDRICAL SHELLS OF STAINLESS STEEL (LEFT) AND UNI C 60 STEEL (RIGHT) AFTER FRACTURE DUE TO INTERNAL BLAST LOADING

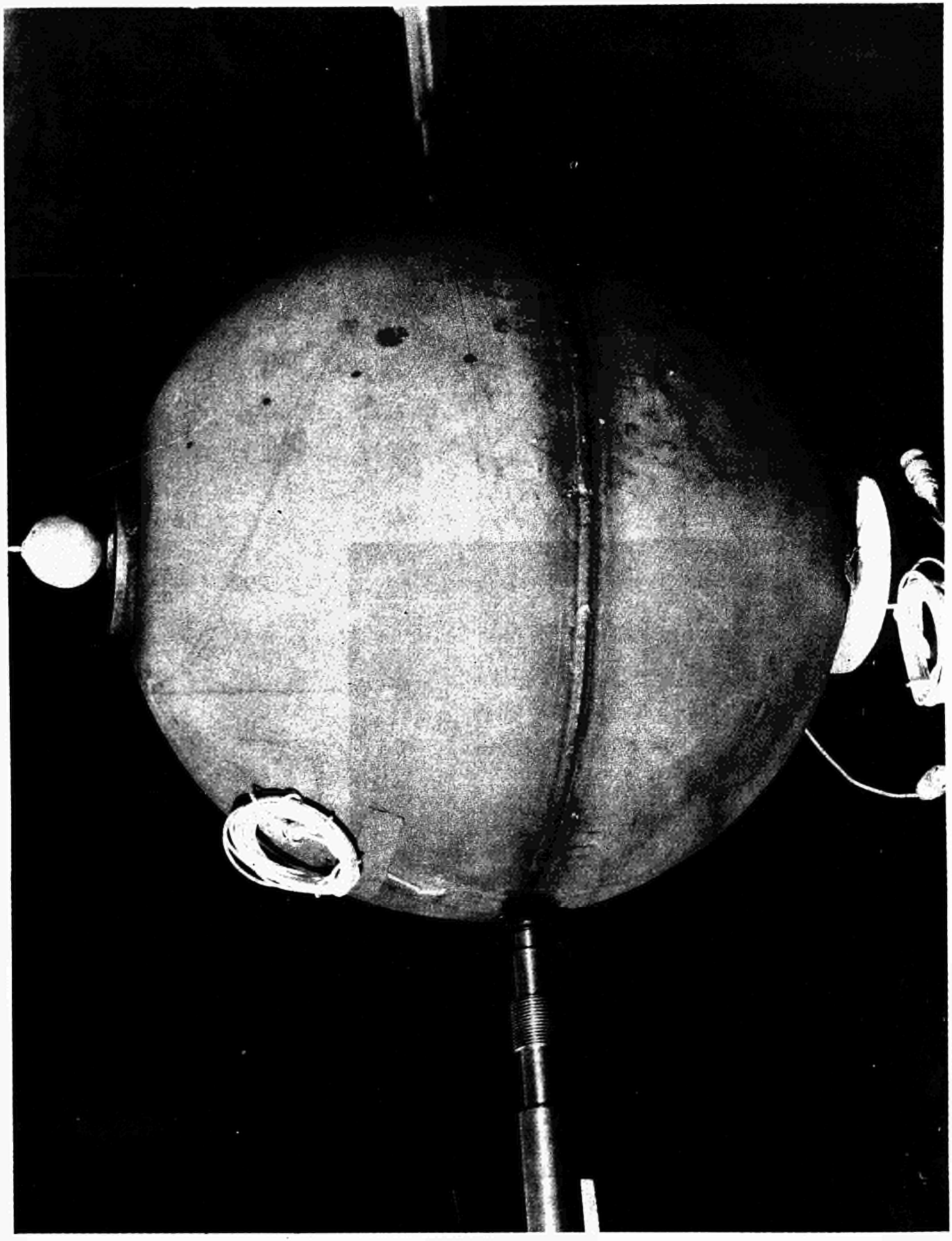

Fig. 22

MOUNTING OF THE SPHERE WITH THE PRESSURE TRANSDUCERS AND STRAIN-GAUGE FOR TESTS IN THE ELASTIC FIELD

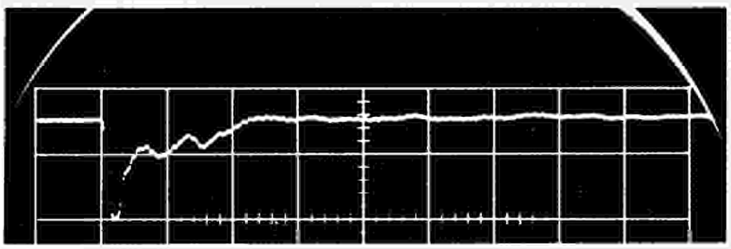

Fig. 23
pressure record

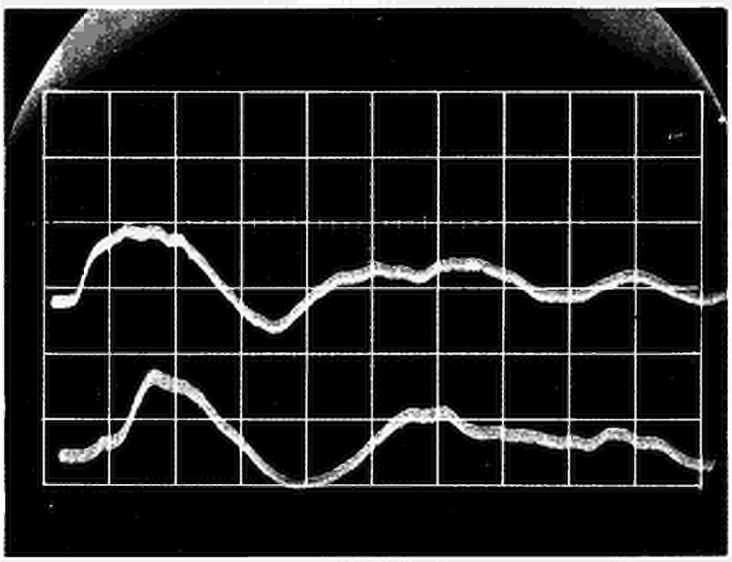

Fig. 24
strain record

PRESSURE AND STRAIN RECORDS FOR A STAINLESS STEEL SPHERE, DIAMETER 400 MM, IN THE ELASTIC FIELD USING A PLASTIT CHARGE OF 25 GR.

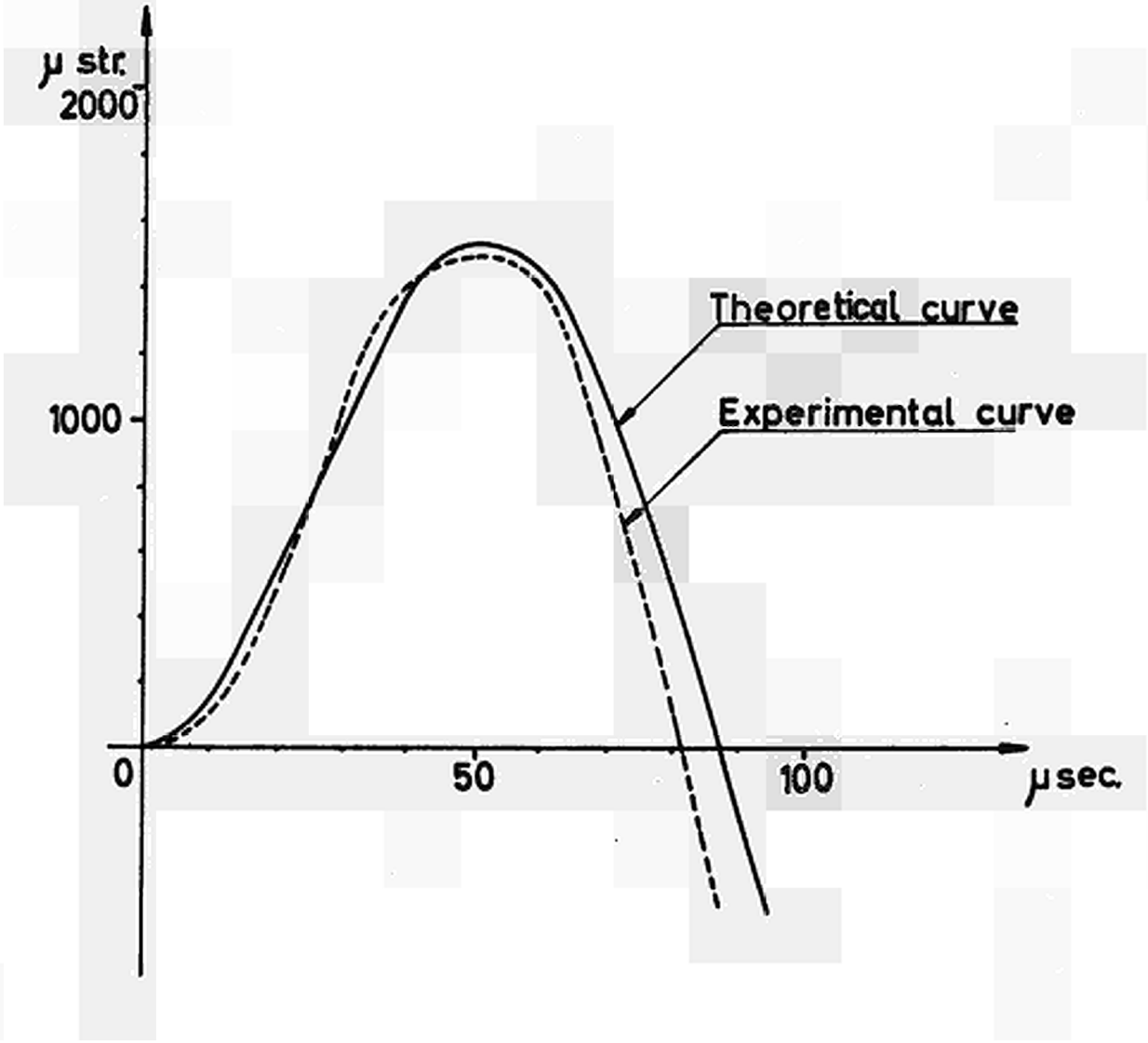

Comparison between the measured and calculated deformations of a sphere Ø 400 ST. 37

FIG. 24a

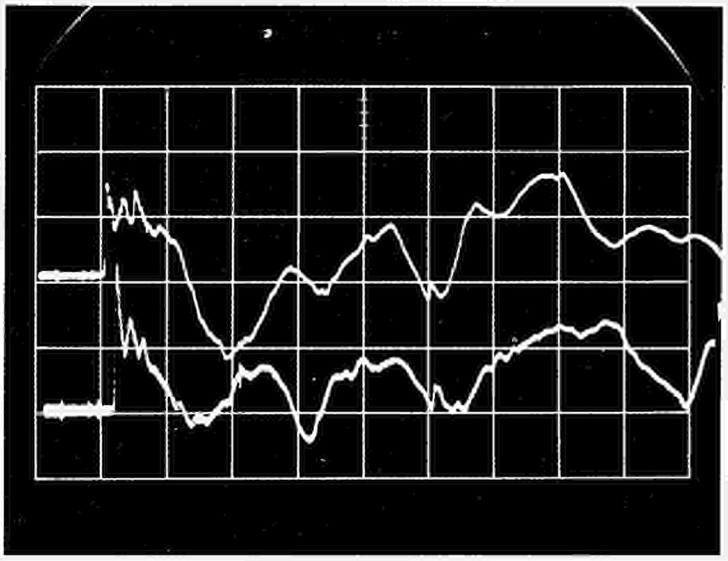

Fig. 25
Pressure record

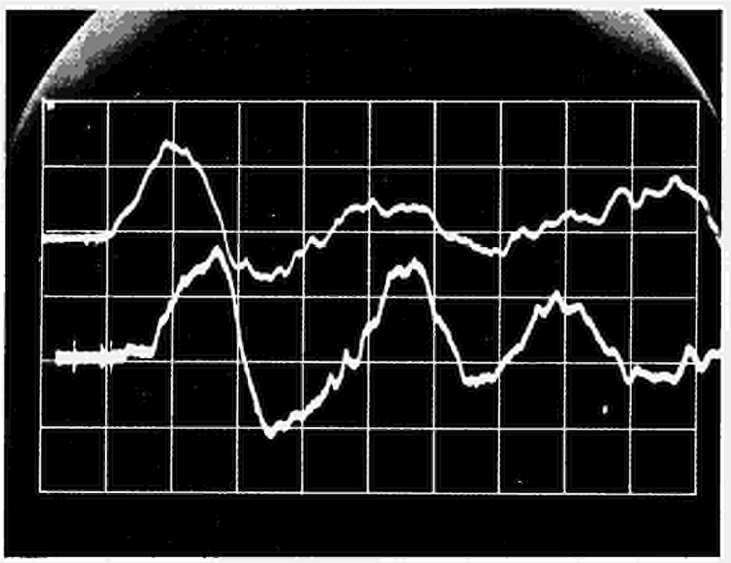

Fig. 26
Strain record

PRESSURE AND STRAIN RECORDS FOR A STAINLESS STEEL SPHERE DIAMETER 400 MM, IN THE ELASTIC FIELD USING A PLASTIT CHARGE OF 20 GR.

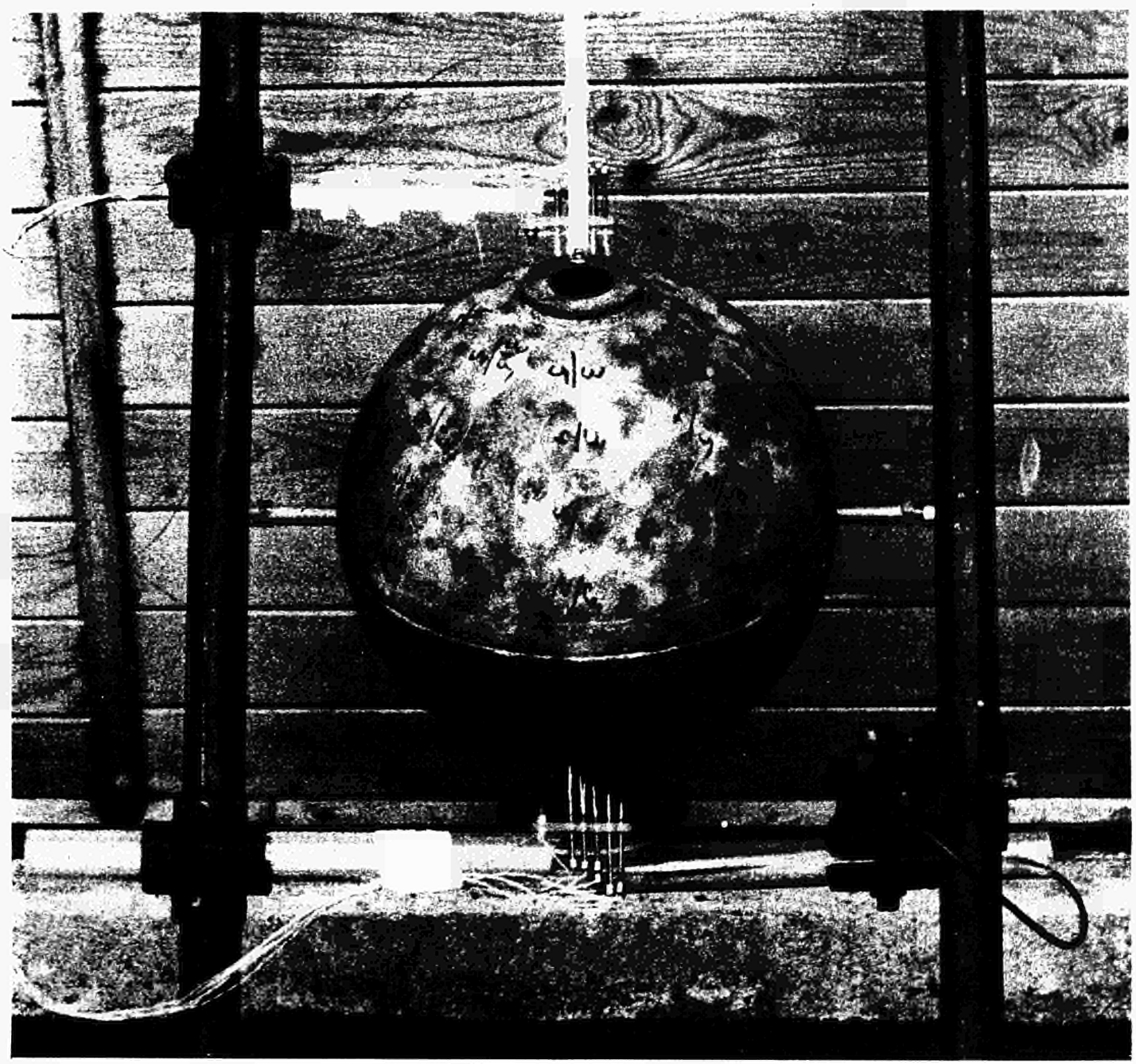

Fig. 27

MOUNTING OF THE SPHERE WITH MULTIPLE PIN CONTACTORS AND A CAPACITY GAUGE FOR DISPLACEMENT MEASUREMENTS

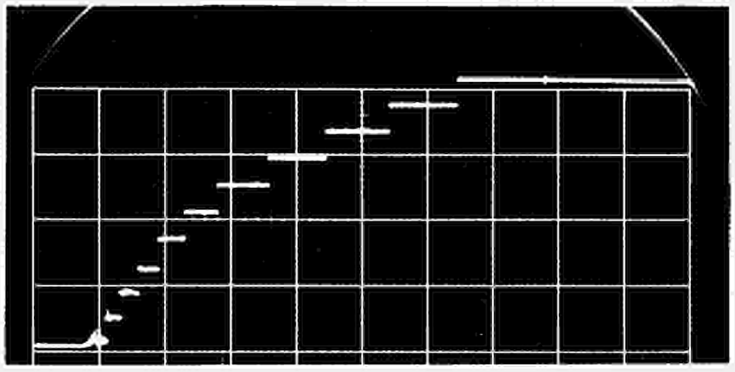

Fig. 28
pin contact signals versus time
60 gr plastit in water

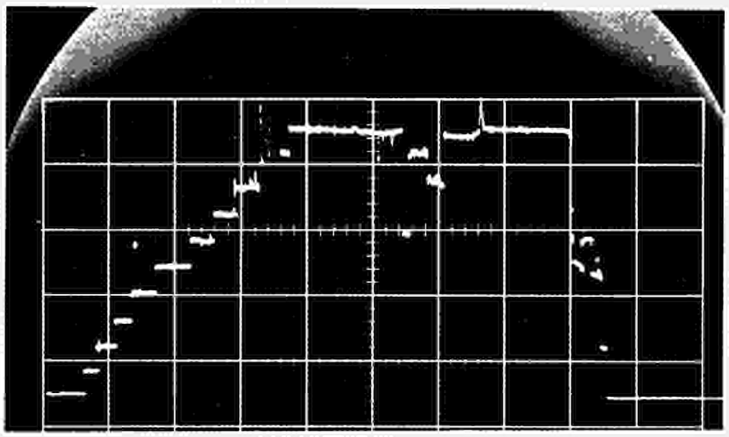

Fig. 29
pin contact signals versus time
100 gr plastit in water

RECORD OF RADIAL DISPLACEMENT VERSUS TIME
OF DIN St. 37, 400 mm DIAMETER SPHERE

Fig. 30
Stainless steel, 250 mm diameter sphere after explosion with 80 gr plastit in air

Fig. 31

St. 37 DIAMETER 400 mm SPHERE AFTER EXPLOSION
WITH 500 gr PLASTIT IN WATER

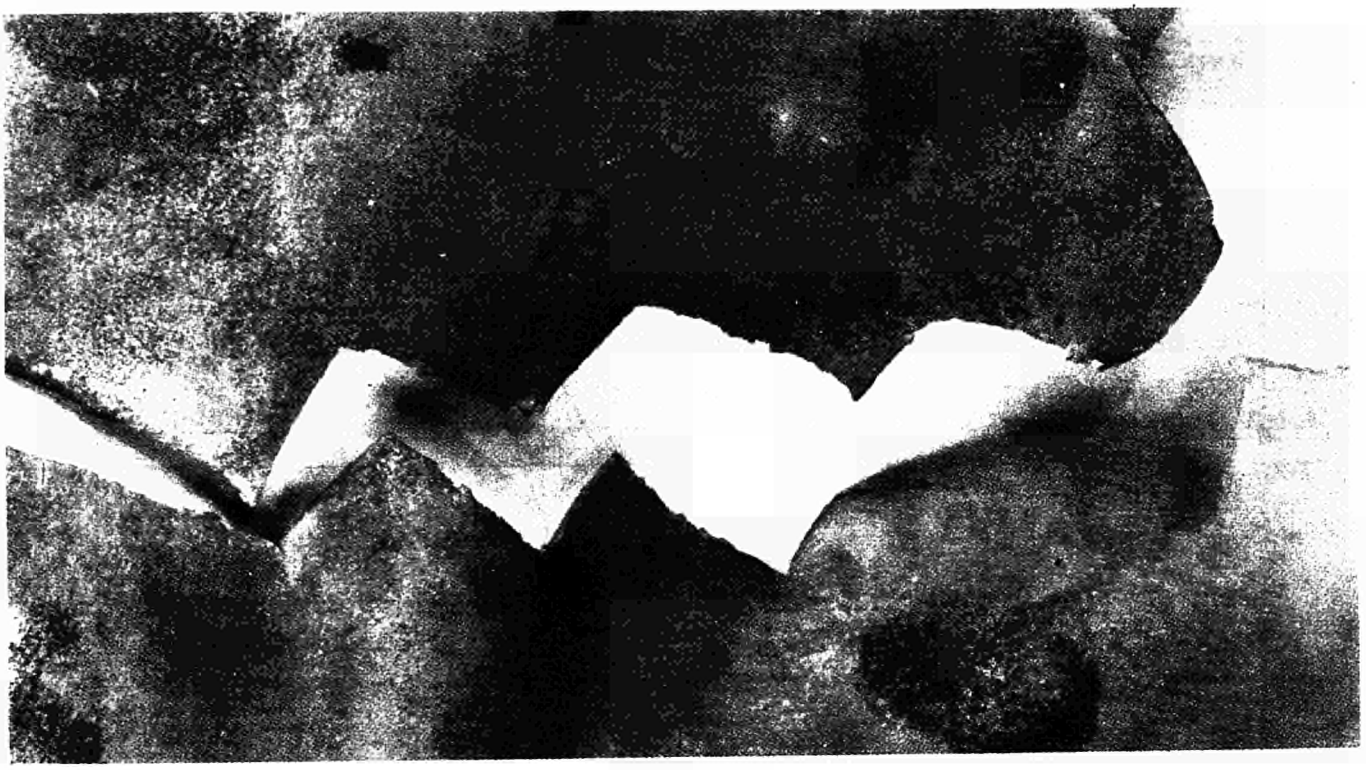

A

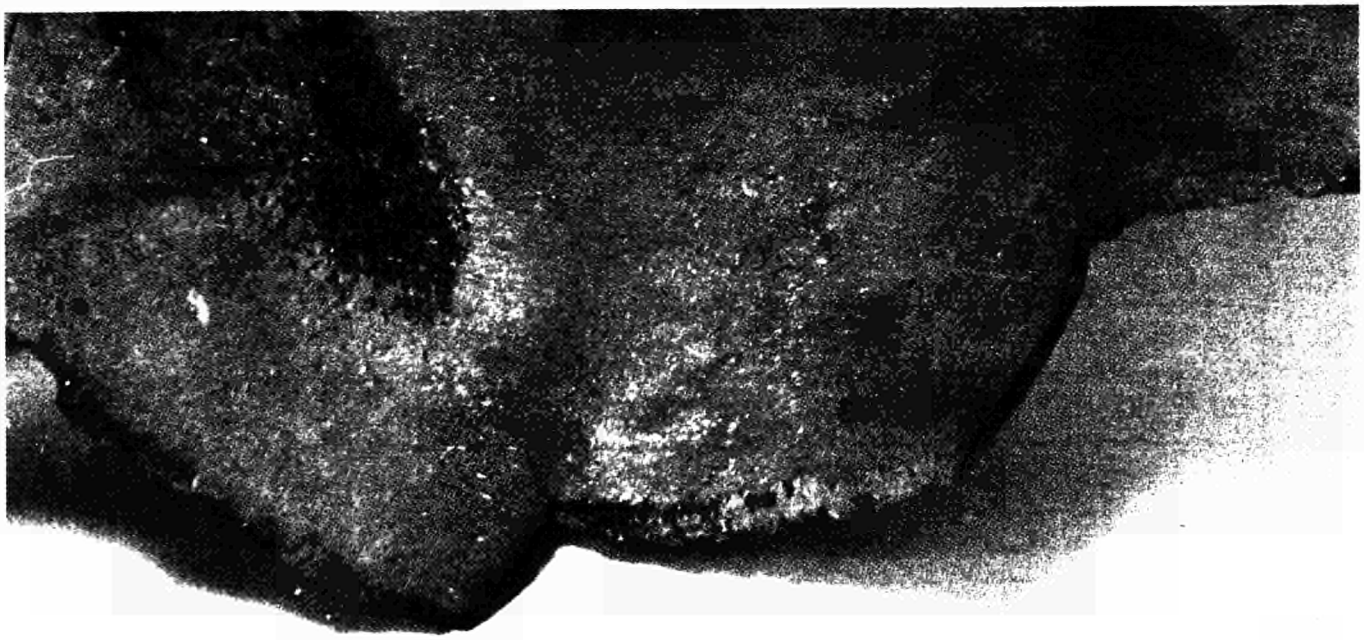

B

Fig. 32

DIN St.37, diameter 400 mm sphere (as in Fig. 31)
details of shear-cleavage fracture
(A: 1.3 x) (B: 1.9 x)

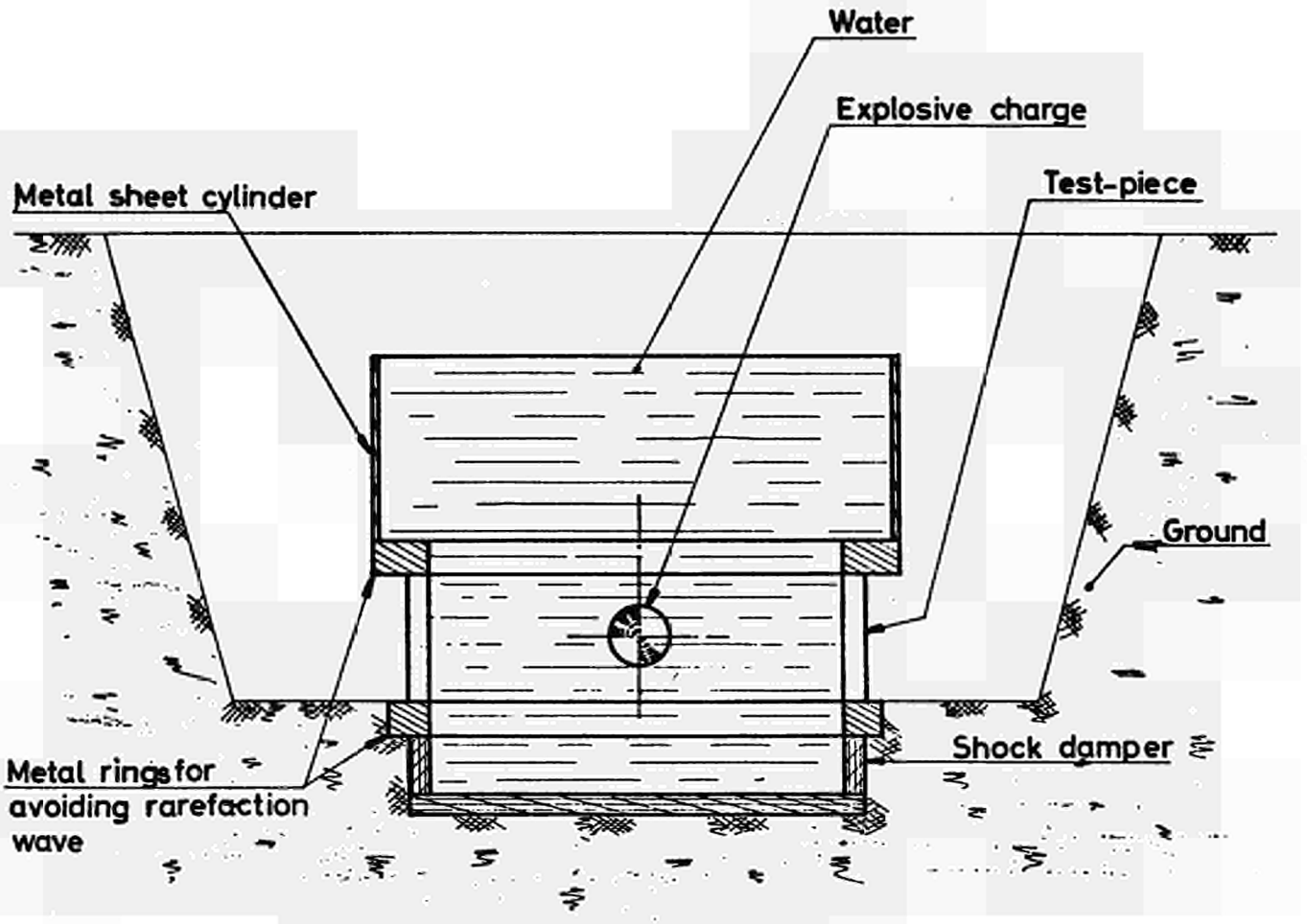

fig_ 33 PROTOTYPE TEST SET-UP

APPENDIX I

MECHANICAL CHARACTERISTICS

Material as cited in report	St. 37	UNI C 60	austenitic 18/8 stainless steel	DIN 4300 stainless steel
Norm	DIN 17100 St. 37-2	2954 UNI C 60	AISI 304	DIN 4300 x 12 CrNi 188
E kg/mm^2	20,900	21,000	19,600	---
$\sigma_{0.01}$ kg/mm^2	21.6	34.5	15.5	
$\sigma_{0.1}$ kg/mm^2	21.9	34.8	24.5	---
$\sigma_{0.2}$ kg/mm^2	21.7	35.2	25.8	36.7
σ_u kg/mm^2	31.8	60.5	59.8	61.6
true strain %	163	91	233	62
uniform strain %	25	17.5	49.5	---

CHEMICAL COMPOSITION

C	0.8	0.6	0.06	0.06
Mn	--	$\leq$ 0.8	$<$ 2	1.6
Cr	--	--	18 + 20	18
Ni	--	--	8 + 12	9.2
Si	--	$\leq$ 0.35	$<$ 1	0.45
P	$\leq$ 0.175	$\leq$ 0.035	$<$ 0.04	0.03
S	$\leq$ 0.063	$\leq$ 0.035	$<$ 0.03	0.017

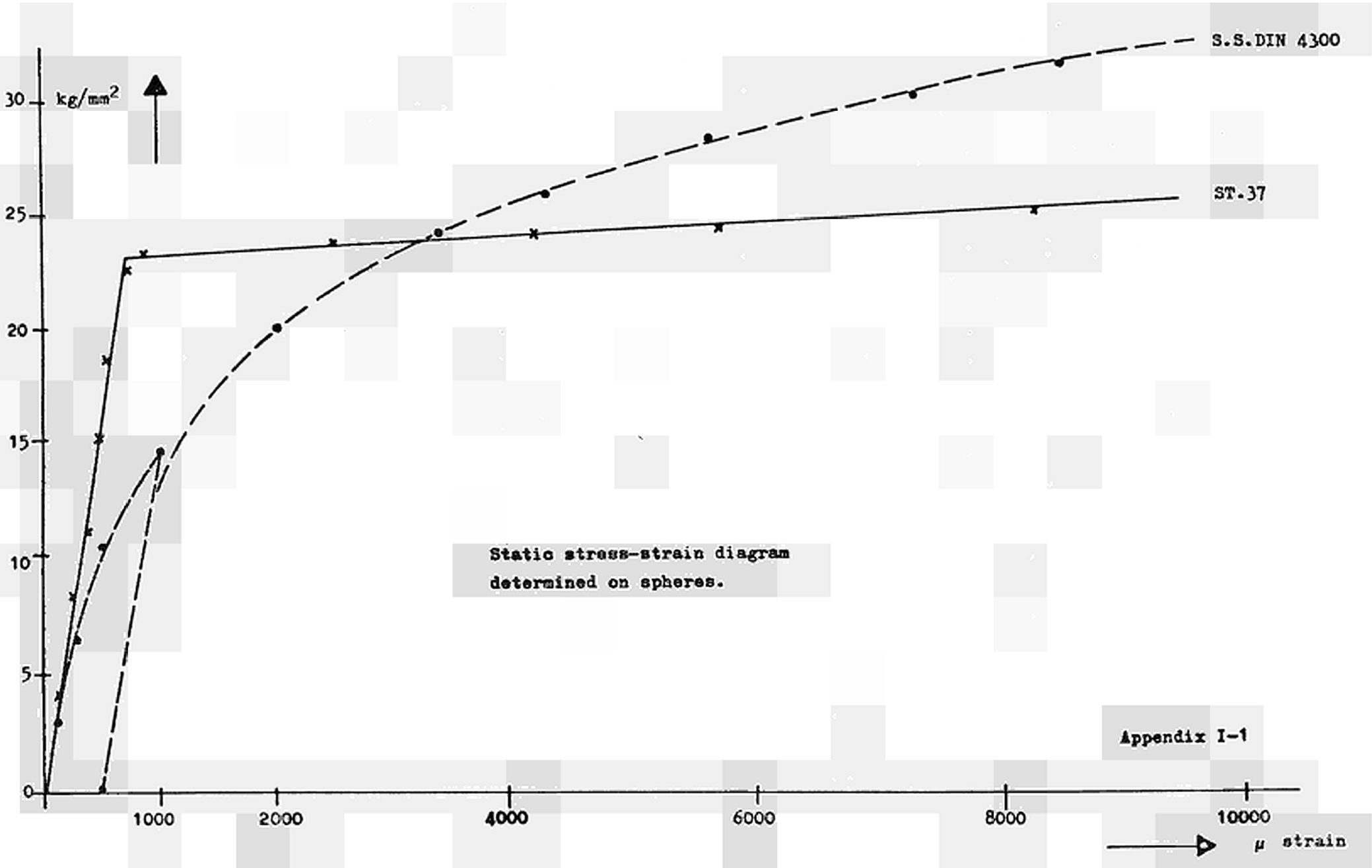

Static stress-strain diagram
determined on spheres.

Appendix I-1

APPENDIX II

APPARATUS FOR IGNITING THE EXPLOSIVE (E. Jorzik)

A circuit diagram of the apparatus for exploding a wire of 0.05 mm diameter has been represented in fig. II-1. The apparatus consists of two main parts: the condenser with a high voltage supply, and the triggering mechanism with a spark-gap.

For a high voltage condenser a Bosch 0.5 μF and 25 KV impulse condenser was chosen. The high voltage was obtained by a leakage transformer with a secondary voltage of 7 KV and a rectifier tube. In this way the condenser is charged to 14 KV.

The spark-gap is directly connected to the condenser terminal. The trigger impulse is fed concentrically to an electrode. A small condenser is switched on by a hydrogen thyratron, and discharges onto the primary windings of a transformer which gives an impulse to the ignition electrode. The control grid of the thyratron receives a steep positive impulse from a switch-transistor.

In order to keep down the total inductance which consists of inductances of the condenser, a connection cable and the explosive wire, two parallel connected coaxial cables were used. The smallest discharge time of the condenser obtained was about 3 μ sec.

The ignition delay is about 0.5 μ sec, and is constant. The noise level resulting from the current-discharge becomes negligible 10 μ sec after the ignition, allowing measurements to be made with an oscilloscope.

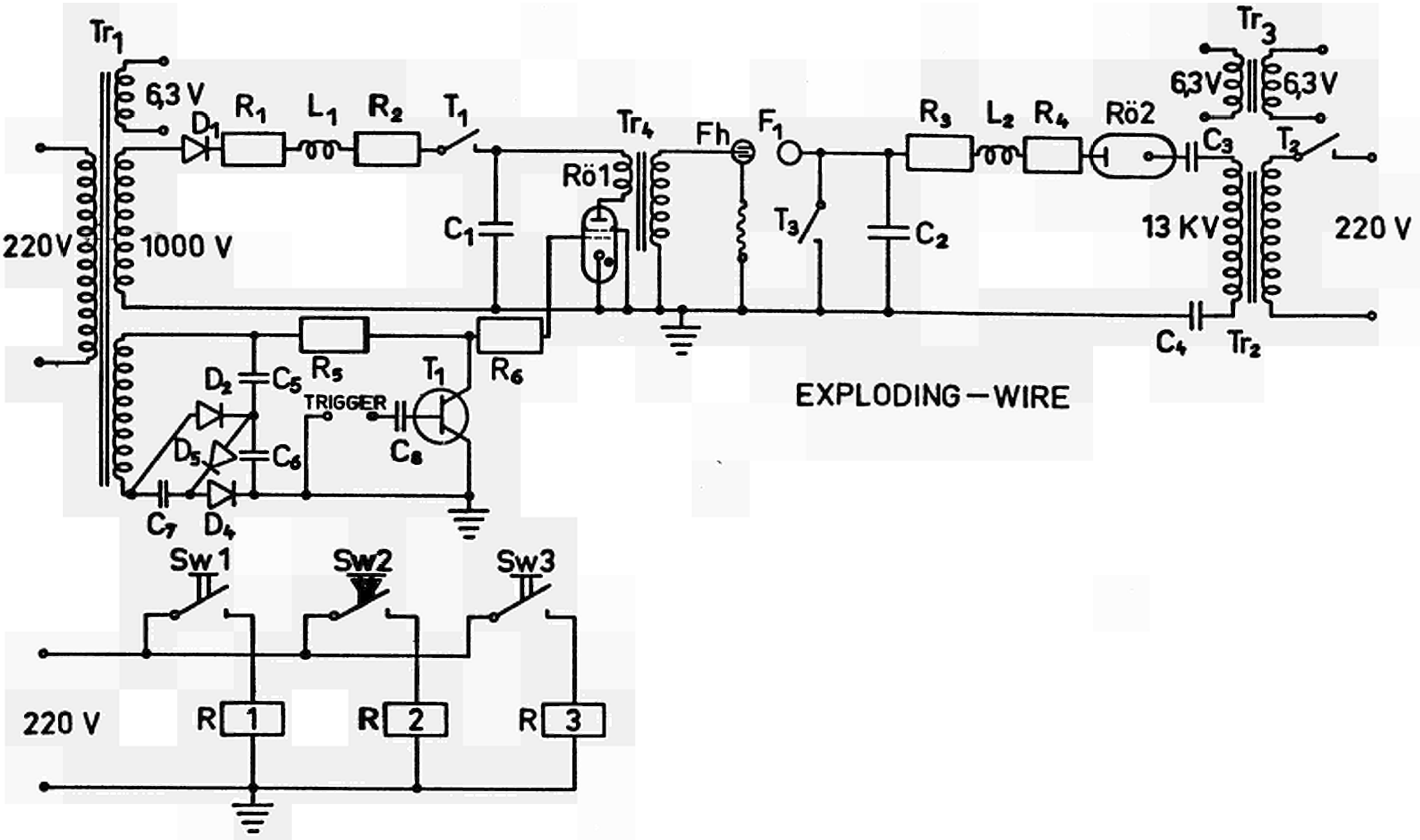

FIG. II 1 CIRCUIT DIAGRAM FOR WIRE EXPLODING DEVICE

APPENDIX III

1. PIN CONTACTOR METHOD

In order to be able to measure the large deformations of a sphere or a cylinder (since the strain-gauges are incapable of following a deformation greater than 7%) it was decided to calculate the mean strain by measuring the global deformation of the structure through ten contacts. The distance between these contacts and the walls is regulated by a screw with a pitch of 0.7 mm. By placing the contact so that it touches the wall, whose displacement it is desired to measure, the zero position of the individual contact is established. In this way the height of the points can be set at known distances from each other and from the wall, with an accuracy of $\pm$ 0.1 mm. The measuring device is shown in the following diagram.

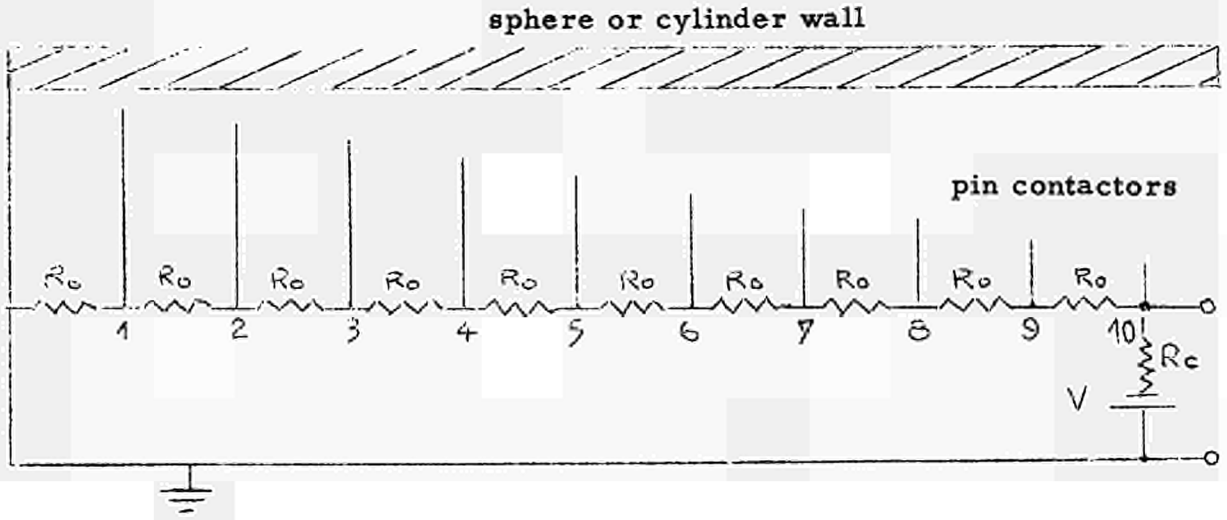

The potential of point 10 decreases by 1/10 of the initial value when it touches the first point, by 2/10 when it touches the second, and by n/10 when it touches the nth. For this relation to be valid it is necessary that $R_c >> 10\ R_o$. By placing the nth point at a distance n times greater than the first, we can make an oscillograph which we can interpret as the curve of the displacement of the wall. The photographs 21, 28 and 29 give examples of the results obtained by this method.

2. CAPACITIVE METHOD (E. Jorzik, Y. Lachapelle)

The capacitive variations are measured between a spherical fixed bowl of 16 cm diameter and the wall of the sphere (fig. III-1). The relative motion be-

tween the plate and the sphere causes a variation in distance between the two poles which is initially of about 7 cm. The capacity variations are transformed linearly into frequency variations by means of an oscillator which is attached to a Southern F. M. amplifier model containing a discriminator circuit.

In this way a signal is obtained on the oscillograph, directly proportional to the capacity variations. Given that the capacity of the condenser is not a linear function of the distance of the two poles, it is necessary to calibrate before every experiment. The measurement system adopted (F. M.) permits a static calibration. Fig. III-2 shows the determination of the displacement curve versus time obtained from the curve signal voltage versus time and from the calibration curve. The maximum recordable frequency of the system is of about 50 Kc/sec.

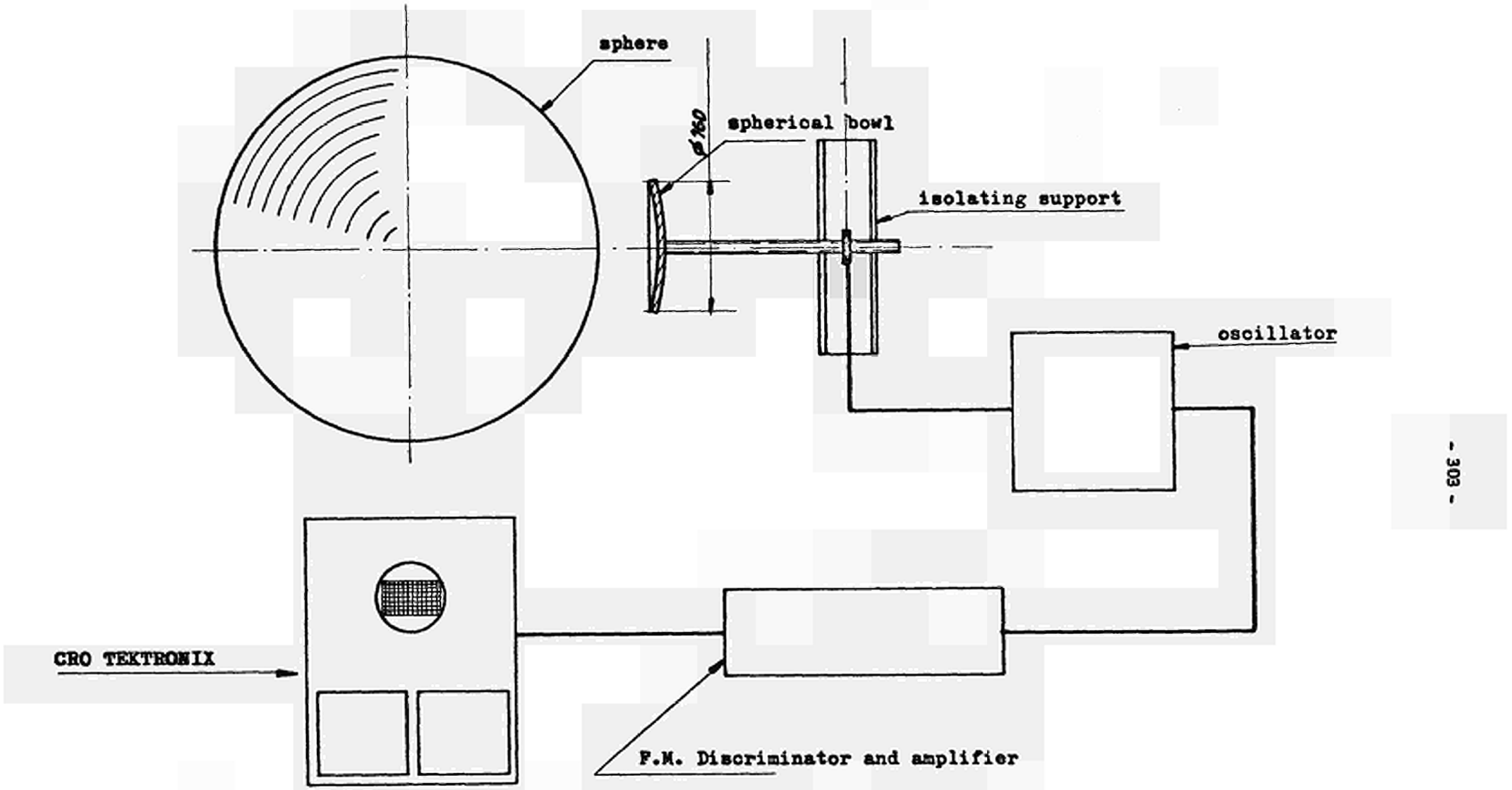

Appendix III-1 - Capacitive displacement measuring system.

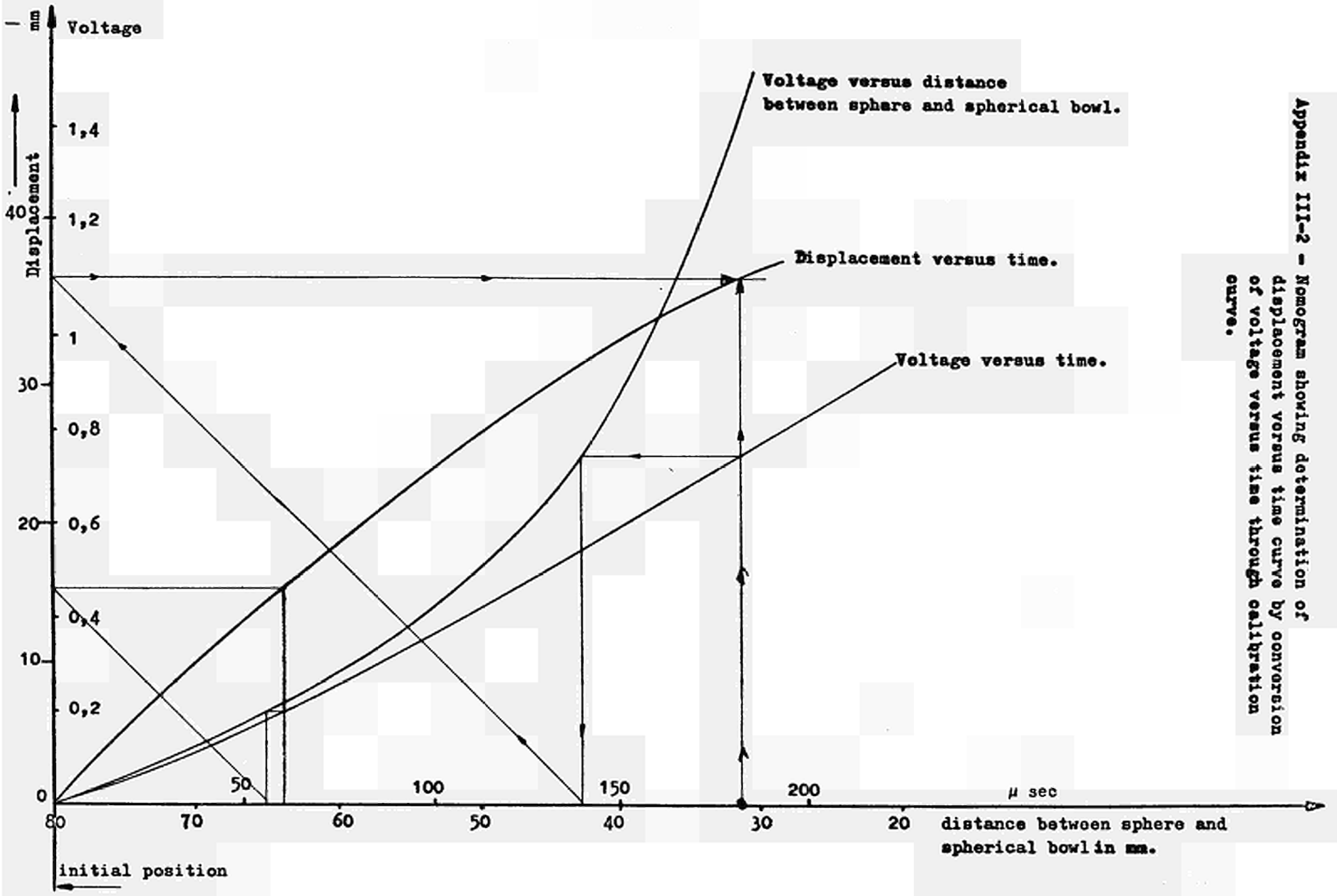

Appendix III-2 - Nomogram showing determination of displacement versus time curve by conversion of voltage versus time through calibration curve.

EXPLOSION TESTS OF ARC WELDED STEEL TUBES

by

H. Kihara* and K. Iida**

University of Tokyo

Tokyo, Japan

1. Introduction

The present paper summarizes two experimental studies[1,2] published in Japanese in 1956 and 1958.

Under dynamic load the brittle fracture of welded steel structure can occur at a temperature higher than the critical temperature under static load, and, as it is widely known, the higher the loading rate is, the brittler the fracture mode tends to be. The fracture mode is also affected by material properties, welding procedures such as manual welding, submerged arc welding and so on, and treatments after welding such as stress annealing, peening and low temperature stress relieving.

The object of the investigation summarized in the present paper was to examine the contributions of the above mentioned factors to brittle fracture characteristics of welded tubes under explosion impact load.

In preliminary tests a mine of TNT was put directly on a welded steel plate and was detonated, but, contrary to the authors' expectation, a layer of steel of almost the same area of the bottom of the explosive came off from the other surface of the plate than the surface on which the explosive was placed.

Accordingly, the method that a mine of TNT set at the center of the tube specimen filled with liquid medium was adopted for the tests, and that was the same procedure Folkhard[3] employed. By this method welded tubes without any particular artificial notch were able to be successfully fractured in a brittle manner.

2. Experimental Technique

2-1. Materials and Specimens

---

* Professor, Dr.-Eng., Department of Naval Architecture, University of Tokyo.

** Assoc. Professor, Dr.-Eng., Department of Nuclear Engineering, University of Tokyo.

18 kinds of tube specimens, whose designations and numbers are listed in Table 1, were used in the explosion impact test to investigate the effect of material, welding method, stress annealing, low-temperature stress relieving and peening on the fracture behaviour of tube specimen. Materials of the specimens were a common structural mild steel (designated as MS steel) and three kinds of high tensile steels with 50 kg/mm^2 or 60 kg/mm^2 tensile strength (designated as 50 HT steel, 60 HT steel and 2H steel respectively). Chemical analysis, mechanical properties and V notch Charpy impact values of the steels used are given in Table 2 and Table 3 respectively.

Figs. 1 and 2 show the details of the tube specimen with dimensions of 20 mm in thickness, 400 mm in inner diameter and 800 mm in length. Details of joint preparation and welding sequence for the specimens with high strength steels are illustrated in Fig.1, and for the mild steel specimen in Fig. 2. All joints of the specimen were but welded in flat position with back chipping after the welding of backing side.

For the mild steel specimen longitudinal joints were welded first by manual welding, and then the circumferential joint was welded. X ray inspection, of which results are given in Table 4, were carried out over the whole length of welded joints. 8 of mild steel specimens (designated as AW specimen) were tested in as-welded condition, and 6 of mild steel specimens (designated as SR specimen) were tested after the stress annealing at 650°C for 1 hour.

High tensile steel specimens were fabricated as follows; two plates cylindrically cold-bent were made into a unit tube by welding longitudinal joints and after X ray inspection of the joints and stress annealing at 650°C for 1.5 hours two unit tubes were assembled by welding a circumferential joint, and then finally the circumferential joint was inspected by X ray radiography.

Specimens with the designation of L in Table 1 were stress relieved by the Linde method with the following condition:

breadth of burner	; 150 mm
location of the center of burner	; 150 mm from the center of circumferential joint
maximum temperature on outer surface	; 230°C
maximum temperature on inner surface	; 190°C

Circumferential joint of the specimen with P designation was peened at

a temperature below 100°C. Peening conditions were as follows:

weight of pneumatic hammer	; 1.8 kg
weight of chisel	; 140 gr
cycling rate	; 3,500 cycle/min
diameter and stroke of piston	; 18 mm and 50 mm respectively
hammering area	; 5 x 6.5 mm^2

2-2. Explosion Test

The significant merit of the explosion test is that a huge amount of energy produced by explosion is given to the specimen. For the purpose of fully making use of the energy by explosion, liquid medium was filled up in the tube specimen, and then the explosive charged at the center of the specimen was detonated by an electric snap cap (Fig. 3).

To test a specimen at various temperature hot water, cold water, ammonium nitrate solution with ice or alcohol with dry ice were used properly as a liquid medium. In case of tests in low temperature a specimen was covered with paper in order to prevent temperature rise before detonation.

Weight of explosive, TNT, for one shot was limited up to 500 gr, but special attention was paid for the purpose of making the distribution of pressure waves similar regardless of weight of TNT: shape of charged explosive was always formed a similar columnar shape, of which height to diameter ratio was 2,5 and besides specific weight of charged explosive was fixed to 0.95.

The tests began with a shot of a small amount of TNT, and weight of TNT for succeeding shots was determined as the case may be according to the degree of deformation of the specimen so that the specimen might be fractured in several shots.

By detonation of explosive the shock wave reaches the inner surface of a steel tube specimen first, and then the pressure waves reach. According to Snay[4] the peak pressure of the front of the shock wave P_M at the standoff R from the center of detonation is given in the form for $1 < R/a_o < 5$

$$P_M = 6.8 \times 10^4 (a_o/R)^{1.95} \qquad (kg/mm^2),$$

where a_o is the radius of spherical explosive charge.
In the case of the present investigation, R, the distance from the detonation center to the inner surface of the specimen, was 200 mm, and the maximum weight

of the explosive charge used in the test was 500 gr in the form of a cylinder with the specific weight of 0.95. Assuming that the shape of explosive is a sphere, R/a_o becomes approximately 4. Therefore, it was estimated that the peak pressure of the shock wave decreased to about 7% of that in the case that $R/a_o=1$, and that the mechanical energy of the shock wave decreased to about 60% of the initial value.

2-3. Strain Measurement

Specimens were fractured in one or several shots. Circumferential strains after each shot including the last shot to fracture were determined by the following two methods; the one was a method that a strain was determined on the basis of change of diameter by using large slide calipers (accuracy: 1×10^{-4} mm/mm), and the other is a method that local strains were directly measured by using a small comparator (accuracy: 2×10^{-3} mm/mm, gauge length: 10 mm), and the other the specimens were axisymmetrically deformed the circumferential strain ε_θ is given in terms of d_n and d_o in the form,

$$\varepsilon_\theta = (d_n - d_o)/d_o \ .$$

The method on the basis of diametral change is easy to apply and has enough accuracy, but, as strains after failure cannot be obtained by the method, the method with a comparator was used jointly.

Diametral changes of gauge lengths for comparator were measured by setting sixteen gauge points each long two circumferential lines 25 mm off the circumferential weld joint, and twenty points each along four generating lines 25 mm and 1/8 of the circumferential girth length off the longitudinal weld joints. Mean values of the strains measured at the symmetrical points were used for the analysis.

3. Results and Discussion

3-1. Dynamic Pressure and Dynamic Strain

For the purpose of measuring hydraulic dynamic pressure applied on the inner surface of a specimen and dynamic strain change in the specimen, a piezo-transducer and a sweep triggering contact switch were set in water filled in the tube specimen, and wire strain gauges were mounted on the specimen as shown in Fig. 4. The strain gauges used were bakelite base type wire

strain gauges of 1,000 ohm in resistance and 10 mm in gauge length. A DC-amplifier was used in the measurement of dynamic pressure response, and for the measurement of short time response of dynamic strain a DC-amplifier was coupled between a wire strain gauge and a cathode ray oscillograph. Long time response of the dynamic strain was measured by AC-amplifier and a magnetic oscillograph.

As the capacity of the piezo-electric transducer was not so large, a mine of 10 gr of TNT was charged at the center position of the specimen. In this case the specific weight and the shape of the mine were the same as used in the other speciments.

Results of pressure measurement are shown in Fig. 5-1. In the figure it is seen that the shock wave reached 60 μS after the beginning of the sweep of beam spot in cathode ray oscillograph, and its duration was about 31 μS. As the time lag of the triggering contact was about 25 μS, it was considered that the shock wave propagated 15 cm in 85 μS, and therefore the propagation speed of the wave was estimated to be 1,770 m/sec. The maximum pressure of the wave was read 2.81 kg/mm^2 referring to the calibration pulse.

A strain-time relation recorded by means of a cathode ray oscillograph is illustrated in Fig. 5-2, which shows that stress began to increase 160 μS after the beginning of the beam sweep, and reached to the maximum value in time of 100 μS. Fig. 5-3 shows a record of long time response of the dynamic strain on the outer surface of the specimen. Maximum value of the dynamic strain was read 25 kg/mm^2 referring to the calibration pulse.

3-2. Relation between Surface Strain and Charge Weight

As an example, longitudinal distributions of circumferential surface strain measured after each shot of explosive of 150 to 200 gr are shown in Fig. 6. The distribution curve shows its maximum at the middle which is the nearest point to the charged explosive. The inclination that the strain at a point in lower half of the specimen is higher than that at the symmetrical point in upper half is observed in the figure, and this inclination is considered to be caused by the effect of reflection of shock wave and pressure waves at the bottom plate and besides the effect of longer duration of the pressure waves on the lower half of the specimen than on the upper half.

Solid points in Fig. 6 represent the strain measured on the generating line located at 25 mm from the center line of a longitudinal weld joint, and

open points the strain measured on the generating line positioned at the middle of two longitudinal joints. Both measured values look to coincide well.

Circumferential distributions of plastic circumferential strain were almost uniform, and values of local strain measured by means of a comparator and strain values determined from change of diameter coincided well, and therefore deformations were regarded to be axisymmetric. Then the mean values of circumferentially distributing strains, defined as ε_θ, were adopted as the basis of analysis.

Relations bètween ε_θ and weight of TNT in each shot ΔW are shown in Fig. 7-1 for the AW specimen and in Fig. 7-2 for the SR specimen. Now, as a method of explosion test an explosive impact test in which the critical weight of explosive to fracture specimen in a single explosion is determined would be developed, but for the reason that the critical weight of explosive naturally changes according to the type of structure and dimensions of the specimen, the critical weight is very hard to be found by tests of small number of specimens. Accordingly, in the present test specimens were fractured as a rule in several numbers of explosion. For example, specimen AW-1, a mild steel specimen in as-welded condition, was fractured by explosion of 200 gr of TNT after shots of 50, 70, 100, 150 gr of TNT. It is seen in Figs. 7-1 and 7-2 that the specimens fractured in general at room temperature irrespective of weight of consumed explosives when the circumferential strain reached to a critical value (approximately 6% for AW specimens and about 11% for SR specimens). AW-6 specimen was fractured in two shots of 400 gr and 150 gr of explosive.

In Fig. 7-1 m-m line was obtained by connecting the points for the first shot. The critical weight of explosive to cause fracture in a single shot will be obtained as the point of intersection of 6% level line of ε_θ and the m-m line. In the same way the critical weight of explosive to cause a single shot fracture of the SR specimen, mild steel specimen in stress annealed condition, is obtained as the intersecting point of the n-n line and the level of 11% of ε_θ. Specimen AW-4, SR-5, SR-2 were tested at $-3^\circ C$, and specimen AW-7 at $-10^\circ C$. It was found that at a low temperature deformation at fracture were smaller as shown in Figs. 7 and 16.

Incremental hoop strain from the (n-1)th shot to n-th shot $\Delta\varepsilon_\theta$ are plotted against weight of explosive in a shot ΔW in Fig.8 for specimens AW and SR. As it is clear in the figure, the incremental strains by the first shots were larger than the incremental strains by the following shots, and the incremental strains in SR specimens are also larger than that in AW

specimens. The former difference is considered to be caused by the effect of strain hardening and the latter by the effect of heat treatment.

The relations between ε_θ and sum of weight of explosive are illustrated in Figs.9-1 and 9-2, in which it is observed that the strain by the first shot is on the line of O-F.

The relations between the ratio of incremental circumferential strain to weight of explosives in a shot $\Delta\varepsilon_\theta/\Delta W$, which represents the capacity for deformation and test temperature are illustrated in Fig.10. $\Delta\varepsilon_\theta/\Delta W$ for the first shot is constant in the range of tested temperature,and the ratio reduces for the second shot or after. $\Delta\varepsilon_\theta/\Delta W$ reduces further for the final shot to failure because the weight of explosives apt to be excessive. The relation between $\Delta\varepsilon_\theta/\Delta W$ for the first shot and test temperature is shown in Fig. 11, which indicates the order of deformability.

The relation between the circumferential strain at fracture ε_f and test temperature for manual welded specimen are shown in Fig. 12. The figure illustrates a dominant factor of material on the fracture strain at the same test temperature. Fig. 13 represents the relations between ε_f and test temperature for all kinds of 50 HT specimens. Test results of peened specimens 5MP is evidently lower than the other, but there is not much difference among the fracture strains of the rest specimens. The same relations for 60 HT specimens and 2H specimens are shown in Figs. 14 and 15 respectively.

By summarizing the test results on fracture strain it can be concluded that, as to the circumferential strain at fracture, the difference in the results of various steels and the deteriorative effect of peening are obvious, but that the difference among the methods of stress relief treatment and welding method is not clear.

3-2. Mode of Fracture

Developed sketches of fractured specimens are arranged in Figs. 16-(a), (b) and (c), where crack paths, crack initiation points, directions of crack propagation (with arrow) are shown.

In the case of mild steel specimens, for both AW and SR specimens, cracks generally initiated in the circumferential welded joints and propagation along generating lines. Fracture surfaces at and near the initiation point exibited brittle and crystalline appearances, and lateral contraction was hardly seen there. Modes of fracture propagation were mainly divided into two; the one was a mode in which a brittle crack propagated through to an end, and the other

was a mode in which a brittle crack was arrested with the increasing shear lips after propagation of some distance. Approaching to the arresting point the brittle fracture changed to shear fracture with gray and fibrous appearance. Shear percentage of fracture surface is stated in figures along the crack path in a sketch for AW and SR specimens.

Starting points of cracks indicated with X marks were generally the dendrite structure in the final pass of the circumferential joints with a few exceptions. It may be because the circumferential joint was subjected to the highest pressure due to the nearest standoff from the charged explosive. In the case of specimens AW-8 and X-1, a crack initiated from an arc strike 65 mm to 150 mm off the circumferential joint. In almost all the cases small cracks initiated at an arc strike on inner surface of the specimen, if any. In the case of AW-4 specimen a crack initiated at a defect with looked like a hot cracking, and propagated with the crack bifurcation. The one crack propagated to meet a crack initiated at the circumferential joint, and the other propagated on the inside surface of the specimen and traversed the circumferential joint. Thus, it is noteworthy, a crack initiated in a region on which the load was lower than at the central portion of the specimen.

Cracks developed by prior shots did not always act as origins of final failure. For example, SR-4 specimen fractured by three shots, and a transverse crack, which developed on the surface of the circumferential joint by the second shot, did not propagate but simply opened a little wider by the third shot.

Almost always the brittle cracks propagated along the generating lines and no crack initiated at the intersecting point of the circumferential and longitudinal joints. Any crack did not propagate in the longitudinal joint, but in some cases cracks propagated in the heat affected zone or embrittled zone.

AW-7 specimen which was tested at $-10^{\circ}C$ was broken into more than four pieces, and the crack path of the specimen changed its direction 90° and traversed a longitudinal joints. That mode of fracture was quite different from the mode of fracture which appeared in the tests at room temperature.

Results of X ray radiography for specimens AW and SR are tabulated in Table 4, in which star marks represent the origin of brittle fracture. In general a clear relation between quality of weld joint classified by X ray inspection and the origin of crack initiation could not be found in the table.

In Figs. 16(a), (b) and (c) crack initiation points of high tensile

steel specimens are indicated with marks, ● , ○ and ⊗ when cracks initiated from the external surfaces, the inner surfaces and central regions of the plate thickness, respectively. When a crack started from an arc strike, a blow hole or a slag inclusion, a mark A, B or S is put close to the initiation point, respectively.

Except the 5MP specimens the initiation points were mostly at the inner surfaces of the specimens, and main cracks propagated along the generator lines from the initiation point. In general one of the cracks which started from a point in heat affected zone propagated in heat affected zone to an end of specimen, and the other crack propagated over the circumferential joint to another end of specimen or bifurcated near the end. However, in the case of 2H steel specimens, a crack which traversed the circumferential weld joint propagated into the base metal 100 mm to 200 mm and then stopped. This feature of 2H steel would show a remarkable crack arresting characteristic which is closely connected with the shear lip.

The initiation points are roughly classified into three groups; the heat affected zone, the deposited of the circumferential joint and the base metal. When a crack initiated in the base metal, the origin was mostly an arc strike, and when a crack initiated in the deposited metal a blow hole was generally the origin. The initiation points were not always clearly correlated to the results of the X ray inspection. Even in the same welded joints, in some case cracks initiated in a region where many blow holes aggregated, but in other case cracks initiated independent of the region of blow hole aggregation.

Explosion test results for high tensile specimens are summarized in Table 5. On an average the specimen of 5MA has 0.86 point of crack initiation in the heat affected zone of the longitudinal weld joints per a specimen, but, on the other hand, the average number of crack initiation points in the circumferential joints is about a half of the number of points in the longitudinal joint, except the case of No.7 specimen of which a crack initiated at an arc strike. However, in the specimen series of 5MR, of which the circumferential joints were annealed, average number of crack initiation points in the deposited metal is larger than in the heat affected zone. Besides the fracture strain at fracture of 5MR specimens was equal to or a little lower than that of 5MA specimens.

Fracture strain of annealed mild steel specimen, SR specimens, was much larger than that of the as-welded mild steel specimen, AW specimens, but as

for the high tensile steels the treatment of stress annealing did not bring out significant increment of fracture strain. The reason why there was not much difference in fracture strain in the cases of the high tensile steels may be that the circumferential joints welded with low hydrogen type electrode would be embrittled by annealing. 5ML specimens had almost the same number of crack initiation points in the heat affected zone and in the deposited metal. Fracture strain of 5MP specimens was very low, and all the crack initiated at the outer surface of the circumferential joints, and it is evident that the peening on the final pass of the weld acted as a deteriorating effect on the brittle fracture of the tube specimen due to explosive impact loading.

In 5MAX specimens main cracks initiated in the heat affected zone of the longitudinal welded joint due to the possible effect of metallurgical notch caused from the hardening of the heat affected zone, as it is the case with 5MA specimens. In the case of HT60 specimen most cracks initiated at the heat affected zones of the longitudinal joints except cases of 6MR specimens. 6MR specimens which were manually welded and annealed showed the same tendency that 5MR specimens did. Most main cracks of 2H steel specimens started from the heat affected zones, and several cracks tended to initiate in the heat affected zone of the same welded joint. This tendency was seen in the cases of 5MAX and 6MA specimens, but not so remarkable as that of 2H steel specimens.

3-3. Shear Lips

When the test temperature was not low, the brittle cracks were accompanied with shear lips. The strain at fracture would represent the resistance to deformation, and the shear lips the resistance to brittle crack propagation. In order to express the shear lip quantitatively, fracture paths were classified into three groups according to material properties in which crack propagated; the mother metal, the heat affected zone and the deposited metal.

Taking the mean width of shear lips which distributed on the top and bottom side of the fracture surface and in the range of 300 mm from the center of the circumferential joint, the relations between the mean width of shear lips and test temperature were obtained as shown in Figs. 17 to 21.

Figs. 17 to 19 show the relations for base metal, and it may be concluded that various factors in welding procedures could hardly influenced on the relation in the case of the same base metal. Relations between test temperature and the mean width of shear lips observed in weld metal and heat affected zone are plotted in Fig. 20, in which difference due to the base metal is hardly

seen. Fig. 21 illustrates the mean curves obtained in Figs. 17 to 21. The order of width of shear lips at the same temperature represents the brittle crack arresting properties as mentioned above.

4. Conclusions

Series of explosion tests were carried out on the arc welded tube specimens made of mild steel and three kinds of high tensile steels with the various conditions of welding procedure and after welding treatment. The explosive of TNT was charged in the center of a specimen filled up with liquid and detonated. Specimens were fractured in brittle manner exhibiting the effect of factors in the specimen series. As the results of the test following conclusions were obtained.

(1) Specimens were fractured in general when the circumferential strain reached to a certain value of strain irrespective of weight of explosive in successive explosion.

(2) Comparing the as-welded specimens with respect to the effect of the quality of steel on the circumferential strain at fracture, it can be concluded that 50 kg/mm^2 high tensile steel (50HT) is the best, and then comes quenched and tempered steel (2H), 60 kg/mm^2 high tensile steel (60HT) and mild steel (MS). And concerning the width of shear lips, quenched and tempered steel comes first and then 50 kg/mm^2 high tensile steel, 60 kg/mm^2 high tensile steel. In other words 50 kg/mm^2 high tensile steel is superior for the brittle crack initiation properties, and the quenched and tempered steel for the brittle crack arresting properties.

(3) So far as the circumferential strain at fraction the effect of stress annealing was hardly observed for high strength steel specimens, while the effect was shown remarkably for mild steel specimens.

(4) Difference of the fracture strain was hardly observed as for the effect of low temperature stress treatment, and for the difference caused by manual or submerged arc welding.

(5) In all the specimens peened on every layer of the outer side of the circumferential joint, the crack initiated at the outer surface of the circumferential joint, and the strain at fracture was the lowest.

(6) With the exception of peened specimens cracks were usually initiated from the inner surface of the tube specimen, especially from the heat affected zone of longitudinal joints, or blow holes in circumferential

joint for high tensile steel specimens, while in the mild steel specimens welded by submerged arc welding cracks initiated from the dendrite structure in the final pass of the circumferential joint.

(7) In almost all the cases cracks initiated at an arc strike. Arc strike may act as a starting point of brittle fracture by impact loading.

References

(1) H. Kihara, S. Ichikawa, K. Masubuchi, Y.Ogura, K. Iida, T. Yoshida and H. Ōba, "Explosion Tests on Arc-Welded Tubes with and without Stress Annealing", J. of Soc. Nav. Arch. Japan, Vol. 100 (1956), 167/175

(2) H. Kihara, S. Ichikawa, K. Masubuchi, Y. Ogura, K. Iida, T. Yoshida and H. Ōba, "Explosion Test on Arc Welded Tubes and Various Welding Procedures", J. of Soc. Nav. Arch. Japan, Vol. 104 (1958), 243/253

(3) E. Folkhard, "Das Verhalten elektrisch geschweißter Rohre für Turbinendruckrohrleitungen bei schärfster geschlagartiger Beanspruchung durch Sprengung", Public Session of the 1955 Annual Meeting of the International Institute of Welding, Sept., 1955

(4) H.G. Snay, "Unterwasser-Explosion Hydromechanische Vorgänge und Wirkungen", J. der Schiffbautechnischen Gesellschaft, Bd. 51 (1957), 222/235

Table 1 Codes and Numbers of Specimens

Type of Steel		50 kg/mm² Mn-Si Steel		60 kg/mm² V-Ti Alloy Steel		Quenched and Tempered Steel		Mild steel
Steel Code		52 HT		60 HT		2 H		MS
Stress Relieving	Welding	Manual(M)	Submerged (U)	Manual(M)	Submerged (U)	Manual(M)	Submerged (U)	Manual
As Weld	(A)	5 MA (8)	5 UA (9)	6 MA (7)	6 UA (3)	2 MA (4)	2 UA (3)	AW (9)
Annealed	(R)*	5 MR (9)	5 UR (3)	6 MR (3)	6 UR (3)	2 MR (4)		SR (6)
Linde	(L)**	5 ML (8)	5 UL (4)	6 ML (3)				
Peened	(P)	5 MP (4)						
As Weld	(AX)***	5 MAX(3)						
		32	16	13	6	8	3	
Total Numbers		48		19		11		15
				93				

Numbers of specimen are shown in round brackets

* Annealed in an electric furnace (600°C, 1.5 hour)

** Low temperature stress relieved by the Linde Method

*** Both longitudinal and circumferential joint were not stress relieved

Table 2 Chemical and Mechanical Properties of Base Metal

Steel Code	Chemical Analysis											Grain Size		Yield Point	Tensile Strength	Elongation (%)	Absorbed Energy at 0°C (V-Charpy)
	C	Si	Mn	P	S	Cu	Ni	Cr	Mo	V	Ti	Al	Austenite	Ferrite	(kg/mm²)	(kg/mm²)	G.L.=200mm	(kg-m/cm²)
52 HT	0.15	0.37	1.21	0.015	0.020	0.18	—	—	—	—	—	0.025	6.5	8.0	38.0	52.0	27.5	13.3
60 HT	0.15	0.37	1.01	0.014	0.011	0.13	0.61	0.24	0.15	0.10	0.022	0.027	6.9	7.5	42.0	68.2	23.3	5.4
2 H	0.16	0.40	1.05	0.012	0.009	0.14	0.19	0.06	0.16	—	—	0.015	5.5	—	56.7	65.0	18.9	27.8
MS	0.13	0.05	0.74	0.024	0.025	0.08	—	0.06	—	—	—	—			29.1	42.6	32.5	5.8

Table 3 Notch Toughness of Base Metal

	As Rolled	650°C Annealed	2% Strain Aged	2% Strain Aged and Annealed
Tr_{15}*	−18	−1	−2	−2
W_0 **	5.8	2.7	3.0	3.0

Note : Tr 15*=15 ft-lb Transition Temperature (°C)

W_0**=Absorbed Energy at 0°C (kg-m/cm²)

Tabl 4 Results of X-Ray Inspecton (JIS Classification)

Specimen Code		ε_g at Fracture	Circumferential Joint						
			0	π/2		π		3/2π	
AW-1	As Weld	5.7%	1	3	1	1*	2	2	1
AW-2		5.9	1	1	2	2	2	1*	3
AW-3		5.9	1	2	2	2	1	2	3*
AW-4		1.4	1	2*	3	2	2	1	2
AW-5		6.8	* 4	2*	6	4*	1	3	6
AW-6		6.8	2*	5*	4	3	6	6	2*
AW-7		0	2*	3*	*3*		1	3*	2*
AW-8		8.5	3	2*	1	1	2	6*	1
X-1		11.0	1	1	1	3	3	2	2
SR-1	Stress Relieved	11.3	2*	4	4*	5*	6	6	6
SR-2*		5.2	4	3	1	1	4*	3	4
SR-3		9.8	1	1*	1	6	1	3	1
SR-4		11.4	6	5*	5*	6*	6	5	6
SR-5		4.0	4*	1	3		1	2	2

* Star mark represents the origin of fracture

Table 5 Summary of Test Results

Code of Specimen		Test Temperature °C	Total Weight of Explosive gr	No. of Shot	Circumferential Strain at Fracture %	Principal Fracture				Shear Lip (Mean.) mm		
						No. of Fracture Line	No. of Initiation Point					
							Weld Metal	Heat Affected Zone	Base Metal	Weld Metal	Heat Affected Zone	Base Metal
5 MA	1	−51	250	1	1.7	3	—	3	—	—	0.5	0.3
	4	−31	500	1	3.7	1	1	—	—	—	0.1	0.2
	6	0	1,600	4	17.8	1	—	1	—	0.5	—	0.4
	7	20	2,900	8	32.3	2	—	1	1	—	—	5.0
	8	10	2,100	7	22.1	2	1	—	—	—	2.1	2.8
	9	−10	1,200	4	15.1	1	—	1	—	—	2.5	—
	10	−17	550	2	6.3	1	1	—	—	0.9	0.1	0.0
	Mean					1.43	0.43	0.86	0.14			
5 MR	1	20	2,000	4	22.2	2	2	—	—	—	—	2.1
	2	− 6	1,950	13	18.6	2	2	—	—	—	—	0.2
	3	−16	850	3	9.3	1	—	1	—	0.0	0.0	—
	5	−34	500	1	3.8	4	2	2	—	—	0.8	0.2
	6	0	1,400	3	15.5	1	1	—	—	—	—	0.4
	8	−48	300	1	1.0	6	2	4	—	0.0	0.4	0.0
	9	0	250	1	3.3	1	1	—	—	—	—	0.2
	10	10	1,590	10	16.2	1	1	—	—	—	—	0.2
	Mean					2.25	1.25	0.88	—			
5 ML	1	−30	400	1	3.1	2	—	2	—	0.0	1.5	0.0
	2	−48	250	1	2.4	2	—	2	—	—	0.1	0.0
	3	40	2,200	5	26.8	1	—	1	—	—	8.9	6.4
	5	0	900	2	10.6	1	1	—	—	—	—	0.6
	6	30	2,500	8	29.7	1	1	—	—	—	—	8.4
	7	10	1,900	4	20.0	2	2	—	—	—	—	5.2
	8	−10	1,300	3	12.9	1	—	1	—	—	2.0	0.5
	10	20	1,800	4	21.4	1	1	—	—	1.6	3.5	1.4
	Mean					1.38	0.63	0.75	—			
5 MP	1	10	900	3	12.7	1	1	—	—	—	—	1.1
	2	0	300	1	2.0	1	1	—	—	—	—	0.5
	3	20	1,100	4	13.5	1	1	—	—	—	—	2.8
	4	−30	300	1	2.3	3	3	—	—	—	—	0.2
	Mean					1.50	1.50	—	—			
5MAX	1	0	3,200	8	37.4	1	—	1	—	—	—	3.2
	3	10	2,500	5	29.4	1	1	—	—	—	—	3.4
	4	−50	350	1	2.6	4	—	4	—	—	1.3	0.0
	Mean					2.00	0.33	1.67	—			
5 UA	1	−30	400	3	4.2	1	1	—	—	—	—	0.0
	2	−10	1,450	4	19.6	2	1	1	—	—	—	0.0
	5	−45	300	1	4.3	2	—	2	—	—	0.0	0.4
	7	−50	400	1	3.8	1	—	1	—	—	0.0	0.0
	8	20	2,100	5	25.8	1	—	1	—	—	1.7	0.1
	9	0	1,750	5	20.5	1	—	1	—	—	1.0	1.4
	10	10	1,200	3	14.5	1	1	—	—	—	0.4	0.0
	Mean					1.30	0.43	0.86	—			
5 UR	2	0	1,400	3	16.9	1	1	—	—	—	—	0.1
	3	10	1,000	2	12.8	1	—	1	—	0.9	0.0	0.0
	4	−51	250	1	2.8	2	—	2	—	0.0	0.0	—
	Mean					1.33	0.33	1.00	—			
5UL	4	−45	250	1	3.6	1.00	—	1.00	—	0.0	—	—
6MA	6	−47	300	1	0.3	1	—	1	—	—	0.4	0.0
	7	40	1,100	3	11.2	2	—	2	—	—	3.5	3.1
	8	20	1,100	5	8.8	2	—	2	—	—	2.0	0.6
	9	0	350	1	3.6	1	—	1	—	—	1.2	—
	10	10	500	1	4.8	1	—	1	—	—	2.1	0.7
	Mean					1.40	—	1.40	—			
6 MR	2	20	500	1	5.1	4	1	3	—	—	4.2	1.8
	3	0	300	1	2.6	3	1	2	—	—	0.4	0.5
	4	10	850	2	7.9	2	1	1	—	—	1.1	1.0
	Mean					3.00	1.00	2.00	—			
6 ML	2	0	400	2	3.1	3	—	3	—	—	0.5	0.0
	3	10	250	1	5.4	1	—	1	—	—	1.1	—
	4	20	500	2	5.5	2	—	2	—	—	3.4	0.9
	Mean					2.00	—	2.00	—			
6 UA	1	10	1,150	3	11.6	3	—	3	—	—	3.4	2.2
	2	20	1,450	7	12.7	2	1	1	—	—	3.0	2.3
	3	0	350	1	3.9	1	—	1	—	—	3.2	0.0
	Mean					2.00	0.33	1.67	—			
6 UR	1	−51	200	1	1.4	3	—	3	—	2.0	0.0	0.1
	2	−46	100	1	0.6	5	1	4	—	1.3	1.4	0.7
	3	−48	50	1	0.2	1	—	1	—	2.4	0.7	—
	Mean					3.00	0.33	2.67	—			
2 MA	1	10	1,000	2	10.0	1	—	1	—	—	3.3	7.0
	2	20	1,900	5	17.4	1	—	1	—	—	2.6	12.0
	3	0	900	3	7.3	1	—	1	—	—	1.0	—
	4	−10	450	2	5.0	1	—	1	—	—	—	—
	Mean					1.00	—	1.00	—			
2 MR	1	10	1,000	3	11.0	1	—	1	—	—	1.0	10.0
	2	0	1,100	4	10.0	2	—	2	—	—	0.8	4.6
	3	−29	350	1	2.3	4	1	3	—	—	0.1	0.1
	4	−50	250	1	1.6	4	1	3	—	—	0.2	0.0
	Mean					2.75	0.50	2.25	—			
2 UA	1	−32	300	1	2.7	3	—	3	—	—	0.8	1.1
	2	0	350	1	4.2	1	—	1	—	—	—	—
	3	10	1,200	3	11.3	1	—	1	—	—	2.3	3.5
	Mean					1.67	—	1.67	—			

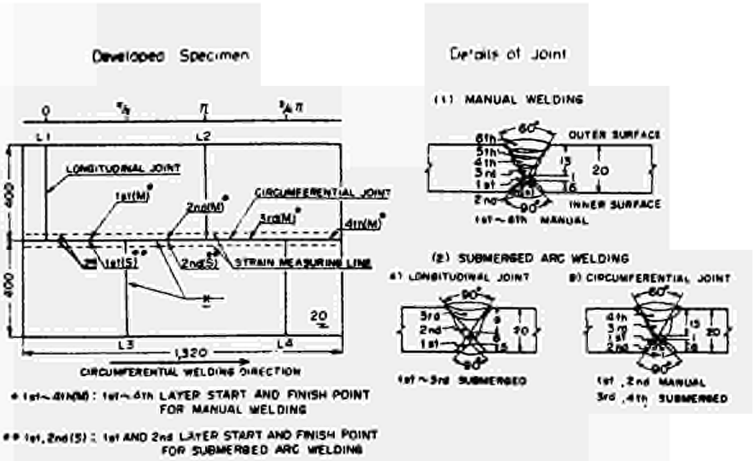

Fig. 1 Details of Specimen and Shape of Joint

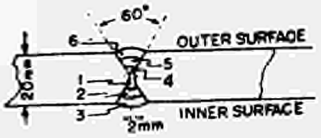

Fig. 2 Welding Procedures

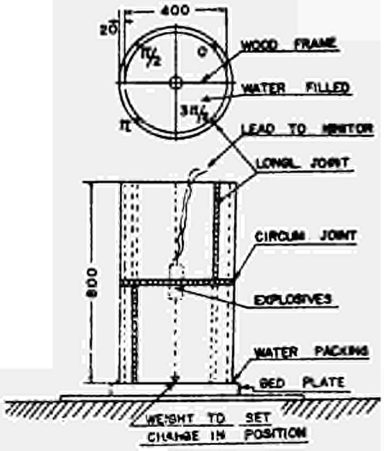

Fig. 3 Tett Specimen prepared for Explosion

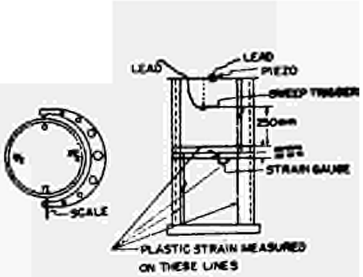

Fig. 4 Nonius for Diameter Measurement (left), and the Arrangement of Static and Dynamic Gauges(right)

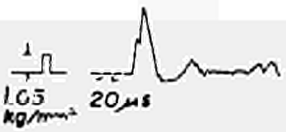

Fig. 5-1 Dynamic Pressure

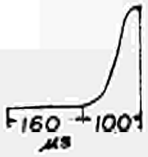

Fig. 5-2 Dynamic Strain

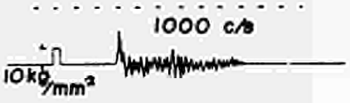

Fig. 5-3 Dynamic Strain

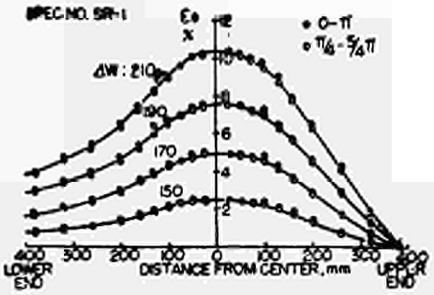

Fig. 6 Longitudinal Distributions of Circumferential Strain ε_θ

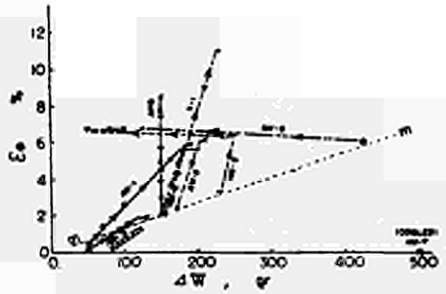

Fig. 7-1 Relation between ε_θ and ΔW (As-weld specimens)

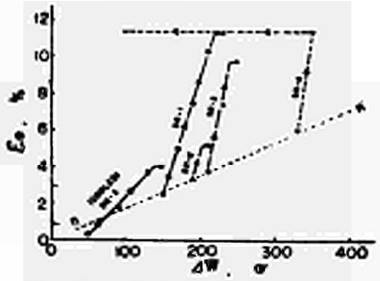

Fig. 7-2 Relation between ε_θ and ΔW (Stress relieved Specimens)

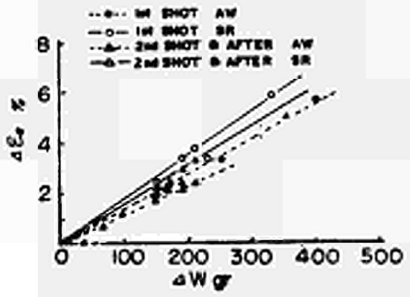

Fig 8 Relation between $\Delta\varepsilon_\theta$ and ΔW

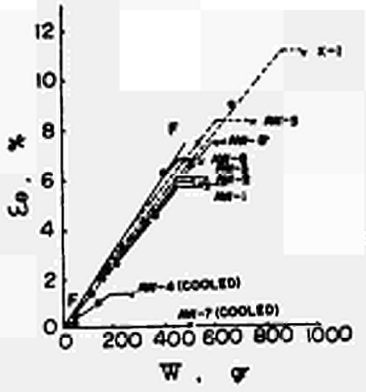

Fig. 9-1 Relation between ε_θ and W (As weld Specimens)

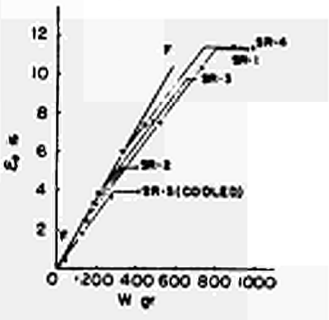

Fig 9-2 Relation between ε_θ and W (stress relieved Specimens)

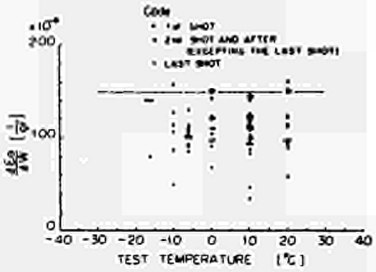

Fig 10 Relation between Temperature and Strain Difference on Each Shot(50kgHT)

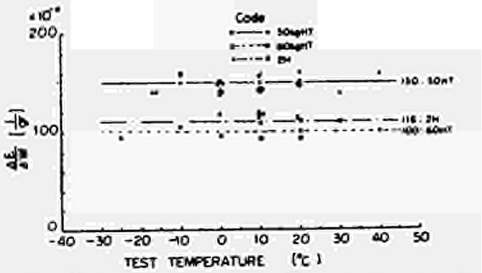

Fig 11 Relation between Temperature and Strain Difference on First shot

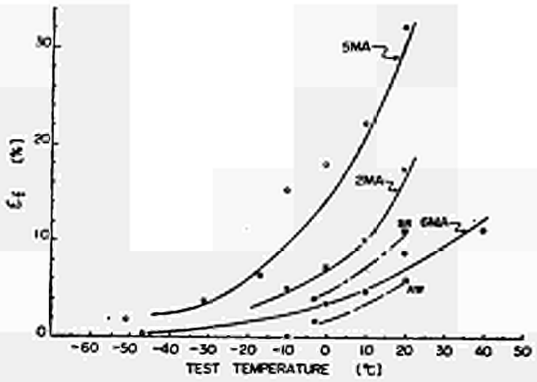

Fig 12 Relation between Test Temperature and Circumferential Strain at Fracture for Manual Weld Specimens

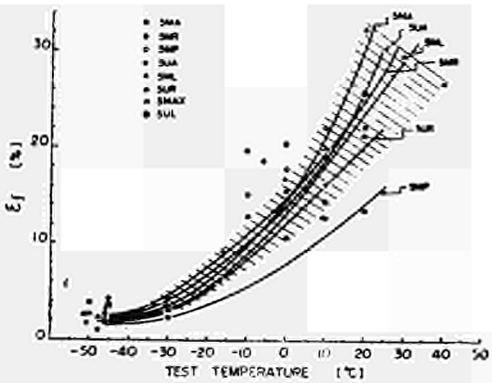

Fig 13 Relation between Circumferential strain at Fracture and Test Temperature (50 HT)

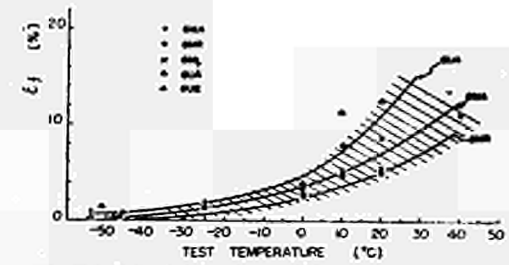

Fig. 14 Relation between Circumferential Strain at Fracture and Test Temperature(60 HT)

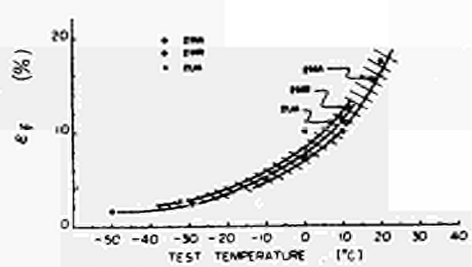

Fig ■ Relation between Circumferential Strain and Test Temperature (2H)

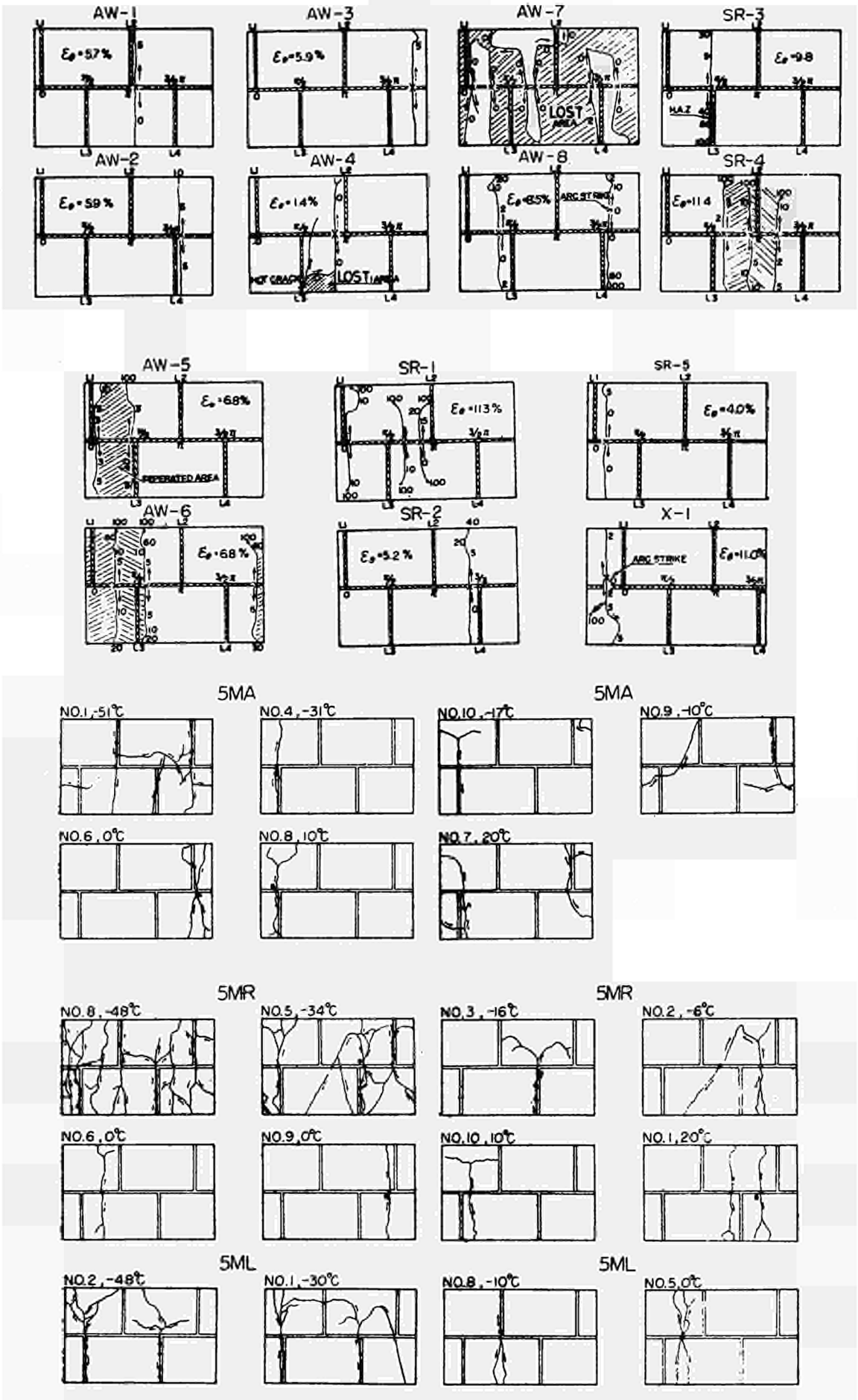

Fig 16(a) Developed Sketch of Fractured Specimens

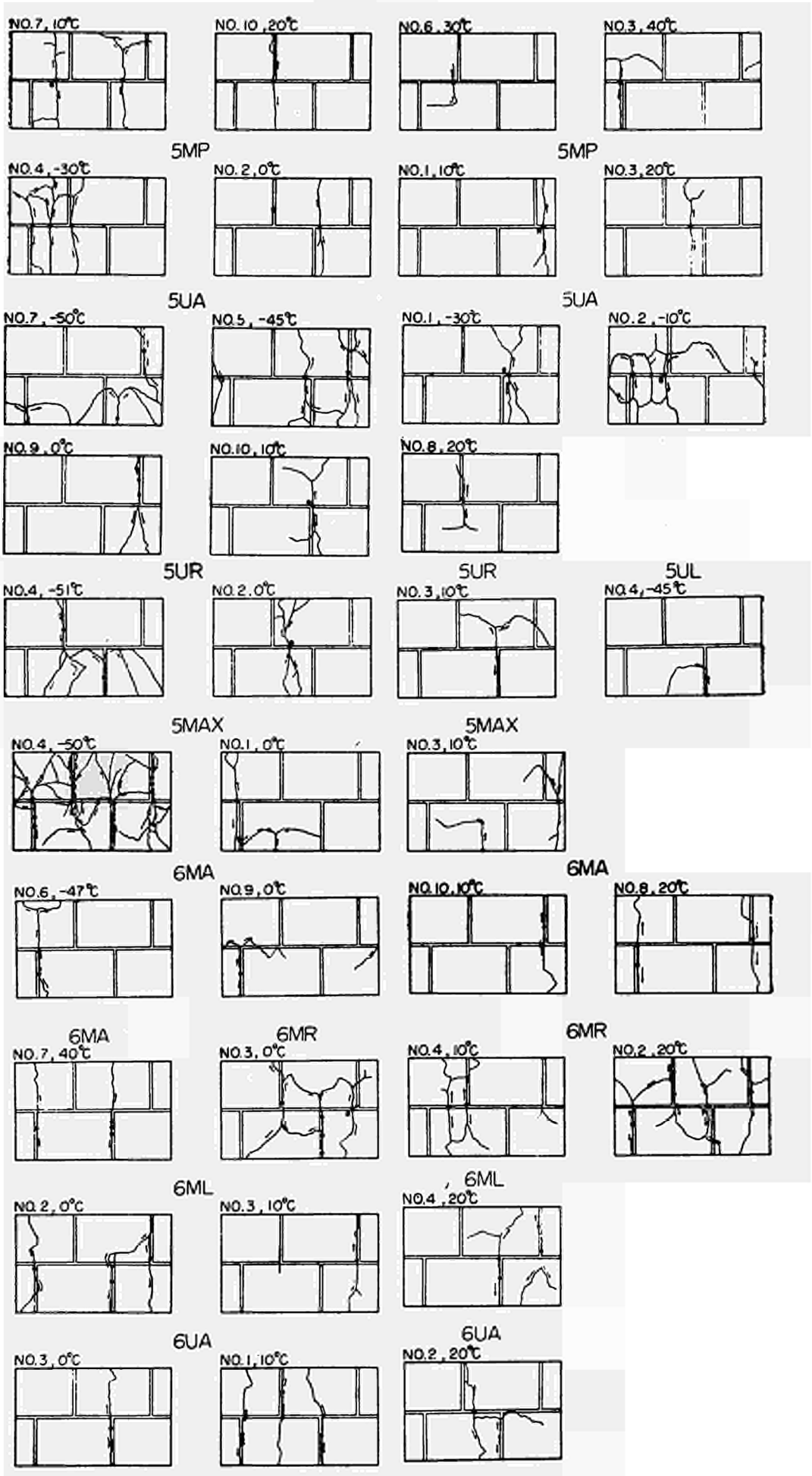

Fig. 16(b) Developed Sketch of Fractured Specimens

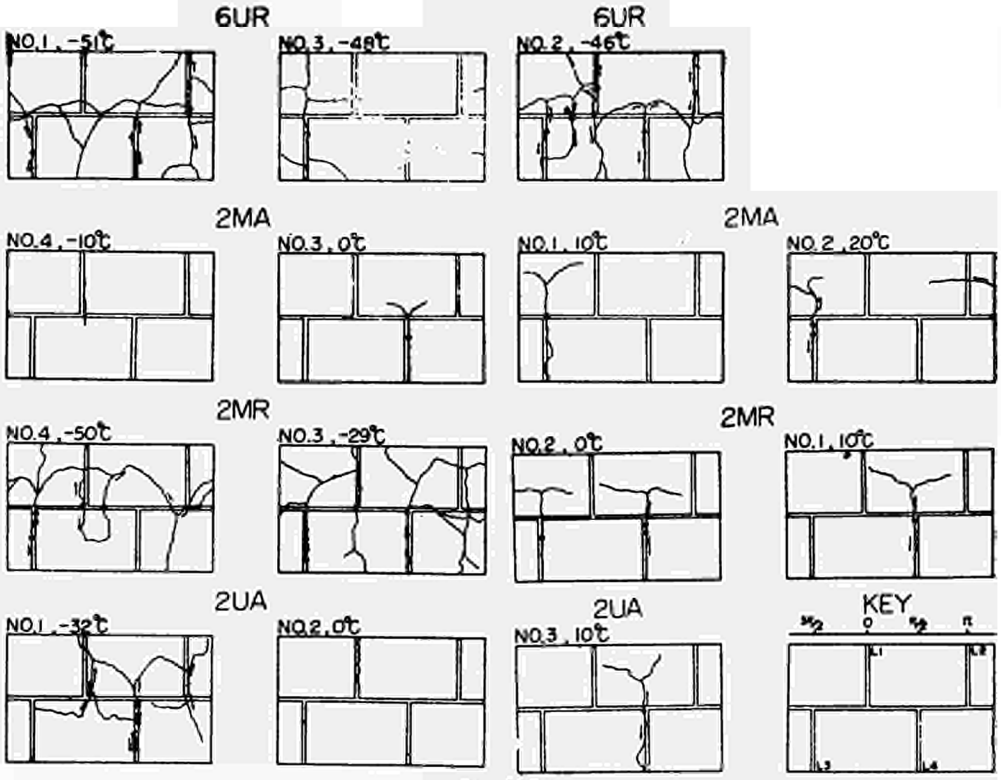

Fig. 16(c)

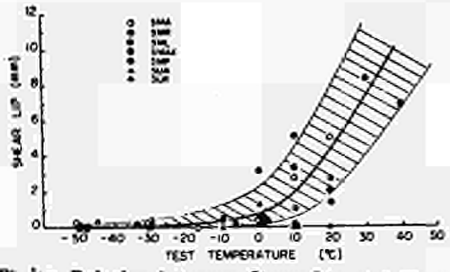

Fig 17 Relation between Shear Lip and Test Temperature (50 HT Base Metal)

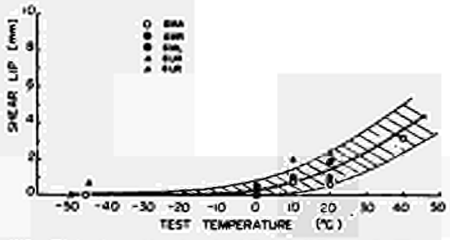

Fig 18 Relation between Shear Lip and Test Temperature (60 HT Base Metal)

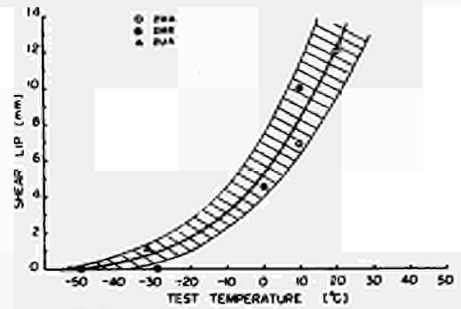

Fig 19 Relation between Shear Lip and Test Temperature (2 H Base Metal)

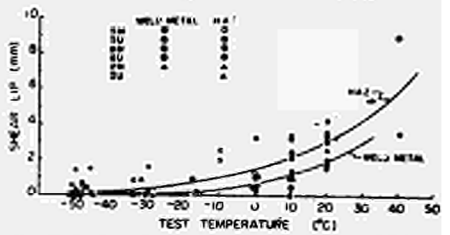

Fig. 20 Relation between Shear Lip and Test Temperature (Weld Metal and Heat Affected Zone)

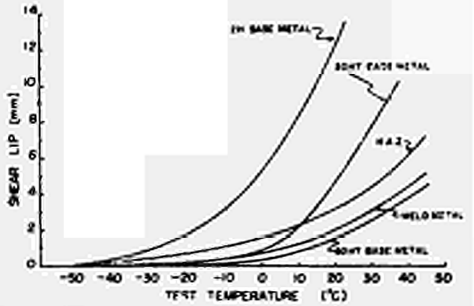

Fig 21 Relation between Shear Lip and Test Temperature

EFFETS MECANIQUES DE LA RUPTURE D'UN TUBE DE FORCE A GAZ SOUS PRESSION DANS UN REACTEUR DU TYPE EL4

par

R. Roche

C.E.N. Saclay
France

1 - LES STRUCTURES DES REACTEURS DU TYPE EL4 -

L'architecture générale et la conception mécanique des réacteurs de la filière eau lourde gaz à tubes de force du type EL4 ont fait l'objet d'un certain nombre de publications (1), (2), (3), (4), (5) ; il suffit donc d'en rappeler les traits et caractéristiques essentiels.

Le réacteur est constitué essentiellement d'une cuve cylindrique de révolution contenant le modérateur. Les éléments combustibles sont contenus dans des tubes rectilignes d'axe parallèle à celui de la cuve et qui traversent la cuve d'un fond à l'autre. Ces tubes sont parcourus par un courant de gaz qui permet de refroidir les éléments combustibles, ce gaz étant sous pression, les tubes doivent résister mécaniquement aux effets de cette pression d'où leur nom de TUBES DE FORCE. Les tubes sont disposés en réseau régulier qui correspond au réseau même du milieu multiplicateur. La cuve elle-même est munie d'exutoires de gros diamètre qui permettent éventuellement l'évacuatuion de l'eau lourde.

Ces dispositions sont visibles sur les planches 1 et 2.

Plus précisément, notons que le canal dans sa partie centrale comprend les éléments combustibles qui sont des grappes de crayons, le tube de guidage entouré d'un isolant thermique et le tube de force lui-même (6). Ce canal est raccordé au circuit caloporteur par deux tubulures de grande longueur et d'un diamètre médiocre.

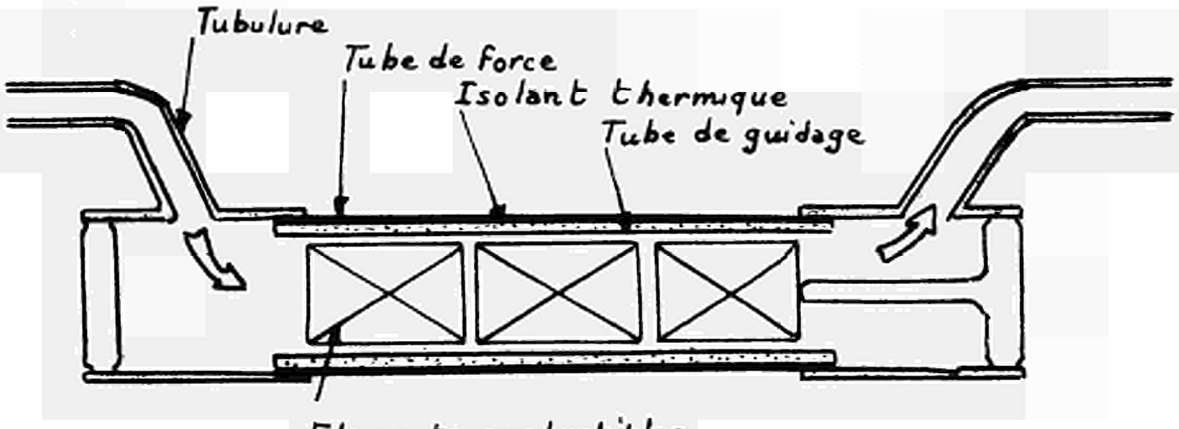

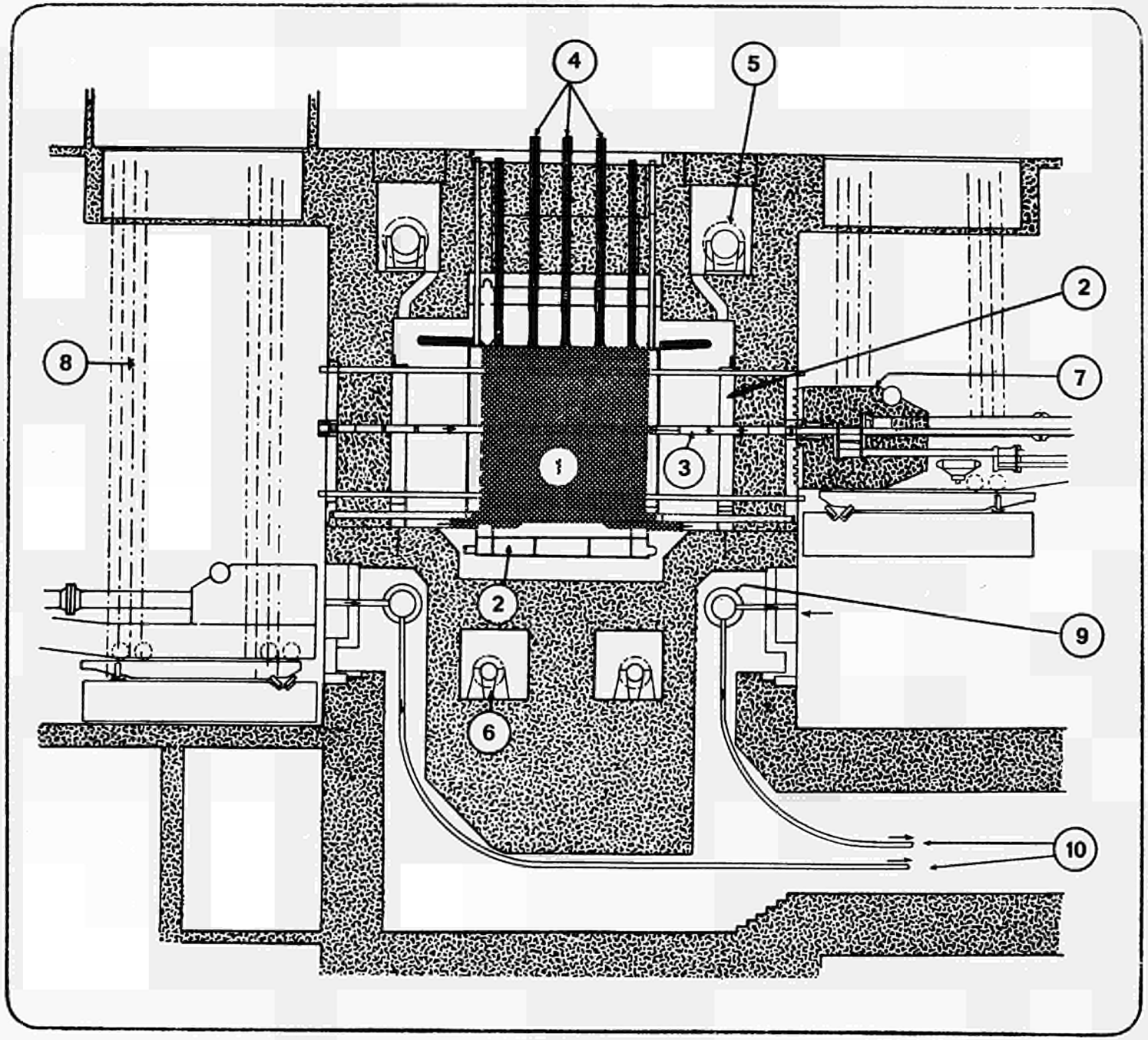

fig. 1

COUPE LONGITUDINALE DU RÉACTEUR

1 Cuve (D_2O)
2 Ecran d'eau de protection
3 Canal
4 Barres de contrôle
5 Collecteur CO_2 chaud
6 Collecteur CO_2 froid
7 Machine de manutention du combustible
8 Chaînes du support de machine
9 Machine d'évacuation du combustible
10 Vers bâtiment du combustible irradié

CANAL (1/2 COUPE)

1 Tape de sécurité
2 Nez d'accrochage
3 Vanne
4 Verrou
5 Bouchons biologiques (coupés)
6 Ecran d'eau
7 Bouchon thermique
8 Tubulures CO^2
9 Lanterne de départ du gaz
10 Raccord vissé soudé
11 Fourreau de fond de cuve
12 Epée
13 Fond de cuve (H_2O)
14 Elément combustible
15 Cuve (D_2O)
16 Tube de force
17 Isolant thermique
18 Tube de guidage

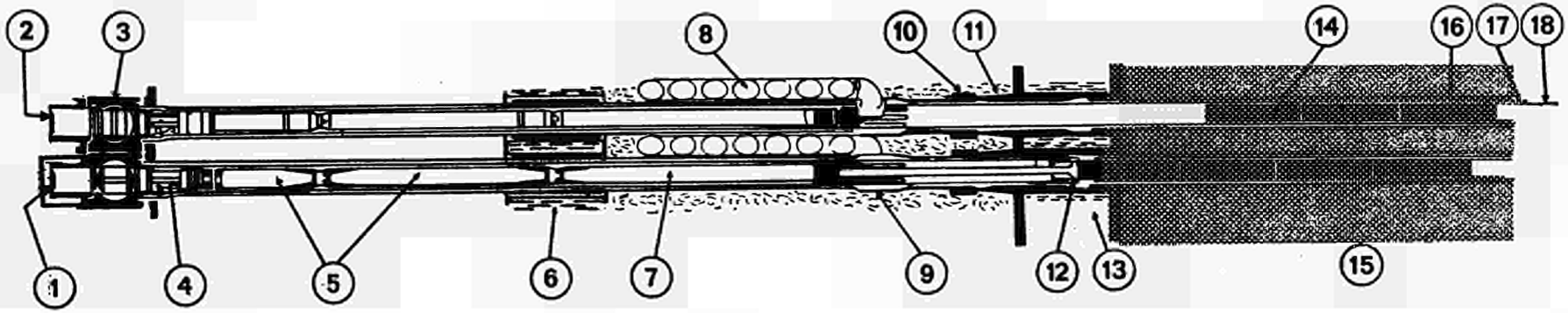

fig. 2

Pour EL4, les caractéristiques essentielles sont les suivantes :

- diamètre cuve : 4,8 m
- longueur cuve : 4,6 m
- épaisseur virole : 20 mm
- exutoires : 2 ∅ 600 mm
- nombre de tubes de force : 216
- matière des tubes de force : Zircalloy 2 recuit
- dimensions : 107 × 113 mm
- pression du gaz : 60 bars

En comparaison, on peut indiquer les caractéristiques d'une centrale de 600 MWe de la filière eau lourde-gaz.

- diamètre cuve : 7,8 m
- longueur cuve : 6,4 m
- épaisseur virole : 30 mm
- exutoire : 1 ∅ 1200
- nombre de tubes de force : 480
- matière des tubes de force : Zircalloy 2
- dimensions : 140 × 148
- pression du gaz : 75 bars

2 - SURETE ET RUPTURE D'UN TUBE DE FORCE -

On trouvera un examen d'ensemble des problèmes de sûreté concernant la filière dans un certain nombre de documents (7), (8). Un point très important concerne la rupture éventuelle du tube de force. Il est en fait difficile d'apprécier la probabilité des diverses causes possibles d'une rupture éventuelle ; en tout état de cause, cette probabilité paraît extrêmement faible. C'est ce que montrent les différents essais concernant la défaillance de l'isolation thermique (point chaud), les défauts éventuels, etc. ...

Il a paru cependant nécessaire d'étudier en détail les conséquences d'une telle rupture et d'essayer de prendre pour EL4 un ensemble de précautions telles que cette rupture n'entraîne pas une mise hors service du réacteur. Ce point de vue se justifie spécialement par le caractère prototype du réacteur dont le fonctionnement doit permettre de mieux connaître et comprendre le comportement du tube de force et de son équipement.

Les conséquences de cette rupture éventuelle sont de plusieurs ordres (effets mécaniques de choc, de pression, effets de réactivité, effets thermiques, etc. ...); mais les effets mécaniques occupent une place de première importance dans cet ensemble, car ils paraissent faire courir les risques les plus importants et les plus immédiats à la cuve du réacteur et à son environnement.

On peut diviser, assez arbitrairement d'ailleurs, les conséquences mécaniques de la rupture d'un tube de

force en deux catégories :

- Les conséquences locales qui concernent plus particulièrement les effets de la rupture sur les tubes voisins : déroulement et fragmentation du tube de force, projection des éléments combustibles, etc. ..., et comportement des tubes les plus proches.

  Les études correspondantes, encore inachevées, ont été menées sur une maquette à l'échelle 1 avec diverses mesures et clichés cinématographiques. On a utilisé pour représenter les tubes de force de matériaux plus fragiles (Zircalloy 2 écroui en particulier) que celui prévu pour EL4 qui, rappelons-le, est du Zircalloy 2 recuit ; le but de cette substitution est de tenir compte dans une certaine mesure des effets de l'irradiation sur les tubes. Ces derniers effets, qui ne sont encore qu'imparfaitement connus, compliquent notablement l'interprétation des résultats obtenus.

- Les conséquences globales qui concernent l'évolution de la pression dans la cuve d'eau lourde à la suite de l'irruption du gaz caloporteur libéré par la rupture du tube. On étudie également la tenue de la cuve à cette évolution de pression.

  Les études correspondantes ont été menées sur deux types de montages : un montage à grande échelle (1/2) destiné à apprécier directement les phénomènes en limitant au maximum les corrections éventuelles d'échelle (déformations, fragilité, dégradations d'énergie) ; un montage à échelle réduite (1/10) destiné à une étude systématique des différents paramètres (dimensions du tube, pression, température, etc. ...).

3 - EFFETS LOCAUX DE LA RUPTURE : TENUE DES TUBES VOISINS -

Le faux canal à échelle 1, malgré ses simplifications, reproduit avec une certaine fidélité le canal du réacteur EL4.

La cuve est figurée par un bac empli d'eau qui assure également la réplique de la géométrie des fonds et de l'amorce des prolongements de canaux. Sur ces prolongements, sont piqués des tubulures figurant les tubulures d'alimentation du canal en gaz caloporteur.

Un de ces prolongements est coulissant dans le fond et permet, grâce à un système de vérin, de placer dans un état de traction convenable le tube de force situé entre les deux prolongements et fixé par ses extrémités à chacun d'eux.

L'ensemble de l'installation (après exécution d'un essai) est représenté sur la planche 3.

Les canaux voisins sont figurés par des tubes sous pression placés autour du tube essayé.

La représentation de l'intérieur du canal proprement dit a exigé le recours à un certain nombre de transpositions dues :

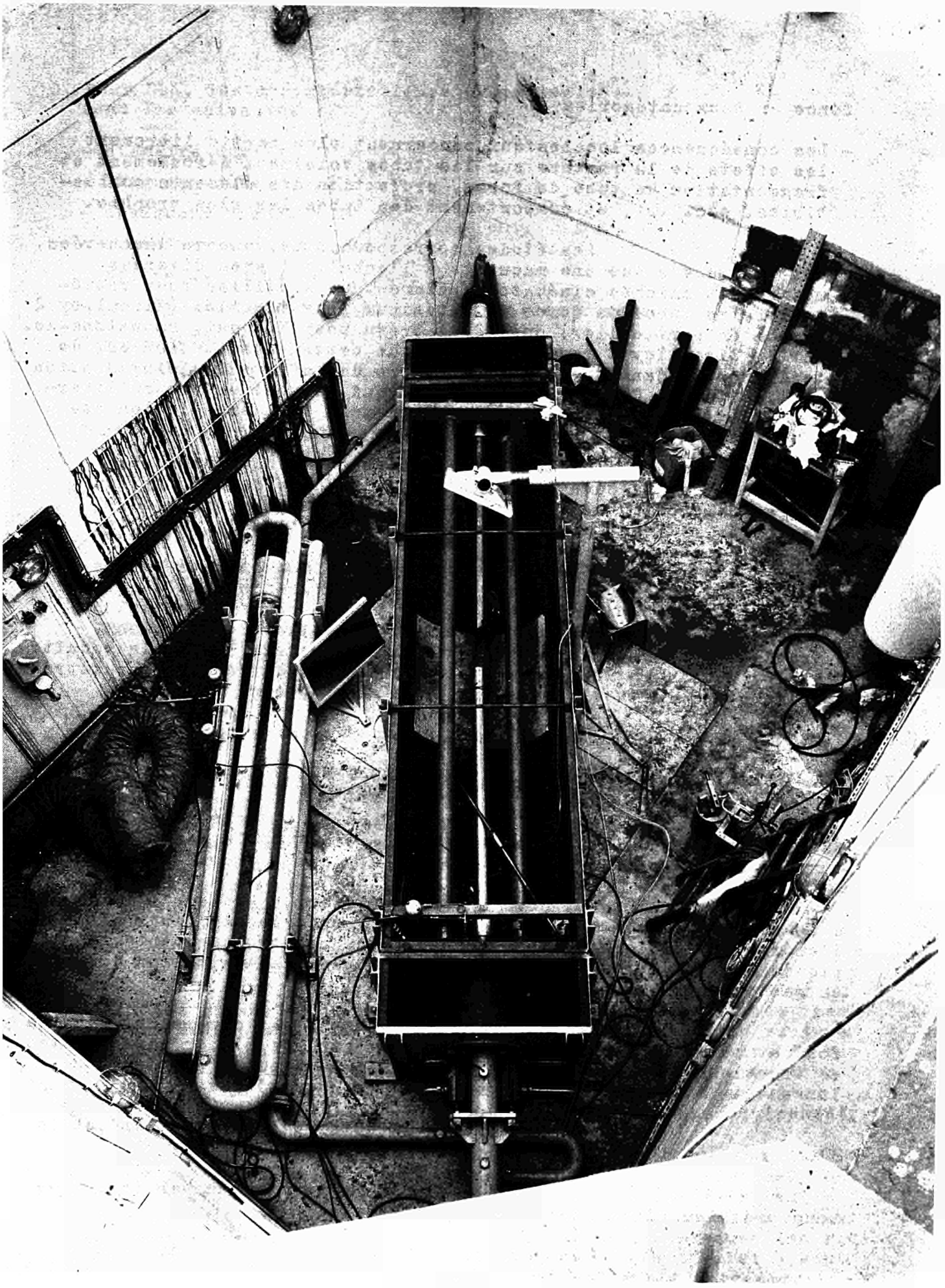

fig. 3

- à la non-circulation du gaz,
- à l'exécution des essais à la température ambiante.

Il a fallu en particulier remplacer le tube de guidage par un tube d'un matériau dont les propriétés à la température ambiante soient comparables à celles du tube réel à sa température de service. De même, l'effet de poussée aérodynamique sur les éléments combustibles a été simulé par un poussoir à ressort.

L'ensemble est installé dans la grande fosse d'essais dangereux de SACLAY, et bénéficie ainsi de l'équipement de mesures y afférent, le dispositif lui-même portant les différents capteurs (pressions, forces) ainsi que certains dispositifs tels que des cibles de tôle de laiton destinées à apprécier les dégâts causés par les projectiles libérés par la rupture.

La rupture elle-même est due à une entaille préalable créant une sous-épaisseur sur une portion de génératrice, c'est donc la pression qui, en croissant, provoque la rupture, à une valeur assez voisine de la pression de service. Du fait de l'incertitude sur l'instant même de la rupture, les mesures sont auto-déclenchées par le phénomène lui-même ; en particulier, pour la cinématographie rapide du phénomène, il a fallu utiliser un système original de caméra à tambour tournant et d'éclairage à éclairs déclenchés par la rupture d'une sonde placée sur les lèvres de la rupture (9).

Résultats des essais - Conséquences -

Ce genre d'essai est assez complexe et ne permet pas une exploration systématique des paramètres principaux ; le nombre d'essais exécutés restant assez faible (une dizaine). Par contre, il permet une assez bonne appréciation des risques et de mettre en évidence les principaux éléments du problème.

Les facteurs les plus importants qui apparaissent concernent :

- la longueur de l'entaille
- le matériau du tube
- la robustesse de la jonction du tube sur les prolongements
- la présence du tube de guidage et de l'isolation thermique

Pour les deux premiers points, nous devons signaler tout d'abord que nous n'avons pas obtenu de fragmentation du tube explosant. D'autres essais portant sur des matériaux très fragiles devront donc être envisagés, mais il semble que pour EL4 du moins, où le tube est utilisé à l'état recuit, le risque de fragmentation reste assez faible (les essais ont porté sur des tubes écrouis dont l'allongement à rupture était plus faible que celui que l'on escompte pour les tubes réels à la fin de leur vie).

Le fait important est l'existence d'une longueur minimale d'entaille en deçà de laquelle le tube ne se déroule pas et ne fait que bailler, ce qui n'entraîne que des dégâts limités. Cette longueur, est pour le tube équipé, de l'ordre d'une vingtaine de centimètres ; elle dépend, bien entendu, du matériau et

de son état d'écrouissage.

La robustesse des jonctions du tube sur les fonds de cuve (prolongements de canaux) est un facteur essentiel lorsqu'on a affaire à une rupture longue (longueur supérieure à la longueur critique définie ci-dessus). Des jonctions affaiblies (saignée locale réduisant l'épaisseur à 60 % de sa valeur) conduisent à la rupture du tube aux jonctions et, par suite, à la séparation du tube en trois tronçons avec une aggravation sensible des dégâts. On a cependant établi que les jonctions non affaiblies (épaisseur entière) permettent d'éviter une telle rupture par flexion sous la réaction du jet.

La présence du tube de guidage et de son isolation thermique ont également une importance extrême ; cet ensemble reste assez ductile et tend à provoquer un net retard à la rupture complète. Du fait de leur présence, la rupture longue a lieu en deux temps.

Un premier temps d'une durée de l'ordre de 20 millisecondes où il n'y a pas de rupture du tube de guidage et où le tube de force baille sans se dérouler. Cette première phase de la rupture mise en évidence par la forme de la variation de pression a été étudiée par cinématographie ultra-rapide autodéclenchée ; la planche 4 reproduit les images obtenues où l'on voit une oscillation des lèvres de la fissure à une fréquence voisine de 600 Hz avec une amplitude de 30 à 40 mm suivie, au bout de 15 millisecondes, de la rupture proprement dite qui laisse à nu les éléments combustibles qui ne tarderont pas à être éjectés après le déroulement du tube de force.

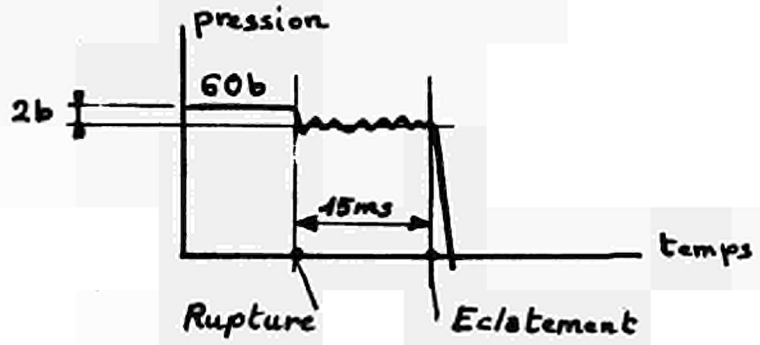

Les dégâts obtenus sont, dans le cas de la rupture courte, limités au baillement des lèvres de la fissure et à l'éjection de fragments de la chemise en graphite. Ces fragments de l'ordre du cm^3 sont susceptibles de percer des tôles de laiton d'épaisseur 2/10 mm, ce qui permet d'apprécier leur énergie qui est très insuffisante pour occasionner des dégâts aux tubes de force voisins.

La rupture longue correspond à des dommages beaucoup plus importants ; le tube se déroule sur la longueur de l'entaille et se sépare des deux tronçons restant accrochés aux prolongements (voir planche 5). Par l'ouverture ainsi créée, les éléments combustibles sont éjectés vers les tubes de force voisins et disloqués dans la cuve. Ce sont eux qui constituent en quelque sorte les projectiles redoutables ; leur vitesse n'a pu être éva-

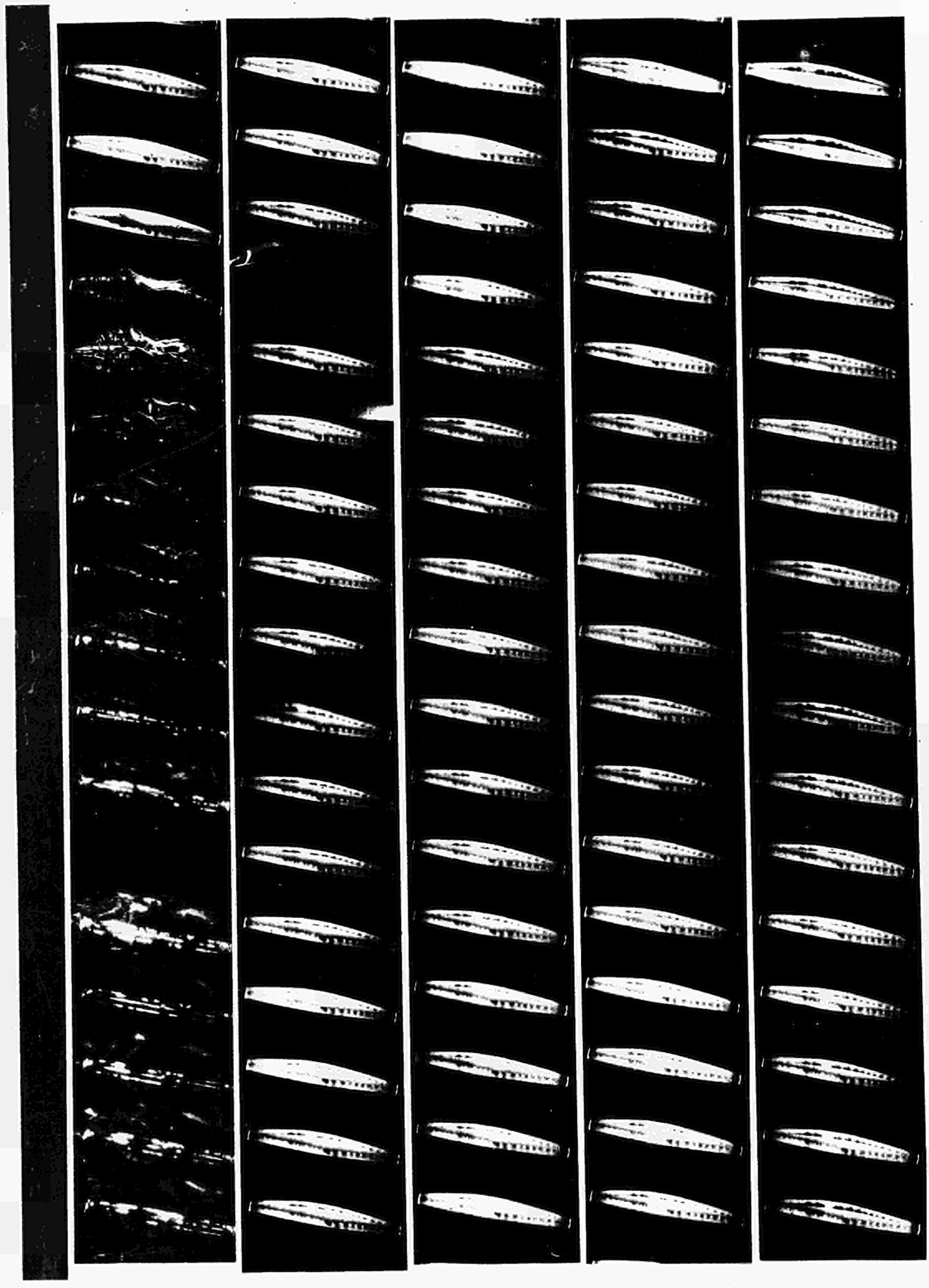

fig. 4

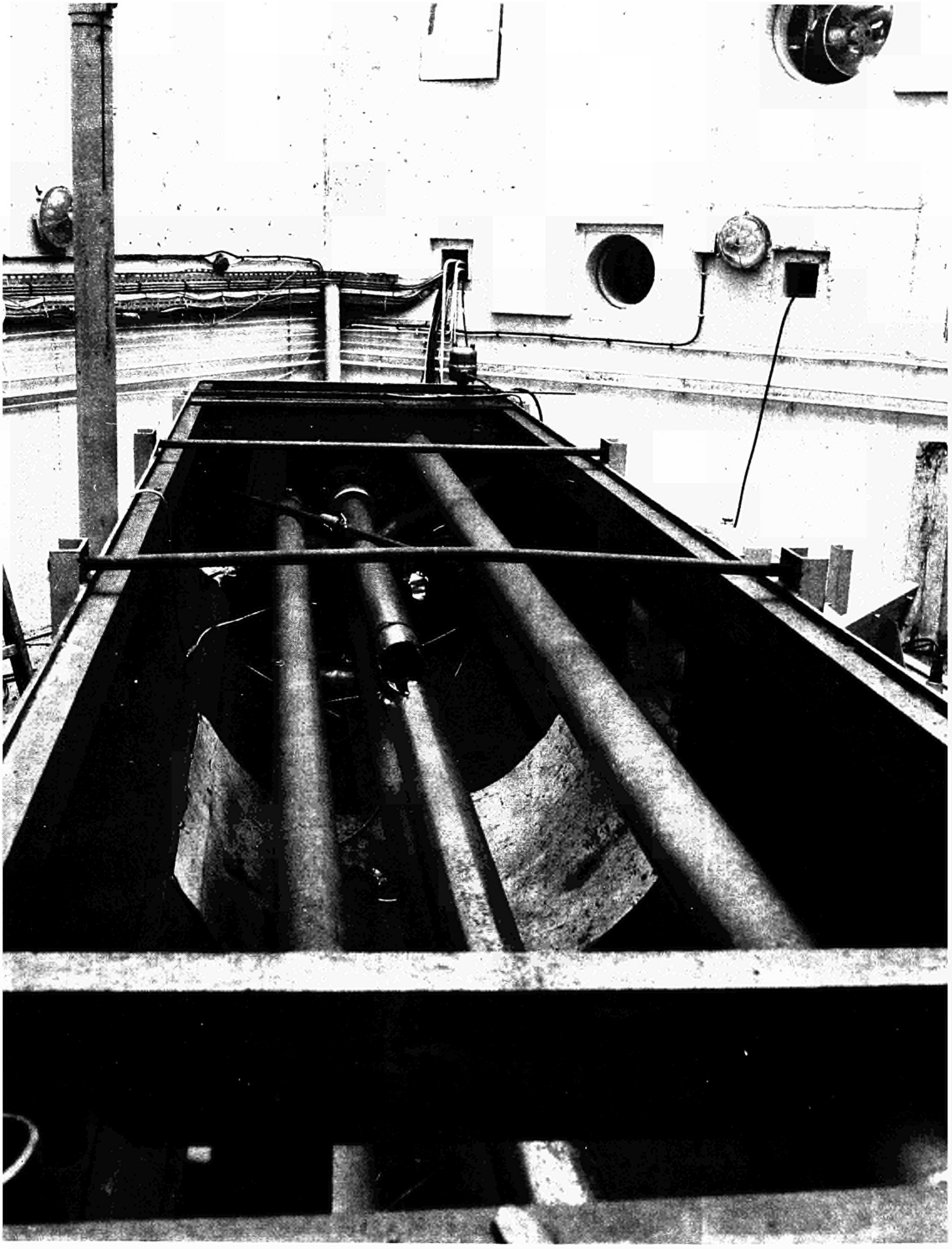

luée que très grossièrement (15 à 20 m/s) mais a jusqu'ici été insuffisante pour détériorer les tubes voisins. La planche 6 représente les éléments éjectés et met en évidence la grande déformation qu'ils subissent au moment de leur sortie (la grappe de gauche a été pliée en forme de U) ce qui entraîne certainement un certain freinage.

4 - EFFETS D'ENSEMBLE DE LA RUPTURE : TENUE DE LA CUVE -

L'étude de la résistance de la cuve et de ses différents accessoires a également fait l'objet d'essais à grande échelle (1/2) qui ont montré le bon comportement général de l'installation. Ces essais très importants, menés à GRENOBLE, ne se sont pas prêtés à une analyse extensive du rôle des différents paramètres qui a été faite sur des maquettes à échelle réduite dont les essais ont été exécutés à SACLAY.

Ces essais ont fait l'objet d'un rapport très complet (10) auquel on voudra bien se reporter pour un examen complet, l'ampleur prévue pour la présente communication ne permettant guère que d'en fournir un résumé complété de la mention de quelques essais complémentaires.

Le matériel d'essai se compose essentiellement de maquettes à l'échelle 1/10 dont certaines sont transparentes pour permettre l'étude par cinématographie ultra-rapide. Le tube de force explosant est figuré par un tube en matière plastique qui permet une rupture rapide et une fragmentation totale.

L'instrumentation consistait en enregistrement, de pression, de contraintes et de force, enregistrement effectué essentiellement sous forme d'oscillogrammes auto-déclenchés.

Le phénomène a, de plus, fait l'objet d'une étude complète par cinématographie ultra-rapide, dont les résultats recoupant ceux des enregistrements ont permis de les interpréter de façon sûre.

Description du phénomène -

Cette étude systématique a permis de distinguer deux phases essentielles dans le phénomène :

- la première phase constituée par une série de pics de pression allant en s'amortissant et où il n'y a pas d'eau éjectée de la cuve ;

- la seconde phase où la pression s'établit à un palier faiblement décroissant et où l'eau est régulièrement éjectée de la cuve *.

Ces deux phases sont évidemment liées par une zone de transition, mais elles sont cependant nettement différenciées dans les films ultra-rapides, on pourra également apercevoir la différence sur la planche 7 représentant un enregistrement des pressions :

- du gaz dans la tubulure d'alimentation (en haut)

fig. 7

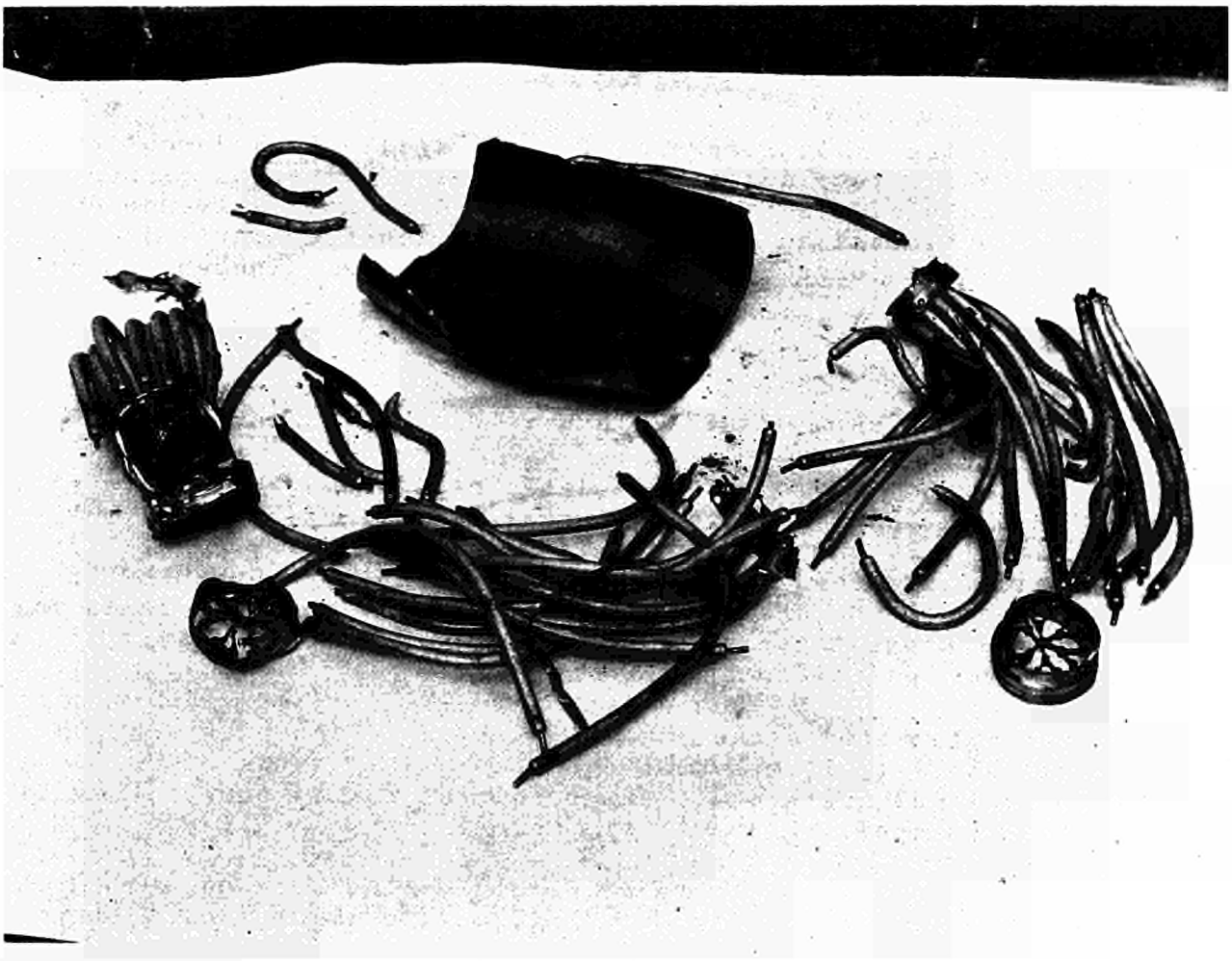

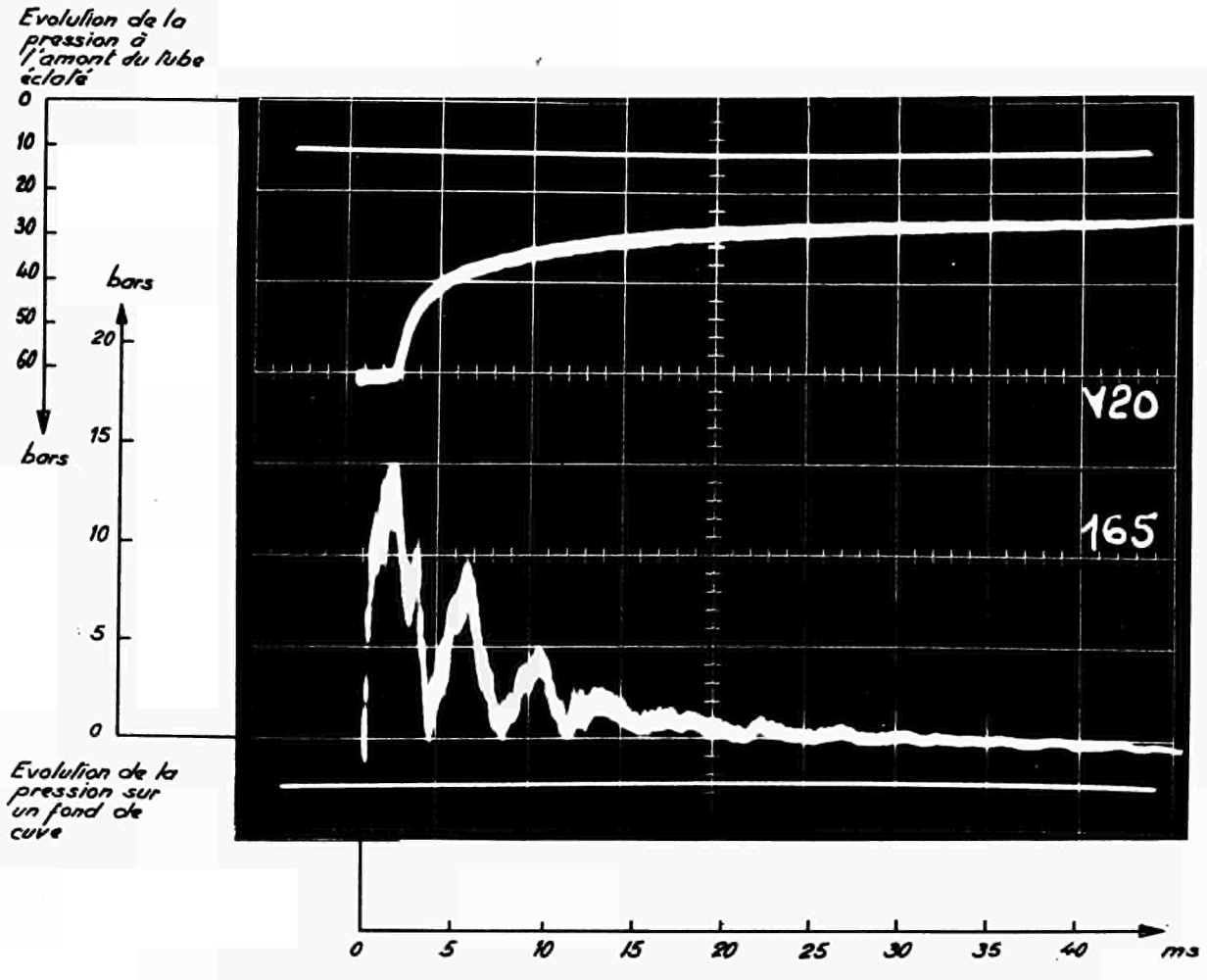

Evolution type de la pression au cours des premières milli-secondes qui suivent l'éclatement (pas de réseau de tubes, source en position basse Z = 0,08).

- de l'eau dans la cuve (au-dessous)

Cette dernière pression peut être schématisée ainsi :

* Nous laisserons de côté une troisième phase, peu intéressante qui s'établit lorsque l'eau lourde a été expulsée et que le gaz s'évacue par l'exutoire.

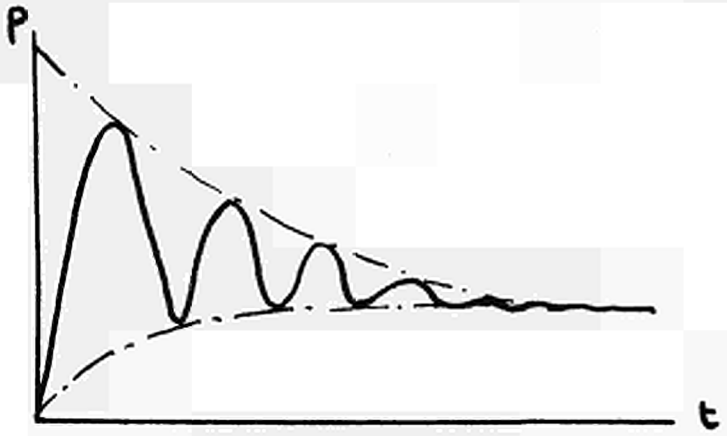

Etude de la pression maximale -

La seconde phase est d'une analyse facile : tous les résultats obtenus montrent qu'elle correspond au régime établi d'arrivée du gaz par le tube et d'éjection de l'eau lourde par les exutoires ; le régime des pressions obtenu correspond nettement à cet état de régime gouverné essentiellement par les dimensions respectives des orifices en présence (tubulures d'arrivée de gaz et exutoires d'évacuation d'eau lourde).

La première phase correspond à des pressions supérieures à celles de la seconde (10 à 15 bars contre 2 à 3) qui apparaissent sous forme de pics assez longs pour que l'on doive considérer qu'ils s'appliquent statiquement sur la cuve ; c'est d'ailleurs ce que l'on constate en analysant les contraintes sur la cuve, ces contraintes correspondent à une extension en phase avec le pic de pression, extension à laquelle il faut superposer des vibrations de flexion. C'est dire que l'étude de la pression maximale atteinte au cours du premier pic est de la plus haute importance puisque c'est à cette pression que correspondent les contraintes d'extension susceptibles de détériorer la cuve.

Il faut donc sélectionner d'abord les paramètres ayant une influence sur la valeur de cette pression, puis expliciter la corrélation entre la pression et lesdits paramètres.

La planche 8 représente l'influence :

- de la section des exutoires (évacuation de l'eau) ;
- de la hauteur d'eau dans les exutoires ;
- de la section d'arrivée de gaz.

On constate aisément que ces paramètres ont l'influence la plus réduite (sauf pour la hauteur d'eau, lorsque la cuve n'est pas pleine). Il s'agit des paramètres concernant la liaison de la cuve avec l'extérieur, ce qui laisse supposer que ce sont les paramètres intérieurs à la cuve qui sont particulièrement significatifs, et c'est ce que l'on constate effectivement, les paramètres importants étant :

- la pression du gaz dans le tube avant rupture p_o
- le volume du tube v_o
- la "flexibilité" de l'ensemble avec cuve-eau F telle que l'accroissement de volume sous une pression p soit FP

On peut donc représenter la valeur de la pression maximale de p_{pic} par une relation

$$p_{pic} = \text{fonction de } (p_o, v_o, F)$$

qui, pour des raisons d'homogénéité, doit s'écrire :

$$\frac{p_{pic}}{p_o} = \text{fonction de } \frac{V_o}{F p_o}$$

La planche 9 montre le résultat obtenu en portant les résultats expérimentaux obtenus sur le diagramme correspondant ; on les voit se regrouper convenablement pour justifier cette analyse et même fournir ainsi un moyen de déterminer la pression de pic à partir des trois paramètres v_o, p_o, F.

Un correctif doit être apporté pour le choix de la valeur de v_o lorsque la partie rompue du tube est très courte ; l'influence du gaz situé dans les parties voisines amène pour ce cas à définir une longueur équivalente. Les résultats correspondants sont portés sur la planche 10 qui montre que pour une longueur inférieure à celle de la cuve, cette correction devient négligeable puisque les résultats deviennent les mêmes que l'on alimente le tube par une ou deux extrémités.

Modèle - Interprétation -

Il est intéressant de tenter de constituer un modèle conduisant à préciser la forme de la relation précédente ; un modèle simple peut en effet s'obtenir en considérant l'oscillation de la masse d'eau entre la bulle de gaz et la virole élastique. L'étude de cinématographie justifie ce point de vue ainsi qu'on peut le voir sur la planche 11 représentant l'évolution simultanée de la pression et du diamètre de la bulle. On obtient ainsi la relation suivante :

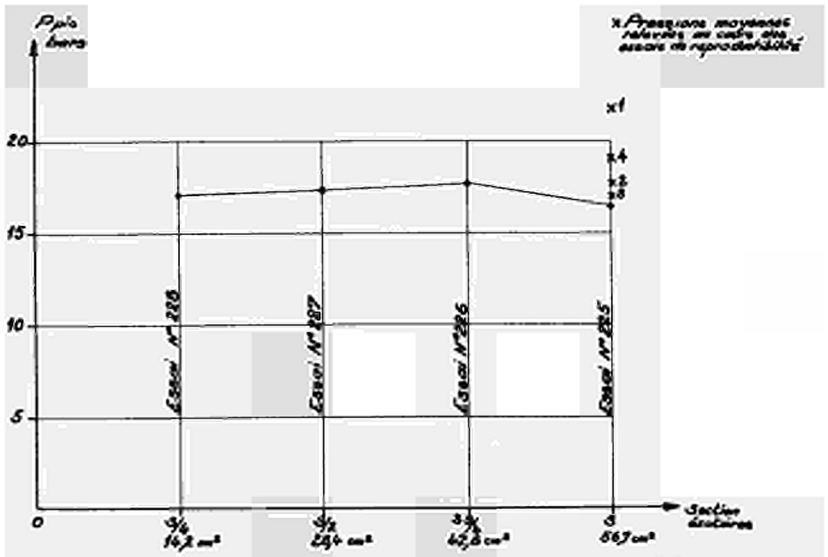

Influence de l'étranglement des orifices de décharge.

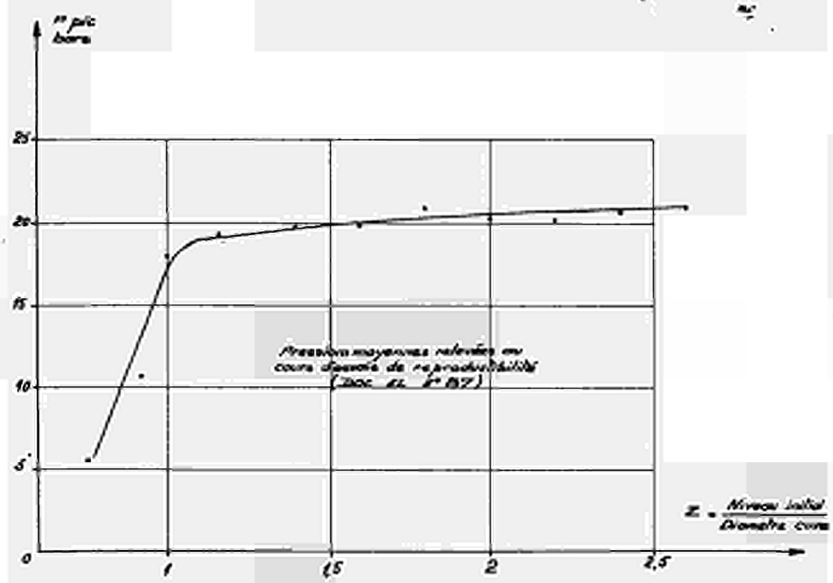

Influence de la hauteur d'eau dans les orifices de décharge.

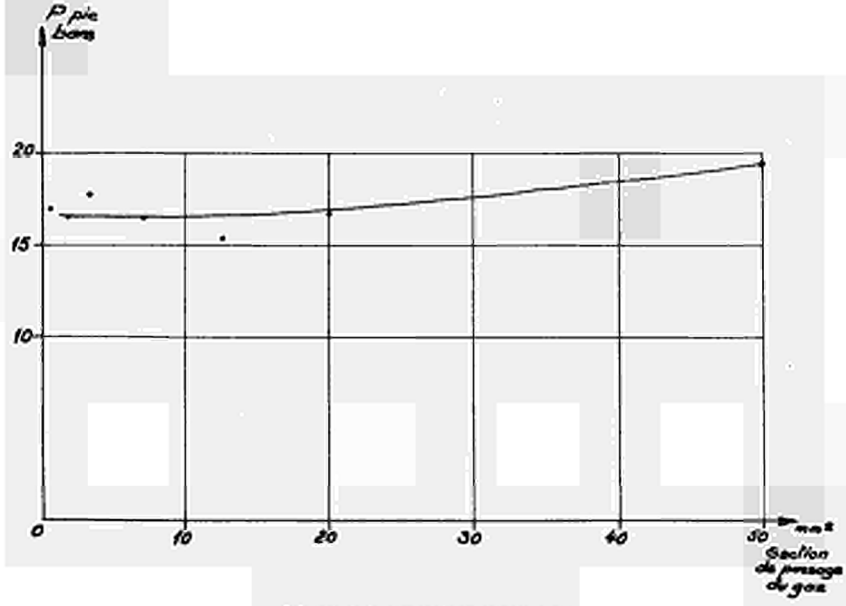

Influence de la section d'alimentation en gaz.

fig. 8

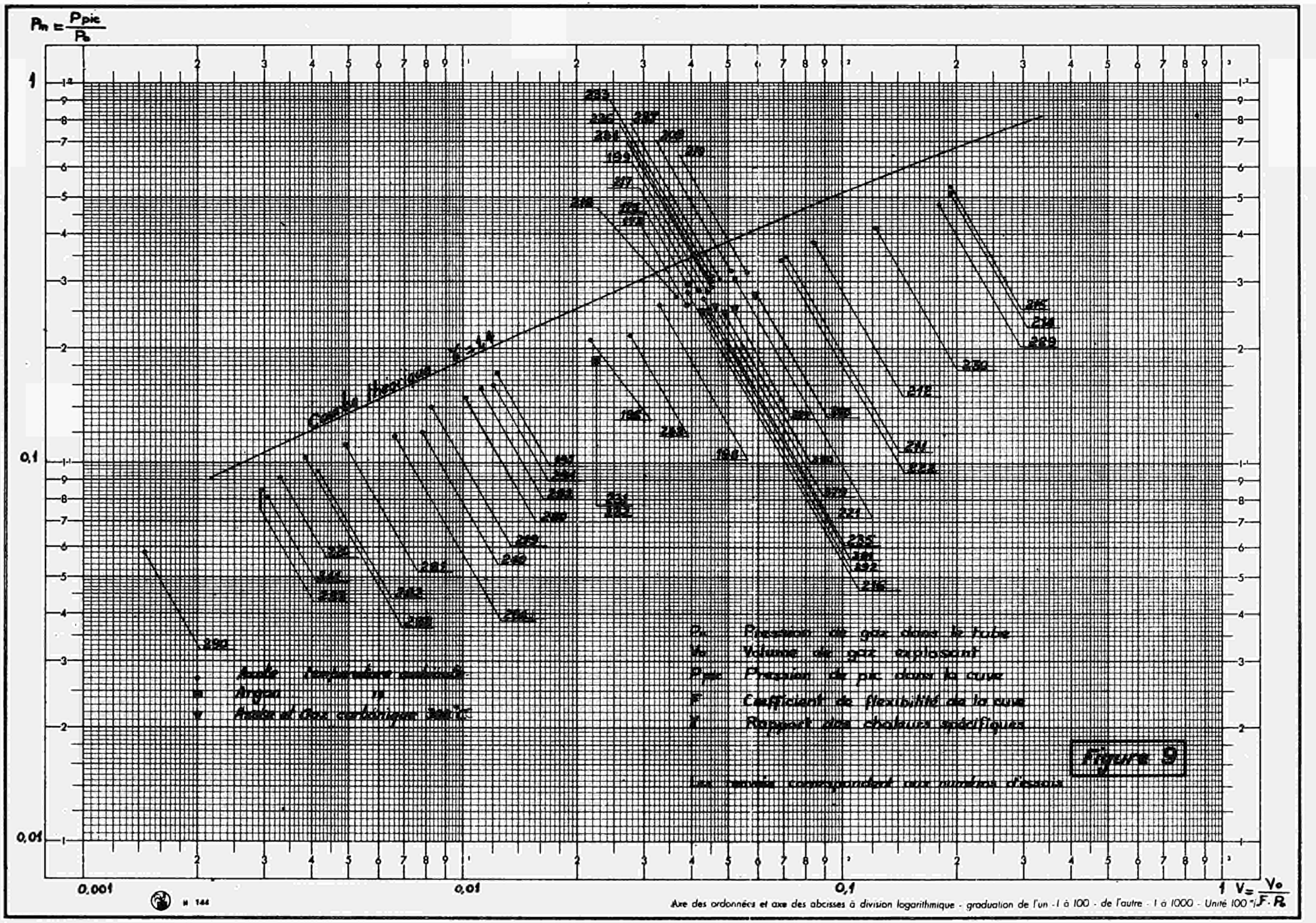
$P_m = \frac{P_{pic}}{P_o}$
Courbe théorique $\gamma = 1,4$
Acide Température ambiante
Argon "
Acide et Gaz carbonique 360°C
P_m Pression du gaz dans le tube
V_o Volume de gaz explosant
P_{pic} Pression de pic dans la cuve
F Coefficient de flexibilité de la cuve
γ Rapport des chaleurs spécifiques
Les traits correspondent aux numéros d'essais
$V = \frac{V_o}{\sqrt{F \cdot R_o}}$
0,001
0,01
0,1
1
Axe des ordonnées et axe des abcisses à division logarithmique - graduation de l'un - 1 à 100 - de l'autre - 1 à 1000 - Unité 100 mm

Figure 9

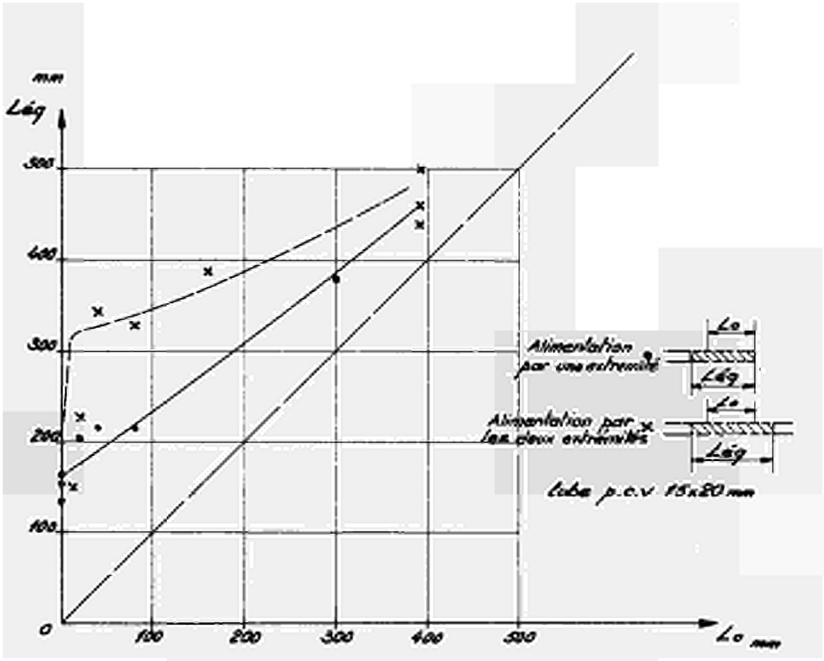

Longueur de tube à considérer en fonction de la longueur réelle de rupture.

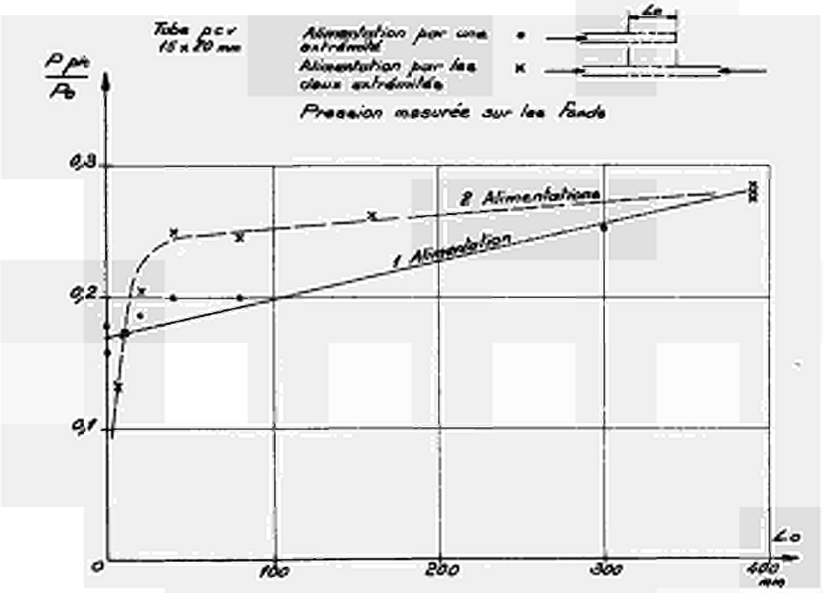

Evolution de la pression de pc en fonction de la longueur de rupture.

fig. 10

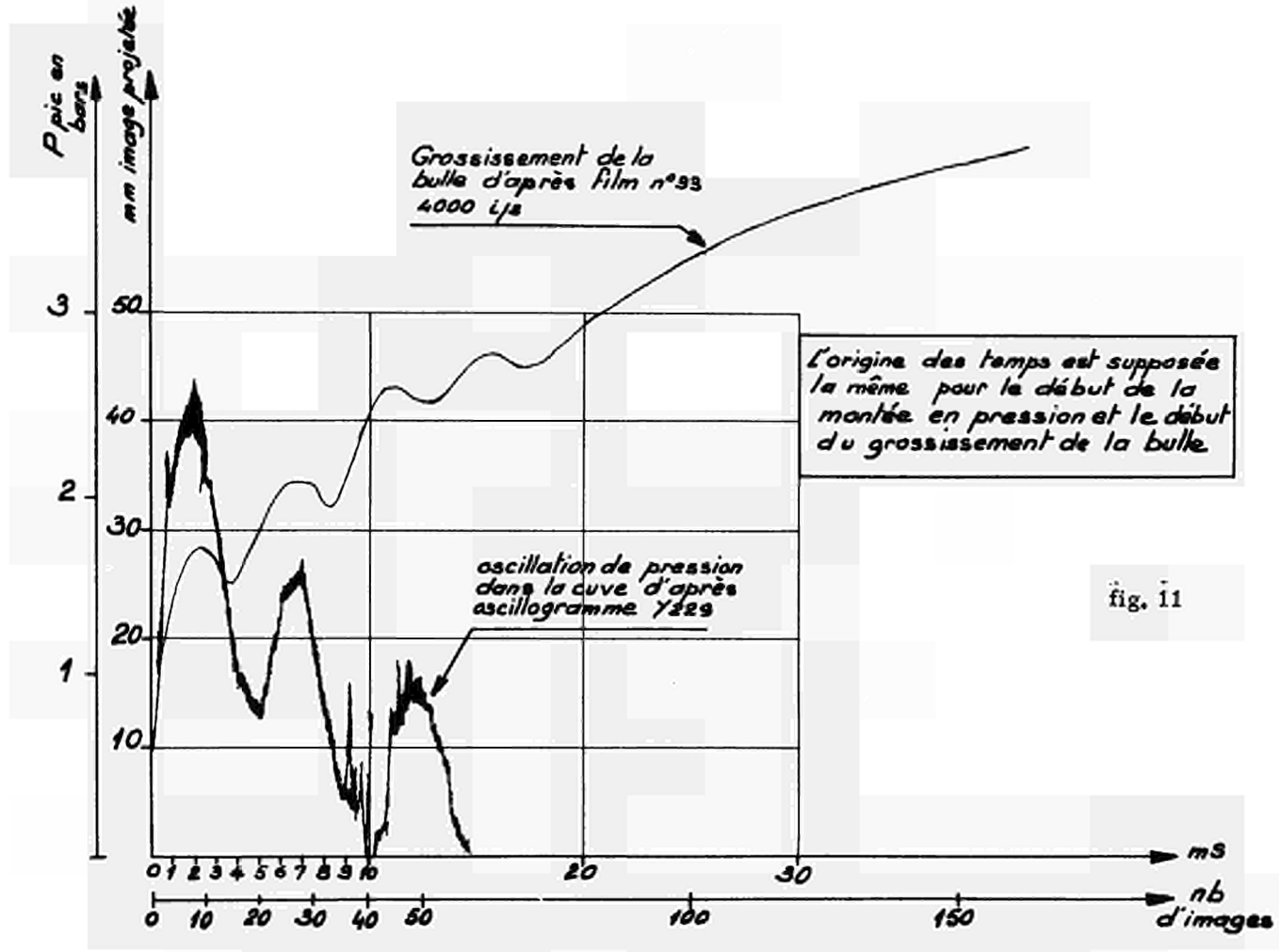

fig. 11

Comparaison de l'oscillation de la bulle enregistrée par cinématographie rapide et de la pression dans la cuve.

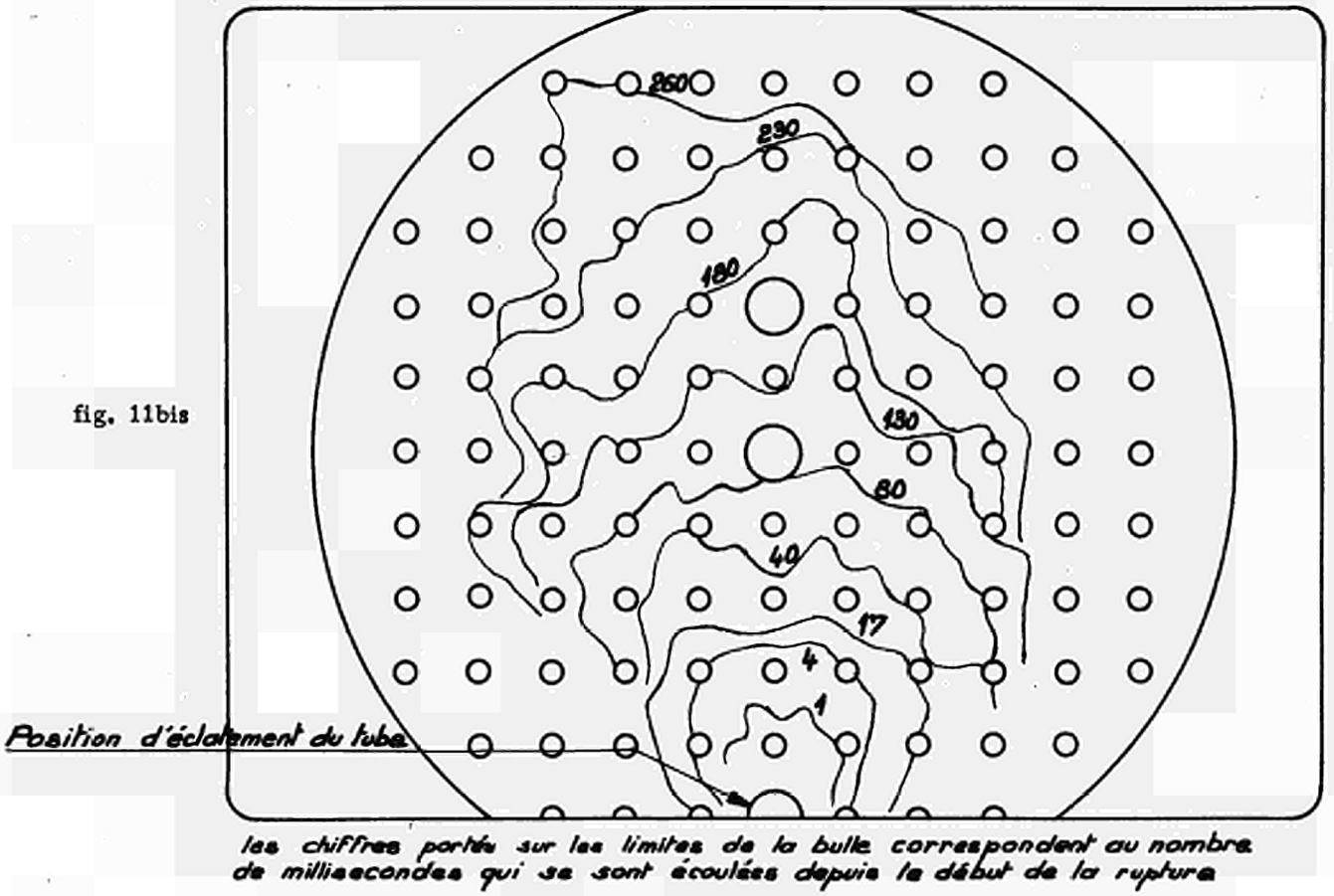

fig. 11bis

Carte du grossissement de la bulle.

$$\left(\frac{P_{pic}}{P_o}\right)^2 = \frac{2}{\gamma-1}\ \frac{v_o}{F p_o}\left\{1-\left(\frac{P_{pic}/P_o}{v_o/F p_o}+1\right)^{1-\gamma}\right\}$$

la courbe correspondant à γ = 1,4 (rapport des chaleurs spécifiques de l'Azote) est portée sur la planche 9 ; on peut voir que les points expérimentaux relatifs à l'Azote se groupent entre 75 et 85 % de la valeur obtenue, ce qui fait penser à un certain amortissement qui correspond sensiblement à celui constaté d'un pic à l'autre (la valeur de cet amortissement ne paraît pas dépendre sensiblement des dimensions de la maquette).

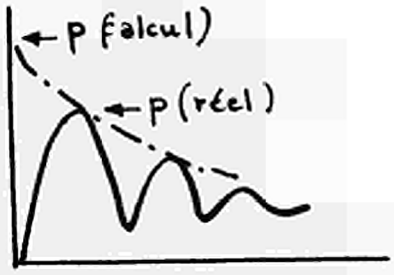

Ce modèle, qui s'adapte bien à la réalité, implique que les échanges de fluides entre la cuve et les systèmes extérieurs n'interviennent pas dans les mécanismes qui gouvernent le phénomène. L'étude par cinématographie ultra-rapide confirme la réalité physique de ce point de vue :

- Pendant les premiers pics de pression, le niveau d'eau dans les exutoires reste immobile : il n'y a pas sortie d'eau. Ceci peut être attribué à l'inertie de la masse d'eau vis-à-vis des mouvements rapides concernés.

- L'évolution de la bulle de gaz montre qu'il y a deux "bouffées", la première correspondant à la première phase, la seconde étant due à l'arrivée continue du gaz qui entame la seconde phase. On peut tenter de comprendre cette césure en considérant que le début de la première phase correspond à l'émission d'une onde de dépression dans les canalisations de gaz, ce qui n'entraîne qu'un faible débit de gaz (le tiers à peu près du régime permanent), alors que la deuxième phase correspond au régime établi de l'arrivée de gaz qui entraîne un débit appréciable. Il existe alors un "trou" entre la première bulle provoquée par le gaz du tube et l'arrivée d'un débit important à la suite des réflexions diverses de l'onde de dépression.

Par suite de cette hypothèse, on doit introduire comme paramètre supplémentaire, le rapport des chaleurs spécifiques du gaz employé. Ce point a été examiné par emploi de gaz tels que l'Argon et le gaz carbonique ; si, pour le premier, on vérifie convenablement la formule, il n'en est pas de même pour le second qui, utilisé à la température ambiante, est loin de se comporter comme un gaz parfait (liquéfaction et solidification partielle momentanées).

Ces essais à température ambiante ont été complétés par des essais avec du gaz chaud ; on a pu constater alors que l'amortissement était légèrement plus important qu'avec le gaz froid (voir planche 9) ; cet effet a été attribué aux échanges thermiques entre eau et gaz sur le front de la bulle.

5 - CONCLUSION -

Les études et essais effectués ont montré que pour la qualité de tube utilisée à EL4 et pour l'équipement interne prévu, il n'y avait pas de risque que la rupture d'un tube de force entraîne des ruptures de tubes voisins. Pour des tubes de force de qualité différente, admettant des contraintes plus élevées, cette conclusion serait à réexaminer.

D'autre part, on a pu déterminer la valeur de la pression maximale règnant dans la cuve et, ainsi, dimensionner convenablement celle-ci de façon qu'elle puisse survivre à l'accident.

Les travaux exposés ci-dessus sont évidemment une oeuvre collective ; néanmoins, l'auteur se plaît à évoquer l'importance de la participation de MM. VRILLON et GARNIER du D.E.P. ainsi que l'aide efficace apportée par M. MEUNIER à ces études de sûreté.

*

* *

- R E F E R E N C E S -

1 - Le projet EL4 par J. HOROWITZ, B. BAILLY DU BOIS et R. NAUDET - Energie Nucléaire (Novembre-Décembre 1961).

2 - EL4 - Centrale Nucléaire des Monts-d'Arée - Plaquette du C.E.A. et E.D.F. (10 Octobre 1963).

3 - Caractéristiques et problèmes de construction d'EL4 par R. CARLE, P. SCHULHOFF, P. SEVIN, J. BUTTIN - Communication à Conférence de GENEVE 1964.

4 - Filière Eau Lourde-Gaz par B. BAILLY DU BOIS, JL. BERNARD, R. NAUDET, R. ROCHE. - Conférence de GENEVE 1964 -

5 - Ensemble du Bulletin d'Informations Scientifiques et Techniques du C.E.A. n° 87 (Octobre 1964).

6 - Structures du coeur du réacteur "Eau Lourde-Gaz" EL4 par JL. BERNARD, H. FOULQUIER et P. THOME - Communication à la 3ème Conférence de GENEVE.

7 - Quelques problèmes de sûreté relatifs à un réacteur à tubes de force par A. MEUNIER, R. ROCHE et B. VRILLON - Bulletin d'Informations Scientifiques et Techniques du C.E.A. (Juillet 1962).

8 - Conception de la sûreté en France et influence des impératifs de sûreté sur la conception des réacteurs par F. DE VATHAIRE etc. .. Communication à la 3ème Conférence de GENEVE.

9 - Cinématographie ultra-rapide d'un éclatement par auto-déclenchement par B. VRILLON - Communication au 7ème Congrès International de Photographie Ultra-rapide de ZURICH (Septembre 1965).

10 - Etude des conséquences de la rupture d'un tube de force dans la cuve d'un réacteur modéré à l'eau lourde et refroidi au gaz par F. HAREUX, R. ROCHE et B. VRILLON - Rapport C.E.A. R 2459.

FULL SCALE EXPERIMENT ON THE CONSEQUENCES OF A PRESSURE TUBE RUPTURE IN ESSOR REACTOR VESSEL

by

H. Holtbecker, M. Montagnani

and

G. Verzeletti

Euratom CCR, Ispra, Italy

1. INTRODUCTION

The ESSOR reactor system is composed of a number of independent units of similar geometry, known as channels.

One object of the core safety study is to ensure that the individual units remain independent even in the event of an accident caused, for instance, by failure of the pressure tube, or by failure of both the pressure tube and the calandria tube.

The events associated with this problem are:

- The pressure waves which are propagated in the moderator and which originate in the contact between the coolant liquid and the heavy water at the moment of failure, and the waves set up by the formation of organic and water vapours and their recondensation through heat exchange between the two components.
- The dynamic loading in the vessel and the other channels, resulting from these pressure waves or from thermal stresses, caused by local heating of the areas struck by the jet of not organic liquid.

As will be seen, not all of the problems quoted can be solved by a direct quantitative calculation, for some of them entail experimental study.

The experiments carried out respected, in the essential part, the real geometry and the real coolant fluid, and light instead of heavy water was used[1]. The reason for respecting the scale was, as will be seen further on, the impossibility of effecting a complete, absolute analogy, since the phenomena we were dealing with depend on parameters whose relative importance was

unknown.

The analogy should be effected on the basis of four fundamental magnitudes:

l	= length	where	$l_{mod} = l^* = \lambda \cdot l$ and similarly
t	= time		$t^* = \tau \cdot t$
K	= forces		$K^* = x \cdot K$
T	= temperature		$T^* = \delta \cdot T$

The limit conditions sought must satisfy the Navier - Stoke or Fourier differential equations for the model and the original, and relate to the description of

- the fields of velocity
- the fields of temperature
- the fields of pressure.

This satisfaction is obtained by equating the parameters in the above-named equations which can be expressed in Re, Gr, Froude, Cauchy, etc., numbers.

To start with, we define the ratio of the inertia forces expressed by Newton's law:

$$x = \frac{m^* b^*}{mb} = \frac{\rho^*}{\rho} \cdot \frac{\lambda^4}{\tau^2} \text{ , which where } \frac{\rho^*}{\rho} = 1 \text{ becomes } x = \frac{\lambda^4}{\tau^2} \qquad (1)$$

No potential flow can be assumed for the liquid in our case; the friction forces must therefore be taken into account in determining the fields of both velocity and temperature.

The ratio for the forces, as defined above, must remain constant.
Then:

$$x = \frac{\eta^* \cdot dw^* \cdot F^*}{dn^*} \cdot \frac{dn}{\eta \cdot dw \cdot F} \quad ;$$

it is assumed that the type of liquid or material will not be changed and then

$$x = \frac{\lambda^2}{\tau} = \frac{\lambda^4}{\tau^2} \rightarrow \tau = \lambda^2 \qquad (2)$$

which corresponds to Reynold's model law.

At this point the ratios λ, τ and x are fully determined and can be calculated. In the problem to be dealt with, other forces such as those due to gravity, or elastic stresses, should be reproduced in the same ratio as those already treated.

Two further relations are obtained from

$$x = \frac{\gamma^* \cdot V^*}{\gamma \cdot V} = \lambda^3 \qquad \text{with (1)} \quad \frac{\lambda^4}{\tau^2} = \lambda^3 \rightarrow \tau = \sqrt{\lambda} \qquad (3)$$

which corresponds to Froude's law;

$$x = \frac{E^* \cdot \varepsilon^* \cdot F^*}{E \cdot \varepsilon \cdot F} = \lambda^2 \text{ with (1)} \quad \lambda^2 = \frac{\lambda^4}{\tau^2} \rightarrow \tau = \lambda \qquad (4)$$

which is Cauchy's law.
It is then clear that (2), (3) and (4) are only satisfied if $\lambda = 1$.

Moreover, there are a great many phenomena requiring study - including the formation of vapours and their recondensation versus place and time, which are of particular value to this work - which it has so far not been possible to deal with by model laws, and the study of dynamic events on model, where the time scale varies, involves significant variations of the characteristics of the material (elastic limit versus strain-rate, brittle behaviour of the material at high strain-rates).

Apart from these theoretical considerations, the decision to carry out the experiments on the real scale was also influenced by planning requirements; for the time available was only 18 months, from the start of designing the test rig to the completion of three experiments which were to provide data that could be reliably interpreted to determine the safety of the reactor, already at an advanced stage of design.

2. RIG CHARACTERISTICS

The failure of an ORGEL channel was simulated by reproducing the maximum pressure and temperature (30 atm., 420°C) and injecting into the vessel, through the crack in the channel, the organic throughput calculated from the ESSOR multiple circuit geometry (see fig. 1).

As the flowsheet shows (fig. 2) the organic liquid from the pump delivery

enters tank S_2 ($3\,m^3$ capacity), passes into the test channels and enters tank S_3 which simulates the expansion tank ($2\,m^3$ capacity). Tank S_2 allows of simulating the 170 l/sec delivery of the two pumps, by means of a gas blanket which reproduces their head. The calculated organic delivery in case of failure is shown in fig. 3. (2)

Design data for the circuit are:

pressure:	50 at
temperature:	450°C

The water circuit is connected to the vessel and to four feeding elements located in the experimental area. Both vessel and water circuit are constructed for an overpressure of 12 kg/cm^2 and a temperature of 190°C.

The vessel comprises two areas - the test area amounting to a quarter of the vessel cross-section, where the real material and geometry of the channels for the reactor are respected, and the second area where plain 99.5 Al tubes simulate the relevant channels.

The feeding elements, as also the control and safety rods, are guided in special gates on the false bottom of the vessel. The vessel is anchored to 4 solid cantilevers which rest on a prestressed concrete structure capable of supporting a static horizontal load of 18 metric tons. The installation has two nitrogen circuits. One, of high capacity, keeps the pressure in tank S_2 constant even while the organic liquid is pouring into the vessel; the other is connected only to a set of cylinders and allows of independent pressurizing of the vessel and tanks S_2 and S_3, by means of pressure-reducing valves operated from a bunker which houses all the remote controls and measuring gear.

3. DISCUSSION OF THE RESULTS

3.1 Effects of the pressure wave produced by a burst channel

The pressure tube fails along a purposely weakened generatrix, and as a result pressure rises in the annular heat-insulating gap and the inside of

the calandria tube comes in contact with the hot organic liquid.

The calandria tube, which is weakened in the same way as the pressure tube, normally fails some instants after the failure of the pressure tube. Fig. 4 shows the variations of pressure on the upper part of the pressure-tube during the first second after the burst. The moment at which the calandria tube fails is clearly visible, coinciding with the maximum static pressure in the annular gap. At the moment and place where coolant and moderator come into contact, a dilatation wave is propagated towards the inside of the tube in the organic part, while a pressure wave, generated by the elastic energy of the organic liquid, is propagated through the water. Even assuming, pessimistically, that the crack travels with the speed of sound, the wave front in the water will form an angle with the tube axis that can be calculated from the expression:

$$\operatorname{tg} \alpha = \frac{\text{speed of sound in } H_2O}{\text{speed of sound in Al}} = \frac{1500 \text{ m/sec}}{7000 \text{ m/sec}} = 0.214; \quad \alpha = 12.1^{\circ}$$

Thus the pressure to which the adjacent tubes or the vessel wall will be subjected will not amount to the same value simultaneously over a whole generatrix.

Furthermore, since the pressures in play are fairly low, they cannot build up a shock front but will propagate a series of sound waves. Shock waves form only when there are appreciable variations in the density of the water, with the resultant major dispersive effects.

The wave motion is described by the law of acoustic disturbances which in its integrated form allows of calculating the pressure peak decay with distance. Fig. 5 shows two theoretical curves corresponding to a decay in $\frac{1}{\sqrt{x}}$ and $\frac{1}{x}$.

A number of experimental points are shown, obtained from the diagram which records the pressures measured at two points on the vessel shell. The gauge pressures are lower than the calculated values, because no allow-

ance was made in the calculations for the pressure decay caused by deformation of the channel or for the diffraction due to the obstacles encountered by the pressure wave before it reaches the wall of the vessel.

In order to calculate the maximum strain energy provided by the impact of a wave on the channel, the total energy contained in the wave must be calculated. The maximum energy available has been calculated here on the basis of certain pessimistic assumptions:

- failure over the whole length of the channel;
- no allowance for energy losses due to dissipation in the liquid or plastic deformation of the tube.

The internal energy of the liquid is given by the expression [3]:

$$E_1 = c_p \cdot T_1 - v_o \cdot \beta \cdot p_1 \cdot t_1 + \frac{v_o p_1^2}{2K} + C$$

Passing adiabatically from condition $(p_1 T_1)$ to $(p_2 T_2)$ the energy released per unit of weight is:

$$E_1 - E_2 = T_1 \cdot c_p \left(1 - \frac{T_2}{T_1}\right) - v_o \cdot \beta \cdot T_1 \left(p_1 - p_2 \cdot \frac{T_2}{T_1}\right) + \frac{v_o}{2K}\left(p_1 - p_2^2\right)$$

The ratio $\frac{T_2}{T_1}$ is obtained by integrating the entropy equation

$$ds = \frac{c_p}{T} dT - \beta v_o \, dp = 0, \text{ giving } \frac{T_2}{T_1} = e^{\beta \frac{v_o}{c_p}(p_2 - p_1)}$$

The modulus of compression is obtained from the expression $c \cdot \rho^2 = K$, where C = 1000 m/sec $\pm$ 5% is the speed of sound in the organic liquid measured at 200°C.

The calculation shows that the temperature drop values for expansions of 30 atm. in this process are very small (< 1°C) and that the maximum energy released is that of the elastic expansion of the liquid, which is obtained by the expression:

$$E_i = \frac{v_o}{2K}(p_1^2 - p_2^2)$$

The energy thus calculated is compared with the strain energy of the guide tube for a feeding element assumed to have built-in or pinned extremities and to be subjected to a force concentrated in its middle area

$E = -\frac{1}{2}\int_1 My'' \, dx$ where $y'' = -\frac{M}{EI}$ is the differential equation of the bending line

therefore

$E = -\frac{1}{2}\int_1 \frac{M^2}{EI}$ and from $\sigma = \frac{M}{W}$ the channel bending stress is obtained as a function of the burst pressure

Fig. 6 gives the values of σ and of the released energy as functions of p_1.

It is clear that the values for the stress thus calculated would be negligible and, indeed, not even measurable. To these forces, however, must be added those due to organic and water evaporation and to the dynamic effect of the jet.

As the passage of the first sonic wave, caused by the decompression of the organic liquid, is related to the velocity of sound in water, it is a very short-lived event by comparison with the subsequent phenomena that occur in the vessel, such as the generation of pressure-waves through vaporization of the organic liquid and through organic/water heat exchange.

Moreover, the channel's own vibrations set up by the first wave will already be damped down by the time the subsequent events occur. Hence the effects of the first liquid decompression wave can be dealt with separately from those provoked by the subsequent loading phenomena.

The high-speed photographs show a sizeable formation of organic vapour immediately where the jet emerges when the initial organic temperatures are higher than boiling temperatures at atmospheric pressure; with low

temperatures (250°C), however, only steam forms, at some distance from the jet outlet (see also figs. 7 and 7a). These events, which first affect the adjacent channels about 0.01 sec after the burst, explain the increased load on the channel, which varies with the organic temperature or with the pressure in the tank (depending on the amount of water and organic liquid evaporated) where the channel burst pressure is kept constant.

The hydrodynamic force of the jet can be calculated by multiplying the jet dynamic pressure by the axial cross-section struck by the jet.

$$K = \frac{\rho}{2} w^2 \cdot F \cdot cw$$

The resistivity value can be assessed at 0.5. In the table below, load values thus calculated are compared with those recorded during experiments 4 and 6 on an 18/8 stainless steel channel of the feeding zone.

	Experiment 4	Experiment 6
length of crack	320 mm	407 mm
cross-section of passage	29 cm^2	140 cm^2
throughput in first second	70 dm^3	75 dm^3
velocity of organic liquid	8.9 m/sec	5.4 m/sec
calculated dynamic load	113 kg	52 kg
max. stress value calculated from strain measurement	9.5 kg/mm^2	15 kg/mm^2
static load calculated from strain measurement	175 kg	280 kg

This comparison shows that the hydrodynamic load only partly accounts for the load measured on the channels, thus demonstrating that the vaporization of the organic liquid and the heat exchange provide the rest of the impulse required to produce the strain measured on the channels.

3.2 Pressure transients due to vaporization and fast condensation of moderator

The temperature difference between the organic liquid and the water at the

moment of contact is about 320°C. The heat transmitted to the water will depend on the evolution of the heat exchange value and the exchange surface versus time. The pressure, temperature and strain records indicate a characteristic periodic profile (figs. 8 and 11).

After the channel bursts the first pressure wave is registered, followed 0.2 seconds later by pressure peaks of considerable amplitude which are repeated roughly every 0.2 seconds.

The nature of these peaks was investigated with a view to determining their maximum amplitude and impulse. The maximum amplitude registered by standard slow transducers positioned on the vessel shell and the special fast piezo-electric transducers mounted in the water in no case exceeded 15 atm. The pressure rise times are of the order of 0.5 milli-seconds.

Experiments effected with water at 100°C and atmospheric pressure and repeated by injections in water at 70° and 50°C demonstrated that the peaks are caused by rapid condensation of vapour bubbles which periodically break away from the generation area and encounter regions of water at subcooled temperature.

The three records are compared in fig. 9. Fig. 10 shows how the peak frequency varies with the varying water temperature.

The measurements effected with strain-gauges on the channels show that the major loads are due to the waves caused by the collapsing of steam bubbles (fig. 11). These loads caused the collapse of the Al channels (thickness 2 mm, diameter 110 mm) simulating the feeding element guide-tubes, and crashed some of the safety rods (Al 2 mm thick, diameter 75 mm) against the wall of the vessel (see fig. 12).

It was therefore necessary to ascertain the mechanical strength of each type of channel against the maximum wave measured during the tests. This calculation was of fundamental value as regards the safety rod guide-tubes and the ORGEL channels, i.e. for the purpose of preventing a chain failure.

The collapse of the safety rod guide-tubes in the first 2/10 sec, the period when the greatest peaks are recorded, might have prevented the insertion of the rods and seriously jeopardized the safety of the reactor. Consequently, in the final design a Zr-2 safety rod guide-tube has been chosen avoiding the problem.

The maximum strains were registered on the 18/8 stainless steel tube (fig. 11), simulating a feeding zone element.

By means of a static calculation, we found via the measured bending strain a load value of 350 kgf, which is assumed to be concentrated in the central area of the tube. We assumed that this load value could also act on a channel or a control rod and we calculated the stresses for each component.

For the channel the field of the bending moments was determined and in respect of each tube length, of various geometry and material, the ratio was calculated between the moment acting in that section and the relative moment of inertia. These M/I ratios are considered as so many separate forces acting in the various tube lengths, and in this way the elastic strain line can be plotted graphically (fig. 13).

The load acts first on the calandria tube, and when a deflection of 3 mm has developed on that tube the load distributes itself over the pressure tube as well.

The following values were found:

σ max SAP = 5 kg/mm^2, σ rupture = 8 kg/mm^2 at 420°C
σ max Zircaloy = 12 kg/mm^2, σ rupture = 20 kg/mm^2 at 380°C

Using the same calculating system for the safety rod, we found:

$$\sigma \text{ max Zircaloy} = 17 \text{ kg/mm}^2$$

It should be noted, of course, that this simplified calculating system is really only applicable where the effective bending line virtually conforms to a static loading pattern. On the other hand, where there are dynamic loads impinging on the tube at different points and instants, conditions arise that are hard to interpret from the tube deformation. In fact, alternations of tensile and com-

pressive stresses have been observed, indicating a disorderly buffeting of the tube.

The interpretation of this complex field of loading will be brought somewhat nearer by research into the following events:

- determination of the mechanical energy released on collapse of a bubble,
- transversal buckling strength of a tube subjected to the lateral impact of a pressure wave,
- propagation of a longitudinal bending wave along a tube,
- propagation of a wave in water in complex geometries (reflection and refraction phenomena).

3.3 Static loading of vessel

The development of the static pressure and temperature in the vessel gas blanket is shown in fig. 14. Injection of the organic liquid at or above the water level is particularly avoided, by means of a tube which encases each channel and by which any organic liquid escaping in the upper part of the channel would be ducted down to the water.

It is possible to work back to the measured pressures via a calculation based on:

- the increase of the liquid volume in the vessel, through thermal expansion of the water and the injection of organic liquid;
- the rise in the blanket-gas temperature;
- the partial pressure of the saturated vapour in the gas blanket.

From this calculation it emerges that practically all the heat lost by the organic liquid is used to heat the entire volume of water in the vessel, in a uniform manner.

In the case of experiment 2 (fig. 14), the total water evaporation was only 0.4 kg, in 11 seconds of injection.

3.4 Temperature rise in channels affected by organic jet

The jet enters at a certain velocity into the water, which fractionates it; this reduces the velocity and at the same time increases the cross-section.

When the organic liquid reaches a temperature of over 357°C, it can no longer continue in the liquid state at atmospheric pressure and partial evaporation will occur (fig. 15).

According to the theory, the reduction of velocity of the turbulent jet in water and the increase in the jet cross-section can be described by the following equations [4]:

$$b = c_1 \cdot x \quad \text{and} \quad w_{max} = c \cdot \frac{1}{x} \sqrt{\frac{I}{\rho}} ,$$

where I is the jet impulse.

High-speed cinematography revealed a different jet behaviour from that predicted by the theory. It will be seen from fig. 16 that the path of the jet in the relevant field can be described by the equation

$$x = x_o (1 - e^{-Cot}) ,$$

from which is obtained the velocity

$$w(t) = w_o \cdot e^{-Cot} = Co (x_o - x),$$

i.e. the velocity decreases linearly with distance.

It should be remarked that the jet can only be visually observed during the initial phase, before it has attained the condition of permanent flow and when the escaping or escaped organic liquid is already partially evaporating. The experiments showed that in spite of the jet's reduced velocity, evaporation, and immixture in water, the temperatures reached at the stagnation point on the tubes at distances of 100 mm may be as high as the jet temperatures. This finding is confirmed by a calculation of the temperature decay with distance, in which the theoretical laws for the behaviour of the jet are assumed to be valid.

We obtain $$T = T_{water} + (T_{org} - T_{water}) \cdot e^{C/2(R_o^2 - R_f^2)}$$

with

$$C = \frac{2\alpha}{C_1 R_o^2 \cdot v_o \cdot \rho \cdot c_p}$$

With $tg\,\gamma = C_1 = 0.4$; $\alpha = 6$ Kal/m^2 sec ^oC ; $R_o = 25$ mm; and $x = 100$ mm, we obtain

$$T = T_{water} + (T_{org} - T_{water}) \cdot 0.982$$

A small rig was employed for experiments on the heating of tubes affected by a jet at distances including some greater than the minimal distances encountered in the ESSOR network, with the object of obtaining more general information.

Examination of the experimental data obtained during reduced-scale injections reveals that up to distances of 180 mm the maximum temperature at the stagnation point remains more or less constant, while for distances of 275 mm and 360 mm the values are noticeably lower. From fig. 17 it is possible to determine a jet-destruction distance after which there is a substantial change in the surface heating mechanism. For whereas at short distances the central region of the jet is not yet mixed with the water, at long distances there is a mixture of organic liquid and water, both of them in vapour and liquid phase.

Furthermore, the heating may be greater with low injection temperatures than with high. The explanation of this phenomenon is that at injection temperatures higher than the boiling temperatures the jet is destroyed through evaporation of the organic liquid.

We endeavoured to give a more complete picture of the circumferential and axial temperature distribution on the different channels, by positioning thermocouples on various sections directly affected by the organic jet.

A characteristic record of the temperature measurements at various points distributed over the circumference of a tube struck by the jet is given on fig. 18. From these diagrams the surface distribution of the temperature over the channel can be read instant by instant. A number of characteristic

profiles for channels struck directly or only touched in passing by the jet are shown in figs. 19, 20, 21. This irregular temperature distribution may set up stresses of thermal origin in the tube.

A look at the distribution on fig. 19 where the temperature difference between two points on the circumference is greatest, shows that the curves can be assimilated to cosinusoidal curves.

Thus: $T(\varphi) - Ti = (To - Ti) \cos \varphi$ for $0 \leqslant \varphi \leqslant 90^{o}$

For the field $90^{o} < \varphi < 270^{o}$ it may be accepted that the temperature remains at the initial value Ti($\varphi = 0$ for the stagnation point). Assuming a balanced system of internal stresses and a tube anchored so as to form a statically determined system, it was possible to calculate for this particular case the distribution of the thermal stresses which are greatest at points of low temperature.

The study will have to be supplemented by a more precise investigation of the effects produced by the continual varying of the circumferential and axial temperature distribution over the tube during injection.

SYMBOLS

b = acceleration
c_p = specific heat
E = modulus of elasticity
F = surface, cross-section
I = moment of inertia
M = momentum
p = pressure
R = jets diameter
T = temperature
t = time
v = specific volume
V = volume
w = velocity
x = distance

β = thermal expansion factor
γ = specific weight, jets opening angle
ε = strain
ρ = density
σ = stress

ACKNOWLEDGEMENTS

The test rig was designed and constructed in collaboration with the firm of CIFA, Milan, and more especially with Messrs. G. Ausenda, E. Cacciari, S. Balzanelli and C. Petronilli.

Mr. P. Golinelli, ably assisted by Mr. E. Soma, carried out the mechanical assembly of the test-section and the preparation of the experiments.

Mr. V. Andrighetti and Mr. W. Schnabel were responsible for the instrumentation of the test section.

The pressure measurements with standard and specially constructed transducers were effected by Mr. E. Jorzik.

We are much indebted to Mrs. D. Doyen and Miss E. Zenner for the translation and preparation of the document.

REFERENCES

(1) P. W. BRIDGMAN, Journal of Chemical Physics, 1935 "The Pressure, Volume, Temperature Relations of the Liquid and the Phase Diagram of Heavy Water".

(2) G.A.A.A. - INTERATOM, Internal Report 1965, "Rupture d'un tube de force".

(3) CLEMENS SCHAEFER, "Einführung in die theoretische Physik".

(4) SCHLICHTING, "Grenzschicht-Theorie".

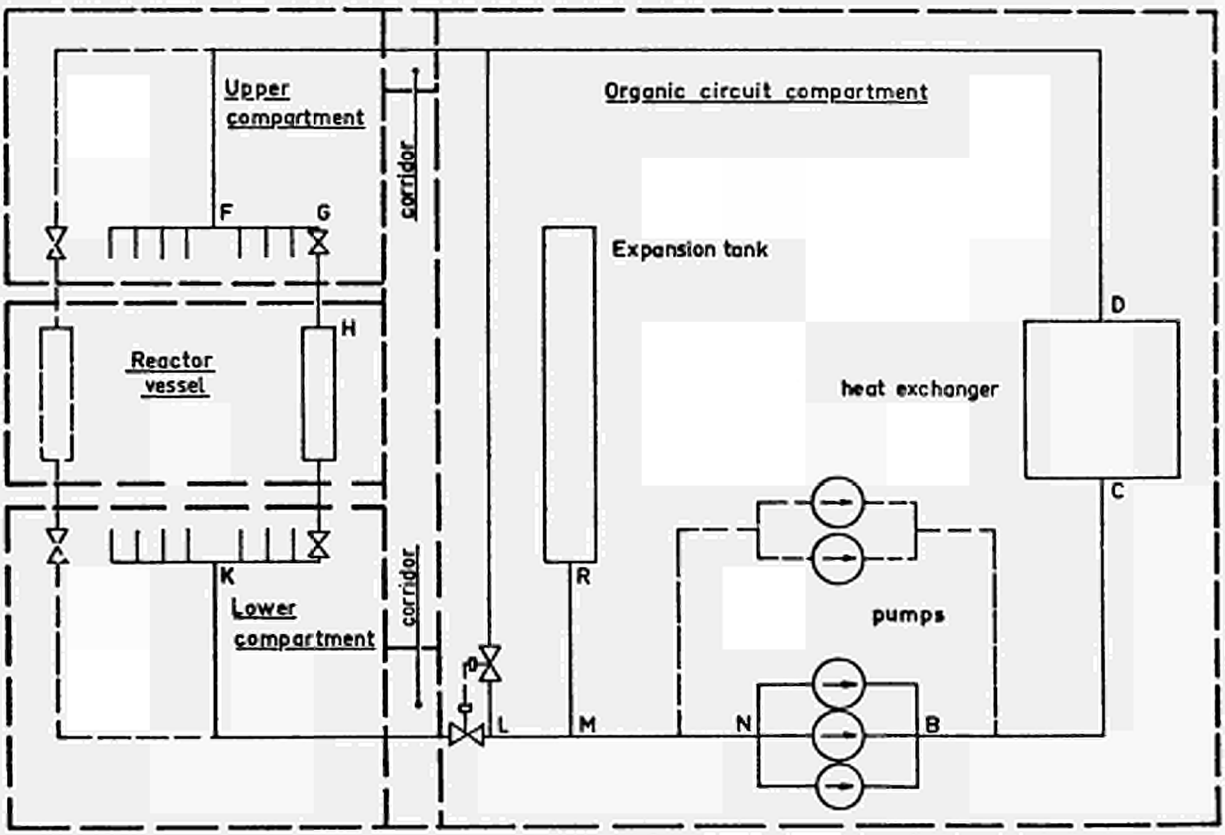

FLOW SHEET OF THE PRIMARY CIRCUIT IN THE ESSOR REACTOR FIG.1

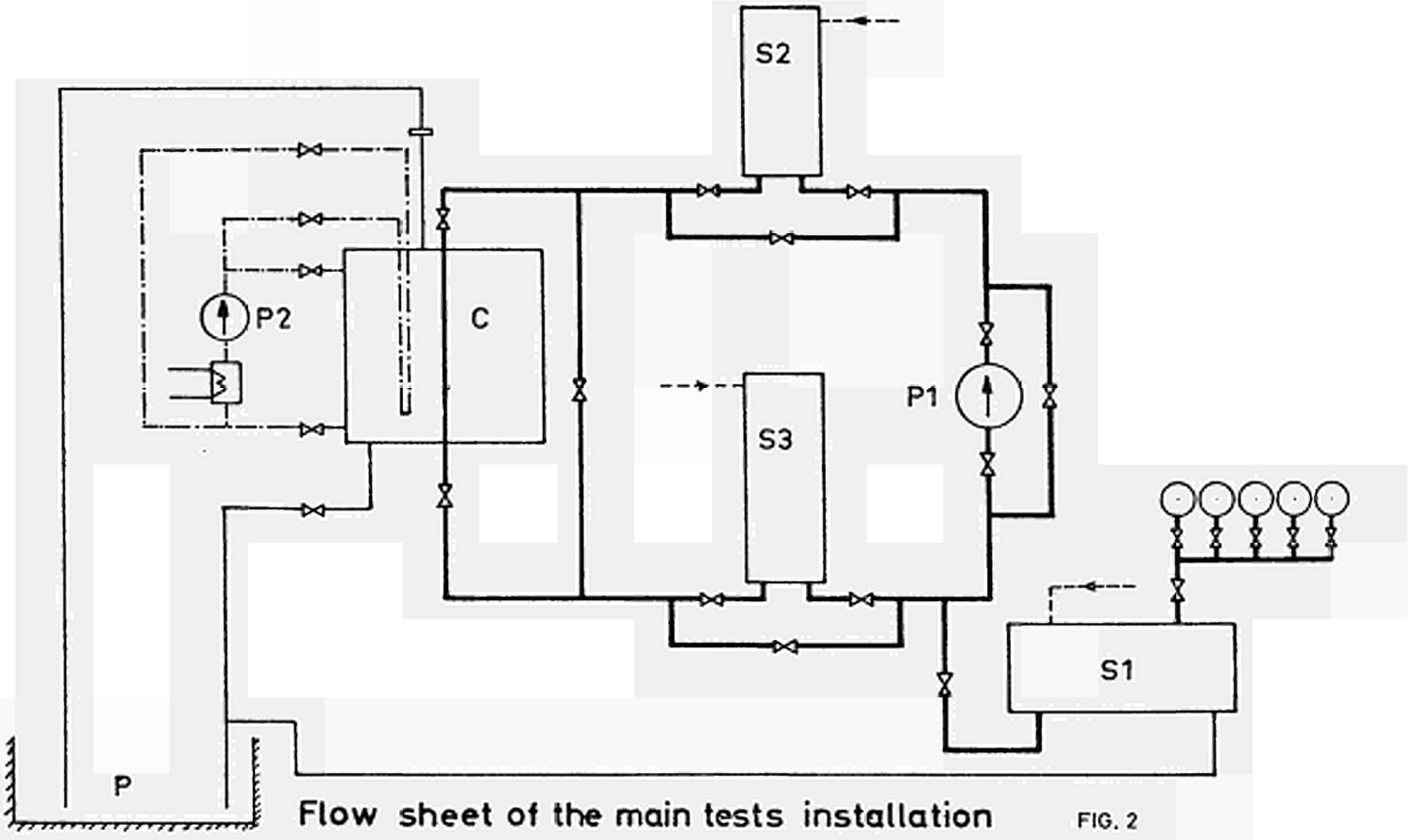

Flow sheet of the main tests installation FIG. 2

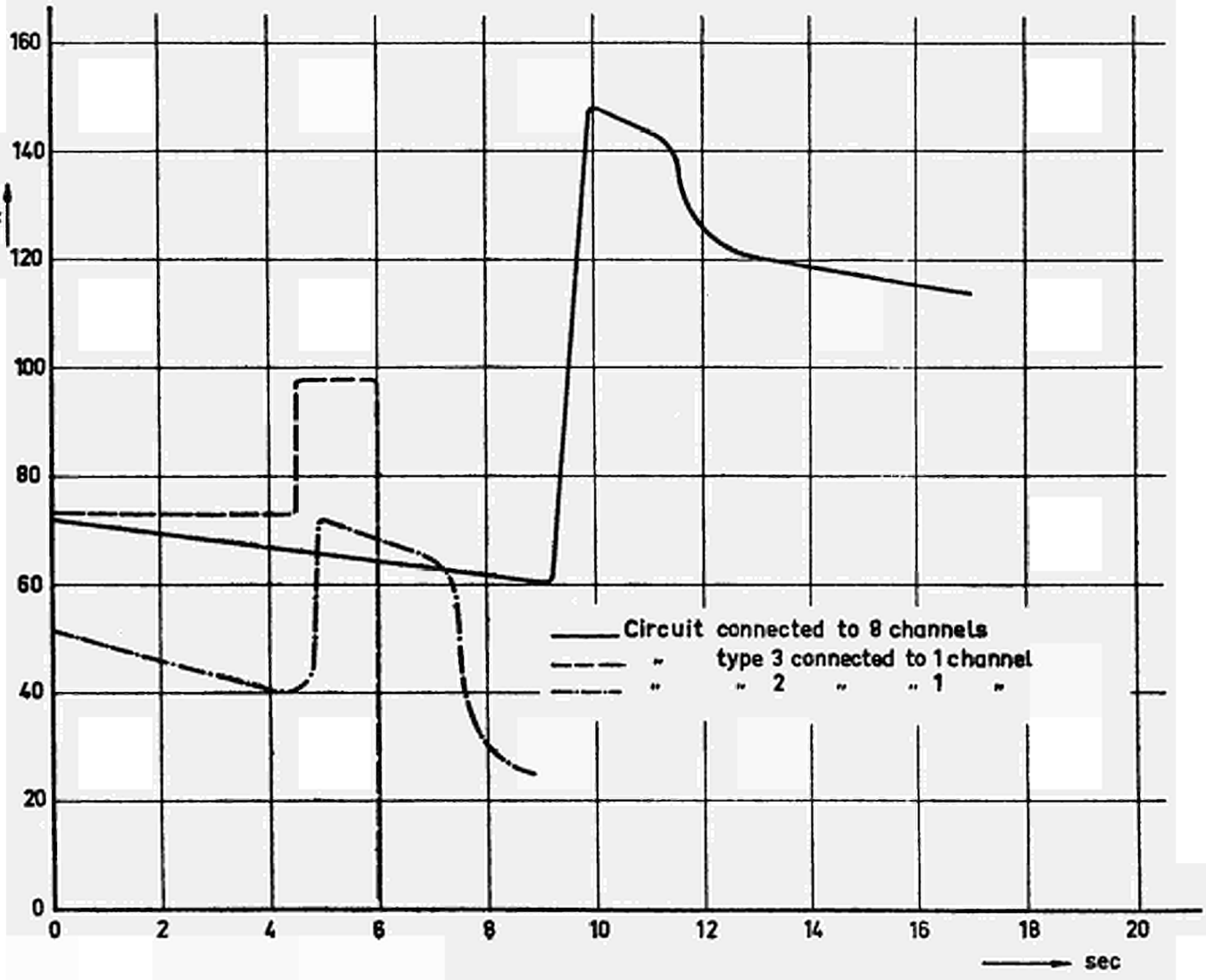

FIG. 3

Flow rate of organic liquid heavy water as a consequence of channel rupture

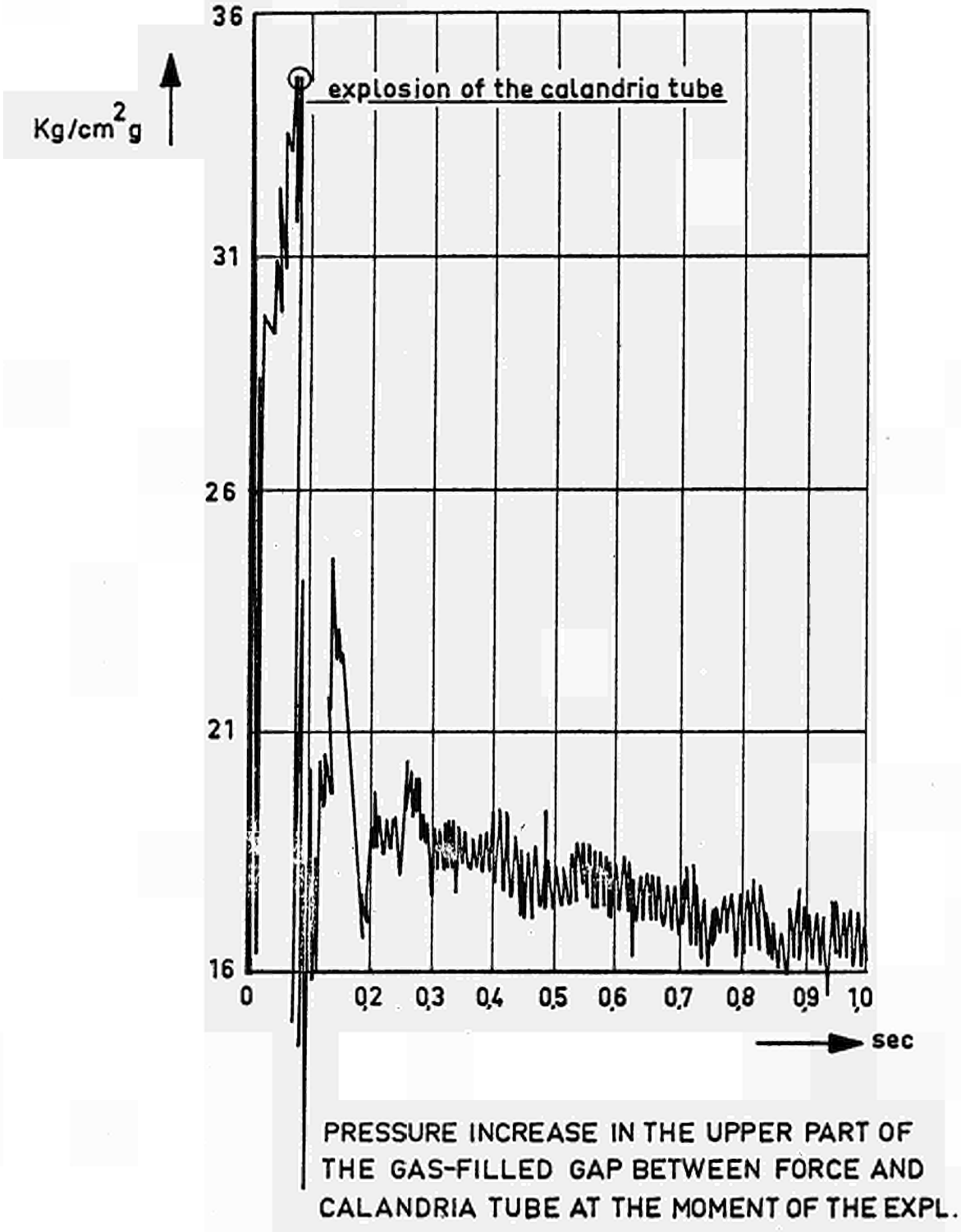

FIG. 4 PRESSURE RELEASE IN THE UPPER PART OF THE CHANNEL AT THE MOMENT OF THE EXPLOSION

FIG. 5 DECREASE OF THE PRESSURE PEAK AS A FUNCTION OF DISTANCE FROM THE GENERATION POINT

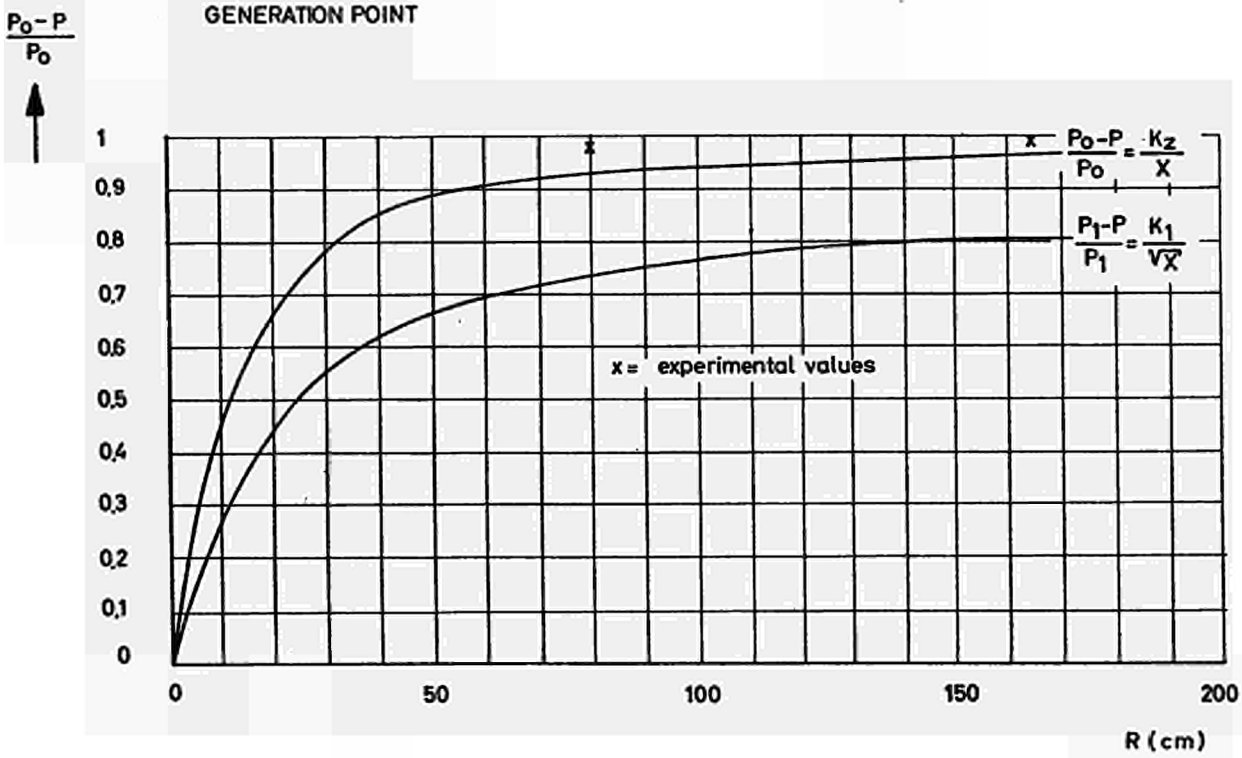

FIG. 6 ENERGY RELEASE OF 8,5 kg OF ORGANIC LIQUID AND MAXIMUM BENDING STRESS OF A FEEDING CHANNEL AS A FUNCTION OF THE EXPLODING PRESSURE

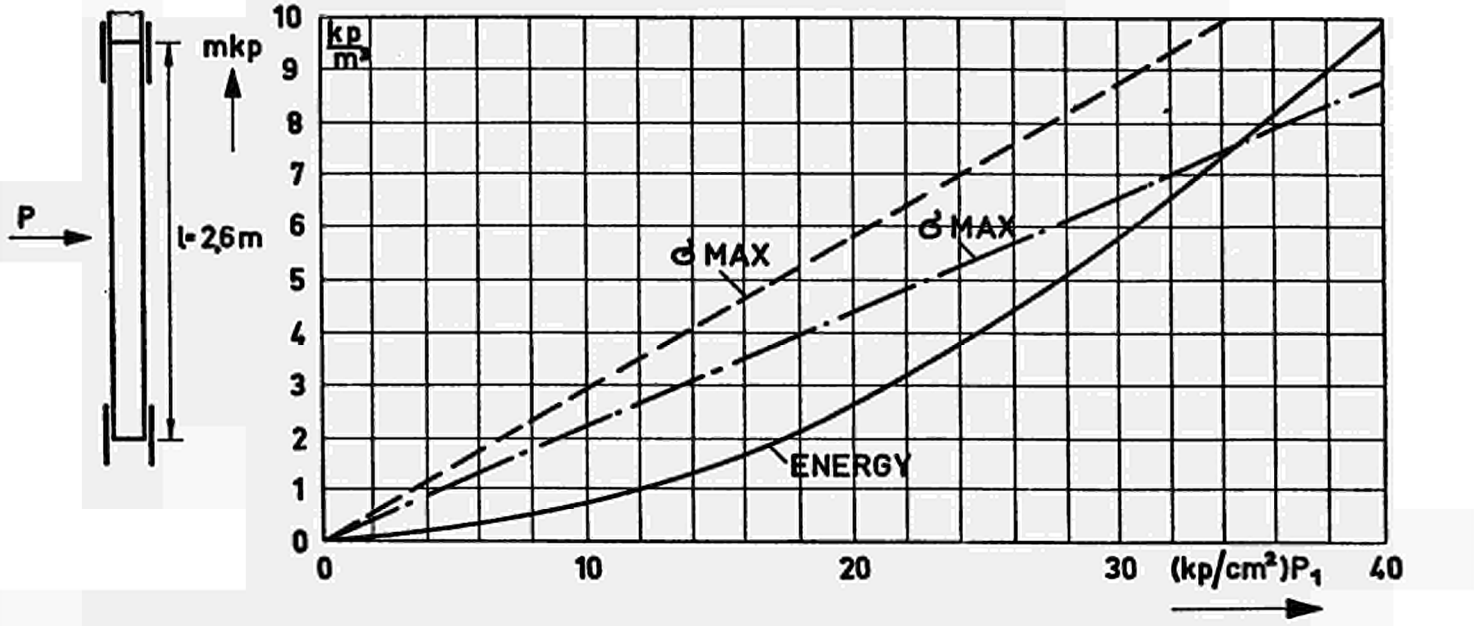

—·—·— σ MAX CALCULATED FOR THE CHANNEL BUILT IN AT ITS EXTREMITIES

– – – – " " " " " " PINNED " " "

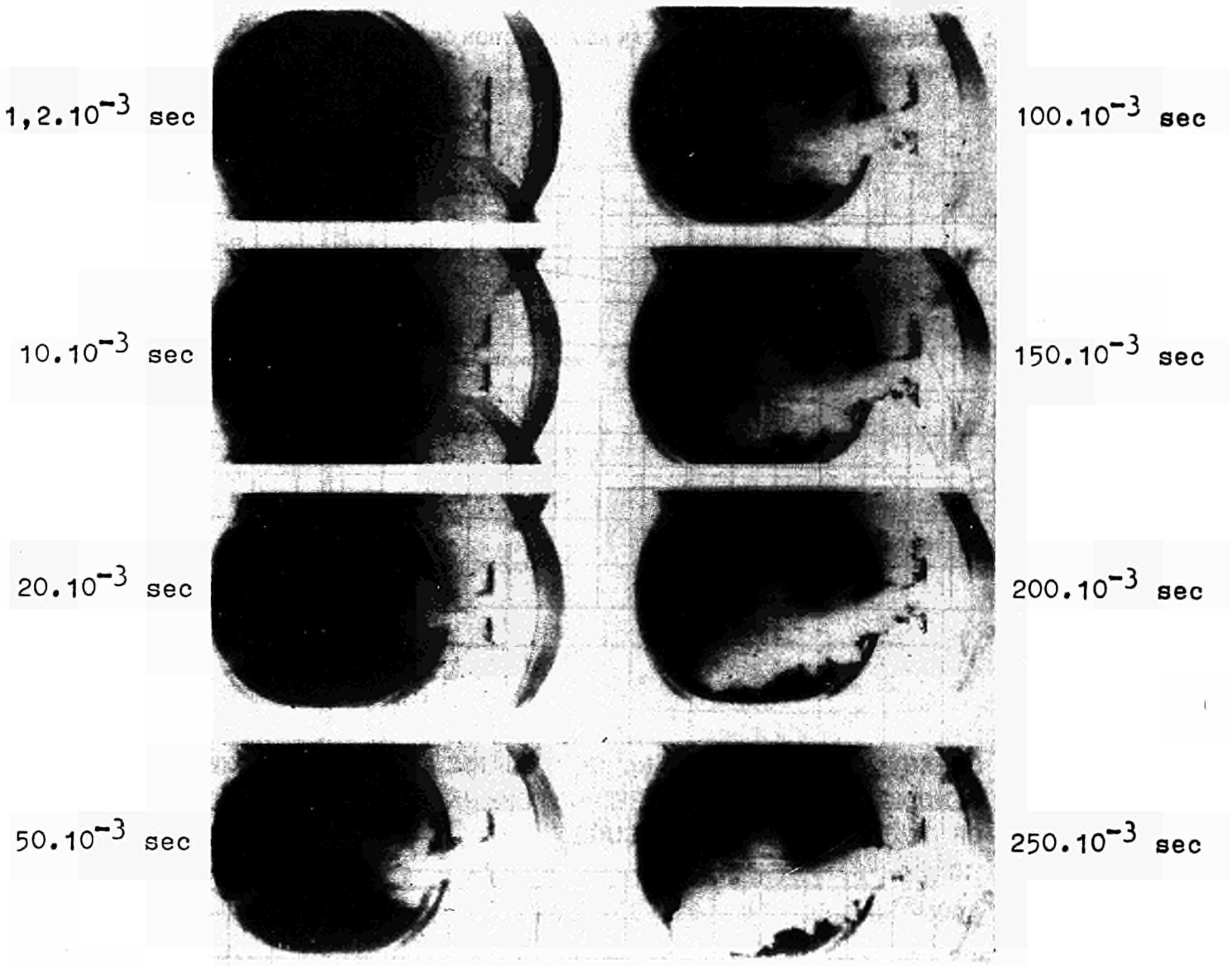

Fig. 7

250°C jet of organic liquid into water
form and velocity of jet as shown by high-speed cinematography

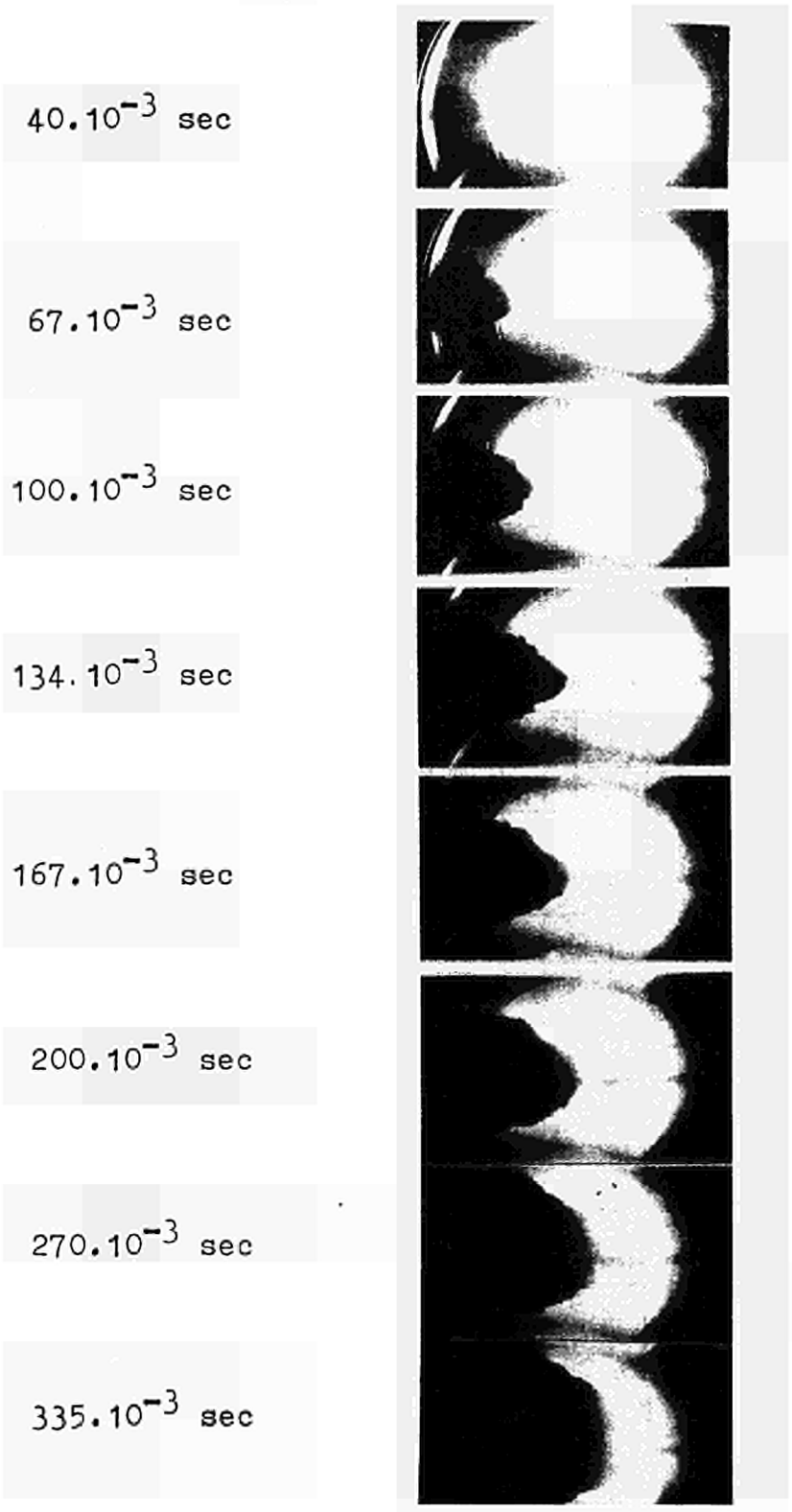

Fig. 7a

390°C jet of organic liquid into water

form and velocity of jet as shown by high-speed cinematography

FIG. 8 PRESSURES ON THE WALL OF THE VESSEL AS A FUNCTION OF TIME AFTER THE EXPLOSION

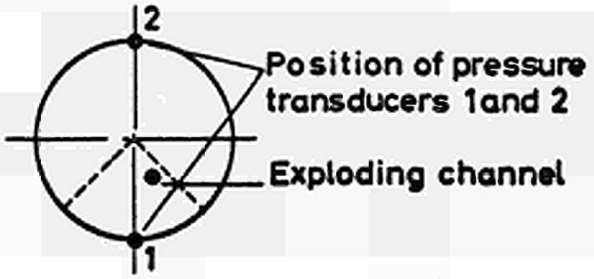

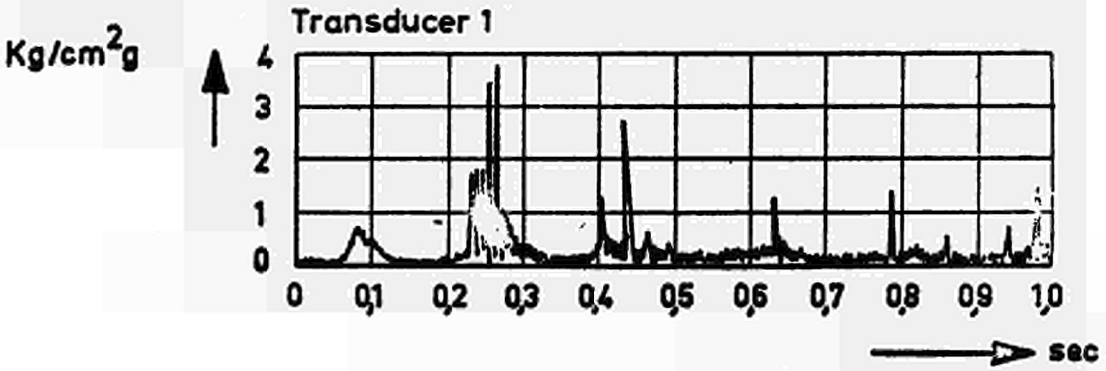

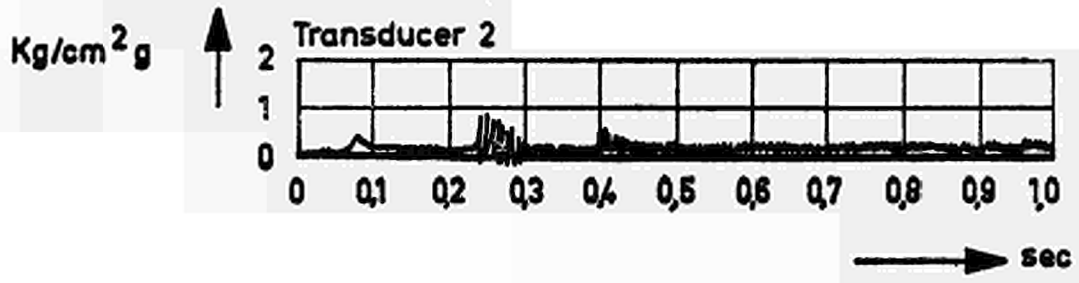

EXPERIMENT 8

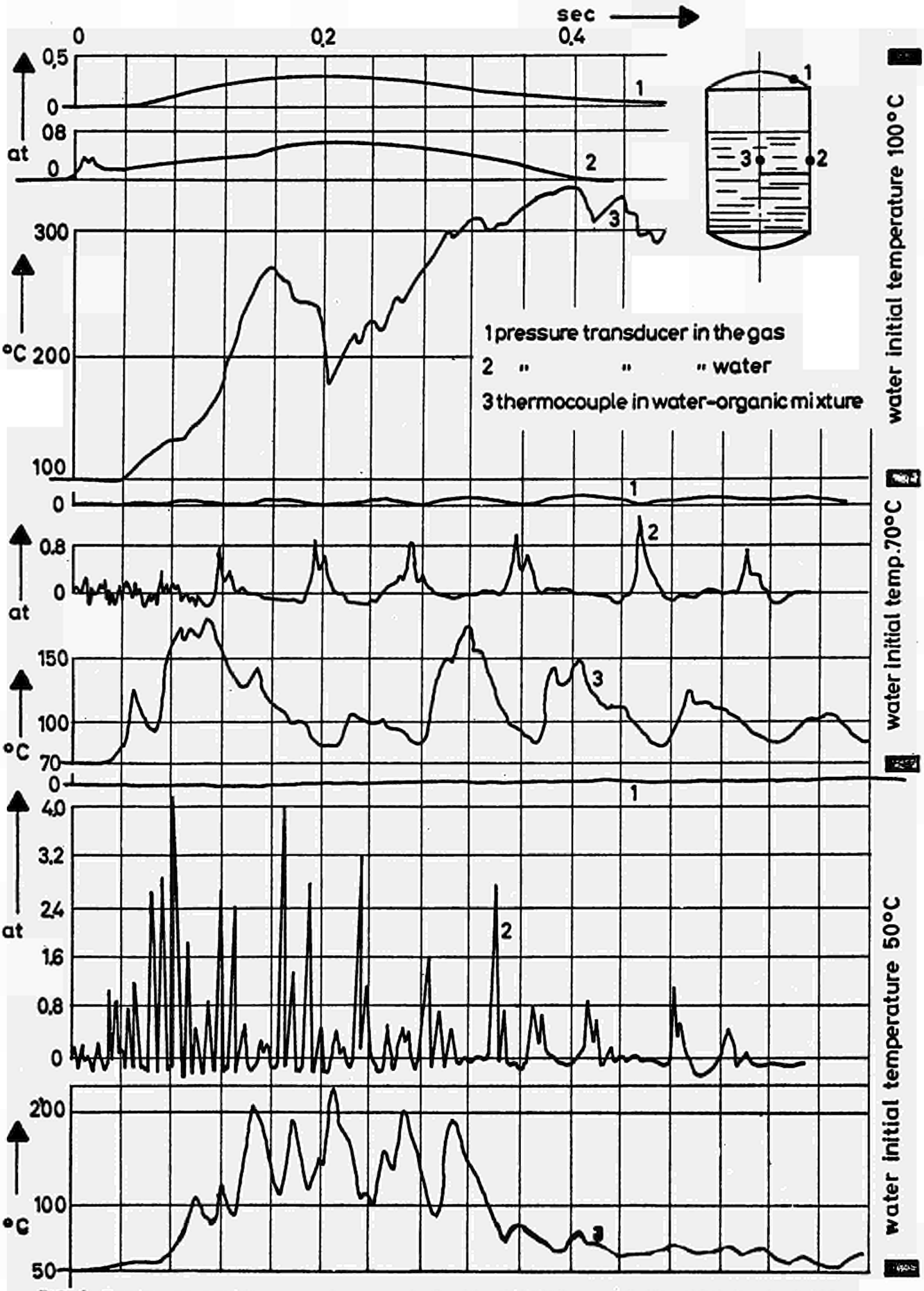

FIG. 9 Pressure and temperature records for 400° C organic liquid injected into water at 100°, 70° and 50°C.

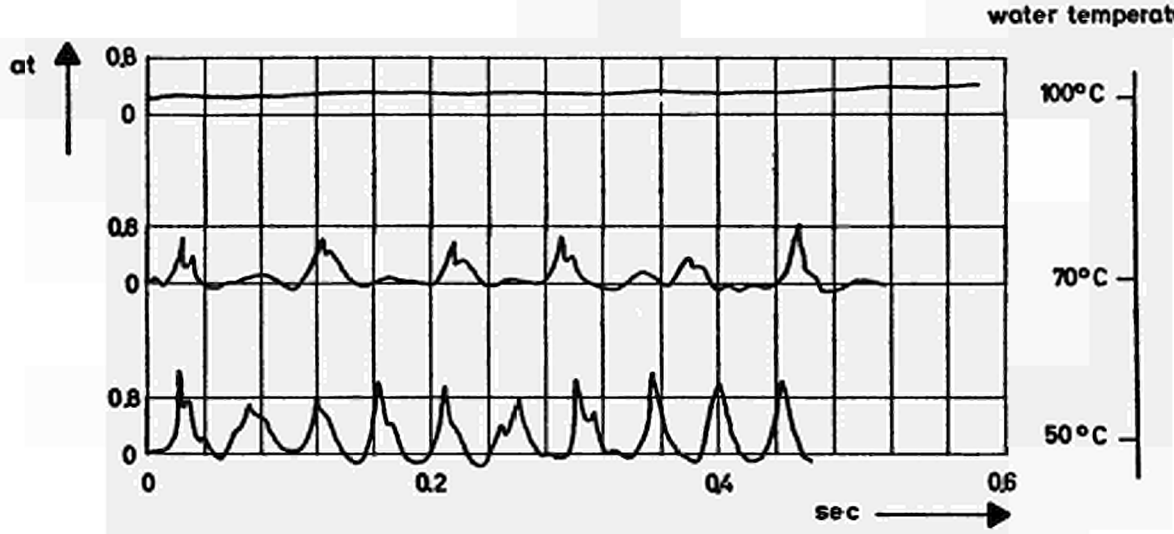

FIG.10 Peak frequency variation with the varying of water temperature

Experiment: 4 Channel: 6

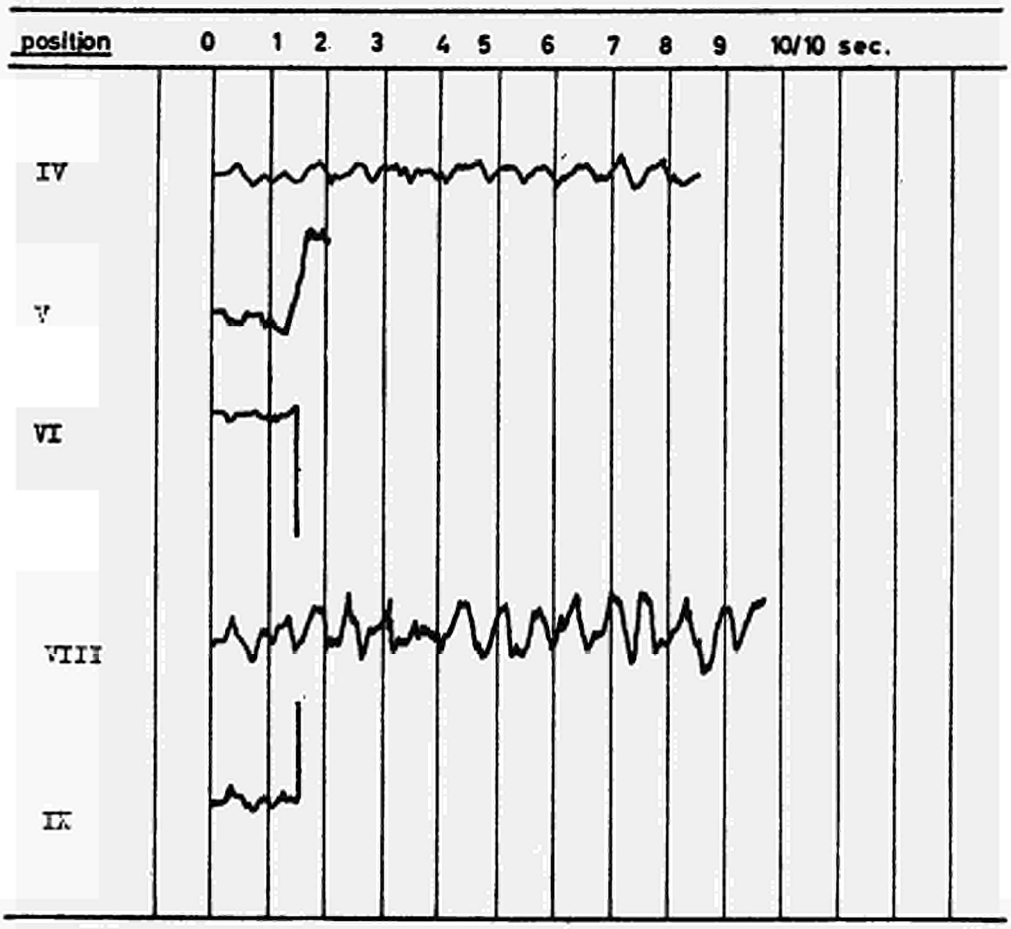

scale: 89 $\frac{\mu/m}{mm}$

Strain measurements as a function of time after explosion FIG.11

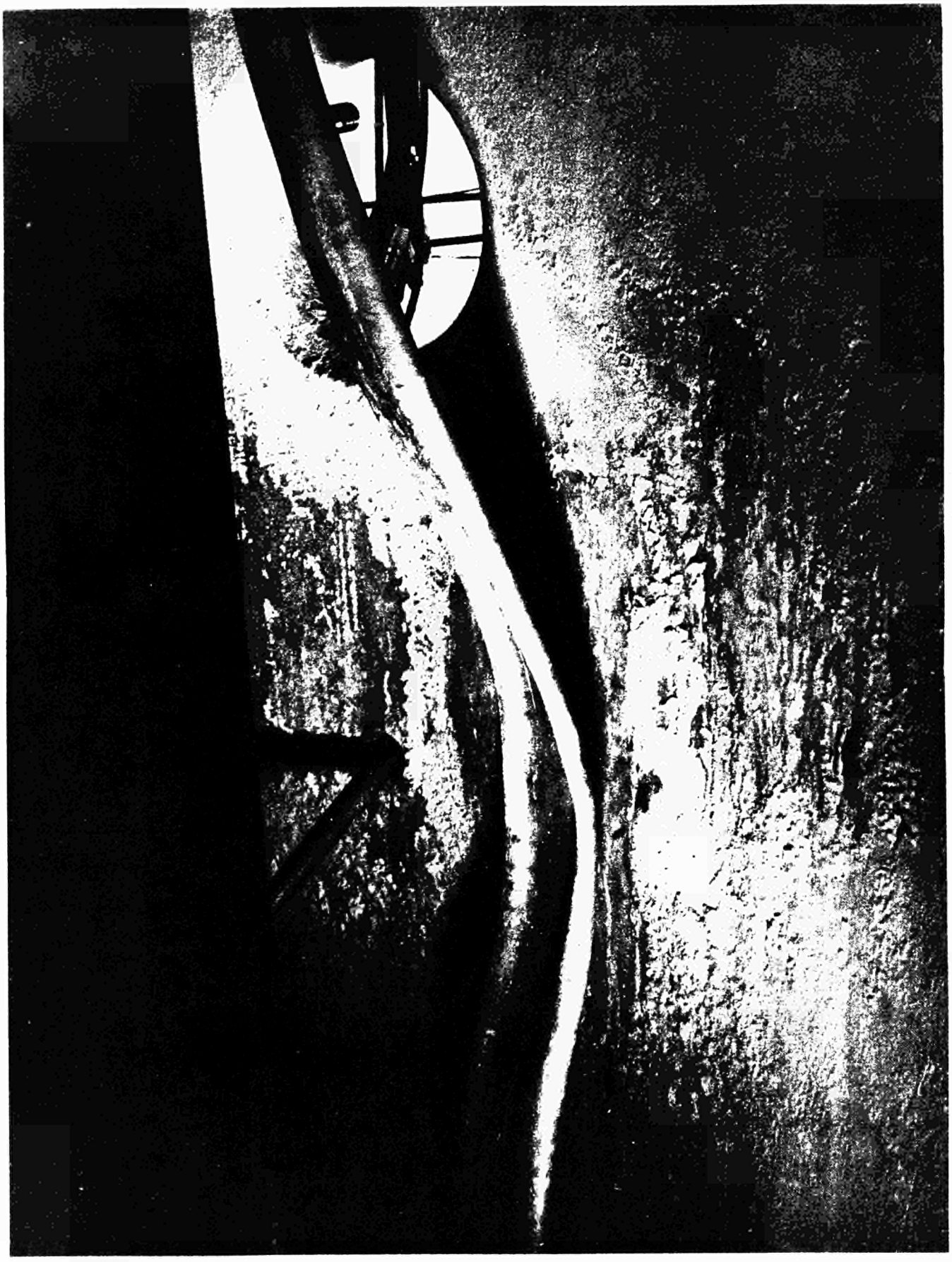

Fig. 12

SAFETY ROD (Al 2 mm thick, diameter 75 mm)
crashed against the wall of the vessel
Experiment 4

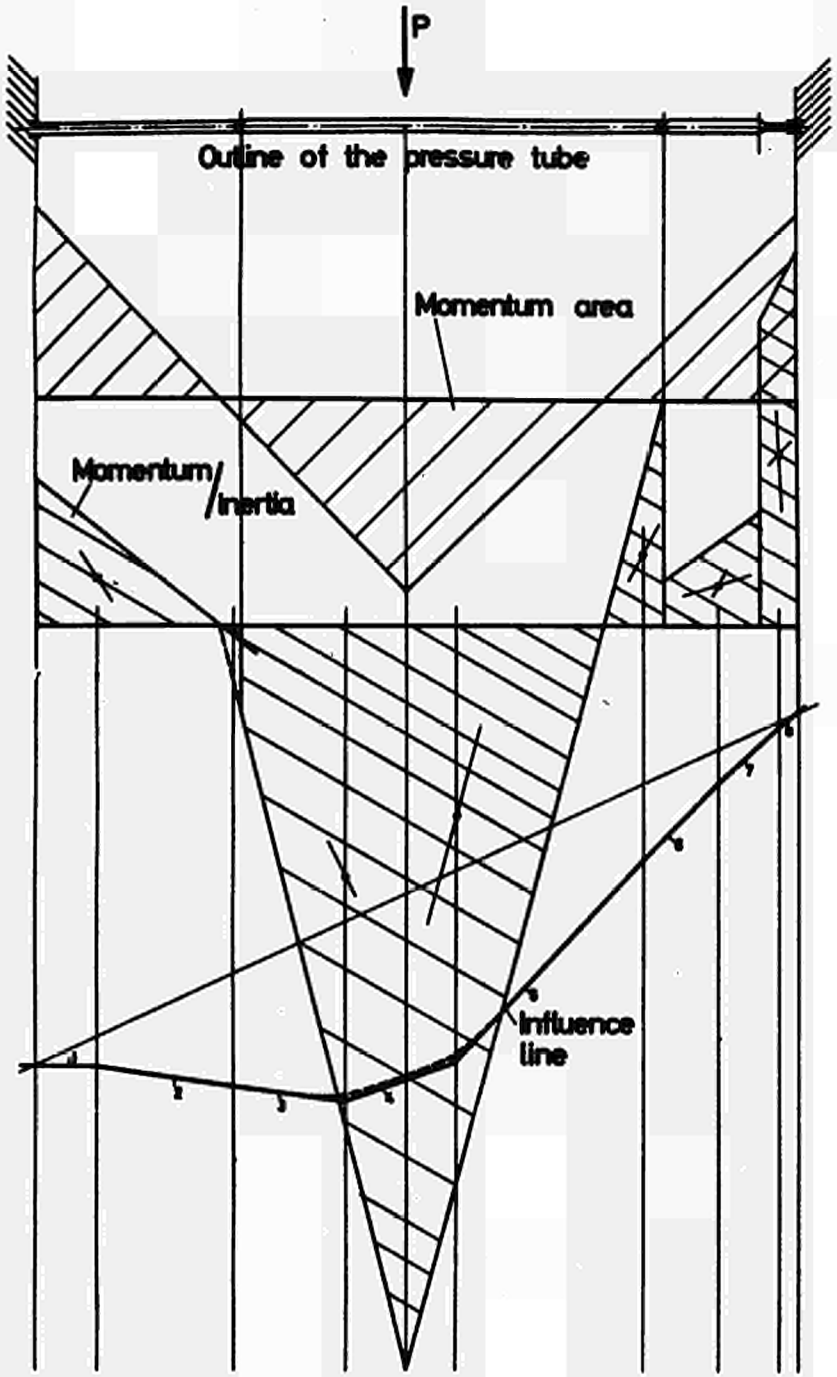

FIG. 13 CONSTRUCTION
OF THE INFLUENCE LINE
OF THE PRESSURE TUBE

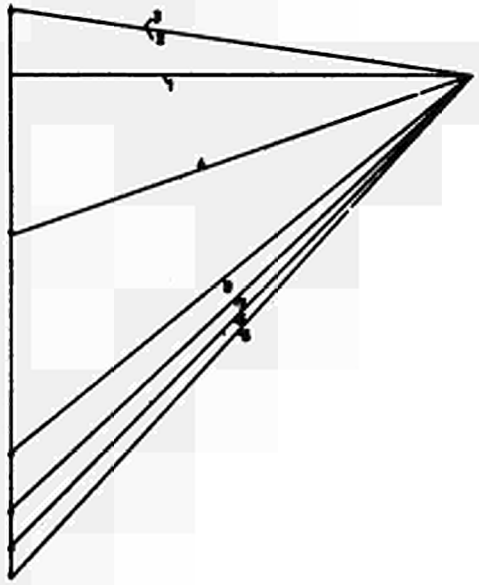

FIG. 14 PRESSURE AND TEMPERATURE RISE IN THE NITROGEN-FILLED UPPER PART OF THE VESSEL AS A FUNCTION OF TIME AFTER EXPLOSION

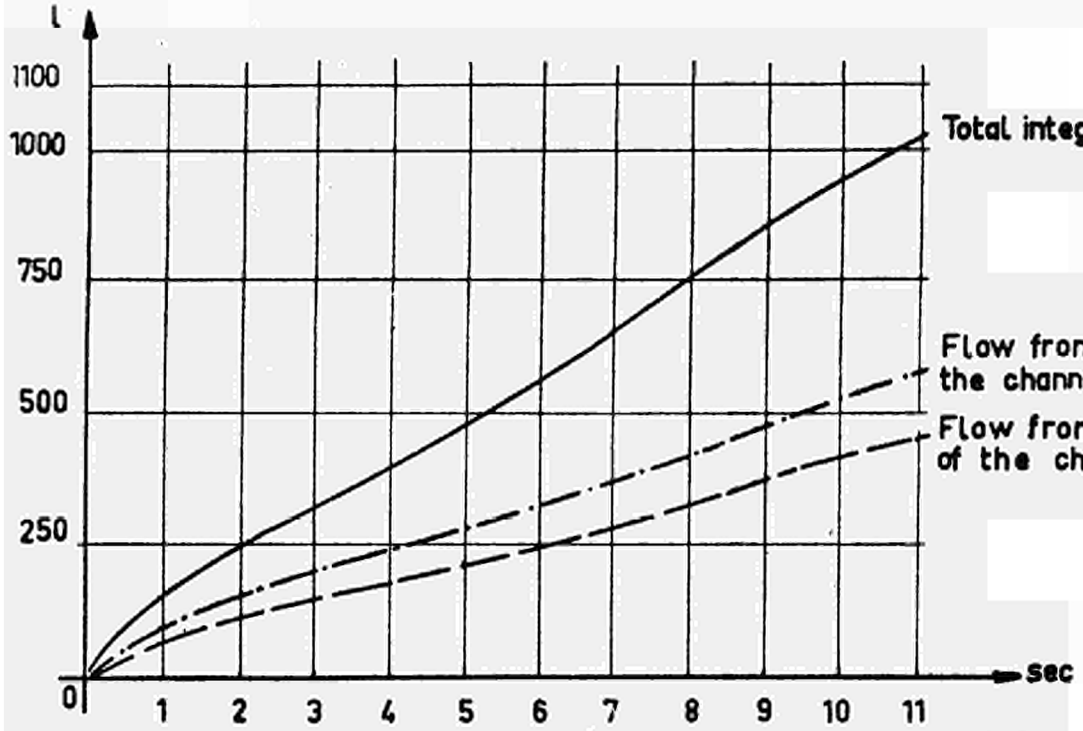

INTEGRATED FLOW OF ORGANIC LIQUID INTO WATER AS A FUNCTION OF TIME

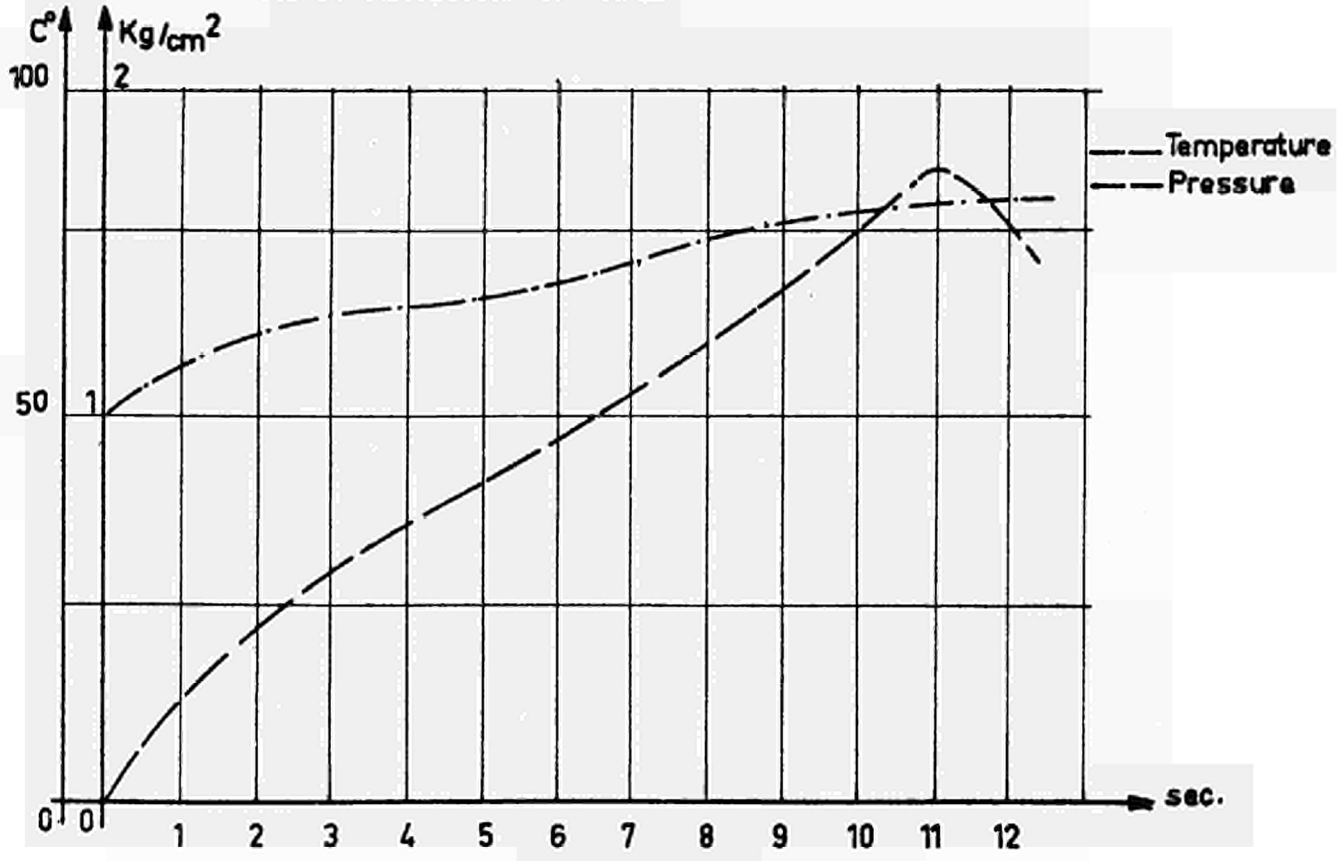

EXPERIMENT 2

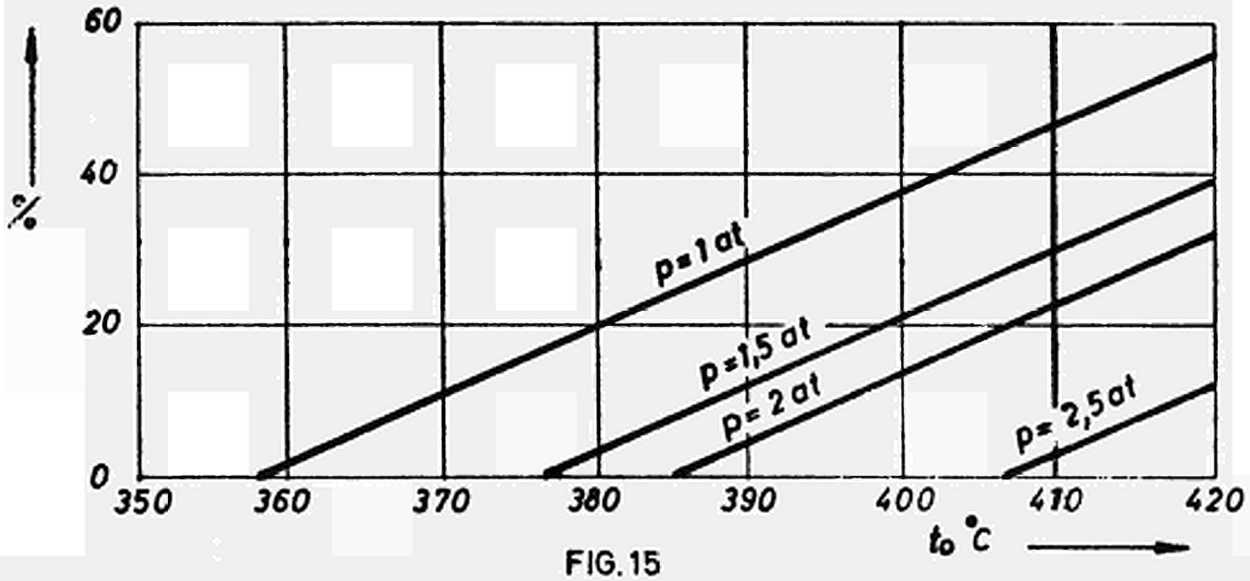

FIG. 15

Percentage of evaporated liquid as a function of temperature

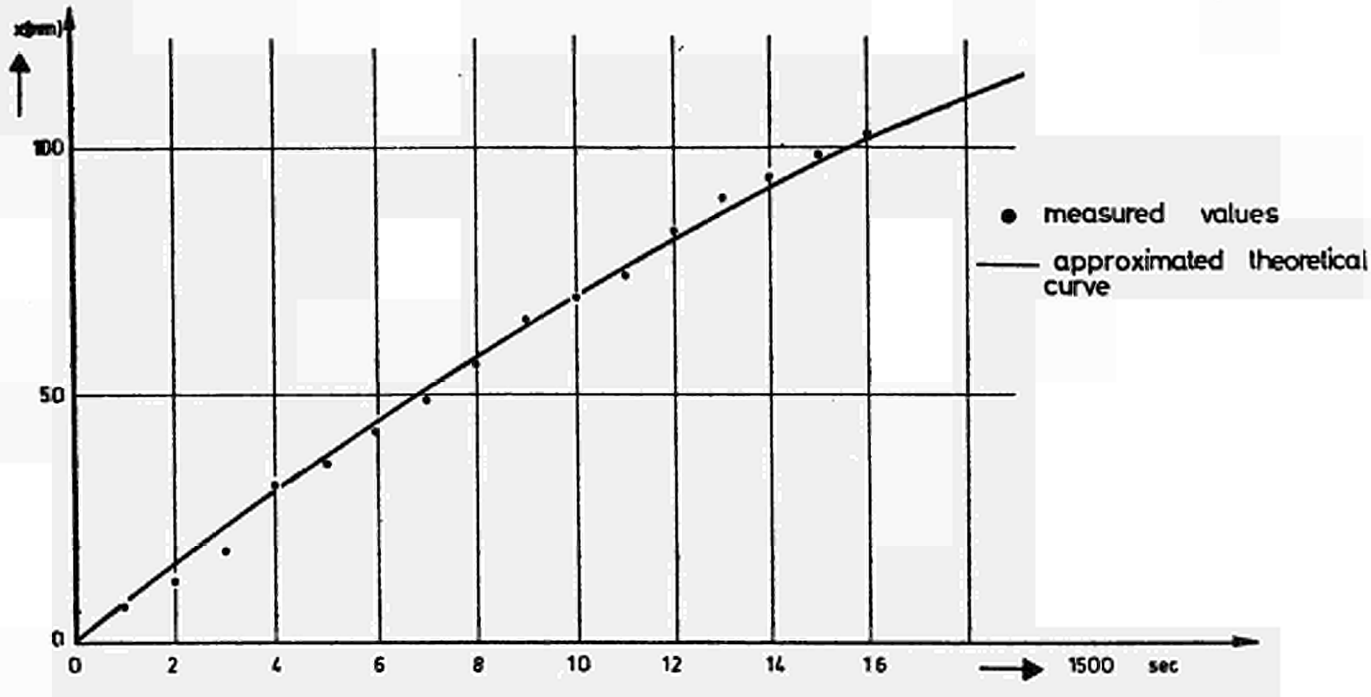

FIG. 16 POSITION OF JET FRONT VERSUS TIME

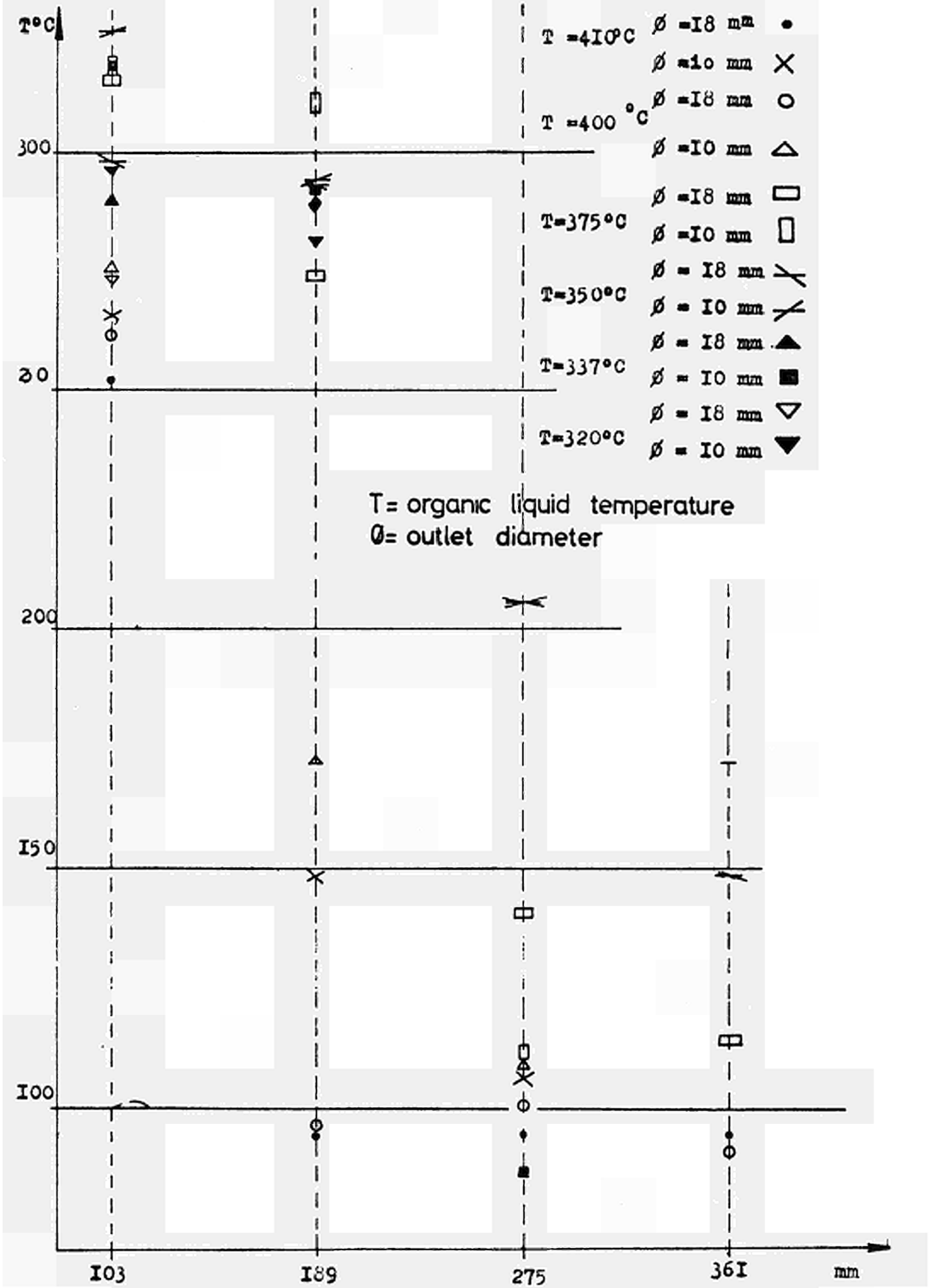

Maximum stagnation point temperature versus distance from the outlet

FIG. 17

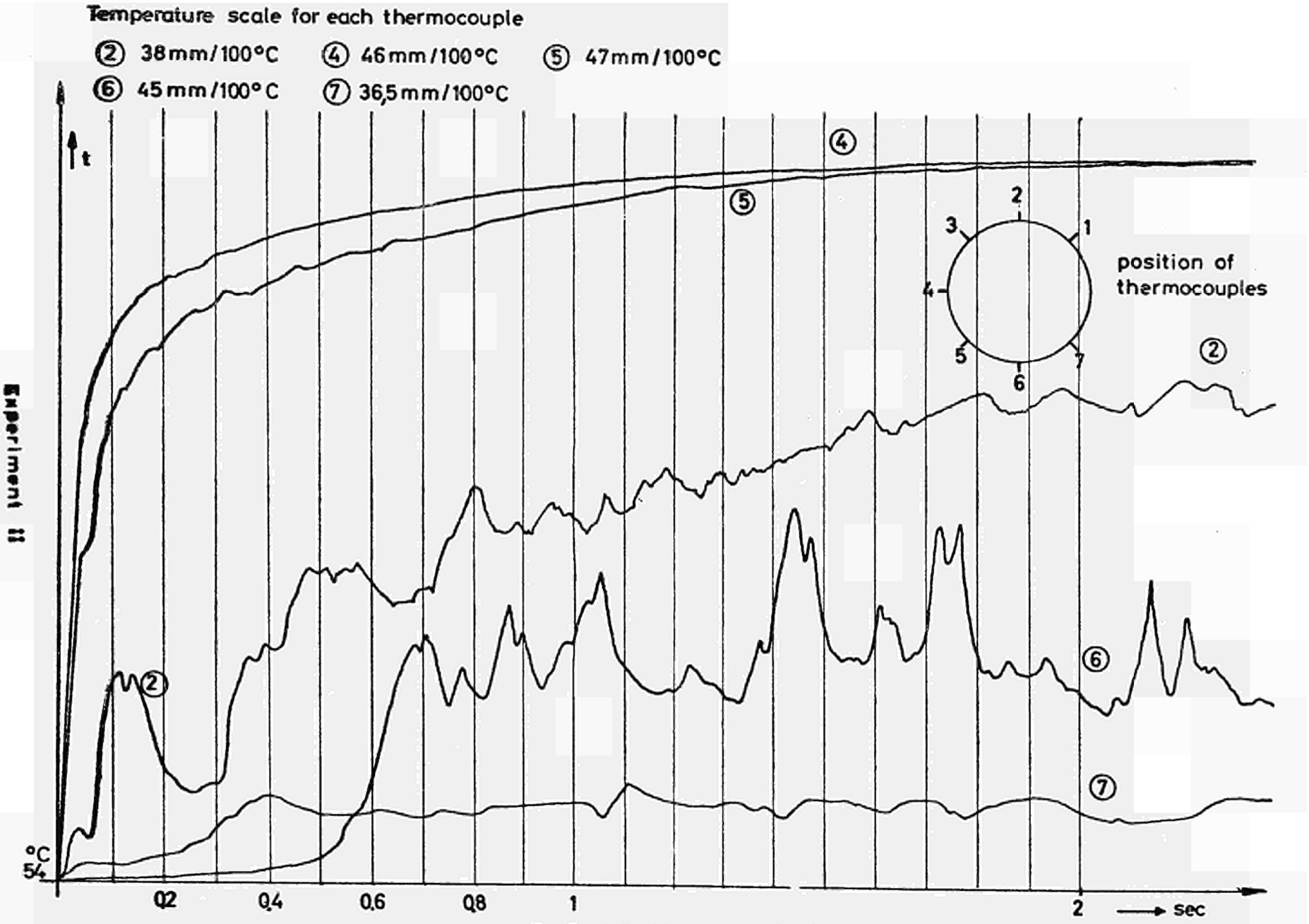

FIG. 18

Surface temperature distribution of zircaloy calandria tube (upper cross section)

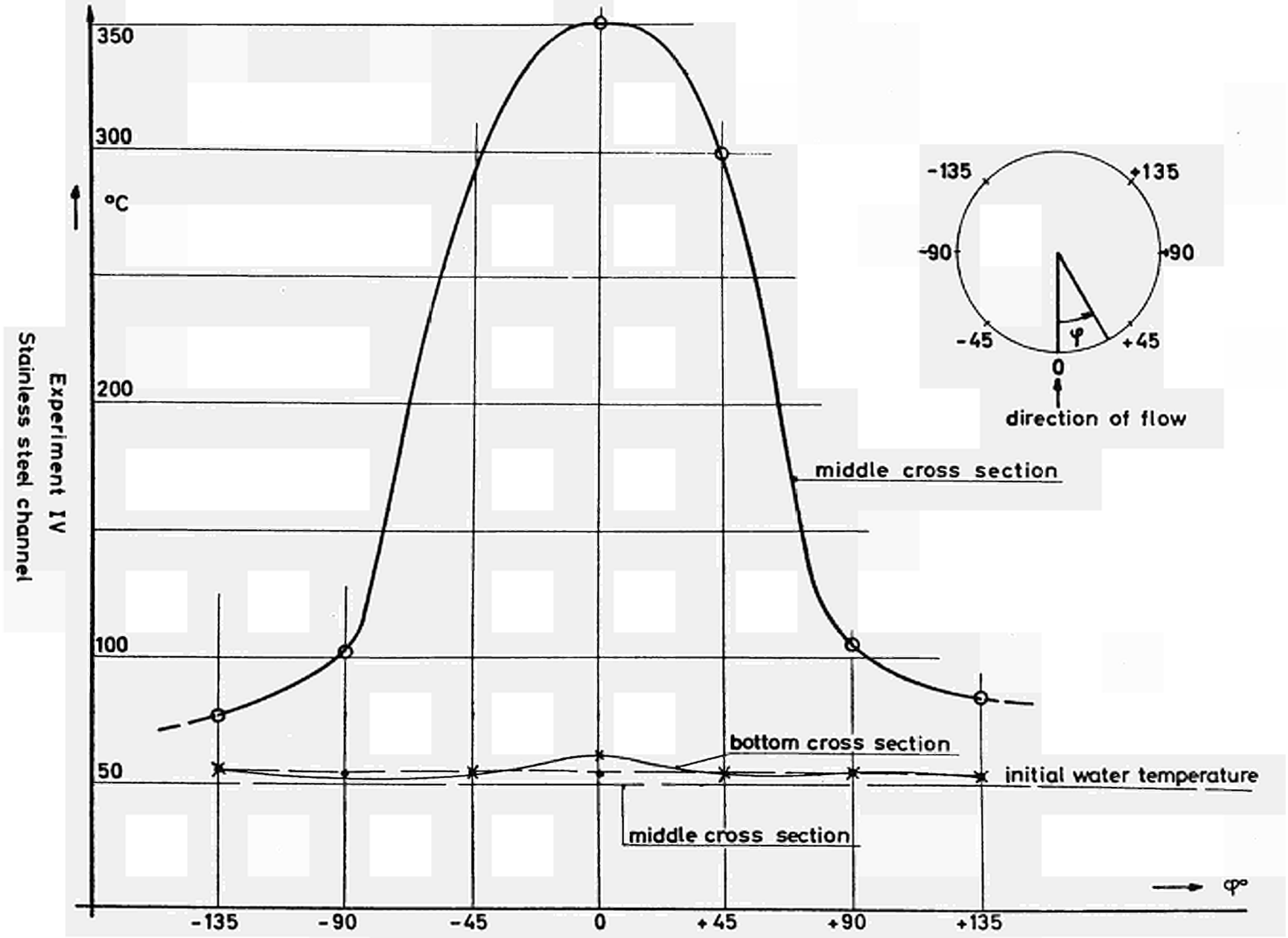

FIG. 19

Surface temperature distribution on 3 cross sections of a channel of the feeding zone 0,88 sec after explosion

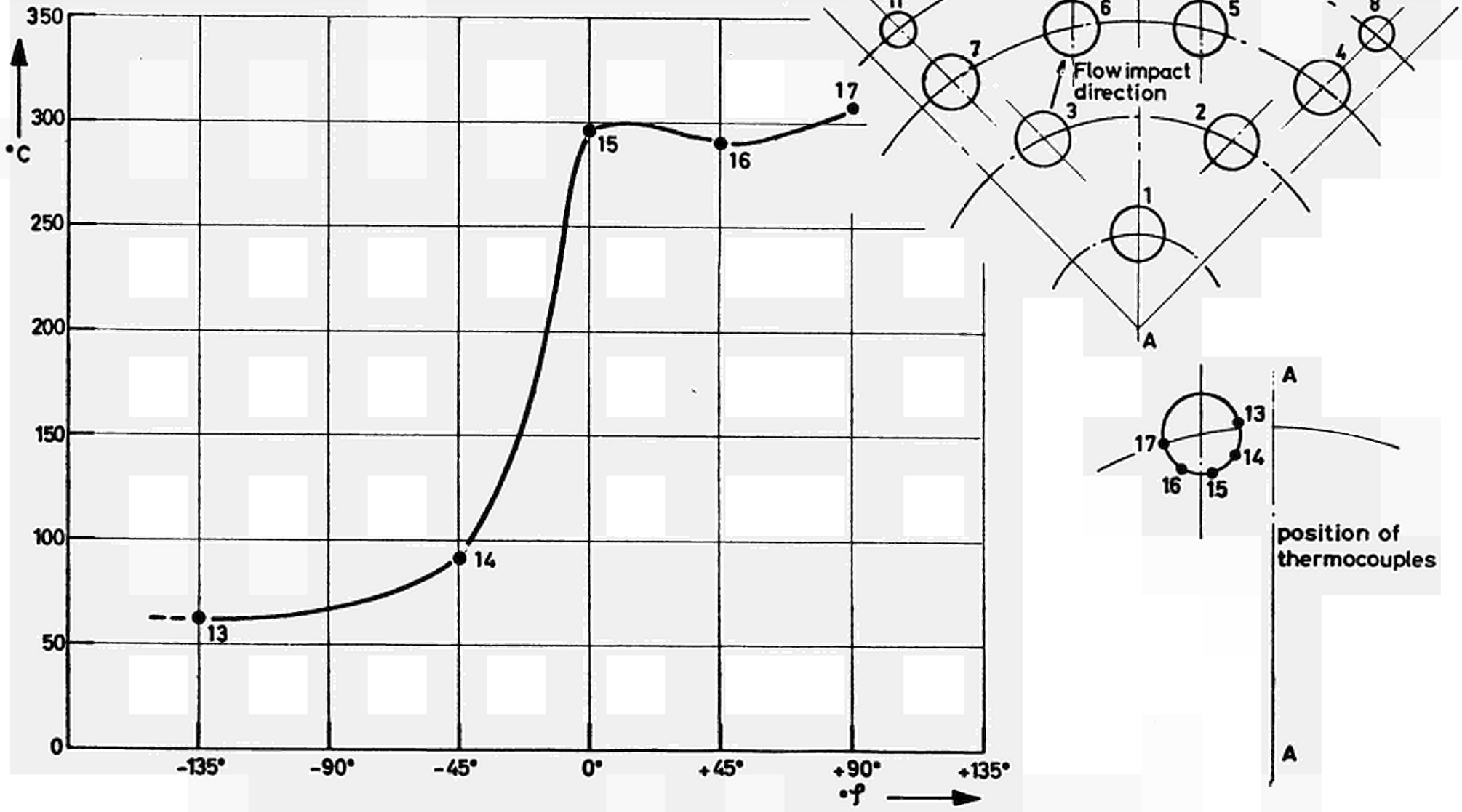

FIG 20 SURFACE TEMPERATURE DISTRIBUTION ON THE MIDDLE CROSS SECTION OF TUBE 10 10sec AFTER EXPLOSION (EXPERIMENT 6)

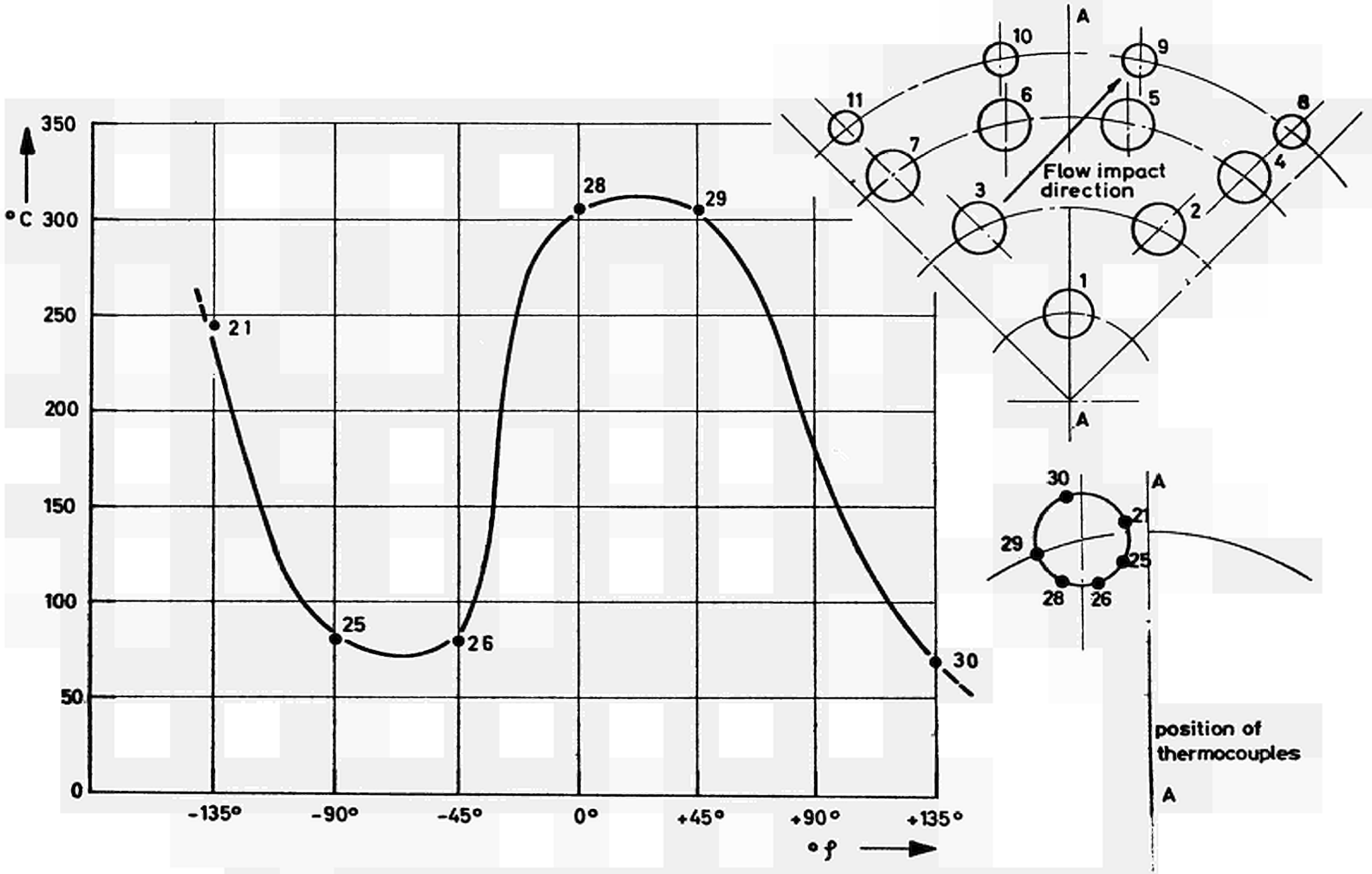

FIG 21 SURFACE TEMPERATURE DISTRIBUTION ON THE MIDDLE CROSS SECTION OF TUBE 6 4sec AFTER EXPLOSION (EXPERIMENT 7)

THE CALCULATION OF THE RESPONSE OF MODEL AND FULL SCALE REACTOR STRUCTURES TO DYNAMIC LOADINGS

by

N.J.M. Rees, UKAEA, Foulness

1. Introduction

Model testing of reactor systems to establish their mechanical safety to internal explosion has been carried out in the UK for some years (1). One early, though fairly typical, example for an investigation of explosion containment on single tank fast reactors has been recently published (2). In these experiments a charge of chemical explosive was used to simulate the rapid energy release in the core of a fast reactor under maximum accident conditions. The model reactor tank was an overstrong cylindrical vessel of 24 in. diameter, 24 in. deep closed by a loose fitting core access plug of $7\frac{3}{4}$ in. diameter in the centre of the roof. Water was used to simulate the hot sodium coolant. The roof, plug and walls of the reactor model were instrumented with pressure gauges to measure the transient pressure loading on these overstrong containment structures. The measured pressure loadings on the walls of the main tank clearly showed the direct shock wave from the explosion, the shock reflected from the base of the tank and the reflected rarefaction from the water surface. The pressure loading on the roof was due to the impact of the water thrown upwards when the direct shock wave was reflected at the free coolant surface.

The pressures that are measured acting on the major containment structures i.e. the roof, core access plug and the main tank, are used to interpret the sequence of the main physical events that result from the explosion in the core. In addition the effect of these pressure loadings on both the model and full scale structures can be calculated in suitable cases. In model experiments important forces such as the roof hold-down force can be measured and compared with the hold-down force calculated from the pressure loading to ensure that they are consistent, one with the other.

We are currently examining the effect of an explosion in the core of the Prototype Fast Reactor using models having linear dimensions 1/16th of the full scale reactor (1,3). A cross-section and plan of this PFR model are shown in Figures 1, 1A and 2, together with an explanation of the instrumentation

used to measure the forces acting on the core plug and roof of the model reactor structure. The size of the explosion simulated is conservatively larger than current calculations of the energy released by the collapse of the core under gravity (4). Our experiments have shown that the main sodium tank is unlikely to be ruptured by the explosion. The roof, however, will deflect under the impact pressure loading and it is possible that some of the numerous penetration seals might rupture. Thus the response of the model roof to the impact pressure loading is an important feature of this experiment. We hope to demonstrate the integrity of the roof penetration seals under the explosion loading conditions.

2. Deflexion of an Edge fixed roof panel under dynamic pressure loading

Consider a panel (Figure 3) with cartesian coordinates (x,y,Z) with the Z axis normal to the undisturbed position of the panel surface. Take the origin at the centre of the cross-section where the maximum deflexion is to occur. Thus in our case of a circular vault roof the origin would be at the centre of the roof. The positive direction of Z is taken upwards in the same direction as the force on the roof produced by the pressure loading. The panel is supported by uniformly distributed edge supports attached to a ring frame. The ring frame and the roof edge supports are capable of uniform motions Z_F in the Z direction only (Figure 4, Table I).

The displacement of the mid-section of the panel with reference to a fixed origin is thus

$$Z + Z_F = Z\, f(x,y) + Z_F \qquad \text{.....(2.1)}$$

Z_F represents the translation of the whole roof panel, its edge supports and the ring frame, while Z is the deflexion of a point (x,y) with reference to the translated position of the undisturbed roof section. (Figure 4). $f(0,0) = 1$ and Z is the deflexion of the point of maximum displacement produced by a uniform loading per unit area $\frac{1}{A} F(Z)$ applied very slowly to the panel. A is the total area of the panel exposed to the pressure loading. It is assumed later on that f(x,y) is the same function when the panel is stressed by non-uniform dynamic pressure loading.

$$\text{Let } \bar{f} = \frac{1}{A} \int\int f\,(x,y)\, dx\, dy \qquad \text{.....(2.2)}$$

and $$\bar{f}^2 = \frac{1}{4}\iint f^2\,(x,y)\,dx\,dy \qquad .....(2.3)$$

where integration is taken over the whole of the roof panel. $\bar{f}$ and $\bar{f}^2$ are "form" factors and are assumed to be constant for all values of Z of interest under both static and dynamic deflexions.

The kinetic energy T of the panel at a time t in the first swing is

$$T = 1/2\,\frac{M}{A}\iint \left(\dot{Z} + \dot{Z}_F\right)^2 dx\,dy \qquad .....(2.4)$$

$$= 1/2\,M\left\{\bar{f}^2\,\dot{Z}^2 + 2\bar{f}\,\dot{Z}\dot{Z}_F + \dot{Z}_F^2\right\}$$

Here integration is taken over the whole roof panel of total mass M which is assumed to be uniformly distributed. Z_F is not a function of x and y. The rate of change of kinetic energy is

$$\frac{dT}{dt} = M\left\{\bar{f}^2\,\dot{Z}\ddot{Z} + \bar{f}\,\dot{Z}_F\ddot{Z} + \bar{f}\,\dot{Z}\ddot{Z}_F + \dot{Z}_F\ddot{Z}_F\right\} \qquad .....(2.5)$$

The rate $\frac{dF}{dt}$ at which work is done against gravity and the elastic-plastic forces resisting the bending of the roof and resisting the translation of the roof is

$$\frac{dF}{dt} = \frac{d}{dt}\left\{\iiint\left[\frac{1}{A}\left(F_1(Z) + Mg\right)\left(\dot{Z} + \dot{Z}_F\right)\right]dx\,dy\,dt\right\}$$

$$= \left(\bar{f}\,\dot{Z} + \dot{Z}_F\right)\left\{F_1(Z) + Mg\right\} \qquad .....(2.6)$$

where $F_1(Z)$ is the force required to produce a dynamic central displacement Z of the roof. If the bending of the roof panel is subject to simple velocity dependent damping, then the rate of working against these forces $\frac{dK}{dt}$ is given by:

$$\frac{dK}{dt} = \frac{d}{dt}\left\{\iiint k\,\dot{Z}^2\,dx\,dy\,dt\right\}$$

$$= kA\bar{f}^2\,\dot{Z}^2 \qquad .....(2.7)$$

Here k is the damping factor per unit area of roof.

The rate at which work is done by the dynamic loading pressure $\frac{dP}{dt}$ is

$$\frac{dP}{dt} = \frac{d}{dt}\left\{\iiint \left(\dot{Z} + \dot{Z}_F\right) P(x,y,t)dx\ dy\ dt\right\}$$

$$= A\left(\bar{f}\,\dot{Z} + \dot{Z}_F\right)\bar{P}(t) \qquad .....(2.8)$$

where $\bar{P}(t)$ is the mean pressure acting on the panel at time t.
The rate of working due to the dynamic pressure loading is equal to the sum of the other rates of working,

$$M\left\{\left(\frac{\bar{f}^2}{\bar{f}} + \frac{\dot{Z}_F}{\dot{Z}}\right)\ddot{Z} + \left(1 + \frac{\dot{Z}_F}{\bar{f}\dot{Z}}\right)\ddot{Z}_F\right\} + \left(1 + \frac{\dot{Z}_F}{\bar{f}\dot{Z}}\right)\left\{F_1(Z) + Mg\right\} + kA\,\frac{\bar{f}^2}{\bar{f}}\,\dot{Z}$$

$$= A\left(1 + \frac{\dot{Z}_F}{\bar{f}\dot{Z}}\right)\bar{P}(t) \qquad .....(2.9)$$

Putting $\lambda = 1 + \frac{\dot{Z}_F}{\bar{f}\dot{Z}}$ then (2.9) becomes

$$M\left\{\left(\frac{\bar{f}^2}{\bar{f}} + \bar{f}\,(\lambda-1)\right)\ddot{Z} + \lambda\,\ddot{Z}_F\right\} + \lambda\left\{F_1(Z) + Mg\right\} + kA\,\frac{\bar{f}^2}{\bar{f}}\,\dot{Z}$$

$$= A\lambda\,\bar{P}(t) \qquad .....(2.10)$$

The "form" factors $\bar{f}^2$ and $\bar{f}$ can be evaluated from the measured shapes of a scale model roof under a "static" loading test to determine the function F(Z). From equation (2.2) putting an equal to the maximum radius of the roof.

$$\bar{f} = \frac{1}{A}\iint \frac{Z}{Z}\,dx\,dy$$

$$= \frac{1}{AZ}\int_0^{2\pi}\int_0^a Zrd\theta\,dr \text{ in polar coordinates}$$

$$= \frac{2\pi}{AZ}\int_0^a r\,Z\,dr \qquad .....(2.11)$$

where $Z = Zf(r)$ is the displacement of the roof mid-section at a distance r from the centre.

$$\text{Similarly } \bar{f}^2 = \frac{2\pi}{AZ^2}\int_0^a z\,Z^2\,dr \qquad .....(2.12)$$

It should be noted that both $\bar{f}$ and $\bar{f}^2$ could be slowly varying functions of

the peak roof deflection, that is, of the total static load F(Z) acting on the roof.

Some simplification of equation (2.10) can be achieved by restricting the motion of edge fixation of the panel. If $|\dot{Z}_F| << |\bar{f}\dot{Z}|$ the $\lambda \to 1$, and equation (2.10) becomes

$$M\left\{\frac{\bar{f}^2}{\bar{f}}\ddot{Z} + \ddot{Z}_F\right\} + F_1(Z) + Mg + kA\frac{\bar{f}^2}{\bar{f}}Z = A\bar{P}(t) \qquad .....(2.13)$$

If $\ddot{Z}_F << \ddot{Z}$ and $\dot{Z}_F << \bar{f}\dot{Z}$ then equation (2.10) becomes

$$\frac{\bar{f}^2}{\bar{f}}\left\{M\ddot{Z} + kA\dot{Z}\right\} + F_1(Z) + Mg = A\bar{P}(t) \qquad .....(2.14)$$

This is the simplest form that the equation of motion of the panel can take and is expressed solely in terms of the central deflexion Z.

3. The Response of a Model Structural Roof to an Impact Pressure Loading

It is important to remember that the acceleration due to gravity is the same for both the model and the full scale structure (1.3). Thus the forces between various parts of the model that depend partly on their weight will not be correctly scaled. A simplified mathematical model of the 1/16th scale model reactor structure is shown in Figure 4 and the various terms used are explained in Table I.

The main forces acting on this structure as a result of the explosion in the core occur in a definite sequence in time after the explosion. The first force F_D acts downwards through the diagrid structure and its support and acts on the ring frame to which the latter is attached. When the shock wave from the explosion reaches the main tank a second downward force F_T acts on the ring frame. The ring frame is supported by a number of columns connected to a thick base plate, which is firmly bolted to the reinforced concrete floor of the laboratory. About 0.5 m.sec after these initial downward forces the pressure on the core plug and roof begins to rise, and a mean pressure loading $\bar{P}(t)$ can be calculated from the individual pressure records.

The equation of motion of the roof, with moveable edge fixations, is given by equation (2.10). However for these initial calculations the

simpler form (2.13)

$$M\left\{\frac{\bar{f}^2}{\bar{f}}\ddot{Z} + \ddot{Z}_F\right\} + k\,A\,\frac{\bar{f}^2}{\bar{f}}\dot{Z} + Mg + F_1(Z) = A\,\bar{P}(t) \quad .....(3.1)$$

obtained by assuming $|\dot{Z}_F| << |\bar{f}\dot{Z}|$ is used. Since the roof hold-down is attached to the ring frame as are the diagrid support and the reactor main tank, all these move together as one lumped mass M_F through a displacement Z_F given by

$$M_F\ddot{Z}_F + K_F\dot{Z}_F + M_Fg = F_1(Z) - F_D - F_T - S_F(Z_F-Z_L) \quad .....(3.2)$$

The model base hold-down to the laboratory floor is assumed to be rigid so that the mass of the base is added to the "dynamic" lumped mass M_L of the laboratory floor for the purposes of this calculation. By "dynamic" lumped mass M_L is meant that fraction of the total floor mass that can be assumed to move with the peak (central) acceleration $\ddot{Z}_L$. With this approximation the equation of motion of the floor becomes

$$(M_L+M_B)\ddot{Z}_L + K_L\dot{Z}_L + (M_L+M_B)g = S_F(Z_F-Z_L) - S_LZ_L \quad .....(3.3)$$

All displacements Z_L, Z_F and Z and forces are taken as positive in an upwards direction.

In order to solve equations (3.1), (3.2) and (3.3) for the roof holddown force and the central roof deflexion Z, the constants and the forcing functions of the equations must be known. The masses and spring rates are found by calculation but the "form" factors $\bar{f}$ and $\bar{f}^2$ and the static total load, deflexion curve for the roof F(Z) are found from a separate experiment. Here a 1/16th scale structural model of the roof is subjected to a static load which was slowly increased in small steps until the roof failed. The profile of the roof was measured during the test and the form factors $\bar{f}$ and $\bar{f}^2$ calculated.

4. The Response of a Full Scale Structural Roof to an Impact Pressure Loading

The reactor vault is a very strong structure of mass M_V resting on a hard rock foundation (Figure 5). Thus in compression from the full scale forces $F'_D(t')$ and $F'_T(t')$ (where t' is now full scale time) it acts as an infinite mass; in tension when the roof is deflected upwards, it acts as a

mass M_V plus the mass of the main tank and coolant M_T and the mass of the diagrid support structure, breeder and reflector M_D. Let 1/S be the scale factor between the full and model scales, then the equation of motion of the roof is

$$M'\left\{\frac{\bar{f}^2}{\bar{f}}\ddot{Z}' + \ddot{Z}_F\right\} + kA'\frac{\bar{f}^2}{\bar{f}}\dot{Z}' + M'g + F_1'(Z') = \bar{P}'(t') \quad .....(4.1)$$

The dashed variables refer to the full scale quantities. The effect of doing work against gravity g, when the roof is displaced is more important on the full scale. Note that (3)

$$M' = S^3 M \quad F_1'(Z') = F_1(Z'/S)$$

and $\bar{P}'(t') = \bar{P}(t'/S)$

The equation of motion of the vault is

$$\left(M_V + M_D + M_T\right)\ddot{x}_V + \left\{F'_D + F'_T\right\} + \left(M_V + M_D + M_T\right)g$$

$$+ P_V A_V = F_1'(Z') \quad .....(4.2)$$

Here x_V is the full scale displacement of the vault, (positive upwards), P_V is the pressure in the vault. A_V is the total base area of the vault, and A' is the full scale area of the vault roof ($A' = S^2A$). Note that the equations are different to the model equations (3.1), (3.2) and (3.3) and that the solution for Z' is such that $Z' \neq SZ$.

5. Solutions

The cases outlines above are the most complex encountered to date and a number of solutions have been obtained using the equations in simplified form. The simplest case that has been calculated is that of a completely rigid model roof, while the response of a full scale roof attached to an infinite mass has been calculated. The model and full scale systems outlined above are also being computed at the present time. The work is carried out on a small PACE analogue computer.

References

1. N.S. Thumpston, "Model Techniques in Reactor Safety Studies" OECD Committee on Reactor Safety Technology. Meeting of Specialists on Shock Structure Interactions in a Reactor. ISPRA June 27th-29th, 1966.
2. N.J. M. Rees, "A Model Investigation of Explosive Containment in Single Tank Fast Reactors". Conference on Safety Fuels & Core Design in Large Fast Power Reactors, Argonne National Laboratory October 11th-14th, 1965. (AWRE Report R5/65)
3. N.J.M. Rees, "Experiments to Examine the Effects of Rapid Strain Rates on Full Scale and Model Scale Reactor Materials" OECD Committee of Reactor Safety Technology. Meeting of Specialists on Shock Structure Interactions in a Reactor. ISPRA June 27th-29th, 1966.
4. E.P. Hicks & D.C. Menzies, "Theoretical Studies of the Fast Reactor Maximum Accident". Conference on Safety Fuels & Core Design in Large Fast Power Reactors, Argonne National Laboratory October 11th-14th, 1965.

TABLE I : DEFINITION OF VARIABLES

x,y,Z	cartesian co-ordinates of roof panel Z axis normal to undisturbed position of panel surface. (in)
Z	central displacement of roof with respect to the edge fixations. (in)
Z_F	displacement of roof panel edge fixations with repsect to fixed origin. (in)
A	area of reactor roof on which loading pressure acts. (in^2)
M	mass of roof (ton $sec^2 in^{-1}$)
$\bar{f}, \bar{f}^2$	"Form" factors see equations (2.2) and (2.3)
T	Kinetic energy of roof at time t. (ton in)
k	velocity damping per unit area of roof. (0.25 critical)
P(x,y,t)	pressure acting at a time t and position (x,y) on roof (tsi)
$\bar{P}(t)$	mean pressure acting at time t on roof. (tsi)
$\lambda = 1 + \frac{\dot{Z}F}{\bar{f}\dot{Z}}$	
F(Z)	Static total load on roof required to produce a maximum central deflexion Z. (ton)
$F_1(Z)$	Dynamic total load on roof required to produce a maximum central deflexion Z. (ton)
M_F	Mass of edge fixations framework, diagrid and main tank. (ton $sec^2 in^{-1}$)

k_F velocity damping of edge fixation framework. (0.25 critical)

S_F Spring rate of frame (ton in^{-1})

F_D downward loading exerted on edge fixations by diagrid support, expressed a function of time. (ton)

F_t downward loading exerted on edge fixations by main tank expressed as a function of time. (ton)

M_B mass of reactor model base. (ton $sec^2 in^{-1}$)

M_L "Dynamic" lumped mass of laboratory floor. (ton $sec^2 in^{-1}$)

S_L central force required to produce unit central deflexion of laboratory floor. (ton in^{-1})

K_L velocity damping of laboratory floor. (0.125 critical)

Z_L Peak central deflexion of laboratory floor. The model is fixed to centre of laboratory floor. (in)

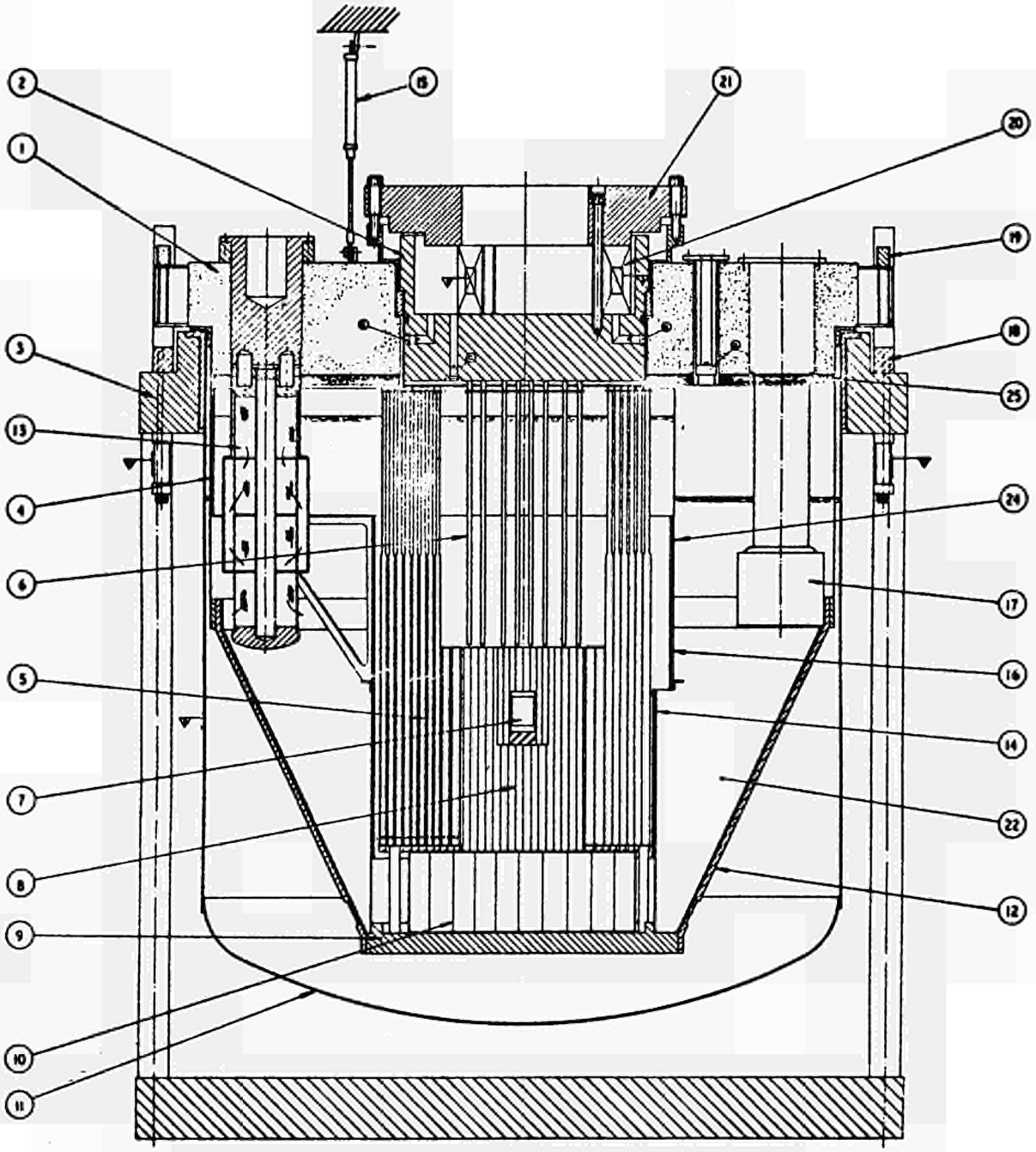

FIGURE 1. SECTION THROUGH 1/16th SCALE P.F.R. MODEL

ITEM	TITLE
1	ROOF
2	CORE PLUG
3	DYNAMIC TEST FRAME
4	COOLANT TRAY (NOTE BRACING FRAMES)
5	NEUTRON SHIELD
6	CONTROL ROD ASSEMBLY
7	CHARGE
8	CORE AND BREEDER ASSEMBLY
9	DIAGRID SUPPORT
10	DIAGRID
11	MAIN TANK
12	DIAGRID SUPPORT STRUCTURE
13	HEAT EXCHANGER
14	RE-ENTRANT PART OF CORE JACKET
15	LINEAR TRANSDUCER
16	CORE JACKET
17	SODIUM PUMP
18	ROOF HOLD-DOWN YOKE
19	HOLD-DOWN BAR
20	STRAIN GAUGE BLOCKS-CORE PLUG
21	CORE PLUG RESTRAINT RING
22	DIAGRID SUPPORT FRUSTRUM
23	
24	THERMAL SHIELD
25	THERMAL INSULATION LAYER

SYMBOLS

DENOTES STRAIN GAUGE POSITIONS

DENOTES PIEZO ELECTRIC TRANSDUCERS

FIGURE 1 (a)

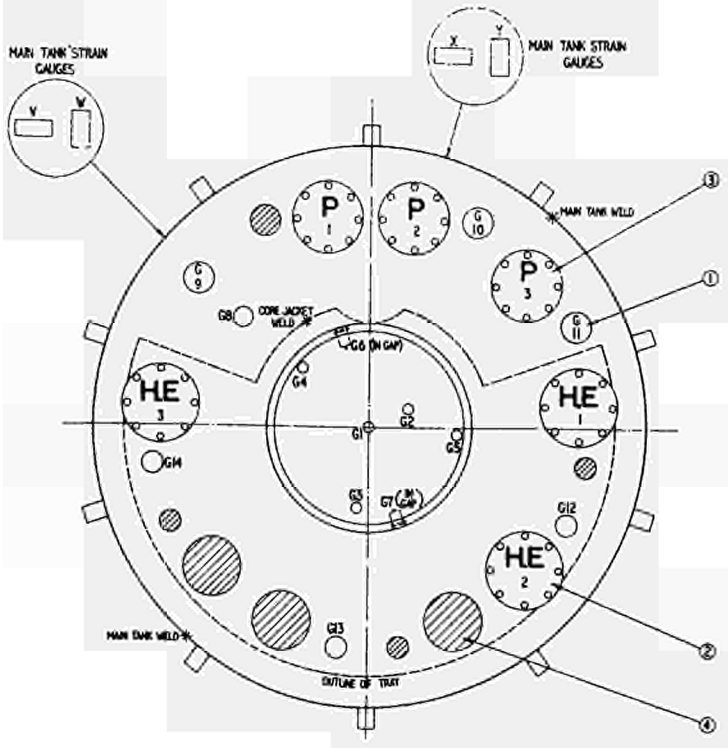

ITEM	TITLE
1	PRESSURE GAUGES (NUMBERS AS INDICATED)
2	HEAT EXCHANGERS (NUMBERS AS INDICATED)
3	SODIUM PUMPS (NUMBERS AS INDICATED)
4	PLUGGED HOLES (ALL CROSS HATCHED)

NOTE

CENTRE OF STRAIN GAUGE PATTERN IS 20" BELOW LIP OF MAIN TANK

FIGURE 2. PLAN VIEW OF 1/16 th SCALE P.F.R. MODEL

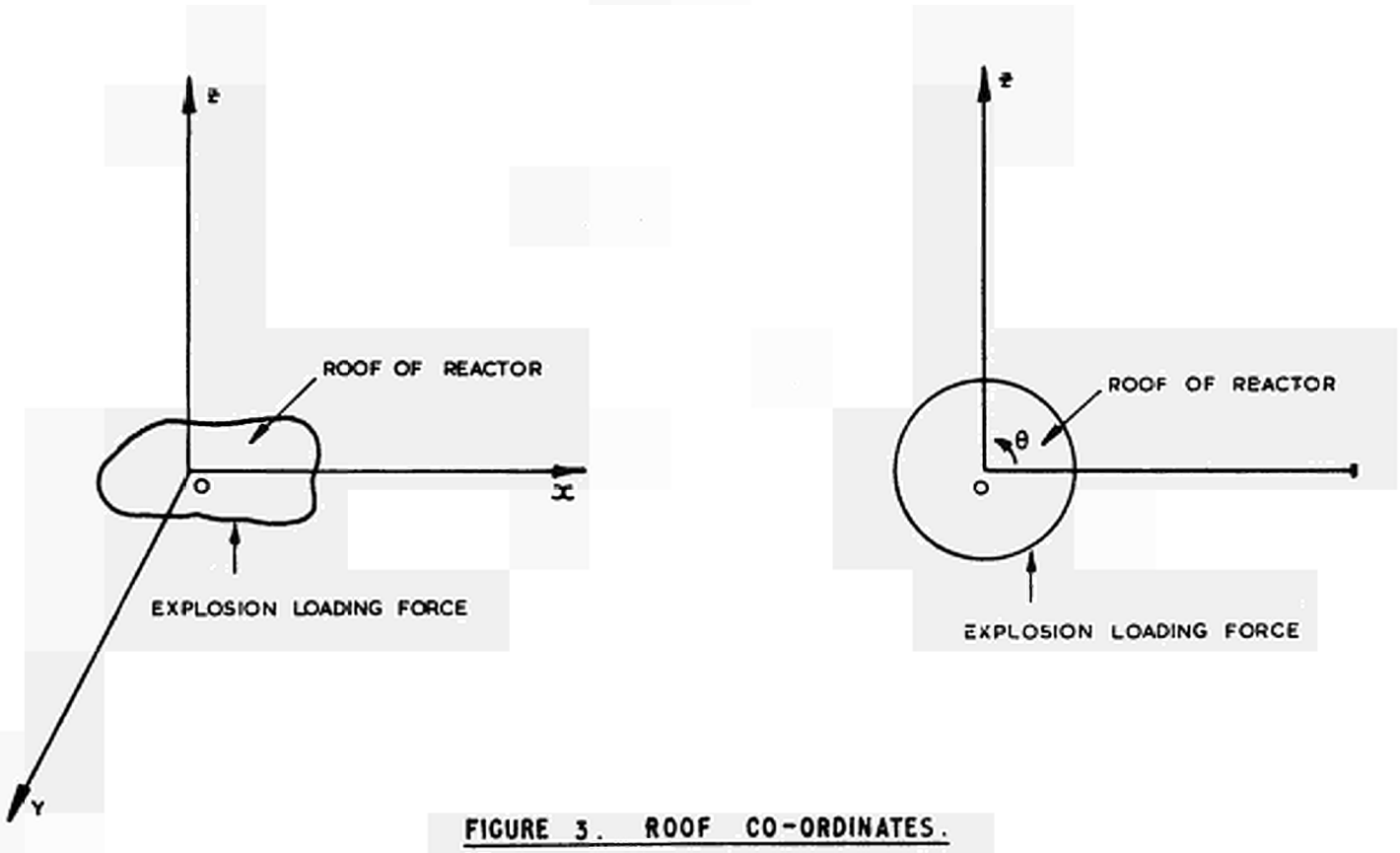

FIGURE 3. ROOF CO-ORDINATES.

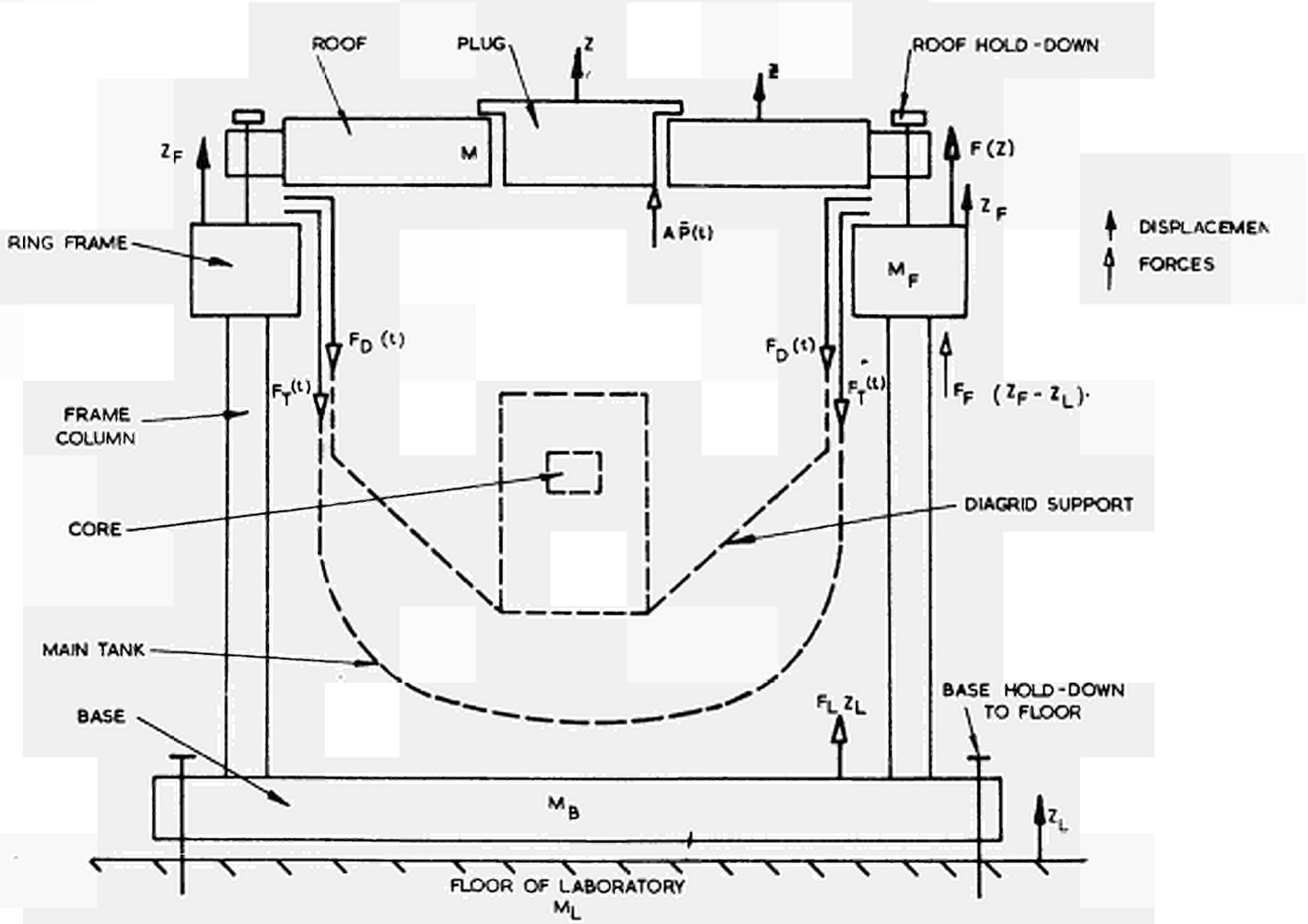

FIGURE 4. SIMPLIFIED MODEL ARRANGEMENT USED FOR CALCULATIONS OF MODEL BEHAVIOUR

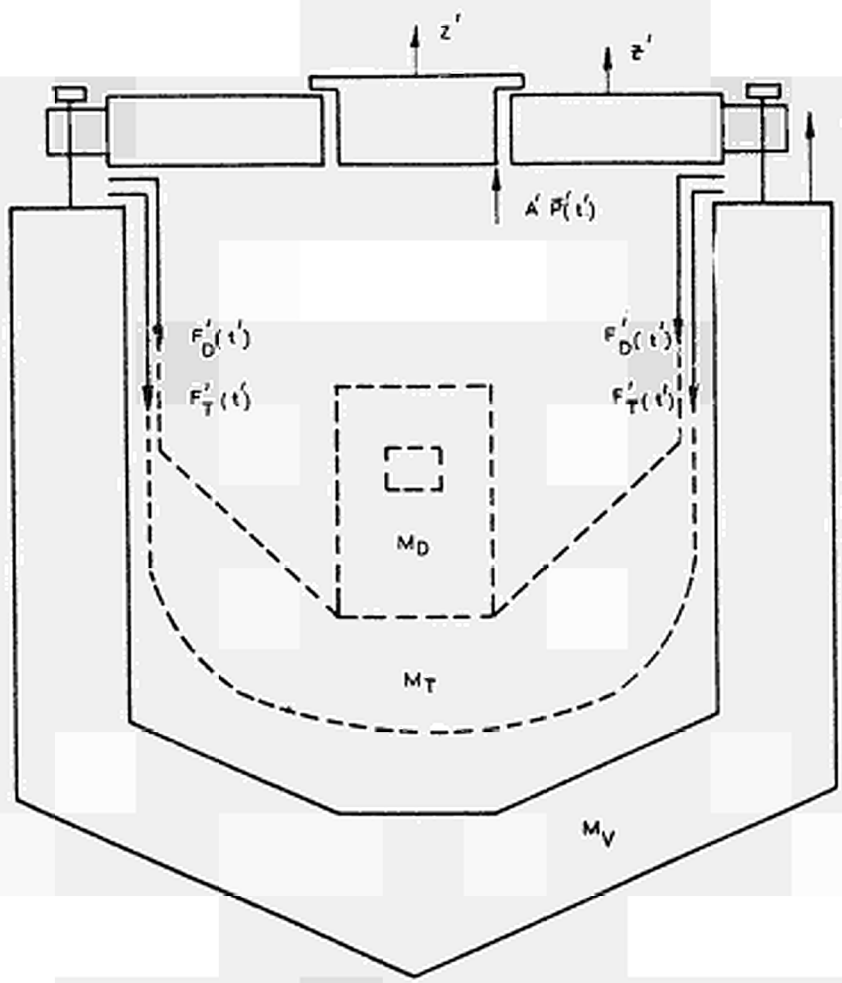

M' = MASS PER UNIT AREA OF FULL SCALE ROC

M_D = MASS OF CORE SUPPORT ASSEMBLY

M_V = MASS OF REACTOR VAULT.

M_T = MASS OF REACTOR TANK AND SODIUM

FIGURE 5. ARRANGEMENT USED TO INTERPRET MODEL RESULTS FOR FULL SCALE REACTOR.

SIMULATION D'ACCIDENTS EXPLOSIFS SUR LES PILES RAPIDES

par

M. Falgayrettes et J.P. Millot

C.E.N. Cadarache
France

I - INTRODUCTION

Bien que l'heure des centrales nucléaires utilisant comme source d'énergie un réacteur rapide à sodium ne soit pas encore venue, un grand nombre de pays dans le monde développent des études en vue de réaliser un prototype.

Dans le domaine de la sûreté, la conception de ces réacteurs doit tenir compte de la nécessité de maintenir le sodium dans une cuve étanche, quel que soit le comportement du coeur au cours d'un accident. La rupture de l'étanchéité peut entraîner en effet des conséquences graves : vaporisation de combustible par manque de refroidissement du coeur, et feu de sodium actif dans l'enceinte. Le maintien de l'étanchéité de l'enceinte du réacteur doit permettre de limiter les conséquences radiologiques d'accidents graves.

L'étude des accidents pouvant conduire à des explosions a été commencée dans différents pays ; cependant, étant donné la complexité de ce problème, il est peu probable qu'elle soit terminée à temps pour la construction des divers prototypes en projet. Afin de donner aux projeteurs des éléments de travail sur les ondes de pression engendrées en cas d'explosion, et sur la tenue des divers composants du réacteur, nous avons, en France, développé une technique de simulation d'explosion. Cette technique consiste à placer dans une maquette à échelle réduite, représentant le réacteur, un explosif au centre du coeur. L'évolution, en fonction du temps, du dégagement d'énergie dans celui-ci est voisine de celle supposée d'un réacteur rapide lors d'un accident de réactivité. Cette technique a été appliquée pour déterminer le comportement du réacteur RAPSODIE. Sur cette maquette, le comportement de la cuve du réacteur, de la cuve d'étanchéité et des bouchons supérieurs du réacteur ont été examinés ; la propagation des ondes de pression, les contraintes engendrées et les déformations des composants ont été mesurées. Afin de préciser l'influence de l'échelle, deux séries d'essais ont été effectuées :

a) G.A.A.A. (Groupement Atomique Alsacienne Atlantique) a effectué, sou contrat, des essais sur une maquette à l'échelle 3/10 ; le sodium était remplacé par de l'eau ;

b) lors des essais suivants, réalisés sur une maquette à l'échelle 1/10, on a étudié les différences de comportement lorsque le sodium est remplacé par de l'eau ; ces essais ont été effectués à CADARACHE, par l'association EURATOM-C.E.A. sur les neutrons rapides, en collaboration avec des spécialistes de l'U.K.A.E.A. de Foulness.

II - DESCRIPTION SOMMAIRE DU REACTEUR RAPSODIE

RAPSODIE est un réacteur rapide refroidi au sodium dont la puissance nominale est de 20 MW. L'élément combustible est constitué d'aiguilles contenant un mélange U O 2 - Pu O 2 gainé d'acier inoxydable et placées dans un boîtier de forme hexagonale. A l'origine, ces éléments étaient constitués d'alliage U - Pu - Mo, et les expériences de simulation ont été effectuées pour ce type d'éléments. Aux deux extrémités du boîtier, des aiguilles d'uranium naturel sous forme d'oxyde constituent les couvertures inférieure et supérieure du coeur. Le coeur est entouré d'assemblages de forme extérieure identique à celle des éléments combustibles ; ces assemblages contiennent de l'uranium naturel sous forme d'oxyde ; ils constituent la couverture latérale du coeur.

Le coeur est refroidi par un courant de sodium de sens ascendant. Une cuve extérieure à double paroi, suspendue, protégée du rayonnement par une série d'écrans de protection interposés entre elle et le coeur, contient l'ensemble. La cuve d'étanchéité est protégée par un isolant thermique et est plaquée sur le béton de protection.

Le chargement et le déchargement s'effectuent par une hotte et par un système de deux bouchons tournants excentrés. Les échangeurs sont placés dans une fosse à l'extérieur de la protection biologique.

La pile est placée dans une enceinte métallique étanche prévue pour résister à une surpression de 2,4 bars.

Les annexes montrent :

- un plan de l'ensemble du coeur (annexe 1)
- un éclaté de la cuve (annexe 2)
- une coupe de l'ensemble du réacteur (annexe 3)

III - PRESENTATION DES EXPERIENCES DE SIMULATION

Le choix des expériences a été effectué à partir des idées suivantes :

(1) il est nécessaire d'effectuer des essais à échelles différentes pour étudier leur influence sur la simulation ;
(2) une simulation à grande échelle permet une représentation assez fidèle de l'ensemble de la pile, mais elle présente des risques au point de vue de la sécurité, étant donné la grande quantité de sodium nécessaire.

Deux séries d'essais ont été choisies :

(1) la première, à l'échelle 3/10, constituait une représentation fidèle de l'ensemble de la pile ; le sodium était remplacé par de l'eau ;
(2) la seconde, à l'échelle 1/10, a permis d'étudier, à l'aide d'une représentation plus symbolique de l'installation, l'influence du remplacement de l'eau par le sodium.

L'étude des accidents explosifs sur RAPSODIE a montré que, dans les conditions les plus pessimistes, les dégagements d'énergie étaient les suivants :

(1) Combustible métallique U - Pu - Mo
Energie 1,6 10^8 calories ou 6,6 10^8 joules
durée du phénomène : 80 microsecondes
(2) Combustible oxyde U O 2 - Pu O 2
Energie 1,2 10^8 calories ou 4,8 10^8 joules
durée du phénomène : 80 microsecondes.

L'explosif a été choisi en tenant compte de ces énergies et du temps de dégagement. Quelques essais ont été effectués avec divers explosifs et ont démontré que, pour des temps de dégagement d'énergie aussi rapides, la quantité de gaz dégagée avait peu d'importance. Néanmoins, l'hexogène a été retenu car il était le seul explosif à fournir une énergie donnée dans un temps donné sous le volume disponible. En outre, parmi les explosifs envisagés, son dégagement en gaz était le plus faible.

1. Première série d'essais à échelle 3/10

Une coupe de la maquette est donnée en annexe 4.

Dans ces essais, la part de l'instrumentation a été assez faible. Le but de ces essais était surtout de déterminer le comportement

des divers composants de la pile en tenant compte de différentes conditions initiales :

- influence de la présence de la couverture latérale
- influence de la hauteur d'eau simulant le sodium
- influence de la présence ou de l'absence de gaz entre le bouchon et l'eau
- influence de la fixation du bouchon supérieur
- influence de la quantité d'explosifs - domaine de variation de 196 à 1.764 g d'hexogène.

Les résultats de ces essais ont été obtenus par l'examen des effets mécaniques sur les composants de la maquette. L'effort sur le bouchon mobile supérieur a été déduit de la hauteur d'envol de celui-ci pendant l'expérience.

2. Seconde série d'essais à l'échelle 1/10

Une représentation du dispositif expérimental est en annexe 5.

La protection du réacteur est symbolisée par une cuve d'acier très solide dans laquelle est placée une cuve de paroi mince contenant une maquette du coeur. L'enceinte est fermée à sa partie supérieure par un couvercle boulonné. La charge est introduite au centre du coeur par un verrin quelques minutes avant l'essai. Elle est placée sous le dispositif et verrouillée par un système mécanique à quart de tour. La charge est placée dans un doigt de gant qui l'isole du réfrigérant. L'ensemble est placé dans une enceinte de sécurité.

Des mesures de contrainte sont effectuées grâce à des jauges placées sur les boulons du couvercle supérieur. Elles donnent une idée de l'effort sur le couvercle. Quatre capteurs de pression sont placés dans le couvercle supérieur.

Au cours de ces essais, l'influence de certaines conditions initiales a été testée :

- influence du remplacement du sodium par de l'eau
- influence de la température initiale
  - de l'eau - domaine de variation de 20° C à 90° C
  - du sodium - domaine de variation de 150° C à 550° C
- influence de la quantité d'explosif.

Ces essais ont été effectués pour 15 g, 30 g et 60 g d'hexogène correspondant à des énergies dissipées de $2 \cdot 10^4$, $4 \cdot 10^4$ et $8 \cdot 10^4$ calories.

IV - PRESENTATION DES RESULTATS OBTENUS

1. Maquette à l'échelle 3/10

Les résultats obtenus dans les 8 essais effectués sur la maquette à l'échelle 3/10 sont contenus dans le tableau donné en annexe 6.

Les effets sur le bouchon mobile sont indiqués dans le tableau donné en annexe 7.

Les effets sur le bouchon fixe sont indiqués dans le tableau donné en annexe 8.

On peut émettre les remarques suivantes sur cette série d'essais :

(a) les effets observés ne dépendent pas seulement de l'énergie de l'explosion, mais des modifications de la géométrie provoquées par l'explosion. Les effets sur les bouchons mobiles, par exemple, augmentent peu parce que la cuve s'est ouverte très vite et qu'une grande partie de l'énergie a été absorbée par l'écrasement des caissons ;

(b) le rendement de l'explosion (fraction de l'énergie utilisée pour mouvoir les bouchons) décroît quand l'énergie augmente et tend vers 10 % environ ;

(c) la couche de béton en vermiculite placée entre le graphite et la virole de béton armé intervient très peu et la tension du béton armé reste faible ;

(d) le fait de maintenir en place le bouchon mobile accroît les effets sur la cuve et sur le bouchon fixe.

2. Essais sur maquette à l'échelle 1/10

Les résultats obtenus lors des essais sont rassemblés dans le tableau donné en annexe 9. Au cours de ces essais, la pression a été mesurée par des capteurs mis au point par l'U.K.A.E.A. La forme générale de l'impulsion de pression est schématisée par la courbe ci-dessous :

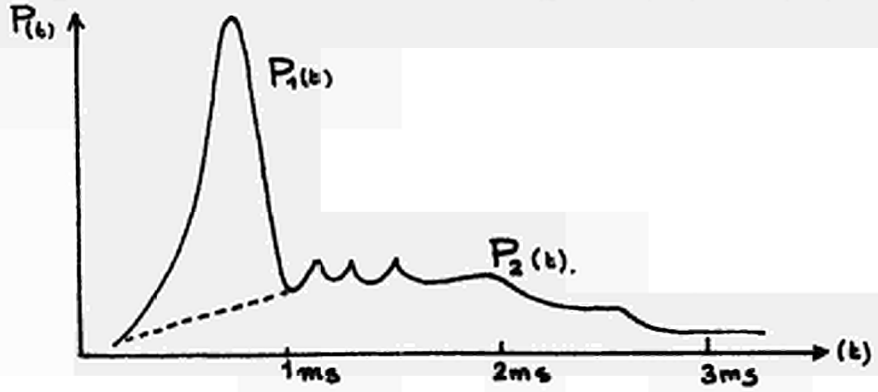

Cette courbe peut être décomposée en deux parties :

(a) le pic de pression $P_1(t)$ provenant probablement de l'impact du liquide sur le couvercle, et représenté par le pic auquel on a déduit la partie en pointillé ;

(b) des oscillations de pression $P_2(t)$ provenant des oscillations de la bulle de vapeur créée par l'explosion de la cuve et des oscillations du volume de gaz produit par le corps détonnant. Ces oscillations représentent le reste de la fonction.

A partir de ces enregistrements, on peut en déduire :

(a) P valeur du pic moyen de pression sur le couvercle - la valeur donnée dans le tableau correspond à une moyenne sur un certain nombre d'essais et sur les différents capteurs placés dans le couvercle supérieur ;

(b) I, impulsion sur le couvercle, correspond à

$I = \int_0^t P_1(t)\,dt$ due à l'impact du liquide sur le couvercle ;

(c) $\Lambda_1 = 16{,}4\ Q^{1/3}$ formule empirique donnant I

(d) Π : pression d'impact.

Cette pression a été calculée par la relation $P = \rho c v$

ρ = densité du liquide
c = vitesse acoustique dans le liquide
v = vitesse d'impact du liquide

v est déterminé par le temps τ mis par le liquide pour parcourir l'espacement entre sa surface et le couvercle.

Cette pression peut être comparée à la valeur de P obtenue expérimentalement. A l'aide du tableau donné en annexe 9, on constate que la pression calculée est légèrement supérieure à la pression mesurée.

Des mesures de contraintes ont été effectuées sur les boulons de fixation du couvercle supérieur et sur le couvercle lui-même. Les enregistrements montrent qu'une première force est appliquée sur le couvercle avant l'impact du liquide sur celui-ci. Elle est due à des efforts transmis par les structures de la maquette. L'effort lié au pic de pression est donné dans l'annexe 9 et comparé (rubrique : force

mesurée par le C.E.A.) à la force déterminée à partir des mesures de pression (rubrique : force maximum par l'U.K.A.E.A.) ; on constate que les efforts déterminés à partir de la réponse des jauges de contraintes sont plus faibles que les efforts déterminés à partir de la réponse des capteurs de pression.

La comparaison des résultats obtenus démontre que les pressions obtenues dans les expériences effectuées avec de l'eau sont plus faibles que celles obtenues dans les expériences avec le sodium ; le facteur est :

- 1,7 pour les charges de 15 g
- 1,5 pour les charges de 60 g

V - CONCLUSIONS

L'utilisation de ces expériences, en vue de la définition des composants, doit être faite avec beaucoup de prudence. La liaison entre les effets mécaniques engendrés par l'explosion d'un réacteur - et l'explosion d'un corps détonnant dégageant la même énergie dans le même temps - est très difficile et, de toute manière, fort peu connue. On peut néanmoins supposer qu'une étude sur maquette, effectuée avec explosif, donne des résultats pessimistes qui peuvent être interprétés de manière rassurante pour la sûreté d'une pile. Cette étude permettrait de définir des normes pour les projeteurs sous réserve que celles-ci ne conduisent pas à des réalisations économiquement catastrophiques.

Ainsi, dans le cas du réacteur RAPSODIE, l'extrapolation des résultats de ces expériences permet de prévoir qu'en cas d'explosion du coeur, avec dégagement de 1,6 10^8 calories, les efforts sur les bouchons seraient les suivants (on estime que cette explosion correspond à une explosion d'hexogene libérant une énergie quatre fois plus faible) :

Bouchons mobiles	
Impulsion totale	$7 \cdot 10^5$ N. S.
Durée de l'impulsion	15 ms
Force totale moyenne	$4{,}4 \cdot 10^6$ kg
Pression moyenne	85 kg/cm^2
Bouchons fixes	
Impulsion	$1{,}2 \cdot 10^5$ N. S.
Durée de l'impulsion	30 ms
Force totale moyenne	$4 \cdot 10^5$ kg
Pression moyenne	5,6 kg/cm^2

On peut, par ailleurs, en déduire que la cuve du coeur est déchirée ; mais la cuve d'étanchéité est préservée car elle est appuyée sur le béton de protection.

Le calcul de ces efforts sur les bouchons permet de définir des systèmes mécaniques suffisamment solides pour éviter l'envol de ceux-ci.

La définition, par les projeteurs, des composants du réacteur permettra de limiter les conséquences d'une explosion ; ainsi :

- la conception des mécanismes de contrôle permettrait d'éviter leur envol ;
- la définition de la position des tuyauteries permettrait d'éviter la propagation à l'extérieur du bloc pile d'ondes de choc qui, transmises par les tuyauteries, pourraient provoquer la rupture de celles-ci.

REFERENCES BIBLIOGRAPHIQUES

1. ETUDES RELATIVES AUX ENCEINTES DE SURETE DE RAPSODIE
G. Drevon, M. Gelée, R. Wustner - Commissariat à l'Energie Atomique - France
A.I.E.A. Symposium sur la sécurité des réacteurs et les méthodes d'évaluation des risques - Vienne - 14 au 18 mai 1962.

2. QUELQUES RESULTATS DE L'ETUDE DES ENVELOPPES DE SECURITE DU REACTEUR RAPSODIE
G. Drevon, M. Falgayrettes - Association EURATOM - C.E.A. Neutrons Rapides
8ème Congrès nucléaire de Rome - Symposium sur les réacteurs rapides - 17 au 19 juin 1963.

3. COMPARISON OF PRESSURE LOADING PRODUCED BY CONTAINED EXPLOSIONS IN WATER AND SODIUM
G.A.V. Drevon, M. F.G. Falgayrettes, F.J. Walford - C.E.A. - U.K.A.E.A.
Conference on Safety, Fuels and Core Design in large fast power reactors - Argonne National Laboratory, October 11th - 14th, 1965.

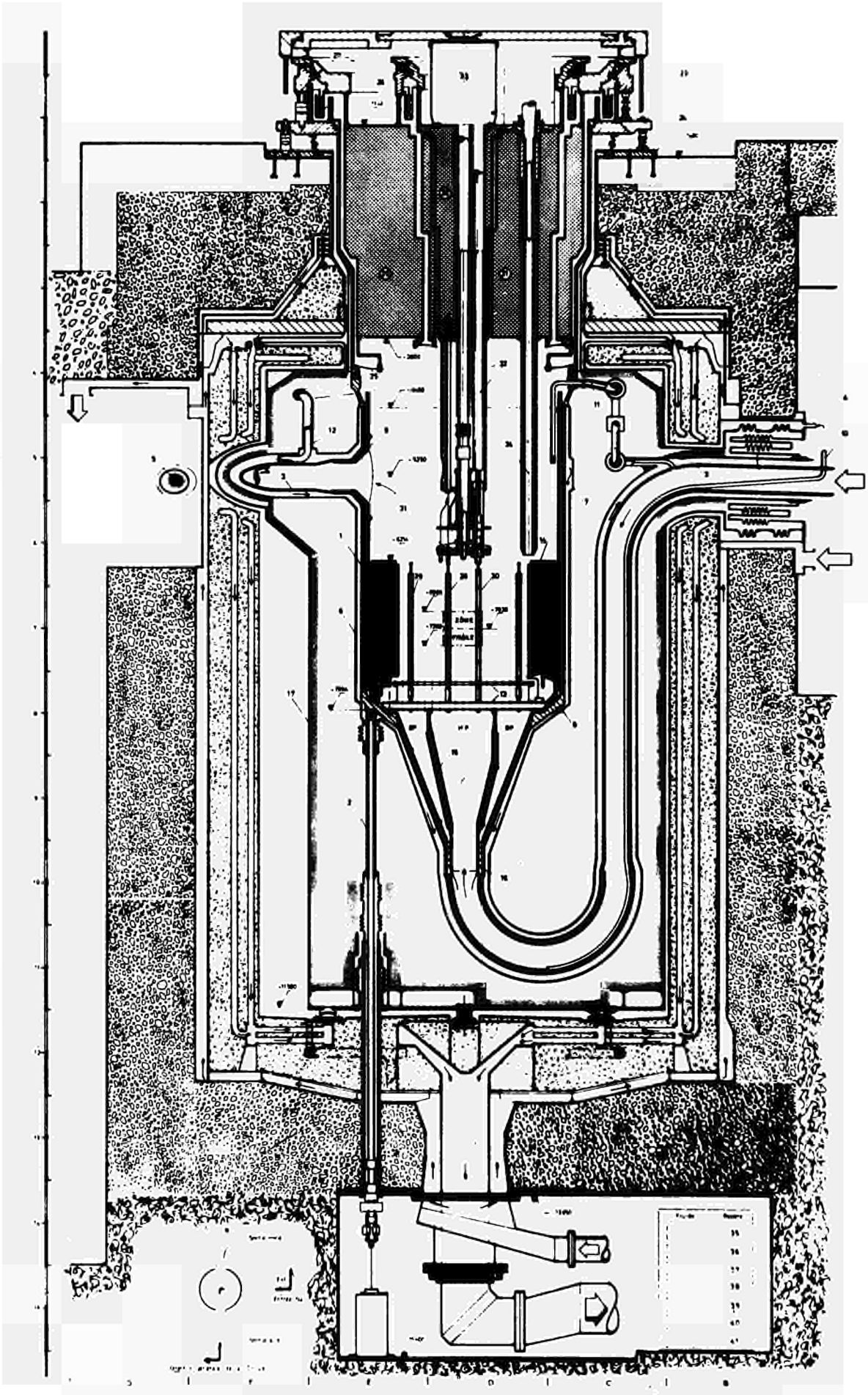

Annexe 1 : RAPSODIE - UN PLAN DE L'ENSEMBLE DU COEUR

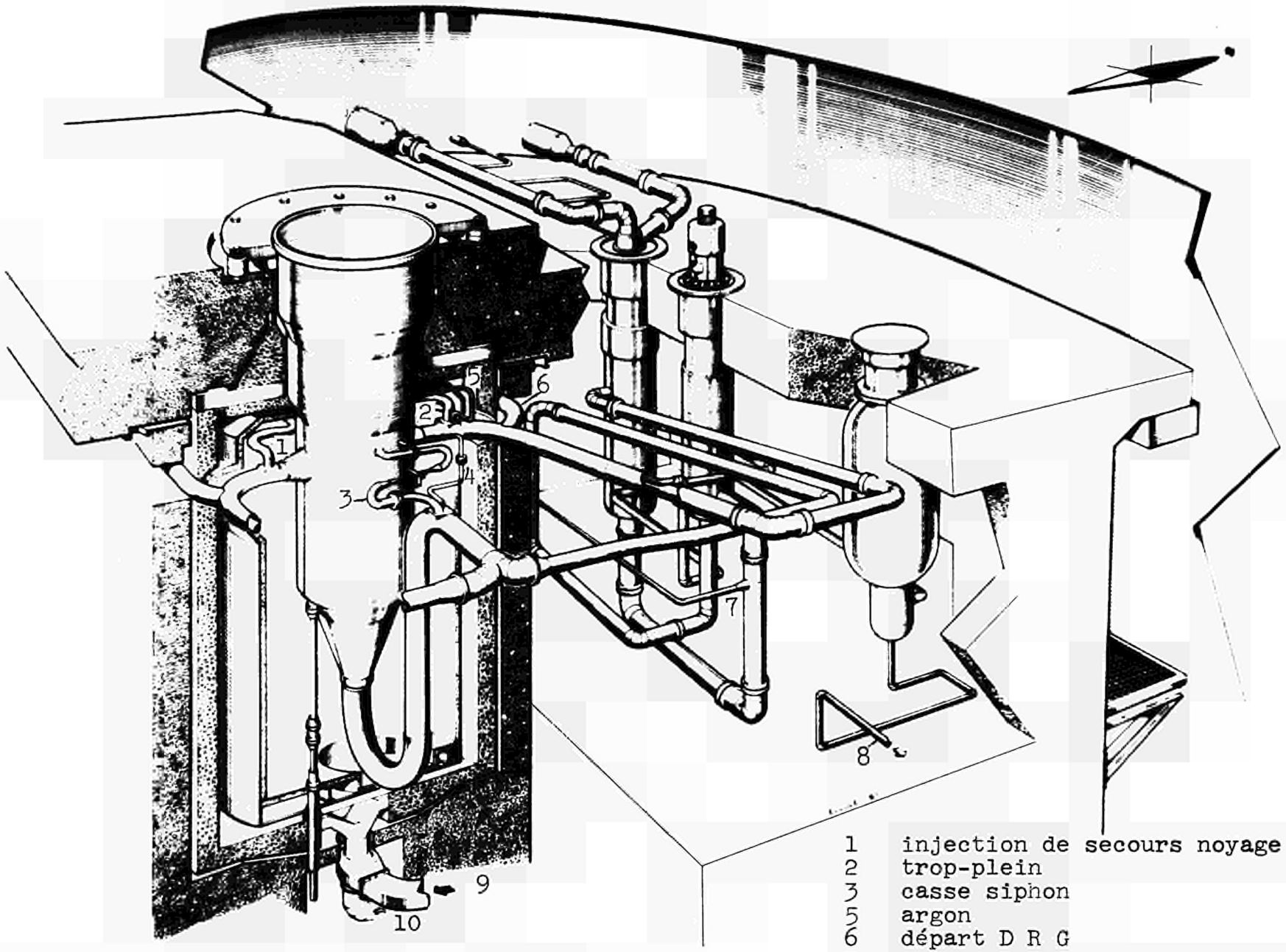

1	injection de secours noyage
2	trop-plein
3	casse siphon
5	argon
6	départ D R G
7	retour D R G
8	vers armoire de purification
9	entrée azote
10	sortie azote

Annexe 2 : RAPSODIE - UN ECLATE DE LA CUVE

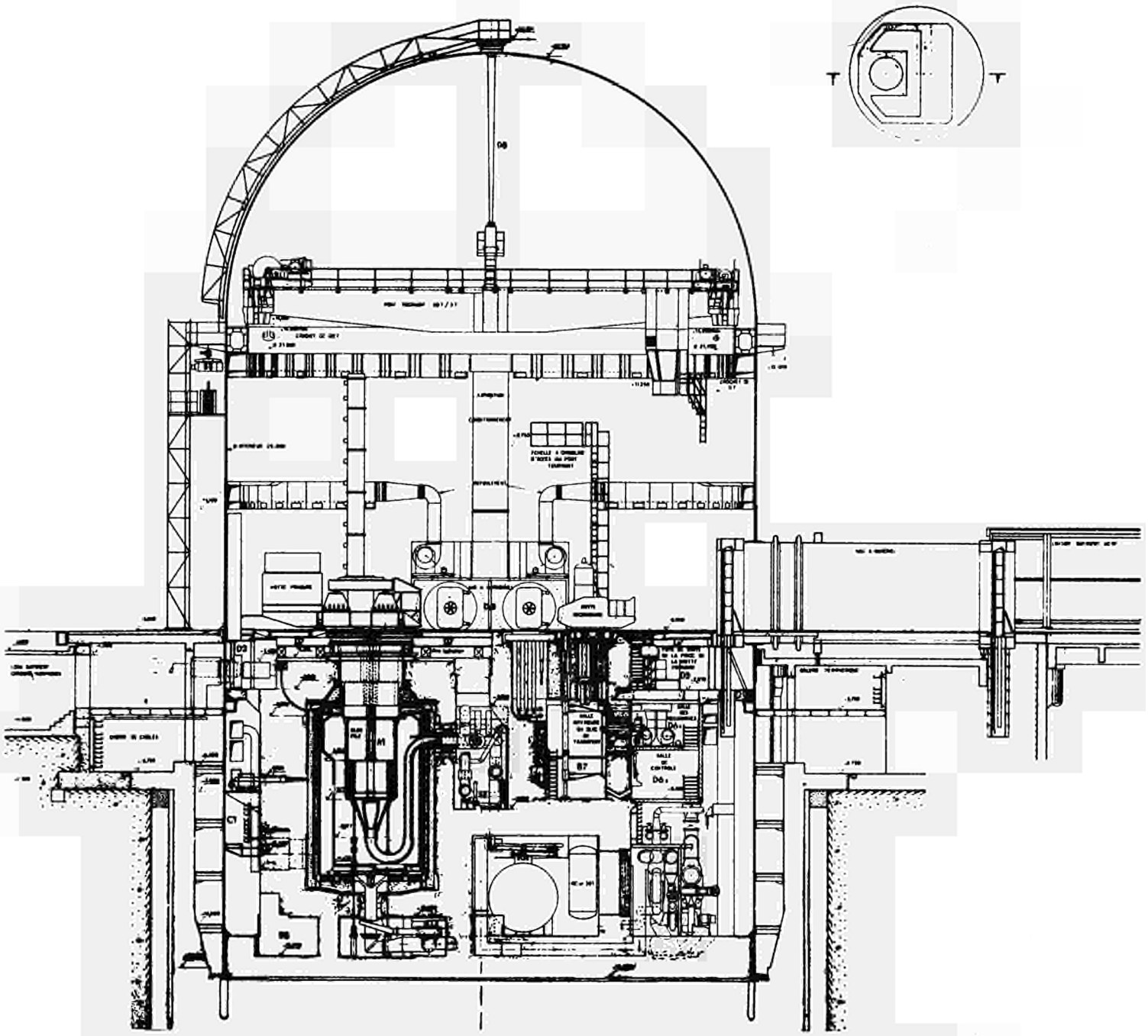

Annexe 3 : RAPSODIE - UNE COUPE DE L'ENSEMBLE DU REACTEUR

COUPE DE LA MAQUETTE

annexe 4

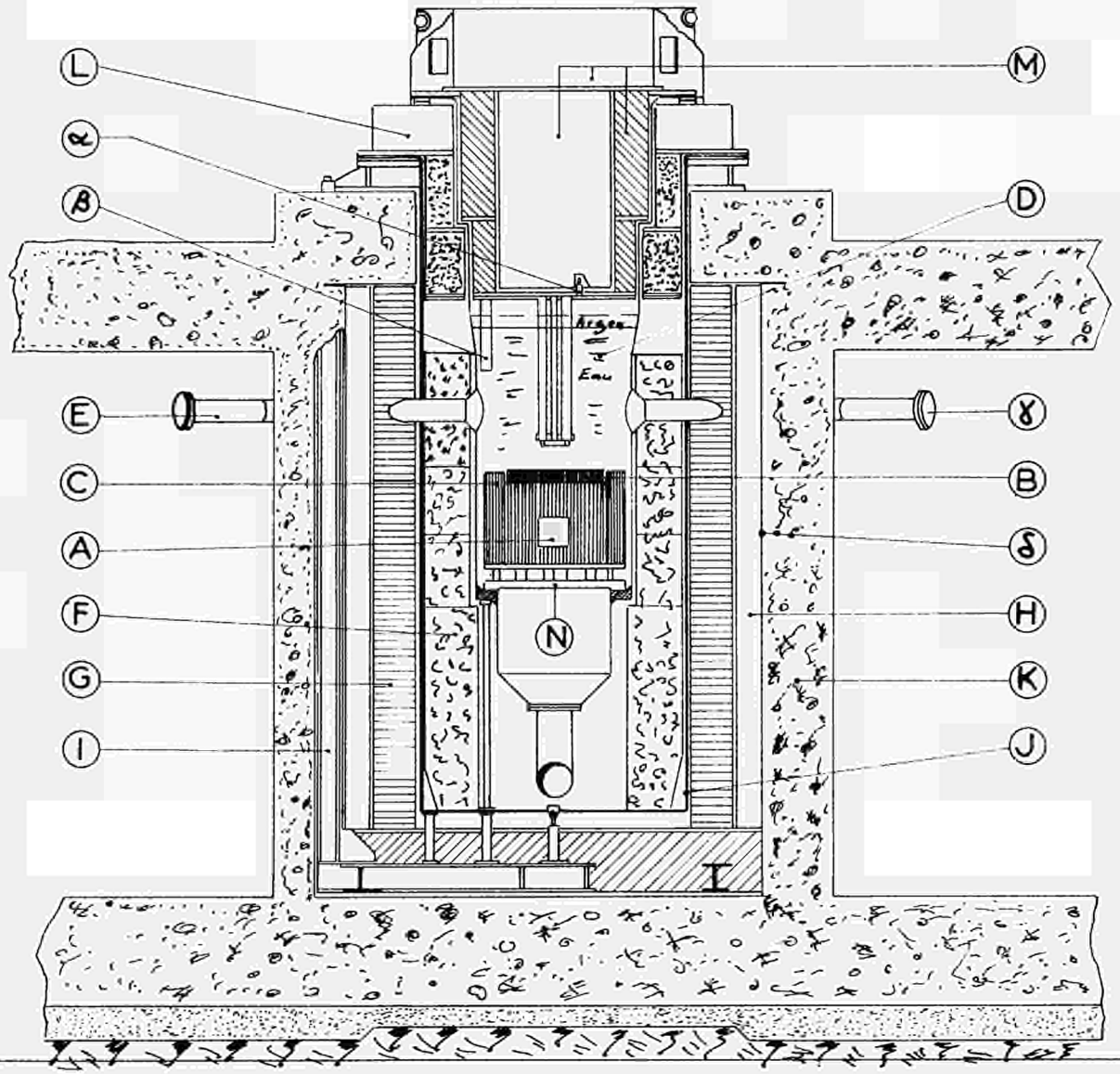

- (A) Charge d'explosif
- (B) Assemblages combustible et couverture
- (C) Virolas neutroniques
- (D) Cuve d'étanchéité
- (E) Sorties sodium
- (F) Caissons calorifuges
- (G) Graphite
- (H) Béton de vermiculite
- (I) Poteaux supports des bouchons
- (J) Cuve de sécurité
- (K) Béton armé
- (L) Bouchon fixe
- (M) Ensemble bouchon mobile
- (N) Sommier
- (α) Capteur dans la cuve au dessus du niveau de l'eau
- (β) Capteur dans la cuve au dessous du niveau de l'eau
- (γ) Capteur sur tuyauterie sodium
- (δ) Capteur sur béton

- Annexe 5 -

MAQUETTE 1.10

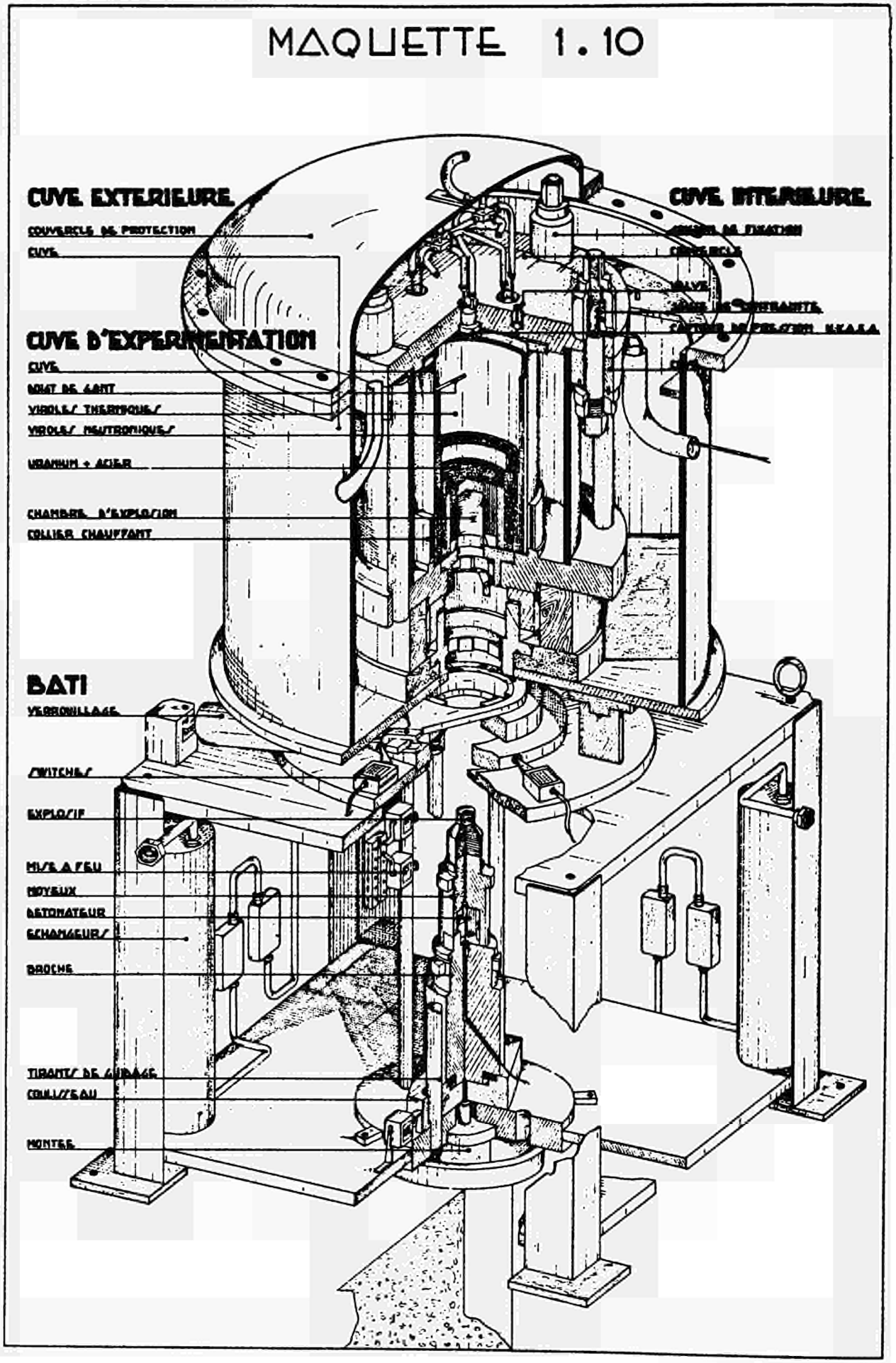

E X P E R I E N C E S S U R L A M A Q U E T T E D E R A P S O D I E A L ' E C H E L L E 3 / 1 0

Résultats généraux définitifs

Numéro de l'expérience	Date	Energie libérée maquette (10^6 cal)	Quantité d'explosif (Hexogène) (g)	Durée de l'explosion maquette (μs)	Conditions particulières de l'expérience	Hauteur de soulèvement du bouchon (cm)	Principales constatations sur les dommages
1	8 juin 1961	0,25	196		Assemblages hexagonaux sans uranium – bouchon 5 862 Kg	(1)	Cuve ouverte au niveau du coeur
2	29 juin 1961	0,25	196		Normales – bouchon 7 789 Kg	11	Pas de rupture mais déformation de la cuve
3	3 oct. 1961	1	784		Normales – bouchon 7 789 Kg	(2)	Cuve rompue en plusieurs points, sommier descendu de 21 mm
4	13 nov. 1961	0,25	196	30 ± 1	Pas de couverture d'argon, (l'eau arrive à 10 cm au-dessus du bas du bouchon – bouchon 7 789 Kg	20,7	Cuve ouverte en plusieurs points, sommier descendu de 2 mm
5	15 fév. 1962	1	784	23 ± 1	Normales – bouchon 7 760 Kg Dispositif de guidage en place	30	Cuve rompue en plusieurs points, notamment sous le bouchon fixe, sommier descendu de 16 mm – quelques caissons déformés près des sorties sodium
6	22 mars 1962	2,25	1 764	23 ± 2	Normales – comme n° 5	38	Cuve séparée en 4 parties, sommier descendu de 83 mm, caissons défoncés et crevés, cuve de sécurité déformée localement au niveau des sorties étanches. Quelques briques de graphite sont cassées.
7	16 nov. 1962	4	3 136	23 ± 2	Normales – comme n° 5	64,6	Cuve séparée en plusieurs parties, sommier descendu de 391 mm, caissons écrasés, cuve de sécurité ayant subi un allongement de 2 % au niveau de l'entrée du sodium, graphite endommagé, quelques briques de vermiculite détruites.
8	27 fév. 1963	2,25	1 764	23 ± 2	Bouchon maintenu par deux IPN de 400 mm		Cuve séparée en plusieurs parties, sommier descendu de 77 mm, cuve de sécurité légèrement déformée, graphite intact.
9	20 juin 1963		Perchlorate Alu	193 μs	Normales	13,6	Cuve séparée au niveau sommier
* 10	12 juil. 1963	1	784	23 ± 1	Bouchon 6 662 Kg bouchon de contrôle simulé absence de caissons	28,2	Cuve rompue en plusieurs points
* 11	21 août 1963	2,25	1 764	23 ± 1	Bouchon 6 662 Kg bouchon de contrôle simulé absence de caissons	31,2	Dégâts très importants dans la partie basse de la cuve

(1) Quelques centimètres, valeur exacte non mesurée

(2) Valeur un peu supérieure à 27 cm mais non connue exactement

* Participation de l'U. K. A. E. A. aux expériences n° 10 et n° 11

- Annexe 7 -

EFFETS SUR LES BOUCHONS MOBILES

toutes les grandeurs sont données à l'échelle de la pile

n° de l'expérience	Energie W 10^8 joules	Hauteur H m	Energie E 10^6 joules	Impulsion I 10^5 N . s	Durée impulsion ms (1)	Force F 10^6 Kg	Pression P Kg/cm^2	I/S N.s/cm^2	R 0/0
2	0,39	1,9	1,3	4,23				8	3,3
3	1,55	non mesurée avec précision							
4	0,39	3,6	2,4	5,8				11	6,3
5	1,55	5,2	3,5	7	16	4,4	85	13,5	2,3
6	3,5	6,65	4,5	7,9	16 à 33	2,5 à 5	48 à 96	15	1,3
7	6,2	11,2	7,6	10	20 à 33	3 à 5	58 à 96	19	1,2
8	3,5			3,6	30	1,3	25	7	
9	1,55 lente	2,35	1,6	4,7	16	2,95	57	9	1,03
10	1,55 sans caisson	4,9	3,3	6,8	de 18 à 27 25 ms	2,7	52	13	2,13
11	3,5 sans caisson	5,4	3,7	7,2					1,06

(1) On a indiqué le cas échéant deux chiffres qui correspondent aux évaluations extrêmes déduites des mesures. Les forces et pressions ont été alors calculées à partir de ces chiffres.

Notations

W = énergie de l'explosif
E = énergie correspondant au soulèvement des bouchons
H = hauteur atteinte par les bouchons supposés solidaires
I = impulsion sur les bouchons
F = force totale moyenne pendant l'impulsion
P = pression moyenne
I/S = impulsion moyenne par unité de surface
R = rendement mécanique de l'explosion $\frac{100\ E}{W}$

EFFETS SUR LE BOUCHON FIXE

- Annexe 8 -

N° de l'expérience	Energie W 10^8 joules	Impulsion I 10^5 N.s	Durée Impulsion ms(1)	Force F 10^5 Kg	Pression P Kg/cm^2	I/S N.s/cm^2
3	1,55	0,33				0,5
4	0,39	pas de mesures valables				
5	1,55	0,5	27	1,85	2,6	0,7
6	3,5	1,75	37 à 50	3,5 à 4,7	5 à 6,7	2,5
7	6,2	6,3	47 à 50	12,6 à 13,5	18 à 19,4	9
8	3,5	4,25	50	8,5	12	6,1
9	1,55	0,4	21	1,9	2,7	0,6
10	1,55	0,65	15	4,1	6	0,95
11	3,5	3,6	41	8,8	12,4	5,2

(1) Toutes les grandeurs sont données à l'échelle de la pile

(2) On a indiqué le cas échéant deux chiffres qui correspondent aux évaluations extrêmes déduites des mesures. Les forces et pressions ont été alors calculées à partir de ces chiffres

Notations

W = énergie de l'explosif

I = impulsion sur le bouchon fixe

F = force totale moyenne sur le bouchon fixe pendant l'impulsion

P = pression moyenne

I/S = impulsion moyenne par unité de surface

Réfrigérant	Q	T_o	P pic moyen de pression	I impulsion	Λ	Π = Pression d'impact calculée	F force maximum mesurée CEA	F force maximum mesurée UKAEA
eau	15 g	20°	290 Kg/cm^2	33 Kg.ms/cm^2	41	335 Kg/cm^2 τ= 2,30 ms	41 . 10^3 Kg	46 . 10^3 Kg
	30 g	20°	480	48	51	630 τ= 1,22 ms	50 . 10^3	79 . 10^3 Kg
		90°	480					
	60 g	20°	920	78	61	940 τ= 0,81 ms	49	74
sodium	15 g	150°	545	54	41	630 τ= 1,83 ms	55	75
		400°	460	47			72	76
	30 g	150°	830	52	51	1 150 τ= 1,00 ms	74	91
		250°	770	52			56	86
		400°	890	49			70	84
		550°	non mesuré				98	97
	60 g	150°	1 230	60	61	1 500 τ= 0,81 ms	85	132
		400°	1 340	88			70	114

La précision de ces mesures est d'environ 15 % à 20 %.

LEGENDES

Q quantité d'explosif en g

T_o température initiale du réfrigérant en ° C

P pic de pression moyenne sur le couvercle en Kg/cm^2

I impulsion de pression sur le couvercle en Kg.ms/cm^2

Λ formule empirique proposée pour détermniner I

Π pression d'impact en Kg/cm^2

τ temps de transit mis par le réfrigérant pour parcourir 5 cm en ms

F force mesurée sur le couvercle en Kg

NOTICE TO THE READER

All Euratom reports are announced, as and when they are issued, in the monthly periodical **EURATOM INFORMATION,** edited by the Centre for Information and Documentation (CID). For subscription (1 year: US$15, £6.5) or free specimen copies please write to:

Handelsblatt GmbH
« Euratom Information »
Postfach 1102
D.4 Dusseldorf (Germany)

or

Office central de vente des publications
des Communautés européennes
2, Place de Metz
Luxembourg

All Euratom reports are on sale at the offices listed below (when ordering, specify clearly the EUR number and the title of the report, which are shown on the internal title page).

OFFICE CENTRAL DE VENTE DES PUBLICATIONS DES COMMUNAUTÉS EUROPÉENNES

2, place de Metz, Luxembourg (Compte chèque postal N° 191-90)

BELGIQUE — BELGIË
MONITEUR BELGE
40-42, rue de Louvain - Bruxelles
BELGISCH STAATSBLAD
Leuvenseweg 40-42 - Brussel

DEUTSCHLAND
BUNDESANZEIGER
Postfach - Köln 1

FRANCE
SERVICE DE VENTE EN FRANCE DES PUBLICATIONS DES COMMUNAUTÉS EUROPÉENNES
26, rue Desaix - Paris 15e

ITALIA
LIBRERIA DELLO STATO
Piazza G. Verdi, 10 - Roma

LUXEMBOURG
OFFICE CENTRAL DE VENTE DES PUBLICATIONS DES COMMUNAUTÉS EUROPÉENNES
9, rue Goethe - Luxembourg

NEDERLAND
STAATSDRUKKERIJ
Christoffel Plantijnstraat - Den Haag

UNITED KINGDOM
H.M. STATIONERY OFFICE
P.O. Box 569 - London S.E.I.

FB 500,—	DM 40,—	FF 50,—	Lit. 6.240	Fl. 36,—	$ 10,—